Cumhuriyet Science Journal   Vol: 46   No:1   Year 2025

Cumhuriyet Science Journal

Cumhuriyet Science Journal (CSJ) is an official publication of Sivas Cumhuriyet University, Science Faculty. The high quality research papers related to the natural sciences are published as online four times a year. CSJ is an open access, free of charge journal and all articles in CSJ have undergone peer review and upon acceptance are immediately and permanently free for everyone to read and download.

Cumhuriyet Science Journal (CSJ)

Abstracted&Indexeding

ULAKBİM TR-Dizin   Clarivate Analytics   Crossref   WorldCat   Arastirmax Bilimsel Yayın Indeksi

Bielefeld Academic Search Engine (BASE)   Google Scholar   Research Gate   Idealonline

CONTENTS

Cumhuriyet Science Journal

Investigation of Antioxidant Effect of Origanum Hypericifolium Extracts in Different Solvents

Muhammed Sufi [1,a], Ceylan Hepokur [1,b,*], Mehmet Çiçek [2,c]

[1] Department of Biochemistry, Faculty of Pharmacy, Sivas Cumhuriyet University, Sivas, Türkiye

[2] Department of Molecular Biology and Genetics, Faculty of Science and Arts, Pamukkale University, Denizli, Türkiye

*Corresponding author

Research Article

ABSTRACT

Origanum hypericifolium is one of the most widely distributed endemic species of the family Lamiaceae. Origanium hypericifolium contains mostly monoterpenes. Monoterpenes are volatile compounds with 10 carbons and are widely found in the plant kingdom. Monoterpenes, which are used as fragrances in perfumes and foodstuffs, have anti-fungal, anti-bacterial, anti-oxidant and anti-cancer effects. Various in vitro assays can be used to determine the antioxidant activity of *Origanium hypericifolium* extracts. In our study, total polyphenolic, total flavonoid content, iron reducing power, cupric ion reducing capacity and radical scavenging activity were evaluated to the antioxidant properties of various extracts of Origanum hypericifolium. TAS and TOS levels were also analyzed. The highest DPPH radical scavenging acitiviy value was 3.09±0.01 µg/mL in ethanol extract, Total polyphenol 144.00±1.89 µg GAE /g in ethanol extract, Total polyphenol 17. 08±0.85 µg CE /g in ethanol extract, FRAP 942.46±1.89 µg TE /g ethyl acetate and CUPRAC 2.54±0.01 mmol TE/g ethyl acetate extract.

Keywords: Antioxidants, Free radicals, Origanum hypericifolium.

a 🔗soufi1990ha@gmail.com   🆔 https://orcid.org/0009-0006-2626-310X   b🔗cozsoya@gmail.com   🆔 https://orcid.org/0000-0001-6397-1291
c 🔗mcicek@pau.edu.tr   🆔 htpps://orcid.org/0000-0003-4058-3717

Introduction

Nowadays, studies on treatment methods with herbal medicines are increasing due to their low cost and easy availability. It is known that components isolated from plants are still being used in some types of cancer. For this reason, the search for new and effective herbal components continues.

Our country has a remarkably rich flora in terms of plant diversity. This richness is due to the fact that it is located at the intersection of three phytogeographic regions, it is a bridge between the flora of Southern Europe and South West Asia, and the centers of origin of many genera and sections are located in Anatolia. The flora of our country has a rich composition with 12.301 taxa. Of these taxa, 3963 are endemic and constitute 32.2% of our flora. In this respect, the possible pharmacological effects of many endemic species remain to be investigated. Origanum L. is a genus of the Lamiaceae family and includes 21 endemic species in Turkey, including Origanum hypericifolium O. Schwartz & P.H. Davis [1-3]. Members of this family are distributed mainly in the Mediterranean basin countries, but also in Australia, South West Asia and South America. Origanium hypericifolium includes the monoterpenes such as carvacrol, thymol and terpenes.

Members of the Lamiaceae family constitute a part of useful plants since ancient times. There are old records that the plants in this family are used in the treatment of various diseases [4-6]. O. hypericifolium, which is also found in Denizli region, is an endemic plant. It is a perennial O. hypericifolium, semi-shrub form, 30-105 cm tall and hairy. The leaves are petiolate, acute, greenish scaly, with black punctate glandular hairs [3]. O. hypericifolium is used as an herbal tea in the treatment of diabetes, as well as powdered and added as a spice to cheese and dishes [7]. The essential oil of the plant contains monoterpenes such as basic cymene, carvacrol, thymol and γ-terpinene [8,9]. Flavonoids, triterpenoids and monoterpenes are mostly distributed in the aerial parts of plants, especially in flowers and leaves, while phenolic acids and diterpenoids are mainly found in roots [10].

The purpose of the present work was to evaluate the antioxidant capacity of the extracts of Origanum hypericifolium, an Endemic herb, obtained in various solutions.

Methods

Preparation of Origanum Hypericifolium (EOH) Extracts in Different Solvents

C2 Muğla; Köyceğiz, Sandras Mountain, 1410 m, clearings of Pinus nigra (black pine forest), 16.09.2017, collected by M. Çiçek 2017-7-1 (Herb. M. Çiçek). While 55 g of Origanum hypericifolium was weighted, 1000 mL solvent was added to each one separately (Ethanol, ethyl acetate and n-hexane) and was sonicated at 45°C, 150 rpm

for 45 min. This process was repeated twice. The obtained samples were evaporated and the extracts were kept at -20oC until the experimental period [11].

Origanum Hypericifolium HPLC Analyses

Samples were eluted through 0.20 μm filters on a Perkin Elmer high pressure liquid chromatography (HPLC) and were analyzed on a Brownlee Analytical C18 (4.6 x 250mm, 5μm) colon (Perkin Elmer) with a DAD detector (Diode-Array Detector; Perkin Elmer Model Flexar, USA). Solvent A (orthophosphoric acid) and Solvent B (acetonitrile) were used. Samples were eluted from the column with a gradient of acetonitrile in 100%-57% water at 25 ºC and a flow rate of 0.8 mL/min (0-10 min 100% A, 8 min 100%-91% A, 10 min 91%-87% A, 8 min 87%-67% A, 14 min 67%-57% A) [12].

Determination of DPPH Radical Scavenging Activity

The method is based on the loss of the initial purple-violet colour of the DPPH (2,2-diphenyl-1-picrylhydrazyl] solution as a result of electron exchange with a hydrogen atom donating substance (antioxidant). 4 mg DPPH is dissolved in 10mL methanol. Thus, 100mL DPPH solution of 1 mM is prepared. The sample was mix with DPPH-radical (1:1) and was incubated in the dark for 50 min. At the end of the incubation period, absorbance is read at 517 nm (yellow colored reduced form). In this method, the change in absorbance of DPPH reacted with different sample concentrations is measured and the absorbance graph corresponding to the concentration is drawn. In the slope equation y=ax+b obtained from the graph, the amount of sample that halves the DPPH concentration is determined in μg/mL and expressed as the effective concentration 50 (IC50) value. The amount of antioxidant used to reduce the initial DPPH concentration by 50% is expressed as IC50 value [13,14].

Total Phenolic Substance Analysis

Total phenolic matter was analyzed by Folin-Ciocalteu assay. The method is based on the reduction of phosphotungstic acid. Folin-Ciocalteu reagent (10%) was added to samples diluted to different concentrations. This mixture was mixed with saturated sodium carbonate solution. The mixture was incubated in the dark for 30 min and then measured at 700 nm in a spectrophotometer. Total phenolic matter was expressed as gallic acid equiv (GAE) using the gallic acid calibration line [15].

Total Flavonoid Analysis

Total flavonoid content analysis performed according to Chang et al. The method is essentially the complexation of $AlCl_3$ by flavones. Samples were incubated with 80% ethanol, 10% $Al(NO_3)_3$ solution and 1 M KCH_3COO solution for 40 minutes at shade and absorbance was detected by spectrophotometer at 415 nm. Quercetin was used as standard [16,17].

Determination of FRAP Antioxidant Power

FRAP [Iron (III) reduction anti-oxidant capacity] determination was carried out according to the method developed by Benzie and Strain. According to this method, the main FRAP reagent, Phosphate Buffer and $FeCl_3$ solutions were mixed with the sample, incubated for 20 minutes in the shade and the absorbance was determined at 700 nm (Trolox was used as standard) [18].

Total Antioxidant Capacity Method Using Cu (II) as Oxidant (CUPRAC)

Cuprac ion reduction antioxidant capacity was determined according to the method of Arkan,T. CuCl2, neocuproin solutions were added to the sample and stored in the shade for 30 min and then the absorbance was measured at 450 nm in a UV-VIS [19].

Total Antioxidant Status (TAS) Assay

TAS was measured using Rel Assay, a novel assay method invented by Erel. In this technique, a hydroxyl radical is formed. This technique can be used to measure the anti-oxidative activity of the sample in response to strong free radical reactions initiated by the generated hydroxyl radical. The test has excellent sensitivity values of > 97% [20].

A2-A1=ΔA After taking the difference between absorbances, it is calculated according to equation 1 below.

$$x = \frac{\Delta A(sample)}{\Delta A(standart)} x20 \tag{1}$$

Total Oxidant Status (TOS)

TOS determination was performed according to the method developed by Erel. In this method, R1 reagent (prepared by dissolving xylenol orange and NaCl in H_2SO_4 (pH=1.75) and adding glycerol), R2 reagent (prepared by dissolving ferrous ammonium sulphate hexahydrate and o-dianisidine dihydrochloride in H_2SO_4) were used. R1 and R2 reagents were added to the sample and incubated for 5 minutes at room temperature and the absorbance was measured at 530 nm [21].

A2-A1=ΔA   After taking the difference between absorbances, it is calculated according to Equation 1.

Statistical Analysis

The analyses were conducted using SPSS version 22.0 (SPSS, Chicago, IL, USA). Measurement data are presented as mean ± standard deviation (SD). Statistical analyses involving multiple groups were conducted using either one-way ANOVA or the Kruskal-Wallis test. The mean IC50 values were calculated, and the averages were graphed using SigmaPlot version 12.0. A p-value of less than 0.05 was considered statistically significant.

Results

Since the antioxidant properties of Origanum Hypericifolium ethanol extract were found to be better, the content analysis was performed by HPLC. The chromatogram obtained is given as supplementary data 1 and the content is expressed in Table 1.

Table 1. Origanum Hypericifolium ethanol extracts of HPLC analysis

Sample No	Standart Name	Retion time	mg /g plant
1	Naringenin	14,6	90,4626
2	Rosmarinic asit	17,1	287,3615
3	Carvacrol	30	141,0442
4	Thymol	32,4	173,4577
5	Caffeic acid	33	204,5225
6	Coumaric acid	33,8	696,1726
7	Myricetin	34,7	539,198

As a result of HPLC analysis, the main components of carvacrol, thymol, caffeic acid, coumaric acid and myricetin were found abundantly in the ethanol extract (Supplementary 1).

DPPH radical is used to determine the free radical scavenging activity of natural antioxidants. The free radical scavenging effects of *Origanum Hypericifolium* extracts of different solvents were determined by DPPH radical. DPPH solution is purple in colour. When the antioxidant interacts with a compound, its structure changes and forms a yellow colour and a new compound is formed. The rate of colour change is proportional to the concentration of the antioxidant. The concentration (C)-% inhibition graphs of the DPPH free radical scavenging activities of Origanum Hypericifolium extracts and ascorbic acid in the study are shown in Figure (1).

a.Ethanol solvent

b. Ethyl acetate solvent

c. n- hexane solvent
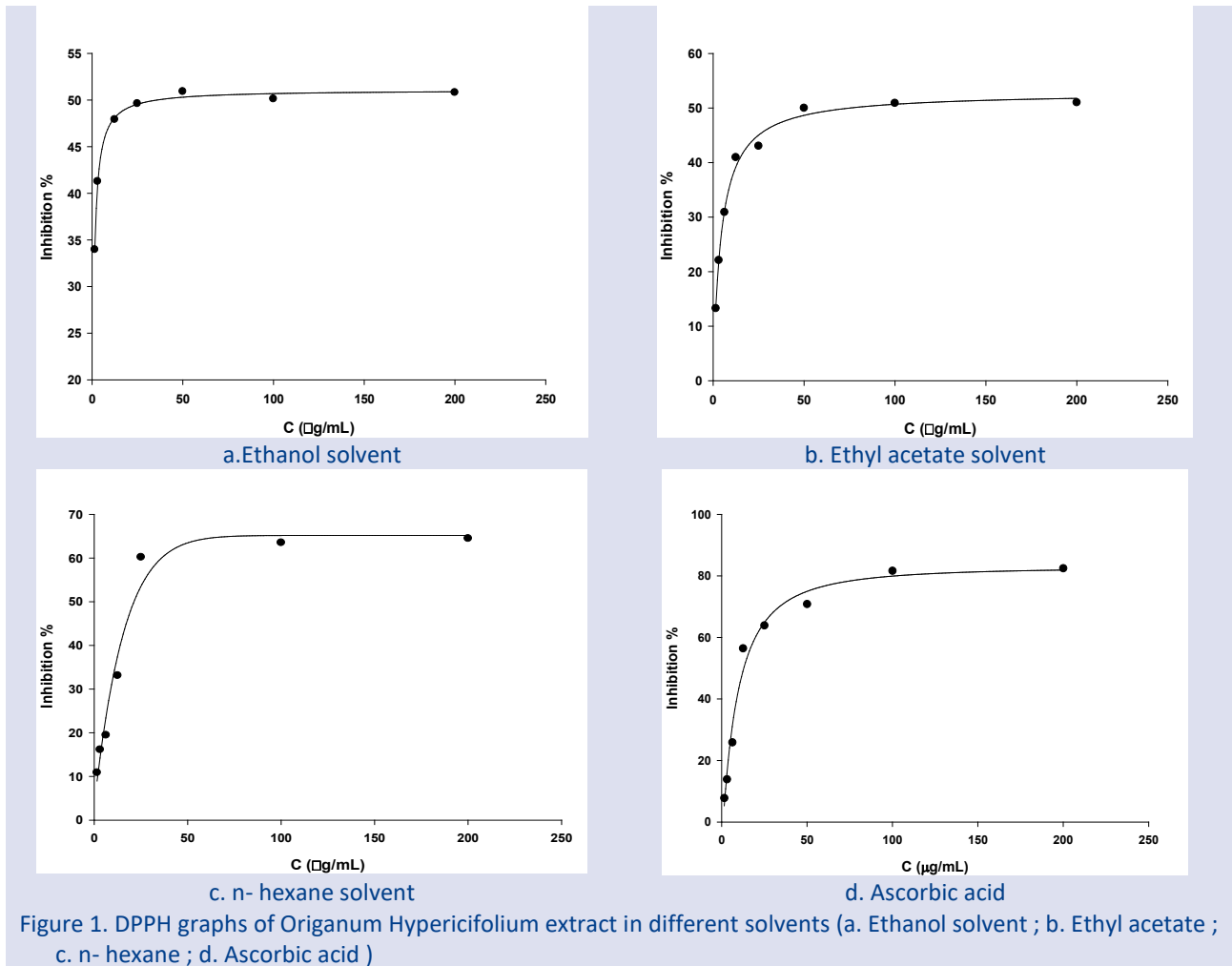
d. Ascorbic acid

Figure 1. DPPH graphs of Origanum Hypericifolium extract in different solvents (a. Ethanol solvent ; b. Ethyl acetate ; c. n- hexane ; d. Ascorbic acid)

The results of DPPH radical scavenging activity of *Origanum Hypericifolium* ethanol, ethyl acetate and n-hexane extracts are shown in Table 2.

Table 2. DPPH IC$_{50}$ values

IC$_{50}$	Ethanol	Ethyl Acetate	n-Hexane	Ascorbic Acid
(µg/mL)	3.09±0.01	13.71±0.54	14.70±0.98	11.07±0.75

Total phenolic matter of the Origanum Hypericifolium was determined as gallic acid eq. Gallic acid was used as standard. Gallic acid calibration graph was found as $y=0.0370+0.0006x$ ($R^2=0.9993$).

The results of the total phenolic content of *Origanum Hypericifolium* ethanol, ethyl acetate and n-hexane extracts are shown in Table 3.

Table 3. Total Phenolic Substances

(µg GAE /g)	Ethanol	Ethyl Acetate	n-Hexane
	144.00±1.89	138.94±1.78	30.50±1.08

Total flavonoid content of the extracts of Origanum hypericifolium in different solvents was calculated as quercetin equivalent. Quercetin was used as standard. The equation y=0.0433+0.0648x (R2=0.9999) was found from the quercetin standard graph.

The results of total flavonoid content of Origanum Hypericifolium ethanol, ethyl acetate and n-hexane extracts are shown in Table 4.

Table 4. Flavonoid values

(µg CE /g)	Ethanol	Ethyl Acetate	n-Hexane
	17.08±0.85	15.69±0.66	7.09±0.47

The amount of FRAP antioxidant power was calculated as trolox equivalent. Trolox was used as the standard. The standard graph of trolox was found as y=0.1511+0.0005x (R2=0.8772).

The results of FRAP antioxidant power of Origanum Hypericifolium ethanol, ethyl acetate and n-hexane extracts are shown in Table 5.

Table 5. FRAP values

(µg TE/g)	Ethanol	Ethyl Acetate	n-Hexane
	683.11±1.76	942.46±1.89	200.46±1.01

Calculation of total antioxidant capacity value equivalent to trolox in solid samples is done by using Equation 2 given below. When the total antioxidant capacity value is to be calculated as the equivalent of a different antioxidant, the molar absorption coefficient of the relevant antioxidant compound should be used in the formula.

$$TAC(mmol \frac{TR}{g} - sample = \frac{A}{\epsilon} \times \frac{Vt}{Vs} \times DF \times \frac{Ve}{m} \qquad (2)$$

A: Absorbance, Ɛ: Molar absorption coefficient (16700 L mol-1.cm-1),Vt: Total volüme, Vs: Sample volüme, DF: Dilution factor ,Ve: Volume of prepared extract, m: Weight of sample in the extraction process (g)

Cu (II) results of *Origanum Hypericifolium* ethanol, ethyl acetate and n-hexane extracts as oxidant are shown in Table 6.

Table 6. CUPRAC values

(mmol TE/g)	Ethanol	Ethyl Acetate	n-Hexane
	1.64±0,09	2.54±0.01	1.35±0.06

Total antioxidant status and Total oxidant status results of *Origanum Hypericifolium* ethanol, ethyl acetate and n-hexane extracts are shown in Figure 2.
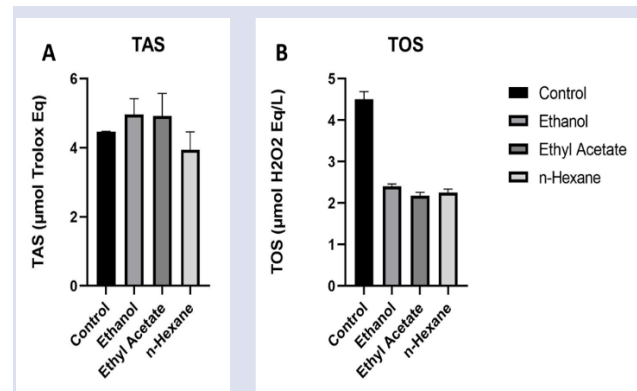
Figure 2. Total antioxidant status (A) and Total oxidant status (B) results of *Origanum Hypericifolium* Extracts

Table 7. The Antioxidant Values of Origanum hypericifolium Extracts in Various Solvents

	Ethanol	Ethyl Acetate	n-Hexane	Ascorbic acid	Control	p-value
DPPH (µg/mL)	3.09±0.01	13.71±0.54	14.70±0.98	11.07±0.75	-	p<0.0000
Polifenol (µg GAE /g)	144.00±1.89	138.94±1.78	30.50±1.08	-	-	p<0.0000
Flavonoid(µg CE /g)	17.08±0.85	15.69±0.66	7.09±0.47	-	-	p<0.0000
FRAP (µg TE /g)	683.11±1.76	942.46±1.89	200.46±1.01	-	-	p<0.0000
CUPRAC (mmolTE/g)	1.64±0,09	2.54±0.01	1.35±0.06	-	-	p<0.0000
TAS (µmol Trolox Eq)	5.25±0.19	5.15±0.21	3.99±0.13	-	4.22±0.02	0.0000152
TOS(µmol H_2O_2 Eq/L)	2.35±0.01	2.13±0.06	2.28±0.07	-	4.58±0.34	0.000000380

* In statistical analysis, a p-value of less than 0.05 is considered significant.

Dissucions

Medicinal plants have been used since ancient times for the treatment of many diseases. Today, at least 132 different active substances derived from these plants are currently in use and recognized as important medicines [22]. In this context, new medicinal plants are continuously researched and contribute to the literature and new treatments.

There are some literature studies investigating the anatomical, morphological, cytotaxonomic, palynological, biosystematic, chorological and chemical characteristics of Origanum genera in Turkey [23]. Origanium hypericifolium essential oil contains monoterpenes such as p-cymene, carvacrol, thymol and γ-terpenes. In our content analysis (by HPLC), carvacrol, thymol, caffeic acid, coumaric acid and myricetin were abundant in the ethanol

extract of Origanium hypericifolium. Carvacrol and thymol are monoterpenes; while caffeic acid is a phenolic group; coumaric acid and myricetin are in the polyphenol group. Monoterpenes have antifungal, antibacterial, antioxidant, anticancer, antispasmodic, hypotensive and vasorelaxant effects [8,9].

Antioxidant is the general name for a group of compounds that stop oxidation reactions caused by free radicals. These compounds neutralize free radicals, preventing the body from being affected by them and allowing it to regenerate itself. Determination of the total amount of phenolic substances in foods is important in terms of giving an idea about the hydroxyl groups that provide antioxidant activity. Generally, there is a good linear correlation between total phenol content and antioxidant activity. Various in vitro assays can be used to determine the antioxidant activity of natural product extracts [24]. Oxygen Radical Absorbance Capacity (ORAC) Method, Total Radical Scavenger Parameter (TRAP) Method, Crocin Whitening Method, Total Oxyradical Quenching Capacity (TOSC) Method, Trolox Equivalent Antioxidant Capacity (TEAC or ABTS) Method, DPPH Radical Scavenging Capacity Method, CUPRAC Method, Iron (III) Ion Reducing Antioxidant Power (FRAP) Method, Folin-Ciocalteu Reagent (FCR) and Total Phenolic Method [25]. In our study, total polyphenolic, total flavonoid content, iron reducing power, cupric ion reducing capacity and radical scavenging activity were evaluated to the antioxidant properties of various extracts of Origanum hypericifolium. TAS and TOS levels were also analyzed.

In our study, the DPPH radical sacvenging activity of Origanum Hypericifolium ethanol extract was the strongest. The IC50 value of DPPH radical was 3.09±0.01μg/ml for ethanol, 13.71±0.54 for ethyl acetate, 14.70±0.98 for n-hexane and 11.07±0.75μg/ml for ascorbic acid as standard. The IC50 value of DPPH radical of Origanum Hypericifolium essential oil collected from the dry limestone slopes of Korkuteli district, Antalya was determined as 4.88 mg/ml. Hossain, M. et al. found the IC50 value of DPPH radical in Methanol extracts of Origanum species to be 20.10 μg/g [26]. Sökmen M. et al. determined the IC50 values of DPPH radical in methanol, dichloromethane (DCM) extracts of Origanum species as 18.0 ± 2.0, 49.5 ± 3.5 μg /mg, respectively [27]. Roby, M. et al. reported that the IC50 values of DPPH radical in methanol, ethanol, diethyl ether, hexane extracts of Origanum species were 11.00±0.1, 13.00±0.1, 13.00±0.1, 13.00±0.2, 22.00±0.5 mg GAE/g, respectively [28].

In our study, the total polyphenol content of ethanol extract of Origanum Hypericifolium was 144.00±1.89, ethyl acetate 138.94±1.78, 30.50±1.08 n-hexane μg GAE / g. Celik A. et al. reported 1.2480±0.03 mmol GAE/L total polyphenolic content in Origanum Hypericifolium essential oil collected from Sandras mountain [29]. Fakir H. et al. reported 104.928±2.389 mg GAE/g total polyphenolic content in Origanum Hypericifolium essential oil collected from Denizli Honaz Mountain [30]. Sökmen M. et al. found total polyphenolic content as 151.5± 12.0, 154.0 ± 9.6 and 1.9 ± 0.4 μg /mg in methanol,

dichloromethane and hexane extracts of Origanum species, respectively [27]. Roby et al. reported 24.66±3.90, 14.80±200, 10.30±2.08, 4.21±2.65 mg GAE/g of total polyphenolic content in methanol, ethanol, diethyl ether, hexane extracts of Origanum species [28]. Cervato, G. et al. found total polyphenolic content of 5±0.1 μg GAE /g in methanol extracts of Organum vulgare [31]. Hossain, M. et al. determined total polyphenolic content of 11.87 μg/g in Methanol extracts of Origanum species [26].

Our study, amount of total flavonoid of extracts was 17.08±0.85, 15.69±0.66 and 7.09±0.47 μg CE/g in ethanol, ethyl acetate and n-hexane, respectively. In a study by Özkan, G. et al. total flavonoid content in hexane and ethyl acetate extracts were 716.86±1.17 / 1291.69±1.67 μg CE/g, respectively [32]. In the study by Kaurinovic, B. et al. on different species of Origanum, the total flavonoid content in the extracts prepared in ethyl acetate and chloroform solvents was found to be 9.37 ± 0.06 / 13.12 ± 0.05 mg / g, respectively [33].

In our study, iron reducing power determination was 683.11±1.76, 942.46±1.89 and 200.46±1.01 μg TE /g in ethanol, ethyl acetate and n-hexane, respectively. According to the study conducted by Baddal, M. et al. iron reducing power determinations in hexane, dichloromethane, chloroform, acetone, methanol extracts were 0.117 ± 0.010, 1.237 ± 0.033, 0.343 ± 0.008, 1.272 ± 0.001, 1.583 ± 0.110 mg CE/mg respectively [34]. Sarikurkcu, C. et al. found iron reducing power 17.18 ± 0.27 mg /g [35].

In our study, CUPRAC ion reduction capacity was 1.64±0.09, ethyl acetate 2.54±0.01, n-hexane 1.35±0.06 mmol TE/g for ethanol. In a study by Yılmaz, H. et al. the CUPRAC ion reducing capacity of ethanol extracts was found to be 0.9 mmol /g [36]. According to another study by Sarikurkcu, C. et al. the CUPRAC ion reducing capacity was found to be 46.64 ± 0.37 mg /g [35].

The total antioxidant capacity of Origanum Hypericifolium was studied and 4.96±0.46, 4.92±0.65, 4.94±0.72 mmol TE/L for ethanol, ethyl acetate, n-hexane were found. Celik A. et al. reported a total antioxidant content of 1.5358±0.06 mmol GAE/L in Origanum Hypericifolium essential oil collected from Sandras mountain [29]. Fakir H. et al. found the total antioxidant content of Origanum Hypericifolium essential oil collected from Denizli Honaz Mountain as 9.979±0.309 mg GAE/g [30].

According to the results of the total oxidant capacity of Origanum Hypericifolium extract obtained in different solvents, it was found as 2.40±0.06, 2.18±0.08, 2.25±0.09 μmol H_2O_2 / L for ethanol, ethyl acetate, n-hexane. According to the study of Celik A. et al. total oxidant capacity was found as 95±2 μmol H_2O_2 / L [29].

When the literature is examined, it is observed that the results of total polyphenol, flavonoid, iron reducing power (FRAP), radical scavenging activity (DPPH), CUPRAC, TAS and TOS analyzes are compatible with the literature in our study with different extracts of Origanum

Hypericifolium. Further studies are needed to determine the effects of Origanum Hypericifolium.

Conclusions

About 50% of medicines used for therapeutic purposes are herbal. Although plants have many active molecules, there are many factors in secondary metabolites whose effectiveness has not yet been elucidated. Thus, due to the need for effective bioactive agents, research on phytochemical and bioactivity properties of plants based on ethnobotanical approach has gained momentum [37]. Although metabolites in plant products are generally of low risk, some pure compounds may be toxic. Therefore, in vitro and in vivo screening tests of herbal products are important to demonstrate their toxic effects [38].

In conclusion, Origanum Hypericifolium was observed to have high antioxidant properties. Clarification and characterization of the compounds active in herbs and a greater understanding of the respective preservative mechanisms are essential for their possible use in pharmaceuticals industry.

Conflicts of interests

No conflicts of interest have been declared by the authors.

References

[1] Başer K.H.C.,(2002). The Turkish Origanum Species, In:Oregano, The Genera Origanum and Lippia, Ed.: S.E.Kintzios, Taylor and Francis, UK.

[2] Başer K.H.C., Tümen G., Özek T. ve Kürkçüoğlu M., Composition of the Essential Oil of Origanum sipyleum of Turkish Origin, *Journal of Essential Oil Research*, 4(1) (1992)139-142.

[3] Davis P.H., (1982). Flora of Turkey and the East Aegean Islands, vol: 7. Edinburg University Press, Edinburgh.

[4] Baytop T. (1999). Türkiye'de bitkiler ile tedavi (Geçmişte ve Bugün). İstanbul Üniversitesi Yayınları, İstanbul, Türkiye, 520s.

[5] Baytop T., (1994).Türkçe Bitki Adları Sözlüğü, Atatürk Kültür, Dil ve Tarih Yüksek Kurumu, Türk Dil Kurumu Yayınları: 578, s.33, 206, Ankara.

[6] Kütükcü Z.M. (2016). Deneysel diyabetik dişi sıçan genital sisteminde Origanum Hypericifolium Esansiyel yağının etkilerinin ince yapı düzeyinde araştırılması (Master's thesis, Pamukkale Üniversitesi Sağlık Bilimleri Enstitüsü).

[7] Sonmez C., Effect of different harvest times on some yield and essential oil characteristics in Origanum onites L. *Turkish Journal Of Field Crops*, 24(1) (2019)106-110.

[8] Marino M., Bersani C., Comi G., Impedance measurements to study the antimicrobial activity of essential oils from Lamiaceae and Compositae. *International journal of food microbiology*, 67(3) (2001) 187-195.

[9] Özcan M, Erkmen O,, Antimicrobial activity of the essential oils of Turkish plant spices, *European Food Research and Technology,* 212(6) (2001) 658-660.

[10] Topçu G., Bioactive triterpenoids from Salvia species. *J Nat Prod,* 69 (2006) 482–487.

[11] Tutar U., Hepokur C., Misir S., Hepokur A.I., DUMAN F., Antimicrobial, Antioxidant, Cytotoxic and Wound Healing Effects of Thymbra sintenisii Extract. *Indian Journal of Pharmaceutical Sciences*, 80(5) (2018).

[12] Gök H. N., Luca S. V., Ay S.T., Komsta Ł., Salmas R. E., Orhan I. E.,Skalicka-Woźniak K., Profiling the annual change of the neurobiological and antioxidant effects of five Origanum species in correlation with their phytochemical composition. *Food Chemistry*, 368 (2022) 130775.

[13] Cuendet M., Potterat O., Salvi A., Testa B.,Hostettmann K., A stilbene and dihydrochalcones with radical scavenging activities from Loiseleuria procumbens. *Phytochemistry*, 54(8) (2000) 871-874.

[14] Berköz M., Yalın S., Normal ve preeklamptik gebelerde lipid peroksidasyonu ve antioksidan aktivite. *ADÜ Tıp Fakültesi Dergisi* 10 (2009) 52-58.

[15] Dinçer Y., Akçay T., DNA Hasarı. *Türk Biyokimya Dergisi*,25(2) (2000)73-79.

[16] Lima C.F., Fernandes-Ferreira M., Pereira-Wilson C. Phenolic compounds protect HepG2 cells from oxidative damage: Relevance of glutathione levels. *Life Sciences*, 79 (2006)2056-2068.

[17] Chang C.C., Yang M.H., Wen H.M., Chern J.C., Estimation of total flavonoid content in propolis by two complementary colorimetric methods. *J Food Drug Anal,* 10(3) (2002)178-82

[18] Yu L., Haley S., Perret J., Harris M., Wilson J., Qıan M., Free radical scavenging properties of wheat extracts. *J Agric Food Chem,* 50(6)(2002)1619-24.

[19] Arkan T. (2011). Daphne oleoides subsp. oleoides ve Daphne sericea'nın farklı çözücülerle antioksidan özellikleri (Doctoral dissertation, Selçuk Üniversitesi Fen Bilimleri Enstitüsü).

[20] Erel O., A novel automated direct measurement method fortotal antioxidant capacity using a new generation, morestable ABTS radical cation. *Clin Biochem,* 37(2004) 277–285.

[21] Erel O.,A new automated colorimetric method for measuring total oxidant status. *Clin Biochem,* 38 (2005)1103–1111

[22] Emine F., (2013). Isparta ve Afyon illerinde tıbbi ve aromatik amaçlı kullanılan bitkilerin satılma, toplanma ve kullanılma durumları. Doktora tezi, Ankara Üniversitesi Fen Bilimleri Enstitüsü.

[23] Azize T.,(2010). Türkiye'de yetişen Orıganum L. (Labıatae) cinsi üzerinde epidermal incelemeler. Yüksek lisans tezi. İnönü Üniversitesi Sağlık Bilimler Enstitüsü.

[24] Jin D., Mumper R.J., Plant phenolics: extraction, analysis and their antioxidant and anticancer properties. *Molecules,* 15(10) (2010)7313-52.

[25] Okan O. T., Varlıbaş H., Mehmet Ö.Z., Deniz İ., Antioksidan analiz yöntemleri ve doğu Karadeniz bölgesinde antioksidan kaynağı olarak kullanılabilecek odun dışı bazı bitkisel ürünler. Kastamonu Üniversitesi Orman Fakültesi Dergisi, 13(1) (2013) 48-59.

[26] Hossain M.B., Brunton N.P., Patras A., Tiwari B., O'donnell C.P., Martin-Diana A.B., Barry-Ryan C., Optimization of ultrasound assisted extraction of antioxidant compounds from marjoram (Origanum majorana L.) using response surface methodology. *Ultrasonics sonochemistry*, 19(3) (2012)582-590.

[27] Sökmen M., Serkedjieva J., Daferera D., Gulluce M., Polissiou M., Tepe B., Sokmen A., from herbal parts and callus cultures of Origanum acutidens. *Journal of agricultural and food chemistry*, 52(11)(2004) 3309-3312.

[28] Roby M. H. H., Sarhan M. A., Selim K.A.H., Khalel K.I. Evaluation of antioxidant activity, total phenols and phenolic compounds in thyme (Thymus vulgaris L.), sage (Salvia officinalis L.), and marjoram (Origanum majorana L.) extracts. *Industrial Crops and Products*, 43 (2013) 827-831.

[29] Celik A., Nur Herken E., Arslan İ., Zafer Özel M.,Mercan N. Screening of the constituents, antimicrobial and antioxidant activity of endemic Origanum hypericifolium O. Schwartz & PH Davis. *Natural product research*, 24(16) (2010)1568-1577.

[30] Fakir H., Us A.A., Sagdic M.,Tornuk F.,Essential Oil Composition, Antimicrobial and Bioactive Properties of Origanuim hypericifolium, An Endemic Plant Species grown in Turkey. *Research Journal of Biotechnology*,10, 11(2015).

[31] Cervato G., Carabelli M., Gervasio S., Cittera A., Cazzola R.,Cestaro B., Antioxbdant properties of oregano (Origanum vulgare) leaf extracts. *Journal of Food Biochemistry*, 24(6) (2000). 453-465.

[32] Özkan G. (2007). Türkiye'de Lamiaceae (Labiatae) familyasına ait baharat veya çeşni olarak kullanılan bazı bitkilerin fenolik bileşenleri ile antioksidan ve antimikrobiyal etkilerinin belirlenmesi (Doctoral dissertation, Selçuk Üniversitesi Fen Bilimleri Enstitüsü).

[33] Kaurinovic B., Popovic M., Vlaisavljevic S., Trivic S. Antioxidant capacity of Ocimum basilicum L. and Origanum vulgare L. extracts. *Molecules,* 16(9) (2011) 7401-7414.

[34] Baddal M.K. (2010). Origanum Minutiflorum bitkisinin antioksidan özelliklerinin incelenmesi (Doctoral dissertation, SDÜ Fen Bilimleri Enstitüsü).

[35] Sarikurkcu C., Zengin G., Oskay M., Uysal S., Ceylan R., Aktumsek A., Composition, antioxidant, antimicrobial and enzyme inhibition activities of two Origanum vulgare subspecies (subsp. vulgare and subsp. hirtum) essential oils. *Industrial Crops and Products,* 70 (2015)178-184.

[36] Yılmaz H., Çarıkçı S., Kılıç T., Dirmenci T., Arabacı T., Gören A.C., Screening of chemical composition, antioxidant and anticholinesterase activity of section Brevifilamentum of Origanum (L.) species. *Records of Natural Products,* 11(5) (2017).

[37] Elhardallou S.B., Cytotoxicity and biological activity of selected Sudanese medicinal plants. *Research Journal of Medicinal Plant*, 5(3) (2011) 201-29.

[38] Taraphdar A.K., Roy M., Bhattacharya R.K. Natural products as inducers of apoptosis: Implication for cancer therapy and prevention, *Curr Sci*, 80 (2001) 1387-1396.

Cumhuriyet Science Journal

Evaluation Of Hepcidin And Iron Concentrations With Liver And Kidney Functions In Beta-Thalassemia Patients

Othman Rashid Al Samarrai [1,a,*], Hazem Mohammed Abd [2,b], Mohammed Hameed Mahal [3,c], Ali Rasheed Hameed Al Samarrai [4,d]

[1]Department of Chemistry, College of Education, University of Samarra, Samarra, Iraq

[2]The General Directorate of Education in Diyala Province, Baquba, Iraq

[3]Department of Biotechnology, College of Applied Sciences, University of Samarra, Samarra, Iraq

[4]Altaleem Aldeeney-Sunni affairs, Samarra, Iraq

*Corresponding author

Research Article

ABSTRACT

The goal of this research was to estimate the concentrations of iron and hepcidin with liver and kidney functions in beta-thalassemia patients, the study involved the collection of 80 blood samples from both sexes, and the samples were distributed into 45 samples for beta thalassemia patients, their ages ranged between 15-25 years, the samples were collected from the Thalassemia Specialization Center in Baquba General Hospital, and 35 blood samples for healthy people as a control group, their ages extended from 15 to 25. years, during the period from the beginning of March 2023 until the end of May 2023. The study's findings revealed a considerable increase in the concentrations of hepcidin and iron in patients group compared with the healthy ones. It also displayed a significant reduce in the patients' albumin and creatinine concentrations as compared with healthy group, while the results here were no significant variations in total protein, urea and uric acid levels.

Keywords: Beta-thalassemia, Hepcidin, Iron, Liver, Kidney.

[a] othman.samarrai@uosamarra.edu.iq https://orcid.org/0000-0002-1487-4054 [b] hazimm.abed@gmail.com https://orcid.org/0000-0002-1488-4055
[c] mohammedhameed@uosamarra.edu.iq https://orcid.org/0000-0002-7207-3140 [d] ali.rasheed86@gmail.com https://orcid.org/0000-0001-9963-4449

Introduction

Thalassemia refers to a range of genetic blood disorders that impact the inability of a person to make hemoglobin, which causes anemia, leading to anemia [1], or it is a genetic disorder resulting from a defect in the composition of a globin chain or several globin chains, meaning that the alpha and beta chains in hemoglobin are made equally in normal cases, but in the case of thalassemia, the speed of making one of these two chains is slower than the other, and as a result the chain increases the other compared to the first, and an abnormality of hemoglobin occurs in an abnormal form that leads to a decrease [2].

In the nations that surround it—the Middle East, India, the Mediterranean, and the Far East—thalassemia is a major problem. The Maldives has the highest percentage of thalassemia carriers 18%, Cyprus has 14 percent, Sardinia has 10.3%, and Southeast Asia has 3-5 percent [3]. Due to population mobility and interethnic marriages, thalassemia has spread around the world as a result of the selection pressure of sickle Plasmodium malaria in these areas [4].

The pathogenesis of thalassemia is mainly related to incompetent erythropoiesis and hemolysis, which hemoglobinopathies are a diverse set of hereditary illnesses characterized by impaired production of the alpha or beta chains of hemoglobin, which function as oxygen-carrying components of red blood cells. α/β-globin chain ratio leading to chronic hemolytic anemia, compensatory hematopoietic expansion [5]. If there is insufficient production of these two chains by the body, red blood cells do not form properly and are unable to carry enough oxygen, leading in anemia that begins in early childhood and lasts throughout one's life. Thalassemia is a hereditary condition that requires at least one of the parents to be a carrier. It is caused by a genetic mutation or deletion of specific essential natural components [6].

Thalassemia comes in two forms: alpha [α-] and beta (β-). Whereas beta thalassemia occurs when all four -globin genes are damaged or altered, alpha thalassemia is caused by changes or deletions in one or more of the four -globin genes [6,7]. Unique of the greatest frequent danger elements for thalassemia is consanguineous marriage. [7]. The legacy of faulty and altered genes intricate in the manufacture of hemoglobin from the parents is one of the causes of thalassemia. Another explanation is that if one of the parents has thalassemia, even if the child has no symptoms the child might grow up to carry the illness. The youngster may possibly have thalassemia minor, in which case his symptoms may be minimal [8].

Hepcidin is a peptide hormone that was first identified in 2000. It is mostly produced by hepatocytes and consists of 25 amino acids as well as four disulfide bridges [9]. By enabling iron from daily meals to cross the oral-enteric membrane by means of a divalent metallic transporter,

where it is either delivered to the plasma by hepcidin or stored as ferritin. Hepcidin is involved in the regulation of the iron balance in the human body, hepcidin is an acute-phase reactant, one of many molecules whose plasma concentration changes in response to inflammation. During acute or chronic inflammation, hepcidin and other acute-phase reactant levels rise, which causes serum iron levels to decrease as hepcidin levels rise. Elevated hepcidin is associated with the pathophysiology of chronic disease anemia; elevated inflammation lowers serum iron levels because hepcidin decreases iron transport out of cells; on the other hand, a lack of hepcidin production can lead to iron overload, as in hereditary hemochromatosis [10,11].

This study aimed to determine the concentrations of hepcidin and iron with liver and kidney functions in beta-thalassemia patients.

Materials and Methods

Samples Collection

A total of 45 Patients diagnosed with beta-thalassemia at the Thalassemia Center at Baquba General Teaching Hospital in Diyala Governorate provided blood samples. The age range of the patients was 15 to 25 years old, and 35 blood samples were taken from healthy individuals in the same age range. The patients' information was recorded using a customized questionnaire form that was created specifically for each patient.

Blood Collection

Blood samples were taken using disposable plastic syringes to draw (4-6) ml of venous blood. The blood was then placed in test tubes and allowed to coagulate for 30 minutes at room temperature. The separated sera were then centrifuged for 15 minutes at 5000 x g and stored at -20 ° C for further biochemical analysis.

Biochemical Parameters

By means of the hepcidin kit manufactured by Shanghai Biological Technologies, identified by the numeral YHB1535Hu, the concentration of hepcidin was measured make use of the enzyme-linked immunosorbent assay (ELISA) method, while iron, total protein, albumin, urea, creatinine and uric acid determined by using the analyzer Autonomous Cobas integra 400 puls system supplied by the German company Roche.

Statistical analysis

The mean and standard deviation (SD) for each measurement were used in the SPSS statistical software to examine the results that were obtained. To compare biochemical variables between two groups, the T-test was run at the probability level (P≤ 0.05).

Results

Table 1 displays the findings of study, Mean ± SD of hepcidin and iron concentrations in the two groups of patients and healthy people.

Table 1: The mean ± SD of hepcidin and iron in the two groups.

Parameters	Control (n=35)	Patients (n=45)	P-value
Hepcidin (ng/ml)	531.048±211.343	1539.846±601.945	0.001*
Iron (µmol/L)	21.587±3.3152	40.673±7.352	0.001*

* This sign means different significant at P ≤0.05.

Table 1 shows that the concentrations of hepcidin and iron in thalassemia patients were 1539.846 ± 601.945 ng/ml and 40.673 ± 7.352 µmol/L respectively, while it was 531.048 ± 211.343 ng/ml and 21.587 ± 3.3152 µmol/L respectively in the healthy people. Results showed that the concentrations of hepcidin and iron increased significantly (p ≤ 0.05) in the thalassemia patients compared to healthy people, as evidenced by figures 1 and 2.
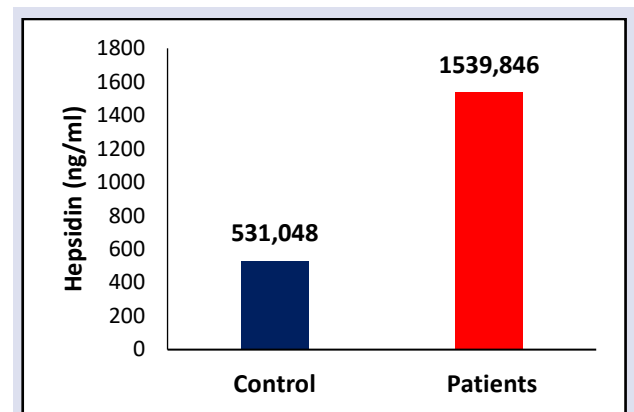
Figure 1: The mean of hepcidin concentration in two groups.
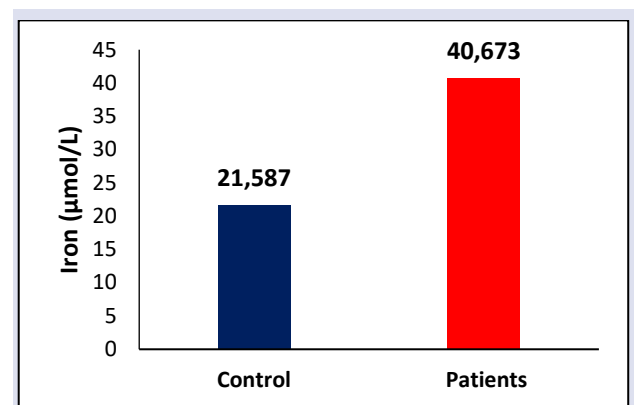
Figure 2: The mean of iron concentration in two groups

Liver and kidney functions were also evaluated in both groups of patients and healthy by measuring the concentrations of total protein, albumin, urea, uric acid and creatinine, as shown in Table 2.

Table 2: Mean ± SD levels of liver and kidney functions in the two groups.

Parameters	Control (n=35)	Patients (n=45)	P-value
Total protein (g/dl)	68.930±11.818	66.392±7.918	0.224
Albumin (g/dl)	51.092±5.505	46.404±5.978	0.001*
Urea (mg/dl)	27.627±8.398	25.965±8.922	0.35
Uric acid (mg/dl)	4.976±1.046	5.032±1.731	0.849
Creatinine (mg/dl)	0.785±0.182	0.388±0.088	0.001*

* This sign means different significant at P ≤0.05.

Table 2 shows that the mean ± SD of total protein and albumin levels in thalassemia patients were (66.392 ± 7.918) g/dl and (46.404 ± 5.978) g/dl respectively, while were (68.930 ± 11.818) g/dl and (51.092±5.505) g/dl respectively in the healthy group.

There were no significant variations in total protein level, according to the findings, but there was a significant reduce in the level of albumin at a probability level of p ≤ 0.05 in the patients group matched to the healthy group, as showen in figures 3 and 4.
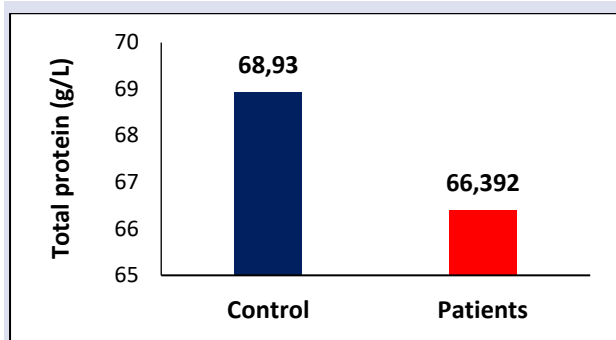
Figure 3: Total protein concentration in two groups.
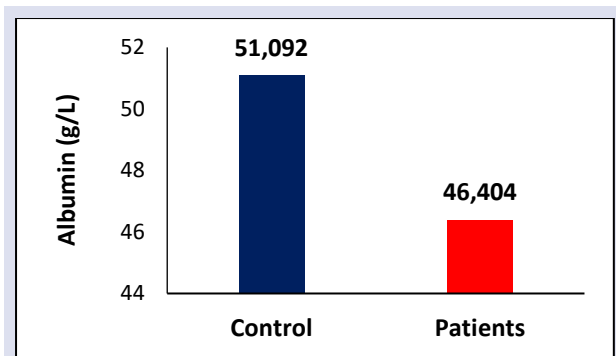
Figure 4: Albumin concentration in two groups.

Table 2 showed that the mean ± SD of urea levels of (25.965 ± 8.922) mg/dl, uric acid (5.032 ± 1.731) mg/dl, and creatinine (0.388 ± 0.088) mg/dl, respectively in thalassemia patients, while it was (27.627 ± 8.398) mg/dl and (4.976±1.046) mg/dl and (0.785±0.182) mg/dl respectively in the healthy group.

Results displayed that there were no significant differences at the probability levels of ≤ 0.05 in each of urea and uric acid in patients group compared to the healthy group, while creatinine level decreased significantly at the probability of ≤ 0.05 in the patients compared to the healthy group as in figures (5-7).
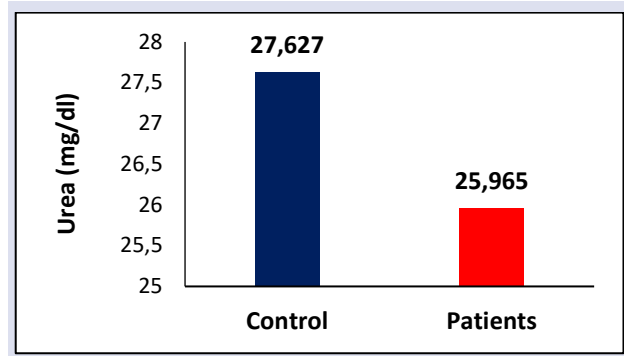
Figure 5: Urea concentration in two groups
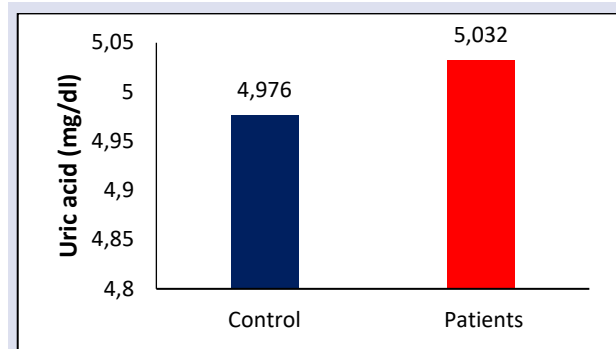
Figure 6: Uric acid concentration in two groups.
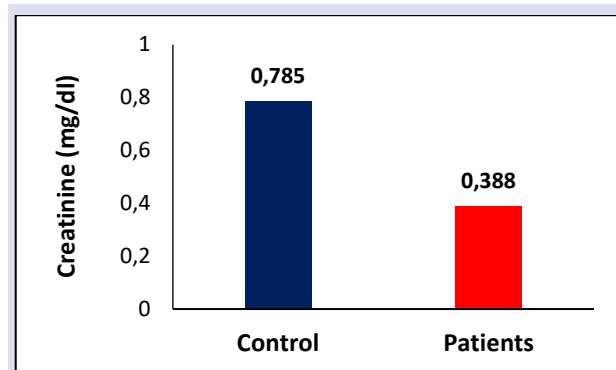
Figure 7: Creatinine concentration in two groups.

Discussion

The findings of this study are consistent with the study of Abd and Al Samarrai [12], as they suggest that the reason of high hepcidin was due to regular blood transfusions, and blood transfusions inhibit the red blood cell move, so that both lead to an increase in hepcidin in thalassemia patients.

Hepcidin is secreted primarily by hepatocytes into the circulation, it is an important controller of iron homeostasis in the body, and it plays a job in a variety of iron metabolism metabolic pathways. It acts by directly inhibiting ferroportin, a protein that transports iron out of its storage cells, and this protein is present in intestinal absorption cells and macrophages, hepcidin blocks intestinal absorption cells from secreting iron in the hepatic portal system by blocking ferroportin, limiting iron absorption and preventing iron from exiting macrophages., liver, spleen, endothelial cells and

duodenum, preventing its export to the plasma, and thus leads to iron balance in the body. Hepcidin gene expression is down-regulated by low tissue oxygen tension and by increased erythropoietic demand and up-regulated by increased body iron stores and infection or inflammation [13].

The recent study discovered that iron levels in beta-thalassemia patients had increased, and are in agreement with Hasoon's et al findings [12,14], the excessive iron levels in beta-thalassemia patients were caused by both the frequent red blood cell transfusions and high iron absorption, these results indicate insufficient chelation.

Excess iron is harmful to many tissues, including the liver, endocrine glands, and heart, according to a research [15], resulting in a variety of consequences that cause sickness, and death in Mention the name of the disease studied by Neufeld et al [15]. Iron can work a major job and is essential for oxidation of membrane cell, aging, and the production of cell antigen, which is one of the key erythrocyte clearance pathways. Additionally, patients' significantly elevated blood iron levels are caused by defects in the control of iron absorption, including the genetics of hemochromatosis. Recurrent blood transport also raises blood iron levels because recipients lack the biological mechanisms of iron excretion, which results in higher than normal levels of iron stores in the body [16]. The present study's findings agreed with the results of Hosen et al [17], who noticed that there were no significant differences for total protein level in patients compared to healthy controls, and also agreed with the results of Abd et al. [18], who discovered that thalassemia patients' albumin levels were much lower than healthy controls.

Total protein is the most abundant compound in the blood serum and includes enzymes, hormones, and antibodies, as well as regulators of osmotic pressure balance. The decrease in total protein in the serum of thalassemia patients is related to the liver's inability to synthesize secondary protein [19].

Albumin is the main component of serum protein (usually more than 50%) and is synthesized in the liver and aids in osmotic pressure, nutrient transport, and waste removal [20]. Albumin is the major fatty acid-binding protein in plasma and has seven fatty acid-binding sites with medium and high affinity [21], and it regulates osmotic pressure, transports fatty acids, bilirubin, and cholesterol. Also, it has been proven to play a key function in blood plasma's antioxidant capability against *reactive oxygen species* [22]. Albumin is produced mainly by hepatocytes and hepatic dysfunction, malnutrition, or systemic inflammation can lead to low serum albumin levels [23].

Our study results agreed with the results of Althanoon and Alkazzaz [24], who they noted that there were no significant differences in the concentration of urea and uric acid with a significant decrease in creatinine in serum of thalassemia patients compared to healthy controls. The result also agrees with the study of Ghazala et al., [25],

who they noted that there were no significant differences in urea concentration between thalassemia patients and healthy controls. Outcomes of study also agreed with Shanaki et al [26], as they observed a significant reduce in the concentration of creatinine in thalassemia patients compared to healthy controls.

Increased transfusion frequency and hypercalcemia are linked to impaired renal function in thalassemia patients, highlighting the significance of monitoring calcium levels in thalassemia patients on a regular basis, as it is considered a risk factor for renal function [27,28]. And that the reason for the low concentration of creatinine in the blood is related to a decrease in body mass index due to a delay in growth or a decrease in body muscle mass in thalassemia patients, the creatinine is the most widely used measure in knowing the functions of the kidneys, and this in turn leads to the disruption of the filtration process carried out by the kidneys [29,30]. The low concentration of creatinine in the blood is due to a deficiency in the functions of the kidneys that reduce the glomerular filtration process, and that the glomerular filtration rate is clinically important because it is a measure of kidney function [30].

Conclusion

According to the current study, there has been Hepcidin and iron concentrations in beta-thalassemia patients were significantly higher than in healthy controls. Also showed a significant difference in some liver and kidney functions in beta-thalassemia patients compared to healthy controls.

Conflict of interest

There are no conflicts of interest in this work.

Acknowledgments

References

[1] Oltean A., & IM C.. Mentzer Index in pediatric thalassemia trait, Jurnalul Pediatrului, 23 (89-90) (2020) 35-40.

[2] JLT J. M. B. Lubert Stryer editor, BIOCHEMISTRY. 5th ed. W. H. Freeman, (2002) 596. ISBN-10: 0716746840, ISBN-13: 978-0716746843.

[3] Rivella S., β-thalassemias: paradigmatic diseases for scientific discoveries and development of innovative therapies, *Haematologica*, 100 (4) (2015) 418.

[4] Bajwa H., Basit H., Thalassemia, StatPearls Publishing, Treasure Island (FL), 2023.

[5] Mathur S., Sutton J., Personalized medicine could transform healthcare, *Biomedical Reports*, 7 (1) (2017) 3-5.

[6] Danjou F., Anni F., Galanello R., Beta-thalassemia: from genotype to phenotype, *Haematologica*, 96 (11) (2011) 1573.

[7] Prathyusha K., Venkataswamy M., Goud K. S., Ramanjaneyulu K., Himabindu J., Raj K. S., Thalassemia-A Blood Disorder, its Cause, Prevention and Management, *Research Journal of Pharmaceutical Dosage Forms and Technology*, 11 (3) (2019) 186-190.

[8] Casu C., Oikonomidou P. R., Chen H., Nandi V., Ginzburg Y., Prasad P., Rivella S., Minihepcidin peptides as disease modifiers in mice affected by β-thalassemia and polycythemia vera, Blood, *The Journal of the American Society of Hematology*, 128 (2) (2016) 265-276.

[9] Rauf A., Shariati M. A., Khalil A. A., Bawazeer S., Heydar M., Plygun S., Aljohani A. S. Hepcidin, an overview of biochemical and clinical properties, *Steroids*, 160 (2020) 108661.

[10] Keohane E. M., Otto C. N., Walenga J. M., Rodak's Hematology-E-Book: Rodak's Hematology-E-Book, Elsevier Health Sciences, (2019).

[11] Papanikolaou G., Tzilianos M., Christakis J. I., Bogdanos D., Tsimirika K., MacFarlane J., Nemeth E. Hepcidin in iron overload disorders, *Blood*, 105 (10) (2005) 4103-4105.

[12] Abd H. M., Al Samarrai O. R., Evaluation of hepcidin, ferritin and iron levels with liver enzymes of β-thalassemia patients in Diyala governorate, Iraq, In AIP Conference Proceedings, 2450 (1). (2022) AIP Publishing.

[13] Goodnough L. T., Iron deficiency syndromes and iron-restricted erythropoiesis (CME), *Transfusion*, 52 (7) (2012) 1584-1592.

[14] Hasoon I. G., Shani W. S., Radi A. M., The association of hepcidin with some inflammatory markers in β-thalassemia major patients of Basrah Province, *EurAsian Journal of BioSciences*, 14 (2) (2020) 7285-7289.

[15] Neufeld E. J., Update on iron chelators in thalassemia, Hematology 2010, *The American Society of Hematology Education Program Book*, 2010 (1) (2010) 451-455.

[16] Kosman D. J., Redox cycling in iron uptake, efflux, and trafficking, *Journal of Biological Chemistry*, 285 (35) (2010) 26729-26735.

[17] Hosen M. B., Karmokar N. C., Karim M. F., Al Mahmud R., Mesbah, M., Association of AST, ALT, ALB and total protein with beta-thalassemia in Bangladeshi population, *International Journal*, 3 (1) (2015) 991-995.

[18] Abd I. K., Zainal I. G., Assessment of biochemical parameters and study its correlation in ß-Thalassemia major patients and healthy controls in Kirkuk City, Iraq, *Medical Journal of Babylon*, 17 (2) (2020) 172-176.

[19] Malik A. M., Malik E. M., Al-Shammaa N. M., Al-Rubaei Z. M., A Comparative Biochemical Study of Proteins Profile in Iraqi Children and Adolescent with β–Thalassemia, *Iraqi J. Pharm. Sci.*, 19 (2) (2010) 19-23.

[20] Walter P. B., Macklin E. A., Porter J., Evans P., Kwiatkowski J. L., Neufeld E. J., Harmatz, P., Inflammation and oxidant-stress in β-thalassemia patients treated with iron chelators deferasirox (ICL670) or deferoxamine: an ancillary study of the Novartis CICL670A0107 trial, *Haematologica*, 93 (6) (2008) 817-825.

[21] Pieniazek A., Gwozdzinski L., Zbrog Z., Gwozdzinski K., Alterations in conformational state of albumin in plasma in chronic hemodialyzed patients, *PLoS One*, 13 (3) (2018) e0192268.

[22] Taverna M., Marie A. L., Mira J. P., Guidet B., Specific antioxidant properties of human serum albumin, *Annals of Intensive Care*, 3 (2013) 1-7.

[23] Oki S., Toiyama Y., Okugawa Y., Shimura T., Okigami M., Yasuda H., Kusunoki M., Clinical burden of preoperative albumin-globulin ratio in esophageal cancer patients, *The American Journal of Surgery*, 214 (5) (2017) 891-898.

[24] Althanoon Z. A., Alkazzaz N. A., Comparison of The Effects of Deferasirox And Deferoxamine On Uric Acid And Renal Function In Patients with Beta Thalassemia, *Systematic Reviews in Pharmacy*, 11 (11) (2020).

[25] Ghazala M. M., Abdellateif S. S., Taher M. M. S., Abdelmohsen E. A., Bakheet O. H., Assem A. A. A., Serum hepcidin and growth differentiation factor 15 in patients with β-thalassemia and its relation to blood transfusion, *Al-Azhar International Medical Journal*, 2 (3) (2021) 43-48.

[26] Shanaki M., Ehteram H., Nasiri H., Azad M., Kouhkan F., Pakzad R., Mobarra N., Assessment of Liver and Kidney Functional Parameters along with oxidative Stress and Inflammatory Biomarker in Patients with β-Thalassemia major, *Iranian Journal of Pediatric Hematology and Oncology*, 6 (4) (2016) 249-260.

[27] Jalali A., Khalilian H., Ahmadzadeh A., Sarvestani S., Rahim F., Zandian K., Asar S., Renal function in transfusion-dependent pediatric beta-thalassemia major patients, *Hematology*, 16 (4) (2011) 249-254.

[28] Sadeghi-Bojd S., Hashemi M., Karimi M., Renal tubular function in patients with beta-thalassaemia major in Zahedan, southeast Iran, *Singapore Med. J.*, 49 (5) (2008) 410-2.

[29] Majeed A. M. H., Hameed O. R., Effect of endothelin-1, Vimentin and some biochemical variables on men with type 2 diabetes mellitus, diabetic patients with hypertension, and diabetic patients with renal impairment, *Samarra Journal of Pure and Applied Science*, 4 (3) (2022) 61-78.

[30] Younus Z. M., Alhially Y. A. H., Bashi A. Y. D., Evaluation of conventional renal function tests in β-thalassemia major patients in Nineveh province, *Tikrit Journal of Pharmaceutical Sciences*, 8(1) (2012) 6-14.

Cumhuriyet Science Journal

Isocitrate Dehydrogenase: Three Subunits in Different Cancer Types—Changes in Gene Expression, Mutation Status, and Cancer Progression.

Esra Bulut Atalay [1,a,*]

[1] Department of Biochemistry, Faculty of Science, Sivas Cumhuriyet University, Sivas, Türkiye
*Corresponding author

Research Article

ABSTRACT

The isocitrate dehydrogenase (IDH) gene encodes three protein isoforms (IDH1, IDH2 and IDH3). IDH3 exists in three subunits (IDH3A, IDH3B, and IDH3G). Examining the gene expression level and mutation status of IDH3 subunits could help find new diagnoses or treatment options for specific cancer types. Until now, studies on the IDH3 enzyme have been focused on the IDH3A subunit and a few types of cancer. In our study, the effect of IDH3A, IDH3B, and IDH3G expression changes on cancer progression and survival in the ten major cancer types were investigated using bioinformatic tools. Then, the impact of mutation status on cancer progression was examined in the TCGA database. The expression level of IDH3 subunits increased as the bladder, breast, colon, esophageal, lung, and stomach cancers progressed. The elevated expression level of all IDH3 subunit expressions leads to poor prognosis in colon, esophageal, lung, prostate, and stomach cancers. The cumulative alteration rates revealed low-frequency (0.3-5.9 %) mutations in all IDH3 subunits. IDH3A, IDH3B, and IDH3G expression was significantly altered after mutation among all types of cancer studied except the prostate. Our data showed that there may be correlation between the mutation status of the IDH3 subunits and breast, esophageal, lung and stomach cancer progression.

Keywords: Cancer, Biomarker, IDH3A, IDH3B, IDH3G.

a ✉ esrabulut@cumhuriyet.edu.tr   🆔 https://orcid.org/0000-0002-1615-0535

Introduction

Isocitrate dehydrogenase (IDH) is one of the critical regulator enzymes in the tricarboxylic acid (TCA cycle). IDH plays a role in the α-KG (α-ketoglutarate) production from isocitrate with the formation of NADH or NADPH, which is essential for the metabolism of normal mammalian cells [1]. There are three IDH isoforms, IDH1, IDH2, and IDH3, and their molecular structure, subcellular localization, catalytic mechanism, and cofactor requirement are different [2]. NADP+-dependent IDH1 and IDH2 enzymes are homodimeric, and the reactions catalyzed by IDH1 and IDH2 are reversible [3]. IDH1 catalyzes the oxidative decarboxylation of isocitrate to α-KG in the cytoplasm and peroxisomes, whereas IDH2 carries out the same reaction in the mitochondria [2]. On the other hand, the NAD+-dependent IDH3 enzyme has structurally different heterotetrameric chemistry. IDH3 catalyzes the irreversible conversion of isocitrate to α-KG, one of the rate-limiting steps in the TCA cycle, acts as a part of the mitochondrial respiratory system [4]. This enzyme has multiple subunits: α, β, and γ. In mammals, IDH3 consists of the αβ- and αγ-subunits, which together form α2βγ heterotetramers [5]. The α subunit is catalytic, the β subunit plays a structural role, and the γ subunit has the regulatory role of activating the holoenzyme. To show complete activity, IDH3 needs the assembly and synergistic function of αβ and αγ heterodimers [6]. The IDH3A gene (chromosome 15q25.1), IDH3B gene (chromosome 20p13), and IDH3G gene (chromosome

Xq28) abundantly encode the α, β-and γ-subunits in the mitochondria-rich tissues, respectively [7.] Hartong et al. (2008) found that IDH3B is required for IDH3 activity in most tissues [8]. In another study, loss of the IDH3B in the mice led to isocitrate accumulation in the TCA cycle [9]. It is known that IDH3 is a disease-causing gene, and IDH3A and IDH3B subunits are significantly related to different diseases such as pseudo-coloboma, epileptic encephalopathy, and retinal degeneration [8,10]. The expression level of IDH subunits is significantly altered in human cancer types. The studies about IDH3's role in tumorigenesis are deficient and generally focus on IDH3A [11].

Cancer is derived from changes resulting from mutations in processes such as cell division and metabolism. The mutations cause cells to undergo atypical metabolic changes in energy production reactions [12]. According to GLOBOCAN estimations, 19.3 million new cancer cases were observed worldwide in 2020; unfortunately, 9.96 million patients died [13]. Recently, the diagnosis and treatment of cancer disease have been studied with increasing interest. In addition to protooncogenes and oncogenes, mutations in metabolic enzymes such as IDH and oncometabolite that cause transcriptional changes are also very important in the development and progression of cancer [14]. IDH1 is an atypical gene that acts as a tumor suppressor in cases where mutation causes loss of function and as an

oncogene where mutation causes gain of function [2]. In the literature, it is known that wild-type IDH isoforms (IDH1 and IDH2) have a role in the growth and progression of different tumors (breast, colon, esophageal, lung, and pancreas [15-19]. However, the expression levels of IDH3 subunits (IDH3A, IDH3B, and IDH3G) in different cancer types and the role of mutations in cancer progression have not been given adequate research attention.

It has been determined that there are more than 200 types of cancer [13]. Breast, lung, cervix, colon, and stomach cancer are the most common types of cancer that cause death in women. The six most common cancers that lead to death for men were lung, liver, stomach, prostate, esophageal, and colon cancer in 2022 [20]. Knowing the gene that is explicitly overexpressed for the cancer type is vital. The specific expression of IDH isoforms or subunits to cancer type and the expression level change as cancer progresses cause metabolic rearrangement. This situation can potentially be used to diagnose and treat various cancers [14]. In the literature, Iscan et al. (2021) investigated the expression profile of two isoforms of the TP73 gene in the most common human cancers by using publicly available data. They found that TAp73α is overexpressed in lung squamous and breast invasive carcinoma, whereas the second isoform DNp73α is downregulated in these cancer types [21]. In another study, Guneri-Sozeri and Erkek-Özhan (2022) studied one of the frequently mutated genes (ELF3) in bladder cancer. They provide essential information about gene expression changes in all cancer types in the TCGA Gen Atlas Project [22].

In the present study, the effect of expression changes of IDH3A, IDH3B, and IDH3G genes on cancer progression and survival probability was analyzed in the bladder, breast, colon, esophageal, kidney, lung, pancreas, prostate, and stomach cancer types by using bioinformatic tools such as TSVdb, cBioPortal for Cancer Genomics, and UALCAN. Then, the mutation frequency of these subunits and the impact of mutation status on cancer progression were investigated. All results showed that IDH3A, IDH3B, and IDH3G might be potential targets for diagnosing and treating colon, esophageal, lung, prostate, and stomach carcinomas.

Experimental Methods

The Level of IDH3A, IDH3B, IDH3G Expression in ten Major Cancer Tissues

The analysis of genomic data was performed in tumor and normal samples using TCGA data via the UALCAN web portal [23] to determine the level of IDH3A, IDH3B, and IDH3G expression based on samples types in the ten major cancers including bladder urothelial carcinoma (BLCA), breast invasive carcinoma (BRCA), colon adenocarcinoma (COAD), esophageal carcinoma (ESCA), kidney renal clear cell carcinoma (KIRC), lung adenocarcinoma (LUAD), lung squamous cell carcinoma (LUSC), pancreas adenocarcinoma (PAAD), prostate adenocarcinoma (PRAD), and stomach adenocarcinoma (STAD). 4616

tumors and 458 non-tumor tissues were analyzed. Fig. 1 and Supplementary Fig. 2 was generated using the GraphPad Prism software, version 8.0 (GraphPad Software, USA). p values less than 0.05 were considered statistically significant and marked on the Figures.

IDH3A, IDH3B, and IDH3G expression based on individual cancer stages in the most common cancer types were also investigated in the TCGA dataset via the UALCAN web portal [23]. The "Expression" and "Individual Cancer Stages" functions were used, respectively, and the cancer stages were defined. All results were combined in Fig. 2.

Our previous report [24] described how to construct the heatmap used in Supplementary Fig. 1.

The Protein Level of IDH3A, IDH3B, IDH3G Expression in five Major Cancer Tissues

To investigate the protein level of IDH3A, IDH3B, and IDH3G expression, the "Proteomics" function was used in UALCAN web portal [23] for the five major cancer types including BRCA (Normal n = 18, Tumor n = 125), COAD (Normal n = 100, Tumor n =97), LUAD (Normal n = 111, Tumor n = 111), LUSC (Normal n = 102, Tumor n = 110), PAAD (Normal n = 74, Tumor n = 137) and Supplementary Fig. 2 was generated.

Investigation of Patient Survival Probability

To investigate the relationship between elevated expression of IDH3 subunits and clinical outcomes, the "Survival" function of the UALCAN web portal [23] was used. All results with a poor prognosis were combined in Fig. 3.

Analyze the Mutation Status

The alteration status of IDH3A, IDH3B, and IDH3G was examined on the cBioPortal for Cancer Genomics using TCGA PanCancer Atlas data of the ten major cancer types. Genetic alterations of the IDH3 subunits were analyzed for both mutations and copy numbers and finally, we achieved the cumulative alteration rates (Fig. 4; Supplementary Fig. 5). BLCA, BRCA, COAD, ESCA, KIRC, LUAD, LUSC, PAAD, PRAD, and STAD samples in the TCGA PanCancer Atlas were chosen as sample queries. In addition, the mutation types and frequencies were also determined using cBioPortal for Cancer Genomics web tool [25] (Supplementary Fig. 3; Supplementary Fig. 4).

Gene Expression Analysis According to Mutation Status

The effect of mutations on the gene expression of IDH3 subunits (IDH3A, IDH3B, IDH3G) was examined using the "Plot" function of the cBioPortal for Cancer Genomics web tool [25]. Boxplots were combined in Fig. 5.

Statistical Analysis:

Statistical analysis was carried out by GraphPad Prism 8.0 (GraphPad Software, CA, USA). One-way ANOVA was used to compare differences between two or more

groups, followed by Tukey's multiple comparison test. Asterisks (* for p<0.05, ** for p<0.01, *** for p<0.001, **** for p<0.0001) are used on the graph to indicate statistical significance.

Results and Discussion

Expression Status of IDH3 Subunits (IDH3A, IDH3B, and IDH3G) in the ten Major Types of Cancer

IDH enzymes that catalyze the rate-limiting step in the TCA cycle dramatically affect cell metabolism [4]. Wild-type IDH1/2 enzymes are overexpressed in some cancer tissues compared to healthy tissue to meet the increased energy and substrate needs of the cancer cell [15].

In the first step, the expression level of IDH3A, IDH3B, and IDH3G was investigated by using TCGA data via UALCAN web portal for the ten major cancer types, including BLCA, BRCA, COAD, ESCA, KIRC, LUAD, LUSC, PAAD, PRAD, and STAD. According to the TCGA data, the expression of IDH3A increased in esophageal, lung, and stomach tumor tissues. In contrast, it decreased in bladder, colon, kidney, and prostate tumor tissues compared to normal tissue (Fig. 1A). The bladder, esophageal, lung, and stomach cancer types displayed a significant upregulation of IDH3B. In contrast, breast and kidney cancers showed significant downregulation (Fig. 1B). IDH3G's expression level is elevated in all tumor

tissues except kidney and pancreas tumors (Fig. 1C). The expression of all subunits in only cancer tissues was examined in the Heatmap constructed in GEPIA. Interestingly, the expression of IDH3A, IDH3B, and IDH3G showed specific differences and heterogeneity (Supplementary Fig. 1). In addition, the expression levels of all subunits only increased in esophageal, lung, and stomach tumor tissues and decreased in kidney cancer types according to control tissue (Fig. 1A-C). It was found that IDH3 subunit expressions (IDH3A, IDH3B, and IDH3G) were high in the different tumor types according to normal tissue, and their expression showed heterogeneity.

To corroborate the findings about mRNA expression, protein expression analysis was curated by using TCGA data via UALCAN web portal for the five major cancer types, including BRCA, COAD, LUAD, LUSC, and PAAD. According to the TCGA data, the protein expression of IDH3A decreased in breast, colon, and prostate primary tumor tissues compared to normal tissue (Supplementary Fig. 2A). The lung cancer displayed a significant upregulation of IDH3B protein level. In contrast, breast, colon, and prostate cancers showed significant downregulation (Supplementary Fig. 2B). IDH3G's protein level is decreased in breast, colon, and lung primary tumor tissues (Supplementary Fig. 2C). The IDH3A protein level in colon cancer and IDH3B protein level in the breast and lung showed similarity with the mRNA expression level.
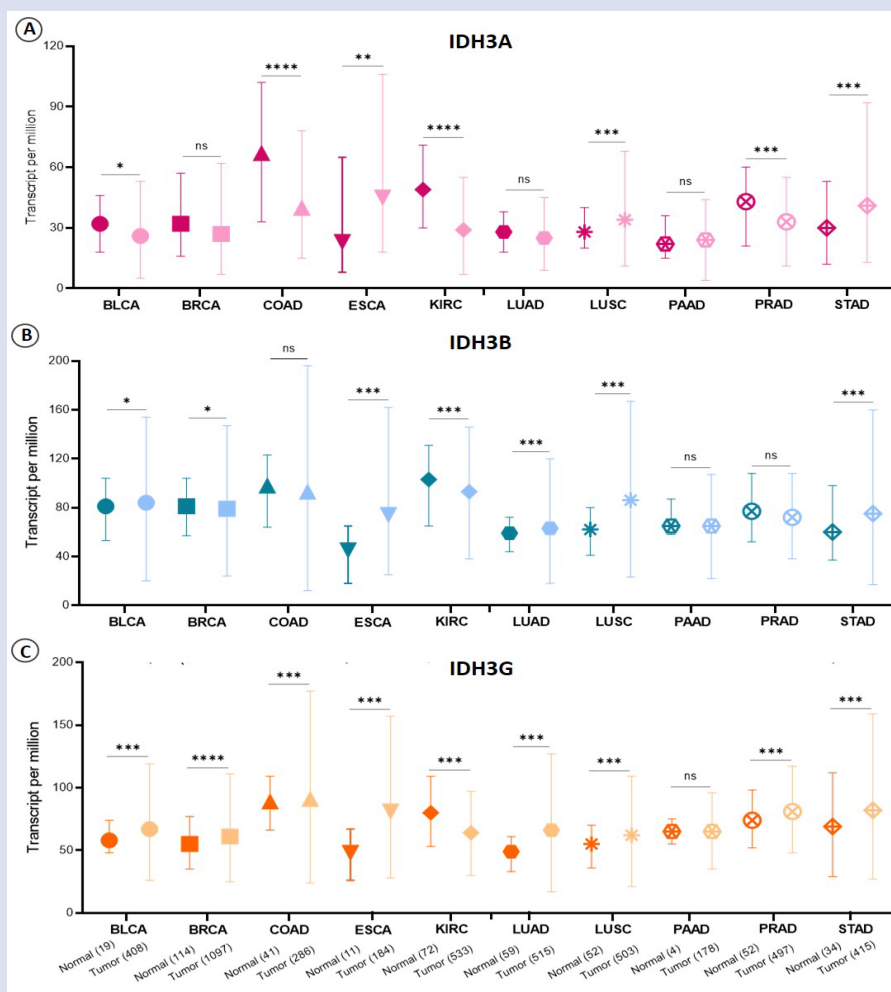
Figure 1. IDH3 subunits (IDH3A, IDH3B, IDH3G) gene expression in the ten most common cancer types.

Box-Whisker plot showing the mRNA expression levels of IDH3 (A), IDH3B (B), and IDH3G (C) in normal and primary tumor tissues of most common human cancers. The IDH3 subunits expressions were collected from UALCAN web portal for BLCA (Normal n = 19, Tumor n = 408), BRCA (Normal n =114, Tumor n = 1097 tumors), COAD (Normal n = 41, Tumor n =286), ESCA (Normal n = 11, Tumor n = 184), KIRC (Normal n = 72, Tumor n = 533), LUAD (Normal n = 59, Tumor n = 515), LUSC (Normal n = 52, Tumor n = 503), PAAD (Normal n = 4, Tumor n = 178), PRAD (Normal n = 52, Tumor n = 497), and STAD (Normal n = 34, Tumor n = 415) tumors. The cancer types are represented on the x-axis. The expression values (transcript per million) are represented on the y-axis. The mRNA levels of IDH3A, IDH3B, and IDH3G (A-C) were analyzed through the UALCAN web portal (http://ualcan.path.uab.edu/).

The responses to treatment are closely associated with tumor progression [26]. In the next step, we investigated how the expression of IDH3 subunits changes as cancer progresses in cancer types that displayed upregulation for this subunit. The expression level of IDH3A was highly elevated in esophageal, lung squamous cell, and stomach cancer types as the tumor progressed (Fig. 2A, B, C). There was no significant increase in the mRNA level of IDH3A in stage 4 of LUSC according to normal tissue (Fig. 2B). The expression level of IDH3B was increased in bladder, esophageal, lung, lung cell squamous, and stomach cancer types along with the tumor advancement (Fig. 2D, E, F, G, H). The mRNA level of IDH3B was not changed at stage 1 of BLCA according to normal tissue (Fig. 2M). The expression IDH3G was highly expressed in bladder, breast, colorectal, esophageal, lung, lung squamous, and stomach cancer types as the tumor progressed (Fig. 2I, J, K, L, M, N, O). There was no significant increase in IDH3G mRNA level at Stage 1 in BLCA and COAD (Fig. 2I, K) and Stage 4 in LUSC according to normal tissue (Fig. 2N).

The stage-specific results showed slight variations in the expression of IDH3 subunits based on individual cancer stages. On the other hand, all IDH3 subunits were highly expressed along with advancing tumor stages in different cancer types.
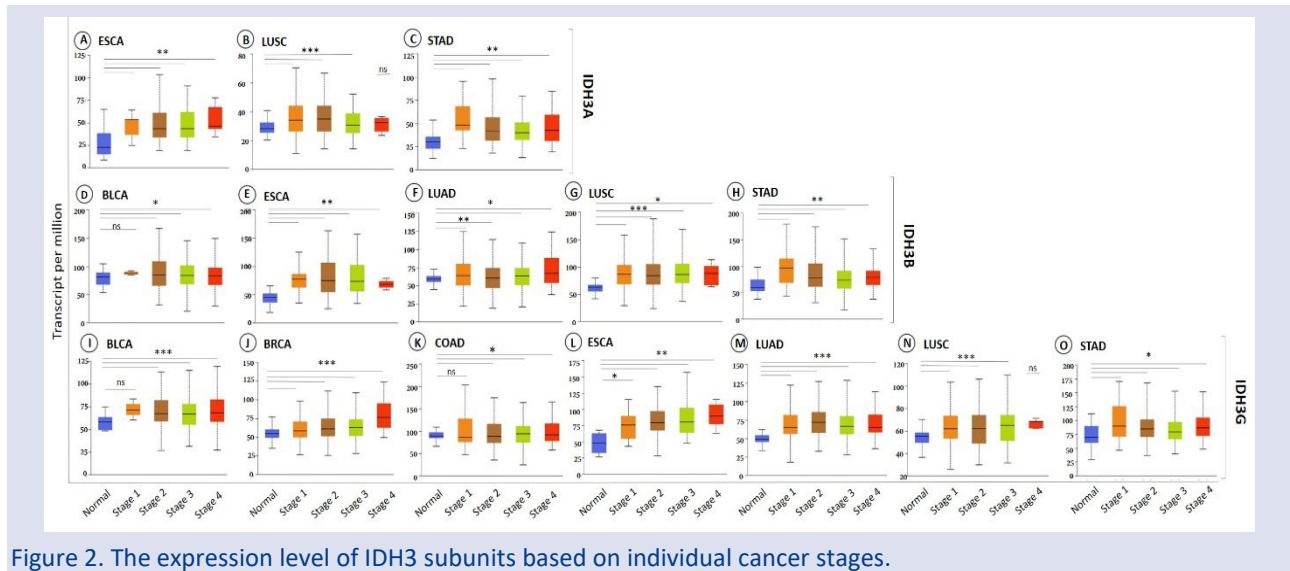
Figure 2. The expression level of IDH3 subunits based on individual cancer stages.

The mRNA level of IDH3A (A-C), IDH3B (D-H), and IDH3G (I-O) was analyzed through the UALCAN web tool. The number of samples for each stages are Normal n = 19, Stage 1 n = 2, Stage 2 n = 129, Stage 3 n = 137, Stage 4 n = 132 in BLCA, Normal n = 114, Stage 1 n = 183, Stage 2 = 615, Stage 3 n = 247, Stage 4 n = 20 in BRCA, Normal n = 41, Stage 1 n = 45, Stage 2 n = 110, Stage 3 n = 80, Stage 4 n = 39 in COAD, Normal n = 11, Stage 1 n = 13, Stage 2 n = 78, Stage 3 n = 55, Stage 4 n = 9 in ESCA, Normal n = 59, Stage 1 n = 277, Stage 2 n = 125, Stage 3 n = 85, Stage 4 n = 28 in LUAD, Normal n = 52, Stage 1 n = 243, Stage 2 n = 157, Stage 3 n = 85, Stage 4 n = 7 in LUSC, Normal n = 34, Stage 1 n = 18, Stage 2 n = 123, Stage 3 n = 169, Stage 4 n = 41 in STAD. The cancer stages and normal tissue are represented on the x-axis. The expression values (transcript per million) are represented on the y-axis.

The Effect of IDH3 Subunit Expression Level on Patient Survival Probability

In order to be a biomarker, it is not sufficient to provide information about disease progression. This gene should also significantly affect the treatment response. Information about the relevance of the target gene to the cancer patient survival allows reaching points that cannot be achieved with the gene expression analysis results of the biomarker [26]. The next step is to examine how the elevated expression of IDH3 subunits affects survival probability as cancer progresses. It is known that high expression levels of wild-type IDH isoforms (IDH1, IDH2) in tumor tissues lead to poor prognosis [33]. Among the cancer types in which IDH3A is overexpressed, high IDH3A expression caused decreased survival probability in the bladder, esophagus, lung squamous cell, and stomach carcinoma (Fig. 3A, C, D, E). In addition, the high

expression of IDH3A caused reduced survival probability in breast cancer whose expression was not significantly altered (Fig. 3B). High IDH3B expression led to decreased survival probability in the bladder, lung squamous cell, and stomach carcinoma (Fig. 3F, H, J). The expression of IDH3B was increased in colon and prostate cancer types where the expression of IDH3B was not significantly altered (Fig. 3G, I). The elevated IDH3G expression led to

a decreased survival probability in colon, prostate, and stomach cancers (Fig. 3K, L, M).

The clinical significance, critical in determining a biomarker, was examined using survival probability analysis. The results showed that IDH3A has clinical significance for the colon, IDH3B for the prostate, and IDH3G for liver cancer.
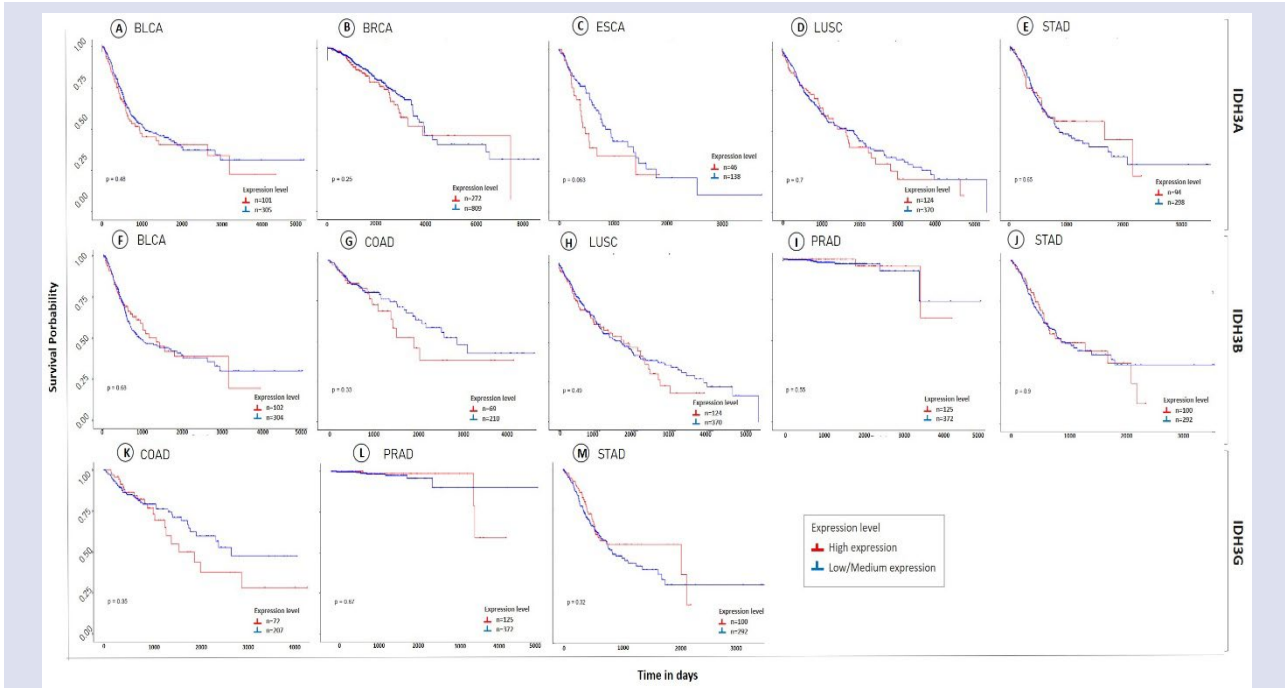
Figure 3. The effect of IDH3 subunits expressions on patient survival status.

Kaplan Meier plot showing the survival status of cancer patients in high and low gene expression of IDH3A (A-E), IDH3B (F-J), and IDH3G (K-M). The x-axis represents days and the y-axis represents the survival probability. The survival probability data were collected from the UALCAN web portal.

The Mutations in all IDH3 Subunits were low Frequency in the ten Major Cancer Types

Mutations in the metabolic enzymes have an essential role in the carcinogenesis. The effect of D-2-HG oncometabolite, which is produced with mutant IDH 1/2 enzymes, has mainly been studied in different types of cancer progression, such as breast and colon [15,17]. However, the mutation status in IDH3 subunits and the effect of these mutations on gene expression are not very well known in the ten major cancer types. The alteration status of IDH3A, IDH3B, and IDH3G was examined on PanCancer Atlas data of the ten major cancer types by cBioPortal for Cancer Genomics [25]. The analysis included both mutations and copy numbers in 4954 samples. Mutation types and locations on IDH3A, IDH3B, and IDH3G genes are presented in Supplementary Fig. 3 and Supplementary Fig. 4.

The cumulative alteration rates revealed low-frequency mutations in all IDH3 subunits (Fig. 4). Among

all subunits, the highest mutation and copy number alterations were observed in the IDH3G, with a cumulative alteration rate of 5.9 % in STAD (Fig. 4C). Afterwards, cumulative alteration frequency was observed in the IDH3B in BRCA (2.46 %) (Fig. 4B). The lowest cumulative alteration frequency was observed in the IHD3A. The highest IDH3A mutation and copy number alterations were observed in LUSC (1.66 %) (Fig. 4A). Focusing on only mutation frequency, the highest mutation rate of the IDH3G gene is 1.5 %, and they mostly contain missense mutations (23) (Supplementary Fig. 3; Supplementary Fig. 4C; Supplementary Fig. 5C). The highest mutation rate of IDH3A and IDH3B genes are 1.1 % in COAD and ESCA, respectively (Supplementary Fig. 5A, B). There is no mutation in prostate cancer in all IDH3 subunits (Supplementary Fig. 5). Genetic alterations of mutated IDH3A and IDH3B are missense, truncating, and splice mutations (Supplementary Fig. 3). However, the frequencies differ for genes (Supplementary Fig. 4A, B). In addition, inframe mutations are also observed in mutated IDH3G (Supplementary Fig. 4C). The locations of mutations in all IDH3 subunits are also included in Supplementary Fig. 3, and the results showed that there have been mutational overlaps in all IDH3 subunits.
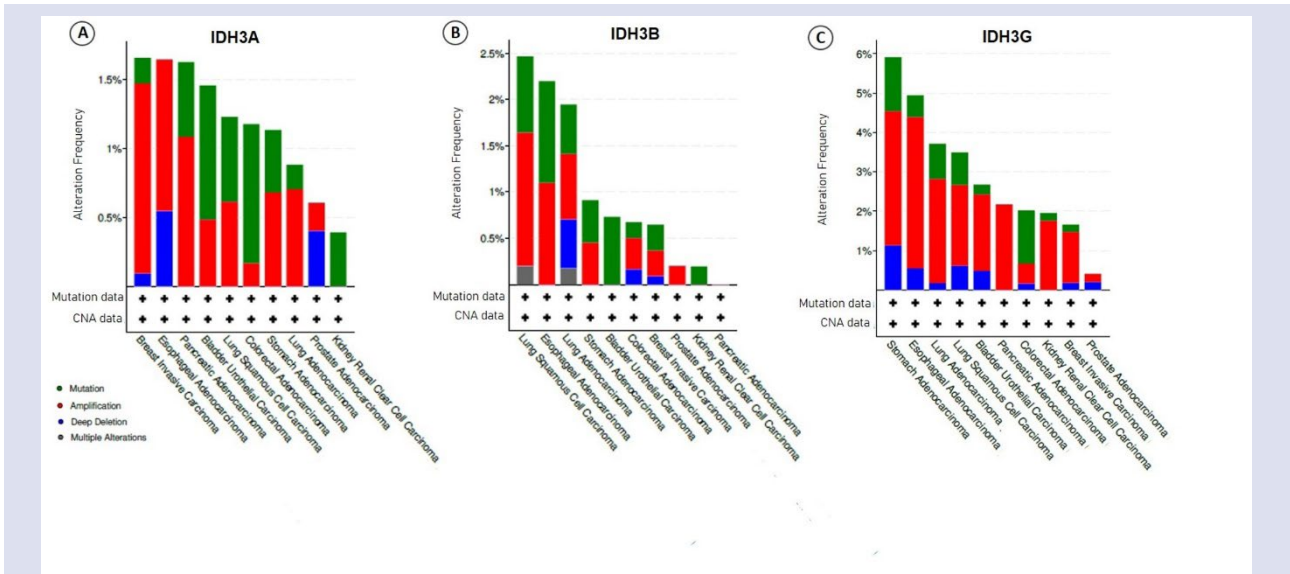
Figure 4. Alteration frequency of IDH3 subunits in TCGA PanCancer datasets.

The cumulative mutation rate of IDH3A (A), IDH3B (B), and IDH3G (C) were analyzed through the cBioPortal web tool by using samples (n=4954) in the TCGA PanCancer Atlas Study. In addition to mutation, amplification, deep deletion, and multiple alterations in IDH3 subunits are observed in the ten most common cancer types (A-C).

The Mutations in the IDH3 Subunits Directly Affect the Gene Expression

After investigating the mutation status of IDH3 subunits, the effect of mutations on the gene expression of IDH3 subunits was examined through the cBioPortal for Cancer Genomics [25]. Mutations in the IDH3A caused a moderate decrease in gene expression in BLCA (Fig. 5A).

The IDH3A expression was highly decreased after mutations in KIRC, LUSC, and STAD (Fig. 5D, F, H) and highly increased in BRCA, COAD, LUAD, and PAAD (Fig. 5B, C, E, G). Mutations in the IDH3B and IDH3G generally caused a decrease in gene expression in all cancer types. The IDH3B expression was moderately decreased after mutations only in the COAD (Fig. 5K) and highly decreased in the BLCA, ESCA, KIRC, LUAD, and LUSC (Fig. 5I, L, M, N, O). It was moderately and highly increased in BRCA and STAD after mutation, respectively (Fig. 5J, P). Mutations in the IDH3G did not affect the expression of the IDH3G gene in BLCA (Fig. 5R). Mutations in the IDH3A caused a moderate decrease in gene expression in BRCA, KIRC, and LUAD (Fig. 5S, V, Y), and it caused a slight decrease in COAD, ESCA, LUSC, and STAD carcinoma (Fig. 5T, U, Z, X).
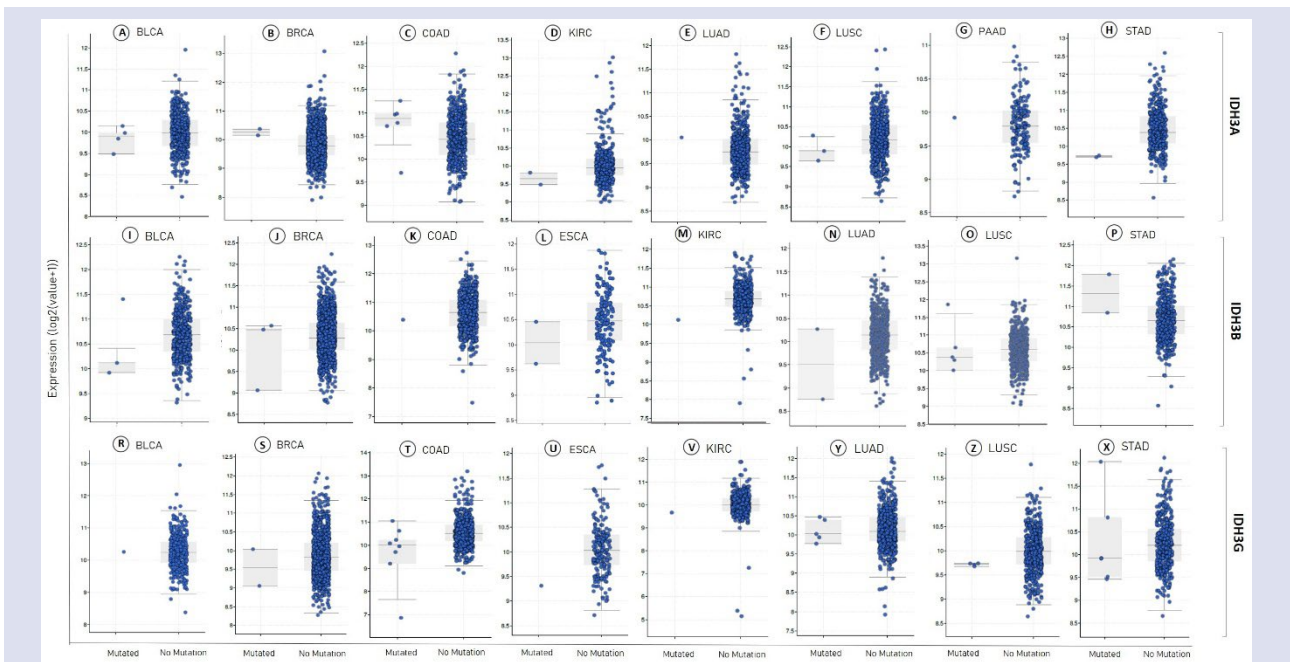
Figure 5. The IDH3A, IDH3B, and IDH3G gene mutations directly affect gene expression.

Box plots exhibit the expression level of IDH3A (A-H), IDH3B (I-P), and IDH3G (R-X) in IDH3A (A-H), IDH3B (I-P), and IDH3G (R-X) mutant and non-mutant in the bladder, breast, colorectal, esophageal, kidney, lung, pancreas, prostate, and stomach cancers.

The most up-to-date sources should be used in the discussion

Discussion

The IDH enzyme was first isolated in 1972 from *E.coli* [27], and later studies focused on its potential catabolic role in the TCA cycle [1]. It is essential for the metabolism of normal mammalian cells because it is located at the key branching point in carbohydrate metabolism and carries out the reaction of the rate-limiting step [14, 41]. All IDH-mediated reactions that result from α-KG, NADH, NADPH, or isocitrate production are of great moment for tumor cells. IDH serves a diverse biological function, which role in cellular defence against oxidative damage, determines the $NADP^+/NADPH$ ratio, and participates in lipid metabolism [28, 29]. In addition to their roles, IDH1/2 isoforms promote tumor proliferation in different cancer types [14-19]. However, the studies about IDH3 are limited [30-31], and no studies have investigated the effect of gene expression profiles in the IDH3 subunits on the various cancer progressions and the relation between mutation frequencies of IDH3 subunits and cancer progression.

As known, a biomarker gene should be associated with disease progression and treatment response [26]. It was found that the expression level of IDH3A, IDH3B, and IDH3G is higher in esophageal, lung squamous cell, and colon tumors according to normal tissues, respectively (Fig. 1). The expression level of IDH3 subunits increased as the bladder, breast, colon, esophageal, lung, and stomach cancers progressed (Fig. 2). High IDH3 subunit expression led to decreased survival probability in colon, esophageal, lung, prostate, and stomach carcinomas (Fig. 3). All results are combined in Supplementary Fig. 6. IDH3A showed higher gene expression and lower survival probability for esophageal, lung, and stomach (Supplementary Fig. 6 A, B, C), IDH3B showed higher gene expression and lower survival probability for lung and stomach (Supplementary Fig. 6 D, E), and IDH3G showed higher gene expression and lower survival probability for colon, prostate, and stomach cancers (Supplementary Fig. 6 F, G, H). All the data indicate that IDH subunits are predictive value for cancer detection.

Investigating how the expression of IDH isoforms changes according to cancer stages is essential for pathophysiological studies. Obtaining cancer stage-specific data has clinical implications in various aspects, such as early diagnosis of cancer and improving personalized treatment [32]. In our study, target gene expression levels were investigated in the different cancer stages. We found that the expression of IDH3A, IDH3B, and IDH3G interestingly showed specific differences and heterogeneity in the ten major types of cancer (Fig. 1; Fig.

2; Supplementary Fig. 1). Then, mRNA levels of IDH3A, IDH3B, and IDH3G based on tumor grade were examined, and the data showed a direct relationship between the expression of IDH subunits and the progression of cancer (Fig. 2). In our study, the gene expression of three subunits of IDH3 was also changed in the same tumor types. Another study found that IDH3A is associated with tumorigenesis of hepatocellular carcinoma and glioblastoma [30-31]. However, no study is related to the expression level of IDH3 subunits in the different cancer types. We have examined the effect of elevated IDH3 expression on survival probability, and it was found that high expression of IDH3 subunits in the bladder, colon, esophageal, lung, prostate, and stomach tumor tissues leads to a poor prognosis (Fig. 3), similar to a previous study [11].

Wild-type IDH1 and IDH2 are essential enzymes that have a role in the growth and progression of different kinds of tumors. In addition to wild-type isoforms, the mutant IDH1/2 enzymes perform oncogenic activities [33]. Some tumor types, the mutation frequencies of the IDH1 and IDH2 genes are very high [34]. In contrast to its isoforms IDH1 and IDH2, the mutation in the IDH3 does not lead to 2-hydroxyglutarate production [14]. Our study found that cumulative alteration rates were low frequency in all IDH3 subunits (Fig. 4). However, it has been dramatically affecting gene expression in some cancer types such as the bladder (Fig. 5I), breast (Fig. 5B), colon (Fig. 5C), esophageal (Fig. 5L, U), kidney (Fig. 5M), lung (Fig. 5E, F, N), and stomach (Fig. 5H, P). To comprehend the spatial expression profiles of the subunits and their role in carcinogenesis, the correlation between the mutation frequencies of IDH3 subunits and cancer progression is examined and results were combined in Supplementary Fig. 7. The highest mutation frequency of IDH3A was observed in breast invasive carcinoma and esophageal adenocarcinoma, and a relationship was observed between mutation frequency and cancer progression (Supplementary Fig. 7A). The relation between high mutation frequency of IDH3B and cancer progression was observed in lung squamous cell carcinoma and esophageal adenocarcinoma (Supplementary Fig. 7B). The relation between high mutation frequency of IDH3G and cancer progression was observed in stomach and esophageal adenocarcinoma (Supplementary Fig. 7C). In the literature, most studies related to mutations in IDH3 subunits focus on diseases such as pseudo-coloboma, epileptic encephalopathy, and retinitis pigmentosa [9-10, 35-36]. Krell et al. (2011) found that IDH3 mutations were not glioblastoma-associated in cancer-related studies [37]. However, our data showed that there may be a relation between the mutation of IDH3 subunits and different kinds of cancer progression.

In the present study, cancer-specific IDH3 subunits were determined for the ten major cancer types, and we found target cancer types for IDH3A, IDH3B, and IDH3G. Until now, studies on the role of IDH3 subunits in tumor development and progression are limited to a few tumors. Zeng et al. (2015) find that IDH3A can be a therapeutic

target for breast and lung cancers [11]. Wu et al. (2019) studied the role of IDH3B in esophageal cell proliferation *in vitro* and *in vivo* [38]. The results demonstrated that overexpression of IDH3B contributes to esophageal cell proliferation and is related to poor prognosis in patients with ESCC. In another study, it was found that the level of IDH3G was higher in gastric cancer tumor tissue than in normal tissue [39]. Knockdown of IDH3G leads to the sensitization of gastric cancer cells to drugs (epirubicin, cisplatin) [40]. In another way, some inhibitors (Vorasidenib and ivosidenib) are using for mutant IDH1 and IDH2 enzymes to combat with different type of cancers [42, 43].

In conclusion, our data showed that there might be a relation between the mutation of IDH3 subunits and breast, esophageal, lung, and stomach cancer progression. The results demonstrated that strategies targeting IDH3A and IDH3B for lung and stomach cancers, IDH3A for esophageal cancer, and IDH3G for colon, prostate, and stomach cancers might greatly benefit cancer management. However, these results were obtained only as a result of bioinformatics analyses and in vitro experiments were not performed. It is planned to study the IDH3 subunits in their related cancer types to find the effect of mutation on cancer progression by *in vitro* methods.

Conflict of interest

There are no conflict of interest in this work.

Acknowledge

Ethical Approval Statement

Any human subjects and animals are not used in this study.

References

[1] D'Adamo Jr A.F., Haft D.E., An alternate pathway of α-ketoglutarate catabolism in the isolated, perfused rat liver: I. Studies with dl-glutamate-2-and-5-14C, *Journal of Biological Chemistry*, 240 (2) (1965) 613-617.

[2] Pollard P.J., Ratcliffe P.J., Puzzling patterns of predisposition, *Science*, 324 (5924) (2009) 192-194.

[3] Rosiers C., Fernandez C.A., David F., Brunengraber H., Reversibility of the mitochondrial isocitrate dehydrogenase reaction in the perfused rat liver. Evidence from isotopomer analysis of citric acid cycle intermediates, *Journal of Biological Chemistry*, 269 (44) (1994) 27179-27182.

[4] Barnes L.D., Kuehn G.D., Atkinson D.E., Yeast diphosphopyridine nucleotide specific isocitrate dehydrogenase. Purification and some properties, *Biochemistry*, 10 (21) (1971) 3939-3944.

[5] Huang Y.C., Colman R.F., Subunit location and sequences of the cysteinyl peptides of pig heart NAD-dependent isocitrate dehydrogenase, *Biochemistry*, 29 (36) (1990) 8266-8273.

[6] Ma T., Peng Y., Huang W., Liu Y., Ding J., The β and γ subunits play distinct functional roles in the α2βγ heterotetramer of human NAD-dependent isocitrate dehydrogenase, *Scientific Reports*, 7 (1) (2017) 41882.

[7] Huh T.L., Kim Y.O., Oh I.U., Song B.J., Inazawa J., Assignment of the Human Mitochondrial NAD+-Specific Isocitrate Dehydrogenase α Subunit (IDH3A) Gene to 15q25.1→q25.2 by in Situ Hybridization, *Genomics*, 2 (32) (1996) 295-296.

[8] Hartong D.T., Dange M., McGee T.L., Berson E.L., Dryja T.P., Colman R.F., Insights from retinitis pigmentosa into the roles of isocitrate dehydrogenases in the Krebs cycle, *Nature Genetics*, 40 (10) (2008) 1230-1234.

[9] Zhu S., Huang J., Xu R., Wang Y., Wan Y., McNeel R., Schwaid A.G., Chen X., Zhang Y., Du J., Isocitrate dehydrogenase 3b is required for spermiogenesis but dispensable for retinal viability, *Journal of Biological Chemistry*, 298 (9) (2022).

[10] Sun W., Zhang Q., A novel variant in IDH3A identified in a case with Leber congenital amaurosis accompanied by macular pseudocoloboma, *Ophthalmic Genetics*, 39 (5) (2018) 662-663.

[11] Zeng L., Morinibu A., Kobayashi M., Zhu Y., Wang X., Goto Y., Harada H., Aberrant IDH3α expression promotes malignant tumor growth by inducing HIF-1-mediated metabolic reprogramming and angiogenesis, *Oncogene*, 34 (36) (2015) 4758-4766.

[12] Bhat, G.R., Sethi, I., Sadida, H.Q., Rah, B., Mir, R., Algehainy, N., Albalawi, I.A., Masoodi, T., Subbaraj, G.K., Jamal, F., Singh, M., Kumar, R., Macha, M.A., Uddin, S., Al-Shabeeb Akil, A.S., Haris, M., Bhat, A.A. Cancer cell plasticity: From cellular, molecular, and genetic mechanisms to tumor heterogeneity and drug resistance. *Cancer and Metastasis Reviews*, 43(1) (2024) 197-228.

[13] Sung H., Ferlay J., Siegel R.L., Laversanne M., Soerjomataram I., Jemal A., Bray F., Global cancer statistics 2020: GLOBOCAN estimates of incidence and mortality worldwide for 36 cancers in 185 countries, *CA: a cancer journal for clinicians*, 71 (3) (2021) 209-249.

[14] Nadhan R., Kashyap S., Mertens K., The role of isocitrate dehydrogenase in cancer and aging, *Journal of Clinical Medicine*, 9 (4) (2020) 1135.

[15] Atalay E.B., Kayali H.A., Aydin N., Yilmaz G., The elevated D-2-hydroxyglutarate level found as a characteristic metabolic change of colon cancer in both in vitro and in vivo models, *Biochemical and Biophysical Research Communications*, 627 (2022) 191-199.

[16] Atalay E.B., Senturk S., Kayali H.A., Aydin N., Wild-type IDH1 Knockout Leads to G0/G1 Arrest, Impairs Cancer Cell Proliferation, Altering Glycolysis, and the TCA Cycle in Colon Cancer, *Biochemical Genetics*, (2023) 1-17.

[17] Špačková J., Gotvaldová K., Dvořák A., Urbančoková A., Pospíšilová K., Větvička D., Mottl R., Smolková K., Biochemical background in mitochondria affects 2HG production by IDH2 and ADHFE1 in breast carcinoma, *Cancers*, 13 (7) (2021) 1709.

[18] Li H., Li J.J., Lu W., Yang J., Xia Y., Huang P., Targeting Mitochondrial IDH2 Enhances Antitumor Activity of Cisplatin in Lung Cancer via ROS-Mediated Mechanism, *Biomedicines*, 11 (2) (2023) 475.

[19] Zarei M., Hajihassani O., Hue J.J., Graor H.J., Rothermel L.D., Winter J.M., Targeting wild-type IDH1 enhances chemosensitivity in pancreatic cancer, *BioRxiv*, (2023) 2023-03.

[20] Chhikara B.S., Parang K., Global Cancer Statistics 2022: the trends projection analysis, *Chemical Biology Letters*, 10 (1) (2023) 451-451.

[21] Iscan E., Karakülah G., Ekin U., Ozturk M., Uzuner H., Suner A., TAp73α is Upregulated in the Most Common Human Cancers, *Molecular Biology*, 56 (2) (2022) 251-256.

[22] Guneri-Sozeri P.Y., Erkek-Ozhan S., Identification of the gene expression changes and gene regulatory aspects in ELF3 mutant bladder cancer, *Molecular Biology Reports*, 49 (4) (2022) 3135-3147.

[23] Chandrashekar D.S., Bashel B., Balasubramanya S.A.H., Creighton C.J., Ponce-Rodriguez I., Chakravarthi B.V., Varambally S., UALCAN: a portal for facilitating tumor subgroup gene expression and survival analyses, *Neoplasia*, 19 (8) (2017) 649-658.

[24] Atalay E.B., Aydin N., Yilmaz G., Ozturk M., Gene expression changes of isocitrate dehydrogenase 1 and isocitrate dehydrogenase 2 affect carcinogenesis and survival probability, *Gümüşhane University Journal Science Technology*, 14 (1) (2024) 370-378.

[25] Cerami E., Gao J., Dogrusoz U., Gross B.E., Sumer S.O., Aksoy B.A., Angarita F.A., Delong L., Reese M., Schaefer C.F., Zhang W., Gabrielli A., Wang W., Sander C., Schultz N., The cBio cancer genomics portal: an open platform for exploring multidimensional cancer genomics data, *Cancer Discovery*, 2 (5) (2012) 401-404.

[26] Sheng K.L., Kang L., Pridham K.J., Dunkenberger L.E., Sheng Z., Varghese R.T., An integrated approach to biomarker discovery reveals gene signatures highly predictive of cancer progression, *Scientific Reports*, 10 (1) (2020) 21246.

[27] Reeves H.C., Daumy G.O., Lin C.C., Houston M., NADP+-specific isocitrate dehydrogenase of Escherichia coli: I. Purification and characterization, *Biochimica et Biophysica Acta (BBA)-Enzymology*, 258 (1) (1972) 27-39.

[28] Koh H.J., Lee S.M., Son B.G., Lee S.H., Ryoo Z.Y., Chang K.T., Moon Y., Huh T.L., Cytosolic NADP+-dependent isocitrate dehydrogenase plays a key role in lipid metabolism, *Journal of Biological Chemistry*, 279 (38) (2004) 39968-39974.

[29] Jo S.H., Son M.K., Koh H.J., Lee S.M., Song I.H., Kim Y.O., Lee J.H., Lee H.J., Huh T.L., Control of mitochondrial redox balance and cellular defense against oxidative damage by mitochondrial NADP+-dependent isocitrate dehydrogenase, *Journal of Biological Chemistry*, 276 (19) (2001) 16168-16176.

[30] Liu X., Qiao Y., Ting X., Si W., Isocitrate dehydrogenase 3A, a rate-limiting enzyme of the TCA cycle, promotes hepatocellular carcinoma migration and invasion through regulation of MTA1, a core component of the NuRD complex, *American Journal of Cancer Research*, 10 (10) (2020) 3212.

[31] May J.L., Kouri F.M., Hurley L.A., Liu J., Tommasini-Ghelfi S., Ji Y., Xu Z., Morrow J.L., Westfield G., Stegh A.H., IDH3α regulates one-carbon metabolism in glioblastoma, *Science Advances*, 5 (1) (2019) eaat0456.

[32] Bensalah K., Montorsi F., Shariat S.F., Challenges of cancer biomarker profiling, *European Urology*, 52 (6) (2007) 1601-1609.

[33] He Q., Chen J., Xie Z., Chen Z., Wild-Type Isocitrate Dehydrogenase-Dependent Oxidative Decarboxylation and Reductive Carboxylation in Cancer and Their Clinical Significance, *Cancers*, 14 (23) (2022) 5779.

[34] Carosi, F., Broseghini, E., Fabbri, L., Corradi, G., Gili, R., Forte, V., Roncarati, R., Filippini, D.M., Ferracin, M., Targeting isocitrate dehydrogenase (IDH) in solid tumors: Current evidence and future perspectives. *Cancers*, 16 (15) (2024) 2752.

[35] Fattal-Valevski A., Eliyahu H., Fraenkel N.D., Elmaliach G., Hausman-Kedem M., Shaag A., Tene O., Kanner A., Elpeleg O., Homozygous mutation, p. Pro304His, in IDH3A, encoding isocitrate dehydrogenase subunit is associated with severe encephalopathy in infancy, *Neurogenetics*, 18 (2017) 57-61.

[36] Peter V.G., Nikopoulos K., Quinodoz M., Granse L., Farinelli P., Superti-Furga A., Andréasson S., Rivolta, C., A novel missense variant in IDH3A causes autosomal recessive retinitis pigmentosa, *Ophthalmic Genetics*, 40 (2) (2019) 177-181.

[37] Krell D., Assoku M., Galloway M., Mulholland P., Tomlinson I., Bardella C., Bourton T., Wilkins S., Screen for IDH1, IDH2, IDH3, D2HGDH and L2HGDH mutations in glioblastoma, *PloS One*, 6 (5) (2011) e19868.

[38] Wu Q., Zhang W., Xue L., Wang Y., Fu M., Ma L., Zhang L., Li B., Lin X., Zhan Q.M., APC/C-CDH1–Regulated IDH3β Coordinates with the Cell Cycle to Promote Cell Proliferation, *Cancer Research*, 79 (13) (2019) 3281-3293.

[39] Wang X., Xu B., Du J., Xia J., Lei G., Zhou C., Feng Y., Zhang H., Li Y., Characterization of pyruvate metabolism and citric acid cycle patterns predicts response to immunotherapeutic and ferroptosis in gastric cancer, *Cancer Cell International*, 22 (1) (2022) 1-20.

[40] Zhou J., Yong W.P., Yap C.S., Vijayaraghavan A., Sinha R.A., Singh B.K., Kwok T.C., Leung T., Tan H.M., Koh Y.W., Wong R.S., Lam K.P., An integrative approach identified genes associated with drug response in gastric cancer, *Carcinogenesis*, 36 (4) (2015) 441-451.

[41] Huang K., Han Y., Chen Y., Shen H., Zeng S., Cai C., Tumor metabolic regulators: key drivers of metabolic reprogramming and the promising targets in cancer therapy, *Molecular Cancer*, 24(1) (2025) 7.

[42] Mellinghoff I. K., Lu M., Wen P. Y., Taylor J. W., Maher E. A., Arrillaga-Romany I., Peters K.B., Ellingson B.M., Rosenblum M.K., Chun S., Le K., Tassinari A., Choe S., Toubouti Y., Schoenfeld S., Pandya S.S., Hassan I., Steelman L., Clarke J.L., Cloughesy T.F., Vorasidenib and ivosidenib in IDH1-mutant low-grade glioma: a randomized, perioperative phase 1 trial, *Nature medicine*, 29(3) (2023) 615-622.

[43] Zarei M., Hajihassani O., Hue J. J., Loftus A. W., Graor H. J., Nakazzi F., Naji P., Boutros C.S., Uppin V., Vaziri-Gohar A., Shalaby A.S., Asara J. M., Rothermel L.D., Brody J.R., Winter J.M., IDH1 inhibition potentiates chemotherapy efficacy in pancreatic cancer, *Cancer Research*, 84(18) (2024) 3072-3085.

Cumhuriyet Science Journal

Investigation of Anti-CA II Antibodies in The Sera of *Helicobacter Pylori* Infected Patients

Sibel Yiğit Alaşalvar [1,a] , , Elif Şahin [1,b,*], Eşref Edip Keha [1,c]

[1] Department of Medical Biochemistry, Faculty of Medicine, Karadeniz Technical University, Trabzon, Türkiye
*Corresponding author

Research Article

ABSTRACT

It has been postulated that there may be a correlation between gastric infection caused by *Helicobacter pylori (H. Pylori)* and autoimmune pancreatitis (AIP). An increase in carbonic anhydrase II (CA II) autoantibodies was found in the sera of patients with AIP and it was suggested that measurement of these autoantibodies could be used in the diagnosis of AIP. In this study, the levels of CA II autoantibodies have been determined in the sera of the patients with *H. pylori*-infected gastritis and gastric ulcer. Anti-CA II antibody levels in the sera of these individuals were measured by ELISA method. There were significant differences between the control group and the *H. pylori*-infected gastric ulcer group and the gastritis group. When the *H. pylori*-infected and non-infected gastric ulcer and gastritis groups were compared, it became apparent that there were notable differences. The results indicated that the CA II antibodies in the sera of the *H. pylori*-infected patients were present at a rate of 8.3%. This led to the conclusion that CA II antibodies may not be a reliable marker for *H. pylori* infection. However, the investigation did demonstrate a clear increase in the levels of CA II antibodies for *H. pylori*-infected patients.

Keywords: Helicobacter pylori, anti-CA II, autoimmune disease, ELISA.

[a] sibelalasalvar@gmail.com   https://orcid.org/0000-0003-4472-7554   [b] elifsahin@ktu.edu.tr   https://orcid.org/0000-0001-5864-9548
[c] edipkeha@yahoo.com   htpps://orcid.org/0000-0002-2271-5811

Introduction

It has been suggested that *Helicobacter pylori*, a bacterium that has been linked to conditions such as peptic ulcer, gastritis and stomach cancer, may encode carbonic anhydrase II (CA II, EC 4.2.1.1), which could be a potential antibacterial drug target [1]. It is thought that the enzyme is involved in a number of important physiological processes in various tissues, including the transport of CO_2 and ions, renal and male reproductive tract acidification, electrolyte secretion, the formation of gastric acid, bone resorption, ureagenesis, gluconeogenesis, lipogenesis and body fluid generation [2,3]. It is interesting to note that *H. pylori* produces two distinct forms of HpCA, α and β, which exhibit differential localisations within the bacterial cell. α-HpCA, which is highly homologous to CA-II, is anchored to the surface of the bacterium. Consequently, it represents an optimal target for host immunity, as a surface antigen. From a functional perspective, α-HpCA appears to play a role in gastric colonization and acid acclimation in the gastric environment, which could be important for the survival and proliferation of *H. pylori* [4].

Autoimmune diseases are understood to originate from the immune responses of the body to its own antigens [5]. Autoimmune pancreatitis (AIP) is a specific form of pancreatitis that may present with obstructive jaundice, pancreatic masses, lymphoplasmacytic infiltrate and fibrosis, and a marked response to steroids. AIP is estimated to account for 4.6–6% of all chronic pancreatitis

cases and is often associated with other autoimmune diseases, particularly Sjögren's syndrome [6]. Inagaki et al. [7] were the first to report the presence of anti-CA II antibodies in the sera of patients with systemic lupus erythematosus (SLE) and Sjögren's syndrome (SjS). Furthermore, it was demonstrated that autoimmune sialoadenitis and immune-mediated pancreatitis could be induced in animal models by immunization with human CA II. Subsequent studies have demonstrated the presence of autoantibodies against CA I and/or CA II in sera from patients with a range of autoimmune disorders, including SjS, SLE, endometriosis, type 1 diabetes, primary biliary cirrhosis, idiopathic chronic pancreatitis, and ulcerative colitis [3]. Antibodies against human CA-II, an enzyme located in the pancreatic ductal epithelium, and lactoferrin are frequently present in the serum of patients affected by AIP, thus suggesting a role for these proteins as autoantigens in the disease [8,9]. In particular, the significance of anti-CA-II autoantibodies in the diagnosis of AIP has been recently corroborated [10]. The theory of microbiological triggering of autoimmunity has been proposed for several decades, based on epidemiological data indicating an increased prevalence of autoimmune diseases following specific infections. A relationship between gastric infection by *H. pylori* and AIP has been reported in the scientific literature. An increase in anti-CA II antibodies has been demonstrated in AIP, and their measurement in the sera of AIP-affected subjects has

been proposed as a diagnostic tool [11]. Furthermore, a striking similarity between the *H. pylori* α-hpCA enzyme and CA II has been demonstrated through *in silico* methods. It has been postulated that α-CA antibodies may exhibit analogous autoimmune effects as CA II autoantibodies [12,13]. In order to confirm the *in silico* results by in vitro methods, the levels of CA II autoantibodies have been determined in the sera of patients with *H. pylori*-infected gastritis and gastric ulcer.

Materials and Methods

Determination of Study Groups

Once the approval had been received from the Karadeniz Technical University Medical Faculty Ethical Committee, Trabzon, Turkey, informed consent was obtained from all subjects (2006/18). Patients with *H. pylori* diagnosed by a gastroenterology consultant and healthy volunteers were recruited. The groups were formed according to the patients' status and the presence of *H. pylori*, as detailed in Table 1. The gender of the patients was not taken into account when the groups were formed.

Table 1. The ages and gender distribution of the study groups

Groups	Control	*H.pylori* (-) ulcer	*H.pylori* (-) gastritis	*H.pylori* (+) ulcer	*H.pylori* (+) gastritis
Age distribution	19-66	22–65	25-67	25-70	24–68
Sex (male/female)	19/11	13/17	16/14	13/17	10/20

Enzyme-linked immunosorbent assay (ELISA) for serum antibody to CA II

The ELISA method developed by Hosoda et al. [14] was modified and used to determine CA II autoantibody levels of the individuals in the study groups. Measurements were repeated twice for each sample.

Assay protocol

Blood samples were collected from the brachial vein using the venipuncture technique at the time of presentation. Serum specimens were obtained using Vacutainer tubes and subjected to centrifugation at 3000 rpm for a period of 10 minutes. The specimens to be utilized for the measurement of anti-CA II antibody blood concentrations were transferred into Eppendorf tubes and stored at a temperature of -80°C. Human CA II, purified from erythrocytes by electrophoresis, was purchased from Sigma Chemical Co. (St. Louis, MO). The presence of anti-CA II antibodies in serum was determined by ELISA. In brief; the wells in the ELISA plate were coated with 50 μL of CA-II diluted in coating buffer (carbonate buffer 0.05 mM, pH: 9.6) with a concentration of 10 μg/mL

and incubated at +4°C for 18 hours. The plate was washed with phosphate buffer (pH 7.0) 3 times at 5 min intervals. After washing, 200 μL of blocking buffer (2% skim milk in phosphate buffer) was added to the wells and incubated on a shaker for 2 hours at room temperature. After blocking, the plate was washed 3 times with phosphate buffer containing 0.05% Tween-20. The wells were incubated with 100 μL of serum diluted with dilution buffer (1:200) for two hours at room temperature. Following the washing step, each well was incubated with 100 μL antibody (peroxidase-conjugated anti-human IgG anti-serum) diluted 1/2000 with dilution buffer containing 1% BSA and kept on shaker for two hour at room temperature. The plate was washed 3 times with phosphate buffer containing 0.05% Tween-20. After washing, the wells were incubated with 100 μL of substrate solution and kept in the dark for 25 minute at room temperature. The reaction was stopped by pipetting 100 μL of 2M H_2SO_4 into all wells. Absorbance was read at 485 nm on an ELISA reader.

All assays were performed in duplicate, and the specific binding of serum antibody to CA II was calculated as follows: the average absorbance of the antigen-coated wells was subtracted from the average absorbance of the control wells (specific binding = A_{coated} - $A_{control}$)

Statistical Analysis

SPSS (IBM SPSS Statistics 17) programme was used for statistical analysis of the data. The conformity of the groups to normal distribution was determined by Kolmogorov-Smirnov test. The statistical difference between the mean values of the groups was tested by One-way ANOVA and Post Hoc Tukey test. Results were expressed as mean and standard deviation (X±SD). $p < 0.05$ was considered statistically significant.

Results

The sera of 30 control, 30 H. Pylori negative ulcer, 30 H.pylori negative gastritis, 30 H.Pylori positive ulcer, 30 H.Pylori positive gastritis patients were analysed and the binding of CA II autoantibodies against pure human CA II was determined with ELISA method. Sera with a mean absorbance value > 0.437 were considered to have a positive reaction. This value was calculated by adding 3 SD values (0.225) to the mean absorbance value (X=0.212) of the sera of the control group. (X±S.D) values of the other groups are shown in Table 2. According to the cut off value of the control group, there were 0 positive results in the control group, 2 (6.6%) in the *H.Pylori* (-) ulcer group, 1 (3.3%) in the *H.Pylori* (-) gastritis group, 2 (6.6%) in the *H.Pylori* (+) ulcer group and 3 (10%) in the *H.Pylori* (+) gastritis group. As stated, no positive results were found in the control group (Figure 1). The values showing the significance level of the difference between the groups are given in Table 3. The antibody-positive prevalence rate and the mean absorbance value of *H.Pylori* (+) ulcers (0.307 ± 0.119) and *H. Pylori* (+) gastritis (0.291 ± 0.119) were found to be significantly higher compared with that of control subjects. There was no significant difference in

the prevalence rates and the mean absorbance value between *H. Pylori* (-) ulcers (0.253 ± 0.088) and *H. Pylori* (-) gastritis (0.192 ± 0.083) and control subjects. The antibody-positive prevalence rate and the mean absorbance value of H. pylori-(+) ulcers (0.307 ± 0.119) were found to be significantly higher than those of H. Pylori (-) ulcers (0.253 ± 0.088). The antibody-positive

prevalence rate and the mean absorbance value of H. Pylori (+) gastritis (0.291 ± 0.119) were found to be significantly higher than that of H. Pylori (-) gastritis (0.192 ± 0.083). There was no significant difference in the prevalence rates and the mean absorbance value between H. Pylori (+) gastritis (0.291 ± 0.119) and H. Pylori (-) gastritis (0.192 ± 0.083).

Table 2. Serum Anti CA II antibody levels in groups

	Control	*H.pylori* (-) ulcer	*H.pylori* (-) gastritis	*H.pylori* (+) ulcer	*H.pylori* (+) gastritis
Anti CA II antibody	0.212±0.075	0.253±0.088	0.192±0.083	0.307±0.119	0.291±0.119

The data were expressed as mean ± standard deviation (X±SD).

Table 3. p values between the groups (* statistically signficant $p<0.05$)

Groups	Control	*H.pylori* (-) gastritis	*H.pylori* (-) ulcer	*H.pylori* (+)gastritis	*H.pylori* (+) ulcer	
Control		0.980	0.062	*0.001	*0.00041	P
H.pylori (-) gastritis	0.980	0.104		* 0.00038		P
H.pylori (-) ulcer	0.062			* 0.048		P
H.pylori (+) gastritis	*0.001	* 0.00038				P
H.pylori (+) ulcer	*0.00041		* 0.048			P
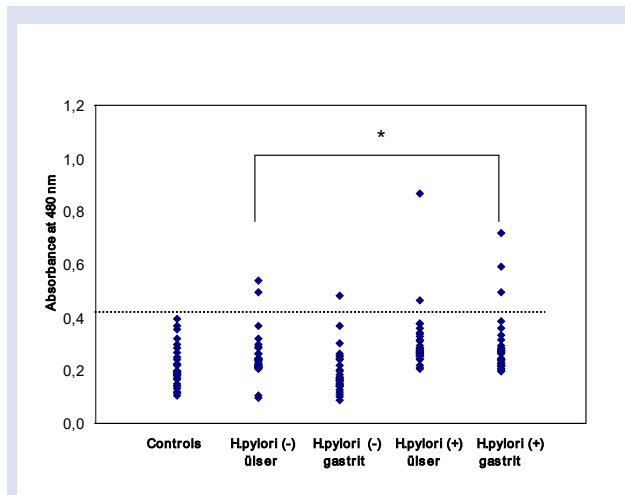
Figure. 1 The presence of anti-CA II antibodies in sera from patients and healthy controls was investigated. The dotted line indicates the mean value plus three standard deviations of healthy control sera (A_{480} = 0.437). A significant difference was observed in the comparison of the mean ± SD value between GD and normal controls ($p < 0.05$).

Discussion

Carbonic anhydrases are ubiquitous metalloenzymes present in prokaryotes and eukaryotes (14). CA II is widespread enzyme, present in mammals tissues. It catalyzes the irreversible hydration of CO_2 provides bicarbonate, a substrate for many reactions and in acid-base equilibrium and plays important roles in regulation of cardiovascular tonus and control of ion exchange between cell compartments [15]. Autoantibodies may be developed response to injured or antigenically altered tissues. In 1991, Inagaki et al. [7] first investigated anti CA II antibodies in the sera of patients of systemic lupus

erythematosus and Sjögren's syndrome. It couldn't be explained that as a sytoplasmic enzyme how CA II antibodies causes cellular damage that seen in autoimmune diseases. But in the recent years the investigation of anti CA II antbodies in the sera of patients with autoimmune pancreatitis (AIP) gave rise to tought use of the positivity of anti CAII antibodies as a criteria in the diagnosis of this disease. Guarneri et al. [11] mentioned that subjects infected by Helicobacter pylori and have genetically bent have had AIP and AIP-anti CAII and based on the occurrence of AIP in some genetically predisposed individuals and the association of AIP-anti CA II, they determined a large amount of homology between the H. pylori α-hpCA enzyme and CA II in a fully computerized (in silico method). It was reported that α-hpCA antibodies may exhibit autoimmune effects similar to anti CA II.

In this study, *in vitro* determination in the sera of *H. pylori* infected individuals was aimed according to the hypotesis of Guarneri et al. suggested the data obtained from *in silico* method. For this purpose, five study group of thirty subjects each of those was evaluated by a gastroeneterologist were formed.The ELISA method developed by Hosoda et al. [16] was used with minor modifications to investigate the anti-CA II antibodies in the sera of the individuals in the study groups. The results and the standart deviations obtained from ELISA are shown in table 2. The cut off point that was used for evaluating the positivity of the study groups was taken as the avarage of the control group sum with 3SD (X ± 3SD= 0.437) , because if it was evaluated among 3SD there would be no positive result in the control group and this enhanced the reliability of the method. The results of the groups are given together in the same graph (Fig 1.)**.** It is seen that there are 3 positive in *H.pylori* (+) gastritis group (10 %), 2 in *H.pylori* (+) ulcer group (6,6 %), 1 in *H.pylori* (-

) gastritis group (3,3 %), 2 in *H.pylori* (-) ulcer (6,6 %) and in the sum 8 positive results were obtained (5,3 %) . Here, anti CA II antibodies were detected in the sera of only 5 (8,3%) of 60 *H.pylori* infected subjects with the ELISA method. It was concluded that altough there was no positive value in the control group,as a good indicator of high specificity, this number meant a low sensivity, so determination of anti-CA II antibodies in the serum with ELISA could not be a marker for *H.pylori* infection. One positive value in *H.pylori* (-) gastritis group and in *H.pylori* (-) ulcer could be arise from some subjects of these groups might have a treated *H.pylori.* as a result of advanced statistical anlaysis between control group and *H.pylori* (+) gastritis and ulcer groups significant difference was found. (respectively, p=0,001 ve p=0,00041). We do not have chance to compare our results, because of the lack of study in this issue. But when compared with the control group subjects with *H.pylori* (+) ulcer had increased anti-CA II antibodies levels rather than subjects with *H. pylori* (+) gastritis and this difference has been arised from the fact that worse damage and localization of ulcer. Likewise, differences between the *H.pylori*(+) and *H.pylori*(-) gastritis groups and *H.pylori*(+) and *H.pylori*(-) ulcer groups were statistical significant (respectively, p=0,00038 and p=0,048). The results were in concordance with our expectations. Increased anti-CA II antibody levels were found in the sera of *H.pylori* infected subjects. But, here increased CA II might not be the real CA, it could also be the hpCA that belongs to *H.pylori*. Because, the role of anti-CA II antibodies in the pathology of autoimmun disease is not clear. Infections are important enviromental factors that triggers autoimmunity and it was reported that *H. pylori* infection induces AIP, an autimmun disease. It is known that, according as necrosis caused by viruses and microbial agents, antibodies can develop with mechanisms such as molecular mimic against spesific enzymes, cross-links, activation and adjuvant effect of autoreactiveT-cells. Anti-CA II antibodies could be developed in *H.pylori* infected individuals with similar mechanisims. It was demonsrated that human CA II shows antigenic character by inducing humoral and cellular immune reactions with studies performed with various rat species those were constituted autoimmun diseaes. It was seen that genetic factors were also determinative in forming of autoantibodies. F.Guarneri et al found significant homology between CA II and shared segments on DRB1*0405, one of binding motifs of hpCA to HLA and suggested that this was a risk factor for AIP. These findings supported the idea of the association between AIP and HLA DRB1*0405 genotype, present in the shared segments with human and bacteria. Further studies on this genotype will be usefull for identification of autoimmune diseases. On the side, the contribution of *H. pylori* positivity and HLA types to the presence of anti-CA II antibodies in the positive results shoud not be undervalued. Carbonic anhydrase has two isoenzymes in *H.pylori*, including alfa and beta and alfa hpCA has considerable homology with human CA. Alfa hpCA exists on the outer surface of bacterium and this makes easy the interaction of host immunity and antibody and the organism can facilely produces antibodies. Because of the similarity between alfa hpCA and human CA II, alfa hpCA antibodies could be cross-linked to CA II, coated to ELISA plate causing increased anti CA II antibodies.

Conclusions and Recommendation

In this study, the hypothesis proposed by Guarneri et al [11], based on the results obtained by in silico methods, was tested in vitro in the sera of H. pylori infected individuals. There were 8 positive values, 3 (10%) in the H. pylori (+) gastritis group, 2 (6.6%) in the H. pylori (+) ulcer group, 1 (3.3%) in the H. pylori (-) gastritis group and 2 (6.6%) in the H. pylori (-) ulcer group, with a cut-off value of <0.437 in the control group. Statistical analysis revealed a significant difference between the control group and the H. pylori (+) ulcer and H. pylori (+) gastritis groups (p=0.00041 and p=0.001 respectively), between the H. pylori (+) ulcer and H. pylori (-) ulcer groups (p=0.048) and between the H. pylori (+) gastritis and H. pylori (-) gastritis groups (p=0.00038). After evaluating the results obtained, it is recommended that the following additional study be carried out to obtain more conclusive information on this subject*: H.pylori* alpha-hpCA enzyme can be purified, ELISA plates can be coated with this enzyme and anti-CA II can be measured and compared with measurements of CA II coated plates. It can be determined whether the antibody is anti alpha-hpCA or anti CA II.

Conflicts of interest

There are no conflicts of interest in this work.

Ethical Approval Statement

This study was approved by the Karadeniz Technical University Medical Faculty Ethical Committee (Protocol no: 2006/18) and informed consent was obtained from all subjects.

References

[1] Supuran C. T., Novel carbonic anhydrase inhibitors for the treatment of Helicobacter pylori infection, *Expert Opinion on Investigational Drugs*, 33(5) (2024) 523–532.

[2] Bayram E., Senturk M., Kufrevioglu O. I., Supuran C. T., In vitro inhibition of salicylic acid derivatives on human cytosolic carbonic anhydrase isozymes I and II, *Bioorganic & Medicinal Chemistry*, 16(20) (2008) 9101–9105.

[3] Alver A., Menteşe A., Karahan S. C., Erem C., Keha E. E., Arikan M. K., Eminağaoğlu M. S., Deger O., Increased serum anti-carbonic anhydrase II antibodies in patients with Graves' disease, *Experimental and clinical endocrinology & diabetes : official journal, German Society of Endocrinology [and] German Diabetes Association*, 115(5) (2007) 287–291.

[4] Nishimori I., Onishi S., Takeuchi H., Supuran C. T., The alpha and beta classes carbonic anhydrases from Helicobacter pylori as novel drug targets, *Current Pharmaceutical Design*, 14(7) (2008) 622–630.

[5] Janeway C.A., Travers P., Walport M., Immunobiology: The Immune System in Health and Disease, 5th ed. New York: Garland Science; 2001.

[6] Nista E. C., De Lucia S. S., Manilla V., Schepis T., Pellegrino A., Ojetti V., Pignataro G., Zileri Dal Verme L., Franceschi F., Gasbarrini A., Candelli M., Autoimmune Pancreatitis: From Pathogenesis to Treatment, *International Journal of Molecular Sciences*, 23(20) (2022) 12667.

[7] Inagaki Y., Jinno-Yoshida Y., Hamasaki Y., Ueki H., A novel autoantibody reactive with carbonic anhydrase in sera from patients with systemic lupus erythematosus and Sjögren's syndrome, *Journal of Dermatological Science*, 2(3) (1991) 147–154.

[8] Yokode M., Shiokawa M., Kodama Y., Review of Diagnostic Biomarkers in Autoimmune Pancreatitis: Where Are We Now?, *Diagnostics (Basel, Switzerland),* 11(5) (2021) 770.

[9] Goyal S., Sakhuja P., Autoimmune pancreatitis: Current perspectives. *Indian Journal of Pathology & Microbiology*, *64* (2021), S149–S159.

[10] Aparisi L., Farre A., Gomez-Cambronero L., Martinez J., De Las Heras G., Corts J., Navarro S., Mora J., Lopez-Hoyos M., Sabater L., Ferrandez A., Bautista D., Perez-Mateo M., Mery S., Sastre J., Antibodies to carbonic anhydrase and IgG4 levels in idiopathic chronic pancreatitis: relevance for diagnosis of autoimmune pancreatitis, *Gut*, 54(5) (2005) 703–709.

[11] Guarneri F., Guarneri C., Benvenga S., Helicobacter pylori and autoimmune pancreatitis: role of carbonic anhydrase via molecular mimicry?, *Journal of Cellular and Molecular Medicine*, *9*(3) (2005) 741–744.

[12] Iyer R., Barrese A. A., 3rd, Parakh, S., Parker, C. N., Tripp, B. C., Inhibition profiling of human carbonic anhydrase II by high-throughput screening of structurally diverse, biologically active compounds, *Journal of Biomolecular Screening*, *11*(7) (2006) 782–791.

[13] Comay D., Cauch-Dudek K., Hemphill D., Diamandis E., Wanless I., Heathcote E. J., Are antibodies to carbonic anhydrase II specific for anti-mitochondrial antibody-negative primary biliary cirrhosis?, *Digestive Diseases and Sciences*, *45*(10) (2000) 2018–2021.

[14] Sharker M. R., Sukhan Z. P., Sumi K. R., Choi S. K., Choi K. S., Kho K. H., Molecular Characterization of Carbonic Anhydrase II (CA II) and Its Potential Involvement in Regulating Shell Formation in the Pacific Abalone, *Haliotis discus hannai*. *Frontiers in Molecular Biosciences*, *8* (2021) 669235.

[15] Supuran C. T., Structure and function of carbonic anhydrases. *The Biochemical Journal*, *473*(14) (2016) 2023–2032.

[16] Hosoda H., Okawa-Takatsuji M., Tanaka A., Uwatoko S., Aotsuka S., Hasimoto N., Ozaki Y., Ikeda Y., Detection of autoantibody against carbonic anhydrase II in various liver diseases by enzyme-linked immunosorbent assay using appropriate conditions. *Clinica Chimica Acta; International Journal Of Clinical Chemistry*, 342(1-2) (2004) 71–81.

Cumhuriyet Science Journal

Comparative Chemical Composition and Antimicrobial Activities of The Essential Oils and Solvent Extracts of The Flower, Leaf, And Stem of *Epilobium angustifolium* Growing in Türkiye

Büşra Korkmaz[1,a,*], Gözde Bozdal[1,b], Şeyma Arıcı Tüfekci[1,c], Büşra Şahin[1,d], Elif Öztürk[2,e], Şengül Alpay Karaoğlu[3,f], Serdar Makbul[3,g], Nurettin Yaylı[1,h]

[1]Department of Pharmacognosy, Faculty of Pharmacy, Karadeniz Technical University, Trabzon, Türkiye

[2]Department of Nutrition and Dietetics, Faculty of Health Science, Karadeniz Technical University, Trabzon, Türkiye

[3]Department of Biology, Faculty of Arts and Sciences, Recep Tayyip Erdogan University, Rize, Türkiye

*Corresponding author

Research Article

ABSTRACT

Volatile organic compounds (VOCs) of essential oils (EOs) and solid phase microextract (SPME) obtained from the flower, leaf, and stem of *Epilobium angustifolium* L. were analyzed by GC-FID/MS. The EOs and SPMEs consist mainly of monoterpenes and aldehydes, which are major classes of compounds. Limonene was found to be a major compound in flower (HD: 42.9% vs. SPME: 95.5%), in leaf (HD: 60.3% vs. SPME: 4.7%), and in stem (HD: 49.06% vs. SPME: 93.6%). The antimicrobial activity of EOs and the solvent extracts (*n*-hexane, acetonitrile, and methanol) of *E. angustifolium* were screened *in vitro* against nine microorganisms. The EO of the leaf showed the best activity (10.2 µg/mL MIC) against *Mycobacterium smegmatis*. All the EOs and the solvent extracts gave moderate activity against the *Staphylococcus aureus, Bacillus cereus,* and *M. smegmatis* within the range of 10.2-1300.0 µg/mL MIC values. The best antibacterial activity was observed against *S. aureus* and *B. cereus* in the *n*-hexane extract of stem and methanol extract of flower samples.

Keywords: Epilobium angustifolium, Essential oil, SPME, GC-FID/MS, Antimicrobial.

a ✉ busra.yayli@ktu.edu.tr   ⓘ https://orcid.org/0000-0002-3747-8855
b ✉ gzdklc89@hotmail.com   ⓘ https://orcid.org/0000-0003-1248-7912
c ✉ seyma.arici1996@gmail.com   ⓘ https://orcid.org/0009-0001-4791-8287
d ✉ busra.sahintr@gmail.com   ⓘ https://orcid.org/0000-0002-2727-9801
e ✉ yayli.elif@hotmail.com   ⓘ https://orcid.org/0000-0002-0809-6145
f ✉ sengul.karaoglu@erdogan.edu.tr ⓘ https://orcid.org/0000-0003-1047-8350
g ✉ serdar.makbul@erdogan.edu.tr ⓘ https://orcid.org/0000-0001-8798-0926
h ✉ yayli@ktu.edu.tr   ⓘ https://orcid.org/0000-0003-4174-3014

Introduction

Among the known medicinal plant species is *Epilobium* taxa, a worldwide traditional medicinal herb known as fireweed or rosebay willowherb. It is known that the extracts obtained from this plant exhibit various pharmacological effects in traditional medicine [1]. From the past to the present, the *Epilobium* plant's transition from traditional to pharmacological use has clarified the plant's components and biological activities [1,2]. Certain members are commonly utilized in traditional medicine, primarily for gastrointestinal and prostate issues in Türkiye [3] and other countries [4,5]. In traditional use, *Epilobium* taxa are used as a tea to treat headaches, insomnia, infection, anemia, and colds. It has been reported that *Epilobium angustifolium* L. extracts are used for therapeutic purposes in gastrointestinal diseases such as diarrhea, dysentery, ulcers, and urinary diseases such as prostate [1,2,6]. *E. angustifolium* extracts have been shown in investigations to be antiproliferative [7], antiaging [8], antioxidants [9, 10], anti-inflammatory [11], and antibacterial [12-15]. *Epilobium* is a genus of around 185 herbaceous perennial species from the Onagraceae family [1]. *E. angustifolium* (also known as *Chamaenerion angustifolium* (L.) Holub) is native to the temperate Northern Hemisphere [16, 17].

Previous pharmacognostic studies have shown that essential oil from the *E. angustifolium* plant grown in China was obtained using the supercritical CO_2 method, and GC-MS analysis was reported [13]. Headspace-SPME GC-MS was used to investigate the volatile contents of dried and fresh *E. angustifolium*, which grows in Lithuania [18, 19]. Chemical composition, antioxidant, antifungal properties, and skin penetration of *E. angustifolium* grown in Poland were reported. The major components of *E. angustifolium* essential oil were mainly terpenes such as β-linalool, camphor, β-caryophyllene, α-caryophyllene oxide, eucalyptol, and (S)-carvone [20]. Furthermore, there have been a few publications on the phytochemical research done on *E. angustifolium*; these reports mostly focus on the investigation of flavonoids, triterpenoids, polyphenols, and phenolic compounds, and they indicate that these compounds have both antibacterial and immunomodulatory properties [13]. The anticancer properties of *C. angustifolium* were also reported [5, 7, 21-23], and activity was attributed to the oenothein B [24].

Currently, no study has focused on the volatile contents (EOs) and antimicrobial effects for the flower, leaf, and stem of *E. angustifolium* growing in Türkiye. This study explores the antimicrobial activity and chemical

variety of EOs and solvent extracts (*n*-hexane, acetonitrile, and methanol) from the stem, leaf, and flower of *E. angustifolium*. This is the first comparative analysis of the phytochemical content of *E. angustifolium* based on a literature survey. Such a study demonstrates how plant parts alter volatile components and antimicrobial activities.

Materials and Methods

Chemical and Reagents

All solvents (*n*-hexane, acetonitrile, methanol, and dimethyl sulfoxide) and other chemicals (Na₂SO₄, Dabouraud dextrose agar, ampicillin, streptomycin, and fluconazole) used were purchased from Sigma-Aldrich in analytical grade.

Plant Material

Wild-grown *E. angustifolium* was collected from Erzurum (SE part of Türkiye) in August 2022 at an altitude of 1960 m. The fresh plant materials were separated into flower, leaf, and stem parts and air-dried in the shade at room temperature. The plant was identified according to the Flora of Türkiye by Professor Dr. Serdar Makbul [2]. The voucher specimen (Okur 38 & S. Makbul) was deposited in the Herbarium of Recep Tayyip Erdogan University, Department of Biology (RUB), Rize, Türkiye.

Hydrodistillation Apparatus and Procedure

The aerial parts (flowers, leaves, and stems) of *E. angustifolium* (~70 g, fresh) were ground with a mill into small pieces. Grounded parts of the plants were hydrodistillated (HD) with a modified Clevenger-type apparatus (7 °C using Chiller, 3 h), yield (v/w): 0.010%, 0.012%, and 0.011%, respectively. The obtained EOs were extracted using *n*-hexane (0.5 mL, HPLC grade), dried on anhydrous Na₂SO₄, and kept in brown glass bottles in the refrigerator at -10 °C until use [24, 25].

The Solvent Extract of the Flower, Leaf, and Stem of E. Angustifolium

The dried and ground parts of *E. angustifolium* were placed into nine separate 50 mL flasks: flower (8.80 g, 8.92 g, and 8.18 g), leaf (8.62 g, 8.66 g, and 9.20 g), and stem (8.55 g, 8.58 g, and 9.36 g). The materials were extracted three times using analytical grade *n*-hexane, acetonitrile, and methanol (10 mL x 3; 12 h, each). Following solvent filtration, the same extracts were combined and evaporated at 40 °C to yield crude *n*-hexane, acetonitrile, and methanol extracts (0.037 g/0.039 mg/11.3 g), leaf (0.044 g/0.028 g/0.106 g), and stem (0.025 g/0.024 g/0.089 g), respectively.

SPME Analysis

The dry aerial part (flower, leaf, and stem) of *E. angustifolium* (~1.1 g each) was placed in a sealed SPME vial (10 mL) with a silicone-rubber septum cap and exposed to an SPME system (Supelco, USA). A DVB/Carboxen/PDMS coated fiber was utilized to get volatile components. The SPME fibers were heated for conditioning in the GC injector for 5 minutes at 250 °C. Extraction was accomplished utilizing magnetic stirring at 80°C for 5 minutes of incubation and 10 minutes of extraction. After that, fiber containing a volatile chemical extract was injected into the GC injector. A Shimadzu QP2010 Ultra mass selective detector connected to the 2010 Plus chromatograph was used for GC-FID/MS analysis. Helium was the carrier gas with 1 mL/min flow rate. The injection was done in split mode (1:30) at 230 °C. The sample was reported after analysis. The temperature, incubation period, and extraction time were determined based on the previous experiment described [26-28].

GC-FID/ MS Analysis

A Shimadzu QP2010 ultra-GC-FID/MS (Shimadzu Class-5000 Chromatography Workstation software) was used to analyze the EOs. Restek Rxi-5MS capillary column (30 mm x 0.25 mm × 0.25 μm) was used. Injection of the EOs into GC-FID/MS was done in split mode (1:30) at 230°C. The essential oil solution (1 μL) in *n*-hexane (HPLC grade) was injected and analyzed. The column was kept at 60ºC for 2 minutes and then elevated to 240ºC using a 3ºC/min heating ramp. The oven program was as follows: the initial temperature was 60ºC for 2 minutes, then rose to 240ºC after 3 minutes, and finally held at 250ºC for 4 minutes. The carrier gas utilized was helium (99.999%) at a steady flow rate of 1 mL/min. The ionization voltage was set at 70 eV, the detection was carried out in electronic impact mode (EI), and mass acquisition was done using scan mode (40-450 m/z). Each sample was evaluated, and the average was given [26, 27]. The volatile components were identified by comparing the literature RI and library mass values (NIST, Wiley7NL, FFNSC1.2, and W9N11) [25-34].

Antimicrobial Activity

All test microorganisms were obtained from the Hıfzısıhha Institute of Refik Saydam (Ankara, Türkiye). They were *Bacillus cereus* 709 ROMA; Candida *albicans* ATCC 60193, *Enterococcus faecalis* ATCC 29212, *Escherichia coli* ATCC 25922, *Mycobacterium smegmatis* ATCC607, *Pseudomonas aeruginosa* ATCC 27853, *Saccharomyces cerevisiae* RSKK 251, *Staphylococcus aureus* ATCC 25923, and *Yersinia pseudotuberculosis* ATCC 911. The plant solvent extracts were dissolved in *n*-hexane, acetonitrile, and methanol to prepare an extract stock solution. Antimicrobial susceptibility of the EOs, *n*-hexanes, acetonitrile, and methanol extracts of *E. angustifolium* were screened using the agar-well diffusion method [27, 35, 36]. Each bacterium and yeast were cultured in Mueller Hinton (MH) (Difco, Detroit, MI) broth and yeast extract broth, respectively. Then, the microorganisms were diluted with approximately 10⁶ colony-forming units (CFU) per mL. Sabouraud Dextrose Agar (SDA) (Difco, Detriot, MI) was used for yeast-like fungi. Microorganisms were "flood-inoculated" onto MH and SD agars and dried under aseptic conditions. 50 μL of essential oils and solvent extracts of *E. angustifolium* were

delivered into wells (5 mm diameter), opened on agar plates, and incubated at 35 °C for 18h. The *M. smegmatis* was grown for 3 to 5 days on MHA plates at 35 °C. Microbial activity was evaluated by measuring the inhibition zone diameters. Antimicrobial agents such as Ampicillin (10 μg/mL), streptomycin (10 μg/mL), and fluconazole (5 μg/mL) were used as the positive control.

Agar Dilution MIC Assay

The antimicrobial assay of EOs, *n*-hexane, acetonitrile, and methanol extracts of *E. angustifolium* was worked quantitatively in respective broth media using double microdilution method. The antibacterial and antifungal assays were carried out in Mueller-Hinton broth (MH) at pH. 7.3 and buffered Yeast Nitrogen Base at pH 7.0, respectively. The microdilution test plates were incubated at 35°C for 18h [27-29]. Brain Heart Infusion broth was used for *M. smegmatis* and incubated at 35°C for 48-72h. The MIC was defined as the lowest concentration that showed no growth. Ampicillin (10 μg/mL), streptomycin (10 μg/mL), and fluconazole (5 μg/mL) were used as standard antibacterial and antifungal drugs. Dimethyl sulfoxide with a dilution (1:10) was used as solvent control.

Results and Discussion

Chemical Constituents of EOs and SPME

A total of 34/15, 45/32, and 39/21 constituents were discovered in the flower, leaf, and stem of *E. angustifolium*, accounting for 91.8-98.8% in HD and 92.3-99.7% in SPME, according to GC-FID/MS analysis for the flower, leaf, and stem of *E. angustifolium*, respectively. The volatile organic components of EOs and SPME in the flower, leaf, and stem of *E. angustifolium*, as well as their KI and percentages, are listed in Table 1.

The EOs were characterized by comparing mass spectra in the libraries (NIST, Wiley7NL, FFNSC1.2, and W9N11) and utilizing the Kovats index [27, 33]. The EOs have been analyzed on the Rxi-5MS column [24-26]. Eighty-one volatile compounds were detected in the EOs and SPME of *E. angustifolium* by the GC-FID/MS analysis. Results had shown that EOs had higher chemical diversity than SPMEs (Table 1). Significant quantitative and qualitative differences were observed between EOs and SPME and among the flower, leaf, and stem samples (Table 1). A variety of chemical classes, including aliphatic hydrocarbons, aldehydes, alcohols, esters, acids, and other hydrocarbons, as well as monoterpenes, sesquiterpenes, and terpene-related substances, are among the components that have been found. The EOs and SPMEs consisted mainly of monoterpenes (flower, HD: 50.9% vs. SPME: 98.1%; leaf, HD: 68.6% vs. SPME: 72.3%; stem, HD: 57.5% vs. SPME: 96.1%), and aldehydes (flower, HD: 7.9% vs. SPME: 0.9%, leaf, HD: 6.5% vs. SPME: 6.2%, stem, HD: 4.7% vs. SPME: 1.3%). Limonene (flower, HD: 42.9% vs. SPME: 95.5%, leaf, HD: 60.3% vs. SPME:

4.7%, stem, HD: 49.06% vs. SPME: 93.6%) was a major compound of the EOs and SPMEs of *E. angustifolium.* Sesquiterpenoids were the minor constituents for only EOs in all parts (flower, HD: 1.6%, leaf, HD: 0.2%, stem, HD: 0.1%) of the *E. angustifolium.* The quantitative alterations in compounds and the appearance/disappearance of volatiles were the two effects of *E. angustifolium* extractions on the plant's composition. Specific molecules, such as (*Z*)-3-hexenol, 2-heptanol, tetradecane, methyl palmitate, *n*-hexadecanoic acid, ethyl palmitate, methyl linolenate, and phytol were found only in EOs samples of *E. angustifolium*. At the same time, (*E*)-2-hexenal, *β*-ocimene, and *β*-cadinene existed only in the SPME samples of *E. angustifolium.* Out of 81 chemicals, only five were found in all samples, including *n*-hexanal (0.5%, 0.1%, 0.5%, 0.2%, 0.7%, and 0.2%), *α*-pinene (1.5%, 0.31%, 1.5%, 2.7%, 1.1%, and 0.4%), sabinene (0.2%, 0.3%, 0.6%, 2.0%, 0.4%, and 0.3%), *β*-mycrene (1.7%, 1.7%, 2.0%, 1.3%, 1.6%, and 1.8%), and limonene (42.9%, 95.51%, 60.3%, 4.7%, 49.0%, and 93.6%), respectively. The quantitative makeup of the volatiles changed depending on where the sample came from. For example, the percentage content of limonene in EO samples varied from 42.9% to 60.3%, and in SPME samples were in the range of 4.7% and 95.5% (Table 1). The variety in chemical components, as reported in the literature [24-30], could be attributed to differences in plant parts and extraction procedures-consequently, the flower, leaf, and stem of *E. angustifolium* growing in Türkiye exhibit distinct chemotypes. A comparative investigation of the plant's sections revealed that monoterpenes (flower, 98.1%, leaf, 72.3%, and stem, 96.1%) were the major components of *E. angustifolium* SPMEs. Some of the identified compounds may form by auto-oxidation during the HD. In our study, eugenol was seen only in the flower essential oil isolated by HD. The numbers of terpenes/terpenoids identified from *E. angustifolium* using HD and SPME were different (flower, HD: 11 vs. SPME: 10; leaf, HD: 17 vs. SPME: 22; stem, HD: 18 vs. SPME: 13).

In the literature, the EO of *E. angustifolium* was obtained by supercritical carbon dioxide. Linoleic acid (17.1%), 1-docosene (11.4%), hexadecanoic acid (10.6%), and linolenic acid (7.3%) were reported to be major constituents, and only 13 out of 78 compounds were the same as in our case [13]. EO also inhibited *E. coli*, *Bacillus subtilis*, *Micrococcus luteus*, and *Enterobacter aerogenes* [13].The essential oil for the dried herbs of *E. angustifolium* from Poland yielded 24 compounds and gave the highest concentration of cosanes (23.70%), 5-methyl docosane (14.95%), and *α*-caryophyllene oxide (8.57%) [20].The volatile constituents of fresh and air-dried samples of *C. angustifolium* were analyzed using HS-SPME GC-MS. Trans-2-hexenal (16.0-55.9% of all volatiles) and trans-anethole (2.6-46.2%) were present only in the dried samples, while *cis*-3-hexenol (17.5-68.6 %) was only in fresh samples and 11 out of 42 constituents were the same as in our result [18]. α/β-Caryophyllenes were reported in all analyzed samples, contributing from 2.4% to 52.3% (fresh or dried).

Table 1. Volatile organic compounds for the flower, leaf, and stem of *E. angustifolium*

No	Compounds	RI*	RIᵃ	(%)ᵇ					
				Flower		Leaf		Stem	
				HD	SPME	HD	SPME	HD	SPME
1.	2-Ethylfuran	728	733	-	-	-	0.1	-	-
2.	Methylbenzene	782	789	-	-	-	0.1	-	-
3.	Hexanal	803	802	0.5	0.1	0.5	0.2	0.7	0.2
4.	(*E*)-2-Hexenal	852	848	-	0.2	-	5.7	-	0.2
5.	(*Z*)-3-Hexenol	858	859	1.6	-	3.0	-	1.3	-
6.	2-Heptanol	894	891	2.1	-	1.2	-	0.6	-
7.	2,4-Hexadienal	907	904	-	-	-	0.2	-	-
8.	α-Thujene	931	930	-	-	-	1.4	-	-
9.	α-Pinene	940	938	1.5	0.3	1.5	2.7	1.1	0.4
10.	Benzaldeyhde	960	963	4.2	-	2.4	-	2.4	-
11.	Sabinene	978	976	0.2	0.3	0.6	2.0	0.4	0.3
12.	β-Pinene	980	981	1.6	-	2.0	9.3	1.8	-
13.	β-Mycrene	992	989	1.7	1.7	2.0	1.3	1.6	1.8
14.	Octanal	1003	1001	-	0.4	1.1	-	-	0.2
15.	α-Phellandrene	1002	1006	-	-	-	0.1	-	-
16.	α-Terpinene	1018	1018	-	-	-	0.5	-	-
17.	o-Cymene	1022	1027	0.4	-	0.1	15.1	0.4	-
18.	Limonene	1031	1035	42.9	95.5	60.3	4.7	49.0	93.6
19.	Benzene acetaldeyhde	1052	1055	2.9	-	1.2	-	1.0	-
20.	β-Ocimene	1046	1045	-	0.3	-	5.8	-	0.1
21.	γ-Terpinene	1060	1059	2.6	-	2.1	29.4	2.8	-
22.	Octanol	1063	1068	-	-	0.7	-	-	-
23.	Linalool oxide	1073	1073	-	-	0.6	-	-	-
24.	α-Terpinolene	1191	1089	-	-	-	-	0.4	-
25.	2-Nonanol	1097	1097	4.3	-	-	-	-	-
26.	2-Ethyl-*p*-xylene	1085	1089	-	-	-	7.4	-	-
27.	Linolool	1098	1096	-	0.1	5.5	0.7	6.0	0.1
28.	Nonanal	1101	1101	0.3	-	0.1	-	-	-
29.	Citronella	1148	1151	-	-	0.1	-	-	-
30.	(*Z*)-2-Nonenal	1142	1142	-	-	-	-	0.1	0.6
31.	4-Terpineol	1192	1190	0.8	-	1.1	-	-	-
32.	α-Terpineol	1191	1189	0.3	-	0.9	0.1	0.3	0.9
33.	Decanal	1201	1201	-	0.2	0.8	0.1	0.4	0.1
34.	β-Cyclocitral	1220	1223	-	-	0.4	-	-	-
35.	Geraniol	1240	1249	-	-	-	-	-	0.1
36.	Neral	1235	1240	-	-	0.2	-	-	-
37.	Geranial	1264	1268	-	-	-	-	-	0.1
38.	Tridecane	1300	1297	2.4	-	1.3	0.1	2.9	-
39.	Undecanal	1305	1302	-	-	0.1	-	-	-
40.	Bicyloelemene	1333	1331	-	-	-	-	-	0.1
41.	Eugenol	1356	1358	1.9	-	-	-	-	-
42.	Decanoic acid	1364	1364	-	-	0.3	-	-	-
43.	β-Cubenene	1387	1390	-	-	-	0.1	-	-
44.	α-Copaene	1374	1370	-	0.1	0.3	-	-	0.1
45.	β-Damascenone	1383	1387	-	-	0.3	-	0.3	-
46.	Tetradecane	1400	1403	2.4	-	1.0	-	2.8	-
47.	β-Elemene	1389	1394	-	-	-	6.1	-	-
48.	α-Bergamotene	1411	1414	-	-	-	-	-	0.2
49.	Dodecanal	1408	1409	-	-	0.1	-	0.1	-
50.	β-Caryophyllene	1417	1416	-	0.2	0.9	2.7	-	0.1
51.	β-Copaene	1430	1430	-	-	-	0.1	-	-
52.	Geranyl acetone	1145	1444	-	-	-	-	0.3	
53.	Neryl acetone	1435	1439	-	-	0.1	-	-	-
54.	α-Humulene	1460	1460	-	-	0.3	0.6	-	-
55.	Valencene	1496	1495	-	0.2	-	-	0.2	0.1
56.	D-Germacrene	1484	1487	-	-	-	0.1	-	-
57.	β-Ionone	1487	1487	0.2	-	0.7	-	0.3	0.3
58.	β-Selinene	1493	1493	-	-	-	0.1	-	-
59.	α-Farnesene	1505	1504	-	-	-	2.1	-	-
60.	Methyl laurate	1526	1528	-	-	-	-	0.1	-
61.	β-Cadinene	1518	1516	-	0.1	-	0.1	-	0.1
62.	α-Cadinene	1526	1537	-	-	-	-	0.3	-
63.	Dodecanoic acid	1526	1528	-	-	-	-	0.1	-
64.	α-Cadinol	1652	1651	-	-	0.1	-	0.1	-
65.	α-Bisabolol	1685	1686	1.6	-	0.2	-	-	-
66.	Methyl myristate	1726	1727	0.1	-	0.1	-	-	-
67.	Tetradecanoic acid	1763	1765	0.1	-	-	-	0.1	-
68.	Ethyl myristate	1790	1786	0.2	-	0.1	-	-	-

No.	Compound								
69.	Hexahydrofarnesyl acetone	1847	1848	-	-	0.1	-	0.1	-
70.	Nonadecane	1900	1900	0.3					
71.	Methyl palmitate	1926	1928	0.1	-	0.4	-	1.0	-
72.	n-Hexadecanoic acid	1966	1968	3.4	-	0.3	-	5.6	-
73.	Ethyl palmitate	1990	1986	3.7	-	0.5	-	1.7	-
74.	Heneicosane	2100	2098	6.3	-	-	0.1	-	-
75.	Methyl linolenate	2101	2097	5.4	-	1.7	-	5.2	-
76.	Phytol	2110	2110	0.5	-	0.3	-	0.2	-
77.	Linoleic acid	2131	2132	0.4	-	-	-	1.2	-
78.	Oleic acid	2152	2156	-	-	0.4	0.4	3.5	-
79.	Ethyl stearate	2194	2195	0.1	-	-	-	-	-
80.	Docosane	2200	2199	-	-	-	-	-	-
81.	Tricosane	2300	2298	1.8	-	0.2	0.2	0.8	-

Chemical classes	Area% [b] and NC [c]					
Monoterpene hydrocarbons	50.9:7	98.1:5	68.6:7	72.3:11	57.5:8	96.2:5
Monoterpenoids	3.0:3	0.1:4	8.8:7	0.8:2	0.9:2	1.2:4
Sesquiterpene hydrocarbons	-	0.6:1	1.5:3	12.0:9	0.5:2	0.7:6
Sesquiterpenoids	1.6:1	-	0.2:2	-	0.1:1	-
Terpene related to compounds	0.2:1	-	1.2:4	-	1.0:4	0.3:1
Aliphatic hydrocarbons	13.2:5	-	2.5:3	0.4:3	6.5:3	-
Aldehydes	7.9:4	0.9:4	6.5:8	6.2:4	4.7:6	1.3:5
Alcohols	8.0:3	-	4.9:3	-	1.9:2	-
Esters	9.6:6	-	2.8:5	-	8.0:5	-
Acids	3.9:3	-	1.0:3	0.4:1	10.5:5	-
Others	0.5:1	-	0.3:1	0.2:2	0.2:1	-
Total	98.8:34	99.7:15	98.3:45	92.3:32	91.8:39	99.7:21

* Retention Index of references; [a] Retention Index calculated from retention times relative to that of *n*-alkane (C6-C32) series; [b] Percentages obtained by FID peak-area normalization; [c] NC: Number of compounds.

The ethanolic extract's total phenolic compounds and the DPPH free radical scavenging activity (in fresh sample 238.6-557.1 mg/g) were also reported [18]. In another work, 42 aliphatic hydrocarbons, aldehyde, and alcohols were mentioned from the *t*-butyl methyl ether extract of *C. angustifolium* leaf and stem [21]. Total phenolic contents, antioxidant activity, and volatile constituents of *C. angustifolium,* collected in six different locations in Lithuania, were reported using SPME GC-MS. Volatile analysis of all samples had been classified into two significant chemotypes, such as *α*-/*β*-caryophyllenes and anethole [19]. Alcohol for the EO and SPME and aromatic hydrocarbons for the SPME of the *n*-hexane extract of *Epilobium hirsutum* L. were reported to be major classes of constituents [37].

As previously stated, the cost of extraction is advantageous for the SPME approach in terms of time and decomposition. The chemical variations in the VOCs on *Epilobium* taxa may be due to environmental and analysis conditions. This work showed that the extraction methods used had remarkable changes in volatile constituents. The literature also demonstrated the differences in volatile composition [30, 34]. However, using different extraction methods allows the appearance of new compounds to have a positive effect on the quality of *E. angustifolium*. Limonene (95.5% and 93.6%) was highly content determined from the SPMEs of the flower and stem, respectively. It was found that *E. angustifolium* oil rich in monoterpene in the range of 50.9% to 98.1% which showed significant inhibitory activity against *C. albicans,*

Candida glabrata, Aspergillus nigerand, Bacillus subtilis, and *P. aeruginosa*. However, no activity was reported against the *Y. pseudotuberculosis*. The evaluation of antimicrobial activities for the pure compounds of *E. angustifolium* was beyond the scope of this work. However, according to the above-mentioned published data [6-19], EOs and solvent extracts of this herb can also be of therapeutic value.

The amounts of monoterpenes found by SPME were greater in HD volatiles for the flower and stem, such as limonene (flower, HD: 42.9% vs. SPME: 95.58%, and stem, HD: 49.0% vs. SPME: 93.6%). This is probably related to the volatility because of a shorter extraction time (10 min for SPME vs. 3 h for HD). Thus, limonene could be used as a taxonomical marker for classifying *E. angustifolium*.

Antimicrobial Activities

The antimicrobial activity of EOs and solvent extracts (*n*-hexane, acetonitrile, and methanol) of the flower, leaf, and stem of *E. angustifolium* was tested using the agar well diffusion method against *E. coli, Y. pseudotuberculosis, Y. coli, P. aeruginosa, E. faecalis, S. aureus, B. cereus, M. smegmatis, C. albicans*, and *S. cerevisiae* (Table 2) [35, 36]. In general, EOs and *n*-hexane extract showed moderate antimicrobial activities against *S. aureus, B. cereus, M. smegmatis, C. albicans*, and *S. cerevisiae* with the inhibition 6-27 mm range, respectively (Table 2).

Table 2. Antimicrobial assay of EOs and solvent extracts for the flower, leaf, and stem of *E. angustifolium*

Sample Extracts	Plant parts	Const. (µg/ml)		Microorganisms, inhibition zone (mm), and MIC (µg/mL)								
				Gram (-)			Gram (+)			No Gr.	Fungi	
				Ec	*Yp*	*Pa*	*Ef*	*Sa*	*Bc*	*Ms*	*Ca*	*Sc*
Os	Flower	17900	mm	-	-	-	-	6	7	15	-	-
			MIC	-	-	-	-	895	895	223.8	-	-
	Leaf	26000	mm	-	-	-	-	6	9	27	7	10
			MIC	-	-	-	-	1300	1300	10.2	1300	650
	Stem	16900	mm	-	-	-	-	6	6	18	-	-
			MIC	-	-	-	-	845	845	105.6	-	-
-Hexane	Flower	19000	mm	-	-	-	-	14	14	15	12	15
			MIC	-	-	-	-	118.8	118.8	59.4	118.8	59.4
	Leaf	17000	mm	-	-	-	-	8	8	16	16	20
			MIC	-	-	-	-	425	425	53.1	53.1	13,3
	Stem	12500	mm	6	-	-	-	12	14	15	16	20
			MIC	625	-	-	-	78.1	39.1	39.1	19.5	9.7
CH₃CN	Flower	29300	mm	6	-	12	18	15	15	15	-	8
			MIC	1465	-	732.5	366.3	366.3	366.3	91.6	-	1465
	Leaf	16400	mm	6	-	13	14	10	14	15	-	-
			MIC	820	-	410	410	410	410	51.3	-	-
	Stem	10300	mm	-	-	-	-	10	11	8	-	6
			MIC	-	-	-	-	515	515	515.0	-	515
CH₃OH	Flower	61100	mm	6	-	15	10	14	15	12	-	-
			MIC	1527	-	190	381.9	95.5	95.5	95.5	-	-
	Leaf	60000	mm	-	-	10	10	8	10	15	-	-
			MIC	-	-	750	750	750	750	93.8	-	-
	Stem	44700	mm	-	-	10	8	17	14	12	-	-
			MIC	-	-	558.8	1117	69.9	69.9	69.9	-	-
Amp.		10		10	10	18	10	35	15			
Strep.		10								35		
Flu.		5									25	25

Ec: E. coli, Yp: Y. pseudotuberculosis, Pa: P. aeruginosa, Sa: S. aureus, Ef: E. faecalis, Bc: B. cereus, Ms: M. smegmatis, Ca: C. albicans, Sc: S. cerevisiae, Amp.: Ampicillin, Strep.: Streptomycin, Flu.: Fluconazole, (-): no activity of test concentrations.

The best activity was observed for the EO of the leaf against *M. smegmatis* with 27 mm inhibition. Acetonitrile flower extract gave better activity against the *P. aeruginosa, E. faecalis, S. aureus, B. cereus,* and *M. smegmatis* with 12 mm, 18 mm, 15 mm, 15 mm, and 15 mm inhibition zones, respectively. The methanol extract showed moderate antimicrobial activity against all tested microorganisms except *Y. pseudotuberculosis, C. albicans,* and *S. cerevisiae.* The results have shown that the EOs and extracts' antimicrobial activity are more susceptible to gram-(+) bacteria and *M. smegmatis.* The MIC of the EOs and the extracts from the parts of *E. angustifolium* were observed within the range of 10.2-1465.0 µg/mL against *E. coli, P. aeruginosa, E. faecalis, S. aureus, B. cereus,* and *M. smegmatis,* respectively (Table 2). Limonene (varied from 42.9% to 95.5%) was the major compound in the EOs and SPME of all, except *γ*-terpinene (29.4%) was the main constituent in the SPME of the leaf, which has been reported to have antibacterial properties [38]. Thus, the bactericidal activity of the EOs and solvent extracts of *E. angustifolium* may be mainly related to the high content of monoterpenes. Other constituents present in the extracts were reported to have antibacterial activities and may also have made a remarkable contribution to the bactericidal activities of EOs and solvent extracts. The antibacterial activity differences are possibly due to the composition, the concentration of EOs, and extraction methods.

A phytochemical study (six flavonoids and 4 phytosterols) and antimicrobial activity of the aqueous and ethanolic extracts of *E. angustifolium* were reported [16]. 92 Neutral compounds (triterpenoids, polyprenols, and dolichols) were mentioned from *C. angustifolium* leaves [21]. Antibacterial, antifungal, antioxidant activities, total phenolic content, DNA-binding activity for the methanolic, ethanolic, and aqueous extracts of *E. angustifolium* were mentioned [6]. Ethanol extracts of *E. angustifolium* leaf and flower tested against the of *S. aureus*, *B. subtilis*, *E. coli*, *P. aeruginosa*, *Proteus mirabilis*, *C. albicans*, *C. tropicalis*, *C. dubliniensis* and *S. cerevisiae* with MIC values between 4.6±0.2 and 18.2±0.8 mg/mL [14]. Total flavonoid content, antioxidant activity, elastase, tyrosinase, and lipoxygenase inhibitor capacity of the aqueous extract of *E. angustifolium* were reported. The aqueous extracts of *E. angustifolium* exhibited strong elastase (EC₅₀ = 42.72

± 2.38 µg/mL), tyrosinase (EC$_{50}$ = 33.03 ± 3.71 µg/mL), and lipoxygenase inhibitory activities (EC$_{50}$ = 0.57 ± 0.06 µg /mL) [12]. The antimicrobial activity for the ethanolic extracts of *Epilobium* species (*E. angustifolium*, *E. hirsutum*, *E. palustre*, *E. tetragonum,* and *E. rosmarinifolium*) was mentioned, and all the ethanolic dry extracts gave antimicrobial activity in a range of 10 µg/mL to 650 µg/mL [16]. The antimicrobial activities of the EO of *E. hirsutism* have been reported, and it showed activity against *E. coli* with an inhibition zone of 10 mm [37].

Conclusion

Eighty-one volatile constituents were characterized from the flower, leaf, and stem of *E. angustifolium*, resulting in variations containing different VOCs. The amounts of monoterpenes identified by SPME of *E. angustifolium* were more significant in EOs for the flower and stem of *E. angustifolium.* Limonene (varied from 42.9% to 95.5%) was the major compound in the EOs and SPME of all, whereas *γ*-terpinene (29.4%) was the main constituent in the SPME of the leaf. Experimental results showed that different extraction methods and parts of the plant used gave chemical variation as in the literature. The amount of limonene was so high that it could be the source to produce it. All EOs and the solvent extracts gave good activity against the *M. smegmatis* within the range of 10.2-223.8 µg/mL (MIC). In general, the leaf's most significant activity of EO was observed at 10.2 µg/mL MIC value against *M. smegmatis*. *n*-Hexane of leaf extract gave better antimicrobial activity against the *S. aureus, B. cereus,* and *M. smegmatis* with 39.1 µg/mL, 39.1 µg/mL, and 78.1 µg/mL MIC values, respectively. *n*-Hexane extracts of the leaf and stem of the plant gave good activity against yeast fungi (antifungal activity). According to MIC values, the highest antimicrobial activity was observed against gram (+) bacteria and *M. smegmatis*. Limonene was used as an aroma to mask the bitter taste of alkaloids in pharmaceutical production. It was used industrially in food production, perfumery, and personal care products such as shaving lotions. Therefore, the overall antimicrobial activity results suggested that EOs and extracts of *E. angustifolium* may have promising prospects for industrial or pharmaceutical applications. In future work, activity-guided phytochemical studies could be carried out for the solvent extract of *E. angustifolium.*

Acknowledgments

Conflict of Interest

No potential conflict of interest was reported by the author(s).

References

[1] Schepetkin I.A., Ramstead A.G., Kirpotina L.N., Voyich J.M., Jutila M.A., Quinn M.T., Therapeutic potential of polyphenols from *Epilobium angustifolium* (Fireweed), Phytother. Res., 30(8) (2016) 1287-1297.

[2] Lans C., Possible similarities between the folk medicine historically used by First Nations and American Indians in North America and the ethnoveterinary knowledge currently used in British Columbia, Canada. J. Ethnopharmacol., 192 (2016) 53-66.

[3] Zeybek N., Zeybek U., Pharmaceutical botany. Ege University Faculty of Pharmacy Publication, Izmir (1994).

[4] Granica S., Piwowarski J.P., Czerwińska M.E., Kiss A.K., Phytochemistry, pharmacology and traditional uses of different *Epilobium* species (Onagraceae): A review, J. Ethnopharmacol., 156 (2014) 316-346.

[5] Sayik A., Yusufoğlu A.S., Leyla A., Türker G., Aydin B., Arslan L., DNA-Binding, Biological Activities and Chemical Composition of Wild Growing *Epilobium* angustifolium L. Extracts from Çanakkale, Turkey, J. Turk. Chem. Society, 4(3) (2017) 811-840.

[6] Vitalone A., Guizzetti M., Costa L.G., Tita B., Extracts of various species of *Epilobium* inhibit proliferation of human prostate cells. J. Pharm. Pharmacol., 55(5) (2003) 683-690.

[7] Vitalone A., Bordi F., Baldazzi C., Mazzanti G., Saso L., B. Tita, Anti-proliferative effect on a prostatic epithelial cell line (PZ-HPV-7) by *Epilobium angustifolium* L., Farmaco. 56 (5-7) (2001) 483-489.

[8] Ruszová E., Cheel J., Pávek S., Moravcová M., Hermannová M., Matějková I., Spilková J., Velebný V., Kubala L., *Epilobium angustifolium* extract demonstrates multiple effects on dermal fibroblasts in vitro and skin photo-protection *in vivo*, Gen. Physiol. Biophys., 32(3) (2013) 347-359.

[9] Tóth B.H., Blazics B., Kéry Á., Polyphenol composition and antioxidant capacity of *Epilobium* species. J. Pharm. Biomed. Anal., 49(1) (2009) 26-31.

[10] Onar H.C., Yusufoglu A., Turker G., Yanardağ R., Elastase, tyrosinase and lipoxygenase inhibition and antioxidant activity of an aqueous extract from *Epilobium angustifolium* L. leaves, J. Med. Plant Res., 6(5) (2012) 716-726.

[11] Juan H., Sametz W., Hiermann A., Anti-inflammatory effects of a substance extracted from *Epilobium angustifolium,* Agents and Actions, 23(1-2) (1988) 106-107.

[12] Kosalec I., Kopjar N., Kremer D., Antimicrobial activity of Willowherb *(Epilobium angustifolium L.)* leaves and flowers, Curr. Drug Targets, 14(9) (2013) 986-991.

[13] Zeng Q., Wu J., Lin P., Chemical composition and antimicrobial activity of the essential oil from *Epilobium angustifolium*, Chem. Nat. Compd., 52(6) (2016) 1113-1115.

[14] Battinelli L., Tita B., Evandri M.G., Mazzanti G., Antimicrobial activity of *Epilobium spp.* Extracts*,* Farmaco., 56(5-7) (2001) 345-348.

[15] Silló S., Varga E., Belák Á., Maráz A., Phytochemical and antimicrobial investigation of *Epilobium angustifolium* L, Acta Pharm. Hung., 84(3) (2014) 105-110.

[16] Baum D.A., Sytsma K.J., Hoch P.C., A phylogenetic analysis of *Epilobium (Onagraceae)* based on nuclear ribosomal DNA sequences, Systematic Botany*,* 19(3) (1994) 363-388.

[17] Chamberlain D., Raven P.H., Epilobium *L.* Flora of Turkey and The East Aegean Island*.*, Edinburgh University Press (1972) 183-196.

[18] Kaškonienė V., Stankevičius M., Drevinskas T., Akuneca I., Kaškonas P., Survilienė K.B., Maruška A., Ragažinskienė O., Kornyšova O., Briedis V., Ugenskienė R., Evaluation of phytochemical composition of fresh and dried raw material of introduced *Chamerion angustifolium* L. using chromatographic, spectrophotometric and chemometric techniques, Phytochem., 115 (2015) 184-193.

[19] Kaškonienė V., Maruška A., Akuņeca I., Stankevičius M., Ragažinskienė O., Bartkuvienė V., Kornyšova O., Briedis V., Ugenskienė R., Screening of antioxidant activity and volatile compounds composition of *Chamerion angustifolium (L.)* Holub ecotypes were grown in Lithuania, Nat. Prod. Res., 30(12) (2016) 1373-1381.

[20] Nowak A., Duchnik W., Makuch E., Kucharski L., Ossowicz-Rupniewska P., Cybulska K., Sulikowski T., Moritz M., Klimowicz A., *Epilobium angustifolium* L. Essential oil-biological activity and enhancement of the skin penetration of drugs-*in vitro* study, Molecules, 26(23) (2021) 7188.

[21] Kukina T., Frolova T., Salnikova O., Neutral constituents of *Chamaenerion angustifolium* leaves, Chem. Nat. Compd*.,* 50(2) (2014) 233-236.

[22] Kiss A., Kowalski J., Melzig M., Induction of neutral endopeptidase activity in PC-3 cells by an aqueous extract of *Epilobium angustifolium* L. and oenothein B, Phytomedicine, 13(4) (2006) 284-289.

[23] Kiss A.K., Bazylko A., Filipek A., Granica S., Jaszewska E., Kiarszys U., Kośmider A., Piwowarski J., Oenothein B's contribution to the anti-inflammatory and antioxidant activity of *Epilobium* sp., Phytomedicine, 18(7) (2011) 557-560.

[24] Schepetkin I.A., Kirpotina L.N., Jakiw L., Khlebnikov A.I., Blaskovich C.L., Jutila M.A., Quinnet M.T., Immunomodulatory activity of oenothein B isolated from *Epilobium angustifolium*, J. Immunol. Res., 183(10) (2009) 6754-6766.

[25] Tosun G., Kahriman N., Albay C., Karaoğlu Ş.A., Yaylı N., Antimicrobial activity and volatile constituents of the flower, leaf, and stem of *Paeonia daurica* grown in Turkey, Turk. J. Chem., 35(1) (2011) 145-153.

[26] Renda G., Özel A., Barut B., Korkmaz B., Yaylı N., The Volatile Chemical Compositions of the Essential Oil/SPME and Enzyme Inhibitory and Radical Scavenging Activities of Solvent Extracts and the Essential oils from *Coronilla orientalis* Miller and *C. varia* L. grows in Turkey, Iran. J. Pharm. Res., 18(4) (2019) 1831-1842.

[27] Renda G., Celik G., Korkmaz B., Karaoglu S.A., Yaylı N., Antimicrobial activity and analyses of six *Geranium* L.

species with headspace SPME and hydrodistillation, J. Essent. Oil-Bear. Plants, 19(8) (2016) 2003-2016.

[28] Yaylı B., Tosun G., Karaköse M., Renda G., Yaylı N., SPME/GC-MS analysis of volatile organic compounds from three *Lamiaceae* species *(Nepeta conferta Hedge & Lamond, Origanum onites* L. and *Satureja cuneifolia Ten*.) growing in Turkey, Asian J. Chem., 26(9) (2014) 2541-2544.

[29] Yaylı N., Yaşar A., Yaylı N., Albay M., Coşkunçelebi K., Essential Oil Analysis and Antimicrobial Activity of *Paeonia mascula* from Turkey, Nat. Prod. Commun., 3(6) (2008) 941-944.

[30] Iskender N.Y., Yaylı N., Yildrim N., Cansu T.B., Terzioglu S., The volatile constituents of the flower, leaf, and stem of *Verbascum wiedemannianum* grown in Turkey, J. Oleo Sci., 58(3) (2009) 117-121.

[31] Yılmaz G., Çiçek M., Demirci B., Başer K.H.C., Composition of the essential oils of five subspecies of *Scutellaria orientalis* from Turkey, J. Essent. Oil Res., 32(5) (2020) 429-435.

[32] Verma R.S., Verma S.K., Tandon S., Padalia R.C., Darokar M.P., Chemical composition and antimicrobial activity of *Java citronella (Cymbopogon winterianus Jowitt ex Bor)* essential oil extracted by different methods, J. Essent. Oil Res., 32(5) (2020) 1-7.

[33] Adams R.P., Identification of essential oil components by gas chromatography/mass spectrometry. Allured publishing corporation Carol Stream, IL (2007).

[34] Üçüncü O., Yaylı N., Yaşar A., Terzioğlu S., Yaylı N., Chemical Composition of the Essential Oils from Flower, Leaf, and Stem of *Senecio trapezuntinus* Boiss. Grown in Turkey, Nat. Prod. Commun., 3(6) (2008) 925-928.

[35] Barry A.L., Standards NCCLS document, Methods for determining bactericidal activity of antimicrobial agents: approved guideline. National Committee for Clinical Laboratory Standards Wayne (1999).

[36] Woods G.L., Brown-Elliott B.A., Conville P.S., Desmond E.P., Hall G.S., Lin G., Pfyffer G.E., Ridderhof J.C., Siddiqi S.H., Wallace R.J., Warren N.G., Witebskyet F.G., Susceptibility testing of mycobacteria, nocardiae, and other aerobic actinomycetes. Wayne (PA): Clinical and Laboratory Standards Institute (2011).

[37] Kılıç G., Korkmaz B., Erik İ., Fandaklı S., Yaylı S.S., Faiz Ö., Karaoğlu Ş.A., Yaylı N., Antimicrobial, antioxidant, tyrosinase activities and volatile compounds of the essential oil and solvent extract of *Epilobium hirsutum* L. growing in Turkey, Turkish Journal of Analytical Chemistry, 2(2) (2020) 87-94.

[38] Erasto P., Viljoen A.M., Limonene-A review: Biosynthetic, ecological and pharmacological relevance, Nat. Prod. Commun., 3(7) (2008) 1190-1202.

Cumhuriyet Science Journal

Cytotoxic Activity, Anti-migration and *in silico* Study of *o*-Coumaric acid on H1975 Non-small Cell Lung Cancer Cells

Dogukan Mutlu [1,a,*]

[1] *Department of Molecular Biology and Genetics, Faculty of Engineering and Natural Sciences, Üsküdar University, Istanbul, Türkiye*
*Corresponding author

Research Article

ABSTRACT

Lung cancer represents the most common malignancy and remains the primary cause of cancer-related deaths worldwide. Phenolic acids, including o-coumaric acid (OCA), have attracted considerable attention due to their diverse biological activities, particularly their anticancer properties. This study evaluates the cytotoxic activity of OCA, along with its anti-migration effects and molecular docking analysis. The in vitro cytotoxicity of OCA on H1975 cells was assessed using the MTT assay and Acridine orange/ethidium bromide (AO/EB) staining, while its impact on cell migration was analyzed through an in vitro scratch assay. OCA demonstrated cytotoxic activity against H1975 cells, with an IC50 value of 8.107 mM, and inhibited cell migration by 38%. Additionally, in silico molecular docking was performed to investigate its interaction with the epidermal growth factor receptor (EGFR). Although OCA exhibited notable binding interactions with EGFR, including hydrogen bonding and pi-alkyl interactions, its binding affinity (−5.9 kcal/mol) was lower compared to Gefitinib (−8.5 kcal/mol), a known EGFR inhibitor. These findings suggest that while OCA holds potential as a therapeutic agent against non-small cell lung cancer, its efficacy may be enhanced through structural modifications, including the synthesis of derivatives, warranting further research into its industrial and clinical applications.

Keywords: o-Coumaric acid, Lung cancer, Cytotoxicity, Anti-migration, Molecular docking.

[a] ✉ *dogukan.mutlu@uskudar.edu.tr* (iD) *https://orcid.org/0000-0003-3259-5822*

Introduction

Lung cancer is a leading cause of cancer-related mortality globally, with non-small cell lung cancer (NSCLC) being the predominant subtype, accounting for over 80% of cases [1]. Most NSCLC patients are diagnosed at advanced metastatic stages, which renders them unsuitable for surgical intervention [2]. Chemotherapy remains a key treatment modality for cancer patients; however, chemotherapeutic agents often induce only temporary tumor regression. Over time, many cases develop drug resistance, leading to disease progression [3]. Consequently, numerous studies have been dedicated to elucidating the mechanisms underlying this resistance.

OCA, also known as trans-2-hydroxycinnamic acid, is a naturally occurring hydroxycinnamic acid widely found in various natural sources [4]. OCA is part of the human diet and contributes to the health benefits associated with consuming fruits, vegetables, whole grains, and mushrooms [5,6]. Its presence in these dietary sources is one reason why diets rich in fruits and vegetables are often recommended for their potential health-promoting properties.

OCA belongs to the group of phenolic compounds and has attracted the attention of researchers due to its various biological activities, particularly its potential anticancer effects [7-9]. The simple chemical structure of cinnamic acid, which includes a hydroxyl group (-OH) attached to the benzene ring, forms the basis for the antioxidant properties of extracts obtained from natural

products containing OCA. These properties allow OCA to scavenge free radicals, protect cells from oxidative damage, and reduce the risk of diseases such as cancer [10-12].

However, studies on the biological activities of OCA are limited, and there are only a few reports on its anticarcinogenic activity. In this study, we evaluated the cytotoxic and anti-migration effects of OCA on H1975 cells, which are commonly used in NSCLC research due to their EGFR L858R/T790M double mutation. This mutation is known to cause resistance to first-generation tyrosine kinase inhibitors (TKIs), such as Gefitinib and Erlotinib, which target EGFR [13]. The presence of this mutation contributes to acquired resistance, making these drugs less effective in treating NSCLC patients with the L858R/T790M mutation [14,15]. Therefore, H1975 cells offer a useful model for investigating both the biology of EGFR-mutated NSCLC and the therapeutic potential of novel compounds like OCA. The findings suggest that OCA may have the potential to be developed as an anti-metastatic drug for human lung cancer.

Material and Methods

Cell Culture

Human non-small lung cancer (H1975) cell line was purchased from American Type Culture Collection (ATCC). Cells were cultured with Dulbecco's Modified Eagle's

Medium (DMEM, Sigma-Aldrich, Germany) with 10% fetal bovine serum (FBS, Capricorn, Germany) and 100U/ml of penicillin, and 100 µg/ml of streptomycin (Capricorn) at 37 °C in a humidified 5% CO_2, as previously described [16].

Cytotoxicity Assay

Cytotoxicity was evaluated using the MTT (3-(4,5-Dimethylthiazol-2-yl)-2,5-Diphenyltetrazolium Bromide) assay, as described previously [17]. H1975 cells were plated into 96-well plates (2×10^3 cells/well). OCA was obtained from Sigma-Aldrich was dissolved in dimethyl sulfoxide (DMSO, Carlo Erba). Then different concentrations (0.625, 1.25, 2.5, 5, and 10 mM) of OCA were used to cytotoxicity for 24 hours. The final concentration of DMSO was kept below 1% (v/v), and the control group was treated with DMSO alone. After treatment, the culture medium was removed, 10 µl of MTT solution (5 mg/ml, Merck, USA) was added into each well and cells were kept at 37 °C. After 4 h incubation, the culture medium was aspirated and 100 µl of DMSO was added to each well, for solubilization of formazan crystals using an orbital shaker for 15 min at room temperature. Finally, cell viability was measured at 590 nm using an Epoch microplate spectrophotometer (BioTek, USA). The results are expressed as percentages of the treatment group compared to the control group. IC_{50} values was calculated using GraphPad Prism 9 (GraphPad Software, CA, USA).

AO/EB Double Staining Assay

H1975 cells were incubated, and treated with OCA at IC_{50} concentration as mentioned, after 95% alcohol fixation, cells were stained with acridine orange/ethidium bromide (AO/EB) mixture (1:1, 100 µg/ml), as described previously [18]. After washing for two times, the results were observed and photographed by fluorescent microscope (BX53F, Olympus, Japan).

In vitro Scratch Assay

The effect of OCA on the migration ability of H1975 cells was investigated by the scratch assay, as described previously [19]. Cells were seeded in 6-well plates (3×10^4 cells/well) and incubated for 24 hours. Then, the cell monolayers were scratched with a sterile 200 µl tip. After scratching, the wells were washed with phosphate buffered saline (PBS) twice to discard cell debris, and the DMEM was refreshed. Then, H1975 cells were treated with the IC_{50} dose of OCA for 24 hours. The wound areas were captured at 0, 24, 48, and 72 h with an inverted microscope (Oxion Inverso, Euromex, Netherlands) and the migration rate (%) was calculated with ImageJ software 1.53e (USA).

Molecular Docking Study

Molecular docking of OCA with EGFR was completed using the SeamDock web server [20]. Protein-ligand interactions were evaluated using AutoDock Vina with parameters set to a grid spacing of 1 Å, an energy range of 5 kcal/mol, and an exhaustiveness level of 8, while the

docking box dimensions were configured as 33×27×18 Å. The docking models with high scores were selected. Figures were generated with SeamDock and BIOVIA Discovery Studio v.24.1.0. The interactions between OCA and EGFR were analyzed using Discovery Studio. Additionally, the inhibitor that was bound to *EGFR* was removed prior to the docking studies. The data for the three-dimensional (3D) structures of EGFR (PDB ID: 5D41) was used in this study.

Statistical Analysis

GraphPad Prism 9 (San Diego, CA, USA) was used for statistical analysis. The experiments were performed in triplicate, and the data are expressed as means ± SD. For comparisons between control and treatment groups, one-way ANOVA followed by Dunnett's test was performed.

Results and Discussion

MTT Assay

The MTT assay was conducted over a 24-hour incubation period to assess the cytotoxic activity of OCA against H1975 cells. As shown in Figure 1, within the concentration range of 0.625 to 2.5 mM, OCA did not exhibit statistically significant cytotoxicity. However, at higher concentrations, it inhibited cell viability in a dose-dependent manner, with an IC_{50} value of 8.107 ± 0.068 mM.
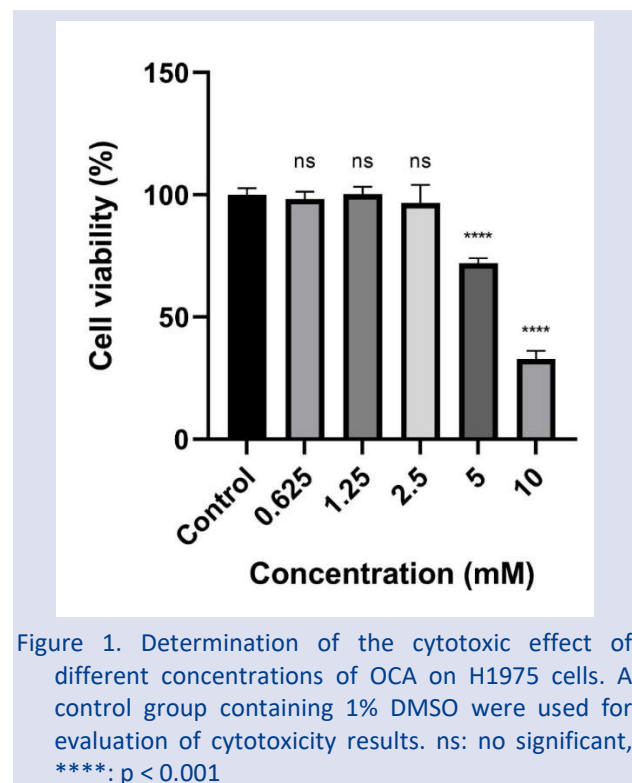
Figure 1. Determination of the cytotoxic effect of different concentrations of OCA on H1975 cells. A control group containing 1% DMSO were used for evaluation of cytotoxicity results. ns: no significant, ****: p < 0.001

Morphological Examination

After 24 hours of incubation, H1975 cells exposed to the IC50 concentration of OCA exhibited significant morphological changes compared to the control group (Fig. 2). These changes included nuclear condensation,

cellular degeneration, and a rounded morphology. In contrast, cells treated with 1% DMSO maintained a morphology similar to the control group after the incubation period.
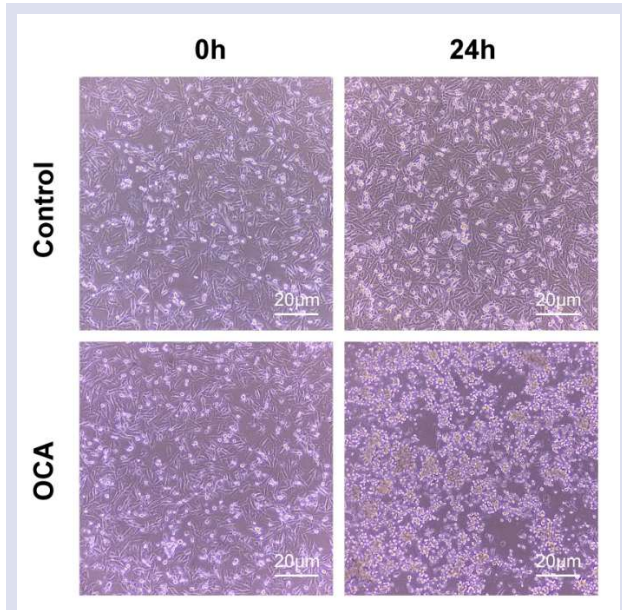
Figure 2. Morphological changes were observed in H1975 cells exposed to OCA at the end of 24 hours of incubation, compared to the control group at 10X magnification.

Fluorescence Microscopy

Fluorescence microscopy analysis was performed on AO/EB (100 µg/mL AO and 100 µg/mL EB) double-stained H1975 cells, both control and OCA-treated, following 24 hours of incubation. Viable cells have uniform green nuclei and the decrease in cell density is consistent with the MTT results (Fig. 3).
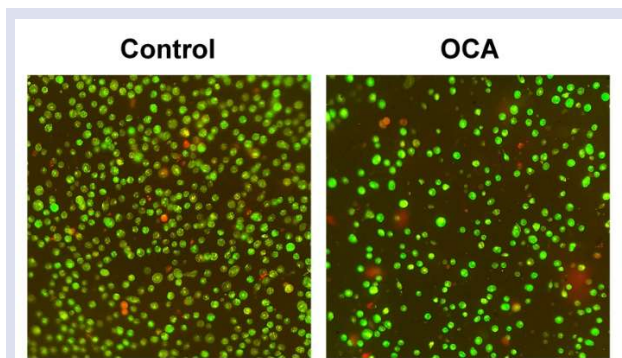
Figure 3. Fluorescence images of AO/EB staining. Viable cells have uniform green nuclei while dead and apoptotic cells exhibit a red and orange, respectively at 20X magnification.

Cell Migration

A scratch assay was performed to assess the effects of OCA on the migration of H1975 cells (Fig. 4). After a 24-hour treatment period, the medium containing the IC50 concentration of OCA was carefully removed from each well, the cells were washed twice with PBS, and fresh

medium was added. The control group received culture medium supplemented with 1% DMSO as the final concentration.
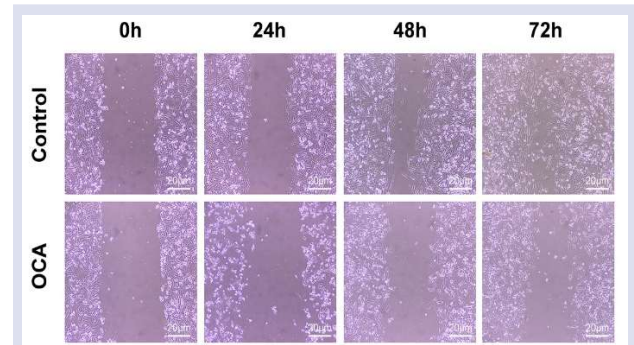
Figure 4. Representative photographs of cell migration using the *in vitro* scratch assay of OCA treated H1975 cells at 10X magnification. Photos were taken at 0, 24, 48, and 72 h.

In this study, the migration of control cells reached 90% at 72 h. However, the migration rate of cells treated with OCA was found to be 52% (Fig. 5). In other words, cell migration was restricted approximately two times (1.7-fold) compared to the control cells.
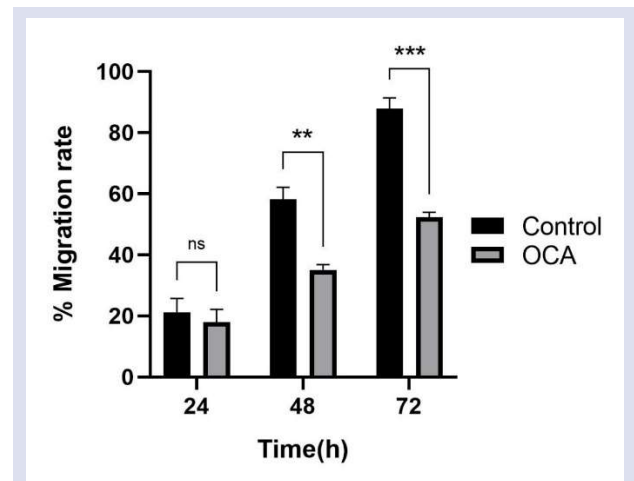
Figure 5. Percentage of migration rate for OCA treated cells compared to the control at 0, 24, 48, and 72 h. ns: no significant, **: $p<0.002$, ***: $p<0.0002$

Interaction Analysis

The 3D structure of EGFR was obtained from the PDB database as the receptor protein. The SMILES code of OCA (CID: 637540) and Gefitinib (CID: 123631) were retrieved from PubChem. OCA's binding interactions with the amino acids in the active site of EGFR were investigated through molecular docking studies. As shown in Figure 6, OCA revealed interactions with ALA1000, GLU1004, ASN771, VAL774, ARG776, GLN791, and LYS852, with a binding affinity of −5.9 kcal/mol in the best pose.

The molecular docking study of OCA with EGFR revealed the following bonding interactions between the ligand and protein residues: 2.10 Å and 2.58 Å long hydrogen bonds with GLN791 and VAL774, respectively;

2.97 Å and 1.40 Å long unfavorable donor-donor interactions between ASN771 and LYS852 of the target protein and OCA, respectively; 4.78 Å and 5.26 Å long pi-alkyl interactions with ARG776 and ALA1000, respectively; and a 4.75 Å long pi-anion interaction with GLU1004.

Gefitinib, a known EGFR inhibitor, demonstrated a binding affinity of −8.5 kcal/mol in the best pose, outperforming OCA in its interaction strength with the EGFR active site (Fig. 6). Gefitinib formed hydrogen bonds with key residues, including ASP770 (2.58 Å), ARG776 (2.03 Å), ARG999 (2.35 Å), GLU1005 (2.75 Å), and ASP1006 (1.97 Å). Additionally, it exhibited a pi-cation interaction with LYS852 (4.58 Å) and a Pi-anion interaction with GLU1005 (4.26 Å). Gefitinib also established alkyl interactions with ARG999 (4.98 Å) and ALA1000 (3.91 Å), as well as a Pi-alkyl interaction with ARG776 (4.56 Å). These interactions highlight Gefitinib's strong and versatile binding capability with the EGFR active site.
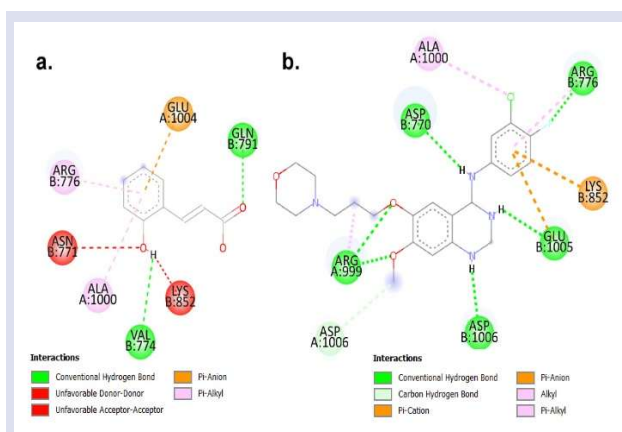
Figure 6. Representative images of molecular docking. Dotted lines show the interactions of a. OCA with EGFR (binding affinity: −5.9 kcal/mol) and b. Gefitinib with EGFR (binding affinity: −8.5 kcal/mol)

This higher affinity can be attributed to the formation of a greater number of hydrogen bonds, as well as diverse secondary interactions (pi-cation and pi-anion interactions) with residues critical for EGFR binding. While OCA demonstrated notable interactions with residues such as GLU1004, GLN791, and VAL774, it showed unfavorable donor-donor interactions with ASN771 and LYS852, potentially reducing its binding efficiency. In contrast, Gefitinib formed favorable interactions with key residues, including ASP770, ARG776, and GLU1005, which are essential for robust binding. Furthermore, Gefitinib's interaction with LYS852 via a pi-cation bond and its engagement with both GLU1005 and ARG776 through pi-anion and pi-alkyl interactions, respectively, underscore its versatility in binding modes.

Numerous in vitro studies have demonstrated the ability of OCA to induce apoptosis in various cancer cell lines. For instance, OCA has been shown to trigger apoptosis in human breast adenocarcinoma MCF-7 cells by activating caspase enzymes, which play a pivotal role in the apoptotic process [21]. Cai et al. (2021) highlighted that OCA inhibits prostate cancer cell growth by targeting

the androgen receptor (AR)/β-catenin axis and initiating apoptosis [22]. Similarly, Jung et al. (2012) observed that OCA induced apoptosis in glioblastoma cells through reactive oxygen species (ROS) production and activation of caspase-dependent pathways [23]. In colorectal cancer cells, OCA suppressed proliferation and induced apoptosis by interfering with the TGF-β signaling pathway [24].

Additionally, OCA has been reported to inhibit cell proliferation in both malignant (HSG1) and non-malignant (S-G; GN61) cells. The NR50 value was determined as 6.4 mM for HSG1 cells, while the values for S-G and GN61 cells were 6.7 mM and >10 mM, respectively [7]. Sen et al. (2013) further demonstrated the anti-proliferative effects of OCA, with EC50 values of 4.95 mM in MCF-7 cells and 7.39 mM in HepG2 cells. Their findings also revealed OCA's ability to induce apoptosis in breast cancer cells, alongside its impact on xenobiotic metabolism and potential drug interactions [8,9].

While prior studies have reported OCA's anticancer effects in various cancer types, this study is the first to explore and confirm OCA's cytotoxic and anti-migration effects on EGFR-mutated H1975 NSCLC cells, a clinically relevant model of drug-resistant lung cancer. After 24 hours of treatment, OCA exhibited significant cytotoxicity at concentrations above 2.5 mM, reducing H1975 cell viability to approximately 30% at a 10 mM concentration. Consistent results were observed in the AO/EB assay. Moreover, OCA markedly inhibited migration in H1975 cells compared to the control group. Unlike previous studies that primarily focused on apoptosis induction or proliferation suppression, our findings also highlight OCA's strong anti-migration properties in lung cancer cells, which are critical for metastasis prevention.

However, the IC_{50} value of OCA in H1975 cells (8.107 mM) is relatively high, suggesting that achieving effective cytotoxicity in clinical settings may be challenging due to physiological limitations. For instance, a recent study reported cytotoxic effects within a dose range of 100–500 μM in U-138 MG glioblastoma cells treated with OCA derivatives [25]. These findings underscore the necessity of developing strategies to enhance OCA's efficacy at lower concentrations. Potential approaches include structural modifications to produce more potent derivatives, combination therapies to exploit synergistic effects with other chemotherapeutic agents, and advanced drug delivery systems to optimize its pharmacokinetics and bioavailability. Such advancements are critical for bridging the gap between OCA's promising in vitro effects and its potential clinical applications.

It is well known that many cases of NSCLC involve overexpression of EGFR. As such, EGFR is a targeted receptor in the treatment of lung cancer [26]. The use of currently available EGFR inhibitors for NSCLC treatment still faces various shortcomings, particularly the high failure rate due to resistance [27]. For this reason, OCA was docked with the EGFR macromolecule, and the results showed that OCA has the potential to inhibit receptors that are overexpressed in NSCLC. The docking results suggest that while OCA shows some potential as an EGFR

ligand, its lower binding affinity and the presence of unfavorable interactions make it less effective compared to Gefitinib. Future studies could explore structural modifications of OCA, including the synthesis of derivatives, to enhance its binding properties and interaction profile, potentially improving its inhibitory activity against EGFR.

This study contributes to the understanding of OCA's anticancer properties by demonstrating its specific activity against H1975 cells. While further research is necessary to validate these findings, the results highlight OCA's potential role as a supplementary or alternative approach in lung cancer treatment, particularly in addressing the challenges posed by drug resistance.

Conclusion

This study suggests that OCA may serve as a promising alternative bioactive agent for NSCLC. This is the first examination of the antiproliferative effects of OCA on H1975 cells. Further research is needed to elucidate the molecular mechanisms underlying the potential anti-cancer activities of OCA.

Conflict of interest

There are no conflicts of interest in this work.

Acknowledgments

References

[1] Siegel R.L., Giaquinto a.N., Jemal A., Cancer statistics, *CA Cancer J. Clin.*, 74 (2024) 12–49.

[2] Siegel R.L., Miller K.D., Jemal A., Cancer statistics, *CA Cancer J Clin.*, 68 (2018) 7-30.

[3] Anand U., Dey A., Chandel A.K.S., Sanyal R., Mishra A., Pandey D.K., De Falco V., Upadhyay A., Kandimalla R., Chaudhary A., Dhanjal J.K., Dewanjee S., Vallamkondu J., Pérez de la Lastra J.M., Cancer chemotherapy and beyond: Current status, drug candidates, associated risks and progress in targeted therapeutics, *Genes Dis.*, 4 (2022) 1367-1401.

[4] Mead J.A.R., Smith J.N., Williams, R.T., Studies in detoxication. 72. The metabolism of coumarin and of o-coumaric acid, *Biochemical Journal*, 68 (1) (1958) 67.

[5] Sellami I.H., Maamouri E., Chahed T., Wannes W.A., Kchouk M.E., Marzouk B., Effect of growth stage on the content and composition of the essential oil and phenolic fraction of sweet marjoram (Origanum majorana L.), *Ind Crops Prod.*, 30(3) (2009) 395-402.

[6] Cayan F., Deveci E., Tel-Cayan G., Duru M.E., Phenolic acid profile of six wild mushroom species by HPLC-DAD, *Chem. Nat. Compd.*, 54 (2018) 985-986.

[7] Babich H, Visioli F., In vitro cytotoxicity to human cells in culture of some phenolics from olive oil, *Farmaco.*, 58(5) (2003) 403-407.

[8] Sen A., Terzioglu G., Atmaca P., Celik G., Ozgun O., Arslan S., Modulatory actions of o-coumaric acid on carcinogen-activating cytochrome P450 isozymes and the potential for drug interactions in human hepatocarcinoma cells, *Pharmaceutical Biology*, 53(9) (2015) 1391–1398.

[9] Sen A., Atmaca P., Terzioglu G., Arslan S., Anticarcinogenic effect and carcinogenic potential of the dietary phenolic acid: o-coumaric acid, *Nat Prod Commun.*, 8(9) (2013) 1269-74.

[10] Boutellaa S., Zellagui A., Öztürk M., Bensouici C., Ölmez Ö.T., Menakh M., Duru M.E., HPLC-DAD profiling and antioxidant activity of the butanol extract from aerial parts of Algerian L., *Acta Scientifica Naturalis*, 6(1) (2019) 8-16.

[11] Suleiman J.B., Mohamed M., Abu Bakar A.B., Nna V.U., Zakaria Z., Othman Z.A., Aroyehun A.B., Chemical profile, antioxidant properties and antimicrobial activities of Malaysian Heterotrigona itama bee bread, *Molecules*, 26(16) (2021) 4943.

[12] Sun Y., Ren G., Shi Q., Zhu H., Zhou N., Kong X., Jiang D., Liu C., Identification of a novel coumarins biosynthetic pathway in the endophytic fungus Fusarium oxysporum GU-7 with antioxidant activity, *Appl. Environ. Microbiol.*, 89(1) (2023) e01601-22.

[13] Pao W., Miller V., Zakowski M., Doherty J., Politi K., Sarkaria I., Singh B., Heelan R., Rusch V., Fulton L., Mardis E., Kupfer D., Wilson R., Kris M., Varmus H., EGF receptor gene mutations are common in lung cancers from "never smokers" and are associated with sensitivity of tumors to gefitinib and erlotinib, *Proc. Natl. Acad. Sci. U.S.A.*, 101(36) (2004) 13306-13311.

[14] Pao W., Chmielecki J., Rational, biologically based treatment of EGFR-mutant non-small-cell lung cancer, *Nat Rev Cancer*, 10 (2010) 760-774.

[15] Rosell R., Carcereny E., Gervais R., Vergnenegre A., Massuti B., Felip E., Palmero R., Garcia-Gomez R., Pallares C., Sanchez J.M., Porta R., Cobo M., Garrido P., Erlotinib versus standard chemotherapy as first-line treatment for European patients with advanced EGFR mutation-positive non-small-cell lung cancer (EURTAC): a multicentre, open-label, randomised phase 3 trial, *Lancet Oncol.*, 13 (2012) 239-246.

[16] Yılmaz C., Arslan S., Mutlu D., Konus M., Kayhan A., Kurt-Kızıldoğan A., Otur Ç., Ozok O., Kivrak A., Identification of 3-Bromo-1-Ethyl-1H-Indole as a Potent Anticancer Agent with Promising Inhibitory Effects on GST Isozymes, *Anticancer Agents Med Chem.*, 21(10) (2021) 1292-1300.

[17] Konus M., Çetin D., Yılmaz C., Arslan S., Mutlu D., Kurt-Kızıldoğan A., Otur C., Ozok O., Algso M.A.S., Kivrak A., Synthesis, biological evaluation and molecular docking of novel thiophene-based indole derivatives as potential antibacterial, GST inhibitor and apoptotic anticancer agents, *ChemistrySelect*, 5 (2020) 5809.

[18] Liu K., Liu P.C., Liu R., Wu X., Dual AO/EB staining to detect apoptosis in osteosarcoma cells compared with flow cytometry, *Med Sci Monit Basic Res.*, 9 (2015) 15-20.

[19] Mutlu D., Seçme M., Arslan S., Effects of Usnic Acid on Cytotoxicity, Colony Formation and Migration in SK-UT-1 Human Uterine Leiomyosarcoma Cells, *SDUFASJS*, 18 (3) (2023) 195–202.

[20] Murail S., de Vries S.J., Rey J., Moroy G., Tufféry P., SeamDock: an interactive and collaborative online docking resource to assist small compound molecular docking, *Front Mol Biosci.*, 8 (2021) 716466.

[21] Nair V.D., Panneerselvam K., Effect of o-coumaric acid on cytotoxicity and apoptosis in human breast

adenocarcinoma MCF-7 cells, *Prev Nutr Food Sci*, 5 (2) (2015) 115-122.

[22] Cai X., Wang X., Li J., Chen S., Sun Z., O-Coumaric Acid Inhibits Proliferation, Migration, and Invasion of Prostate Cancer Cells by Targeting AR/β-Catenin Axis, *Front. Oncol.*, 11 (2021) 679972.

[23] Jung S.H., Kim B.K., Park Y.K., Kim, K.S., Lee S.J., Kim J.R., Moon S. H., Cytotoxic activity of o-coumaric acid in glioblastoma cells is mediated via apoptosis induction and reactive oxygen species production, *Toxicol. In Vitro*, 26 (5) (2012) 699-709.

[24] Li C., Shi Y., Wang W., Li D., O-coumaric acid inhibits cell proliferation and induces apoptosis in colorectal cancer via inhibiting the TGF-β signaling pathway, *IJCEM*, 10 (10) (2017) 14116-14123.

[25] Gutiérrez Mercado Y.K., Mateos Díaz J.C., Ojeda Hernández D.D., López Gonzalez F.J., Reza Zaldivar E.E., Hernández Sapiens M.A., Gómez Pinedo U.A.; Estrada R.S., Macías Carballo M., Canales Aguirre A.A., Ortho-coumaric acid derivatives with therapeutic potential in a three-dimensional culture of the immortalised U-138 MG glioblastoma multiforme cell line, *Neurol Perspect*, 2 (2022) 19-30.

[26] Morgillo F., Della Corte C.M., Fasano M., Ciardiello F., Mechanisms of resistance to EGFR-targeted drugs: lung cancer, *ESMO open*, *1*(3) (2016) e000060.

[27] Chung E.K., Yong S.H., Lee E.H., Kim E.Y., Chang Y.S., Lee S.H., New Targeted Therapy for Non-Small Cell Lung Cancer, *Tuberc Respir Dis.* (Seoul)., 86 (1) (2023) 1-13.

Cumhuriyet Science Journal

Synthesis of Isatin Monohydrazone, Spectroscopic Analysis, DFT Studies, and Molecular Docking Applications to MCF-7 Cell Line

Ceylan Alkaya Yıldız [1,a,*], Sultan Erkan [1,b]

[1] Chemistry Department, Science Faculty, Sivas Cumhuriyet University, Sivas, Türkiye
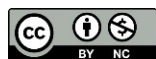
*Corresponding author

Research Article

ABSTRACT

In this study, 3-hydrazinoindolin-2-one (S), an isatin monohydrazone compound, was synthesized. Spectroscopic (IR and ^{1}H-NMR) analyses were performed for the synthesized isatin monohydrazone compound. To compare the experimental spectroscopic data obtained, isatin was optimized at B3LYP/6-31G(d,p). The calculated data were found to be compatible with the experimental data obtained for structural analysis. Contour diagrams and MEP maps were also obtained to identify the electrophilic and nucleophilic attack sites of the synthesis compound. To evaluate their compatibility with biomolecular system, the synthesized compounds were fused with target protein representing MCF-7 cell line. The PDB ID of the synthesized compound: 1M17 and 3HY3 were calculated as -5.70 and -5.73 kcal/mol with the target proteins, respectively. Based on the obtained molecular docking parameters, it was determined to be suitable for anti-cancer applications.

Keywords: Synthesis, Computational chemistry, Molecular docking

[a] Ceylanalkaya21@gmail.com   https://orcid.org/0000-0003-0322-2699   [b] sultanerkan58@gmail.com   https://orcid.org/0000-0001-6744-929X

Introduction

The closed formula for the indole chemical, which has an abundance in nature and is found in the heterocyclic ring structure, is C_8H_7N. 2,3-Benzopyrrole, sometimes known as 1-H indole or simply benzopyrrole, is the indole ring. The closed formula for isatin, an organic molecule produced from indole, is C8H5NO2. It is also known as tribulin, 2,3-dioxindole or 1H-indole-2,3-dione. Isatins serve as building blocks for the production of indole compounds, which have significant biological functions [1]. It is a heterocyclic molecule with two carbonyl groups attached to the polyfunctional indole nucleus are given Figure 1.
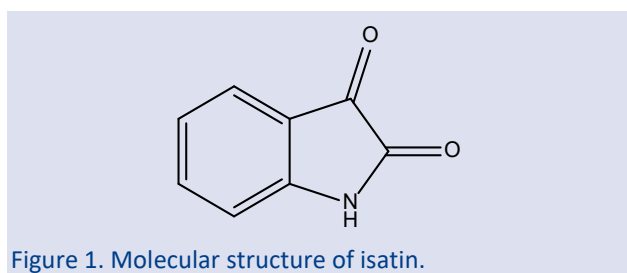
Figure 1. Molecular structure of isatin.

Structurally, isatin consists of two rings with six-membered aromatic and five-membered anti-aromatic characters. Many species replace certain regions in the structure of the isatin skeleton. Therefore, isatin is an important starting material in the synthesis studies of new isatin derivatives [2,4]. Isatin and its derivatives are also used as precursors in drug synthesis. These molecules are used in drug treatment such as anticancer, antibiotics, and antidepressant drugs and have many more clinical applications [3,5]. As an anticancer efficacy study of isatin, Vine et al synthesized a series of substituted 1H-indole-2,3-diones (isatins) and examined there in vitro cytotoxicity against the human monocyte-like histiocytic lymphoma (U937) cell line. Studies have been developed on the structure-activity relationships of di- and tri-halogenated isatins. These compounds showed greater selectivity against leukemia and lymphoma cells over breast, prostate and colorectal carcinoma cell lines. Of the most active compounds, 5, 6, 7-tribromoisatin was found to be antiproliferative at low micromolar concentrations. These results suggest that di- and tri-substituted isatins may be useful guides for future anticancer drug development [6]. When isatin and its derivatives are examined in the literature, it is noteworthy that it has been studied in a broad perspective and there are many noteworthy findings.

Murukan et al. synthesized iron (III), cobalt (III), and manganese (III) complexes of bishydrazone and investigated their antibacterial activity. They found that the 2-hydroxy-1-naphthaldehyde-3-isatin-bishydrazone ligand exhibited enhanced antibacterial properties upon metal complexation [7]. Pandeya et al. synthesized Schiff bases by reacting isatin and its derivatives with 4-(4'-chlorophenyl)-6-(4''-methyl phenyl)-2-aminopyrimidine and evaluated their anti-HIV activity [8]. In a recent study, Sindhu Kumari et al. synthesized coumarin-isatin monohydrazone and their cobalt(II), nickel(II), copper(II) and zinc(II) metal complexes. They used human cancer cell lines such as breast cancer cell (MCF-7) and leukemia

cancer cell (K-562) for in vitro anticancer activity. The results showed moderate activity compared to the standard drug [9]. The DFT (Density Functional Theory) approach is based on modeling electron correlation through electron density functions. This method, rooted in the Hohenberg-Kohn theorem, provides a computational framework for analyzing the electronic structure of molecules, making it essential in chemistry, biology, and physics [10].

In this study, isatinmonohydrazone (S) was synthesized and structurally characterized using spectroscopic methods. The B3LYP/6-31G(d,p) level of theory was employed to compute and compare its spectroscopic data with experimental results. Furthermore, contour diagrams, molecular electrostatic potential (MEP) maps, and frontier molecular orbitals (FMOs) were analyzed to gain insights into its electronic properties. A key objective of this study is to assess the anti-cancer potential of isatinmonohydrazone through molecular docking. To achieve this, molecular docking studies were conducted against target proteins associated with the MCF-7 breast cancer cell line. The docking simulations were performed using PDB IDs: 1M17 [11] and 3HY3 [12], providing insights into the binding interactions that could contribute to the compound's potential as an anti-cancer agent.

Calculation Techniques

Input files of the synthesized isatin monohydrazone were prepared with GaussView 6.0 [13]. All calculations were performed via TR-Grid [14]. With Gaussian 16 Linux version. The molecules were fully optimized using the DFT/B3LYP/6-31G(d,p) level [15,16]. Leading molecular orbitals such as high-energy occupied molecular orbital (E_{HOMO}) and low-energy unoccupied molecular orbital (E_{LUMO}) were calculated according to Koopmans theorem [17].

$$I = -E_{HOMO}$$
$$A = -E_{LUMO}$$

Molecular electrostatic potential (MEP) is related to electronic density and is a very useful descriptor for identifying active sites for electrophilic attacks and nucleophilic attack. Electron-withdrawing and electron-donating parts of the synthesized compounds will be determined with MEP maps.

Docking process DockingServer also MOPAC2009 [18]. Ligands and proteins were optimized using the PM6

method. The parameters of torsion step (0.2 Å), rigid body orientation step (5°), dihedral angle step (5°) and square root of deviation tolerance (2.0 Å) were used in the calculation [19]. All docking calculations are based on AutoDock connection parameters [20]. The binding affinity was measured in kcal/mol, with lower values indicating stronger binding interactions. The docking simulations targeted the active binding pockets of the respective proteins, ensuring alignment with previously reported binding sites. Validation Procedures: The docking protocol was validated using a re-docking approach, and RMSD calculations were performed to assess the accuracy of ligand placement.

Materials and Methods

Chemicals and Solvents Used

Isatin, Hydrazine monohydrate, ethanol are the chemicals and solvents used. Bought from BLDpharm and Sigma-Aldrich brands.

Devices and Computer Programs Used

NMR measurements were taken by dissolving isatin monohydrazone ^{1}H-NMR spectra in DMSO (Dimethyl sulfoxide) -D6, which was synthesized in two stages. Recorded on JEOL (400 MHz) JNM-ECZ400S/L1 NMR Device. Synthesis compound rod models were drawn and added in ChemDraw Professional 15.1. Optimized, MEP, HOMO and LUMO views of the compounds were obtained with GaussView 6.0 computer programs.

Synthesis of Isatine Monohydrazone

It was synthesized according to the reported procedure [21] with minor modifications. Isatin (1g, approximately 7mmol) was dissolved in some ethanol (25ml) and 0.4g of hydrazine hydrate solution was added by dissolving in a small amount of ethanol (2ml). The prepared solution was taken on a heating tablet and left to the reflux system for 3 hours with mixing and temperature. After 3 hours, the reaction was terminated and TLC (thin layer chromatography) was performed to observe the formation of a new product. Then, the newly formed reaction was kept in the fume hood with its mouth open for crystal formation. Crystal formation was observed during the day. The resulting product was washed with ether and filtered on filter paper. A yellow solid was obtained. After the product dried, it was dissolved with ethanol again and excess solvent was removed by Rotary. It was allowed to recrystallize. Yield: 72%.
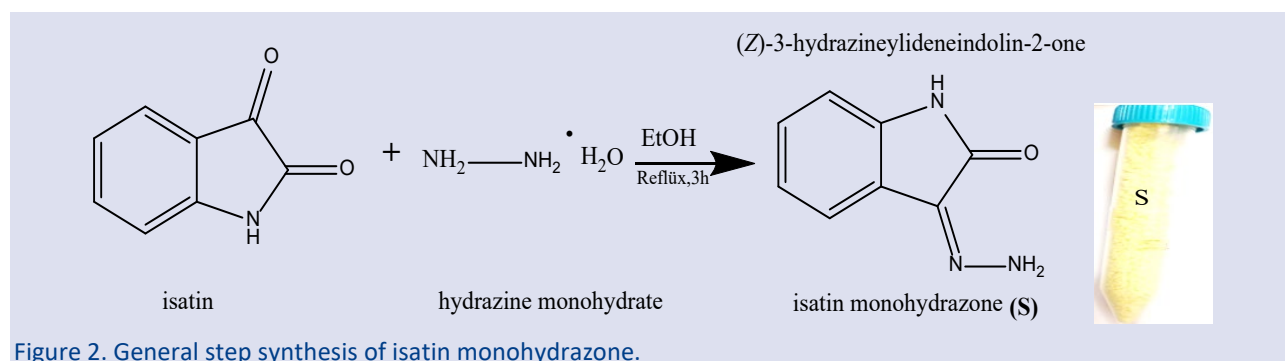
Figure 2. General step synthesis of isatin monohydrazone.

Result and Discussion

Optimized Structure

The molecular structure of synthesized S compound is shown in GaussView 6.0.16 program. Calculations at the B3LYP/6-31G(d,p) level were created using Gaussian16 IA32W-G16RevB.01, Gaussian09 AS64L-G09RevD.01. Figure 3 shows the optimized structure of S compound.
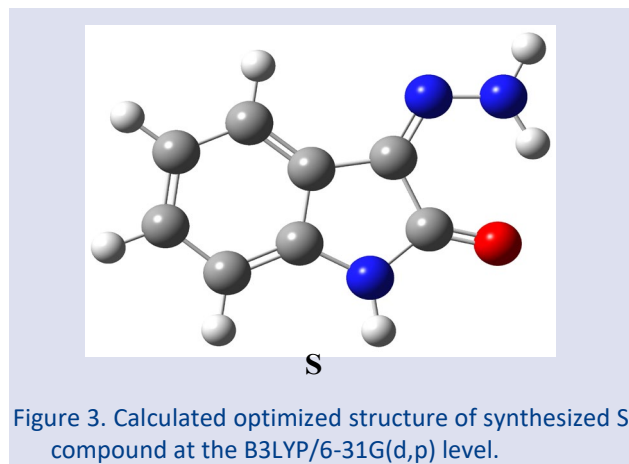
Figure 3. Calculated optimized structure of synthesized S compound at the B3LYP/6-31G(d,p) level.

^{1}H-NMR Calculation-Experimental

Chemical shifts of the ^{1}HNMR spectrum are calculated based on TMS (tetramethylsilane). Structural characterization and ^{1}HNMR spectrum of the synthesized isatin monohydrazone (S) were calculated and the peaks were labeled. TMS proton is calculated as 31.6412 ppm. ^{1}HNMR spectra were calculated at the B3LYP/6-31G(d,p) level and are given in Figure 4.

Table 1. Calculated proton chemical shifts for S.

^{1}H-NMR (ppm)	H9	H10	H11	H12	H18	H19
S	7.42	6.90	7.02	6.50	6.57	5.98
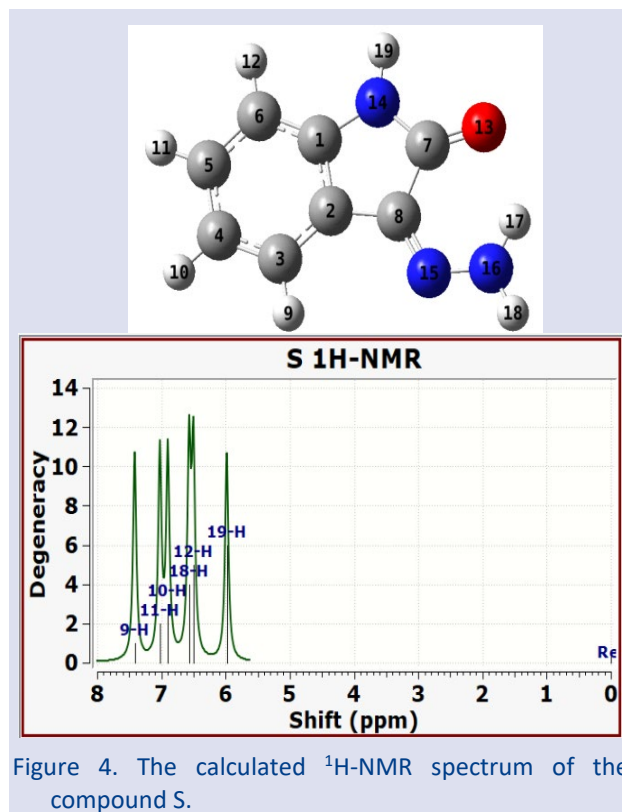
Figure 4. The calculated ^{1}H-NMR spectrum of the compound S.

(Z)-3-hydrazineylideneindolin-2-one (isatin monohydrazone, S)

Yellow powdery substance, Yield %72. ^{1}H NMR (400 MHz, DMSO-D6) δ 10.63, 10.49 (d, J = 14.6 Hz, 1H), 9.49 (d, J = 14.7 Hz, 1H), 7.31 (d, J = 7.5 Hz, 1H), 7.10 (td, J = 7.7, 1.3 Hz, 1H), 6.92 (td, J = 7.6, 1.1 Hz, 1H), 6.81 (d, J = 7.7 Hz, 1H).
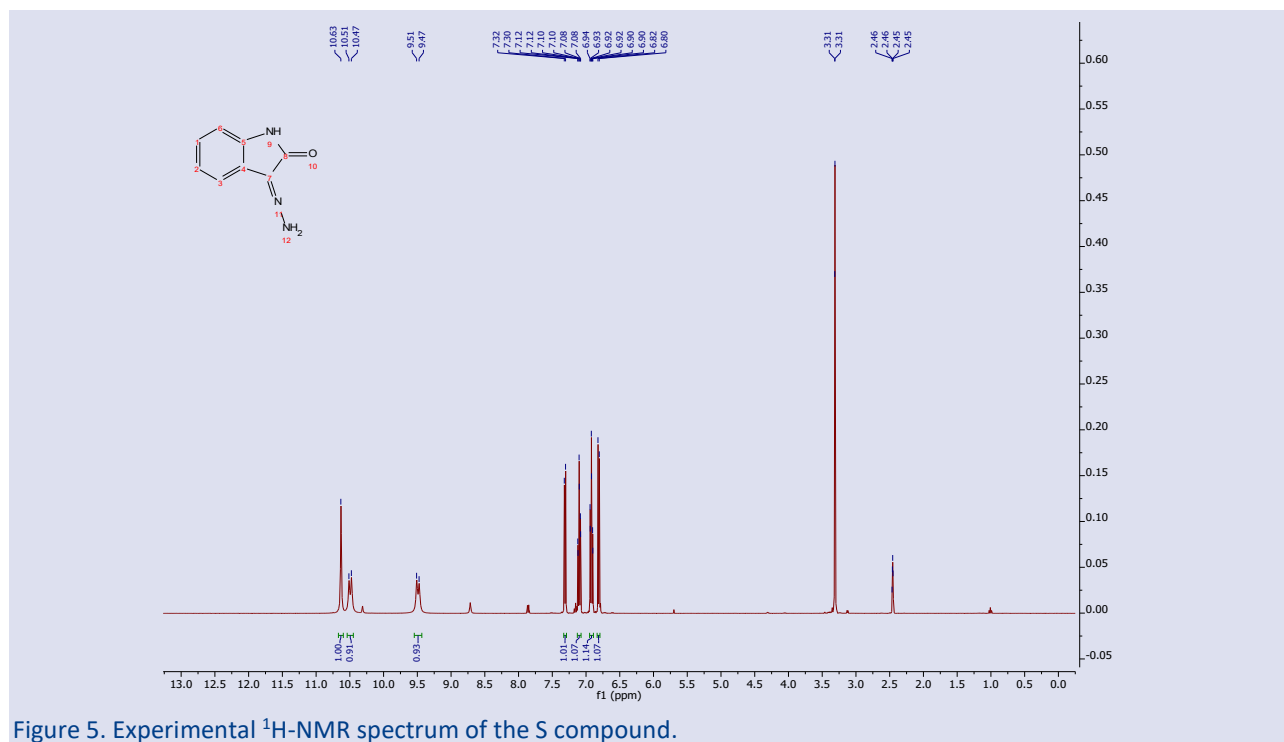
Figure 5. Experimental ^{1}H-NMR spectrum of the S compound.

IR Calculation

The IR spectra of compound S were calculated with the B3LYP/6-31G(d,p) level. The calculated IR spectrum is given in Figure 6. The frequencies obtained by calculation methods are the harmonic frequencies. A measurement factor of 0.967 was used to convert harmonic frequencies into anharmonic frequencies. The calculated anharmonic frequencies of S compounds and their labelling are given in Table 2.
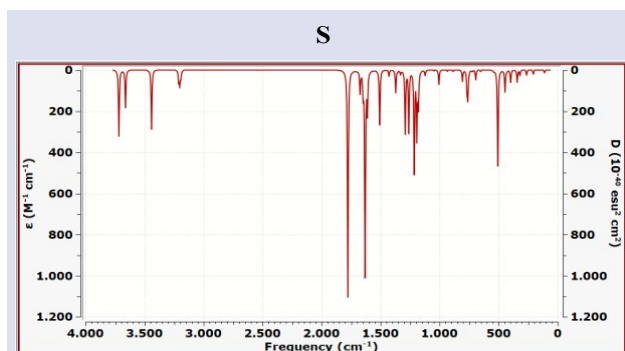
Figure 6. Calculated IR spectrum of the synthesized compound S.

Isatin is a chemical structure containing -C=N-N2, -NH and =O functionals in its monohydrazone structure. νN-H (3541.3 cm^{-1}) vibration refers to the stretching vibration of the N-H bond. Amine (N-H) and amide (N-H) groups are usually seen between 3500-3300 cm^{-1}. This frequency indicates the presence of hydrazone (-NH-N=) or amide structure in the compound. νCaro-H (3087.7 cm^{-1}), the stretching vibration of the C-H bonds in the aromatic ring is seen in this region. C-H vibrations of aromatic compounds usually occur between 3100-3000 cm^{-1}. νC=O (1719.1 cm^{-1}) is defined as the stretching vibration of the carbonyl (C=O) bond.

It is usually seen between 1700-1750 cm^{-1} and indicates the presence of ketone, amide or acid carbonyl group in the compound. Here, the value of 1719.1 cm^{-1} shows the typical vibration of the carbonyl group in the isatin structure. νC=C (1594.0 cm^{-1}) is defined as the stretching vibration of the double bonds (C=C) in the aromatic ring. C=C vibrations of aromatic systems are found between 1600-1450 cm^{-1}. This value confirms that the compound has aromatic character. νC=N (1577.8 cm^{-1}), the stretching vibration of the C=N bond is seen in this region. Values between 1600-1550 cm^{-1} indicate the presence of hydrazone (-C=N-NH2) or imine (-C=N) groups. The vibration of the hydrazone (C=N) group in the isatin monohydrazone structure is observed here. νC=C + ωCH (1458.2 cm^{-1}), CH bending (wagging) vibrations are observed together with the stretching of the C=C bond. It is a frequently encountered mode in aromatic systems. νCN + ωNH + ωCH (1381.6 cm^{-1}), NH and CH bending (wagging) vibrations are observed together with C-N stretching vibrations. This supports the presence of hydrazone (-C=N-NH2) or amine (-NH2) functional groups in the compound. νCN (1310.8 cm^{-1}), C-N stretching vibration is generally observed between 1300-1200 cm^{-1}. This value represents the C-N bonds found in the hydrazone (C=N-NH2) structure. νNN (1248.9 cm^{-1}), stretching vibration of N-N bond, especially seen in hydrazone and azine (N-N) structures. This value is a strong indicator of hydrazone structure. ωCH + ωCH (1175.0 cm^{-1}), CH bending (wagging) vibrations in aromatic ring are seen in this region. CH bending vibrations are common between 1200-1100 cm^{-1}. ωCH (1085.5 cm^{-1}), aromatic CH bending (wagging) vibration is observed as a lower frequency mode.

Frontier Molecular Orbitals

HOMO and LUMO orbitals, also known as boundary molecular orbitals, are when a molecule interacts with another molecule. HOMO, the highest occupied molecular orbital and LUMO, the lowest unoccupied molecular orbitals are used in quantum chemical parameters studies. These orbitals are comparable in their ability to donate and gain electrons. The HOMO orbital represents the electron donating potential. The data show that electron exchange is easy by donating electrons, and the energy gap between the LUMO orbital energy and the HOMO and LUMO orbitals. To indicate the chemical state of a molecule, the energy difference between the HOMO and LUMO orbitals is looked at. When this difference is calculated, information about the stability of the molecule is obtained. It is a pioneer in experimental studies by obtaining theoretical ideas with quantum mechanical studies. With HOMO and LUMO molecular orbitals, inferences can be made about inhibitory reactive sites. B3LYP/6-31G(d,p) level in Figure 7 shows the boundary molecular orbitals of S [22,23].

Table 2. Calculated frequencies (cm^{-1}) and their labelling for compound S.

Modes	Calc.
νN-H	3541.3
νC-H(aro)	3087.7
νC=O	1719.1
νC=C	1594.0
νC=N	1577.8
νC=C+ωCH	1458.2
νCN+ωNH+ ωCH	1381.6
νCN	1310.8
νNN	1248.9
ωCH +ωCH	1175.0
ωCH	1085.5
ν: stretching, δ: Scissoring, ω; Wagging	
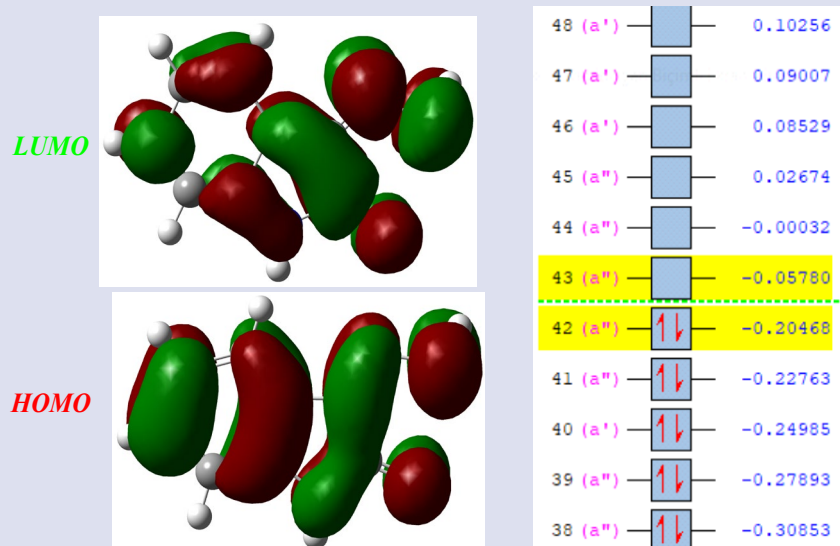
Figure 7. Frontier molecular orbital contour diagrams of S.

As seen in Figure 7, the regions shown in green and red indicate that the electron is localized. LUMO vacant orbitals gain electrons in the red and green portions of the molecule. The HOMO filled orbitals define the electron donating sites in the molecule.

Molecular electrostatic potential (MEP) maps

It provides information about the reactivity of that molecule by showing the same or different colors in each region of the molecule. Electrophilic and nucleophilic attack regions of molecules can also be viewed from MEP maps. In addition, MEP maps are used about the electrostatic potential data of the molecule, the shape of the molecule and the size of the molecule. The colors used to define electrostatic potentials and the order of their potentials are from small to large; red-orange-yellow-green-blue [24,25].
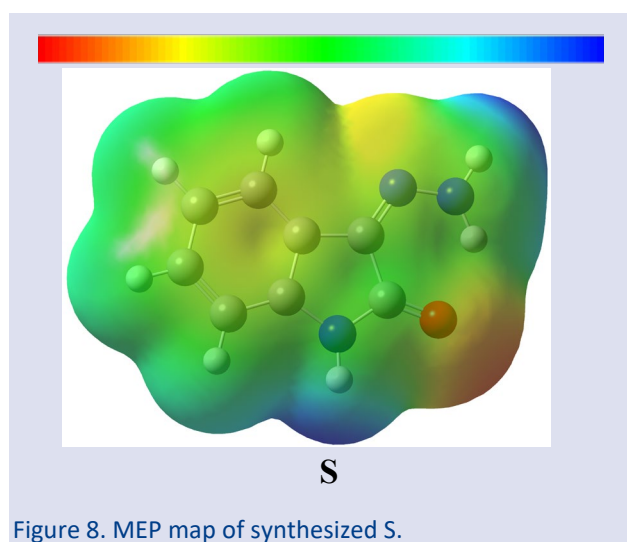
Figure 8. MEP map of synthesized S.

The green areas on the MEP map are neutral regions. Electron donating groups such as -C=N-NH$_2$, NH in the S compound, for example =NH-N=, NH are positively charged and their presence makes that region poor in terms of electrons. Also shown in blue. These synthesized compounds are shown in yellow and red when looking at

the MEP map. The presence of oxygen in the -C=O group is negatively charged and electron rich regions. Therefore, red regions are active regions. MEP maps gave results consistent with contour diagrams of HOMO and LUMO boundary molecular orbitals.

Molecular Docking Studies

The molecular docking method is used in many fields of chemistry and cancer research. Computational studies are a priority in drug design. The molecular docking method is used to understand binding energies and ligand-receptor interaction between proteins. For many types of cancer, the selected target protein can be bound by the binding energy between the selected protein and the compounds studied by molecular docking. The selected cancer cell matches the target protein derived from the protein database [26]. The effect and biological activities of different substituents will be determined by docing studies. The synthesized S is isatin, an organic compound derived from indole. A molecular docking study was performed with target proteins PDB ID= 1M17 [27] and PDB ID= 3HY3 [28] corresponding to the MCF-7 cell line. Docking calculations were performed with DockingServer [29]. Est. between the studied isatin monohydrazone and target proteins. Free Energy of Binding, Est. Inhibition Constant, Ki, vdW + Hbond + desolv Energy, Total Intermolec. Energy and Interact. Surface is given in Table 3.

Additionally, the interaction poses between the synthesis compound and target proteins are given in Figure 9.

Table 3. Docking results between isatin monohydrazone compound and target proteins.

Docking results	1M17	3HY3
Est. Free Energy of Binding (kcal/mol)	-5.70	-5.76
Est. Inhibition Constant, Ki (µM)	65.97	59.50
vdW + Hbond + desolv Energy (kcal/mol)	-5.65	-5.83
Total Intermolec. Energy	-6.00	-6.06
Interact. Surface	458.004	494.986

S-1M17

S-3HY3

Figure 9. Interaction modes between ligand and protein.
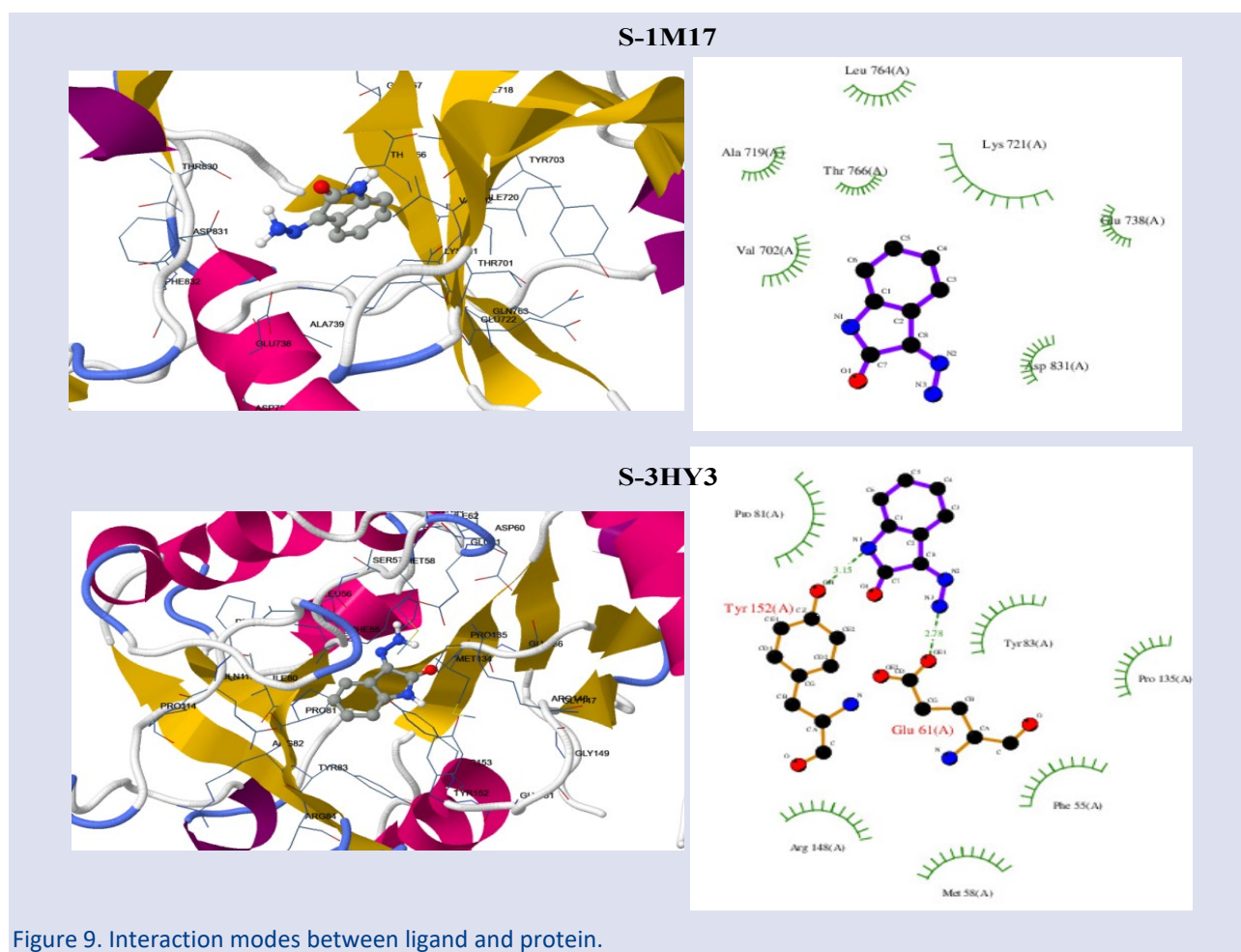
According to the docking results given in Table 3, compound S shows that it is active against breast cancer. The greater the binding energy in absolute value, the higher its anticancer activity. Similar trends are vdW + Hbond + desolv Energy (kcal/mol) and Total Intermolec. It is the same for energy values. When examined in general, large differences in the activity of molecules with small volumes that do not contain functional groups may not be expected. The binding energy between the S molecule and the 1M17 target protein is -5.70 kcal/mol, and the binding energy between the 3HY3 target protein is -5.76 kcal/mol. Although there is not much difference between the activities against different protein sequences of the cancer cell, the activity against the 3HY3 target protein is higher. Considering the interaction poses given in Figure 6, the H-bond between the S molecule and the 3HY3 target protein is noteworthy. The binding energy of 3HY3 with the target protein may have increased due to the energy of the H-bond. The S molecule interacts polarly with amino acid residues LYS721, GLU738 and ASP831 of the 1M17 target protein. It makes hydrophobic interactions with amino acid residues VAL702, ALA719 and LEU764. The nitrogen atom of the S molecule formed an H-bond with the GLU61 and TYR152 amino acid residues of the 3HY3 target protein. In addition, it interacts polarly with GLU61, ARG148 and TYR152, and

hydrophobicly with MET58 and PRO81. As a result, compounds that can be synthesized with the S molecule can be evaluated biochemically.

Conclusion

The synthesized isatin monohydrazone (S) was synthesized and examined by computational chemistry method. Starting from the widespread use of Density functional theory (DFT), which is a computational chemistry method, to support experimental data and correlate the biological activities of the molecule, its relationship with experimental data was also examined by applying the quantum chemical calculation method. Contour diagrams and molecular electrostatic potential maps (MEP) of the synthesized S were visualized. In the MEP map, it was determined that oxygen atoms were electron withdrawing regions. Nitrogen regions were determined to be electron donor regions. Structural characterization of compound S was determined by both experimental and computational ^{1}H-NMR chemical shift. Their activities against different protein sequences of breast cancer were examined by molecular docking. The results obtained showed that it has activity and can be used as a starting material for new molecules.

Conflicts of interest

The authors have made the following contributions to this article. Ceylan Alkaya Yıldız: Methodology, Investigation. Sultan Erkan: Writing, Methodology, Investigation.

References

[1] Kaya Y., Erçağ, A., Serdaroğlu G., Kaya S., Grillo I.B., Rocha G.B., Synthesis, Spectroscopic Characterization, DFT Calculations, and Molecular Docking Studies of New Unsymmetric Bishydrazone Derivatives, *Journal of Molecular Structure*, (2021) 1244, 131224.

[2] Mathur G., Nain S., Recent Advancement in Synthesis of İsatin as Anticonvulsant Agents: A review, *Med chem.*, 4(4) (2014) 417-27.

[3] Cheke R.S., Patil V.M., Firke S.D., Ambhore J.P., Ansari I.A., Patel H.M., Snoussi M., Therapeutic Outcomes of İsatin and its Derivatives Against Multiple Diseases: Recent Developments in Drug Discovery, *Pharmaceuticals*, 15(3) (2022) 272.

[4] Nath R., Pathania S., Grover G., Akhtar M.J., Isatin Containing Heterocycles for Different Biological Activities: Analysis of Structure Activity Relationship, *Journal of Molecular Structure*, 1222 (2020) 128900.

[5] Vine K.L., Locke J.M., Ranson M., Pyne S.G., Bremner J.B., In Vitro Cytotoxicity Evaluation of Some Substituted İsatin Derivatives, *Bioorganic & Medicinal Chemistry,* 15(2) (2007) 931-938.

[6] Murukan B., Mohanan K., Synthesis, Characterization and Antibacterial Properties of Some Trivalent Metal Complexes With [(2-Hydroxy-1-Naphthaldehyde)-3-İsatin]-Bishydrazone, *Journal of Enzyme Inhibition and Medicinal Chemistry*, 22(1) (2007) 65-70.

[7] Pandeya S. N., Sriram D., Nath G., De Clercq E., Synthesis and Antimicrobial Activity of Schiff and Mannich Bases of İsatin and its Derivatives With Pyrimidine, *Il Farmaco,* 54(9) (1999) 624-628.

[8] Retnam C.G., Rose S.V., Kumari B.S., Synthesis, Characterization, Biological Activity and Molecular Docking Study of Transition Metal Complexes from Heterocyclic Ligand System, *Journal of Molecular Structure*, 1282 (2023) 135162.

[9] Ernzerhof M., Scuseria G.E., Perspective on "Inhomogeneous Electron Gas" (2000). Hohenberg P, Kohn W., Phys Rev 136: B864, Theoretical Chemistry Accounts, 103 (1964) 259-262.

[10] Stamos J., Sliwkowski M.X., Eigenbrot C., Structure of the Epidermal Growth Factor Receptor Kinase Domain Alone and in Complex With a 4-Anilinoquinazoline İnhibitor, *Journal of Biological Chemistry.*, 277(48) (2002) 46265-46272.

[11] Wu D., Li Y., Song G., Cheng C., Zhang R., Joachimiak A., Liu Z. J., Structural Basis for the İnhibition of Human 5, 10-Methenyltetrahydrofolate Synthetase by N10-Substituted Folate Analogues, *Cancer Research*, 69(18) (2009) 7294-7301.

[12] Dennington R., Keith T.A., & Millam J.M., GaussView Version 6.1. In., (2016).

[13] Frisch M.J., Trucks G.W., Schlegel H.B., Scuseria G.E., Robb M.A., Cheeseman J.R., Scalmani G., Barone V., Petersson G.A., Nakatsuji H., Li X., Caricato M., Marenich A. V., Bloino J., Janesko B. G., Gomperts R., Mennucci B., Hratchian H.P., Ortiz J.V., Fox D.J., Gaussian 16 Rev. C.01. In., (2016).

[14] Becke A.D., Density-Functional Thermochemistry. I. The Effect of the Exchange-Only Gradient Correction, *The Journal of Chemical Physics*, 96(3) (1992) 2155-2160.

[15] Blaudeau J.P., McGrath M.P., Curtiss L.A., Radom L., Extension of Gaussian-2 (G2) Theory to Molecules., (1997).

[16] Phillips J.C., Generalized Koopmans' Theorem, *Physical Review*, 123(2) (1961) 420.

[17] Stewart J.J., Stewart computational Chemistry, http://openmopac. net/., (2007).

[18] Bikadi Z., Hazai E., Application of the PM6 Semi-Empirical Method to Modeling Proteins Enhances Docking Accuracy of AutoDock, *Journal of Cheminformatics.*, 1 (2009) 1-16.

[19] Huey R., Morris G.M., Olson A.J., Goodsell D.S., A Semiempirical Free Energy Force Field with Charge-Based Sesolvation, *Journal of Computational Chemistry*, 28(6) (2007) 1145-1152.

[20] Devi J., Batra N., Synthesis, Characterization and Antimicrobial Activities of Mixed Ligand Transition Metal Complexes with İsatin Monohydrazone Schiff Base Ligands and Heterocyclic Nitrogen Base, Spectrochimica Acta Part A: *Molecular and Biomolecular Spectroscopy*, 135 (2015) 710-719.

[21] Kaya S., Erkan S., Karakaş D., Computational İnvestigation of Molecular Structures, Spectroscopic Properties and Antitumor-Antibacterial Activities of Some Schiff Bases, *Spectrochimica Acta Part A: Molecular and Biomolecular Spectroscopy*, 244 (2021) 118829.

[22] Özdemir E.Ç., Akyol H., The Development of a Reading Comprehension Test, *Universal Journal of Educational Research*, 7(2) (2019) 563-570.

[23] Küçükterzi Ö., Theoretical İnvestigation of the Structure and Spectroscopic Properties of N-trans-Cinnamilidene-M-Toluidine Schiff Base Molecule by DFT and HF Methods, Master's thesis, Ankara University (Turkey)., (2020).

[24] Khalid H.H., Erkan S., Bulut N., Halogens Effect on Spectroscopy, Anticancer and Molecular Docking Studies for Platinum Complexes, *Optik*, 244 (2021) 166324.

[25] Kaya S., Erkan S., Karakaş D., Computational İnvestigation of Molecular Structures, Spectroscopic Properties and Antitumor-Antibacterial Activities of Some Schiff Bases, Spectrochimica Acta Part A: *Molecular and Biomolecular Spectroscopy*, 244 (2021) 118829.

[26] Erkan S., Structural, Spectroscopic and Anti-Cancer Properties of Hydroxy-and Sulfonamide-Azobenzene Platinum (II) Complexes: DFT and Molecular Docking Studies, *Cumhuriyet Science Journal*, 39(4) (2018) 1036-1051.

[27] Stamos J., Sliwkowski M.X., Eigenbrot C., Epidermal Growth Factor Receptor Tyrosine Kinase Domain with 4-Anilinoquinazoline İnhibitor Erlotinib, URL https://doi. org/10.2210/pdb1m17/pdb., sep 2002.

[28] Wu D., Li Y., Song G., Cheng C., Zhang R., Joachimiak A., Liu Z.J., Structural Basis for the İnhibition of Human 5, 10-Methenyltetrahydrofolate Synthetase by N10-Substituted Folate Analogues, *Cancer Research*, 69(18) (2009) 7294-7301.

[29] Erkan S., Karakaş D., DFT İnvestigation and Molecular Docking Studies on Dinuclear Metal Carbonyls Containing Pyridyl Ligands with Alkyne Unit, *Chemical Papers*, 73 (2019) 2387-2398.

Cumhuriyet Science Journal

Anatomical Investigations on Turkish Vulnerable *Scrophularia* species: *Scrophularia lepidota* Boiss.(Scrophulariaceae)

Hulya Ozpinar [1,a,*], Serhat Bozan [2,b], Mehmet Tekin [2,c]

[1] Department of Pharmaceutical Botany, Faculty of Pharmacy, Sivas Cumhuriyet University, Sivas, Türkiye.

[2] Department of Pharmaceutical Botany, Faculty of Pharmacy, Trakya University, Edirne.

*Corresponding author

Research Article

ABSTRACT

In this study, the root, stem and leaf anatomy of *Scrophularia lepidota*, a narrowly distributed endemic species specific to our country, whose morphological features are known, was investigated. Plant materials were collected from Ziyarettepe, Ulaş district of Sivas, Türkiye and anatomically analyzed. In the root cross-section, root is in the secondary structure, there are 5–8 cell layered periderm in outside and under periderm tissue, there are 6–10 cell layered pericycle. The stem is in primary structure, covered by uniseriate epidermis and stellate epidermal trichomes. Under the epidermis there is cortex tissue which consists of 6–8 cell layers. The leaves are equifasiyal according to the mesophyll layer, and amphistatic according to the presence of stoma. The midrib is oval–circular in shape, and is surrounded by a single cell layered bundle sheath. There are idioblastic cells in leaf cross section. The determined anatomical features of *S. lepidota* were compared with previous anatomical studies on other species of the genus *Scrophularia* and the results were discussed. In this study, the anatomical features of *S. lepidota*, which is endemic to our country, were revealed for the first time. In addition, by determining the anatomical features of *S. lepidota*, a contribution was made to the general anatomical features and systematics of the genus *Scrophularia*.

Keywords: Anatomy, Endemic, S. lepidota, Scrophulariaceae, Turkey.

[a] ✉ hulya1177@yahoo.com.tr   🆔 https://orcid.org/0000-0001-8154-0874   [b] ✉ serhat091994@gmail.com   🆔 https://orcid.org/0009-0009-5199-8265
[c] ✉ mtekin2280@gmail.com   🆔 https://orcid.org/0000-0002-6504-2223

Introduction

Scrophulariaceae Juss. family, which has 200-250 genera and approximately 3000-4000 herbaceous and a few shrub species worldwide, is known as the seventh largest flowering plant family in the world [1,2]. Although the genera belonging to the Scrophulariaceae family are cosmopolitan, they also spread widely in the temperate regions of the Northern Hemisphere to tropical regions, but varies especially in Africa [2-4]. The species of this family are generally autotrophic, semi or rarely fully parasitic plants [5].

Scrophularia L. is the genus that gives its name to the Scrophulariaceae family, and this genus is represented in the world with approximately 300 taxa that generally spread naturally in the Mediterranean Region [6]. The primary diversification center of the genus *Scrophularia* is Southeast Asia [7,8]**.** According to Turkish Flora there are 59 species in which 22 of them are endemic with the endemism ratio 37.2 % belonging to the genus *Scrophularia* spread naturally in Turkey [9]. According to Turkey Plant List (Vascular Plants) with the addition of new species recently discovered in Turkey, *Scrophularia* is represented by 65 species and 85 taxa in Turkey [10].

Anatomical studies on the members of the genus *Scrophularia* in the world and in our country are not sufficient. Anatomical studies on members of the genus *Scrophularia* mostly focused on leaf characteristics. The first brief description of idioblasts found in the leaves of

Scrophularia species was made by Volkens (1887) in *Scrophularia deserti* Delile, and later on other species by Metcalfe and Chalk (1950) [11,12].

Holm (1929) stated that there was not much difference between root and stem anatomies as a result of his examination on five *Scrophularia* species that were close to each other [13]. Pennel (1929, 1935) studied the root, stem and leaf anatomy of 25 species and showed that there are anatomical and morphological differences between these species [14,15]. In another study by Lersten and Curtis (1997), idioblasts and their intracellular secretory structures were examined in detail. As a result of this study conducted on 172 genera and 237 species in the Scrophulariaceae family, secretion structures with different sizes and shapes were discovered [6].

In a recent study published by Lersten and Curtis (1997, 2001), the distribution of idioblast and leaf endocrine system in different Scrophulariaceae taxa was examined, and many important differences were found among the taxa examined [6]. Another explanation of idioblasts in species of the genus *Scrophularia* is Makbul et al. (2006). Makbul et al. (2006) investigated the anatomical features of some Scrophularia taxa and the distribution of idioblasts and found many important differences between the taxa examined [16].

The morphological and anatomical features of 14 Scrophulariaceae taxa naturally distributed in Turkey

were studied by Kaplan and İnceoğlu (2003) but there are no members of the genus *Scrophularia* among these taxa [17]. Although the anatomical characters are very important in the genus *Scrophularia*, there are not enough studies and publications on the species of the genus in Turkey [16]. The subject of this study, *Scrophularia lepidota* Boiss, is a perennial herbaceous plant. It is an endemic plant that spreads naturally only in Sivas and Erzincan provinces in Turkey [18]. The endangered status of the *S. lepidota* species Ekim et al. (2000) in the "Red Book of Plants of Turkey" prepared by taking IUCN criteria into account (VU-May be Harmful) [19].

In this study, the root, stem and leaf anatomy of *S. lepidota*, a narrowly distributed endemic species specific to our country, whose morphological features are known, was investigated.

Material and Methods

In order to obtain plant material, a field study was carried out in Sivas where the species is distributed and the species was reached. Some of the plants collected as a result of the field work were transformed into herbarium material and stored in Cumhuriyet University Faculty of Science Herbarium (CUFH) under the code number M. Tekin 1426. Locality of the collected specimen: B6 Sivas: Ulaş district, Ziyarettepe, 39° 33' 08,9" N, 37° 01' 12,1" E and the date of collection was 11.05.2013.

Anatomical Studies

For anatomical study, fresh plant samples taken from at least 3 different individuals during the field study were preserved in 70% ethyl alcohol. The root, stem and leaf sections of these specimens were manually cut using a razor blade and stained with Safranin-Alcian blue mixture (double staining) to separate the pectin and lignin containing parts. The stained sections were covered with glycerin-gelatin and made into permanent preparations [20]. Photographs of the anatomical sections of all organs were taken with an Olympus DP70 digital camera connected to an Olympus brand BX51 model light microscope. Previous anatomical analysis studies on the Scrophulariaceae family and *Scrophularia* genus were utilized in anatomical studies [8,16].

Dyes and Solutions Used in Anatomical Studies
Preparation of Safranin-Alcian Blue

This staining method is used to see the difference between lignified and non-woody parts in the anatomical structures of plants. Safranin and Alcian blue are prepared separately.

Safranin solution

1 g safranin + 100 ml distilled water; Alcian blue solution: 1 g alcian blue + 3% acetic acid + 100 ml distilled water + 1 thymol crystal (acetic acid is added until pH 2.5).

The procedure followed for staining; sections are soaked in 6 volumes of Safranin: 4 volumes of Alcian blue for 1-2 minutes [21]. The sections removed from the stain are washed in 70% ethyl alcohol and made into permanent preparations using glycerin-gelatin.

Preparation of Glycerin-Gelatin

To prepare glycerin-gelatin, 50 ml glycerin, 8 g gelatin, 0.1 g phenol and 52 ml distilled water are used. The gelatin pieces are left in warm water for 30 min. to swell, glycerin and a small amount of phenol are added and the mixture is heated in a water bath for 15 minutes below 75 °C with

stirring until homogeneous. If the heating is done above 75 °C, the gelatin turns into metagelatin and does not harden at room temperature. The mixture is cooled and stored in the refrigerator. When used, it is melted in an oven at 60 °C. In the anatomical study, layers, tissues and cells were identified and indicated on the photographs taken from the sections of different organs of the plants.

Results

Morphological Features

Dense lepidote, many-stemmed, perennial, 10-35 cm; scales yellowish to whitish-gray, margins stellate-pilose. Leaves thick, 3-7 × 0.3-0.7 cm; margins ± inverted, lower leaves linear-spathulate, narrowing to long petiole; upper leaves (and bracts) linear-oblong, ± sessile; tip of all leaves obtuse or slightly or deeply 3(-5)-dentate or wedge-shaped, otherwise nearly flat.

(A) (B)

(C)

(D)
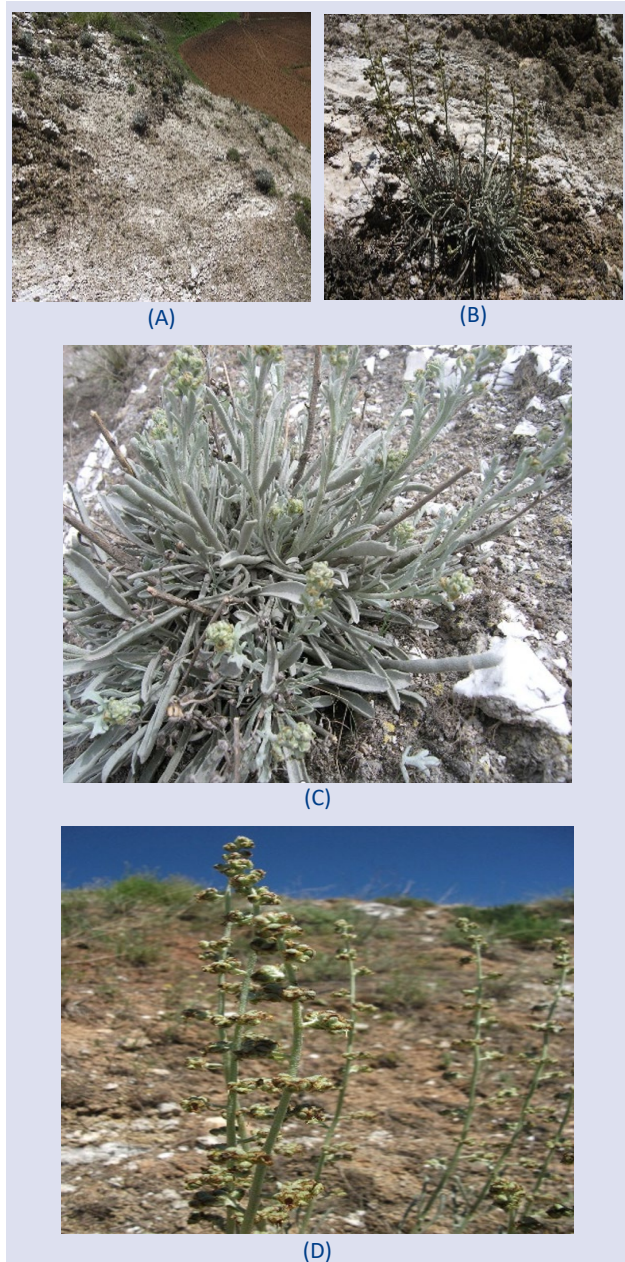
Figure 1. Gypsiferous hills where *Scrophularia lepidota* naturally occurs (A); *Scrophularia lepidota* in its natural habitat (B) *Scrophularia lepidota*' s basal leaves (C) and flower state (D)

Symous 1-5-flowered; peduncle 4-10 mm; bracteoles oblong-linear, obtuse to spatulate, 2-3 mm with pedicels exceeding 1-2 mm. Calyx lobes with lepidote and glandular hairs, ovate to obovate, 3.5-4 × 3.5-4.5 mm; scaly margins yellow to buff, 1-2.5 mm wide, lacerate, ± undulate. Corolla greenish to maroon, 7 mm, all lobes with yellow-green margins. Stamens exserted; staminodes ovate to roundish, lobed. Capsule globose, 4-5 × 4-4.5 mm. Inflorescence 5-6. On dry gypsiferous land, 1200-1500 m [23].

Root Anatomy

The root is circular and secondary in cross-section. Outermost is the periderma consisting of 5-8 cell rows. The cells of the peridermal layer are rectangular, sometimes irregularly shaped.

(A)

(B)

(C)

(D)
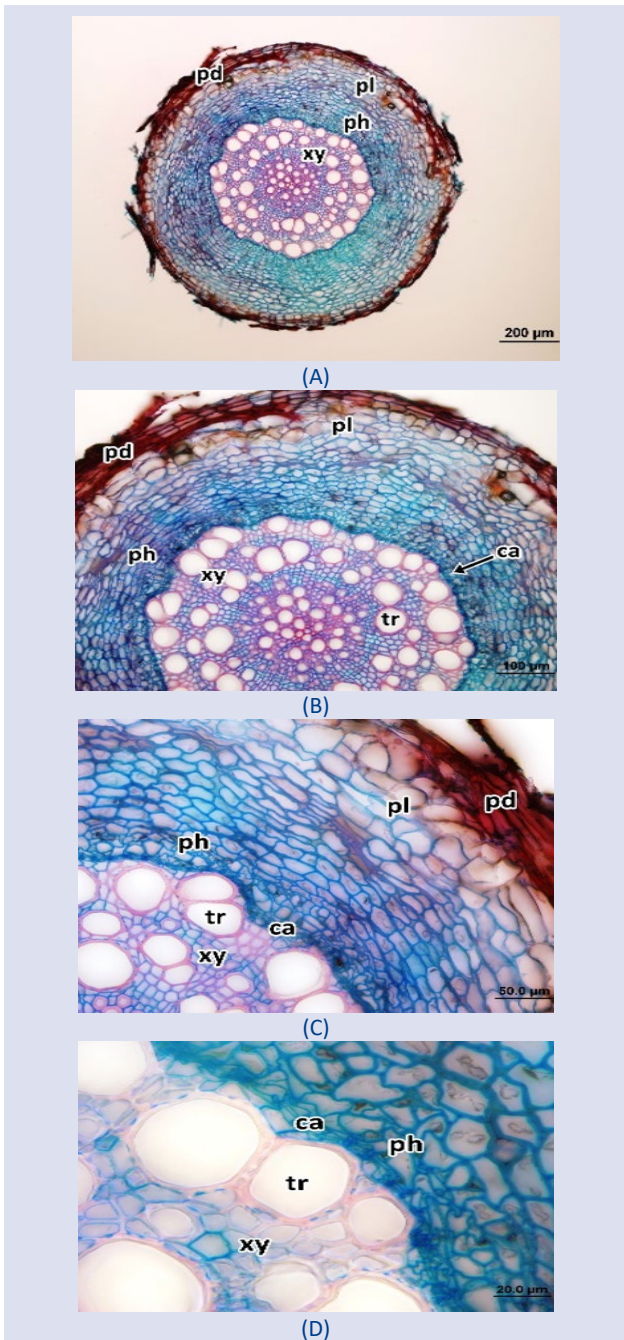
Figure 2. Root anatomy of *Scrophularia lepidota* (A, B, C, D)(ca: cambium; pd: periderm; ph: phloem; pl: pericycle; tr: trachea; xy: xylem)

The cells are usually brown and do not contain intercellular spaces. In the section, it is observed that the outer layers of the periderma are fragmented in places. The fellem layers of the periderma are prominent, whereas the phellogen and phelloderma are not. Immediately below the periderm is the pericycle layer consisting of 6-10 cell rows. The cells of the pericycle layer are rectangular, squarish or generally irregular in shape (Figure 2A, B). There is no space between the cells. Below the pericycle layer is the phloem layer, which usually consists of 9-12 cell rows. Phloem cells are usually irregularly shaped and sometimes rectangular (Figure 2C,D). Phloem cells close to the pericycle layer are larger, while cells located close to the cambium are smaller. The cambium layer separates phloem and xylem. The cambium is composed of 3-4 cell rows and highly flattened irregularly shaped cells (Figure 2B, C, D). The center of the root cross-section is filled by xylem elements. In the xylem, the tracheae close to the cambium are larger in diameter, while those in the center are narrower wider in diameter, while those in the center are narrower (Figure 2C,D).

Stem Anatomy

The epidermis is single-row oval, oblong-oval and rarely square. There are stellate hairs originating from the epidermis (Figure 3A, B). The body is in the primary stage of development. Below the epidermis is the cortex layer with 6-8 cell rows and circular or oval cells. There are intercellular spaces between the cortex cells. Below the cortex is the phloem layer with 3-5 cell rows. Below the phloem is the xylem (Figure 3A, B, and C). Between the phloem and xylem is a layer of sclerenchymatic fibers with 7-13 cell rows, which surrounds the stem as an inner ring. The cambium layer is not prominent. In the radial direction there are pith rays composed of uniseriate parenchymatic cells embedded in the phloem and xylem (Figure 3A, B, and C). The pith region is composed of usually circular, sometimes oval cells with large intercellular spaces, occupying a large area in the stem cross-section (Figure 3A, B, and C).
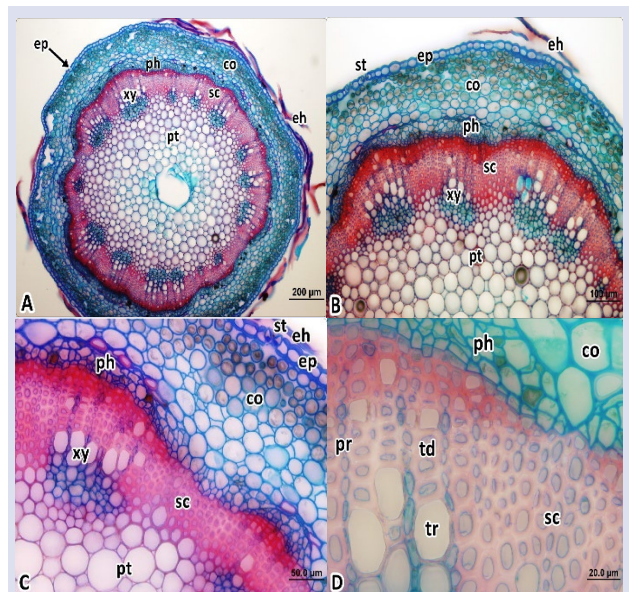
Figure 3. Stem anatomy of *Scrophularia lepidota* (A, B, C, D) (co: cortex; eh: cover hair; ep: epidermis; ph: phloem; pt: pith; sc: sclerenchyma; st: stomata; xy: xylem)

50

Leaf Anatomy

In cross-section, the leaf is surrounded by a single row of epidermis above and below.
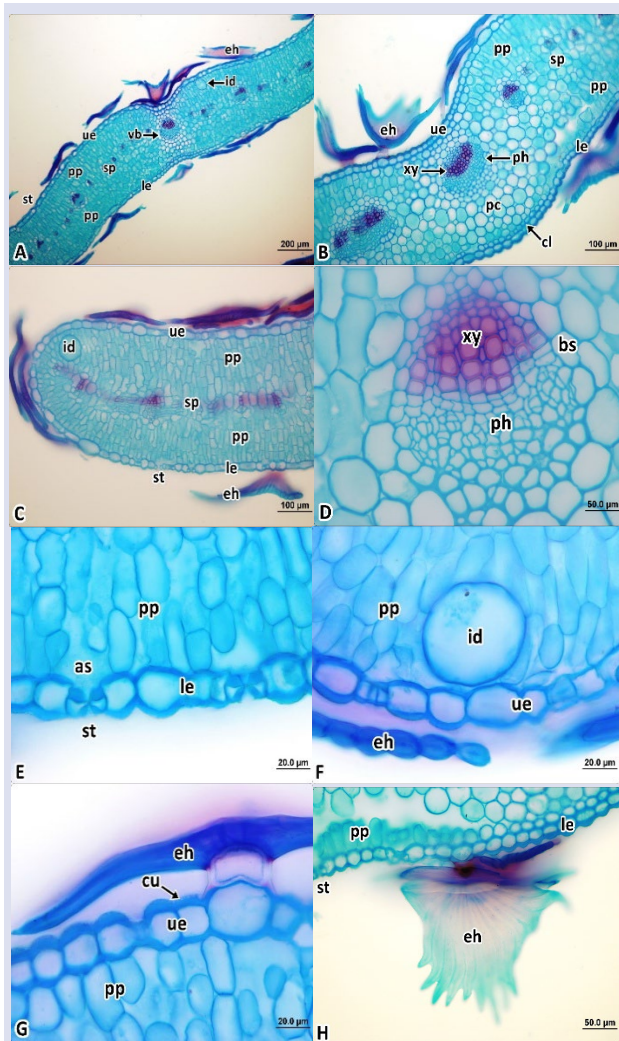
Figure 4. Leaf cross-section photomicrographs of *S. lepidota* (A, B, C, D).Mesophytic stomata in leaf lower epidermis (E); idioblastic cell in leaf mesophyll (F) Detail of stellate cover hair on leaf upper epidermis (G); stellate cover hair on leaf lower epidermis (H) (cl: collenchyma; eh: cover hair; id: idioblast; le: lower epidermis; pc: parenchymatic cells; ph: phloem; pp: palisate parenchyma; sp: sponge parenchyma; st: stomata; ue: upper epidermis; vb: conduction bundle; xy: xylem; as: substomatal space; eh(H): stellate cover hair; cu: cuticle)

It is covered with stellate hairs, more densely on the lower surface of the leaf (Figure 4G, H). The mesophyll layer is quite thick. The leaf is equifacial in terms of mesophyll. There are 3-4 cell rows of palisate parenchyma on the upper and lower epidermis. Palisate cells are usually oblong, oblong-oval and sometimes cylindrical in shape. Sponge parenchyma with 2-4 cell rows is located between the two palisate layers. Sponge parenchyma cells are usually circular, oval or sometimes irregularly shaped (Figure 4A, B, and C). The midrib (leaf main conduction bundle) is oval-circular in shape and surrounded by bundle sheath cells consisting of a single layer of cells.

The midrib is located closer to the upper epidermis in the leaf cross-section and occupies a small area in the cross-section. In the area where the midrib is located, there is a single row of collenchyma just above the lower epidermis. Between the midrib and this single-row collenchyma layer are parenchymatic cells, which are usually circular in shape (Figure 4A, B,and D). The leaf is amphistomatic in terms of stomata and the stomatal cells are located at the same level (mesophytic) as the epidermis cells (Figure 4A, B, C, D, and E).

In the leaf transverse section, idioblastic cells, which were very dense but considerably larger in size than the neighboring palisade parenchyma cells, were also found just below the upper epidermis (Figure 4F).

Discussion

In this study, the anatomical features of *S. lepidota* species were revealed. In terms of many anatomical features, *S. lepidota* has the general anatomical features of Scrophulariaceae family and *Scrophularia* genus given by Metcalfe and Chalk (1950) [12].

For example, Metcalfe and Chalk (1950) reported that the leaves of Scrophulariaceae are usually amphistomatic in terms of stomata and sometimes only the lower epidermis may have stomata (hypostomatic). As a result of this study, the leaves of *S. lepidota* are also amphistomatic in terms of stomata.Furthermore, Metcalfe and Chalk (1950) reported that the endodermis layer is usually seen in stem anatomy sections of species of the genus *Scrophularia*, but this is not a distinctive character; in addition, sclerenchymatic fibers corresponding to the pericycle layer are found as a band in the stem cross-section. In this study, unlike Metcalfe and Chalk (1950), no endodermis layer was observed in *S. lepidota* stem transverse sections. In addition, although Metcalfe and Chalk (1950) stated that sclerenchymatic fibers can be seen as bands in members of the genus *Scrophularia*, in the stem of *S. lepidota*, the sclerenchymatic fiber layer forms a thick layer that surrounds the stem cross-section as an inner ring [12].

Table 1. Comparison of the results of the stem and leaf anatomy of *Scrophularia lepidota* species in this study with the results of the stem and leaf anatomy of six *Scrophularia* species studied by Makbul et al. (2006)

| | Features/Species | This study | Makbul et al. (2006) | | | | | |
		S. lepidota	S. ilwensis	S. capillaris	S. nodosa	S. libanotica var. pontica	S. lucida	S. cinerancens
Stem	Epidermis cell shape	Oval, oblong-oval, rarely square	Rectangular or circular	Rectangular or circular	Not specified	Rectangular or circular	Rectangular or circular	Not specified
	Collenchyma layer under the epidermis	Not available	1–3	Not specified	1–3	1–3	1–3	1
	Cortex cell row number	6–8	6–7	7–8	7–8	6–7	7–8	6–7
	Cortex cell shape	Circular or Oval	Oval	Oval	Oval	Oval	Oval	Oval
	Cambium	Uncertain	Uncertain	Uncertain	Not specified	Uncertain	Uncertain	Uncertain
	Self cell shape	Circular or oval	Cylindric	Cylindric	Cylindric	Cylindric	Cylindric	Cylindric
Leaf	Midrib shape	Oval-Circular	Triangle	Triangle	Not specified	Triangle	Triangle	Triangle
	Size of lower epidermis cells relative to upper epidermis cells	It's big	It's big	It's big	It's big	It's big	It's big	It's big
	Leaf type according to mesophyll	Ecuifacial	Bifacial	Bifacial	Bifacial	Bifacial	Bifacial	Bifacial
	Palisate parenchyma cell row number	3-4 cells below the upper epidermis; 3-4 cells above the lower epidermis	4–5	1–3	2–3	3–4	5–6	3–4
	Sponge parenchyma cell line number	2–4	3–4	2–3	2–3	4–5	5–6	5–6
	Presence of stoma	Amphistomatics	Amphistomatics	Amphistomatics	Amphistomatics	Amphistomatics	Not specified	Not specified
	Presence of idioblast embedded in the palisate parenchyma	Specified	Specified	Specified	Not specified	Specified	Not specified	Not specified

Anatomical studies have been carried out on some species of the genus *Scrophularia* (*S. chrysantha* Jaub. & Spach, *S. scopolii* Hoppe ex Pers. var. *adenocalyx* Somm. & Lev. and *S. olympica* Boiss., *S. sosnowskyi* Kem.-Nath., *S. canina* L.) which are naturally distributed in Turkey. Makbul and Beyazoğlu (2009) studied the stem and leaf anatomy of these species[8]. The stem and leaf anatomy of *S. ilwensis* C. Koch, *S. capillaris* Boiss. & Ball., *S. nodosa* L., *S. libanotica* Boiss. var. *pontica* R. Mill, *S. lucida* L. and *S. cinerascens* Boiss. were also studied by Makbul et al. (2006) [16]. The results of these two studies and the anatomical features of *S. lepidota* species that we have revealed in this study are compared in Table 1 and Table 2 [8, 16]. When the anatomical characteristics of *S. lepidota* determined in our study are compared with these studies, it is seen that some characters show significant differences. For example, in the studies of Makbul et al. (2006) and Makbul and Beyazoğlu (2009), the epidermis cell shape of 9 *Scrophularia* taxa were reported to be rectangular or circular, whereas *S. lepidota* has oval, rectangular-oval, rarely square shaped stem epidermis cells (Table 1 and 2) (Figure 3A, B, and C) [8, 16].

Another important difference in terms of the stem is the presence of collenchyma under the epidermis. In the 10 species shown in Table 1 and Table 2, where the presence of collenchyma is indicated, collenchyma layers ranging from 1 to 3 cell rows were found, whereas no collenchyma was found under the epidermis in *S. lepidota* (Figure 3A, B, C). The stem pith cells were cylindrical in all 10 species studied and characterized by Makbul et al. (2006) and Makbul and Beyazoğlu (2009). However, in *S.*

lepidota, the pith cells appear circular or oval in cross-section (Figure 3A, B, C). In terms of leaves, the most important differences between *S. lepidota* and the species in Table 1 and Table 2 are midrib shape and leaf type relative to the mesophyll. Accordingly, Makbul et al. (2006) and Makbul and Beyazoğlu (2009) reported that the midrib was triangular, kidney or semicircular in all *Scrophularia* taxa studied (Table 1; Table 2). In *S. lepidota*, the midrib was found to be oval circular (Figure 4D). The most significant difference in terms of leaf shape is the leaf shape compared to the mesophyll. While the leaf type of all species studied by Makbul et al. (2006) and Makbul and Beyazoğlu (2009) was bifacial according to mesophyll, *S. lepidota* leaves were found to be equifacial (Figure 4A) [8, 16].

In another study conducted by Shields (1950), he stated that plants having developed palisate parenchyma in their leaves would be directly proportional to their arid character [22]. This is also in agreement with our study. *S. lepidota* is an arid plant and has equifacial type leaves with two different palisate parenchyma (Figure 4A, B, C).

In this study, idioblast cells were observed just below the upper epidermis on *S. lepidota* leaves and again below the epidermis on leaf margins (Fig 4F). Previously, Volkens (1887) observed such idioblasts in species growing in the Middle East [7]. Furthermore, Solereder (1908) reported that "the tannin-bearing idioblasts of the mesophyll of *Scrophularia deserti* are large ellipsoidal cells, the lower end of which is attached to an epidermal cell which penetrates the mesophyll at a very small distance; these idioblasts extend to the middle of the leaf where they are embedded in the ends of the vessels" [23].

Table 2. Comparison of the results of the stem and leaf anatomy of *Scrophularia lepidota* species with the results of the stem and leaf anatomy of five *Scrophularia* species studied by Makbul and Beyazoğlu (2009)

		This study		Makbul and Beyazoğlu (2009)			
	Features/Species	*S. lepidota*	*S. chrysantha*	*S. scopolii* var. *adenocalyx*	*S. olympica*	*S. sosnowskyi*	*S. canina*
Stem	Epidermis cell shape	Oval, oblong-oval, rarely square	Rectangle	Rectangle or circular	Rectangle or circular	Rectangle or circular	Rectangle or circular
	Epidermis altında kollenkima tabakası	Not available	1–3	1	1	1	1–3
	Cortex cell row number	6–8	5–6	4–5	5–6	6–7	5–6
	Cortex cell shape	Circular or oval	Oval	Oval	Oval	Oval	Oval
	Cambium	Uncertain	Uncertain	Not specified	Not specified	Not specified	Uncertain
	Self cell shape	Circular or oval	Cylindric	Not specified	Cylindric	Cylindric	Cylindric
Leaf	Midrib shape	Oval-circular	Triangular or kidney-shaped	Triangular	Semicircle	kidney-shaped	Triangular
	Size of lower epidermis cells relative to upper epidermis cells	It's big	It's big	It's big	It's big	It's big	It's big
	Leaf type according to mesophyll	Ecuifacial	Bifacial	Bifacial	Bifacial	Bifacial	Bifacial
	Palisate parenchyma cell row number	3-4 cells below the upper epidermis; 3-4 cells above the lower epidermis	1–2	1	2–3	3	4–5
	Sponge parenchyma cell line number	2–4	4–5	2–3	3–5	3–4	2–3
	Presence of stoma	Amphistomatics	Amphistomatics	Amphistomatics	Amphistomatics	Amphistomatics	Amphistomatics
	Presence of idioblast embedded in palisate parenchyma	Specified	Not specified	Specified	Not specified	Not specified	Not specified

After these studies, the most comprehensive study on leaf idioblasts of Scrophulariaceae family and *Scrophularia* genus species was conducted by Lersten and Curtis (1997) [6]. As a result of this study, it was reported that 62 of 89 *Scrophularia* species had idioblasts in their leaves, which corresponded to 69.7%. In the aforementioned study, it was also reported that the presence of idioblasts may vary in samples taken from different localities of the same species, and as an example, while there were no idioblasts in samples of *Scrophularia libanotica* taken from one locality, large idioblast cells were found in another sample.

In our study, since *S. lepidota* species is not widespread, the sample taken from a single locality was studied and idioblast cells with primary cell wall and seemingly empty lumen were found. In the study of Lersten and Curtis (1997), idioblasts in all specimens with idioblasts had only primary cell walls and their lumens appeared to be empty. In this respect, our study coincides with the results of Lersten and Curtis (1997) study.

Conclusion

In this study, the anatomical features of *S. lepidota*, which is endemic to our country, were revealed for the first time. The results obtained were compared with the species of the genus *Scrophularia* whose anatomy was previously studied and their similarities and differences were revealed. We believe that the results of this study will contribute to future anatomical studies on the other members of the genus and to determine their place in the systematics.

Conflict of Interest

Authors declare that there are no conflict of interest between them. Also, we note that our manuscript contains original material.

References

[1] Bigazzi M., A survey on the intraclear inclusions in the Schrophulariaceae and their systematic significance, *Nordic journal of botany*, *13*(1) (1993) 19-31.

[2] Sotoodeh A., Histoire biogéographique et évolutive des genres Verbascum et Artemisia en Iran a l'aide de la phylogéniamoléculaire, Ph.D Thesie. Paul Sabatier Université, Ecology, Toulouse, (2015) France.

[3] Seçmen Ö., Gemici Y., Görk G., Bekat L., Leblebici E., Tohumlu Bitkiler Sistematiği, 5. Baskı, İzmir, Ege Üniversitesi Basımevi (1998) 200-220.

[4] Juan R., Pasto J., Fernandez I., Sem and light microscope observations on fruit and seeds in Scrophulariaceae from Southwest Spain and their systematic significance, *Annals of Botany*, 86 (2000) 323–338.

[5] Dayı F., Anatomical Studies on the Parasitic Plants Distributed in Balıkesir, Institute of Science and Technology, Master's Thesis: Balıkesir University, Balıkesir-Turkey (2015).

[6] Lersten N. R., Curtis J. D., Anatomy and distribution of foliar idioblasts in *Scrophularia* and *Verbascum* (Scrophulariaceae), *American Journal of Botany*, 84 (12) (1997) 1638–1645.

[7] Stiefelhagen H., Systematische und pflanzengeographicsche Studien zur Kenhtnis der Gattung *Scrophularia*, *Botanische Fahrbücher*, 44 (1910) 406–496.

[8] Makbul S., Beyazoğlu O., Morphological and anatomical studies on some *Scrophularia* L. (Scrophulariaceae) taxa from NE Anatolia, Turkey, *Iran. J. Bot.*, 15 (2) (2009) 186–195.

[9] Lall S. S., Mill R. R., *Scrophularia* L. in P. H. Davis (ed.) Flora of Turkey and the East Aegean Island. Edinburgh Univ. Press., Edinburgh, (1978), Vol. 6: 603–647

[10] Güner A., Aslan S., Ekim T., Vural M. & Babaç M. T., List of Plants of Turkey (Vascular Plants). Publication of Nezahat Gökyiğit Botanical Garden and Flora Research Association, Istanbul, (2012) 280-282.

[11] Volkens G., Die Flora der aegyptisch–arabischen Wüste auf Grundlage anatomisch–physiologischer Forschungen dargesttellt. Gebrüder Borntraeger, Berlin, (1887) 520-522.

[12] Metcalfe C. R., Chalk L., Anatomy of Dicotyledons. 1st ed. vol. 2 –Clarendon Press, Oxford, (1950):120-122.

[13] Holm T., *Gerardia* L. and *Buchenera* L., With supplementary note on Gratiola an anatomical study, *Am. J. Sci.*,218 (1929) 401–411.

[14] Pennel F. W., Agalinis and allies in North America. II. Proc. Academy of Natural Sciences Philadelphia 81 (1929) 111–249.

[15] Pennel F. W., The Scrophulariaceae of Eastern Temperate North America (41 Gerardia). Acad. Nat. Sci., Phila, Monogr. 1 (1935) 419–476.

[16] Makbul S., Coşkunçelebi K., Türkmen Z., Beyazoğlu O., Morphology and anatomy of *Scrophularia* L. (Scrophulariaceae) taxa from NE Anatolia. *Acta Biological Cracoviensia Series Botanica* 48 (1) (2006) 33–43.

[17] Kaplan A., Inceoğlu Ö., Leaf Anatomy and Morphology of 14 Species Belonging to the Turkish *Rhinantheae* (Scrophulariaceae) Tribe Israel Journal of Plant Sciences,51 (2003) 297–305.

[18] Davis PH., *Scrophulariaceae*. Flora of Turkey and The East Aegean Islands. Edinburgh: Edinburgh University Press, Vol 6: (1978) 458–603.

[19] Ekim T., Koyuncu M., Vural M., Duman H., Aytaç Z., Adıgüzel N., The Red Book of Plants of Turkey. Ankara: Türkiye Tabiatını Koruma Dernegi and Yüzüncüyıl University, (2000) 120-125.

[20] Brown C. A., Palynological Techniques: Baton Rouge. Louisiana State Univ., (1960) 351-353.

[21] Yılmaz G., Determination of toxic effects of herbicide Attribut (propoxycarbazonesodium) and surfactant BioPower (alkylethersulphate sodiumsalt) on *Triticum aestivum* L. cv. Pehlivan. PhD Thesis: Institue of Science University of Trakya,. Edirne-Turkey, (2009).

[22] Shields L. M., Leaf xeromorphy as related to physiological and structural influences. The Botanical Review, 16 (1950) 399-447.

[23] Solereder H., Systematic anatomy of the dicotyledons. Translated from German by L. A. Boodle and D. H. Scott revised from 1899 edition by D. H. Scott Clarendon Press, Oxford, (1908) 180-182.

Cumhuriyet Science Journal

Investigating the Efficacy of Cannabidiol Against Arsenic-Induced Liver Cell Damage

Serkan Şahin[1,a,*], Vugar Ali Türksoy[2,b], Serap Yalçın Azarkan[3,c]

[1] Department of Medical Pharmacology, Faculty of Medicine, Yozgat Bozok University, Yozgat, Türkiye

[2] Department of Public Helath, Faculty of Medicine, Yozgat Bozok University, Yozgat, Türkiye

[3] Department of Medical Pharmacology, Faculty of Medicine, Kırşehir Ahi Evran University, Kırşehir, Türkiye

*Corresponding author

Research Article

ABSTRACT

Arsenic (As) exposure is known to have harmful effects, prompting the search for effective countermeasures. This study investigated the protective effects of cannabidiol (CBD) against arsenic toxicity in liver cell cultures (THLE-2). The IC_{50} values for As were determined, finding 10 µM in 2D and 15 µM in 3D cell lines. To assess CBD's protective efficacy, 5 µM of CBD was administered alongside arsenic at its IC_{50} concentration. The levels of oxidative stress markers, including Glutathione (GSH), malondialdehyde (MDA), myeloperoxidase (MPO), and catalase (CAT), as well as inflammatory cytokines such as tumor necrosis factor-α (TNF-α), interleukin-1β (IL-1β), and interleukin-6 (IL-6), were measured using ELISA kits. Inductively Coupled Plasma Mass Spectrometry (ICP-MS) analysis was conducted to evaluate As uptake in the cells. The results showed that CBD significantly enhanced cell proliferation and reversed the oxidative stress and inflammatory responses induced by arsenic exposure. Furthermore, CBD effectively reduced arsenic uptake into the cells. These findings provide compelling evidence for CBD's protective role against arsenic-induced toxicity, highlighting its potential as a therapeutic agent in mitigating the harmful effects of arsenic.

Keywords: Arsenic, Cannabidiol, Toxicity, THLE-2, ICP-MS.

a🖂 serkan.sahin@bozok.edu.tr 🔾 https://orcid.org/0000-0001-7000-6342   b🖂 v.alitrurksoy@bozok.edu.tr 🔾 https://orcid.org/0000-0002-3545-3945
c🖂 syalcin@ahievran.edu.tr 🔾 https://orcid.org/0000-0002-9584-266X

Introduction

The increasing environmental pollution associated with industrialization and urbanization has led to soil contamination reaching levels that can pose a threat to living organisms. Both the escalating environmental and soil pollution, along with the industrialization, contribute to an increasing likelihood of human exposure to toxic metals. Among these toxic metals, arsenic (As) exposure holds a significant place. As is used in industrial chemicals (primarily wood preservatives), agricultural chemicals (herbicides and desiccants), as well as in the production of glass, batteries, and semiconductor devices in the industry [1]. After exposure to As, the resultant oxidative stress and inflammation can lead to cellular damage and various problems [2, 3]. Health problems caused by As include hyperpigmentation [4], basal cell carcinoma on non-melanin skin [5], hepatomegaly [6], cirrhosis [7], increased incidence of hypertension [8], myocardial damage, cardiomyopathy [9], cardiac arrhythmias [10], confusion and memory loss [11], nephritis, prostate, kidney, ureter cancer [12], and an increased risk of diabetes mellitus [13].

The most commonly used method for heavy metal poisoning is chelation therapy, which aims to increase the elimination of metals [14]. A variety of chelating agents containing sulfhydryl groups such as meso-2,3-dimercaptosuccinic acid, 2,3-dimercapto-propan-1-sulfonate, and British Anti-Lewisite (2,3-dimercaprol) are used in the treatment of As toxicity. The use of these substances aims to increase the elimination of metal from the body [15, 16]. However, these chelators have a range of side effects and are not suitable for high-dose and long-term treatment. Therefore, the search for reliable new substances for prevention or treatment of As poisoning is of great importance.

Cannabidiol (CBD) is one of the compounds derived from the hemp plant [17]. CBD is the primary non-psychotropic cannabinoid derived from hemp plant, commonly referred to as marijuana. It was first isolated in 1940, with its structure and stereochemistry elucidated in 1963 CBD does not produce nearly any psychoactive effects. Additionally, CBD has antiemetic, analgesic, anti-inflammatory, and antioxidant effects [17, 18]. The protective role of CBD is attributed to multiple molecular mechanisms, including its ability to mitigate oxidative stress and inflammation, as well as its potential to interfere with the cellular uptake and accumulation of heavy metals [19].

In our study, the aim was to determine the protective effect of CBD on oxidative stress and inflammation occurring in liver cell cultures after As exposure.

Methods

Acquiring CBD

CBD was obtained in its purest form from the company CB21 Pharma S.R.O. in the Czech Republic.

Providing Test Material

As ionic standard was obtained from Sigma-Aldrich. Glutathione (GSH) (BT LAB, China, Cat.No:EA0142Hu), malondialdehyde (MDA) (Elabscience, USA, Cat.No:E-EL-0060), myeloperoxidase (MPO) (BT LAB, China, Cat.No:E0880Hu), and catalase (CAT) (BT LAB, China, Cat.No:E30053Hu), as well as tumor necrosis factor-α (TNF-α) (BT LAB, China, Cat.No:E0082Hu), interleukin-1β (IL-1β) (BT LAB, China, Cat.No:E0143Hu), and interleukin-6 (IL-6) (BT LAB, China, Cat.No:E0090Hu) ELISA kits, were sourced from commercial companies. The THLE-2 non-cancerous liver cell line (ATCC) was obtained from the Ege University Central Research Test and Analysis Laboratory Application and Research Center.

Development of Cell Lines in 2 Dimensions (2D) and Three-Dimensional (3D)

In the project, a liver cell line called THLE-2 was used to determine the toxic effects of As. THLE-2 cells were produced in two dimensions (2D) in 75 cm^2 and 25 cm^2 flasks at 37°C with 5% carbon dioxide in an incubator using Dulbecco's Modified Eagle's Medium (D-MEM) (High Glucose) supplemented with 10% Fetal Bovine Serum, 1% Gentamycin, and 1% Penicillin. As the surface of the flask was covered by 80% of the cells, the cells were passaged using trypsin.

THLE-2 cell lines were also developed in 3D format. Cells were grown in a spheroid shape using the hanging drop method. The cell lines were expanded globally using the three-dimensional hanging drop method. Subsequently, the cells were cultured at 37°C with 5% CO$_2$ in an incubator.

As Toxicity Analysis

In our study, As trioxide (As$_2$O$_3$) compound was used. To determine the toxic effect levels of As, XTT assay kit (Biological Industries) was used for 2D cell lines, and ATP assay kit (Elabscience) was employed for 3D cell lines. The analyses were conducted following the manufacturer's instructions

Cytotoxicity Experimental Groups

Group I (Control(CONT)): The cell line was only passaged, similar to the other groups, without the application of any additional test substance.

Group II (As): As was added to the cell line's medium at concentrations of 1μM, 5μM, 10μM, 25μM, 50 μM, and 100 μM, and then the cells were passaged in this manner [20]. The determined IC$_{50}$ concentrations for As, which were 10 μM for 2D cell lines and 15 μM for 3D cell lines, were used in the experiments.

Group III (CBD): CBD was added to the cell line's medium at concentrations of 1 μM, 5 μM, 10 μM, 25 μM, 50 μM, and 100 μM, and then the cells were passaged in this manner [21]. The determined IC$_{50}$ concentrations for CBD, which were 1 μM for 2D cell lines and 5 μM for 3D cell lines, were used in the experiments.

Group IV (As+CBD): As at concentrations of 10 μM for 2D cell lines and 15 μM for 3D cell lines, along with CBD at concentrations of 1 μM for 2D cell lines and 5 μM for 3D

cell lines, was added to the cell line's medium. Subsequently, the cells were passaged in this manner [20, 21].

Cytotoxicity Analysis of CBD in 2D and 3D Cell Models

To determine the cytotoxic effect of As and CBD on cells, an XTT assay was conducted. Cells were seeded onto 96-well plates in a manner that resulted in 5000 cells per well. As solution and CBD were separately and jointly applied to the cell models. The prepared solutions were dispensed into wells in serial dilutions. After 72 hours, the formazan dye from the XTT kit was added to each well, and the plate was incubated for 2 to 5 hours. Subsequently, optical densities were determined using an ELISA reader. The calculated results from the reading determined the LD$_{50}$ on cells treated with both the toxic metal and CBD [19].

In the case of cells developed in a 3D environment, the morphologies of the cells were first examined under a microscope to determine the IC$_{50}$ dose. Subsequently, the determined concentration ranges were added to the cells. Then, the viability of the cells was examined using the ATP detection assay (Colorimetric) method. Each sample was conducted in at least three replicates. The viability rates, calculated in comparison to negative and positive controls, were used to plot dose-response curves. Application to cells was performed based on the obtained IC$_{50}$ value [19].

Determination of Oxidative Stress Parameters

Following the application of As and CBD, the levels of GSH, MDA, MPO, and CAT in cells were measured to assess oxidative stress. The levels of these parameters in cells were determined using ELISA microplate readers, following the instructions provided by the commercial test kits. This analysis aimed to evaluate the oxidative stress response induced by As exposure and the potential protective effects of CBD.

Determination of Proinflammatory Cytokines

Following the application of As and CBD, the levels of TNF-α, IL-1β, and IL-6 were measured to assess the inflammatory response. The levels of these cytokines in cells were determined using ELISA microplate readers, following the instructions provided by the commercial test kits. This analysis aimed to evaluate the inflammatory effects induced by As exposure and the potential modulatory effects of CBD.

Toxicological Analysis

Cells obtained from the experimental groups were treated with nitric acid (HNO$_3$), hydrogen peroxide (H2O2), and ultrapure water. These treatments were applied to evaluate how cellular As uptake is influenced by CBD administration. The concentrations of As in the cells were determined using Inductively Coupled Plasma-Mass Spectrometry (ICP-MS).

Statistical Analysis

The results were presented as mean ± standard deviation. The data analysis was performed using the IBM SPSS Statistics 23.0 software package. The distribution characteristics of the data were determined using the

Kolmogorov-Smirnov test. For data showing a normal distribution, one-way analysis of variance (ANOVA) was conducted, followed by Tukey's post hoc test. For data that did not exhibit a normal distribution, Kruskal-Wallis test was applied, followed by Dunnett's T3 post hoc test. The p-value of less than 0.05 was considered statistically significant.

Results

Cell Line Analysis Results

The protective effect of CBD on the toxic effects of As in a liver cell line was investigated in the project. The cytotoxic effect levels (IC_{50}) of As on liver cell lines were determined in both 2D and 3D cell models at different dose ranges (Table 1 and Table 2). According to the obtained results, the IC_{50} value was determined as 10 µM for 2D cell lines and 15 µM for 3D cell lines. In 3D cell models, the toxic dose was found to be higher compared to 2D cell lines. 3D cell models, due to their production in a manner similar to in vivo systems, contain thousands of cells in their structure. Therefore, the dose given to 2D cell lines may not be effective on 3D cells.

Table 1. Cell proliferation rate (%) in 2D THLE-2 cell lines

Groups	Dosage range	24 h	48 h	72 h
As	1 µM	66	60	43
	5 µM	59	55	35
	10 µM	56	48	30
	25 µM	36	30	21
	50 µM	10	5	3
CBD	1 µM	82	74	68
	5 µM	75	64	60
	10 µM	70	65	60
	25 µM	68	65	55
	50 µM	61	56	49
As + CBD	10 µM + 1 µM	68	61	51
CONT	-	100	100	100

Abbreviations: CONT, control group; CBD, group treated with only CBD; As + CBD, group treated with both As and CBD; As, group treated with only As.

Table 2. Cell proliferation rate (%) in 3D THLE-2 cell lines

Groups	Dosage range	24 h	48 h	72 h
As	1 µM	73	64	50
	5 µM	69	56	48
	10 µM	60	53	41
	25 µM	50	40	38
	50 µM	45	32	25
	100 µM	30	21	10
CBD	1 µM	90	83	75
	5 µM	88	76	70
	10 µM	75	70	63
	25 µM	62	58	50
	50 µM	49	40	35
	100 µM	41	32	28
As + CBD	15 µM + 5 µM	76	68	50
CONT	-	100	100	100

Abbreviations: CONT, control group; CBD, group treated with only CBD; As + CBD, group treated with both As and CBD; As, group treated with only As.

As seen in Table 1 for 2D cell lines, exposure to As alone causes more damage to the cells. However, it was observed that when CBD was applied in addition to As,

there was less damage developed in the cells. As seen in Table 2 for 3D cell lines, As alone caused more damage to the cells. However, it was observed that when CBD was applied in combination with As, there was less damage developed in the cells.

Inverted microscope images of 3D cell lines are provided. As observed, the cell density in the group treated with As alone was lower, while the cell density in the group treated with CBD + As was similar to the CONT (Figure 1).
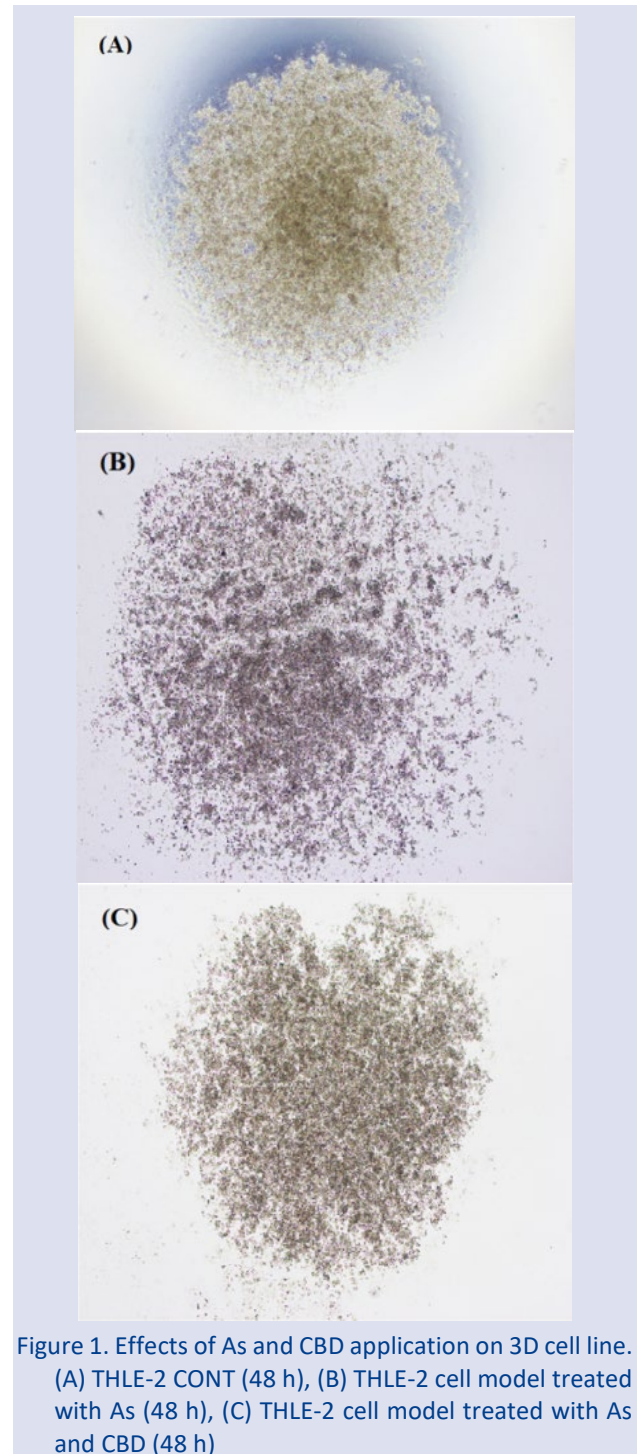
Figure 1. Effects of As and CBD application on 3D cell line. (A) THLE-2 CONT (48 h), (B) THLE-2 cell model treated with As (48 h), (C) THLE-2 cell model treated with As and CBD (48 h)
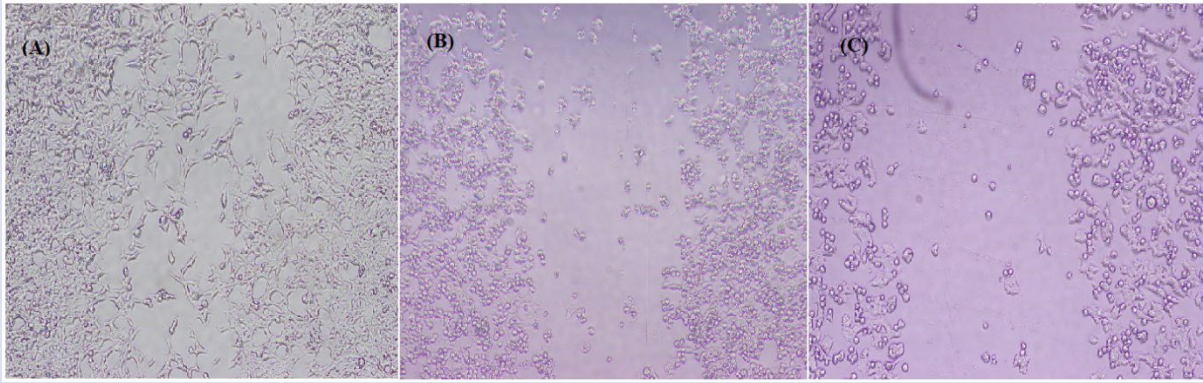
Figure 2. Effects of As and CBD application on 2D cell line. (A) THLE-2 Control (48 h), (B) THLE-2 cell model treated with As (48 h), (C) THLE-2 cell model treated with As and CBD (48 h).

Inverted microscope images of 2D cell lines are provided. As observed, the cell density in the group treated with As alone was lower, while the cell density in the group treated with CBD + As was similar to the CONT (Figure 2).

Evaluation of ELISA and ICP-MS Results

The effect of CBD on As exposure was examined. Levels of GSH, MDA, MPO, CAT, TNF-α, IL-1β, and IL-6 were determined. The decrease observed in GSH and CAT levels in the As group was not observed in the As + CBD group ($p < 0.05$). The increase observed in MPO, MDA, TNF-α, IL-1β, and IL-6 levels in the As group was not observed in the As + CBD group ($p < 0.05$). The level of As detected in the cells of the As group was higher than that in the cells of the As + CBD group ($p < 0.05$) (Figure 3).
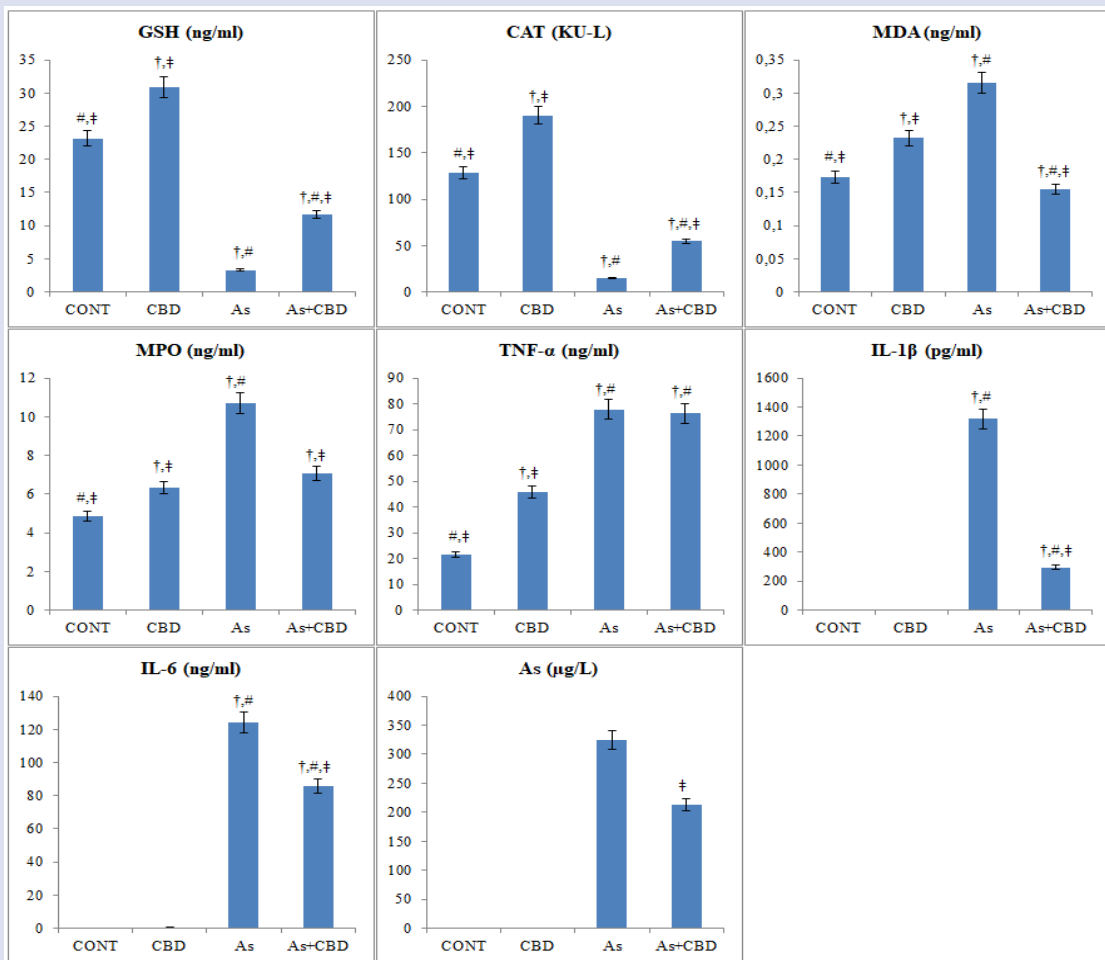
Figure 3. Results of ELISA and ICP-MS in As groups. Abbreviations: CONT, control group; CBD, group treated with only CBD; As+CBD, group treated with both As and CBD; As, group treated with only As. † indicates the group different from the CONT group ($p < 0.05$), # indicates the group different from the CBD group ($p < 0.05$), ‡ indicates the group different from the As group ($p < 0.05$).

Discussion

CBD, an active ingredient of the hemp plant, has attracted significant attention due to its potential therapeutic properties [22, 23]. In recent years, various positive attributes of CBD have been proposed, including its potential protective effects against numerous health conditions [24]. Booz (2011) suggested that CBD activates the immune system and exhibits therapeutic effects in diseases such as rheumatoid arthritis, type 1 and type 2 diabetes, atherosclerosis, Alzheimer's disease, hypertension, metabolic syndrome, ischemia-reperfusion injury, depression, and neuropathic pain induced by oxidative stress [18]. In line with these findings, our study observed a protective effect of CBD in As toxicity in the THLE-2 liver cell culture. Specifically, we found that CBD mitigated oxidative stress markers and proinflammatory cytokine levels elevated due to As exposure, indicating its potential role in counteracting As-induced toxicity. The findings from our study provide experimental evidence that supports the proposed protective effects of CBD, particularly its capacity to modulate oxidative stress and inflammatory responses in human liver cells exposed to As. While previous studies have suggested CBD's therapeutic efficacy in various conditions, including obesity, anorexia, and vomiting [25, 26], our findings contribute to understanding how CBD could potentially protect liver cells from As toxicity through these mechanisms. In support of the therapeutic potential of CBD, various studies have suggested its effectiveness in a range of diseases. For instance, CBD has been investigated for its potential in treating diabetes [27, 28]. In line with these findings, Chen et al. (2016) demonstrated that CBD has a protective effect against oxidative stress, apoptosis, and inflammation induced by hydrogen peroxide in nucleus pulposus cells, which are similar to the stress induced by As in our study [29]. Moreover, CBD has shown promise in alleviating inflammation and oxidative stress in various animal models. For example, Rajesh et al. (2010) reported that CBD administration alleviated myocardial dysfunction, cardiac fibrosis, and oxidative stress in diabetic cardiomyopathy in mice, which supports its broad-spectrum protective effects [30]. While our study did not directly evaluate the effects of CBD on cardiovascular tissues, the observed reduction in oxidative stress markers such as GSH, MDA, MPO, and CAT in the THLE-2 cells after CBD treatment parallels the findings in these animal studies, suggesting similar protective mechanisms. These findings imply that CBD's antioxidant and anti-inflammatory effects extend beyond its effects on the liver and may be relevant in other organ systems exposed to toxic stress.

Various studies have explored CBD's potential therapeutic effects in neurological diseases and other conditions in both animal models and humans. For instance, Campbell and Gowran (2007) evaluated the impact of CBD on Alzheimer's disease, while Sagredo (2012) and Devinsky et al. (2017) investigated CBD's role in Huntington's disease, epilepsy, and other neurological disorders, suggesting positive effects in these conditions [31–33]. Similarly, Hall et al. (2005) highlighted the potential of CBD in reducing pain associated with cancer, emphasizing its therapeutic promise [34]. In our study, although we did not investigate neurological diseases directly, the observed reduction in inflammatory cytokines (TNF-α, IL-1β, IL-6) following CBD treatment aligns with findings from these studies. The modulation of inflammatory responses is a critical aspect of CBD's therapeutic profile, and the suppression of pro-inflammatory cytokines observed in our study suggests that CBD may play a protective role in conditions where inflammation is exacerbated by toxic agents like As. This finding not only supports the anti-inflammatory potential of CBD but also highlights its broad applicability in treating diseases linked to chronic inflammation, including neurodegenerative conditions and cancer.

In studies assessing oxidative stress in response to As exposure, similar protective effects of CBD have been observed. Zhao et al. (2022) investigated the effectiveness of grape skin extract in mitigating As toxicity in mice, reporting that it reversed the elevated levels of MDA and MPO and the reduced levels of GSH following As exposure [2]. In another study by Al Aboud et al. (2021), the protective efficacy of ebselen against As-induced hepatotoxicity in rats was evaluated, showing that ebselen reversed oxidative damage by restoring GSH and CAT levels, while reducing MDA levels [35]. In our study, the As-induced decrease in GSH and CAT levels, along with the increase in MDA levels, was similarly reversed by CBD. These results align with the aforementioned studies, supporting the hypothesis that CBD acts as an antioxidant and can mitigate oxidative stress caused by toxic agents like As. The restoration of these oxidative stress markers in the presence of CBD further confirms its protective role and suggests its potential as a therapeutic agent in preventing or alleviating As-induced liver damage.

In our study, the inflammatory response induced by As exposure, reflected by the elevated levels of pro-inflammatory cytokines (TNF-α, IL-1β, IL-6), was mitigated following CBD treatment. This result is consistent with the findings of Zhao et al. (2022), who reported that grape skin extract reversed the increased mRNA expressions of pro-inflammatory cytokines (TNF-α, IL-1β, IFN-γ) following As exposure in mice [2]. Additionally, CBD has been shown to have a protective effect in various cell types through the suppression of pro-inflammatory and anti-apoptotic pathways [29]. In our study, CBD treatment effectively reduced the cytokine levels that were elevated due to As exposure, suggesting that CBD may exert its protective effects through anti-inflammatory mechanisms. This observation highlights the potential of CBD in modulating the immune response and preventing chronic inflammation, which is often exacerbated by toxic stressors like As. By reducing these inflammatory markers, CBD demonstrates its potential to alleviate inflammation-related damage and may serve as a promising therapeutic option for conditions involving oxidative and inflammatory stress.

Dopp et al. (2004), in their in-vitro studies evaluating the relationship between the uptake, cytotoxic, and genotoxic effects of inorganic and organic arsenic (As) derivatives, indicated that after cellular uptake of inorganic As, it undergoes biotransformation into mono- and dimethylated metabolites. They stated that methylation reactions represent a toxification process rather than a detoxification process and emphasized the importance of cellular uptake mechanisms in the formation of As toxicity [36]. In our study, the lower amount of As observed in the group co-treated with CBD and As, compared to the As-only group, suggests that CBD may reduce cellular As uptake. This may have mediated the protective effect of CBD against As exposure by limiting the conversion of As into toxic metabolites through methylation. The combined reduction in oxidative stress, inflammatory response, and cellular As uptake offers a comprehensive understanding of how CBD may exert its protective effects against As-induced toxicity.

Conclusion

Our study demonstrates that CBD exerts a protective effect against arsenic (As)-induced toxicity in THLE-2 liver cells. By reducing oxidative stress, inflammatory responses, and cellular As uptake, CBD appears to mitigate the harmful effects of As exposure. These findings align with existing literature, which supports the potential of CBD in counteracting various forms of toxicity, including those induced by heavy metals. The observed reduction in As-induced oxidative stress, inflammation, and cellular damage underscores CBD's therapeutic potential in preventing or alleviating As toxicity. Further studies are warranted to explore the mechanisms underlying these effects in greater detail and to evaluate the clinical applicability of CBD in managing environmental toxicities.

Conflicts of interest

There are no conflicts of interest in this work.

Acknowledgment

References

[1] Ishiguro S., Industries Using Arsenic and Arsenic Compounds, *Appl. Organomet. Chem*., 6 (4) (1992) 323–331.

[2] Zhao D., Yi H., Sang N., Arsenic Intake-Induced Gastric Toxicity Is Blocked by Grape Skin Extract by Modulating Inflammation and Oxidative Stress in a Mouse Model, *Ecotoxicol. Environ. Saf*., 233 (2022) 113305.

[3] Liu P., Xue Y., Zheng B., Liang Y., Zhang J., Shi J., Chu X., Han X., Chu L. Crocetin Attenuates the Oxidative Stress, Inflammation and Apoptosisin Arsenic Trioxide-Induced Nephrotoxic Rats: Implication of PI3K/AKT Pathway, *Int. Immunopharmacol*., 88 (2020) 06959.

[4] Mazumder D.N.G., Haque R., Ghosh N., De B.K., Santra A., Chakraborty D., Smith A.H. Arsenic Levels in Drinking Water and the Prevalence of Skin Lesions in West Bengal, India, *Int. J. Epidemiol*., 27 (5) (1998) 871–877.

[5] Abernathy C.O., Liu Y.P., Longfellow D., Aposhian H.V., Beck B., Fowler B., Goyer R., Menzer R., Rossman T., Thompson C., Arsenic: Health Effects, Mechanisms of Actions, and Research Issues, *Environ. Health Perspect*., 107 (7) (1999) 593–597.

[6] Santra A., Gupta J., Das De B.K., Roy B., Mazumder D.N.G. Hepatic Manifestations in Chronic Arsenic Toxicity, *Indian J. Gastroenterol*., 18 (1999) 152–155.

[7] Nevens F., Staessen D., Sciot R., Van Damme B., Desmet V., Fevery J., De Groote J., Van Steenbergen W. Clinical Aspects of Incomplete Septal Cirrhosis in Comparison with Macronodular Cirrhosis, *Gastroenterology*, 106 (2) (1994) 459–463.

[8] Rahman M., Tondel M., Ahmad S.A., Chowdhury I.A., Faruquee M.H., Axelson O. Hypertension and Arsenic Exposure in Bangladesh, *Hypertension*, 33 (1) (1999) 74–78.

[9] Benowitz N.L. Cardiotoxicity in the Workplace, Occup. Med., 7 (3) (1992) 465–478.

[10] Goldsmith S., Arthur H.L., Arsenic-Induced Atypical Ventricular Tachycardia, *N. Engl. J. Med*., 303 (19) (1980) 1096–1098.

[11] Schenk V.W., Stolk P.J., Psychosis Following Arsenic (Possibly Thallium) Poisoning, *Psychiatr. Neurol. Nurochirurgia*, 70 (1) (1967) 31–37.

[12] Guo H.R., Chiang H.S., Hu H., Lipsitz S.R., Monson R.R., Arsenic in Drinking Water and Incidence of Urinary Cancers, *Epidemiology*, 8 (5) (1997) 545–550.

[13] Rahman M., Tondel M., Ahmad S.A., Axelson O., Diabetes Mellitus Associated with Arsenic Exposure in Bangladesh, *Am. J. Epidemiol*., 148 (2) (1998) 198–203.

[14] Zhai Q., Narbad A., Chen W., Dietary Strategies for the Treatment of Cadmium and Lead Toxicity, *Nutrients*, 7 (1) (2015) 552–571.

[15] Gupta R., Flora S.J.S., Therapeutic Value of Hippophae Rhamnoides L. against Subchronic Arsenic Toxicity in Mice, *J. Med. Food*, 8 (3) (2005) 353–361.

[16] Nurchi V.M., Djordjevic A.B., Crisponi G., Alexander J., Bjørklund G., Aaseth J., Arsenic Toxicity: Molecular Targets and Therapeutic Agents*, Biomolecules*, 10 (2) (2020) 235.

[17] Jarjou'i A., Izbicki G., Medical Cannabis in Asthmatic Patients, *Isr. Med. Assoc. J*., 22 (4) (2020) 232–235.

[18] Booz G.W., Cannabidiol as an Emergent Therapeutic Strategy for Lessening the Impact of Inflammation on Oxidative Stress, *Free Radic. Biol. Med*., 51 (5) (2011) 1054–1061.

[19] Şahin S., Azarkan S.Y., Türksoy V.A., Evaluation of the Effect of Cannabidiol on the THLE-2 Liver Cell Line Exposed to Lead, *Sci. Total Environ*., 923 (2024) 170901.

[20] Styblo M., Razo L.M. Del Vega L., Germolec D.R., Lecluyse E.L., Hamilton G.A., Reed W., Wang C., Cullen W.R., Thomas D.J., Comparative Toxicity of Trivalent and Pentavalent Inorganic and Methylated Arsenicals in Rat and Human Cells, *Arch Toxicol*., 74 (2000) 289–299.

[21] Gęgotek A., Atalay S., Domingues P., Skrzydlewska E., The Differences in the Proteome Profile of Cannabidiol-Treated Skin Fibroblasts Following UVA or UVB Irradiation in 2D and 3D Cell Cultures, *Cells*, 8 (9) (2019) 995.

[22] Etienne de M., Fibre Hemp Cultivars: A Survey of Origin, Ancestry, Availabilityand Brief Agronomic Characteristics, *J. Int. Hemp Assoc*., 2 (1995) 67–73.

[23] Fitzcharles M., Clauw D.J., Hauser W.A., Cautious Hope for Cannabidiol (CBD) in Rheumatology Care, *Arthritis Care Res. (Hoboken)*, 75 (6) (2023) 1371–1375.

[24] Niesink R.J.M., van Laar M.W., Does Cannabidiol Protect Against Adverse Psychological Effects of THC?, *Front. psychiatry*, 4 (2013) 130.

[25] Patel P.N., Pathak R., Rimonabant: A Novel Selective Cannabinoid-1 Receptor Antagonist for of Treatment Obesity, *Am. J. Heal. Pharm*., 64 (5) (2007) 481–489.

[26] Gelfand E.V., Cannon C.P., Rimonabant: A Selective Blocker of the Cannabinoid CB1 Receptors for the Management of Obesity, Smoking Cessation and Cardiometabolic Risk Factors, *Expert Opin. Investig. Drugs*, 15 (3) (2006) 307–315.

[27] Penner E.A., Buettner H., Mittleman M.A., The Impact of Marijuana Use on Glucose, Insulin, and Insulin Resistance among US Adults, *Am. J. Med*., 126 (7) (2013) 583–589.

[28] Weiss L., Zeira M., Reich S., Har-Noy M., Mechoulam R., Slavin S., Gallily R., Cannabidiol Lowers Incidence of Diabetes in Non-Obese Diabetic Mice, *Autoimmunity*, 39 (2) (2006) 143–151.

[29] Chen J., Hou C., Chen X., Wang D., Yang P., He X., Zhou J., Li H., Protective Effect of Cannabidiol on Hydrogen Peroxide-induced Apoptosis, Inflammation and Oxidative Stress in Nucleus Pulposus Cells, *Mol. Med. Rep*., 14 (3) (2016) 2321–2327.

[30] Rajesh M., Mukhopadhyay P., Btkai S., Patel V., Saito K., Matsumoto S., Kashiwaya Y., Horvth B., Mukhopadhyay B., Becker L., Cannabidiol Attenuates Cardiac Dysfunction, Oxidative Stress, Fibrosis, and Inflammatory and Cell Death Signaling Pathways in Diabetic Cardiomyopathy, *J. Am. Coll. Cardiol.*, 56 (25) (2010) 2115–2125.

[31] Campbell V.A., Gowran A., Alzheimer's Disease; Taking the Edge off with Cannabinoids?, *Br. J. Pharmacol*., 152 (5) (2007) 655–662.

[32] Sagredo O., Ruth Pazos M., Valdeolivas S., Fernández-Ruiz J., Cannabinoids: Novel Medicines for the Treatment of Huntington's Disease, Recent Pat. *CNS Drug Discov*., 7 (1) (2012) 41–48.

[33] Devinsky O., Cross J.H., Laux L., Marsh E., Miller I., Nabbout R., Scheffer I.E., Thiele E.A., Wright S., Trial of Cannabidiol for Drug-Resistant Seizures in the Dravet Syndrome, *N. Engl. J. Med*., 376 (21) (2017) 2011–2020.

[34] Hall W., Christie M., Currow D., Cannabinoids and Cancer: Causation, Remediation, and Palliation, *Lancet Oncol*., 6 (1) (2005) 35–42.

[35] Al Aboud D., Baty R.S., Alsharif K.F., Hassan K.E., Zhery A.S., Habotta O.A., Elmahallawy E.K., Amin H.K., Abdel Moneim A.E., Kassab R.B., Protective Efficacy of Thymoquinone or Ebselen Separately against Arsenic-Induced Hepatotoxicity in Rat, *Environ. Sci. Pollut. Res. Int*., 28 (5) (2021) 6195–6206.

[36] Dopp E., Hartmann L.M., Florea A.M., Von Recklinghausen U., Pieper R., Shokouhi B., Rettenmeier A.W., Hirner A.V., Obe G., Uptake of Inorganic and Organic Derivatives of Arsenic Associated with Induced Cytotoxic and Genotoxic Effects in Chinese Hamster Ovary (CHO) Cells, *Toxicol. Appl. Pharmacol*., 201 (2) (2004) 156–165.

Cumhuriyet Science Journal

A New Candidate for the Treatment of Alzheimer's Disease; Synthesis, Characterization, Investigation of Drug Properties with *In Silico* Methods

Ömer Dilek [1,a,*], Tolga Acar Yeşil [2,b], Tahir Tilki [3,c]

[1]Central Research Laboratory Application and Research Center, Isparta University of Applied Sciences, Isparta, Türkiye

[2]Department of Property Protection and Security, Türkeli Vocational School, Sinop University, Sinop, Türkiye

[3]Department of Chemistry, Faculty of Engineering and Natural Sciences, Süleyman Demirel University, Isparta, Türkiye

*Corresponding author

Research Article

ABSTRACT

Brain disorder-caused mortality has emerged as the second of all diseases worldwide in the 21st century. Alzheimer's Disease (AD) is the most common disease that takes place among brain disorders according to statistics. Therefore, in this study, potential new drug candidate for AD (2-**a**mino-N'-**b**enzylidene-4-(**t**rifluoromethyl)benzo**h**ydrazide, ABTH) was synthesized, starting from -CF_3 and -NO_2 containing carboxylic acid. The structure of ABTH was elucidated using ^1H, ^{13}C-APT NMR, FTIR, and Mass analyses. ADMEt properties were calculated and from the ADMEt results, it was observed that the ABTH crossed the Blood-Brain Barrier (BBB), the most important property in evaluating new drug candidate in brain disorders. Molecular Docking studies were conducted using proteins related AD. According to docking studies, 2OI0-ABTH was the highest docking score with the -8.9 kcal/mol. Standard drugs (Donepezil, Galantamine, Rivastigmine) used in AD treatment were also docked with the AD proteins to do meaningful comparison. The molecular docking results showed that the ABTH has higher docking score than standards. Since 2OI0-ABTH complex had the best docking score, it was chosen for the MD simulation studies. From the obtained results, It can be suggested that ABTH promising drug candidate for AD after further investigations were done.

Keywords: Alzheimer's disease, Fluorine compounds, Hydrazone, ADMEt, Molecular docking.

[a] omerdilek@isparta.edu.tr   https://orcid.org/0000-0003-1409-782X   [b] tyesil@sinop.edu.tr   https://orcid.org/0000-0001-5983-8447
[c] tahirtilki@sdu.edu.tr   https://orcid.org/0000-0002-1040-2375

Introduction

As the world's population ages in the 21st century, brain diseases, which globally rank as the second most common cause of mortality, such as brain tumors, stroke, neurodegenerative diseases, and other catastrophic illnesses, have grown to pose a serious threat to human life and health [1]. A variety of techniques are used in the current treatment of brain diseases, such as radiation therapy, chemotherapy, and surgery, which are used to treat brain tumors [2]. Based on their causes, symptoms, and effects on the brain, brain disorders can be classified into various categories and impact numerous aspects of brain function. Some common types of brain diseases are dementia, brain cancer, epilepsy, mental disorders, stroke and transient ischemic attack, Parkinson's, and AD.

AD is a neurological illness that worsens over time and mostly impacts behavior, thinking, and memory. It is the most typical cause of dementia, a syndrome marked by a significant enough reduction in cognitive function to cause problems in day-to-day functioning [3]. With a global prevalence of 24 to 34 million cases, AD is the most frequent type of dementia [4]. A variety of proteins, including tau protein, β-amyloid (Aβ), and amyloid precursor protein (APP), are important in the progression and course of AD [5].

Fluorine is known to have a major impact on chemical reactivity, physicochemical behavior, and biological activity due to its size, electronegativity, lipophilicity, and electrostatic interactions [6]. Fluorine's beneficial effects on pharmacological properties have led to a growing interest in fluorinated group (such as F, CF_3, OCF_3, CHF_2, etc.) substances [7].

Hydrazones can be combined with other functional groups to create molecules with distinct chemical and physical properties [8]. Their biological and pharmacological properties make them valuable for the synthesis of heterocyclic compounds and development of new drugs [9]. The biological features of these molecules are noteworthy and include antibacterial, antiviral, analgesic, antidepressant, anticancer, and anti-neuroinflammatory effects [10]. Potential therapies for AD are now being researched, including pharmacologically active hydrazone derivatives with anti-neuroinflammatory potential [11].

The process of developing a new drug can take up to 10-15 years on average, and it can cost up to \$255.8 million to bring a drug to market [12]. Furthermore, only 13% of clinical studies reported in literature for new pharmacological drugs are successful [13]. As a result, in the last few decades, the application of in silico methods

for drug discovery like computer-aided drug design (CADD) has increased significantly [14]. Applications of CADD typically assist in experimental research decision-making by monitoring the major stages of drug development, such as target validation, hit discovery, lead generation, and optimization [15]. CADD mainly deals with drug design based on ligand structure and drug design based on receptors. When developing new drugs, one of the most crucial ADME and Toxicity properties take into account is the BBB permeability of the compounds. The BBB, is a complex biological structure that separates the brain from the systemic blood circulation and is responsible for preserving the homeostasis of the central nervous system (CNS) [16]. The ability of compounds to penetrate the BBB determines how possible drugs are distributed between the blood and the brain. Lipophilic drugs can easily penetrate the BBB through passive diffusion. In contrast, polar molecules are typically unable to pass through the BBB, however occasionally an active transport process can help them [17]. Effective permeability of the BBB is a vital requirement for the development of new drugs intended to treat brain diseases. Molecular docking has increased in significance as an *in silico* drug discovery approach. By modeling the atomic-level interaction between a small molecule and a protein using the molecular docking approach, we can clarify basic biochemical processes and characterize the behavior of small molecules at target protein binding sites [18]. In recent years, MD simulations have become increasingly important in the drug discovery process. MD simulations, which depend on a general model of the physics controlling interatomic interactions, forecast the position of each atom in a protein or other molecular system across time [19].

Because of specified reasons above the ABTH was synthesized. Its structure was verified by using NMR, FTIR, and Mass spectroscopic techniques. *In silico* ADMEt properties were calculated utilizing web servers. Protein-ligand interactions were investigated via Molecular Docking and MD Simulation studies. In molecular docking studies target proteins (PDB ID: 1AAP for amyloid precursor protein (APP); 1O86 for Angiotensin converting enzyme (ACE); 4DJU for β-site APP cleaving enzyme 1 (BACE1); 1Q5K for Glycogen synthase kinase-3 (GSK-3); 2OI0 for TNF-a converting enzyme (TACE)) related with AD were studied. The protein-ligand couple (2OI0-ABTH), which has the best docking score, was used in the MD simulation studies.

Material and Method

General Information

All chemicals used for synthesis and purification were purchased from Aldrich, Merck, and Isolab companies. All reaction conversions were followed by Thin Layer Chromatography (TLC: SIL G/UV254 from MN GmbH & Co). UV light (254 nm) was used for the visualization of spots. Melting points of synthesized compounds were measured in an open glass capillary tube using the Stuart

SMP 30. NMR spectra were recorded by using an Agilent 400 MHz spectrometer and DMSO-d_6 as solvent. Chemical shifts were specified as ppm. Chemical shifts of remaining solvent were adjusted to 2.5 ppm for ^{1}H-NMR, 39.52 ppm for ^{13}C-NMR. A Shimadzu IR Prestige-21 device was used to record FTIR analysis with KBR pellet technique. For mass analyses, the Waters Radian Asap Direct Mass Detector was used. The analytical methods included full scan acquisition mode, ASAP+/ASAP ionization mode, gas (N_2), mass range 100-1200 m/z, cone voltage 10 V, isothermal heater temperature of 600 °C, corona current 3 μA, and capillary dip sampling technique.

Synthesis and Characterization Studies

Synthesis of 2-amino-4-(trifluoromethyl)benzohydrazide (3)

A 100 mL round bottomed two necked flask that was equipped with a magnetic stirring bar and reflux condenser, was charged with 2-nitro-4-(trifluoromethyl)benzoic acid (1, 42.6 mmol; 10.0 g), 6 mL of H_2SO_4 and 100 mL methanol. The flask was heated to reflux via an oil bath for 48 hours. The conversion was also checked by TLC in 6 hours periods. After 48 hours, it was observed that the conversion was completed. The mixture was poured into the cold water and pH was adjusted to 7 with saturated aqueous $NaHCO_3$ solution. Organic components were extracted with three times 100 mL EtOAc. The combined organic extracts were washed with water and brine. So, 10.2 g of the methyl 2-nitro-4-(trifluoromethyl)benzoate(2) was obtained as single product according to TLC in 96% yield. The crude product was converted to its aminohydrazide derivative by using hydrazine hydrate. The 100 mL round bottomed one necked flask containing 10.2 g of the methyl 2-nitro-4-(trifluoromethyl)benzoate and magnetic stirring bar, was charged with 50 mL of hydrazine hydrate, and refluxed for 3 hours. After 3 hours, it was observed that the starting material was converted into the hydrazide derivative. After 3 hours, excess hydrazine hydrate was removed under reduced pressure. The mixture was cooled to room temperature and 50 mL of cold water was added into the flask. The precipitate was filtered and dried. The dried crude product was crystallized with $CHCl_3$/Hexane mixture. 5.82 g of the title compound 2-amino-4-(trifluoromethyl)benzohydrazide (3) was obtained as white solid in 65% yield. Compound 3; Melting Point: 170–172 °C. MS = *m/z*: [M+H]$^+$ Calcd for $C_8H_9F_3N_3O$, 220.18; Found: 220.17.

Synthesis of ABTH

2-amino-4-(trifluoromethyl)benzohydrazide (1 mmol, 219 mg), benzaldehyde (1.1 mmol; 117 mg), catalytic amount AcOH (2-3 drop) and 20 mL absolute ethanol were added into the 100 mL two necked flask that was equipped with magnetic stirring bar and reflux condenser. The mixture was refluxed for 3 hours. The conversion was also followed by TLC. After 3 hours, it was observed that starting material was consumed. The ethanol was removed under reduced pressure. The crude product was

purified by column chromatography using EtOAC/hexane (v/v: 2/1) as eluent. 225 mg of the title compound (ABTH) was obtained in 73% yield. Melting Point: 206–208 °C. FTIR(KBr): $\tilde{v}_{max}$ (cm^{-1}) = 3521 (w), 3462 (w), 3394 (w), 3348 (w), 3223 (br), 3050 (w), 3029 (w), 1647 (s), 1593 (s), 1546 (s), 1437 (s), 1353 (s), 1331 (s), 1250 (s), 1166 (s), 1131 (s). ^{1}H-NMR (400 MHz, DMSO-d_6): δ 11.80 (s, 1H), 8.40 (s, 1H), 7.72 (s, 3H), 7.45 (m, 3H), 7.11 (d, J = 1.2 Hz, 1H), 6.86 (dd, J = 8.2, 1.4 Hz, 1H), 6.68 (s, 2H). ^{13}C{^{1}H}-NMR (APT, 101 MHz, DMSO-d_6): δ 164.20 (C=O), 149.92 (C), 147.75 (CH), 134.28 (C), [132.51, 132.20, 131.90, 131.59, (C, J^2_{C-F} = 30.90 Hz)], 130.06 (CH), [129.59, 129.56, (CH, J^4_{C-F} = 3.2 Hz)], 128.83 (CH), [128.02, 125.30, 122.59, 119.88, (C, J^1_{C-F} = 272.60 Hz)], 127.05 (CH), 116.68 (C), [112.39, 112.36, (CH, J^3_{C-F} = 3.77 Hz)], [110.27, 110.23, 110.20, 110.16, (CH, J^3_{C-F} = 3.59 Hz)]. MS = m/z: [M+H]$^+$ Calcd for $C_{15}H_{13}F_3N_3O$, 308.10; Found: 308.18.

In silico Studies

ADMEt studies

Parameters, such as physicochemical properties, lipophilicity, water solubility, pharmacokinetic and druglikeness properties of the synthesized compound, which play an important role in determining the ADME parameters, were determined by using the SwissADME web server [20]. ProTox-II web server was used to calculate toxicity properties such as LD$_{50}$ and toxicity class [21].

Molecular docking studies

Energy minimization of ABTH and standard drugs were performed by using Avagadro software and UFF parameters before the molecular docking studies [22]. AutodockVina 1.1.2 software was used for Molecular docking studies [23]. UCSF Chimera 1.17.3 for 3D [24] and BIOVIA Discovery Studio Visualizer [25] for 2D were used for all imaging processes. Target proteins specified with PDB ID in Table 1 were used for the molecular docking studies. Selected proteins were downloaded from PDB Bank as .pdb file [26]. All heteroatoms, waters, and non-standard residues were removed from the protein by using UCSF Chimera 1.17.3 software. Dockprep module of UCSF Chimera 1.17.3 was used to add Gasteiger charges. Modeller program was used to homologize selected proteins [27]. The 3D binding coordinates (x,y,z) of selected proteins were calculated utilizing DeepSite web server [28]. A grid box surrounding proteins was used during molecular docking studies.

Table 1. Target Proteins with the PDB ID and 3D binding coordinates

Target Protein	PDB ID	3D Binding Coordinates (x, y, z)
APP	1AAP	10.7; 18.2; 34.7
ACE	1O86	39.0; 39.2; 54.8
BACE1	4DJU	21.2; 32.5; 57.7
GSK-3	1Q5K	8.0; 34.8; 14.4
TACE	2OI0	45.2; 26.8; 1.0

MD simulation studies

Playmolecule web server was utilized for the MD simulation studies [29]. Initially, Force Field (FF) parameterization of ligand was performed by using parameterize module [30]. Then, all selected proteins were prepared for MD simulation with ProteinPrepare module [29]. For the preparing system to MD simulation, the SystemBuilder application based on Playmolecule was used. While the system was being prepared the salt concentration of NaCl was adjusted to 0.15 M. By using AMBER Force Field at 300 K and pH:7.4, the system was prepared for MD simulation. Finally, with the created system in the SystemBuilder of the MD simulation was started by using SimpleRunmodule [31]. MD Simulation was conducted during 12 ns.

Results and Discussion

Synthesis and Characterization

Scope of synthesis studies, the carboxylic acid derivative (1) was converted to its methylester (2) by using methanol and H$_2$SO$_4$. Then, we tried to convert methyl ester to its hydrazide derivative. According to mass analyses (Figure 1) result of obtained product, we observed that not only ester group was converted to hydrazide but also the reduction of nitro group to amine. The aminobenzohydrazide compound 3 was reacted with benzaldehyde (4) in absolute ethanol to give corresponding ABTH in 73% yield. Presence of amine group in the ABTH has also verified with NMR that the broad peak has two protons according to integration in the 6.68 ppm. The synthetic pathway was given in Figure 1. The structure of compound 3 was verified with only mass (Figure 2) and melting point analyses because of the compound commercial available while ABTH was verified with melting point, NMR, Mass, and FTIR analyses. While molecular weight of compound 3 has been theoretically calculated as 219.17 g/mol, it was experimentally observed as 220.17 g/mol in mass analyses in positive mode. The ABTH has eight aromatic region protons, two amine protons, one imine proton, and one hydrazide NH proton. When the ^{1}H-NMR spectrum of ABTH was examined (Figure 3); ^{1}H-NMR result showed that among 6.5-8.5 ppm contain total of eleven protons including aromatic region, amine, and imine protons, and hydrazide proton in the 11.80 ppm. When the ^{13}C-APT NMR spectrum was examined (Figure 4); number of aromatic CH and C carbon atoms was suitable for the suggested structure. Carbon atom of carbonyl group (C=O) was observed in 164.20 ppm. Carbon atom of CF$_3$ group was observed as a quartet signal among 128.02-119.88 with the 272.60 Hz coupling constant. The mass analysis also confirmed the suggested ABTH structure. While the calculated molecular weight of suggested structure was 307.28, It was observed in experimental mass spectra in the positive ionization mode as 308.18 (Figure 5). FTIR analysis of ABTH was also recorded by using KBr pellet technique. When the FTIR spectrum of ABTH was examined, the peaks seen among 3521-3223 cm^{-1} were related with -NH stretching, 3050 and 3029 cm^{-1} aromatic C-H stretching, 1647 cm^{-1} C=O stretching, 1593 C=N, 1546 N-N stretching (Figure 6). The specified peaks were also verified the structure.
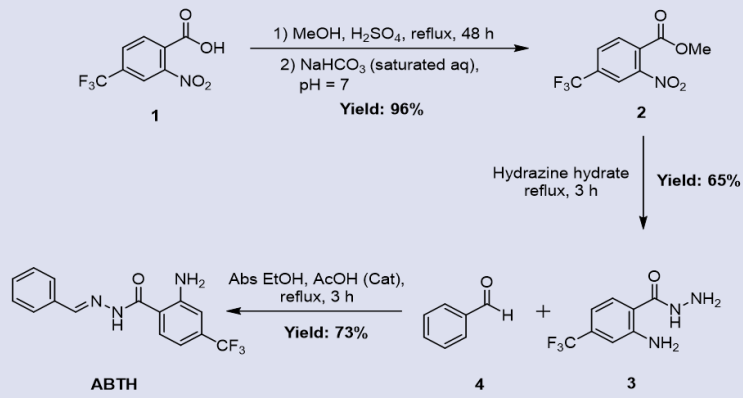
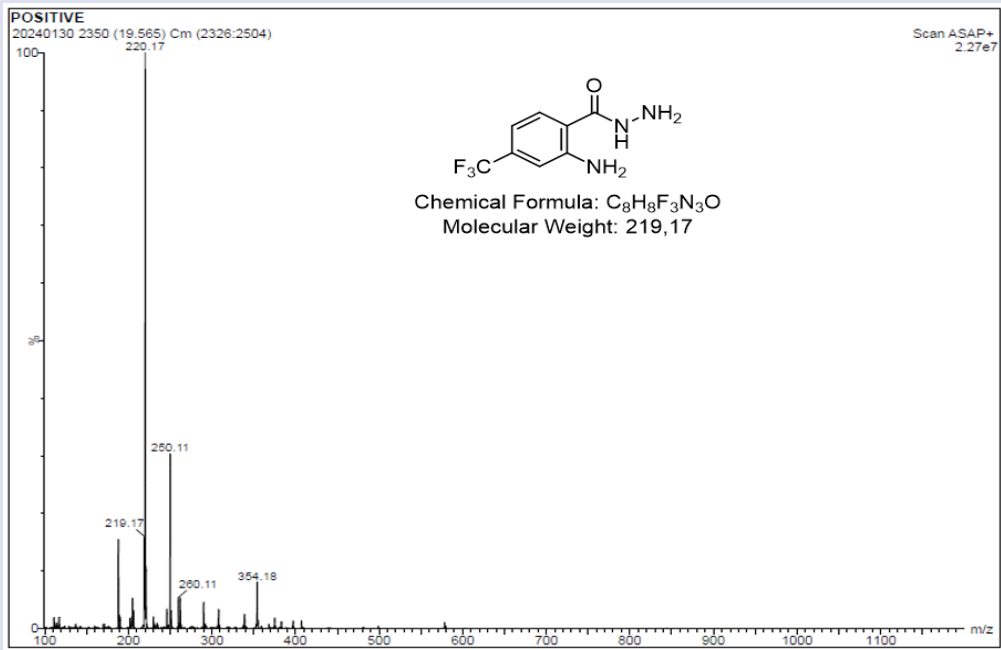Figure 1. Reaction scheme for synthesis of ABTH
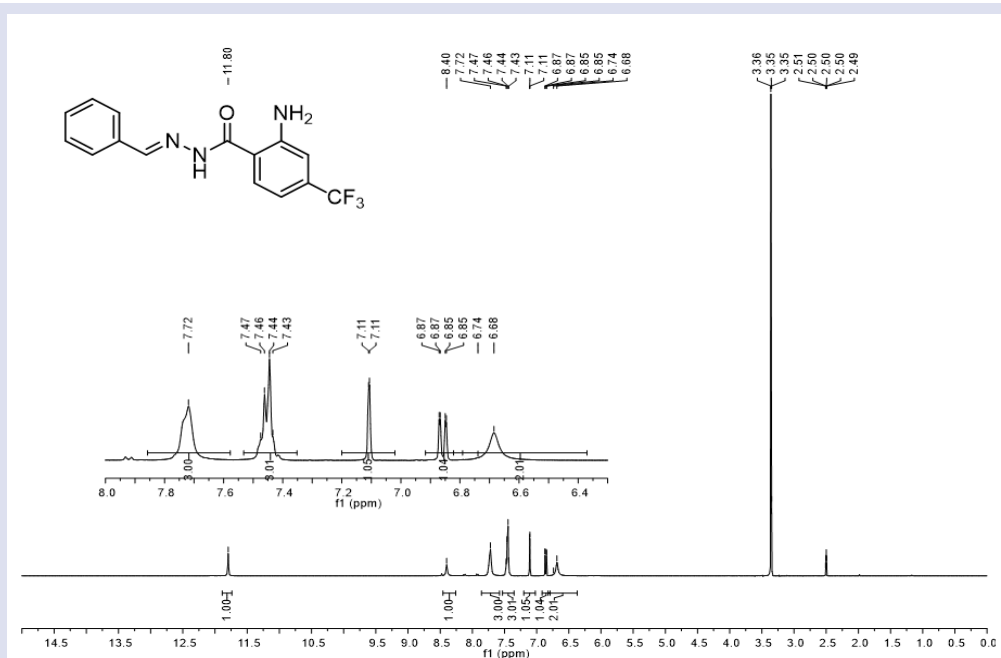

Figure 2. Mass Spectrum of compound 3

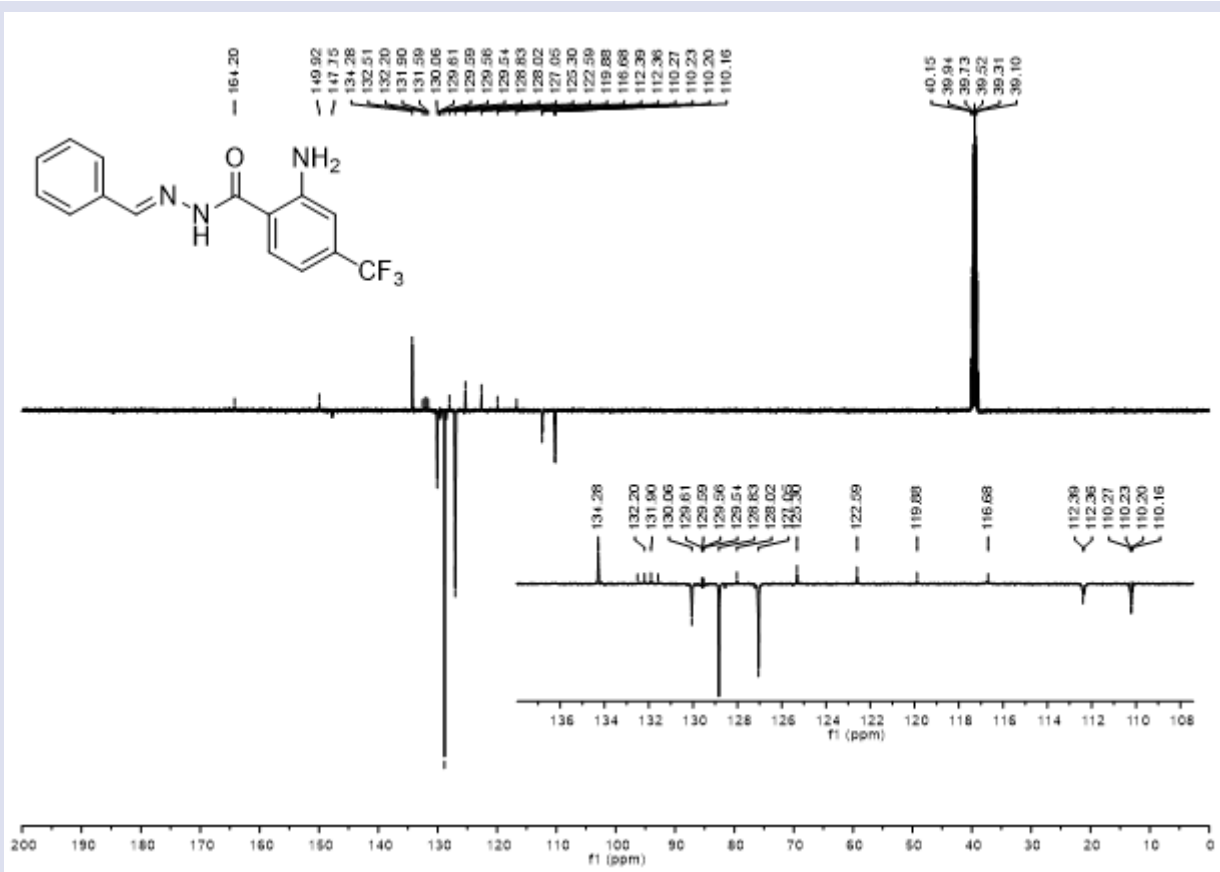Figure 3. ¹H-NMR Spectrum of ABTH

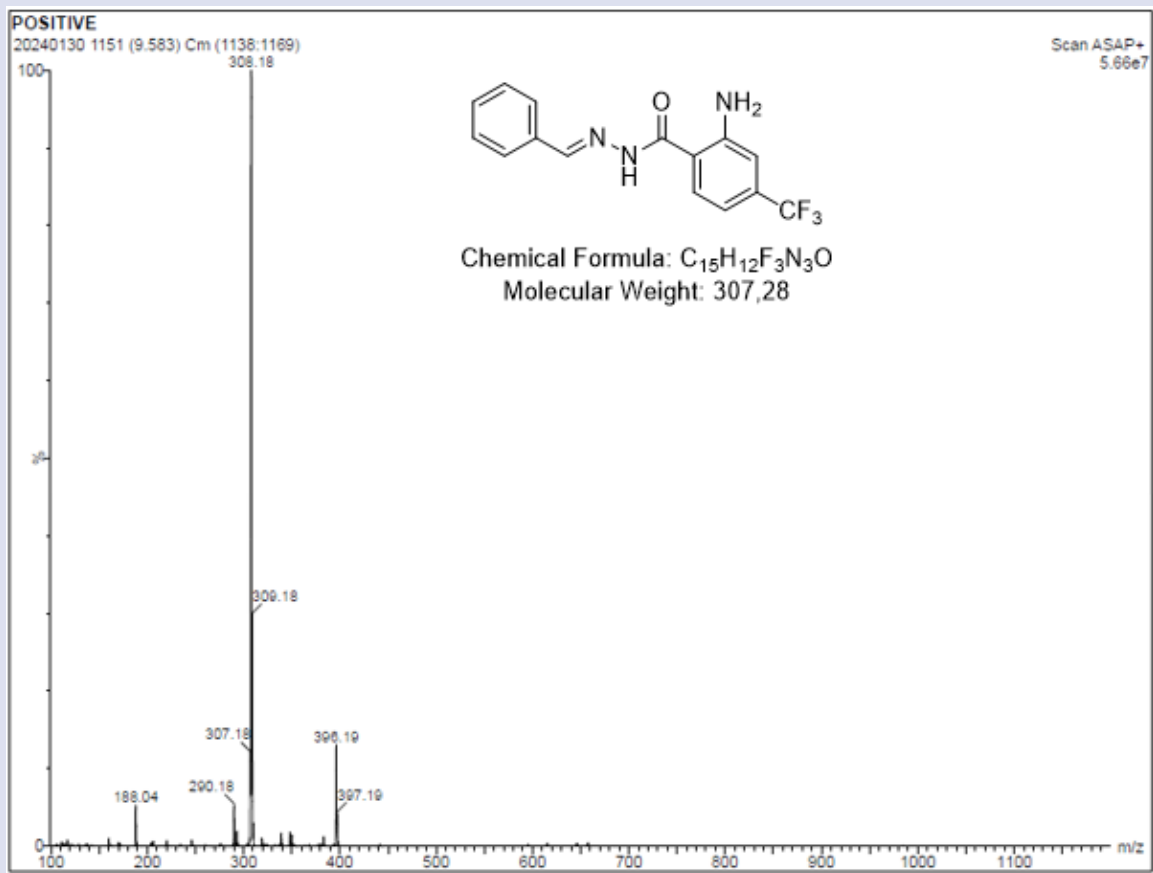Figure 4. ^{13}C-NMR Spectrum of ABTH
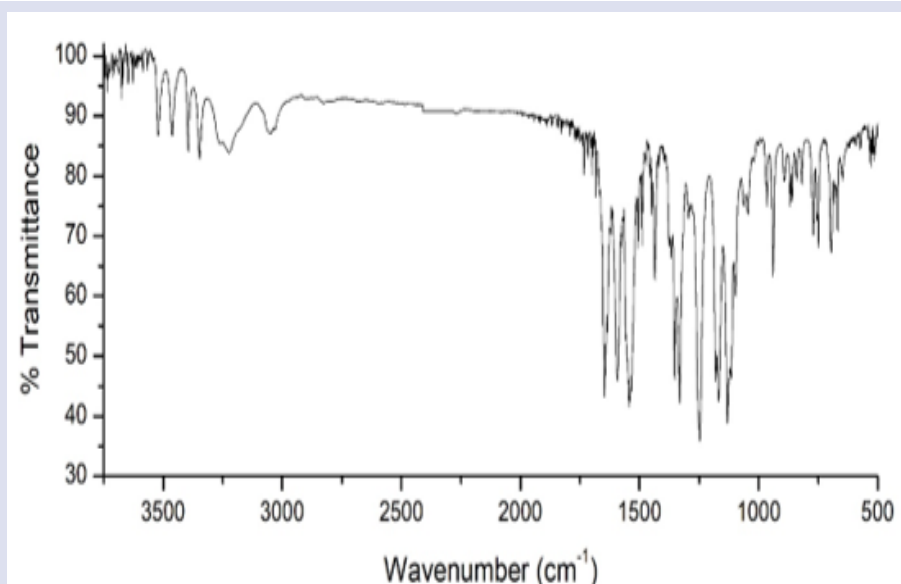

Figure 5. Mass Spectrum of ABTH

Figure 6. FTIR Spectrum of ABTH

In Silico Studies

ADMEt studies

The identification of ADMEt properties of new drug candidates are critical step in the development of any pharmaceutical compounds. Due to several reasons, including their improper pharmacokinetics and drug-likeness, most candidate compounds are eliminated. ADMEt properties of ABTH were depicted in Table 2.

Lipinski's rule of five is important for drug discovery. According to Lipinski's Rules, The drug candidate's molecular weight should be between 150 and 500 g/mol, MLOGP value < 4.15, The number of hydrogen bond acceptor (HBA) atoms < 10, and Number of hydrogen bond donor (HBD) atoms < 5. When ABTH was investigated for all criteria, it was observed that molecular weight of synthesized compound has 307.27 g/mol, MLOGP value has 3.17, HBA atoms have 5, HBD atoms have 2. According to results obtained from calculations, the ABTH compound has been suitable in terms of Lipinski's rule of five. The substance's Topological Polar Surface Area (TPSA) value, which should be less than 140 $Å^2$, is also significant since it determines how well compounds pass through cell membranes [32]. When the TPSA value of ABTH was examined in Table 2, It was lower than 140 $Å^2$ (67.48 $Å^2$). The dispersion of compounds at specified rates between lipids and water is known as lipophilicity. Drug molecules must pass through a number of biological membranes, including as the skin, the gut, and the blood-brain barrier, in order to reach their target areas. Consensus lipophilicity (CLogP$_{o/w}$) value of ABTH was determined to be 3.28.

Water solubility is a crucial property of drug candidates that influences their absorption, distribution, metabolism, and excretion (ADME). Highly soluble drugs dissolve readily in biological fluids, enhancing oral bioavailability and systemic absorption. However, excessively soluble drugs may be rapidly excreted,

reducing their efficacy. Conversely, poorly water-soluble drugs often exhibit limited bioavailability and uneven tissue distribution, necessitating advanced formulation strategies to enhance solubility and absorption. Achieving an optimal balance of water solubility is essential for designing effective and pharmacokinetically favorable drug candidates [33]. When the calculated water solubility value was examined, it was -4.08 (ESOL) corresponding to moderately soluble.

In addition to their pharmacokinetic properties, cytochrome P450 enzyme systems are vital for the metabolism of medications that are ingested. Table 2 analysis revealed that CYP1A2 is likely to inhibit ABTH, whereas CYP2C9, CYP3A4, CYP2C19, and CYP2D6 are not likely to do so. Druglikeness skills were examined in addition to other criteria. Lipinski (Pfizer), Ghose (Amgen), Veber (GSK), Egan (Pharmacia), and Muegge (Bayer) [20] are different rules that are searched by drug companies for drug candidates. The ABTH compound synthesized within the scope of the study met all these rules, as shown in Table 2.

For the LD$_{50}$ values, toxic dosage limits are often expressed as mg/kg body weight. The dosage at which 50% of test subjects pass away after being exposed to a substance is known as the median lethal dose, or LD50. The globally harmonized method of classifying and labeling substances (GHS) establishes toxicological classifications. The classes were arranged from worst to best, from non-toxic to deadly, and from first to sixth. Protox-II web server, a popular tool to calculate toxicity in chemical compounds, was used to determine the toxicity features of ABTH. When Table 2 was examined, LD$_{50}$ (Lethal Dose) value of ABTH was found to be 1440 mg/kg. The toxicity class of ABTH was also determined by using Protox-II web server. It was found to be fourth class, when the toxicity level was from 1st (the worst) to 6th (the best).

Table 2. ADMEt properties of ABTH

Physicochemical Properties		Value	Druglikeness Properties		Value	Compatible
Properties		ABTH	Requirement		ABTH	ABTH
			Lipinski's Rule			
Molecular Formula		$C_{15}H_{12}F_3N_3O$	MW ≤ 500		307.27	
Molecular weight (MW, g/mol)		307.27	M LOGP ≤ 4.15		3.17	Yes
Number of heavy atoms		22	HBA Atoms ≤ 10		5	
Number of aromatic heavy atoms (AHA)		12	HBD Atoms ≤ 5		2	
Number of rotatable bonds (RB)		5	Ghose's Rule			
Number of H-bond acceptors (HBA)		5	160 ≤ MW ≤ 480		307.27	
Number of H-bond donors (HBD)		2	-0.4 ≤ WLOGP ≤ 5.6		4.21	Yes
Molar Refractivity (MR)		77.02	40 ≤ MR ≤ 130		77.02	
TPSA (Å²)		67.48	20 ≤ atoms ≤ 70		34	
Lipophilicity			Veber's Rule			
Log $P_{o/w}$ (iLOGP)		2.16	RB ≤ 10		5	Yes
Log $P_{o/w}$ (XLOGP3)		3.59	TPSA ≤ 140		67.48	
Log $P_{o/w}$ (WLOGP)		4.21	Egan's Rule			
Log $P_{o/w}$ (MLOGP)		3.17	WLOGP ≤ 5.88		4.21	Yes
Consensus Log $P_{o/w}$		3.28	TPSA ≤ 131.6		67.48	
Pharmacokinetics			Muegge's Rule			
GI absorption		High	200 ≤ MW ≤ 600		307.27	
BBB permeant		Yes	-2 ≤ XLOG3 ≤ 5		3.59	
P-gp substrate		No	TPSA ≤ 150		67.48	
CYP1A2 inhibitor		Yes	Number of rings ≤ 7		2	
CYP2C19 inhibitor		No	Number of carbon > 4		15	Yes
CYP2C9 inhibitor		No	Number of heteroatoms > 1		4	
CYP2D6 inhibitor		No	RB ≤ 15		5	
CYP3A4 inhibitor		No	HBA ≤ 10		5	
Log K_p (skin permeation, cm/s)		-5.63	HBD ≤ 5		2	
Water Solubility			Toxicity Properties			
Log S (ESOL)		-4.08	LD$_{50}$ (mg/kg)		1440	
Class		Moderately soluble				
Log S (Ali)		-4.69	Toxicity Class		4	
Class		Moderately soluble				
Log S (SILICOS-IT)		-5.52				
Class		Moderately soluble				

Figure 7. depicts the Boiled-Egg model, with TPSA on the x-axis and WLOGP on the y-axis. The model's yellow region determines whether or not the drug crosses the BBB, while the white region is in charge of gastrointestinal absorption. It was determined by looking at the Boiled-Egg model in Figure 6 that the red dot was in the yellow region and chemical ABTH passed to the BBB.
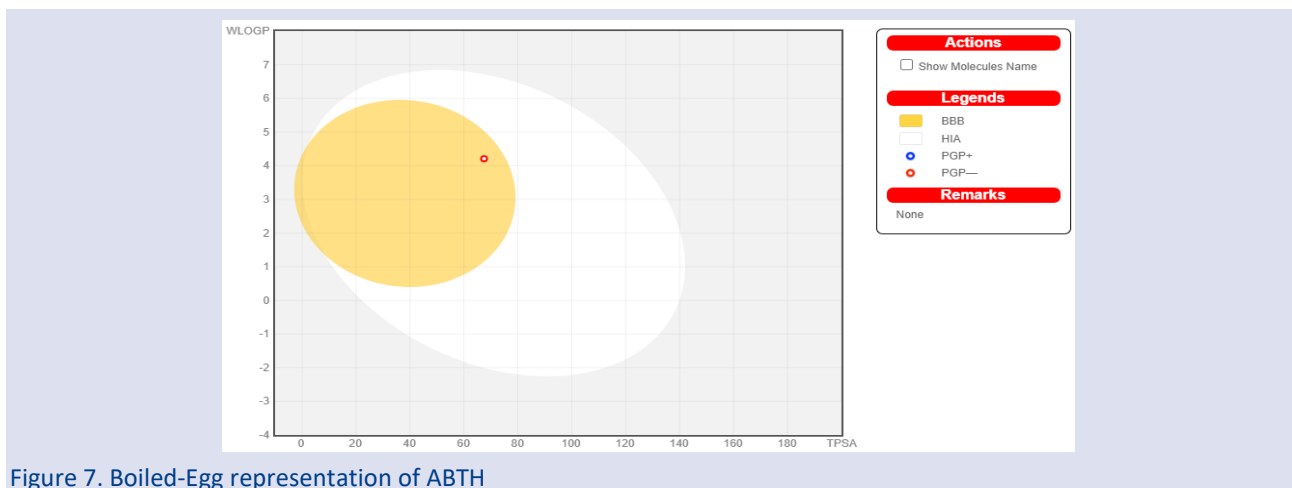

Figure 7. Boiled-Egg representation of ABTH

Molecular Docking Studies

Molecular docking studies was performed using AutoDock Vina 1.1.2 software. AD related proteins [34] were chosen for the molecular docking studies. The primary link between APP and Alzheimer's disease is its involvement in the synthesis of amyloid-beta (Aβ) peptides, which leads to the development of amyloid plaques. The typical symptoms of Alzheimer's disease, including memory loss and cognitive decline, are brought on by these plaques, which impair neuronal function, cause inflammation, and contribute to neurodegeneration. Developing therapies to stop or reduce Alzheimer's disease requires an understanding of APP processing and how it contributes to the illness's progression [35]. Understanding the structure of the ACE protein is essential to comprehending its enzymatic activity, which includes its function in the breakdown of Aβ. Through its impacts on vascular health and amyloid metabolism, ACE may have a doubled influence on Alzheimer's disease. The relationship is complicated, though, and further research is required to determine whether ACE or its inhibitors can be successfully targeted in Alzheimer's treatments [36]. BACE1 is an aspartic acid protease that plays a crucial role in the development of Alzheimer's disease by initiating the production of Aβ peptides. The primary function of the aspartic acid protease BACE1 is in Alzheimer's disease (AD). A crucial stage in the synthesis of Aβ peptides, it is in charge of the first cleavage of the amyloid precursor protein (APP) at the βsite. Alzheimer's disease is characterized by plaques that are formed in the brain by the accumulation of these peptides. The 4DJU structure is crucial in knowing how to block BACE1, an enzyme that is essential to the pathophysiology of Alzheimer's disease. This knowledge provides a basis for creating treatment approaches that target Alzheimer's disease [37, 38]. The 1Q5K structure provides crucial structural information for the creation of more powerful and selective medications by demonstrating precisely how AR-A014418 binds to GSK-3, which is crucial for the development of GSK-3 inhibitors. The development of focused treatments for Alzheimer's disease may benefit from this [39]. The activation of TNFα, a cytokine implicated in neuroinflammation linked to Alzheimer's disease, is significantly influenced by TACE. PDB entry 2OI0, which represents the crystal structure analysis, provides important information for the creation of specific TACE inhibitors, which may be used as therapeutic medicines to modulate neuroinflammation in Alzheimer's disease [40].

In view of given informations above, the specified proteins (PDB ID: 1AAP, 1O86, 4DJU, 1Q5K, 2OI0) were selected for the molecular docking studies. Obtained results of ABTH with the selected proteins were depicted in Table 3. The standard drugs used in treatment of AD were also docked with the same proteins to do meaningful comparison. While the lowest docking score was found to be -6.9 kcal/mol between 1AAP and ABTH complex, the highest one -8.9 kcal/mol between 2OI0 and ABTH. The all protein-ABTH complexes showed higher docking scores than all protein-standard drugs.

Table 3. Molecular Docking scores of ABTH and Standard drugs with the selected proteins

	Docking Scores (kcal/mol)			
PDB ID	ABTH	Donepezil*	Galantamine*	Rivastigmine*
1AAP	-6.9	-7.9	-6.8	-6.0
1O86	-8.5	-8.9	-8.1	-6.5
4DJU	-8.6	-6.9	-7.8	-6.6
1Q5K	-8.8	-8.4	-8.6	-6.5
2OI0	-8.9	-7.9	-7.3	-7.4

* Standard drugs

The 2OI0-ABTH complex, which has the highest score among all of protein-ligand complexes, were selected to investigate binding properties. The 2D figure, which contains binding properties bond types, and bond lengths, was demonstrated in Figure 8 and 3D figures in Table 4. When the 2D representation of 2OI0-ABTH complex was examined, it was observed that the complex has hydrogen bonds, hydrogen-carbon bonds, halogen, π-cation, π-donor hydrogen bond, π-π stacked, alkyl, and π-alkyl pairs. Among the protein-ligand interactions, hydrogen bonding is the most important one for the stability of the complex. When the 2D figure was examined, there were 3 hydrogen bonds 2OI0-ABTH complex. These bonds have a length of 2.51 Å between GLU406 aminoacid of protein and proton of amine group, 2.64 Å between HIS405 aminoacid and oxygen of carbonyl group, and 2.93 Å between HIS415 aminoacid and oxygen of carbonyl group. Halogen interactions were also observed in 2OI0-ABTH complex. These bonds were between ABTH and LEU401, VAL434 aminoacids with the 3.12, 3.39, 3.44 Å, respectively.
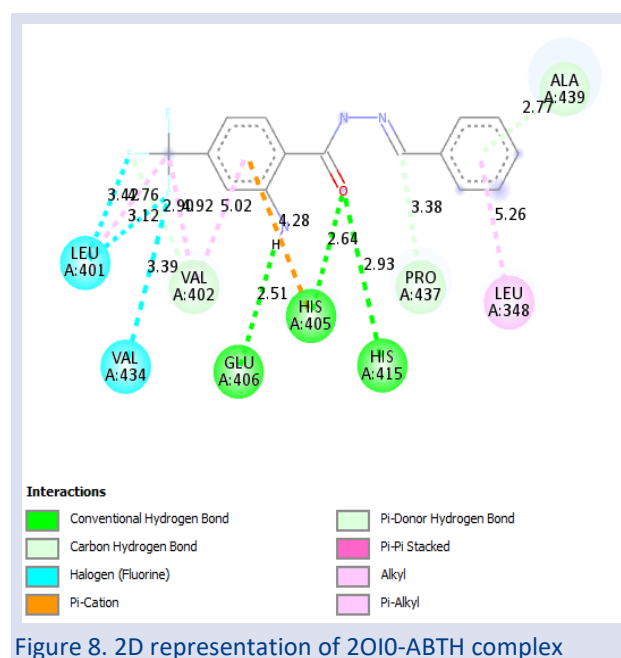
Figure 8. 2D representation of 2OI0-ABTH complex

Table 4. 3D interactions and hydrophobicity surfaces of 2OI0-ABTH complex

a) Zoom out interaction	b) Zoom in interaction
c) Zoom out hydrophobicity	d) Zoom in hydrophobicity
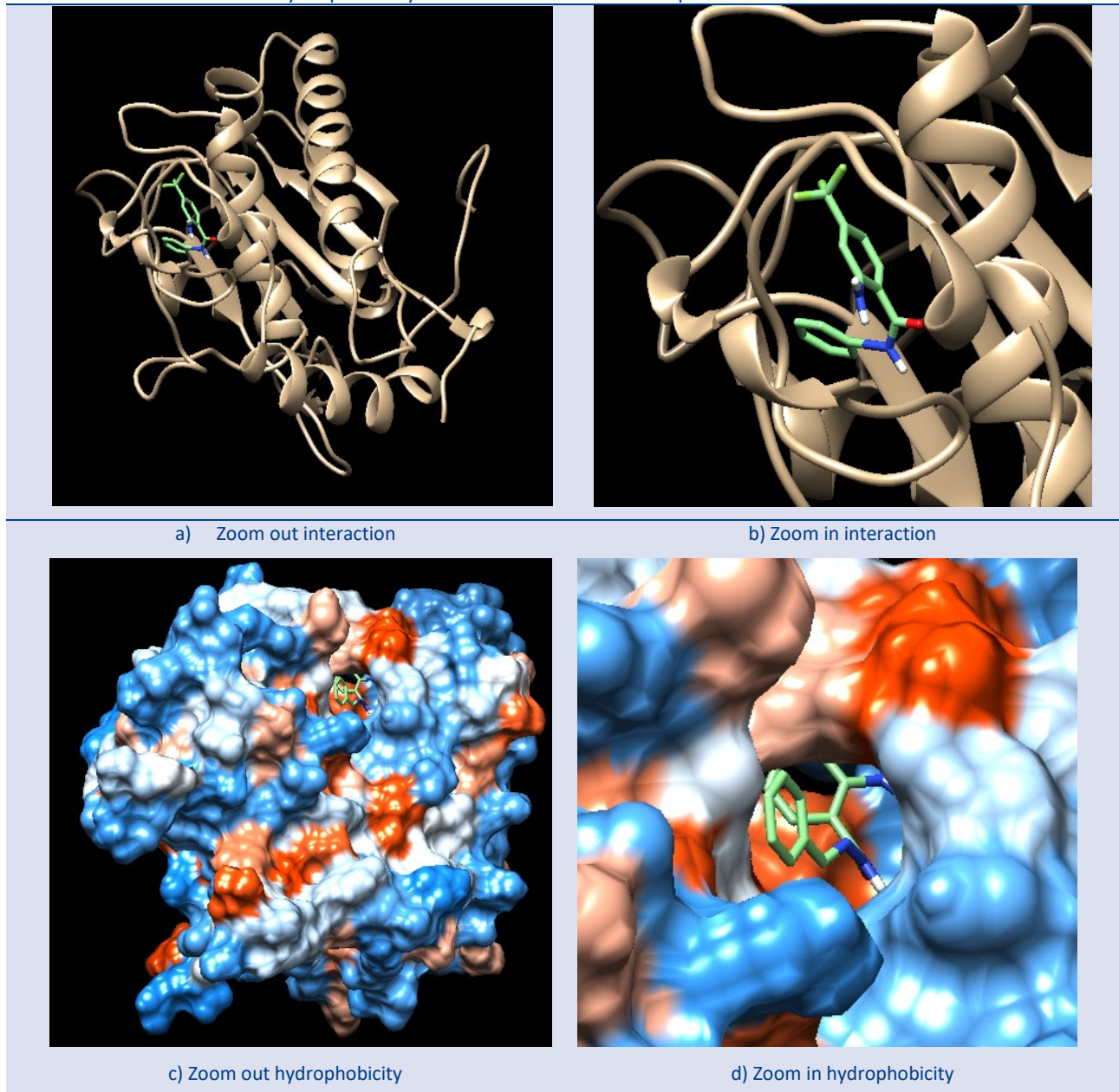
MD Simulation Studies

Stability of the 2OI0-ABTH system was investigated utilizing MD simulation via playmolecule web server during 12 ns. For the MD simulation investigation, the RMSD (Root Mean Square Deviations) of the ligand and system's sidechain/backbone values were determined. The RMSD graph was depicted in Figure 9. For the backbone/sidechain value, the mean RMSD was 2.5 Å, whereas for the ABTH ligand, it was 1.5 Å. During the 12 ns MD simulation, the backbone/sidechain's RMSD graph remained unchanged. For the complex to be stable, the RMSD value needs to be less than 3 Å. The 2OI0-ABTH complex's stability was confirmed by the RMSD values that were acquired from the MD simulation.
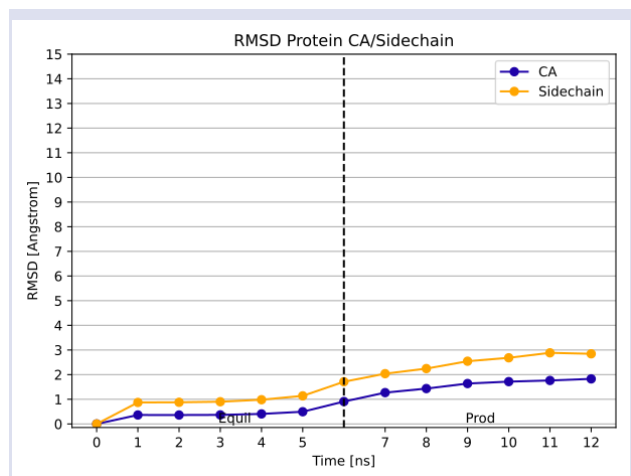
Figure 9. RMSD value of backbone and sidechain for the system during MD simulation

In molecular dynamics simulations, the term "RMSF" (Root Mean Square Fluctuation) describes how much individual atoms or groups of atoms move or fluctuate about their average position during the simulation. To calculate RMSF, the difference between each atom's average location and its positions at each time step is taken and its root mean squared. The stability or flexibility of different molecular constituents can be better understood by knowing how to analyze RMSF. Higher mobility or flexibility is correlated with lower RMSF values, which are correlated with greater stiffness or stability. RMSF values of 2OI0 were shown in Figure 10. Based on the calculated RMSF values, the residue index positions 150-160 had the biggest protein fluctuations during the simulation. In order to ensure the stability of the complex, the RMSF value must also be less than 3 Å. The 2OI0-ABTH complex's stability was further supported by the observation that, aside from these amino acids, the protein in the complex's structure changed very little. The complex's stability was also confirmed by the RMSF value, which was less than 3 (Figure 10).

Figure 10. RMSF graph of protein (2OI0) during MD simulation

Conclusion

In this work, we synthesized a new compound as abbreviated ABTH, starting with carboxylic acid containing -CF$_3$ and -NO$_2$ groups. Its structure was characterized by sp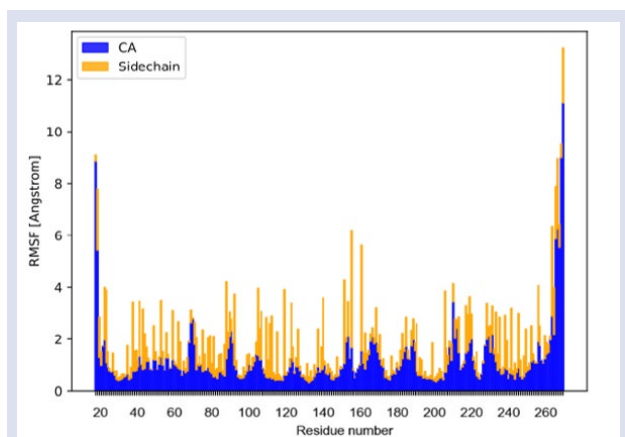ectroscopic methods such as NMR, FTIR, and Mass. ADMEt properties were investigated. From the results ABTH has all criteria in terms of druglikeness and crossed the BBB in terms of pharmacokinetic properties. Crossing the BBB is important to be potential drugs for treatment of AD. Target proteins associated with AD were chosen, and Molecular Docking studies were carried out by using these proteins. The highest docking score was -8.9 kcal/mol formed complex between 2OI0 protein and ABTH ligand. Standard drugs were also used in the molecular docking studies to compare whether ABTH has highest score or not. It was concluded that ABTH has higher docking score than standards. As the 2OI0-ABTH complex has the highest docking score, Additionally, a study using MD simulation was conducted to bolster the stability of the 2OI0-ABTH complex. The complex demonstrated to be stable during the 12 ns simulation, according to the MD simulation results. It can be concluded from all of the results that our synthesized ABTH is an effective candidate for AD, after deeply research have been performed.

Conflicts of interest

There are no conflicts of interest in this work.

Acknowledgment

References

[1] Lu D., Sun Y., Luan Y., He W., Rational design of siRNA-based delivery systems for effective treatment of brain diseases, *Pharmaceutical Science Advances*, (2) (2024) 100041.

[2] Harder B.G., Blomquist M.R., Wang J., Kim A.J., Woodworth G.F., Winkles J.A., Loftus J.C., Tran N.L., Developments in Blood-Brain Barrier Penetrance and Drug Repurposing for Improved Treatment of Glioblastoma, *Frontiers in Oncology*, (8) (2018) 462.

[3] Burns A., Robert P., The National Dementia strategy in England, *BMJ*, (338) (2009) b931–b931.

[4] Brookmeyer R., Johnson E., Ziegler-Graham K., Arrighi H.M., Forecasting the global burden of Alzheimer's disease, *Alzheimer's & Dementia*, (3) (2007) 186–191.

[5] Hashimoto M., Rockenstein E., Crews L., Masliah E., Role of Protein Aggregation in Mitochondrial Dysfunction and Neurodegeneration in Alzheimer's and Parkinson's Diseases, *NeuroMolecular Medicine*, (4) (2003) 21–36.

[6] Hagmann W.K., The Many Roles for Fluorine in Medicinal Chemistry, *Journal of Medicinal Chemistry*, (51) (2008) 4359–4369.

[7] Nair A.S., Singh A.K., Kumar A., Kumar S., Sukumaran S., Koyiparambath V.P., Pappachen .LK., Rangarajan T.M., Kim H., Mathew B., FDA-Approved Trifluoromethyl Group-Containing Drugs: A Review of 20 Years, *Processes*, (10) (2022) 2054.

[8] Tatum L.A., Su X., Aprahamian I., Simple Hydrazone Building Blocks for Complicated Functional Materials, *Accounts of Chemical Research*, (47) (2014) 2141–2149.

[9] Verma G., Marella A., Shaquiquzzaman M., Akhtar M., Ali M., Alam M., A review exploring biological activities of hydrazones, *Journal of Pharmacy and Bioallied Sciences*, (6) (2014) 69.

[10] Rollas S., Küçükgüzel S., Biological Activities of Hydrazone Derivatives, *Molecules*, (12) (2007) 1910–1939.

[11] AlFadly E.D., Elzahhar P.A., Tramarin A., Elkazaz S., Shaltout H., Abu-Serie M.M., Janockova J., Soukup O., Ghareeb D.A., El-Yazbi A.F., Rafeh R.W., Bakkar N.M.Z., Kobeissy F., Iriepa I., Moraleda I., Saudi M.N.S., Bartolini M., Belal A.S.F., Tackling neuroinflammation and cholinergic deficit in Alzheimer's disease: Multi-target inhibitors of cholinesterases, cyclooxygenase-2 and 15-lipoxygenase, *European Journal of Medicinal Chemistry*, (167) (2019) 161–186.

[12] DiMasi J.A., Grabowski H.G., Hansen R.W., Innovation in the pharmaceutical industry: New estimates of R&D costs, *Journal of Health Economics*, (47) (2016) 20–33.

[13] Zhong F., Xing J., Li X., Liu X., Fu Z., Xiong Z., Lu D., Wu X., Zhao J., Tan X., Li F., Luo X., Li Z., Chen K., Zheng M., Jiang H., Artificial intelligence in drug design, *Science China Life Sciences*, (61) (2018) 1191–1204.

[14] Cui W., Aouidate A., Wang S., Yu Q., Li Y., Yuan S., Discovering Anti-Cancer Drugs via Computational Methods, *Frontiers in Pharmacology*, (11) (2020) 733.

[15] Ramírez D., Computational Methods Applied to Rational Drug Design, *The Open Medicinal Chemistry Journal*, (10) (2016) 7–20.

[16] De Vries H.E., Kuiper J., de Boer A.G., Van Berkel T.J., Breimer D.D., The blood-brain barrier in neuroinflammatory diseases. *Pharmacological Reviews*, (49) (1997) 143–155.

[17] Narayanan R., Gunturi S.B., In silico ADME modelling: prediction models for blood–brain barrier permeation using a systematic variable selection method, *Bioorganic & Medicinal Chemistry*, (13) (2005) 3017–3028.

[18] Karabacak Atay Ç., Dilek Ö., Tilki T., Dede B., A novel imidazole-based azo molecule: synthesis, characterization, quantum chemical calculations, molecular docking, molecular dynamics simulations and ADMET properties, *Journal of Molecular Modeling*, (29) (2023) 226.

[19] Karplus M., McCammon J.A., Molecular dynamics simulations of biomolecules, *Nature Structural & Molecular Biology*, (9) (2002) 646–652.

[20] Daina A., Michielin O., Zoete V., SwissADME: a free web tool to evaluate pharmacokinetics, drug-likeness and medicinal chemistry friendliness of small molecules, *Scientific Reports*, (7) (2017) 42717.

[21] Banerjee P., Eckert A.O., Schrey A.K., Preissner R., ProTox-II: a webserver for the prediction of toxicity of chemicals, *Nucleic Acids Research*, (46) (2018) W257–W263.

[22] Hanwell M.D., Curtis D.E., Lonie, Vandermeersch T., Zurek E., Hutchison G.R., Avogadro: an advanced semantic chemical editor, visualization, and analysis platform, *Journal of Cheminformatics*, (4) (2012) 17.

[23] Trott O., Olson A.J., AutoDock Vina: Improving the speed and accuracy of docking with a new scoring function, efficient optimization, and multithreading, *Journal of Computational Chemistry*, (31) (2010) 455–461.

[24] Pettersen E.F., Goddard T.D., Huang C.C., Couch G.S., Greenblatt D.M., Meng E.C., Ferrin T.E., UCSF Chimera--A visualization system for exploratory research and analysis, *Journal of Computational Chemistry*, (25) (2004) 1605–1612.

[25] BIOVIA, 2021 Discovery Studio Visualizer, version 21.1.0.20298. Dassault Systèmes, San Diego, CA.

[26] Berman H.M., The Protein Data Bank, *Nucleic Acids Research*, (28) (2000) 235–242.

[27] Webb B., Sali A., Comparative Protein Structure Modeling Using MODELLER, *Current Protocols in Bioinformatics*, (54) (2016) 5.6.1-5.6.37.

[28] Jiménez J., Doerr S., Martínez-Rosell G., Rose A.S., De Fabriiis G., DeepSite: protein-binding site predictor using 3D-convolutional neural networks, *Bioinformatics*, (33) (2017) 3036–3042.

[29] Martínez-Rosell G., Giorgino T., De Fabritiis G., PlayMolecule ProteinPrepare: A Web Application for Protein Preparation for Molecular Dynamics Simulations, *Journal of Chemical Information and Modeling*, (57) (2017) 1511–1516.

[30] Galvelis R., Doerr S., Damas J.M., Harvey M.J., De Fabritiis G., A Scalable Molecular Force Field Parameterization Method Based on Density Functional Theory and Quantum-Level Machine Learning, *Journal of Chemical Information and Modeling*, (59) (2019) 3485–3493.

[31] Doerr S., Harvey M.J., Noé F., De Fabritiis G., HTMD: High-Throughput Molecular Dynamics for Molecular Discovery, *Journal of Chemical Theory and Computation*, (12) (2016) 1845–1852.

[32] Veber D.F., Johnson S.R., Cheng H.Y., Smith B.R., Ward K.W., Kopple K.D., Molecular Properties That Influence the Oral Bioavailability of Drug Candidates, *Journal of Medicinal Chemistry*, (45) (2002) 2615–2623.

[33] Savjani K.T., Gajjar A.K., Savjani J.K., Drug Solubility: Importance and Enhancement Techniques, *International Scholarly Research Notices Pharmaceutics*, (2012) (2012) 1–10.

[34] Gnanaraj C., Sekar M., Fuloria S., Swain S.S., Gan S.H., Chidambaram K., Rani N.N.I.M., Balan T., Stephenie S., Lum P.T., Jeyabalan S., Begum M.Y., Chandramohan V., Thangavelu L., Subramaniyan V., Fuloria N.K, In Silico Molecular Docking Analysis of Karanjin against Alzheimer's and Parkinson's Diseases as a Potential Natural Lead Molecule for New Drug Design, Development and Therapy, *Molecules*, (27) (2022) 2834.

[35] Hardy J., Selkoe D.J., The Amyloid Hypothesis of Alzheimer's Disease: Progress and Problems on the Road to Therapeutics, *Science*, (297) (2002) 353–356.

[36] Qıu W., Folsteın M., Insulin, insulin-degrading enzyme and amyloid-β peptide in Alzheimer's disease: review and hypothesis, *Neurobiology of Aging,* (27) (2006) 190–198.

[37] Vassar R., Bennett B.D., Babu-Khan S., Kahn S., Mendiaz E.A., Denis P., Teplow D.B., Ross S., Amarante P., Loeloff R., Luo Y., Fisher S., Fuller J., Edenson S., Lile J., Jarosinski M.A., Biere A.L., Curran E., Burgess T., Louis J.-C., Collins F., Treanor J., Rogers G., Citron M., β-Secretase Cleavage of Alzheimer's Amyloid Precursor Protein by the Transmembrane Aspartic Protease BACE, *Science,* (286) (1999) 735–741.

[38] Ghosh A.K., Cárdenas E.L., Osswald H.L., The Design, Development, and Evaluation of BACE1 Inhibitors for the Treatment of Alzheimer's Disease, *Alzheimer's Disease II*, (2016) 27–85.

[39] Kremer A., GSK3 and Alzheimer's disease: facts and fiction…, *Frontiers in Molecular Neuroscience*, (4) (2011) 17.

[40] Plantone D., Pardini M., Righi D., Manco C., Colombo B.M., N. De Stefano, The Role of TNF-α in Alzheimer's Disease: A Narrative Review, *Cells,* 13 (2023) 54.

Cumhuriyet Science Journal

Isolation of Traditional Yogurt Yeast *Kluyveromyces marxianus* and Investigation of Major Probiotic Properties

Serap Çetinkaya [1,a,*]

[1] Department of Molecular Biology and Genetics, Faculty of Science, Sivas Cumhuriyet University, Sivas, Türkiye
*Corresponding author

Research Article

ABSTRACT

The aim of this study was to evaluate the probiotic potential of *Kluyveromyces marxianus* K3 yeast strain isolated from cow yogurt. *Kluyveromyces marxianus* yeast strain was isolated from yogurt and identified based on ITS sequences. The isolated strain showed high tolerance to low pH conditions. This feature can be associated with the ability of the strain to survive in acidic environments such as stomach acid. In addition, the strain showed tolerance to simulated human gastric and intestinal fluids, indicating that it can move healthily in the digestive system. It was determined that the isolate was resistant to antibiotics, indicating its potential to help protect the intestinal flora. It was determined that the strain grew well at human body temperature, exhibited hydrophobic properties and had deconjugation ability against bile salts. The research findings indicate that *Kluyveromyces marxianus* strain obtained from yogurt has the potential to be used as a probiotic in different food products. This species is an important candidate that can be included in food supplements or new probiotic formulations. In conclusion, this study reveals that yogurt is a rich source of probiotic yeast species and *Kluyveromyces marxianus* K3 strain may play an important role in this field.

Keywords: Immunity, Isolation, Yeast, Probiotic, Yoghurt.

a✉ serapcetinkaya2012@gmail.com https://orcid.org/0000-0001-7372-1704

Introduction

The term probiotic is derived from the Greek word "pro bios" meaning "for life" [1]. Probiotics are defined as live microorganisms that are generally found in the intestines and benefit the host organism. These microorganisms can aid nutrient absorption and support the immune system by balancing the digestive system [2]. Additionally, they can have positive effects on health by preventing the establishment of pathogenic microorganisms. In recent years, beneficial fungal communities among probiotics have also attracted attention and new products are being developed in this field [3].

Probiotic mushrooms have attracted the attention of researchers and industries. Yeasts are widely found in various ecological niches, plants, water, airborne particles, and traditional fermented and unfermented food products [4, 5]. These creatures are also important as normal components of the gastrointestinal flora. Yeasts play important roles in food processing and fermentation technologies. In these processes, they contribute to increasing and preserving the flavor and nutritional value of foods. Since ancient times, various fungal communities have provided various benefits to human societies. It has had impacts on food processing, medical practices, and even ecological balance. Nowadays, probiotic mushrooms are the subject of intensive research and development studies, especially due to their health benefits [6, 7].

The unique cell architecture of fungi may make them a better class of probiotics than commercially available probiotic bacteria. In particular, the cell membrane of yeasts consists of two layers: an outer layer made of mannan (phosphopetidomannan or phospholipomannan) and an inner layer containing chitin and 1,3- and 1,6-β-glucan [8, 9]. This structure ensures safe passage through the gastrointestinal environment, which is an important factor in ensuring the probiotic effect. Additionally, many fungal species can grow optimally at different temperatures, indicating their ability to adapt to various environmental conditions. The antagonistic properties of fungi are also notable; Thanks to these properties, they can prevent the growth of pathogenic bacteria in the intestine. Therefore, the use of mushrooms as probiotics has the potential to provide positive effects on digestive health and the overall immune system.

Members of a group of fungal genera are novel probiotics: *Candida humilis*, *Debaryomyces hansenii*, *Debaryomyces occidentalis*, *Kluyveromyces lactis*, *Kluyveromyces lodderae*, *Kluyveromyces marxiamus*, *Saccharomyces cerevisiae var. boulardii*, *Pichia kluyveri*, *Issatchenkia orientalis*, *Pichia kudriavzevii*, *Candida tropicalis*, *Meyerozyma caribbica*, *Candida saitoana*, *Candida pintolopesii*, *Cryptococcus albidus* and *Torulaspora delbrueckii* [10, 11]. The best studied yeast is *Saccharomyces boulardii*.

Current reports suggest that the use of yeast strains alone or in combination with other probiotics has digestive health-promoting effects. These effects can occur by increasing good bacterial populations and at the

same time reducing pathogenic microorganisms through competition for space and food [12, 13]. This may play an important role in maintaining and improving gastrointestinal function. Various findings indicate that fungal-based probiotics affect the host organism in various aspects. These effects may include positive effects such as supporting digestive system health, strengthening the immune system and maintaining metabolic balance. In addition, the potential benefits of yeast strains can be better understood with more research and their use in probiotic therapeutic applications may increase.

The antimicrobial activity of probiotic yeasts plays an important protective role in the gastrointestinal tract. This activity ensures the integrity of the intestinal barrier by helping to maintain tight junctions between epithelial cells, particularly through E-cadherin recycling. In this way, it can contribute to reducing the population of pathogenic bacteria and potentially preventing intestinal infections [14, 15]. In addition, probiotic yeasts can also affect the intestinal microflora balance thanks to their metabolic activities. In particular, by increasing the synthesis of metabolites such as short-chain fatty acids, they can promote the production of compounds such as butyrate, which are important for intestinal health [16, 17]. These fatty acids are used as an energy source for intestinal cells and also have inflammation-reducing effects. These mechanisms of probiotic yeasts offer a potentially effective strategy to maintain and support digestive health. Therefore, the use of these yeast strains is increasingly being investigated in the treatment and prevention of gastrointestinal diseases.

The aim of the study is to identify the yeasts found in cow yoghurt, one of the traditional fermentation products, at the species level, to determine their biotechnological properties and to determine the probiotic properties of these organisms so that they can be used in industrial-scale fermentation processes.

Materials and Methods

Isolation of Yeast Isolates

Yeast was isolated from a traditional yoghurt sample (Budaklı, Sivas, Türkiye). Serial dilutions were made from homemade yoghurt and incubated on YEPD agar (20 g/L peptone, 20g/L glucose, 10g/L yeast extract, pH 6.3) at 25 °C for 3-5 days. Colonies exhibiting different morphologies were inoculated onto YEPD agar plates. Colonies were purified by the smear method on clean agar plates and gram staining was used for morphological identification under a light microscope. Purified isolates were then stored in 20% glycerol at – 80°C [18].

Molecular Identification of the *Kluyveromyces marxianus*

Genomic DNA was extracted [(EurX GeneMATRIX Plant & Fungi DNA isolation kit (Poland)] (https://eurx.com.pl/docs/manuals/en/e3595.pdf). The DNA was quantified (Thermo Scientific Nanodrop 2000,

USA). Internally transcribed spacer (ITS) DNA was copied using ITS1 and ITS4 oligomers (5' TCCGTAGGTGAACCTGCGG 3' and 5' TCCTCCGCTTATTGATATGC 3', respectively, and 0.3µM each). Amplification of DNA (35µL, final volume) was started with a denaturation step (5 min, 95°C), and continued with 40 recycles of extension (denaturation, 45s, 95°C; annealing, 45s, 57°C; extension, 60s, 72°C; and an extension step, 5min, 72°C) (Kyratec, Australia), using DNA Polymerase, 2u, (Solis Biodyne FIREPol Estonia) in the presence of 1.5mM MgCl$_2$, and 0.2µM dNTPs. Amplification product was resolved (1.5% agarose gel). The band of interest was cut out and eluted (HighPrep™ PCR Clean-up System, MAGBIO, AC-60005, MD, USA). Nucleotide data generated by Sanger method (ABI 3730XL, Applied Biosystems, Foster City, CA, USA), showed 99.73% with *Kluyveromyces marxianus* (BLAST, ncbi.nlm.nih.gov). The nucleotide sequence information was deposited in GenBank (Accession No.: PP998224) and a dendrogram was produced for it (Figure 1).

Potential Probiotic Experiments
Growth at human body temperature

Yeast isolates were placed in 10 ml tubes in K3 YEPD broth pH 6.3 at 25℃, inoculated from stock strains and incubated for 24 hours. 100 µl samples were taken from activated liquid cultures, streaked onto solid media and incubated for 10 days [19].

Tolerance to low pH conditions

The active culture was inoculated into YEPD broth medium (pH 2.0, 3.0, 4.0 and 6.3) and incubated at 37℃ for 3 hours. After incubation, 100 µl sample was taken from the active culture and planted on YEPD agar medium using the pour-plate method. It was incubated for 24 hours [20].

Tolerance to simulated human gastric juice

10 ml of active culture, incubated for 24 hours, was centrifuged at 2500 g for 10 minutes. Supernatant was removed. Cells were suspended in 1 ml of 0.85% sterile saline solution. 1 ml pepsin solution (pH 3) was added and incubated at 37℃ for 3 hours. 50 µl of the prepared cell pepsin solution mixture was streaked onto YEPD agar medium. Cell mixture without pepsin was used as a control. It was incubated for 24 hours [19]. Tolerance was evaluated by the cast plate method.

Tolerance to simulated human ıntestinal juice

Trypsin (1 g/L) solution was prepared in PBS (pH 8). 9 ml of the prepared trypsin solution was taken into tubes and 1 ml of active culture was added. Line seeding was done on 100 µl YEPD agar plates. It was incubated at 37℃ for 24 hours. As a control, pure cells were seeded in their own medium. It was checked for 24 hours [21].

Hydrophobicity

10 ml of activated yeast cultures were centrifuged at 5000 g for 5 minutes for 24 hours. The cell pellet was washed with Ringer's solution (6% NaCl, 0.0075% KCl, 0.01% CaCl$_2$, 0.01% Na$_2$CO$_3$). It was resuspended by adding 10 ml of Ringer's solution. 4 ml of sample was separated and optical density was measured using a 600 nm

spectrophotometer. The remaining 6 ml sample was divided into three equal volumes. The same volume (2 ml) of n-hexadecane, n-hexane, xlenes was added and mixed. Phase separation was allowed to occur by vortexing for 2 minutes. At the end of 30 minutes, the upper phase was removed and the aqueous phase optical density of the solution was measured using a spectrophotometer at 600 nm. Percent hydrophobicity was calculated as the decrease in OD_{600nm} using the following formula:

$$\% \text{ hidrofobisite} = \frac{OD0 - OD}{OD} \times 100$$

Here, OD_0 and OD are OD_{600nm} before and after extraction with n-hexadecane, n-hexane, xylenes, respectively [21].

Auto-aggregation

The culture was activated for 24 hours and mixed by vortex for 15 seconds. The optical density of the cells was measured using a spectrophotometer at 660 nm. It was incubated at 37℃ for 4 hours. 10 ml of active culture was centrifuged at 5000 g for 15 minutes. Cells were suspended in 1 ml of PBS (pH 7.4). 400 µl of the sample was taken and inoculated into 20 ml of medium. It was incubated at 37℃ for 24 hours. The optical density of the cells was measured every hour using a spectrophotometer at 660 nm.

$$\% \text{ Otoagregasyon} = \left[1 - \left(\frac{ODt}{D0} \right) \right] \times 100$$

Here OD is OD_{600} nm before incubation and OD_t is OD_{600nm} after incubation [19].

Antibiotic resistance screening

A smear of active culture (100 µl) was inoculated onto YEPD agar plates. Antibiotic discs were placed on the plates using sterile forceps. It was incubated at 37℃ for 48 hours. Inhibition zones were determined [22].

Bile salt deconjugation test

The ability of the strains to deconjugate bile salts was examined [23]. YEPD agar medium was prepared with 0.5% sodium salts (sodiumglycocholate hydrate, sodium taurodeoxycholate, sodium taurocholic acid). The cells were dipped onto agar plates and incubated for 24 hours at 37℃ [21]. Tolerance is indicated by the presence of precipitated bile acids (white opaque halo) around the colonies.

Results and Discussion

Isolation and Identification of Yeast Isolates

Morphological characterization of the yeast strain isolated from cow yoghurt was performed. The obtained sequences were scanned in the GenBank database and a new analysis data was created, including the closest species at the subfamily and genus level. Using this data, phylogenetic trees were constructed using maximum likelihood (ML) and neighbor joining (NJ) methods. On NJ trees, red numbers indicate branch lengths and black numbers indicate bootstrap support values. The resulting DNA sequence reads were used to create a phylogenetic tree. Sequences containing the ITS1 and ITS2 rRNA gene regions, created using forward and reverse raw chromatogram data, are used as DNA barcoding tools for yeasts. The ITS region provides sufficient data for the identification of the fungal sample. Sample K3 was identified and identified by DNA sequence as *Kluyveromyces marxianus* (Figure 1).
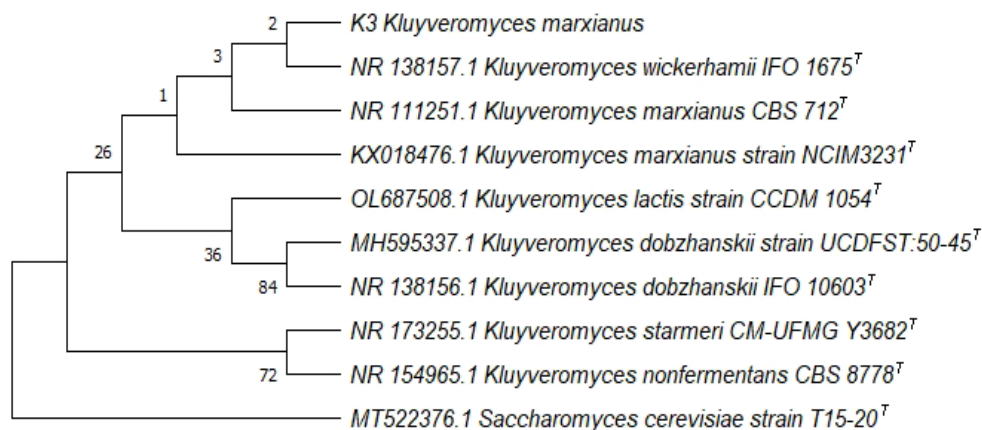
Figure 1. Dendrogram of *Kluyveromyces marxianus* including K3 isolate

Growth at Human Body Temperature

Isolate K3 was successfully grown on YEPD agar (Table 1). A single colony was obtained for each isolated strain. The yeast isolate grew successfully at 37°C. Its growth at human body temperature is important for yeasts to be

evaluated as a potential probiotic. Strains were identified as yeast using macroscopic analysis based on morphological features. The *Kluyveromyces marxianus* isolate was observed to be smooth and white. It has been reported in the literature as smooth in strains isolated from kefir [18].

Table 1. Morphological and numerical characterization of yeast isolate K3

Yeast isolate	K3
Colony morphologies	Smooth-white
Cell morphologies	Global budding
Number of cells (Log 10 cfu/ml)	5.55

Table 2. Degradation capacity for sodium salts

Sodium salts	Isolate K3
Sodium glycocholate hydrate	+
Sodium taurodeoxycholate	+
Sodium taurocholic acid	+

Low PH Tolerance and Bile Salt Resistance

Tolerance to low pH is one of the main selection criteria [24,25]. Because in order for probiotics to reach the small intestine, the stomach must have stressful conditions [26]. It was determined that *Kluyveromyces marxianus* K3 isolate could tolerate low pH values.

Microorganisms considered probiotics must have the ability to survive and grow under stressful conditions. In particular, the ability for bile salt hydrolysis is one of the desirable properties of a probiotic strain. This feature plays an important role in removing cholesterol from the human body [27]. Certain species of the native microflora of the human intestine develop deconjugated bile salts (amino acid residues of bile salts conjugated with glycine or taurine). This process depends on the presence of an enzyme called bile salt hydrolase (BSH). BSH activity occurs by hydrolyzing amino acid residues of bile salts and bile acid.

To detect the presence of BSH activity, YEPD agar plates containing 0.5% sodiumglycocholate hydrate, sodium taurodeoxycholate, and sodium taurocholic acid were used. 10-µl aliquots from overnight incubated cultures were spotted onto the plates. Strains that formed precipitation zones or opaque, granular white colonies were considered BSH positive. This method is a widely used technique to evaluate the bile salt hydrolysis ability of potential probiotic strains. BSH positive strains may have the potential to have positive effects on human health by hydrolyzing bile salts (Table 2).

Tolerance to Simulated Human Gastric Juice

The isolated K3 isolate was exposed to pepsin for 3 hours and survival capacities were obtained by counting live cells (Table 3). In this study, it is stated that strain K3 was incubated in pepsin-PBS medium (pH 3.0) for 3 hours and the results showed that this medium did not completely inhibit the growth of isolate K3. Pepsin is a digestive enzyme active in low pH environments and is one of the main components of gastric juice. Therefore, the use of pepsin-PBS solution is intended to simulate the effect of gastric juice. However, according to the results of the study, the isolated K3 strain was able to maintain its ability to grow even in this low pH environment [19]. Probiotic microorganisms are generally consumed in the presence of nutrients such as milk protein and can exert protective effects depending on the initiators (prebiotics) to survive in the acidic environment of the digestive system. Thanks to these properties, probiotics can contribute to the healthy function of the digestive system. In conclusion, the ability of strain K3 to grow after 3 hours of incubation in pepsin-PBS solution (pH 3.0) suggests that this strain may potentially have the ability to survive even in challenging environments such as stomach acid. Such studies may help us understand the health benefits of probiotic microorganisms.

Tolerance to Simulated Human Intestinal Environment

High survival rates of yeast isolates were determined under simulated human intestinal environment conditions (Table 3). The K3 isolate exhibited a resistant profile and was determined to maintain its viability for 24 hours. Under these conditions, survival time of more than 24 hours is a very important criterion for probiotic selection.

Table 3. Probiotic properties of yeast isolate K3

Yeast Isolate	First log10 (cfu/ml)	GIT growth (log10 cfu/ml)	Growth at 37°C	Hydrophobicity %	Aggregation %	SIT growth
K3	5.55	8.1	++++++	n-hexadecane 2,39 n-hexane 10,19 xlenes 13,58	39.3	2.25

Hydrophobicity

Yogurt yeast isolates were analyzed for hydrophobicity (Table 3). Hydrophobicity can be defined as a nonspecific interaction between microbial and host cells. This interaction is mediated by cell surface proteins and lipoteichoic acids. In this study, K3 showed significantly higher hydrophobicity and was therefore capable of interacting with other cell bodies compared to other isolates. Hydrophobicity is crucial and species-specific for the adhesion of probiotic microorganisms to epithelial cells, where they can provide prophylactic and therapeutic benefits [19].

The cell surface hydrophobicity of the isolated strains was examined using two different hydrocarbons, n-hexadecane, n-hexane and xylene. The highest surface hydrophobicity percentage was determined in n-hexadecane and the lowest in n-hexane.

The study reported that the use of this test is limited due to the harmful effects of hexane on cell walls, triggering lysis [28]. However, since the use of n-hexadecane and xylene did not have a negative effect on bacterial cells, this organic solvent was recommended. This result was associated with cell surface hydrophobicity with xylene in our study.

Autoaggregation

Autoaggregation or automatic aggregation can be defined as cells of the same strain coming together to form clusters [29]. This property can vary depending on factors such as hydrophobicity on the surface of cells and is one of the important properties of probiotics. In particular, this property also determines the capacity to adhere to eukaryotic cells, especially the mucosal epithelium. The autoaggregation capacities of isolated strains are usually measured after 24 hours of incubation at 37 °C and are usually measured at a wavelength of 600 nm. The autoaggregation percentages of yogurt isolates in this study are shown in Table 3, and these results were found to be consistent when compared with previous studies. Automatic assembly of cells may provide protection against environmental stresses. For this reason, it has been stated that the autoaggregation abilities of yeasts are species-specific and different yeast strains may differ in this feature [19]. Such studies help us understand the physiological properties of probiotic yeast strains and evaluate the impact of these properties on health benefits.

Antibiotic Tests

Antibiotic resistance models were generated using the disk diffusion method [30]. An important feature of probiotic bacteria is that they do not carry any infectious antibiotic resistance genes. The results obtained from this study (Table 4) show that only K3 from three different isolates is sensitive to 7 different antibiotics. Vancomycin 30 µg/ml, Neomycin 30 µg/ml, Rifampin 5 µg/ml, Erythromycin 15 µg/ml, Penicillin 2 µg/ml, Gentamicin 30 µg/ml, Chlorophenicol 30 µg/ml and the relevant inhibition zone obtained is Table 3. is also shown. The appearance of the medium is also given in Figure 2. Antimicrobial activity can also be considered one of the most important selection criteria for probiotics. The fact that only one of the isolates was sensitive may be due to the fact that the species are from different sources and the antibiotic tests are species-specific [22].
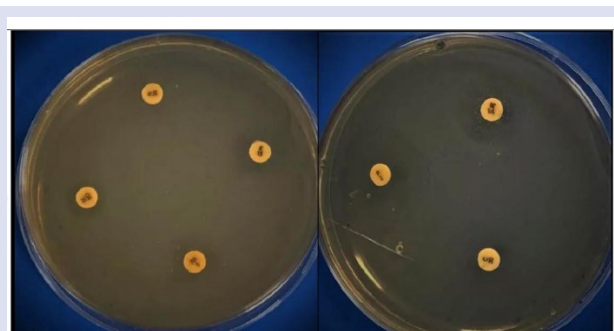

Figure 2. Antibiotic inhibition zones of isolate K3

Table 4. Antibiogram results of isolate K3

Antibiotic	Shortening	Concentration (µg/ml)	Zones of Inhibition (cm)
Vancomycin	VA	30 µg/ml	1.9
Neomycin	N	30 µg/ml	0.8
Rifampicin	RA	5 µg/ml	1.1
Erythromycin	E	15 µg/ml	1.2
Penicillin	P	2 µg/ml	2.7
Gentamicin	CN	30 µg/ml	1.0
Chlorophenicol	C	30 µg/ml	---

Conclusion

This study shows that *Kluyveromyces marxianus* K3 strain can be considered as a potential probiotic. This isolated strain has the ability to survive in acidic stomach and intestinal pH conditions and has a good growth performance at human body temperature. It was also found to be sensitive to antibiotics, suggesting that these strains may be potential candidates for new probiotic formulations or food supplements. However, further research is required to clearly determine whether these strains are truly effective probiotics. In particular, further studies on their potential to adhere to intestinal mucosa and clinical analyses are important. Such studies will help us understand the potential benefits of strains on human health and optimize the use of probiotic yeast. In conclusion, increasing the knowledge about potential probiotic yeast strains such as *Kluyveromyces marxianus* K3 is of great importance in terms of improving the effectiveness and areas of use of probiotics.

Acknowledgements

Conflicts of interest

There are no conflicts of interest in this work.

References

[1] Yeşilyurt N., Yılmaz B., Ağagündüz D., Capasso, R., Involvement of probiotics and postbiotics in the immune system modulation, Biologics, 1 (2) (2021) 89-110.

[2] Yoo J.Y., Groer M., Dutra S.V.O., Sarkar A., McSkimming D.I, Gut microbiota and immune system interactions, Microorganisms, 8 (10) (2020) 1587.

[3] Gurunathan S., Thangaraj P., Kim J.H., Postbiotics: functional food materials and therapeutic agents for cancer, diabetes, and inflammatory diseases, Foods, 13 (1) (2023) 89.

[4] Rima H., Steve L., Ismail F., Antimicrobial and probiotic properties of yeasts: from fundamental to novel applications, Front Microbiol., 421 (3) (2012).

[5] Lloyd-Price J., Abu-Ali G., Huttenhower C., The healthy human microbiome, Genome medicine, 8 (2016) 1-11.

[6] Holzapfel W.H., Appropriate starter culture technologies for small-scale fermentation in developing countries, Int. J. Food Microbiol., 75 (3) (2002) 197–212.

[7] Leroy F., De Vuyst L., Lactic acid bacteria as functional starter cultures for the food fermentation industry, Trends in Food Science & Technology, 15(2) (2004) 67-78.

[8] Lipke P.N., Ovalle R., Cell wall architecture in yeast: new structure and new challenges, Int. J. Bacteriol., 180 (15) (1998) 3735–3740.

[9] Ghassemi N., Poulhazan A., Deligey F., Mentink-Vigier F., Marcotte I., Wang T., Solid-state NMR investigations of extracellular matrixes and cell walls of algae, bacteria, fungi, and plants, Chemical reviews, 122(10) (2021) 10036-10086.

[10] Amorim J.C., Piccoli R.H., Duarte W.F., Probiotic potential of yeasts isolated from pineapple and their use in the elaboration of potentially functional fermented beverages, Food Res. Int., 107 (2018) 518–527.

[11] El-Baz A.F., El-Enshasy H.A., Shetaia Y.M., Mahrous H., Othman N.Z., Yousef A.E., Semiindustrial scale production of a new yeast with probiotic traits, *Cryptococcus sp.* YMHS, isolated from the Red Sea, Probiotics Antimicrob. Proteins, 10 (1) (2018) 77–88.

[12] Sartor R.B., Therapeutic manipulation of the enteric microflora in inflammatory bowel diseases: antibiotics, probiotics, and prebiotics, Gastroenterol., 126 (6) (2004) 1620–1633.

[13] Glassner K. L., Abraham B. P., Quigley E. M., The microbiome and inflammatory bowel disease, Journal of Allergy and Clinical Immunology, 145(1) (2020) 16-27.

[14] Bisson J.F., Hidalgo S., Rozan P., Messaoudi M., Preventive effects of different probiotic formulations on travelers diarrhea model in wistar rats, Dig. Dis. Sci., 55 (4) (2010) 911–919.

[15] Ooi C.Y., Dilley A.V., Day A.S., *Saccharomyces boulardii* in a child with recurrent Clostridium difficile, Pediatr. Int., 51 (1) (2009) 156–158.

[16] Swidsinski A., Loening-Baucke V., Verstraelen H., Osowska S., Doerffel Y., Biostructure of fecal microbiota in healthy subjects and patients with chronic idiopathic diarrhea, Gastroenterology, 135 (2) (2008) 568–579.

[17] Czerucka D., Piche T., Rampal P., Yeast as probiotics–Saccharomyces boulardii, Aliment Pharmacol. Ther., 26 (6) (2007) 767–778.

[18] Azhar M.A., Abdul Munaim M.S., Identification and evaluation of probiotic potential in yeast strains found in kefir drink samples from Malaysia, Int. J. Food Eng., 15 (7) (2019) 20180347.

[19] Gut A.M., Vasiljevic T., Yeager T., Donkor, O.N., Characterization of yeasts isolated from traditional kefir grains for potential probiotic properties, J. Funct. Foods, 58 (2019) 56-66.

[20] de Oliveira Coelho B., Fiorda-Mello F., de Melo Pereira G.V., Thomaz-Soccol V., Rakshit S.K., de Carvalho J.C., Soccol C.R., In vitro probiotic properties and DNA protection activity of yeast and lactic acid bacteria isolated from a honey-based kefir beverage, Foods, 8 (10) (2019) 485.

[21] Kocabay S., Çetinkaya S., Probiotic properties of a *Lactobacillus fermentum* isolated from new-born faeces, Journal of oleo science, 69 (12) (2020) 1579-1584.

[22] Borah T., Gogoi B., Khataniar A., Gogoi M., Das A., Borah D., Probiotic characterization of indigenous Bacillus velezensis strain DU14 isolated from Apong, a traditionally fermented rice beer of Assam, Biocatalysis and agricultural biotechnology, 18 (2019) 101008.

[23] Iyer R., Tomar S.K., Kapila S., Mani J., Singh R., Probiotic properties of folate producing Streptococcus thermophilus strains, Int. Food Res., 43 (2010) 103-110.

[24] Çetinkaya S., Kocabay S., Yenidunya A., An investigation of the probiotic properties of *Lactobacillus fermentum, Int J. Life Sci. Biotechnol.*, *3* (2) (2020) 180-191.

[25] Çakır İ., Determination of some probiotic properties on *Lactobacilli* and *Bifidobacteria*, PhD Thesis, Ankara University, Ankara (2003).

[26] Bhatt V.D., Vaidya Y.H., Kunjadia P.D., Kunjadia, A.P., Isolation, characterization of probiotic bacteria from human milk, International Journal of Pharmaceutical Science and Health Care*, 3* (2012) 62-70.

[27] Vinderola G., Capellini B., Villarreal F., Suarez V., Quıberoni A., Reinheimer J., Usefulness of a set of simple in vitro tests for the screening and identification of probiotic candidate strains for dairy use, LWT-Food Science and Technology, 41 (2008) 1678-1688.

[28] Draksler D., Gonzálesa S., Olıver G., Preliminary assays for the development of a probiotic for goats, Reprod. Nutr. Dev., 44 (2004) 397–405.

[29] Nikolic M., Jovcic B., Kojic, M., Topsirovic, L., Surface properties of Lactobacillus and Leuconostoc isolates from homemade cheeses showing auto- aggregation ability, Eur. Food Res. Technol., 231 (2010) 925-931.

[30] Mathara J.M., Schillinger U., Guigas C., Franz C., Kutima P.M., Mbugua S.K., Shin H.K., Holzapfel W.H., Functional characteristics of *Lactobacilus ssp.* From traditional Maasai fermented milk products in Kenya, *Int. J. Food Microbiol.,* 126 (2008) 57-64.

Cumhuriyet Science Journal

Exploring the Impacts of Substitution Position on Structural, Electronic, and Energetic Characteristics of Selected Chalcone Derivatives by DFT Method: A Quantum Computational Research

Sümeyya Serin [1,a,*]

[1] Inonu University, Scientific and Technological Research Center, 44280, Malatya, Türkiye

*Corresponding author

Research Article

ABSTRACT

Chalcone derivatives are frequently utilized as a versatile scaffold in molecular design studies due to their broad-spectrum activities. Structural modification studies applied to increase their biological activities to a remarkable level reveal the importance of substitution positions on aromatic rings. In this respect, the study aimed to explore the effects of changing substitution positions on molecular properties. Herein, the effects of distinct substitution positions on thermodynamic and physicochemical parameters, reactivity descriptors, absorption characteristics, and intramolecular interactions were investigated utilizing quantum chemical methods. To this end, (Density Functional Theory) DFT-based calculations were performed using the GAUSSIAN 16 software with B3LYP/6-311++G (d, p) level on *ortho*-OH, *meta*-OH, and *para*-OH substituted chalcone derivatives. While the calculated dipole moment and polarizability values differ, very similar results were obtained for the ΔE (total energy), ΔH (enthalpy), and ΔG (Gibbs free energy) parameters. The highest polarizability value, 296.193 a.u., was obtained for the *para*- isomer. The ΔE_g values in the gas phase were calculated as: 4.013 eV (*m*-) > 3.898 eV (*p*-) > 3.832 eV (*o*-). Also, the effects of different solvents on the absorption spectra of the studied isomers were investigated theoretically using (Time Dependent) TD-DFT calculations. Molecular orbitals contributing to electronic transitions were determined for each phase. It is further anticipated that the research findings will offer novel insights to inform future studies on the implications of the substitution position.

Keywords: Chalcone, Substitution position, DFT, Reactivity, Absorption characteristics

[a] ✉ sumeyya.alatas@inonu.edu.tr   ⓘD https://orcid.org/0000-0002-4637-1734

Introduction

Chalcones are plant-derived polyphenolic compounds belonging to the flavonoids family. They have been the subject of numerous studies due to their bioactive nature. Therapeutical applications of chalcone derivatives date back to when plants were utilized in order to treat distinct medical disorders [1]. Over time, research on the design, synthesis and determination of application areas of more specific derivatives has increased. Studies on determining various pharmacological activities such as anticancer [2], antioxidant [3], anti-inflammatory [4], anticonvulsant [5], and antifungal [6] have been frequently encountered in the literature. The typical scaffold in chalcones is the most investigated structure for potential anticancer activity. In particular, hydroxy-substituted chalcones have been demonstrated to exhibit activity as cytotoxic and tumor-reducing agents [7]. Some well-known natural chalcones that are used in pharmaceuticals include isoliquiritigenin, butein, and isobavachalcone (Figure 1.). Modifying the chemical structures of chalcones allowed the examination of their structure-activity relationships to improve pharmacological activity. The types, numbers and positions of substituents have been effective in the preparation of structurally diverse chalcone derivatives. In a study conducted by Ma et al., a series of

hydroxychalcone derivatives were synthesized and appraised for their in vitro inhibitory activities of β-secretase (BACE1) [8]. If we characterize the two phenyl groups in the structure of chalcone as PhC=O and PhC-H, the relevant study focused on how the position of a hydroxyl group in the PhC-H ring affects the inhibitor activity. IC$_{50}$ values of 2.45 ± 0.39 μM, 8.03 ± 0.92 μM, and 33.00 ± 3.75 μM were obtained for *ortho*, *meta*, and *para* substitution, respectively. Therefore, it was determined that the *ortho* position was more effective than other substitution positions. In a recent study by Cyboran-Mikołajczyk et al., the relationship between the biological activities and chemical structure of compounds containing a chloro substituent at various positions of the PhC=O and PhC-H rings of chalcone was investigated, as well as their effects on membranes, cancer cells and bacterial cells [9]. Within the scope of the study, five different 2'-hydroxychalcone derivatives with chlorine atoms in various positions were synthesized. While the chlorine substituent increases the lipophilic character of 2'-hydroxychalcone, the highest n-octanol/water partition coefficient (logP$_{ow}$) of 2.90 was obtained for 2-chloro-2'-hydroxychalcone derivative. Higher lipophilicity value indicates easier membrane permeation. The ability of the derivatives to inhibit bacterial growth and biofilm

formation varies based on the substitution positions in the phenyl rings. Another study carried out by Patil and Zangade focused on the synthesis and anticancer activities of chalconoid based Co (II) complexes with 2-hydroxychalcones containing naphthalene moiety [10]. The anticancer activities of six synthesized complexes were evaluated against the liver cancer cell line (Hep G2). The findings of the study revealed that the complex having –OH substituent at *meta-para* position of PhC-H ring exhibited considerable activity with IC$_{50}$ value of 64.21 µg/mL. In their previously published study, Bronikowska et al. investigated the effects of *ortho-*, *meta-* and *para-*methoxy derivatives of 2'-hydroxychalcones on the release of IL-8, MIF, VCAM-1, ICAM-1 by colon cancer SW480 and SW620 cell lines [11]. Test results revealed that the studied methoxy derivatives exhibited modulating effect on colon cancer cells. Besides, it was reported that *meta-*methoxy derivative at the concentration of 25 µM considerably decreased IL-8 secreted by SW480 and SW620 cancer cells. In another study conducted by Wilhelm et al., cytotoxicity evaluation was carried out on four chalcone derivatives in which the substitution positions and substituents differed [12]. Cytotoxic activity examination was performed in vitro in various cancer cell lines, including breast adenocarcinoma (MCF7), T-lymphoblastic leukemia (CEM), cervical carcinoma (HeLa) lines, malignant melanoma (G-361), and skin fibroblasts (BJ). It has been reported that the best activity was observed against CEM cells. IC$_{50}$ values obtained in the study revealed that the presence of the hydroxy group on the PhC-H ring has a prominent influence on cytotoxicity. Furthermore, one of the important findings emphasized in the study is that *para-*OH substitution exhibited high cytotoxicity and selectivity.
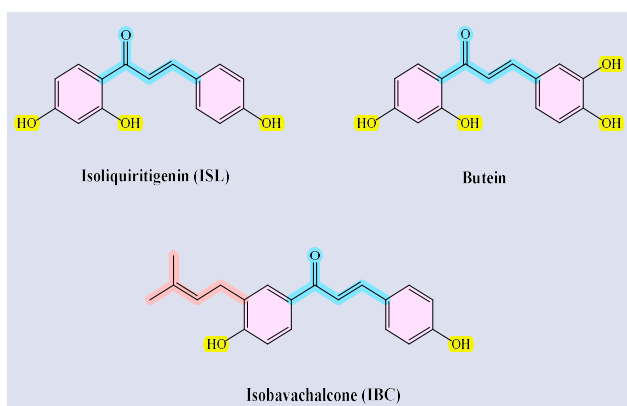

Figure 1. Structures of some naturally derived chalcones.

Keeping these considerations in mind, it is concluded that the bioactivity potential of chalcones is affected by the substitution positions of the substituents on the PhC=O and PhC-H aromatic rings. Therefore, it has becoming more substantial to explore the impacts of positional isomerism on molecules. The use of computational techniques in this laborious exploration duration provides a great advantage to researchers as it ensures the opportunity to evaluate various characteristics of the molecules of interest both numerically and visually [13]. DFT is one of the most versatile techniques available to examine the ground state properties of various molecular systems, especially electronic characteristics. By offering less computational time, excellent accuracy, and being cost-effective compared to other methods, DFT computations remain popular among computational chemists [14]. The theoretical investigation of how the relative position of the substituents affects to the molecular properties motivated this study. Herein, quantum chemical calculations were conducted in three different solvent environments (acetonitrile, DMSO, and water) by selecting *ortho*, *meta*, and *para-*OH substituted chalcone derivatives. The effects of both substituent position and solvent environment on the physicochemical, electronic and molecular properties of OH-substituted chalcone derivatives were examined from a theoretical perspective. A preliminary study of the solvent and/or substituent position effect provides insight into subsequent phase studies. The observation that interaction forces in solution are significantly more pronounced and diversified compared to those in the gas phase enables the modulation of solute properties and reactivities across a range of processes. It is expected that the research findings will provide new perspectives for future studies on the effects of the substitution position.

Computational Methodology

All DFT computations operated in this work were performed by using GAUSSIAN 16 software package [15] with B3LYP hybrid functional and the 6-311++G (d, p) basis [16-18]. Gauss View 6 software [19] was utilized for visualizations of the optimized structure, FMOs, and MEP diagrams. To gain the density of states (DOS) plot, Gauss-Sum 3.0 [20] program was utilized. The solvent phase (acetonitrile, ACN (ε=35.7), DMSO (ε=46.8), and water (ε=78.4)) simulations were carried out by using Integral Equation Formalism Polarizable Continuum Model (IEFPCM) [21]. For computations, optimized structure was verified by the absence of imaginary frequency. The TD-DFT method [22] was utilized to enlighten UV–vis. features such as possible electronic transitions, energies, and oscillator strengths.

The thermochemical quantities, $E_{vib.}$ (vibrational thermal energy), $S_{vib.}$ (vibrational entropy), and $Cv_{vib.}$ (vibrational heat capacity) values were calculated through specific equations ((1)-(5)) defined below in accordance with the principles of quantum mechanics [23-25]. The following explanations refer to the terms presented in the equations: $\Theta_{v,j}=hvj/k$ →vibrational temperature, k→ Boltzmann constant, h→ Planck constant, and vj→ j^{th} fundamental frequency.

$$Q = Q_{trans.} \times Q_{rot.} \times Q_{vib.} Q_{elec.} \tag{1}$$

$$Q_{vib.} = \prod_{j=1}^{3N-6} \frac{e^{-\Theta_{v,j}/2T}}{\left(1 - e^{-\frac{\Theta_{v,j}}{T}}\right)} \tag{2}$$

$$E_{vib.} = Nk \sum_{j=1}^{3N-6} \left(\frac{\Theta_{v,j}}{2} + \frac{\Theta_{v,j}\, e^{-\Theta_{v,j}/T}}{\left(1 - e^{-\frac{\Theta_{v,j}}{T}}\right)} \right) \qquad (3)$$

$$S_{vib.} = Nk \sum_{j=1}^{3N-6} \left[\frac{\Theta_{v,j}/T}{\left(e^{\Theta_{v,j}/T} - 1\right)} \right.$$
$$\left. - ln\left(1 - e^{-\Theta_{v,j}/T}\right) \right] \qquad (4)$$

$$Cv_{vib.} = Nk \sum_{j=1}^{3N-6} \left[\left(\frac{\Theta_{v,j}}{T}\right)^2 \frac{e^{\Theta_{v,j}/T}}{\left(e^{\Theta_{v,j}/T} - 1\right)^2} \right] \qquad (5)$$

According to Koopmans theorem [26], ionization energy (I) (I= - E_{HOMO}) and electron affinity (A) (A= -E_{LUMO}) values can be defined by HOMO (Highest Occupied Molecular Orbital) and LUMO (Lowest Unoccupied Molecular Orbital) energies. Additionally, some quantum chemical reactivity parameters, calculated utilizing I and A values, with their corresponding equations are presented below (6-13) [27-33].

$$\text{Chemical Potential } \mu = -\frac{I + A}{2} \qquad (6)$$

$$\text{Chemical Hardness } \eta = \frac{I - A}{2} \qquad (7)$$

$$\text{Electronegativity } \chi = \frac{I + A}{2} \qquad (8)$$

$$\text{Electrophilicity Index } \omega = \frac{\mu^2}{2\eta} \qquad (9)$$

$$\text{Electron-Accepting Power } \omega^+ \approx (I + 3A)^2 / (16(I - A)) \qquad (10)$$

$$\text{Electron-Donating Power } \omega^- \approx (3I + A)^2 / (16(I - A)) \qquad (11)$$

$$\text{Maximum Charge Transfer Capability } \Delta N_{max} = \frac{I + A}{2(I - A)} \qquad (12)$$

$$\text{Back-Donation Energy } \Delta\varepsilon_{back-donatio} = -\frac{\eta}{4} \qquad (13)$$

NBO (Natural Bond Orbitals) analysis of studied compounds were also performed utilizing the 2nd-order Fock matrix [34-35] at B3LYP/6–311++G (d, p) theory level. Thus, possible donor-acceptor orbital interactions and corresponding stabilization energy predictions were noted. Stabilization energy values were calculated according to the formula specified in equation (14). The terms in the formula are expressed as follows: $E^{(2)}$: Stabilization energy, *qi*: Donor orbital occupancy, *Fij:* Off

diagonal Fock matrix, *εi* and *εj*: diagonal element, donor and acceptor orbital energies.

$$E^{(2)} = \Delta E_{ij} = qi \left[\frac{(Fij)^2}{(\varepsilon j - \varepsilon i)} \right] \qquad (14)$$

Results and Discussion

PES (Potential energy Surfaces) Scan Analysis and Molecular Structure

The investigated chalcone derivatives were optimized in the gaseous state using B3LYP/6- 311++G (d, p) level. X-Ray structures were employed for optimization of *meta*- and *para*- derivatives [12]. The crystal structures were ensured from the Cambridge Crystallographic Data Center (CCDC 2062760 for *m*-OH and 2062757 for *p*-OH) [12]. The resulting DFT-optimized geometries have been represented in Figure 2 ((B) and (C)). In order to evaluate the compatibility of the X-ray structures and the DFT-optimized structures, atom-by-atom superimposition was performed (Figure 3). RMSD is a crucial metric in scientific research, utilized in a variety of ways. It is employed to ascertain the stability of protein-ligand complexes during molecular dynamics simulations, to compare the structural similarity between crystallized and modeled frameworks, and to evaluate the mean change in motion of selected atoms during simulations [36]. The root mean square deviation (RMSD) values were determined as 0.607 Å for *m*-OH isomer and 0.221 Å for *p*-OH isomer. These values are indicative of a satisfactory level of distinction between the structures, suggesting that the observed differences are within an acceptable range. However, since no X-ray structure is available for the ortho isomer, to assign the most stable geometry, conformational analysis has been achieved by operating B3LYP/ 6-311++G (d, p) methodology. The PES computations were carried out in accordance with C14-C4-C2-C5 and C5-C3-C23-27 dihedral angles. The PES scan analysis was conducted by altering the dihedral angles at each step by 10˚ along the specified bond axis. The "Scan of Total Energy" diagrams obtained as a result of the analysis are displayed in Figure 4. The minima (steps 21 and 20) and maxima (steps 29 and 8) points obtained by the rotation of the selected dihedral angles are shown on the diagram. According to PES analysis results, it is revealed that the C14-C4-C2-C5 and C5-C3-C23-27 dihedral angles have rotational potential barrier values of 4.77 and 3.70 kcal/mol. Therefore, the highest value for the energy difference between the most stable conformer and the most unstable conformer was detected in the C14-C4-C2-C5 dihedral angle scan. Namely, minimum energy and improved stability were monitored when rotating round the C14-C4-C2-C5 dihedral angle. Consequently, the lowest energy structure obtained from the relevant dihedral angle scan was used as the basis for further calculations. The DFT-optimized structure of the *ortho* isomer is shown in Figure 2 (A).
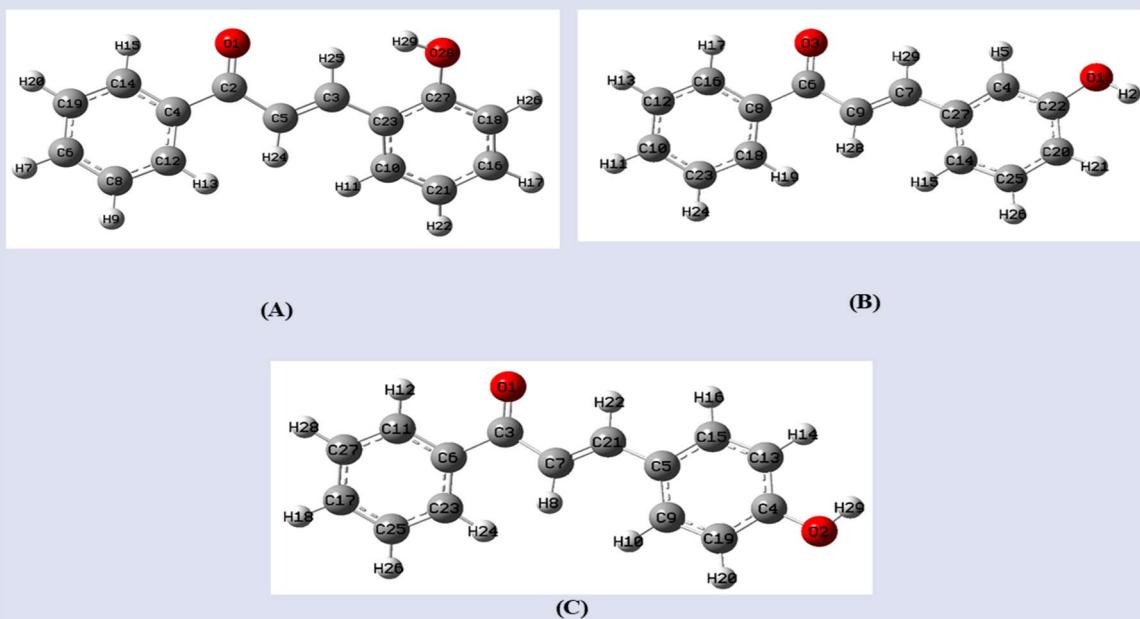
Figure 2. DFT-optimized structures of *o*-OH (A), *m*-OH (B), and *p*-OH (C) derivatives with atomic numbering scheme.
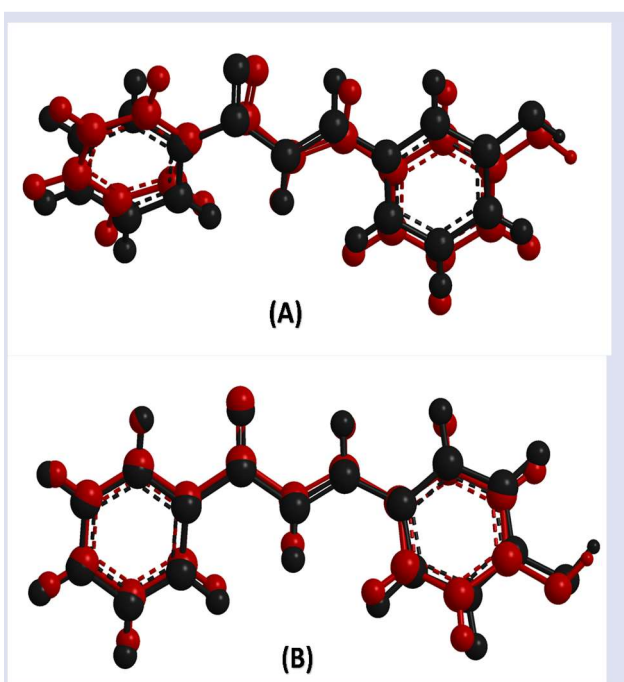

Figure 3. Atom-by-atom superimposition of the DFT-optimized structures (black) and the X-ray structures (red) for *m*-OH (A) and *p*-OH (B) isomers.

Figure 4. Potential energy surfaces scan of *o*-OH substituted isomer

Some of selected bond lengths (Å), bond angles (°), and dihedral angles (°) are listed in Table 1. From Table 1, it is observed that the C=O carbonyl bond lengths of *ortho-*, *meta-*, and *para-* derivatives were calculated as 1.225 Å, 1.223 Å, and 1.225 Å, respectively. The experimental value for the relevant bond length was determined as 1.237 Å. In the case of aromatic ring C-C bond lengths, they were computed in the range of 1.401-1.414 Å for all three compounds. Experimental C-C distances have been reported in the range of 1.385-1.398 Å. The O1-C2-C5 and O1-C2-C4 bond angles of the *ortho-* derivative were estimated as 121.09° and 119.99° respectively.

The equivalents of these angles in *meta-* and *para-* derivatives were calculated as 121.36°/119.89° and 121.57°/119.72°, respectively. Therefore, it is evident that values close to the experimental data (120.40° /119.33°) are obtained. Based on computations of ground state data of dihedral angles, it is concluded that *ortho-*, *meta-* and *para-*substituted isomers exhibit nearly planar molecular structures. Namely, C4-C2-C5-C3/C27-C23-C3-C5, C8-C6-C9-C7/C4-C27-C7-C9 and C6-C3-C7-C21/C15-C5-C21-C7 dihedral angle pairs are calculated as 175.85°/160.69°, 175.48°/177.79° and 175.96°/178.66°, respectively. On the other hand, other dihedral angle pairs mentioned in the Table 1 were determined between -0.04° and -0.65°. All bond parameters of the studied isomers were determined to be in good agreement with other similar structures reported as well as literature data [12, 37-39].

Table 1. Selected bond parameters for studied compounds

Bond Length (Å)	o-OH	Bond Length (Å)	m-OH	Bond Length (Å)	p-OH	Exp.
C2-O1	1.225	C6-O3	1.223	C3-O1	1.225	1.237[a]
C27-O28	1.363	C22-O1	1.367	C4-O2	1.363	1.361[a], 1.362[b] 1.354[c]
C2-C5	1.484	C6-C9	1.484	C3-C7	1.481	1.463[a]
C4-C12	1.402	C8-C16	1.402	C6-C11	1.402	1.398[a]
C4-C14	1.403	C8-C18	1.401	C6-C23	1.401	1.385[a]
C23-C27	1.414	C27-C4	1.401	C5-C15	1.404	1.386[a], 1.404[c]
Bond Angle (°)		**Bond Angle (°)**		**Bond Angle (°)**		
O1-C2-C5	121.09	O3-C6-C9	121.36	O1-C3-C7	121.57	120.40[a]
O1-C2-C4	119.99	O3-C6-C8	119.89	O1-C3-C6	119.72	119.33[a]
C27-C23-C3	120.43	C4-C27-C7	120.95	C15-C5-C21	119.87	120.22[a]
C3-C5-C2	120.12	C7-C9-C6	120.46	C21-C7-C3	120.40	122.63[a]
Dihedral Angle (°)		**Dihedral Angle (°)**		**Dihedral Angle (°)**		
C4-C2-C5-C3	175.85	C8-C6-C9-C7	175.48	C6-C3-C7-C21	175.96	168.96[a]
C27-C23-C3-C5	160.69	C4-C27-C7-C9	177.79	C15-C5-C21-C7	178.66	176.0[a]
C12-C4-C14-C19	-0.65	C16-C8-C18-C23	-0.02	C11-C6-C23-C25	-0.04	0.3[a]
C23-C27-C18-C16	-0.41	C27-C4-C22-C20	-0.1	C5-C15-C13-C4	-0.1	-2.3, 0.7[c]
[a] Ref. [35], [b] Ref. [36], [c] Ref. [37]						

Thermodynamic Parameters

Table 2 demonstrates the calculated physicochemical and thermodynamic parameters of o-, m-, and p-substituted chalcone derivatives in both gas and solvent phases.

Table 2. Thermodynamic and physicochemical parameter estimations at B3LYP/6- 311++G (d, p) level

o-OH	Vacuum	ACN	DMSO	Water
DM (Debye)	3.329	4.726	4.747	4.774
ΔE (a.u.)	-729.212	-729.223	-729.223	-729.224
ΔH (a.u.)	-729.211	-729.222	-729.222	-729.223
ΔG (a.u.)	-729.269	-729.281	-729.282	-729.282
$\Delta E_{thermal}$ (kcal/mol)	152.084	151.993	151.992	151.991
$\Delta E_{vib.}$ (kcal/mol)	150.307	150.215	150.215	150.214
Cv (cal/molK)	55.511	55.586	55.586	55.586
$Cv_{vib.}$ (cal/molK)	49.549	49.624	49.624	49.624
S (cal/molK)	123.903	124.376	124.363	124.330
$S_{vib.}$ (cal/molK)	48.422	48.889	48.876	48.843
α (a.u.)	207.050	284.059	285.115	286.500
m-OH	**Vacuum**	**ACN**	**DMSO**	**Water**
DM (Debye)	4.494	6.413	6.441	6.477
ΔE (a.u.)	-729.213	-729.226	-729.227	-729.227
ΔH (a.u.)	-729.212	-729.225	-729.226	-729.226
ΔG (a.u.)	-729.271	-729.284	-729.284	-729.285
$\Delta E_{thermal}$ (kcal/mol)	151.934	151.972	151.970	151.966
$\Delta E_{vib.}$ (kcal/mol)	150.157	150.195	150.192	150.189
Cv (cal/molK)	55.826	55.653	55.654	55.655
$Cv_{vib.}$ (cal/molK)	49.865	49.691	49.692	49.694
S (cal/molK)	124.825	123.667	123.689	123.720
$S_{vib.}$ (cal/molK)	49.296	48.137	48.158	48.190
α (a.u.)	205.930	281.408	282.465	283.854
p-OH	**Vacuum**	**ACN**	**DMSO**	**Water**
DM (Debye)	2.907	4.456	4.478	4.506
ΔE (a.u.)	-729.214	-729.229	-729.229	-729.229
ΔH (a.u.)	-729.213	-729.228	-729.228	-729.228
ΔG (a.u.)	-729.272	-729.286	-729.287	-729.287
$\Delta E_{thermal}$ (kcal/mol)	152.013	151.951	151.949	151.945
$\Delta E_{vib.}$ (kcal/mol)	150.235	150.174	150.171	150.167
Cv (cal/molK)	55.655	55.534	55.536	55.538
$Cv_{vib.}$ (cal/molK)	49.694	49.572	49.574	49.577
S (cal/molK)	124.137	123.311	123.330	123.357
$S_{vib.}$ (cal/molK)	48.574	47.740	47.760	47.787
α (a.u.)	211.545	293.520	294.675	296.193

In the gas phase, the dipole moment and polarizability values of the isomers changed in the following order: DM (in Debye) 2.907 (p-) < 3.329 (o-) < 4.494 (m-) and α (in a.u.) 205.930 (m-) < 207.050 (o-) < 211.545 (p-). For both parameters, similar trends are observed in the solvent phase values. The highest polarizability value, 296.193 a.u., was obtained for the *para* isomer in the water phase. It can be expressed that *para* substitution on the aromatic ring makes the compound more polarizable. The gas phase total energy values for o-, m-, and p-OH derivatives were calculated as -729.212 a.u., -729.213 a.u., and -729.214 a.u., respectively. The change of substituent position did not create a significant difference in the enthalpy and free energy values, as well as in the total energy values. The highest heat capacity (Cv) and entropy (S) values were determined as 55.826 cal/molK and 124.825 cal/molK, respectively, in the gas phase for the *meta*-substituted derivative.

Vibrational Analysis

In literature reviews, no experimental FT-IR evaluation of the studied derivatives was found except *p*-substituted isomer. However, in the relevant study, only C=O and aromatic ring C-H stretching vibrations were mentioned for the *para* isomer [40]. Therefore, in this section, the vibrational analysis of all three isomers is discussed theoretically. The theoretically predicted FT-IR spectra of studied isomers are shown in Figure 5. Since molecular structures of studied isomers consist of 29 atoms, they reveal total 81 different vibrational modes according to the 3N-6 formula. The selected vibrational mode assignments for mentioned compounds are listed in Table 3.
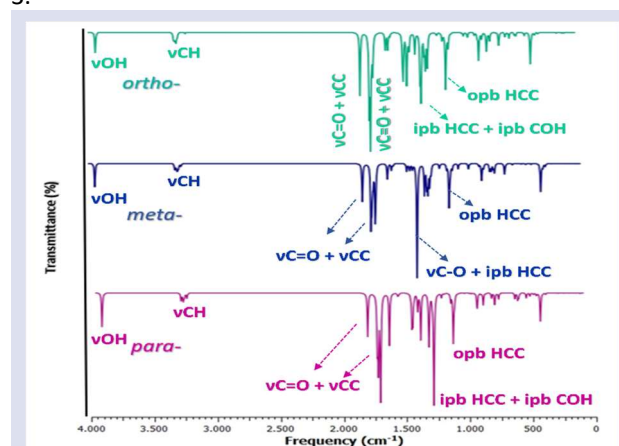

Figure 5. Theoretically simulated IR spectra of studied derivatives

FT-IR analysis facilitates the determination of the C=O stretching vibration band due to its specific region. vC=O stretching vibrations of α,β-unsaturated ketones are observed in the range of 1715-1680 cm^{-1} [41]. Herein, C=O stretching bands of *o*-, *m*-, and *p*- isomers were estimated in the range of 1560-1684 cm^{-1}, 1565-1690 cm^{-1} and 1561-1685 cm^{-1}, respectively. In the literature, the experimental carbonyl stretching vibration for the *p*-isomer has been reported as 1651 cm^{-1} [40]. vOH stretching vibrations are generally observed around 3500-3700 cm^{-1}. The calculated O-H stretching wavenumbers for the studied compounds were assigned at 3766 cm^{-1} (*o*-), 3769 cm^{-1} (*m*-) and 3763 cm^{-1} (*p*-) as pure mode. The theoretical vC-H

(aromatic) bond stretching vibrations of studied isomers appeared at range of 3136-3151 cm^{-1} (*o*-), 3133-3149 cm^{-1} (*m*-), and 3128-3146 cm^{-1} (*p*-) as pure bonding vibrations with lower IR intensities. Also, the predicted peaks in regions 3110-3130 cm^{-1} (*o*-), 3100-3128 cm^{-1} (*m*-), and 3099-3124 cm^{-1} (*p*-) were assigned as C-H (aromatic) bond asymmetric stretching modes. The presence of the phenolic group has been indicated by a broad band at 3350 cm^{-1} for the *p*-isomer [40]. While C-H in-plane bending vibrations were calculated at 1548-1158 cm^{-1} region, out-of-plane bending vibrations were determined at 973-845 cm^{-1} region.

Table 3. The computed approximate frequencies (in cm^{-1}) for *o*-, *m*-, and *p*- isomers

Assignment	I_{IR}	*o*-OH Unscaled	Scaled	I_{IR}	*m*-OH Unscaled	Scaled	I_{IR}	*p*-OH Unscaled	Scaled
vOH	56	3831	3766	86	3834	3769	124	3828	3763
vCH	13	3205	3151	15	3203	3149	11	3200	3146
vCH	11	3201	3147	11	3199	3145	17	3199	3145
vCH	8	3198	3144	1	3195	3141	1	3196	3142
vCH	2	3192	3138	6	3188	3134	5	3188	3134
vCH	14	3190	3136	5	3187	3133	25	3182	3128
v_{as}CH	22	3184	3130	20	3182	3128	1	3178	3124
v_{as}CH	4	3179	3125	9	3176	3122	9	3176	3122
v_{as}CH	10	3174	3120	10	3172	3118	10	3172	3118
v_{as}CH	0	3170	3116	0	3162	3108	0	3162	3108
v_{as}CH	0	3164	3110	10	3154	3100	19	3153	3099
vCH	4	3111	3058	1	3149	3095	1	3144	3091
vC=O + vCC	173	1713	1684	138	1719	1690	158	1714	1685
vC=O + vCC	8	1652	1583	208	1651	1582	1	1654	1585
vC=O + vCC	204	1639	1570	126	1644	1575	185	1638	1569
vC=O + vCC	296	1628	1560	61	1634	1565	255	1629	1561
vCC + ipb HCC	86	1613	1545	167	1617	1549	75	1616	1548
vCC + ipb HCC	28	1610	1542	85	1613	1545	365	1610	1542
vCC + ipb HCC	2	1521	1457	56	1521	1457	190	1541	1476
vCC + ipb HCC	47	1512	1448	0	1520	1456	0	1520	1456
ipb HCC + ipb COH	46	1492	1429	25	1490	1427	10	1475	1413
vCC + ipb HCC	10	1476	1414	7	1475	1413	7	1467	1405
vC-O + ipb HCC	56	1276	1222	415	1285	1231	169	1291	1237
ipb HCC + ipb COH	170	1225	1174	78	1209	1158	185	1225	1174
Ph breathing + opb HCC	3	1016	973	2	1016	973	2	1016	973
opb HCC	0	960	920	10	962	922	0	969	928
opb HCC	10	888	851	11	882	845	2	886	849

Abbreviations; I_{IR}: IR intensity, v: symmetric stretching, v_{as}: asymmetric stretching, ipb: in plane bending, opb: out of plane bending,

FMO (Frontier Molecular Orbital) and MEP (Molecular Electrostatic Potential) Analyses

The outputs obtained from the analysis of frontier molecular orbitals provide valuable information about the distinct chemical characteristics of the molecule of interest by allowing the determination of chemical reactivity parameters. Herein, Table 4 represents the computed DFT-based reactivity parameters of studied isomers. HOMO and LUMO energy values were obtained from calculation outputs performed using density functional theory. The difference between HOMO and LUMO energies (ΔE) is an important merit in determining some properties of a molecule, such as its kinetic stability, chemical reactivity, and chemical hardness. In addition to gas phase, ACN, DMSO, and water phase calculations were also performed using the IEFPCM solvent model to

peruse solvent effects. Accordingly, the energy gap values in the gas phase were calculated as: 4.013 eV (*m*-) > 3.898 eV (*p*-) > 3.832 eV (*o*-). For the solvent phases, the highest ΔE values were also obtained for the *meta*-substituted derivative as 3.835 eV (ACN) > 3.832 eV (DMSO) > 3.829 eV (water). The larger the energy gap value indicates lower chemical reactivity and higher kinetic stability. The same trend was followed in chemical hardness values, and the highest values were obtained for the *meta*- derivative: η, eV, 2.006 (vacuum) > 1.918 (ACN) > 1.916 (DMSO) > 1.915 (water). The electrophilicity index (ω) parameter describes the electrophilic power of the molecule. For all phases studied, the highest electrophilic index values were calculated for the *ortho*-substituted derivative as 5.689 eV (water) > 5.684 eV (DMSO) > 5.682 eV (ACN) > 5.431 eV (vacuum). Therefore, the *o*-OH derivative is expected to exhibit slightly more electrophilic character.

Table 4. The computed chemical reactivity parameters of studied isomers

o-OH	E_{HOMO}	E_{LUMO}	ΔE	η	μ	χ	ω	ω⁺	ω⁻	$ΔN_{max}$	$ΔE_{back}$
Vacuum	-6.478	-2.646	3.832	1.916	-4.562	4.562	5.431	3.390	7.9516	2.381	-0.479
ACN	-6.511	-2.743	3.768	1.884	-4.627	4.627	5.682	3.604	8.2308	2.456	-0.471
DMSO	-6.512	-2.744	3.768	1.884	-4.628	4.628	5.684	3.606	8.2338	2.456	-0.471
Water	-6.513	-2.746	3.767	1.884	-4.630	4.630	5.689	3.610	8.2397	2.458	-0.471
m-OH	E_{HOMO}	E_{LUMO}	ΔE	η	μ	χ	ω	ω⁺	ω⁻	$ΔN_{max}$	$ΔE_{back}$
Vacuum	-6.531	-2.518	4.013	2.006	-4.525	4.525	5.104	3.092	7.617	2.256	-0.502
ACN	-6.545	-2.710	3.835	1.918	-4.628	4.628	5.584	3.510	8.137	2.413	-0.479
DMSO	-6.545	-2.713	3.832	1.916	-4.629	4.629	5.592	3.517	8.146	2.416	-0.479
Water	-6.546	-2.717	3.829	1.915	-4.632	4.632	5.602	3.526	8.157	2.419	-0.479
p-OH	E_{HOMO}	E_{LUMO}	ΔE	η	μ	χ	ω	ω⁺	ω⁻	$ΔN_{max}$	$ΔE_{back}$
Vacuum	-6.281	-2.383	3.898	1.949	-4.332	4.332	4.814	2.892	7.224	2.223	-0.487
ACN	-6.307	-2.587	3.720	1.860	-4.447	4.447	5.316	3.325	7.772	2.391	-0.465
DMSO	-6.308	-2.589	3.719	1.860	-4.449	4.449	5.321	3.329	7.778	2.392	-0.465
Water	-6.309	-2.594	3.715	1.858	-4.452	4.452	5.334	3.340	7.792	2.397	-0.464

Besides, DOS (density of states) diagrams and 3D pictorial presentations of the HOMO & LUMO densities of studied isomers are introduced in Figures 6 and 7, respectively. Through DOS diagrams, the number of molecular orbitals of each isomer at different energy levels can be figured out. Based on Figure 7, it is evident that the HOMO and LUMO densities of all three isomers are quite similar to each other. While LUMOs are spread throughout the molecule, HOMOs are located on the remaining part except the unsubstituted phenyl group. LUMOs exhibit antibonding character. The red and green colors designate negative and positive lobes.
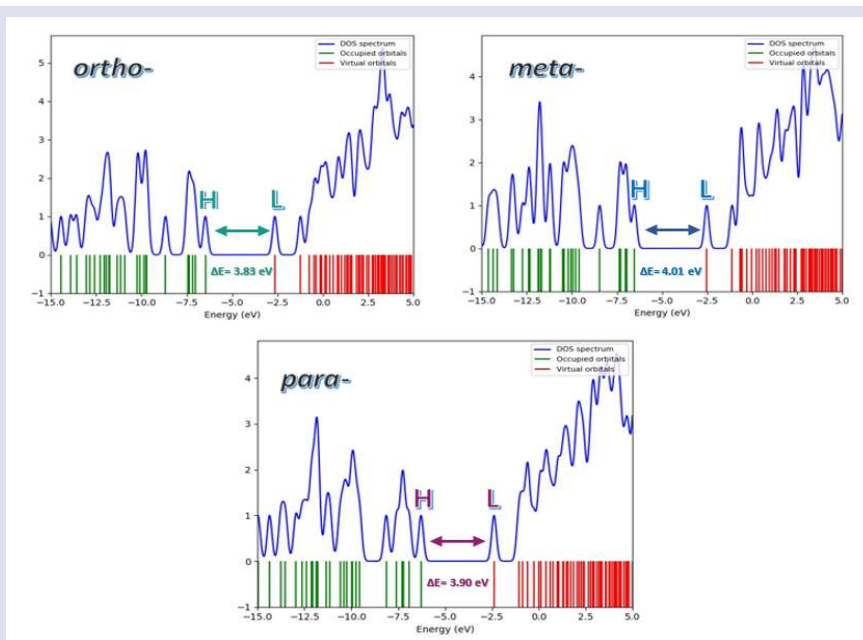

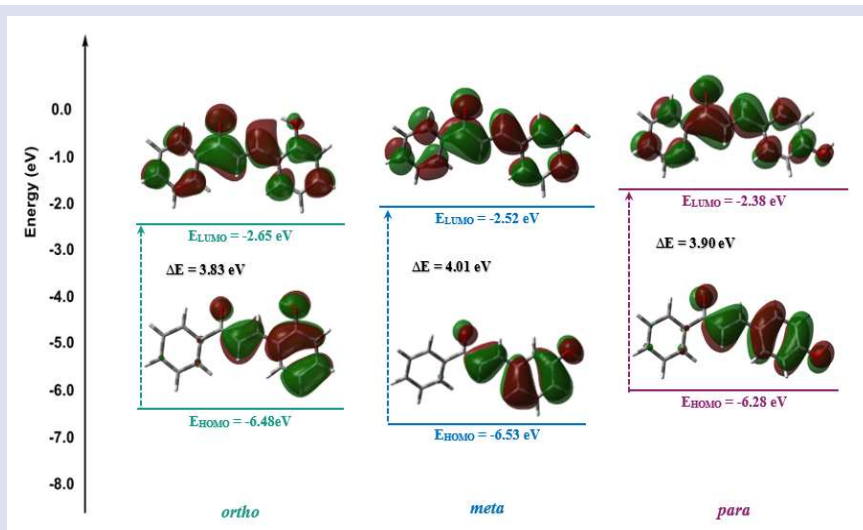Figure 6. DOS diagrams of *o*-, *m*-, and *p*-substituted chalcone derivatives

Figure 7. HOMO & LUMO densities (isoval: 0.02 a.u.) of studied isomers

The molecular electrostatic potential (MEP) mapping was put account to forecast the electrophilic and nucleophilic regions of OH-substituted isomers. Color codes are employed to easily understand the charge distribution [42]. Figure 8 displayed the MEP and ESP surfaces visualized at B3LYP/6-311++G (d, p) theory level. The potential values of MEP and ESP maps of studied isomers are in the range of -006705 a.u (deepest red) /

+0.006705 a.u. (deepest blue) and -0.01286 a.u. (deepest red)/ 0.01286 a.u. (deepest blue). Accordingly, it is obvious that the electron density is higher around aromatic rings (because of π-electron cloud) and oxygen atoms, and there is predominantly red coloration (V<0). Apart from, blue coloration (V>0) is mostly observed around hydrogen atoms.
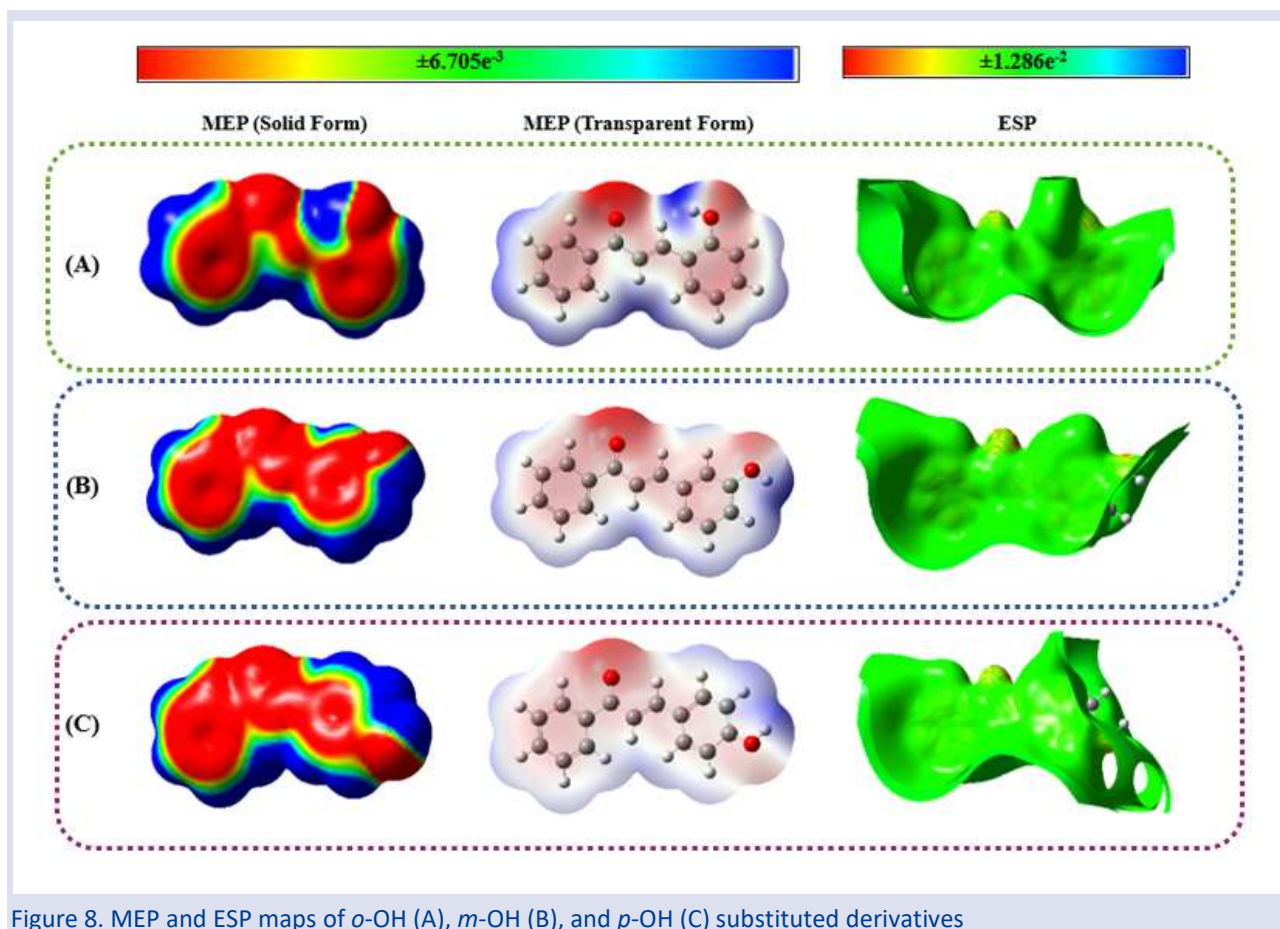

Figure 8. MEP and ESP maps of *o*-OH (A), *m*-OH (B), and *p*-OH (C) substituted derivatives

UV-vis Characterization

The absorption wavelengths of the studied chalcone derivatives were determined by performing TD-DFT calculations in the ACN, DMSO and water phases using the IEFPCM solvent model. Table 5 summarizes possible electronic transitions with relevant data. It is observed for each isomer that the absorption peak values are not significantly affected by the solvent environment. For all three compounds, the studied solvents revealed three distinct wavelengths and oscillator strengths. For *ortho*-OH derivative, water phase wavelengths were computed as 376.91 nm, 325.36 nm, and 288.35 nm, with oscillator strengths (*f*) of 0.3821, 0.3645, and 0.1041, in that order. In ACN and DMSO phases, the wavelengths of the obtained peaks were 377.03/325.32/288.39 nm and 377.94/325.93/288.80 nm, respectively. It has been determined that the following transitions contribute to

the transitions with wavelengths 376.91/325.36/288.35 nm: HOMO-4→LUMO (20%), HOMO→LUMO (66%), HOMO-1→LUMO (66%), HOMO-4→LUMO (52%), HOMO-3→LUMO (34%). It can be seen from Table 5 that the same orbitals contribute to the electronic transitions in acetonitrile and DMSO environments. Although the calculated wavelengths for *meta*-OH and *para*-OH substituted derivatives differed relatively, similar electronic transitions were observed. In the literature review, experimental UV-vis results were found only for *ortho*- and *para*- derivatives. While the λ_max value was reported as 345 nm for the *ortho*- derivative [43], it was recorded as 395 nm for the *para*- derivative [44]. Additionally, for the *ortho*- derivative, plots of the orbitals contributing to electronic transitions in the DMSO phase are shown in Figure 9. With respect to Figure 9, absorption wavelengths can be qualified as π→π* and n→π* transition type.

Table 5. The computed λ_{max}, ΔE, and oscillator strength values of studied isomers in different solvent phases

	Medium	Symmetry	$\lambda_{calc.}$ (nm)	ΔE (eV)	f	Major Contributions
ortho-OH	Water	Singlet-A	376.91	3.2895	0.3821	H-4→L (20%), H→L (66%)
		Singlet-A	325.36	3.8106	0.3645	H-1→L (66%)
		Singlet-A	288.35	4.2998	0.1041	H-4→L (52%), H-3→L (34%)
	ACN	Singlet-A	377.03	3.2885	0.3806	H-4→L (20%), H→L (65%)
		Singlet-A	325.32	3.8112	0.3637	H-1→L (66%)
		Singlet-A	288.39	4.2992	0.1045	H-4→L (53%), H-3→L (33%)
	DMSO	Singlet-A	377.94	3.2805	0.4027	H-4→L (19%), H→L (66%)
		Singlet-A	325.93	3.8040	0.3614	H-1→L (66%)
		Singlet-A	288.80	4.2931	0.1086	H-4→L (53%), H-3→L (33%)
	Medium	**Symmetry**	**$\lambda_{calc.}$ (nm)**	**ΔE (eV)**	**f**	**Major Contributions**
meta-OH	Water	Singlet-A	366.28	3.3850	0.1357	H→L (53%), H-2→L (31%)
		Singlet-A	324.04	3.8262	0.6309	H-1→L (68%)
		Singlet-A	287.00	4.3201	0.0807	H-4→L (55%), H-3→L (30%)
	ACN	Singlet-A	366.36	3.3842	0.1045	H→L (47%), H-2→L (36%)
		Singlet-A	323.93	3.8275	0.6307	H-1→L (68%)
		Singlet-A	286.99	4.3202	0.0809	H-4→L (56%), H-3→L (28%)
	DMSO	Singlet-A	366.71	3.3810	0.1498	H→L (54%), H-2→L (30%)
		Singlet-A	324.84	3.8168	0.6334	H-1→L (68%)
		Singlet-A	287.41	4.3138	0.0843	H-4→L (55%), H-3→L (29%)
	Medium	**Symmetry**	**$\lambda_{calc.}$ (nm)**	**ΔE (eV)**	**f**	**Major Contributions**
para-OH	Water	Singlet-A	364.56	3.4009	0.7226	H→L (66%)
		Singlet-A	358.82	3.4553	0.1251	H-1→L (55%), H-3→L (29%)
		Singlet-A	282.97	4.3816	0.1539	H-3→L (61%), H-1→L (26%)
	ACN	Singlet-A	364.51	3.4014	0.6988	H→L (65%)
		Singlet-A	359.22	3.4515	0.1510	H-1→L (54%), H-3→L (27%)
		Singlet-A	282.98	4.3814	0.1538	H-3→L (62%), H-1→L (26%)
	DMSO	Singlet-A	365.99	3.3877	0.7705	H→L (68%)
		Singlet-A	359.25	3.4512	0.0944	H-1→L (56%), H-3→L (29%)
		Singlet-A	283.38	4.3752	0.1585	H-3→L (61%), H-1→L (26%)

H = HOMO; L = LUMO

HOMO   HOMO-1   HOMO-2

HOMO-3   HOMO-4   LUMO
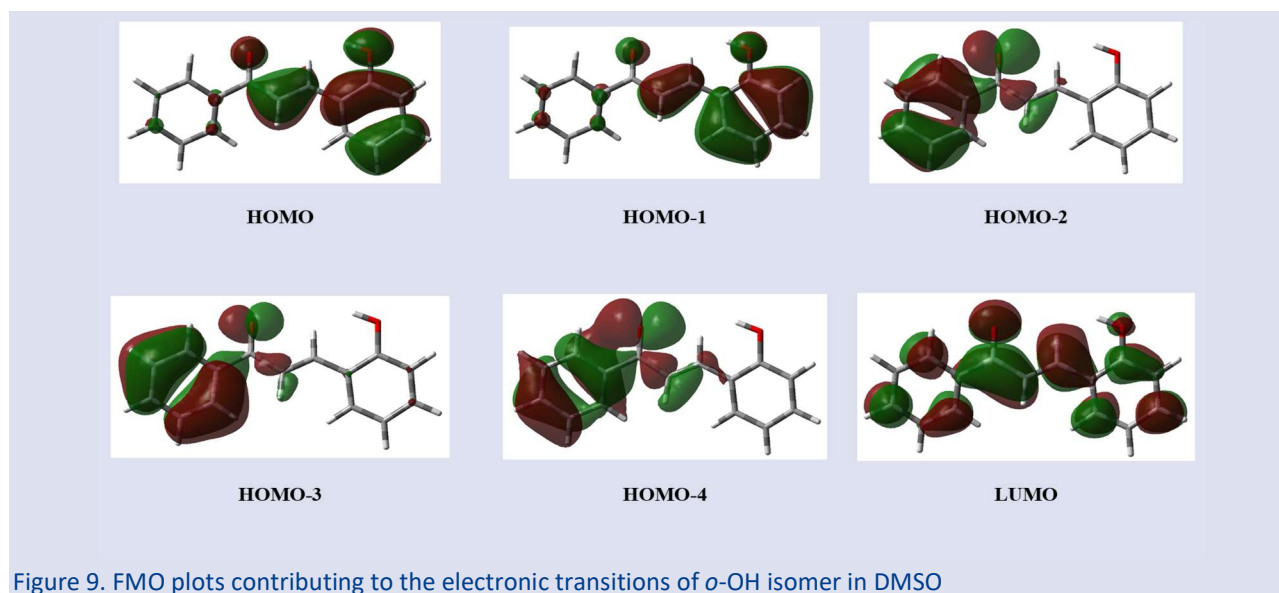
Figure 9. FMO plots contributing to the electronic transitions of *o*-OH isomer in DMSO

NBO Analysis

NBO theory analysis of a particular molecule provides an exhaustive insight into the electron density delocalization from Lewis's donor to non-Lewis's acceptor NBOs. In order to peruse all possible intramolecular interactions of mentioned isomers, the stabilization energy values were computed using the 2nd-order perturbation theory. The findings obtained are listed in Table 6. Interactions with a stabilization energy value of 10 kcal/mol and above were taken into account. As expected, the types of interactions ($\pi \rightarrow \pi^*$, LP $\rightarrow \sigma^*$ and LP $\rightarrow \pi^*$) and energy values are quite close for all three isomers. Some different interactions were determined for the *o*-, *m*-, and *p*-substituted isomers, with energy values ranging from 9.99-28.77, 12.06-26.58, and 11.62-28.67 kcal/mol, respectively. The intramolecular hyperconjugative interactions were observed between π (C-C) and π^* (C-C) bond orbitals and this generated intramolecular charge transfers that resulted in the stabilization of the studied molecules. Moreover,

according to Table 6, it can be concluded that the lone electron pairs (LP) existing on oxygen atoms are involved in intramolecular interactions and largely participate in the stabilization of all three isomers. Namely, for the *o*-OH isomer, the stabilization energies of the LP (2) O1(ED$_i$ = 1.88793e) → σ* C2-C4 (ED$_j$ = 0.06445e), LP (2) O1(ED$_i$ = 1.88793e) → σ* C2-C5 (ED$_j$ = 0.05825e), and LP (2) O28 (ED$_i$ =1.86528e) → π* C23-C27 (ED$_j$ = 0.42508e) transitions were calculated as 18.65, 18.69, and 28.77 kcal/mol, respectively. On the other hand, while the energies corresponding to LP → σ* transitions in *m*-OH and *p*-OH derivatives were calculated as 18.88, 18.02 kcal/mol and 18.96, 18.55 kcal/mol, respectively, the stabilization energy values of LP → π* interactions were determined as 26.58 and 28.67 kcal/mol.

Table 6. NBO analysis results of possible interactions for *o*-, *m*-, and *p*-substituted isomers

o-OH	Donor(i)	ED$_i$/e	Acceptor(j)	ED$_j$/e	E$^{(2)}$ kcal/mol	E(j)-E(i)/a.u	F(i.j)/a.u
	π C3-C5	1.84726	π* O1-C2	0.20829	19.96	0.30	0.070
			π* C23-C27	0.42508	9.99	0.30	0.052
	π C10-C21	1.70219	π* C16-C18	0.31525	21.40	0.29	0.070
			π* C23-C27	0.42508	16.30	0.28	0.062
	π C14-C19	1.65123	π* C4-C12	0.36761	19.46	0.28	0.066
			π* C6-C8	0.32176	21.73	0.28	0.070
	π C16-C18	1.69247	π* C10-C21	0.30386	16.88	0.29	0.062
			π* C23-C27	0.42508	22.73	0.28	0.073
	π C23-C27	1.60589	π* C3-C5	0.11620	16.21	0.29	0.066
			π* C10-C21	0.30386	21.02	0.29	0.071
			π* C16-C18	0.31525	15.88	0.29	0.062
	LP (2) O1	1.88793	σ* C2-C4	0.06445	18.65	0.69	0.103
			σ* C2-C5	0.05825	18.69	0.70	0.103
	LP (2) O28	1.86528	π* C23-C27	0.42508	28.77	0.35	0.097
m-OH	Donor(i)	ED$_i$/e	Acceptor(j)	ED$_j$/e	E$^{(2)}$ kcal/mol	E(j)-E(i)/a.u	F(i.j)/a.u
	π C4-C27	1.97110	π* C7-C9	0.10068	16.25	0.29	0.066
			π* C14-C25	0.31180	17.16	0.28	0.063
			π* C20-C22	0.38293	22.08	0.28	0.071
	π C7-C9	1.83860	π* O3-C6	0.20097	20.35	0.30	0.070
			π* C4-C27	0.37425	12.06	0.30	0.057
	π C8-C18	1.63947	π* O3-C6	0.20097	17.22	0.28	0.064
			π* C10-C23	0.32298	19.02	0.28	0.066
			π* C12-C16	0.28689	19.45	0.29	0.068
	π C10-C23	1.65314	π* C8-C18	0.36581	21.46	0.28	0.070
			π* C12-C16	0.28689	17.77	0.29	0.065
	π C12-C16	1.65158	π* C8-C18	0.36581	19.50	0.28	0.066
			π* C10-C23	0.32298	21.69	0.28	0.070
	π C14-C25	1.69361	π* C4-C27	0.37425	20.61	0.29	0.070
			π* C20-C22	0.38293	16.77	0.29	0.063
	π C20-C22	1.65027	π* C4-C27	0.37425	17.08	0.30	0.064
			π* C14-C25	0.31180	21.22	0.30	0.072
	LP (2) O1	1.87841	π* C20-C22	0.38293	26.58	0.36	0.094
	LP (2) O3	1.88822	σ* C6-C8	0.06548	18.88	0.69	0.103
			σ* C6-C9	0.05888	18.02	0.70	0.102
p-OH	Donor(i)	ED$_i$/e	Acceptor(j)	ED$_j$/e	E$^{(2)}$ kcal/mol	E(j)-E(i)/a.u	F(i.j)/a.u
	π C4-C13	1.64301	π* C5-C15	0.38628	23.27	0.30	0.075
			π* C9-C19	0.28792	15.07	0.30	0.061
	π C5-C15	1.62414	π* C4-C13	0.38565	18.38	0.27	0.062
			π* C7-C21	0.12120	18.26	0.30	0.070
			π* C9-C19	0.28792	20.84	0.28	0.070
	π C6-C23	1.63948	π* O1-C3	0.21011	17.08	0.28	0.064
			π* C11-C27	0.28864	19.49	0.29	0.068
			π* C17-C25	0.32442	19.22	0.28	0.066
	π C7-C21	1.83728	π* O1-C3	0.21011	21.06	0.30	0.071
			π* C5-C15	0.38628	11.52	0.29	0.055
	π C9-C19	1.71275	π* C4-C13	0.38565	22.37	0.28	0.072
			π* C5-C15	0.38628	16.14	0.29	0.063
	π C11-C27	1.65204	π* C6-C23	0.36458	21.80	0.25	0.066
			π* C17-C25	0.32442	24.32	0.25	0.070
	π C17-C25	1.65433	π* C6-C23	0.36458	23.89	0.25	0.070
			π* C11-C27	0.28864	19.96	0.26	0.065
	LP 2 (O1)	1.88850	σ* C3-C6	0.06564	18.96	0.69	0.103
			σ* C3-C7	0.05800	18.55	0.69	0.103
	LP 2 (O2)	1.86766	π* C4-C13	0.38565	28.67	0.35	0.096

Conclusion

This paper presents the main findings of quantum chemical calculations performed on *ortho*-, *meta*- and *para*-substituted chalcones in order to study the effect of substitution position on molecular properties. The bond parameters of the DFT-optimized structures of the relevant isomers were compared with the data available in the literature, and the vibrational allocations of the frequencies were performed by creating theoretical FT-IR spectra. It was observed that the substitution positions of the studied OH-substituted chalcones affected their physicochemical properties and reactivity parameters. With a polarizability value of 296.193 a.u., it was determined that the *para* substitution on the aromatic ring made the molecule more polarizable. However, substituent position variation did not create a considerable distinction in the enthalpy, total energy, and free energy values. Considering the energy gap values, which are an important measure in FMO calculations, the highest values for both vacuum and solvent phases were obtained for the *meta* isomer. Accordingly, in gas phase the chemical reactivity order is predicted as *m*-OH < *p*-OH < *o*-OH. According to results of excited state calculations for the isomers, *ortho*-OH derivative exhibited maximum absorption at 378 nm, while energy required for predominant HOMO → LUMO electronic transition was computed as 3.2805 eV. As a result of *meta*- and *para*-substitution, the λ_{max} value was detected to shift towards slightly lower wavelengths, such as 366.71 and 365.99 nm, respectively. Natural bond orbital analysis was performed to peruse the stabilization energies of various intramolecular interactions of the studied isomers. It is anticipated that the findings obtained in the present study will provide the data needed for future studies. Also, the research outcomes are significant in terms of providing new insights into the effects of the substitution position.

Acknowledgement

Conflicts of interests

There are no conflicts of interest in this work.

References

[1] Narwal S., Devi B., Dhanda T., Kumar S. and Tahlan S., Exploring Chalcone Derivatives: Synthesis and Their Therapeutic Potential, *J. Mol. Struct.,* 1303 (2024) 137554.

[2] Yadav P., Lal K., Kumar A., Guru S.K., Jaglan S., Bhushan S., Green Synthesis and Anticancer Potential of Chalcone Linked-1,2,3-triazoles, *Eur. J. Med. Chem.*, 126 (2017) 944-953.

[3] Wang G., Xue Y., An L., Zheng Y., Dou Y., Zhang L., Liu Y., Theoretical Study on the Structural and Antioxidant Properties of Some Recently Synthesized 2,4,5-trimethoxy Chalcones, *Food Chem.*, 171 (2015) 89-97.

[4] Reddy M.V.B., Hung H.Y., Kuo P.C., Huang G.J., Chan Y.Y., Huang S.C., Wu S.J., Morris-Natschke S.L., Lee K.H. and Wu T.S., Synthesis and Biological Evaluation of Chalcone, Dihydrochalcone, and 1,3-diarylpropane Analogs as Anti-inflammatory Agents, *Bioorg. Med. Chem. Lett.,* 27(7) (2017) 1547-1550.

[5] Sharma C.S., Shekhawat K.S., Chauhan C.S., Kumar N., Synthesis and Anticonvulsant Activity of Some Chalcone Derivatives, *J. Chem. Pharm. Res.*, 5(10) (2013) 450-454.

[6] Parikh K., Joshi D., Antibacterial and Antifungal Screening of Newly Synthesized Benzimidazole-Clubbed Chalcone Derivatives, *Med. Chem. Res.,* 22(8) (2013) 3688-3697.

[7] Abbo H.S., Lai C.H., Titinchi S.J.J., Substituent and Solvent Effects on UV-visible Absorption Spectra of Chalcones Derivatives: Experimental and Computational Studies, *Spectrochim. Acta A Mol. Biomol. Spectrosc.,* 303 (2023) 123180.

[8] Ma L., Yang Z., Li C., Zhu Z., Shen X.,Hu L., Design, Synthesis and SAR Study of Hydroxychalcone Inhibitors of Human β-secretase (BACE1), *J. Enzyme Inhib. Med. Chem.*, 26(5) (2011) 643–648.

[9] Cyboran-Mikołajczyk S., Matczak K., Olchowik-Grabarek E., Sękowski S., Nowicka P., Krawczyk-Łebek A., Kostrzewa-Susłow E., The Influence of the Chlorine Atom on the Biological Activity of 2'-hydroxychalcone in Relation to the Lipid Phase of Biological Membranes - Anticancer and Antimicrobial Activity, *Chem. Biol. Interact.,* 398 (2024) 111082.

[10] Patil P., Zangade S., Synthesis and Comparative Study of Cytotoxicity and Anticancer Activity of Chalconoid-Co(II) Metal Complexes with 2-hydroxychalcones Analogue Containing Naphthalene Moiety, *J. Indian Chem. Soc.*, 99 (2022) 100274.

[11] Bronikowska J., Kłosek M., Janeczko T., Kostrzewa-Susłow E., Czuba Z.P., The Modulating Effect of Methoxy-Derivatives of 2'-hydroxychalcones on the Release of IL-8, MIF, VCAM-1 and ICAM-1 by Colon Cancer Cells, *Biomed. Pharmacother.,* 145 (2022) 112428.

[12] Wilhelm A., Bonnet S.L., Twigge L., Rarova L., Stenclova T., Visser H.G., Schutte-Smith M., Synthesis, Characterization and Cytotoxic Evaluation of Chalcone Derivatives, *J. Mol. Struct.,* 1251 (2022) 132001.

[13] Sahib M.A., Mahdi M.F., Molecular Docking, Synthesis, Characterization and Preliminary Evaluation of some New 3-Ethyl-1H-Indole Derivatives as Potential COX-2 Inhibitors, *Adv. J. Chem. A*, 8(5) (2025) 948-960.

[14] Sandeli A.E., Khiri-Meribout N., Benzerka S., Boulebd H., Gürbüz N., Özdemir N., Özdemir I., Synthesis, Structures, DFT Calculations, and Catalytic Application in the Direct Arylation of Five-Membered Heteroarenes with Aryl Bromides of Novel Palladium-N-Heterocyclic Carbene PEPPSI-Type Complexes, *New J. Chem.*, 45 (2021) 17878-17892.

[15] Frisch M.J., Trucks G.W., Schlegel H.B., Scuseria G.E. et.al. (2016). Gaussian 16 Rev. B.01, Wallingford, CT.

[16] Lee C., Yang W. and Parr R.G., Development of the Colle-Salvetti Correlation-Energy Formula into a Functional of the Electron Density, *Phys. Rev. B.,* 37 (1988) 785–789.

[17] Becke A.D., A New Mixing of Hartree–Fock and Local Density-Functional Theories, *J. Chem. Phys.,* 98 (1993) 1372–1377.

[18] Becke A.D., Density-Functional Thermochemistry. III. The Role of Exact Exchange, *J. Chem. Phys.,* 98 (1993) 5648–5652.

[19] Dennington R., Keith T.A., Millam J.M., GaussView, Version 6 Semichem Inc., Shawnee Mission, KS 2016.

[20] O'Boyle N.M., Tenderholt A.L., Langer K.M.J., cclib: A Library for Package-Independent Computational Chemistry Algorithms, *Comp. Chem.*, 29 (2008) 839.

[21] Tomasi J., Mennucci B., Cammi R., Quantum Mechanical Continuum Solvation Models, *Chem. Rev.*, 105 (2005) 2999–3093.

[22] Casida M.E., Jamorski C., Casida K.C., Salahub D.R., Molecular Excitation Energies to High-Lying Bound States from Time-Dependent Density-Functional Response Theory: Characterization and Correction of the Time-Dependent Local Density Approximation Ionization Threshold, *J. Chem. Phys.*, 108 (1998) 4439–4449.

[23] McQuarrie D.A., Statistical Thermodynamics, Harper & Row Publishers, New York, 1973.

[24] Herzberg G., Molecular Spectra and Molecular Structure III, 1. Edition, D. Van Nostrand Company, Inc., New York, 1964.

[25] Serdaroğlu G., Durmaz S., DFT and statistical mechanics entropy calculations of diatomic and polyatomic molecules, *Indian J. Chem.*, 49 (2010) 861-866.

[26] Koopmans T., Über die zuordnung von wellenfunktionen und eigenwerten zu den einzelnen elektronen eines atoms, *Physica* 1–6 (1934) 104–113.

[27] Parr R.G., Electrophilicity Index, *J. Am. Chem. Soc.,* 121 (1999) 1922-1924.

[28] Parr R.G., Pearson R.G., Absolute Hardness: Companion Parameter to Absolute Electronegativity, *J. Am. Chem. Soc.*, 105 (1983) 7512-7516.

[29] Pearson R.G., Absolute Electronegativity and Hardness Correlated with Molecular Orbital Theory, *Proc. Natl. Acad. Sci. U.S.A*, 83 (1986) 8440-8441.

[30] Perdew J.P. and Levy M., Physical Content of the Exact Kohn-Sham Orbital Energies: Band Gaps and Derivative Discontinuities, *Phys. Rev. Let.*, 51 (1983) 1884-1887.

[31] Perdew J.P., Parr R.G., Levy M. and Balduz J.L, Density-Functional Theory for Fractional Particle Number: Derivative Discontinuities of the Energy, *Phys. Rev. Let.,* 49 (1982) 1691.

[32] Gazquez J.L., Cedillo A. and Vela A., Electrodonating and Electroaccepting Powers, *J. Phys. Chem. A.*, 111(10) (2007) 1966-1970.

[33] Gomez B., Likhanova N.V., Domínguez-Aguilar M.A., Martínez-Palou R., Vela A. and Gazquez J.L., Quantum Chemical Study of the Inhibitive Properties of 2-Pyridyl-azoles, *J. Phys. Chem. B.,* 110(18) (2006) 8928-8934.

[34] Weinhold F., Landis C.R., Glendening E.D., What Is NBO Analysis and How Is It Useful? *Int. Rev. Phys. Chem.*, 35 (2016) 399-440.

[35] Reed A.E., Curtiss L.A. and Weinhold F., Intermolecular Interactions from a Natural Bond Orbital, Donor-Acceptor Viewpoint, *Chem. Rev.* 88(6) (1988) 899-926.

[36] Sahib M.A., Mahdi M.F., Identification of Indole Derivatives as Selective Cyclooxygenase-2 Inhibitors by Virtual Screening and Molecular Dynamic Simulation, *Turkish Comp. Theo. Chem. (TC&TC),* 9(2) (2025) 19-32.

[37] Qiu X.Y., Yang S.L., Liu W.S. and Zhu H.L., (E)-3-(4-hydroxyphenyl)-1-(4-methoxyphenyl) prop-2-en-1-one, *Acta Cryst.* E62 (2006) 3324-3325.

[38] Paixão J.A., Beja A.M., Silva M.R., Alte da Veiga L., Serra A.C., 3-Hydroxybenzaldehyde, *Acta Cryst.* C56 (2000) 1348-1350.

[39] Jasinski J.P., Butcher R.J., Narayana B., Swamy M.T., Yathirajan H.S., Redetermination of 4-hydroxybenzaldehyde, *Acta Cryst.* E64 (2008) o187.

[40] Shubhalaxmi, Hahne S., Zschille C., Jayarama A., Bhat K.S., Crystal Structure Studies and Thermal Characterization of Novel 4-hydroxychalcone Derivative, *Chem. Sci. Trans.*, 2(3) (2013) 841-846.

[41] Prasad A.A., Muthu K., Meenatchi V., Rajasekar M., Agilandeshwari R., Meena K., Manonmoni J.V., Meenakshisundaram S.P., *Spectrochim. Acta A Mol. Biomol. Spectrosc.* 140 (2015) 311–327.

[42] Murray J.S., Sen K., Molecular Electrostatic Potentials: Concepts and Applications, first ed., Elsevier, (Amsterdam, 1996).

[43] Turowska-Tyrk I., Grzesniak K., Trzop E., Zych T., Monitoring Structural Transformations in Crystals. Part 4. Monitoring Structural Changes in Crystals of Pyridine Analogs of Chalcone During [2+2]-Photodimerization and Possibilities of the Reaction in Hydroxy Derivatives, *J. Solid State Chem.*, 174 (2003) 459–465.

[44] Tomečková V., Guzy J., Kušnír J., Fodor K., Mareková M., Chavková Z., Perjési P., Comparison of the Effects of Selected Chalcones, Dihydrochalcones and Some Cyclic Flavonoids on Mitochondrial Outer Membrane Determined by Fluorescence Spectroscopy, *J. Biochem. Biophys. Methods*, 69 (2006) 143–150.

Cumhuriyet Science Journal

Some Factors Affecting Free and Immobilized Amylase Activity

Taner Şahutoğlu [1,a], Derya Kızıloluk [1,b,*]

[1] Department of Biochemistry, Faculty of Science, Sivas Cumhuriyet University, Sivas, Türkiye

*Corresponding author

Research Article

ABSTRACT

In our study, we prepared chitosan beads and immobilized bacterial amylase enzyme on these beads; Parameters such as comparing the optimization conditions (pH, pH stability, temperature, thermal stability, substrate concentration) of free bacterial amylase and amylase immobilized on chitosan beads and investigating the effect of immobilization in its usage areas are included. The immobilized enzyme showed better activity at both lower and higher pH levels compared to the free enzyme. When considering pH stability, the results were consistent with the pH activity values. In other words, both free and immobilized amylase exhibited the highest activity at the same pH levels. However, the free amylase showed less stability at low and high pH levels compared to the immobilized amylase. In terms of temperature-dependent activity, it was found that both free and immobilized enzymes showed the best activity at the same temperature. However, the immobilized enzyme showed activity at higher temperatures than the free enzyme. Moreover, when studying the effect of substrate concentration on free and immobilized enzymes, both types of enzymes exhibited the best activity in the same concentration of starch solution. In this study, factors affecting immobilized and free amylase activity were examined.

Keywords: Chitosan, Amylase, Enzyme immobilization.

a ✉ sahutoglutaner@gmail.com   https://orcid.org/0009-0005-3206-2980   b ✉ deryakiziloluk@cumhuriyet.edu.tr https://orcid.org/0000-0002-0896-6550

Introduction

Enzymes, which are biological catalysts in protein structures, ensure that biological and chemical reactions in living organisms proceed under appropriate and efficient conditions. Enzymes can function outside their natural environment if suitable conditions are provided. They have been successfully utilized in the fields of economy, health, food, cosmetics, industry, and many other everyday applications. The cost-effectiveness of enzyme-catalyzed reactions compared to chemical methods is one of the key reasons for the widespread integration of enzymes into our daily lives [1]. However, its distribution in areas of use is shaped by the activity of enzymes. Some factors affect enzyme activity. Some of these are explained and listed below;

Enzymes show highest activity in a certain pH range. Outside this optimum pH, the activity of enzymes decreases and the reaction rate decreases. The three-dimensional structure of enzymes depends on the pH level. Incorrect pH can cause enzymes to denature (deteriorate their structure). pH can change the binding ability of the substrate by affecting the charge distribution in the active site of the enzyme. This affects the formation of the enzyme-substrate complex. The ionization state of amino acids in the active sites of enzymes depends on pH. This may affect the functionality of the enzymes. Enzymes have evolved to function at various pH levels based on their environment, such as stomach acid or intestinal pH. For these reasons, pH is a critical factor for the activity and functionality of enzymes [2-4].

Enzyme stability involves the balance between the intramolecular interactions of functional groups and their interactions with the environment. These conditions often differ significantly from natural sources of enzymes, such as the presence of organic solvents, unfavorable pH and high ionic strength. This can lead to premature denaturation of enzymes and loss of their activity. For the successful use of enzymes in free or immobilized form, a comprehensive understanding of their long-term stability under various conditions is critical [5-7].

Enzymes show highest activity in certain temperature ranges. At optimum temperature, the reaction rates of enzymes increase. High temperatures can disrupt the structure of enzymes and lead to denaturation. This results in degradation of the enzymes' active sites and loss of functionality. As the temperature increases, the kinetic energy of the enzyme and substrate molecules also increases. This leads to more collisions of molecules, thus increasing the reaction rate. However, after a certain point, this increase in speed can result in denaturation [8,9].

Thermal stability refers to the resistance of enzymes to high temperatures. Some enzymes, especially those from thermophilic organisms, can remain stable at high temperatures, providing an advantage in industrial applications. Enzymes function in different temperature ranges depending on the organisms and environmental conditions in which they are found. Thermal stability makes it possible for them to adapt to these conditions [9,10].

A lot of industrial processes use water-based solutions, and sometimes free enzymes are used as catalysts. When free enzymes are used, it's difficult to recover them from the environment until they have finished their job. This, along with other factors like the contamination of the reaction medium with inhibitors, the limited reusability, and the challenge of removing the enzyme at the right time, makes enzymes expensive and less versatile as catalysts. As a result, using enzymes can drive up costs in industrial settings [11].

The interest in studying enzyme immobilization has grown to tackle various challenges, find effective solutions, and enhance the cost-efficiency and applicability of enzymes, especially in industrial contexts. These studies have been ongoing for almost fifty years. Research on immobilized enzymes has highlighted the role of free enzymes as a bridge connecting immobilized enzymes to their intended applications. However, the primary emphasis has been on the use of immobilized enzymes themselves. In the process of enzyme immobilization, various organic and inorganic substances are utilized as support materials, including chitosan, chitin, cellulose, silica, agarose, phenolic resin, polymers, and bone [12-16]. Many studies in the literature have characterized enzymes by immobilizing them on various supports, with chitosan being one of the most commonly used materials. A comprehensive review outlined the methods for immobilizing catalase enzymes using a range of natural and synthetic polymers, inorganic materials, composite supports, and hybrids. This review emphasized the significance of these immobilization methods in the context of bioreactors and biosensors [17]. Additionally, research has focused on enzyme immobilization and the determination of immobilization conditions using chitosan, a natural polymer derived from the deacetylation of chitin [18,20]. Immobilized enzymes present several advantages compared to free enzymes. Firstly, they can be easily separated from the reaction environment once the reaction is complete, which prevents contamination of the final product. In contrast, free enzymes remain in the reaction environment after the process, potentially affecting the product's quality. Moreover, immobilized enzymes tend to be more resistant to environmental factors such as changes in pH and temperature, making them more stable and reusable. They can also be utilized in continuous processes, allowing for better control over product production and reducing enzymatic degradation. Overall, immobilized enzymes provide a promising solution for continuous multi-step reactions [19,20].

In our study, we utilized chitosan as a support material. Chitosan is a non-toxic and highly biocompatible polymer that is widely used in the biomedical field. Like alginate, chitosan is a biopolymer that can be metabolized in vivo and possesses antitumor properties, as well as the ability to form gels. Additionally, it is effective for treatment due to its bacteriostatic and fungistatic characteristics. Therefore, chitosan and chitin are essential biopolymers for various applications due to their biocompatibility, biological metabolism, adsorption capabilities, and gel-forming properties [20].

In our study, we utilized the bacterial enzyme amylase. This enzyme was selected due to its significant market share, which accounts for nearly half of the industrial enzyme market. Additionally, certain microorganisms produce various enzymes internally to adapt to their environment and then secrete these enzymes through their cell walls. Amylase is one such enzyme, playing a crucial role in breaking down natural raw materials, such as starch. This enzyme, produced through modern methods, has great potential for widespread industrial application and is particularly economically advantageous in a country like Turkey, where there is an abundance of fermentable agricultural residues [21,26].

The bacterial origin of the enzyme contributes to its efficiency and cost-effectiveness, providing it with a significant advantage. Achieving a balance between high efficiency and low cost is challenging for enzymes. Amylase (EC 3.2.1.1) is utilized in various industrial processes, sourced from foods, textiles, paper, and solid waste. This enzyme plays a crucial role in the transformation of starch molecules by hydrolyzing them in the presence of water, resulting in diverse products. Specifically, amylase (1-4-α-glucan-glucanohydrolase) belongs to the hydrolase group, which typically cleaves glycogen and starch-like polysaccharides at alpha-1-4 glycosidic bonds, thereby producing oligosaccharides of various lengths. This enzyme is widely present in many plants, animals, bacteria, and fungi that utilize polysaccharides, making it the primary form of amylase found in humans and other mammals [22].

Amylases and glycoside hydrolases are classified into 13 families. Amylase is a highly valuable industrial enzyme, commonly used in the fruit juice, food, detergent production, pharmaceutical, and textile industries [23-25]. It is also found in seeds that contain starch as a food reserve and is secreted by various fungi.

Material and Method

Chemical Substances Used

Amylase (EC 3.2.1.1) (Sigma- Aldrich), Soluble Starch, (Sigma-Aldrich), Chitosan (Sigma-Aldrich), Sodium Hydroxide- NAOH (Sigma-Aldrich), K/N tartrate (Sigma-Aldrich), Disodium Hydrogen Phosphate Dihydrate- Na_2HPO_4 (ISO-LAB), Sodium Dihydrogen Phosphate Dihydrate- NaH_2PO_4 (ISO-LAB), Boric Acid-H_3BO_3(ISO-LAB), Potassium Chloride- KCl(ISO-LAB), Citric Acid- $C_6H_8O_7$(ISO-LAB), Sodium Citrate, $Na_3C_6H_5O_7$(Merck), DNS (Merck),

Glyoxal (Merck), Glacial Acetic Acid (Sigma-Aldrich), All chemicals used in the study were of analytical purity (≥98%) and double distilled water was used in all stages of the experiments.

Preparation of Chitosan Solution: 3 g of chitosan was suspended in 99 mL of distilled water with a magnetic stirrer. 1 mL of glacial acetic acid was added and stirred for 3 hours at room temperature, and insoluble particles

were separated through a filter. This solution can be used for 1 week at room temperature.

Preparation of Crosslinker Solution: Dissolve 10 g of glyoxal in 250 mL of distilled water. It is dissolved by heating at 80ºC for 10 minutes and cooled at room temperature. This solution is mixed with an equal volume (%4 w/v) of tetrasodium pyrophosphate (pH 8). The solution was prepared fresh and used on the same day.

Preparation of Chitosan Beads

The filtered and rested chitosan solution, which was free of bubbles, was carefully filled into a syringe and slowly dropped into the cross-linker solution one by one (5 mL of cross-linker was dropped into 1 mL of chitosan). The beads were left to mature in this solution for 30 minutes, externally cooled with ice. Then, it was washed 3 times with 0.05 M pH 7 phosphate buffer.

Strengthening of Chitosan Beads with Glutaraldehyde

Freshly prepared beads were incubated in 0.05% (w/v) glutaraldehyde solution for 1 hour. The beads that turned Orange-Brown were washed several times with cold 0.05 M pH 7 phosphate buffer.

Amylase Immobilization into Chitosan Beads

2 mL of stock amylase solution prepared in pH: 7 phosphate buffer at a concentration of 500 ppm was taken. 10 chitosan beads were added and incubated in a shaking incubator for 120 minutes. It was then washed three times with 50 mM phosphate buffer pH:7 to remove unbound enzyme.

$$Q = (C_o - C_1) \backslash m \, X \, Vt \qquad (1)$$

The amount of protein bound to the immobilized support was determined by protein determination. For this purpose, the Bradford (1976) protein determination method was used. The amount of bound protein (Q) was calculated by subtracting the amount of protein remaining after immobilization (C_1) from the initial amount of protein (C_o), dividing by the mass of beads used (m) and multiplying by the total solution volume (Vt) [27].

Investigation of the Activity of Immobilized and Free Amylase in Different Parameters

Amylase activity was determined spectrophotometrically using Bernfeld's partially modified 3,5-dinitrosalicylic acid (DNS) method [7]. 1% soluble starch prepared in 0.05 M pH 7.0 Phosphate buffer was used as the substrate. The components of the standard experimental environment are given in Table 1. and Table 2. Enzyme activity was measured at 530 nm under standard experimental conditions. The amount of reducing sugar formed was calculated from the standard maltose curve. Enzyme activity and specific activity were calculated according to the equations given below.

DNS solution: It was prepared with a ratio of 10g DNS, 16g NaOH, and 300g K/H tartrate (g/L).

1% Starch solution: Weighed 0.1 g of starch, dissolved in 10 mL of 0.05 M phosphate buffer. Heating was applied to dissolve the starch.

$$Volume \ Activity = \frac{Maltose \ (\mu M)}{Incubation \ time \ (dk) \times Enzyme \ Amount \ (mL)} = (U/mL) \qquad (2)$$

$$Specific \ Activity = \frac{Volume \ Activity \ (U/mL)}{mg \ Protein/ \ mL} = (U/mg \ Protein) \qquad (3)$$

The effects of pH, pH stability, temperature and thermal stability on the activity of immobilized and free enzymes were investigated.

Table 1. Free Enzyme Experimental Environment [7].

Sample Tube	Blind Tube
400µL starch	400µL starch
400µL enzyme	-
55°C 20 min. Incubation	55°C 20 min. Incubation
200µL DNS	200µL DNS
-	400µL enzyme
2 min. Cold water bath	2 min. Cold water bath
5 min. Boiling water bath	5 min. Boiling water bath
3 min. Cold water bath	3min. Cold water bath
2000µL distilled water	2000µL distilled water

Table 2. Immobilized Enzyme Experimental Environment [7].

Sample Tube	Blind Tube
400µL starch	400µL starch
10 beads soaked in enzyme	10 empty (non-immobilized) beads
55∘c 20 min. Incubation	55∘c 20 min. Incbation
200µL DNS	200µL DNS
2min. cold water bath	2min. cold water bath
5min. Boiling water bath	5min. Boiling water bath
3min. Cold water bath	3min. Cold water bath
2000µL distilled water	2000µL distilled water

Effect of pH on Immobilized and Free Amylase Enzyme Activity

To determine the optimum pH of free and immobilized amylase, measurements were made using substrate solutions prepared in buffers at different pHs (pH: 4, 5, 6, 7, 8, 9) at the optimum temperature (55 ℃) using the experimental environment described in Table 1. and Table 2. Activity calculations were made and graphs were drawn.

Effect of pH Stability on Immobilized and Free Amylase Enzyme Activity

Free and immobilized amylase were incubated for 1 hour at different pH (pH: 4, 5, 6, 7, 8, 9) and measurements were taken using the experimental environment specified in Table 1. and Table 2. Activity calculations were made and graphs were drawn.

Effect of Temperature on Immobilized and Free Amylase Enzyme Activity

Temperature-dependent activity analysis of free and immobilized enzyme was performed. The construction phase of this experiment is as follows: Activity was measured and graphs were drawn under optimal conditions, provided that the incubation time and other steps in the 3rd step (20 min incubation at 55°C) in Table 1. and Table 2. remained constant and the temperature was changed (25- 35- 45- 55- 65- 75°C).

Effect of Thermal Stability on Immobilized and Free Amylase Enzyme Activity

Free and immobilized amylase were incubated at different temperatures (25- 35- 45- 55- 65- 75°C) for 1 hour before the experimental environment. After incubation, activities under optimal conditions were measured, calculated and graphed.

Results and Discussion

Effect of pH on Immobilized and Free Amylase Enzyme Activity

As a result of this experiment, free amylase showed 100% activity at pH: 7, while immobilized amylase showed 100% activity at pH 9. While the free enzyme was denatured at pH: 4, on the contrary, the immobilized enzyme showed activity at the same pH value. All values are shown in Table 3. These values are shown on the graph in Figure 1.

Table 3. Activity% Values of Free and Immobilized Amylase at Different pH

pH Value	Free Amylase Activity %	Immobilized Amylase Activity %
4	0	24,68
5	12,65	34,92
6	55,83	61,24
7	100,00	78,74
8	97,99	97,95
9	92,97	100,00
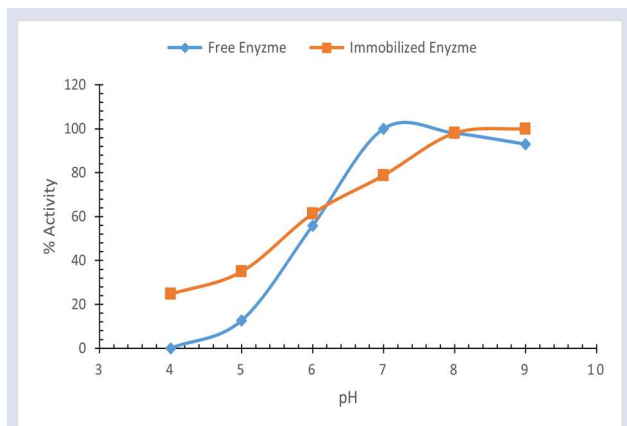
Figure 1. pH Value versus Activity % Value of Free and Immobilized Amylase

Effect of pH Stability on Immobilized and Free Amylase Enzyme Activity

While free amylase was found to have the highest stability at pH 7, immobilized amylase was found to have the highest stability at pH 9. Free amylase was not stable at pH: 4, immobilized amylase, on the contrary, showed low stability at pH: 4. The pH stability of the immobilized enzyme is higher than the stability of the free enzyme. All values are shown in Table 4. These values are shown on the graph in Figure 2.

Table 4. Activity % Values of Free and Immobilized Amylase at Different pHs

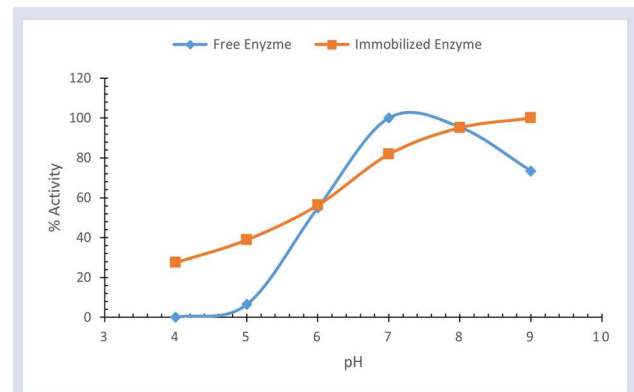| pH Value	Free Activity- Stability %	Immobilized Activity- Stability %
4	0	27,48
5	6,46	38,92
6	54,96	56,32
7	100,00	81,84
8	95,38	95,14
9	73,44	100,00

Figure 2. pH value versus Activity % value of free and immobilized amylase

Effect of Temperature on Immobilized and Free Amylase Enzyme Activity

When the % activity values of free and immobilized amylase depending on temperature were examined, it was observed that both enzymes reached 100% activity at 55°C. Both enzymes showed activity at all temperatures, most of which were different from each other. All values are shown in Table 5. The figure covering these data is drawn in Figure 3.

Table 5. Activity % Values of Free and Immobilized Amylase at Different Temperatures

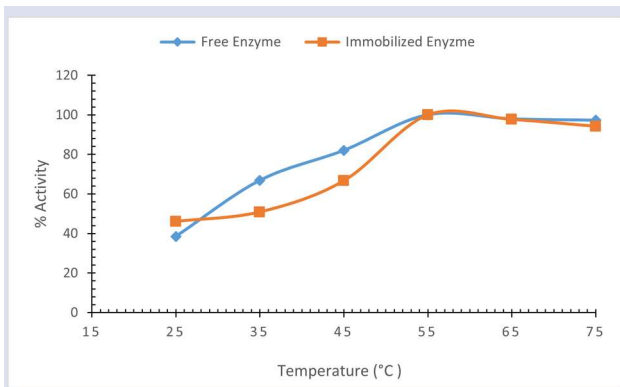| Temperature °C	Free Amylase Activity %	Immobilized Amylase Activity %
25	38,45	46,13
35	66,80	50,93
45	82,00	66,72
55	100,00	100,00
65	97,93	97,72
75	97,237	94,23

Figure 3. Temperature value versus Activity % value of free and immobilized amylase

The optimum temperature was found to be the same 55°C for both enzymes.

Effect of Thermal Stability on Immobilized and Free Amylase Enzyme Activity

After free and immobilized amylase were incubated for 1 hour under known optimum conditions and at different temperatures, activity measurements were made under optimal conditions. A graph of % activity versus temperature was drawn. As a result, both immobilized enzyme and free enzyme showed the best stability between 55°C and 75°C. Both forms of the enzyme showed stability at all temperatures. All values are shown in Table 6. These values are shown on the graph in Figure 4.

Table 6. Activity-Stability % Values of Free and Immobilized Amylase at Different Temperatures

Temperature ºC	Free Activity- Stability %	Immobilized Amylase Activity- Stability %
25	27,76886	35,55369
35	51,84591	47,61008
45	73,51525	75,69218
55	100	93,26022
65	98,39486	97,30234
75	98,39486	100
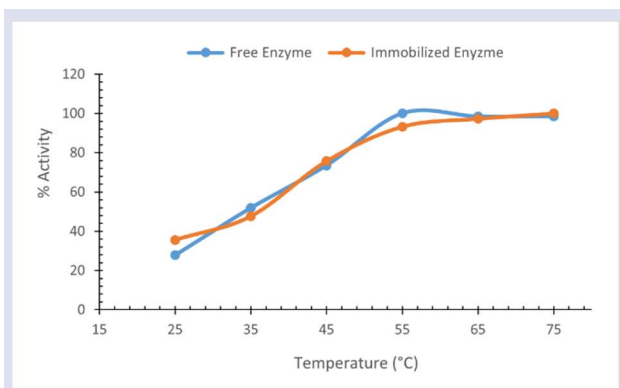
Figure 4. Temperature value of free and immobilized amylase versus Activity-Stability % value

Conclusion

Experiments were performed using different pHs to investigate the effect of pH and pH stability on free amylase and immobilized amylase activity. The optimum pH of the free amylase enzyme was 7, and the optimum pH of the immobilized amylase was 9. Both enzyme forms showed maximum stability at their respective optimum pHs. The variation of maximum activity values with pH is shown in Figure 1 and Figure 2. These figures show a decrease in the maximum activity of free amylase enzyme in acidic and basic regions. One factor that most affects enzymatic reaction rates is the pH of the environment. This enzyme, which has electrolyte properties and therefore enzyme activity is affected by pH, also contains acidic and basic groups in its molecules such as substrate and coenzyme. For this reason, enzymes, substrates, and coenzymes will inevitably be affected by pH. The resulting pH changes affect the stability of the enzyme-substrate complex. Stability and reaction speed are directly proportional. The more stable an enzyme+ substrate complex, the closer the reaction rate is to a maximum. Optimum pH is the pH value at which the enzyme is most active. The enzyme draws a pH curve in the form of a bell curve, the activity and reaction rate of the enzyme irreversibly decreases to zero at the end of both sides of the pH and the enzyme denatures. The optimum pH for enzymes varies depending on various conditions. Factors that cause changes in optimal pH include the source of the enzyme, the type and concentration of substrate on which the enzyme is used, temperature, type of cofactor, and time. The enzyme is not stable at all pH values. Every enzyme has a pH at which it maintains its stability [16,17]. On the other hand, different interactions may occur between enzymes and polymeric support materials. It is known that forces affect pH [18-20].

In our study, amylase was immobilized on chitosan beads as solid support material. Thus, the enzyme was made usable at higher pH values. Because the immobilized enzyme is active at every pH studied, it provides advantages in every field where it is used.

Experiments were carried out at different temperatures to investigate the thermal stability of free and immobilized amylase activity. The optimum temperature of both enzyme forms was determined as 55°C. In thermal stability, this temperature remained at 55°C for the free enzyme, while it was observed at 75°C for the immobilized enzyme. The change of maximum activity-stability values with temperature is shown in Figure 3 and Figure 4. Looking at these figures, a decrease in the maximum activity of free amylase enzyme was observed in regions where the temperature was low and high.

The activities of the enzymes in both forms at their optimum temperatures were accepted as 100% and the other percentages were calculated according to this value. The free and immobilized enzyme showed activity at all temperatures. In free enzyme, when the temperature is lowered or higher than 55°C, the activity decreases, and

when the temperature rises above a certain temperature, the activity of the enzyme drops to zero and the enzyme is irreversibly denatured. However, at low temperatures, when the enzyme freezes or something similar, the enzyme activity reversibly drops to zero, that is, when the temperature is increased to normal conditions again, the enzyme will show activity again, and this is valid for both immobilized and free amylase. The temperature stability of immobilized enzymes is one of the most important reasons for using immobilized enzymes. Enzymes that are immobilized through cross-linking are more resistant to high temperatures compared to free enzymes. This ensures that the immobilized enzyme has constant activity for a certain period during use, facilitating control of the process.

The conformational flexibility of enzymes is affected by immobilization. Immobilization reduces the flexibility of the enzyme and increases its rigidity. This usually manifests itself as increased stability against increasing temperatures. Many studies have shown that the temperature stability of immobilized enzymes, where immobilization reduces their conformational flexibility, is higher than that of free enzymes [21]. Generally, a 10°C increase in temperature approximately doubles the reaction rate. The same situation is observed in biochemical reactions where enzymes in protein structures begin to denature at certain temperatures (above 50 °C) [22]. As the temperature increases, first the tertiary structure and then the secondary structure (α-helical structure) of the enzyme molecule collapse. The active site of the enzyme is also affected by these events and the enzyme loses its activity. When all these are evaluated; The fact that the immobilized enzyme is more stable at higher temperatures than the free enzyme allows this enzyme to be used at high temperatures in its areas of use, thus reducing the cost when considered with pH. This allows it to be more preferred in areas of use.

The narrow parameter ranges of the free enzyme cause the use of the enzyme to be costly. In the experiments, it is seen that the parameter ranges expand with immobilization. This result supports that, with immobilization, the enzyme can now be used under more challenging operating conditions. The immobilization studies were carried out successfully. This study, which can be considered at the initial level in the literature, has been a step towards increasing working conditions to further levels by expanding them.

References

[1] Telefoncu A., Enzimoloji Lisansüstü Yaz Okulu (Ed) Telefoncu A. İçinde: İmmobilize Enzimler. *Ege Üniversitesi. Fen Fakültesi Baskı Atölyesi,* İzmir (1997). 193-248.

[2] Saraydın D., Isıkver Y., and Karadag E. Adsorption of Phenazine Dyes Using Poly (hydroxamic acid) .*Hydrogels from Aqueous Solutions Polymer Engıneerıng and Scıence,* (2018). 310-318

[3] LiuB., Yang Y. H., Wu Z. Y., Wang H., Shen G. L., Yu R. Q.,"A Potentiometric Acetylcholinesterase Biosensor Based on Plasma-Polymerized Film*", Sensors and Actuators B.,* 104 (2005) 186-190.

[4] Doonng R.A., Tsai H. C., "Immobilization and Characterization of Sol-GelEncapsulated Acetylcholinesterase Fiber Optic Biosensor*", Analytica Chimica Acta,* 434 (2001) 239-246

[5] Özçömlekçi E., "Proteaz Enziminin Glutaraldehit Kullanarak Kovalent Bağlanma İle İmmobilazasyonunda Optimum Şartların Belirlenmesi", *Yüksek Lisans Tezi, İstanbul Teknik Üniversitesi Fen Bilimleri Enstitüsü*, İstanbul, Türkiye, (2006).

[6] Tekman Ş., Öner N., *"Genel Biyokimya", İstanbul Üniversitesi Eczacılık Fakültesi,* İstanbul, (1994) 47-49

[7] Bernfeld P., Amylases, alpha and beta. In: Colowick, S.P. and Kaplan, N.O (eds.). Methods in enzymology. New York: *Academic Press.* (1955). v.1 149- 158.

[8] Ali I., Akbar A., Yanwisetpakdee B., Prasongsuk S., Lotrakul P., Punnapayak H., Purification, characterization, and potential of saline waste water remediation of a polyextremophilic α-amylase from an obligate halophilic Aspergillus gracilis, *BioMed. Research International,* (2014) 106937.

[9] Parashar D., Satyanarayana T., A chimeric α-amylase engineered from Bacillus acidicola and Geobacillus thermoleovorans with improved thermostability and catalytic efficiency, *Journal of Industrial Microbiology and Biotechnology*, 43(4) (2016) 473-484.

[10] Sindhu R., Binod P., Madhavan A., Beevi U. S., Mathew A. K., Abraham A., Pandey A., Kumar V., Molecular improvements in microbial α-amylases for enhanced stability and catalytic efficiency, *Bioresource Technology,* 245 (2017) 1740- 1748.

[11] Başak E., Modifiye edilmiş kitosan boncuklar büzerinde katalaz immobilizasyon, *Yüksek lisans tezi,Celal Bayar Üniversitesi Kimya Bölümü,* MANİSA. (2011).

[12] Iyengar L., Prabhakara R., Urease bound to chitin with glutaraldehyde, *Biotechnology and Bioengineering.* 21 (1979) 1333-1343.

[13] Hoffmann C., Pinelo M., Woodley J. M., Daugaard A. E., Development of a thiol- ene based screening platform for enzyme immobilization demonstrated using horseradish peroxidase, *Biotechnology Progress*, 33(5) (2017) 1267-1277.

[14] Gusek T.V., Tyn M.T., Kinsella J.E., Immobilizatiom of serine protease from thermomonospora fusca YX on porous glass, *Biotechnology and Bioengineering,* 36 (1990) 411-416.

[15] Kery V., Haplova J., Tıhlarık K.J., Factors influencing the activity and thermostability of immobilized porcine pancreatic lipase, *Journal of Chemical Technology and Biotechnology,* 48 (1990) 201-207.

[16] Zucca P., Sanjust E., Inorganic Materials as Supports for Covalent Enzyme Immobilization: *Methods and Mechanisms. Molecules,* 19(9) (2014) 14139-14194

[17] Grigoras A. G., Catalase immobilization—A review, *Biochemical Engineering Journal,* 117 (2017) 1–20.

[18] Cao L., Immobilized enzymes: science or art?, *Current Opinion in Chemical Biology*, 9(2) (2005) 217-226.

[19] Vaghari H., Jafarizadeh- Malmırı H., Mohammadlou M., Berenjian A., Anarjan N., Jafari N., Nasiri S., Application of Magnetic Nanoparticles in Smart Enzyme Immobilization, *Biotechnology Letters*, 38(2) (2016) 223–233.

[20] Andersson L., Studies on starch structure and the differential properties of starch branching enzymes, PhD Thesis, *Swedish University of Agricultural Sciences*, Uppsala, 36 (2001).

[21] Zdarta J., Meyer A. S., Jesionowski T., Pinelo M. A., General overview of support materials for enzyme immobilization: characteristics, properties, practical utility, *Catalysts,* 8(2) (2018) 92.

[22] Yarar Ü., α-Amilaz Enziminin Fotoimmobilizasyonu, Yüksek Lisans Tezi, Marmara Üniversitesi, İstanbul (2008).

[23] Najafi M. F., Deobagkar D., Deobagkar,D., Purification and characterization of an extracellular α-amylase from Bacillus subtilis AX20, *Protein Expression and Purification*. 41 (2005) 349-354.

[24] Rana N., Walia A., Gaur A., α-Amylases from microbial sources and its potential applications in various industries, *National Academy Science Letters*, 36(1) (2013) 9-17.

[25] Kalia S., Avérous L., Biopolymers: Biomedical and Environmental Applications*,* Massachusetts, USA: John Wiley & Sons. (2011).

[26] Sharma A., Satyanarayana T., Microbial acid-stable α-amylases: characteristics, genetic engineering and applications, *Process Biochemistry*, 48(2) (2013) 201-211.

[27] Çetinus Ş. A., Şahin E., Saraydin D., Preparation of Cu (II) adsorbed chitosan beads for catalase immobilization, *Food Chemistry*, 114(3) (2009) 962-969.

Cumhuriyet Science Journal

On the Semi-analytical and Hybrid Methods for the Drinfeld-Sokolov-Wilson System Modelling Dispersive Water Waves

Emre Aydın [1,a], İnci Çilingir Süngü [2,b, *]

[1] Department of Mathematics, Ondokuz Mayıs University, Samsun, Türkiye.
[2] Department of Mathematics Education, Ondokuz Mayıs University, Samsun, Türkiye.
*Corresponding author

Research Article

ABSTRACT

In this study, modified variational iteration method (MVIM), modified variational iteration Laplace transform method (MVILTM) and modified variational iteration Sumudu transform method (MVISTM) are used to examine the Drinfeld-Sokolov-Wilson (DSW) system. Semi-analytical solutions have been obtained and compared with the analytical solutions. Moreover, it illustrates the effect of wave parameter on the approximate solutions. The exact solutions and semi-analytical solutions of the DSW system are compared with each other. Tables give maximum errors of semi-analytical solutions for various iteration values. The comparison of relative errors for various iteration values and the effect of change of wave constant is visualized by figures. Also, it commented on the effectiveness and usefulness of the methods when applied to the DSW system.

Keywords: Modified Variational İteration Method (MVIM), Modified Variational İteration Laplace Transform Method (MVILTM), Modified Variational İteration Sumudu Transform Method (MVISTM), The Drinfeld-Sokolov-Wilson (DSW) System.

[a] ✉ emre_aydn_55@outlook.com (ID) https://orcid.org/0000-0001-7480-0965 [b] ✉ incicilingir@gmail.com (ID) https://orcid.org/0000-0001-7788-181X

Introduction

It is applied nonlinear systems of partial differential equations in scientific fields such as plasma physics, plasma waves, solid state physics, fluid mechanics, chemical physics. The purpose of this study is to analyze as semi-analytical the solutions of the Drinfeld-Sokolov-Wilson (DSW) System, which is one of the nonlinear partial differential equation systems. Drinfeld and Sokolov [1], Wilson [2], Drinfeld and Sokolov [3] were introduced firstly the DSW model having an important role in fluid dynamics. A generalized form of the DSW system is given by:

$$\begin{cases} u_t + \alpha v v_x = 0 \\ v_t + \beta v_{xxx} + \gamma u v_x + \varepsilon u_x v = 0. \end{cases} \tag{1}$$

Here α, β, γ and ε are real parameters. The coupled of DSW is a system that modeling of dispersive water waves and it is used a model the translation of shallow water waves. Recently, many studies have been conducted on the DSW model. Gao et al. [4] used q-Homotopy analysis transform method, Saifullah et al. [5] used the Laplace transform combined with Adomian decomposition method, Arora and Kumar [6] used Homotopy analysis method, Azizi and Pourgholi [7] used Sine-Cosine wavelets method, Salim et al. [8] used modified Adomian decomposition method, Eskandari and Taghizadeh [9] used the exp-function method and the rational (G'/G)-expansion method, Ali et al. [10] used new iteration method, Taghizadeh and Neirameh [11] investigated the new complex solutions, Raslan and Entesar [12] used Banach contraction method, Lindeberg et al. [13] used finite difference method, Zhang and Zhao [14] used Lie symmetry analysis and Lie-bäcklund symmetries, Singh et al.

[15] used homotopy perturbation transform method, Al-Rozbayani and Ali [16] used Sumudu transform with Adomian decomposition method, Alam et al. [17] used $S(\xi)$-expansion method, Usman et al. [18] examined Jacobi elliptic solutions, Shahzad et al. [19] used Φ^6-model expansion method, Iqbal et al. [20] examined multiple solitary wave solutions, Younis et al. [21] used improved finite difference technique via Adominian polynomial, Aydemir [22] used generalized unified method, Hakkaev [23] examined spectral stability of periodic waves.

MVIM is a method that uses variational principles by transforming nonlinear terms into power series [24-26]. Respectively, MVILTM and MVISTM are methods obtained by hybridizing the MVIM with Laplace and Sumudu transform. Laplace and Sumudu transform methods are well-known and useful in many problems in which applied mathematics, physics, science and engineering. Also, these methods are suitable to hybrid the variational methods.

In this study, modified variational iteration method, modified variational iteration Laplace transform method and modified variational iteration Sumudu transform method are used to solve semi-analytically the Drinfeld-Sokolov-Wilson system and compare the results. The maximum and relative errors of proposed methods are evaluated and the results are interpreted. The effect of the wave parameter that emerged in the solution of the DSW system for different iteration values in an example is examined with the help of tables and figures.

Material and Method

In this section, the basic idea of modified variational iteration method (MVIM), modified variational iteration Laplace transform method (MVILTM), modified variational iteration Sumudu transform method (MVISTM) will be introduced. Drinfeld-Sokolov-Wilson (DSW) system can be written to explain the basics of MVIM, MVILTM and MVISTM in the following operator form.

$$\begin{cases} L_t u + Nu = 0 \\ L_t v + R_x v + Nv = 0, \end{cases} \tag{2}$$

where $L_t = \frac{\partial}{\partial t}$, $R_x = \beta \frac{\partial^3}{\partial x^3}$ represent linear differential operators and the notation, $Nu = \alpha v v_x$, $Nv = \gamma u v_x + \varepsilon u_x v$ represent nonlinear differential operator.

Modified Variational Iteration Method

The correction functional for Eq. (2) is given by:

$$\begin{cases} u_{n+1}(x,t) = u_0(x,t) + \int_0^t \lambda[Nu_n(x,s)]\,ds \\ v_{n+1}(x,t) = v_0(x,t) + \int_0^t \lambda[R_x v_n(x,s) + Nv_n(x,s)]\,ds. \end{cases} \tag{3}$$

Here λ is a Lagrange multiplier. For $L_t = \frac{\partial^m}{\partial t^m}$, the Lagrange multiplier is given by [27]:

$$\lambda(x,t) = \frac{(-1)^m}{(m-1)!}(t-x)^{m-1}, m \geq 1. \tag{4}$$

Initial approximate functions u_0, v_0 be taken as $u(x,0)$ and $v(x,0)$ respectively. To avoid computational overhead and unnecessary terms, system in Eq. (3) is rearranged in the form:

$$\begin{cases} u_{n+1} = u_0 + \int_0^t \lambda[G_{n-1}]\,ds + \int_0^t \lambda[G_n - G_{n-1}]\,ds \\ v_{n+1} = v_0 + \int_0^t \lambda[R_x v_{n-1} + J_{n-1}]\,ds + \int_0^t \lambda[R_x(v_n - v_{n-1}) + J_n - J_{n-1}]\,ds. \end{cases} \tag{5}$$

By further simplifying and taking $\lambda(x,t) = -1$, system in Eq. (5) is rearranged in the form:

$$\begin{cases} u_{n+1} = u_n - \int_0^t [G_n - G_{n-1}]\,ds \\ v_{n+1} = v_n - \int_0^t [R_x(v_n - v_{n-1}) + J_n - J_{n-1}]\,ds. \end{cases} \tag{6}$$

Here G_n and J_n can be obtained from the following series expansion of nonlinear terms and are convergent functions. So,
$Nu_n = G_n + \text{o}(t^{n+1})$, $Nv_n = J_n + \text{o}(t^{n+1})$, $n = 0,1,\dots$, $G_{-1} = J_{-1} = 0$.
System in Eq. (6) is called the modified correction functional. Consequently, the components $u_0, u_1, u_2, u_3, \dots$ and $v_0, v_1, v_2, v_3, \dots$ are identified and the semi-analytical solutions of the DSW system are determined entirely. The convergence occurs without any conditions. That is, $\lim_{n\to\infty} u_n = u(x,t)$ and $\lim_{n\to\infty} v_n = v(x,t)$.

Modified Variational Iteration Laplace Transform Method

Definition 1. For $\forall t \geq 0$, the Laplace transform of the function $f(t)$ defined is given by [28]:

$$\mathcal{L}\{f(t)\} = F(s) = \int_0^\infty e^{-st} f(t)dt. \tag{7}$$

Taking the Laplace transform of both sides of the system in Eq. (2) and using the derivative properties of the Laplace transform, the system is rewritten as:

$$\begin{cases} \mathcal{L}_t\{u_t\} + \mathcal{L}_t\{\alpha v v_x\} = 0 \\ \mathcal{L}_t\{v_t\} + \mathcal{L}_t\{\beta v_{xxx} + \gamma u v_x + \varepsilon u_x v\} = 0 \end{cases} \tag{8}$$

$$\Rightarrow \begin{cases} sU(x,s) - u(x,0) + \mathcal{L}_t\{\alpha v v_x\} = 0 \\ sV(x,s) - v(x,0) + \mathcal{L}_t\{\beta v_{xxx} + \gamma u v_x + \varepsilon u_x v\} = 0. \end{cases} \tag{9}$$

By rearranging system in Eq. (9), it can be written as:

$$\begin{cases} U(x,s) = \frac{1}{s}u(x,0) - \frac{1}{s}\mathcal{L}_t\{\alpha v v_x\} \\ V(x,s) = \frac{1}{s}v(x,0) - \frac{1}{s}\mathcal{L}_t\{\beta v_{xxx} + \gamma u v_x + \varepsilon u_x v\}. \end{cases} \tag{10}$$

Taking the inverse Laplace transform of both sides of the Eq. (10), it can be rewritten:

$$\begin{cases} \mathcal{L}_t^{-1}\{U(x,s)\} = \mathcal{L}_t^{-1}\left\{\frac{1}{s}u(x,0)\right\} - \mathcal{L}_t^{-1}\left\{\frac{1}{s}\mathcal{L}_t\{\alpha v v_x\}\right\} \\ \mathcal{L}_t^{-1}\{V(x,s)\} = \mathcal{L}_t^{-1}\left\{\frac{1}{s}v(x,0)\right\} - \mathcal{L}_t^{-1}\left\{\frac{1}{s}\mathcal{L}_t\{\beta v_{xxx} + \gamma u v_x + \varepsilon u_x v\}\right\}. \end{cases} \quad (11)$$

By rearranging system in Eq. (11), it can be written as follows:

$$\begin{cases} u(x,t) = u(x,0) - \mathcal{L}_t^{-1}\left\{\frac{1}{s}\mathcal{L}_t\{\alpha v v_x\}\right\} \\ v(x,t) = v(x,0) - \mathcal{L}_t^{-1}\left\{\frac{1}{s}\mathcal{L}_t\{\beta v_{xxx} + \gamma u v_x + \varepsilon u_x v\}\right\}. \end{cases} \quad (12)$$

Taking first derivative of both sides of the system in Eq. (12) with respect to t, it can be as follows:

$$\begin{cases} u_t + \frac{\partial}{\partial t}\mathcal{L}_t^{-1}\left\{\frac{1}{s}\mathcal{L}_t\{\alpha v v_x\}\right\} = 0 \\ v_t + \frac{\partial}{\partial t}\mathcal{L}_t^{-1}\left\{\frac{1}{s}\mathcal{L}_t\{\beta v_{xxx} + \gamma u v_x + \varepsilon u_x v\}\right\} = 0. \end{cases} \quad (13)$$

The modified correction functional of system in Eq. (13) is given by

$$\begin{cases} u_{n+1} = u_n - \int_0^t [G_n - G_{n-1}]\, ds \\ v_{n+1} = v_n - \int_0^t [J_n - J_{n-1}]\, ds. \end{cases} \quad (14)$$

G_n and J_n can always be obtained from the series expansion of nonlinear terms and are convergent functions. That is,

$$\begin{cases} \frac{\partial}{\partial t}\mathcal{L}_t^{-1}\left\{\frac{1}{s}\mathcal{L}_t\{\alpha v v_x\}\right\} = G_n + o(t^{n+1}) \\ \frac{\partial}{\partial t}\mathcal{L}_t^{-1}\left\{\frac{1}{s}\mathcal{L}_t\{\beta v_{xxx} + \gamma u v_x + \varepsilon u_x v\}\right\} = J_n + o(t^{n+1}) \\ u_0 = u(x,0), v_0 = v(x,0), n = 0,1,\dots, \; G_{-1} = J_{-1} = 0. \end{cases} \quad (15)$$

By continuing the iteration process, convergence to the exact solution of the DSW system via modified variational iteration Laplace transform method (MVILTM) occurs without any conditions. That is, $\lim_{n\to\infty} u_n = u(x,t)$ and $\lim_{n\to\infty} v_n = v(x,t)$.

Modified Variational Iteration Sumudu Transform Method

Definition 2. For set $A = \left\{f(t): \exists K, t_1, t_2 > 0, |f(t)| \le K e^{\frac{|t|}{t_n}}, if\ t \in \{(-1)^n x[0,\infty]\}\right\}$, Sumudu transform of the function $f(t)$ is given by [29]:

$$S\{f(t)\} = F(\epsilon) = \int_0^\infty e^{-t} f(\epsilon t)\, dt. \quad (16)$$

Taking the Sumudu transform of both sides of the system in Eq. (2) and using the derivative properties of the Sumudu transform, the system is rewritten as follows:

$$\begin{cases} S_t\{u_t\} + S_t\{\alpha v v_x\} = 0 \\ S_t\{v_t\} + S_t\{\beta v_{xxx} + \gamma u v_x + \varepsilon u_x v\} = 0 \end{cases} \quad (17)$$

$$\Rightarrow \begin{cases} \frac{1}{\epsilon}U(x,\epsilon) - \frac{1}{\epsilon}u(x,0) + S_t\{\alpha v v_x\} = 0 \\ \frac{1}{\epsilon}V(x,\epsilon) - \frac{1}{\epsilon}v(x,0) + S_t\{\beta v_{xxx} + \gamma u v_x + \varepsilon u_x v\} = 0. \end{cases} \quad (18)$$

By rearranging system in Eq. (18), it can be written as follows:

$$\begin{cases} U(x,\epsilon) = u(x,0) - \epsilon S_t\{\alpha v v_x\} \\ V(x,\epsilon) = v(x,0) - \epsilon S_t\{\beta v_{xxx} + \gamma u v_x + \varepsilon u_x v\}. \end{cases} \quad (19)$$

Taking the inverse Sumudu transform of both sides of the system in Eq. (19), it can be rewritten.

$$\begin{cases} S_t^{-1}\{U(x,\epsilon)\} = S_t^{-1}\{u(x,0)\} - S_t^{-1}\{\epsilon S_t\{\alpha v v_x\}\} \\ S_t^{-1}\{V(x,\epsilon)\} = S_t^{-1}\{v(x,0)\} - S_t^{-1}\{\epsilon S_t\{\beta v_{xxx} + \gamma u v_x + \varepsilon u_x v\}\}. \end{cases} \quad (20)$$

By rearranging system in Eq. (20), it can be written as follows:

$$\begin{cases} u(x,t) = u(x,0) - \mathcal{S}_t^{-1}\{\epsilon\mathcal{S}_t\{\alpha v v_x\}\} \\ v(x,t) = v(x,0) - \mathcal{S}_t^{-1}\{\epsilon\mathcal{S}_t\{\beta v_{xxx} + \gamma u v_x + \varepsilon u_x v\}\}. \end{cases} \tag{21}$$

Taking first derivative of both sides of the system in Eq. (21) with respect to t, it can be as follows:

$$\begin{cases} u_t + \frac{\partial}{\partial t}\mathcal{S}_t^{-1}\{\epsilon\mathcal{S}_t\{\alpha v v_x\}\} = 0 \\ v_t + \frac{\partial}{\partial t}\mathcal{S}_t^{-1}\{\epsilon\mathcal{S}_t\{\beta v_{xxx} + \gamma u v_x + \varepsilon u_x v\}\} = 0. \end{cases} \tag{22}$$

The modified correction functional of system in Eq. (22) is given by

$$\begin{cases} u_{n+1} = u_n - \int_0^t [G_n - G_{n-1}]\, ds \\ v_{n+1} = v_n - \int_0^t [J_n - J_{n-1}]\, ds. \end{cases} \tag{23}$$

G_n and J_n can be found from the following convergent series expansion

$$\begin{cases} \frac{\partial}{\partial t}\mathcal{S}_t^{-1}\{\epsilon\mathcal{S}_t\{\alpha v v_x\}\} = G_n + o(t^{n+1}) \\ \frac{\partial}{\partial t}\mathcal{S}_t^{-1}\{\epsilon\mathcal{S}_t\{\beta v_{xxx} + \gamma u v_x + \varepsilon u_x v\}\} = J_n + o(t^{n+1}) \\ u_0 = u(x,0), v_0 = v(x,0), n = 0,1,\dots,\ G_{-1} = J_{-1} = 0. \end{cases} \tag{24}$$

By continuing the iteration process, convergence to the exact solution of the DSW system via modified variational iteration Sumudu transform method (MVISTM) occurs without any conditions. That is, $\lim\limits_{n\to\infty} u_n = u(x,t)$ and $\lim\limits_{n\to\infty} v_n = v(x,t)$

Numerical Experiments and Simulations

In this section, we will examine the following initial value problem for the specific parameters of the Drinfeld-Sokolov-Wilson system in Eq.(1) and get semi-analytical solutions and errors of DSW system with MVIM, MVILTM and MVISTM. Considering the different values of the c wave parameter, the relative errors of the proposed methods for various iteration values will be given with the help of figures.

Example 1. The DSW system with initial value problem for $\alpha = 3, \beta = \gamma = 2, \varepsilon = 1$ in the system in Eq. (1) is given by

$$\begin{cases} u_t + 3v v_x = 0 \\ v_t + 2v_{xxx} + 2u v_x + u_x v = 0 \\ u(x,0) = 0.3\,\text{sech}^2(\sqrt{0.1}x), v(x,0) = 0.2\,\text{sech}(\sqrt{0.1}x). \end{cases} \tag{25}$$

For $c = 0.2$, exact solutions of the DSW system given with initial value problem are

$$u(x,t) = \frac{3c}{2}\,sech^2\left(\sqrt{\frac{c}{2}}(x - ct)\right),\ v(x,t) = c\,\text{sech}\left(\sqrt{\frac{c}{2}}(x - ct)\right). \quad [30]$$

Semi-analytical solutions founded by MVIM for Eq. (25) can be written as follows.

$$u_0 = \frac{0.3000000000}{\cosh(0.3162277660x)^2}$$

$$u_1 = \frac{0.3000000000}{\cosh(0.3162277660x)^2} + \frac{0.03794733192\sinh(0.3162277660x)t}{\cosh(0.3162277660x)^3}$$

$$u_2 = \frac{0.3000000000}{\cosh(0.3162277660x)^2} + \frac{0.03794733192\sinh(0.3162277660x)t}{\cosh(0.3162277660x)^3} + \frac{0.002400000000t^2}{\cosh(0.3162277660x)^2}$$
$$- \frac{0.003600000000t^2}{\cosh(0.3162277660x)^4}$$

$$v_0 = \frac{0.2000000000}{\cosh{(0.3162277660x)}}$$

$$v_1 = \frac{0.2000000000}{\cosh{(0.3162277660x)}} + \frac{0.01264911064\sinh{(0.3162277660x)}t}{\cosh{(0.3162277660x)}^2}$$

$$v_2 = \frac{0.2000000000}{\cosh{(0.3162277660x)}} + \frac{0.01264911064\sinh{(0.3162277660x)}t}{\cosh{(0.3162277660x)}^2} + \frac{0.0003999999990t^2}{\cosh{(0.3162277660x)}}$$
$$- \frac{0.0008000000000t^2}{\cosh{(0.3162277660x)}^3}$$

Semi-analytical solutions founded by MVILTM for Eq. (25) can be written as follows.

$$u_0 = \frac{0.3000000000}{\cosh{(0.3162277660x)}^2}$$

$$u_1 = \frac{0.3000000000}{\cosh{(0.3162277660x)}^2} + \frac{0.03794733192\sinh{(0.3162277660x)}t}{\cosh{(0.3162277660x)}^3}$$

$$u_2 = \frac{0.3000000000}{\cosh{(0.3162277660x)}^2} + \frac{0.03794733192\sinh{(0.3162277660x)}t}{\cosh{(0.3162277660x)}^3} + \frac{0.002400000000t^2}{\cosh{(0.3162277660x)}^2}$$
$$- \frac{0.003600000000t^2}{\cosh{(0.3162277660x)}^4}$$

$$v_0 = \frac{0.2000000000}{\cosh{(0.3162277660x)}}$$

$$v_1 = \frac{0.2000000000}{\cosh{(0.3162277660x)}} + \frac{0.01264911064\sinh{(0.3162277660x)}t}{\cosh{(0.3162277660x)}^2}$$

$$v_2 = \frac{0.2000000000}{\cosh{(0.3162277660x)}} + \frac{0.01264911064\sinh{(0.3162277660x)}t}{\cosh{(0.3162277660x)}^2} + \frac{0.0003999999981t^2}{\cosh{(0.3162277660x)}}$$
$$- \frac{0.0008000000000t^2}{\cosh{(0.3162277660x)}^3} + \frac{6.83372784010^{-13}t^2}{\cosh{(0.3162277660x)}^5}$$

Semi-analytical solutions founded by MVISTM for Eq. (25) can be written as follows.

$$u_0 = \frac{0.3000000000}{\cosh{(0.3162277660x)}^2}$$

$$u_1 = \frac{0.3000000000}{\cosh{(0.3162277660x)}^2} + \frac{0.03794733192\sinh{(0.3162277660x)}t}{\cosh{(0.3162277660x)}^3}$$

$$u_2 = \frac{0.3000000000}{\cosh{(0.3162277660x)}^2} + \frac{0.03794733192\sinh{(0.3162277660x)}t}{\cosh{(0.3162277660x)}^3} + \frac{0.002400000000t^2}{\cosh{(0.3162277660x)}^2}$$
$$- \frac{0.003600000000t^2}{\cosh{(0.3162277660x)}^4}$$

$$v_0 = \frac{0.2000000000}{\cosh{(0.3162277660x)}}$$

$$v_1 = \frac{0.2000000000}{\cosh{(0.3162277660x)}} + \frac{0.01264911064\sinh{(0.3162277660x)}t}{\cosh{(0.3162277660x)}^2}$$

$$v_2 = \frac{0.2000000000}{\cosh(0.3162277660x)} + \frac{0.01264911064\sinh(0.3162277660x)t}{\cosh(0.3162277660x)^2} + \frac{0.0003999999981t^2}{\cosh(0.3162277660x)}$$
$$- \frac{0.0008000000000t^2}{\cosh(0.3162277660x)^3} + \frac{6.83372784010^{-13}t^2}{\cosh(0.3162277660x)^5}$$

Comparison of errors found by MVIM, MVILTM and MVISTM for various iteration values in Eq. (25) are shown in Table 1-6.

Table 1. Comparison of errors for various iteration values in Eq. (25)

	MVIM for $u(x,t)$, $t = 1$			
x	$N = 2$	$N = 3$	$N = 5$	$N = 8$
-6	$6.06160\ 10^{-6}$	$1.13633\ 10^{-7}$	$1.42303\ 10^{-10}$	$4.61369\ 10^{-12}$
-3	$1.10281\ 10^{-5}$	$1.21407\ 10^{-6}$	$7.27618\ 10^{-10}$	$1.02636\ 10^{-11}$
0	$3.19280\ 10^{-6}$	$3.19280\ 10^{-6}$	$7.20005\ 10^{-10}$	$1.31765\ 10^{-12}$
3	$1.35199\ 10^{-5}$	$1.27770\ 10^{-6}$	$8.70581\ 10^{-10}$	$1.00499\ 10^{-11}$
6	$6.28720\ 10^{-6}$	$1.11959\ 10^{-6}$	$1.64544\ 10^{-10}$	$5.41594\ 10^{-12}$

Table 2. Comparison of maximum errors for various iteration values in Eq. (25)

	MVIM for $v(x,t)$, $t = 1$			
x	$N = 2$	$N = 3$	$N = 5$	$N = 8$
-6	$1.16369\ 10^{-6}$	$1.97458\ 10^{-8}$	$5.08659\ 10^{-11}$	$5.27795\ 10^{-12}$
-3	$6.94779\ 10^{-6}$	$2.79873\ 10^{-7}$	$2.71933\ 10^{-10}$	$6.50994\ 10^{-12}$
0	$6.65584\ 10^{-7}$	$6.65584\ 10^{-7}$	$1.081690\ 10^{-9}$	$6.99534\ 10^{-11}$
3	$7.51008\ 10^{-6}$	$2.82411\ 10^{-7}$	$2.96165\ 10^{-10}$	$5.43343\ 10^{-12}$
6	$1.12110\ 10^{-6}$	$2.28447\ 10^{-8}$	$5.27115\ 10^{-11}$	$5.49109\ 10^{-12}$

Table 3. Comparison of maximum errors for various iteration values in Eq. (25)

	MVILTM for $u(x,t)$, $t = 1$			
x	$N = 2$	$N = 3$	$N = 5$	$N = 8$
-6	$6.06161\ 10^{-6}$	$1.13625\ 10^{-7}$	$1.43203\ 10^{-10}$	$6.26648\ 10^{-12}$
-3	$1.10280\ 10^{-5}$	$1.21412\ 10^{-6}$	$6.58228\ 10^{-10}$	$2.01605\ 10^{-11}$
0	$3.19276\ 10^{-6}$	$3.19276\ 10^{-6}$	$7.242262\ 10^{-9}$	$7.61305\ 10^{-11}$
3	$1.35199\ 10^{-5}$	$1.27770\ 10^{-6}$	$8.20719\ 10^{-10}$	$4.33366\ 10^{-12}$
6	$6.28720\ 10^{-6}$	$1.11964\ 10^{-7}$	$1.55581\ 10^{-10}$	$3.83181\ 10^{-12}$

Table 4. Comparison of maximum errors for various iteration values in Eq. (25)

	MVILTM for $v(x,t)$, $t = 1$			
x	$N = 2$	$N = 3$	$N = 5$	$N = 8$
-6	$1.16369\ 10^{-6}$	$1.97432\ 10^{-8}$	5.5985010^{-11}	$1.41204\ 10^{-11}$
-3	$6.94779\ 10^{-6}$	$2.79868\ 10^{-7}$	$2.63163\ 10^{-10}$	$1.72886\ 10^{-10}$
0	$6.65585\ 10^{-7}$	$6.65585\ 10^{-7}$	$1.079563\ 10^{-9}$	$4.736751\ 10^{-9}$
3	$7.51008\ 10^{-6}$	$2.82416\ 10^{-7}$	$3.05784\ 10^{-10}$	$1.39612\ 10^{-10}$
6	$1.12110\ 10^{-6}$	$2.28477\ 10^{-8}$	$4.64987\ 10^{-11}$	$2.48959\ 10^{-12}$

Table 5. Comparison of maximum errors for various iteration values in Eq. (25)

	MVISTM for $u(x,t)$, $t = 1$			
x	$N = 2$	$N = 3$	$N = 5$	$N = 8$
-6	$6.06161\ 10^{-6}$	$1.13625\ 10^{-7}$	$1.43203\ 10^{-10}$	$6.26648\ 10^{-12}$
-3	$1.10280\ 10^{-5}$	$1.21412\ 10^{-6}$	$6.58228\ 10^{-10}$	$2.01605\ 10^{-11}$
0	$3.19276\ 10^{-6}$	$3.19276\ 10^{-6}$	$7.242262\ 10^{-9}$	$7.61305\ 10^{-11}$
3	$1.35199\ 10^{-5}$	$1.27770\ 10^{-6}$	$8.20719\ 10^{-10}$	$4.33366\ 10^{-12}$
6	$6.28720\ 10^{-6}$	$1.11964\ 10^{-7}$	$1.55581\ 10^{-10}$	$3.83181\ 10^{-12}$

Table 6. Comparison of maximum errors for various iteration values in Eq. (25)

	MVISTM for $v(x,t)$, $t = 1$			
x	$N = 2$	$N = 3$	$N = 5$	$N = 8$
-6	$1.16369 \ 10^{-6}$	$1.97432 \ 10^{-8}$	$5.59850 \ 10^{-11}$	$1.41204 \ 10^{-11}$
-3	$6.94779 \ 10^{-6}$	$2.79868 \ 10^{-7}$	$2.63163 \ 10^{-10}$	$1.72886 \ 10^{-10}$
0	$6.65585 \ 10^{-7}$	$6.65585 \ 10^{-7}$	$1.079563 \ 10^{-9}$	$4.736751 \ 10^{-9}$
3	$7.51008 \ 10^{-6}$	$2.82416 \ 10^{-7}$	$3.05784 \ 10^{-10}$	$1.39612 \ 10^{-10}$
6	$1.12110 \ 10^{-6}$	$2.28477 \ 10^{-8}$	$4.64987 \ 10^{-11}$	$2.48959 \ 10^{-12}$

Comparison of relative errors found by MVIM, MVILTM and MVISTM for various iteration values and wave constant c values in Eq. (25) are shown in Figure 1-6.

a) MVIM for u(x,t).

b) **MVILTM** for u(x,t).
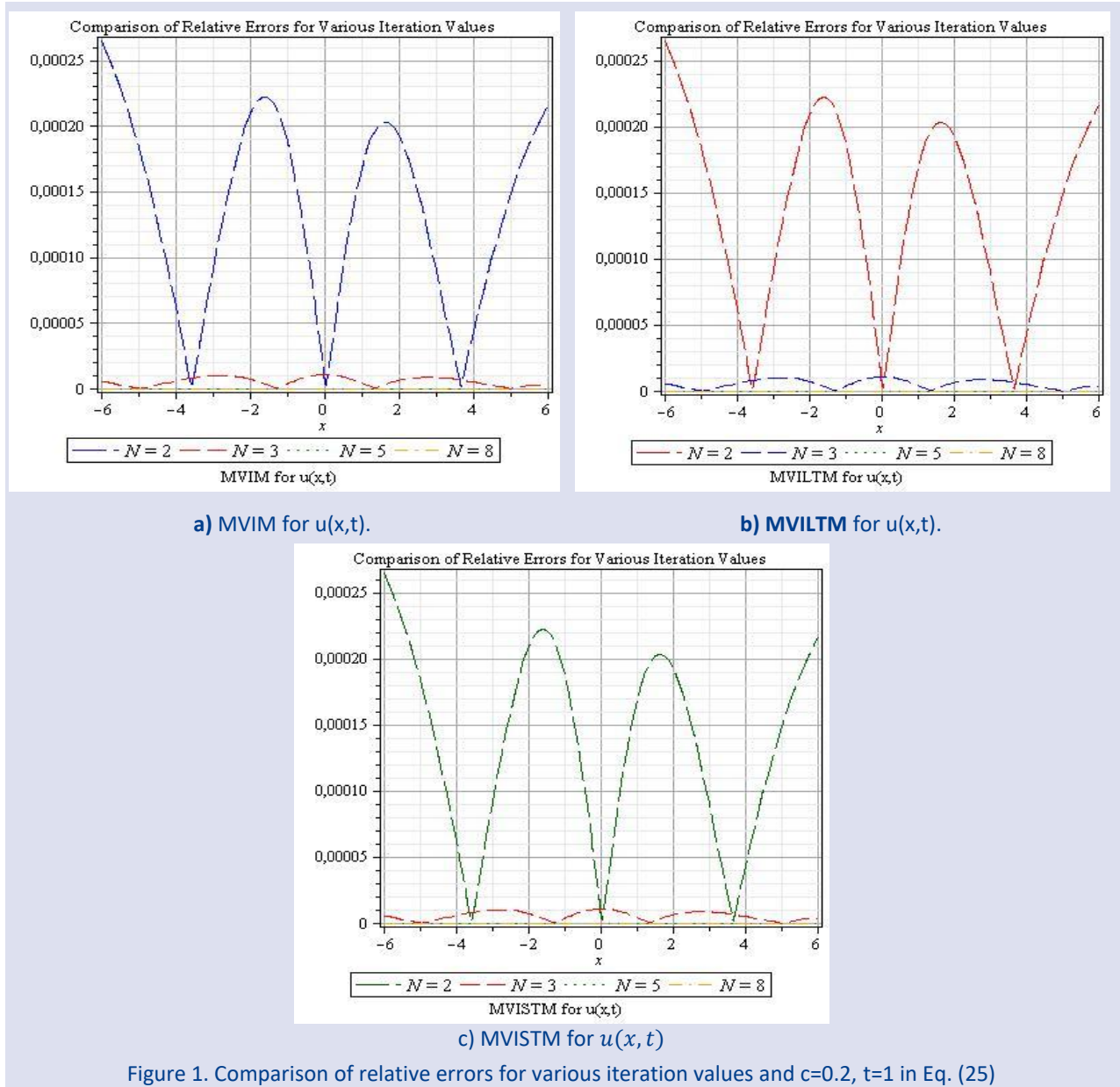
c) MVISTM for $u(x,t)$

Figure 1. Comparison of relative errors for various iteration values and c=0.2, t=1 in Eq. (25)
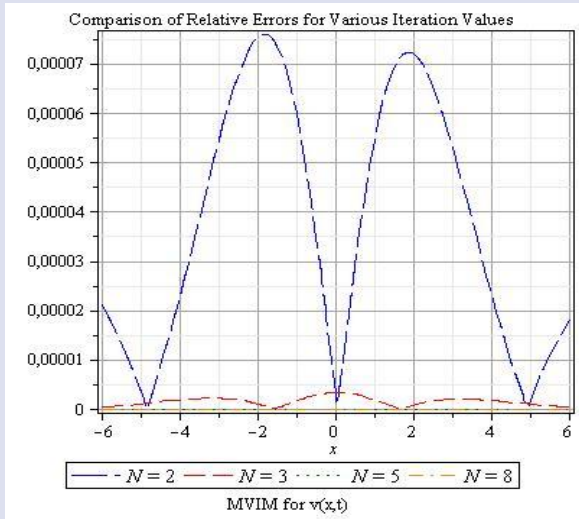
a) MVIM for v(x,t).
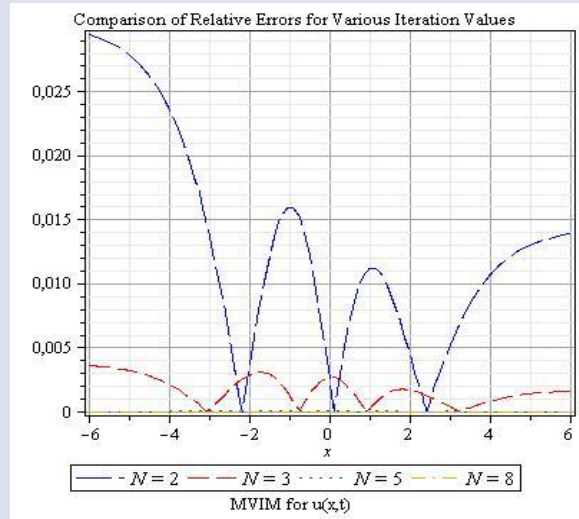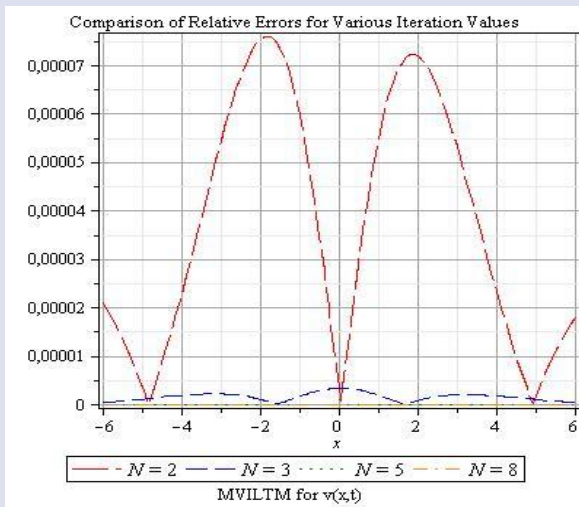
a) MVIM for u(x,t).
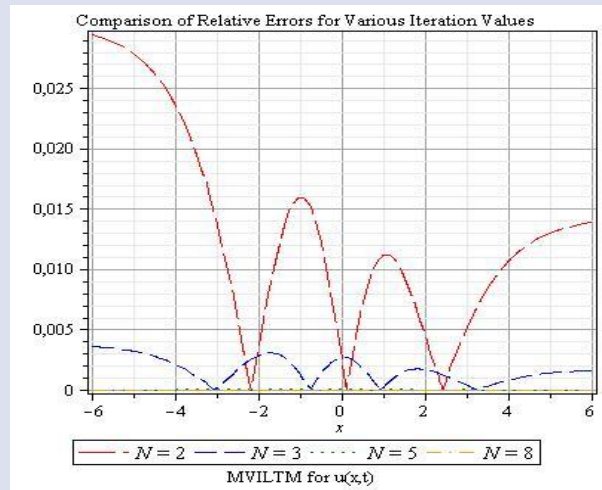
b) MVILTM for v(x,t).
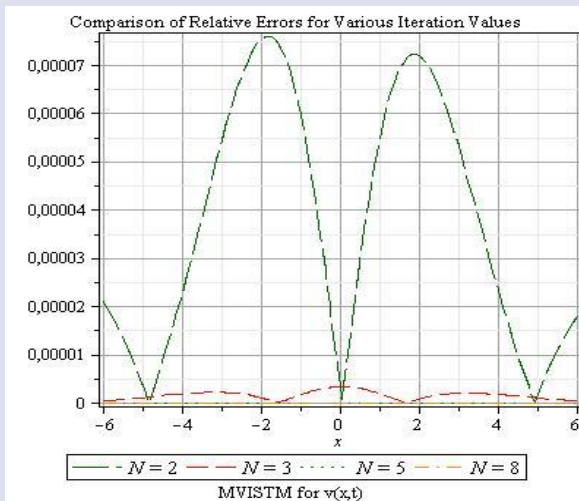
b) MVILTM for u(x,t).
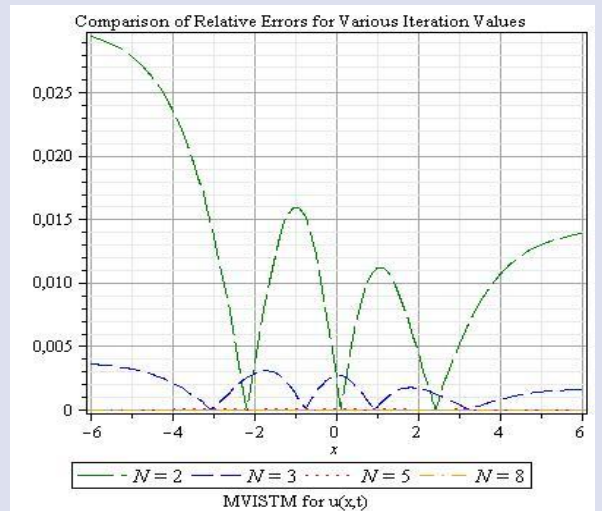
c) MVISTM for $v(x,t)$

c) MVISTM for $u(x,t)$

Figure 2. Comparison of relative errors for various iteration values and c=0.2, t=1 in Eq. (25)

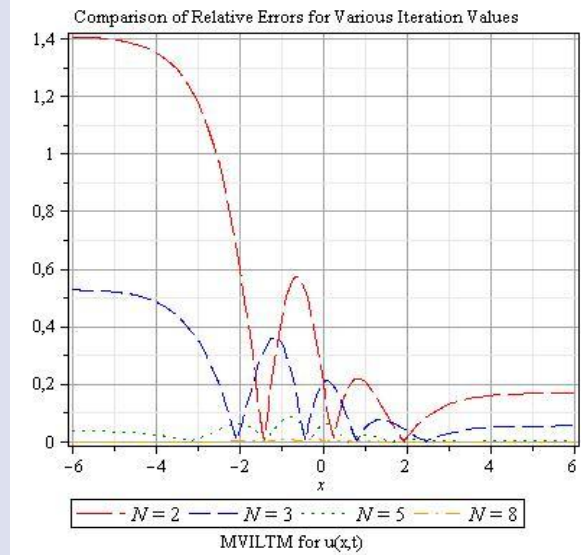Figure 3. Comparison of relative errors for various iteration values and c=0.5, t=1 in Eq. (25)
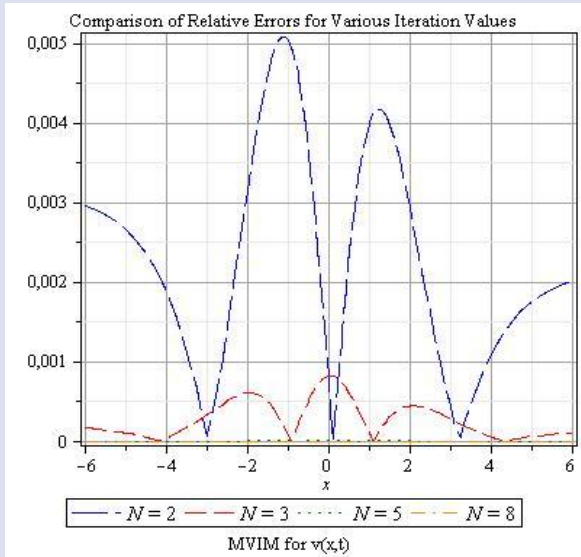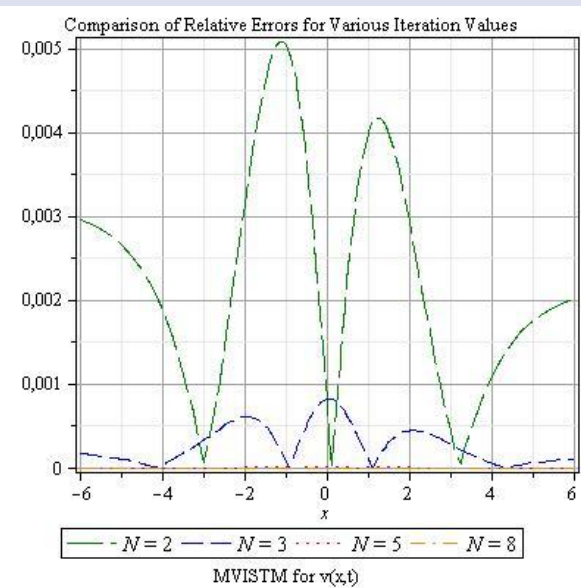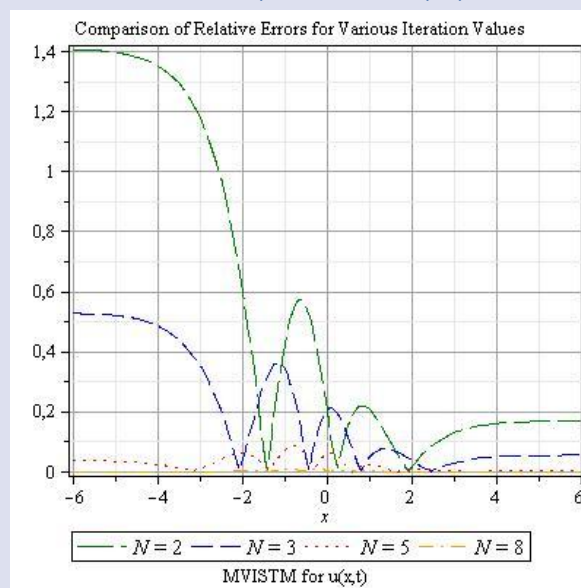
a) MVIM for v(x,t).
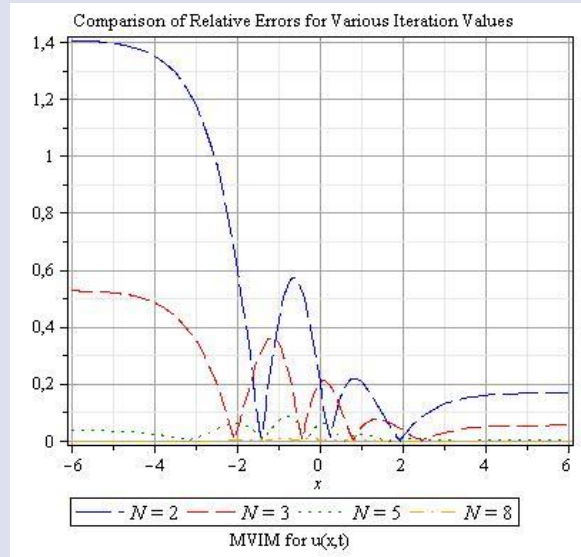
a) MVIM for u(x,t).
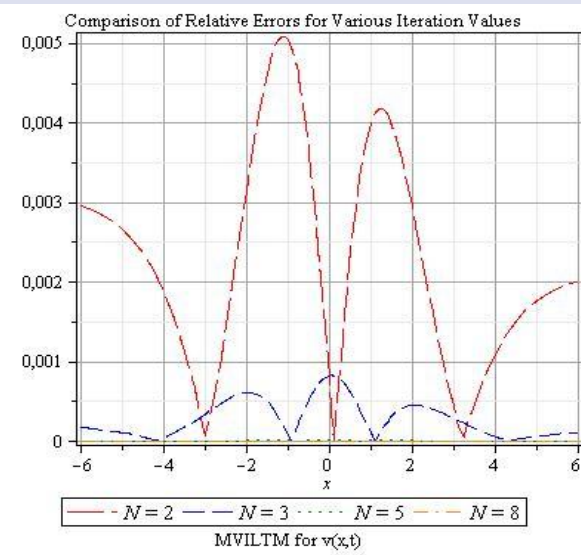
b) MVILTM for v(x,t).

b) MVILTM for u(x,t).

c) MVISTM for v(x, t)

c) MVISTM for u(x, t)

Figure 4. Comparison of relative errors for various iteration values and c=0.5, t=1 in Eq. (25)

Figure 5. Comparison of relative errors for various iteration values and c=1, t=1 in Eq. (25)

a) MVIM for v(x,t).

b) MVILTM for v(x,t).

c) MVILTM for v(x, t)

Figure 6. Comparison of relative errors for various iteration values and c=1, t=1 in Eq. (25)

Conclusion

In this study, MVIM, MVILTM and MVISTM are used to utilize the Drinfeld-Sokolov-Wilson system semi-analytically. Semi-analytical solutions of the DSW system via MVIM, MVILTM and MVISTM are determined. The comparison of maximum errors of MVIM for various iteration values is given in Table 1-6. Also, the c value is a parameter that occurs in the solution of the DSW system and is called the wave parameter r. The comparison of relative errors for various iteration values and wave parameters (c values) are visualized in Figure 1-6.

Via MVIM, MVILTM and MVISTM used to solve the DSW system, the semi-analytical results of proposed methods are obtained in a short time and using less memory. It has been observed that MVIM, MVILTM, MVSTM proposed for the DSW system not only eliminate the complexity and intense processing load of the exact solution but also provide practicality, time saving and effectiveness. Therefore, they are very useful methods in terms of both time and computational cost. It is highly recommended as an alternative to exact solution methods. MVILTM and MVISTM are highly effective, fast, more practical and reliable methods to solve the DSW system as an alternative to MVIM. Also, the maximum errors of proposed methods for c=0.2 in the DSW system are around $10^{-9} - 10^{-11}$. It has been observed that the maximum and relative errors increase as the value of the c parameter increases. Therefore, it has been determined that the c parameter affects convergence. As a result, it has been signed that MVILTM and MVISTM used to solve the DSW system are equivalent methods and have the same effectiveness. It has been shown that MVIM gives more accurate results than MVILTM and MVISTM in solving the DSW problem.

Consequently, proposed semi-analytical solutions can be used instead of exact solutions of the DSW system that models the translation of shallow water waves and the dispersive water waves. These obtained semi-analytical solutions can be more useful and functional in explaining the physical aspects of various models that originated from engineering and science. The parameters in the Drinfeld-Sokolov-Wilson system can be also examined according to spatial. Finally, this study can be taken further by bringing the DSW system to fractional form with the help of fractional derivative definitions.
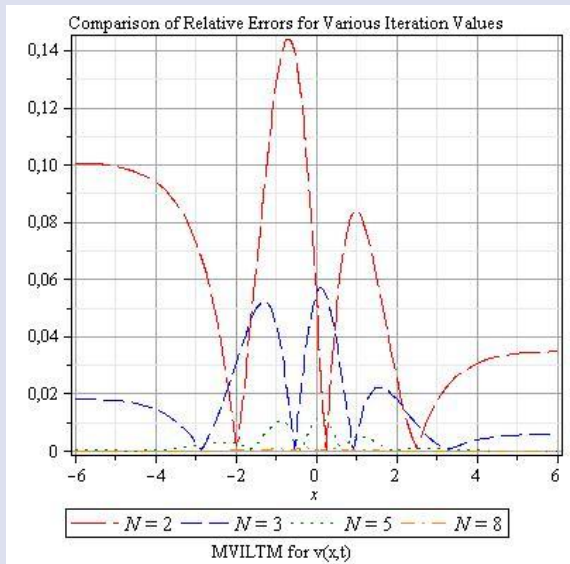
This study was partially presented orally at "The 8th International Conference on Computational Mathematics and Engineering Sciences / 17 – 19 May. 2024, Sanlıurfa – Turkiye".
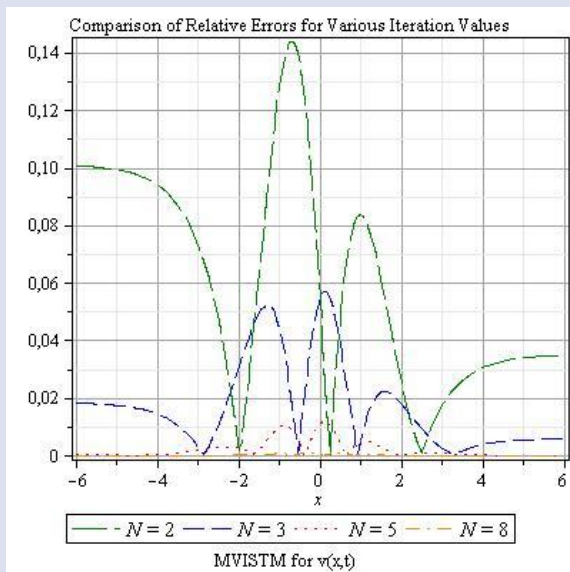
Conflict of interest
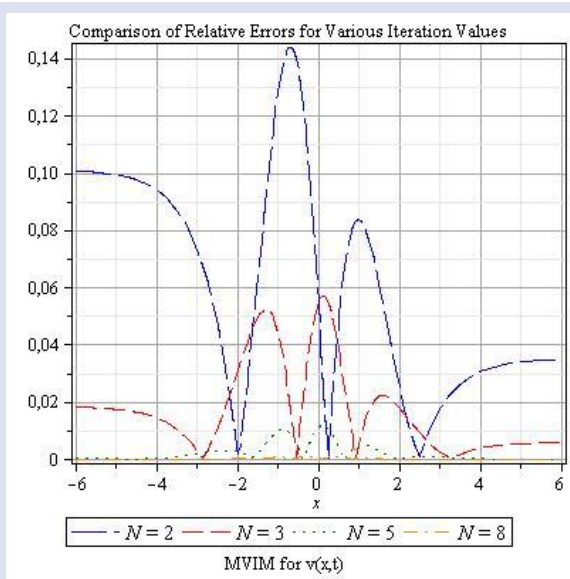
There are no conflicts of interest in this work.

References

[1] Drinfeld V.G., Sokolov V.V., Equations of Korteweg-de Vries type and simple lie algebras, *Dokl. Akad. Nauk*, 258 (1) (1981) 11-16.

[2] Wilson G., The affine lie algebra C_2^1 and an equation of Hirota and Satsuma, *Phys. Lett. A,* 89 (7) (1982) 332-334.

[3] Drinfeld V.G., Sokolov V.V., Lie algebras and equations of Korteweg-de Vries type, *J. Sov. Math.,* 24 (1984) 81-180.

[4] Gao W., Veeresha P., Prakasha D. G., Baskonus, H. M., Yel, G., A powerful approach for fractional Drinfeld-Sokolov-Wilson equation with Mittag-Leffler law, *Alex. Eng. J.,* 58 (4) (2019) 1301-1311.

[5] Saifullah S., Ali A., Shah K., Promsakon C., Investigation of fractal-fractional nonlinear Drinfeld-Sokolov-Wilson system with non-singular operators, *Results Phys.,* 33 (2022) 105145.

[6] Arora R., Kumar A., Solution of the coupled Drienfeld's-Sokolov-Wilson (DSW) system by homotopy analysis method, *Adv. Sci. Eng. Med.,* 5 (10) (2013) 1105-1111.

[7] Azizi N., Pourgholi R., Applications of Sine-Cosine wavelets method for solving Drinfel'd-Sokolov-Wilson system, *Adv. Syst. Sci. Appl.,* 21 (3) (2021) 75-90.

[8] Salim B. J., Jasim O. A., Ali Z. Y., Numerical solution of Drinfeld-Sokolov-Wilson system by using modified Adomian decomposition method, *Indones. J. Electr. Eng. Comput. Sci.,* 21 (1) (2021) 590-599.

[9] Eskondari E. M., Taghizadeh N., Applications of two methods in exact wave solutions in the space-time fractional Drinfeld-Sokolov-Wilson system, *Int. J. Differ. Equ.,* 2022 (2022) 4470344.

[10] Ali N., Yassen M. F., Asiri S. A., Nawaz R., Zada L., Alam M. M., Sene N., New iterative method for solving a coupled system of fractional order Drinfeld-Sokolov-Wilson (FDSW) and fractional shallow water (FSW) equations, *J. Nanomater.,* 2022 (2022) 8370107.

[11] Taghizadeh N., Neirameh A., Complex solutions for Drinfeld's-Sokolov-Wilson system, *Int. J. Eng. Sci. Technol.,* 1 (1) (2011) 1-6.

[12] Raslan A., Entesar A., Enhancing Banach's contraction method using the particle swarm optimization to solve the system Drinfeld-Sokolov-Wilson, *J. Phys. Conf. Ser.,* 2322 (1) (2022) 012031.

[13] Lindeberg L., Dao T., Mattson, K., A high order accurate finite difference method for the Drinfel'd-Sokolov-Wilson equation, *J. Sci. Comput.,* 88 (1) (2021) 18.

[14] Zhang Y., Zhao Z., Lie symmetry analysis, Lie- Backlund symmetries, explicit solutions and conservation laws of Drinfeld-Sokolov-Wilson system, *Bound. Value Probl.,* 154, (2017).

[15] Singh P. K., Vishal K., Som T., Solution of fractional Drinfeld-Sokolov-Wilson equation using homotopy perturbation transform method, *Appl. Appl. Math.,* 10 (1) (2015) 460-472.

[16] Al-Rozbayani A. M. A., Ali A. H., Applied Sumudu transform with Adomian decomposition method to the coupled Drinfeld-Sokolov-Wilson system, *Rafidain J. Comput. Sci. Math.,* 15 (2) (2021) 139-147.

[17] Alam M. N., Bonyah E., Fayz-Al-Asad M., Reliable analysis for the Drinfeld-Sokolov-Wilson equation in mathematical physics, *Palest. J. Math.,* 11 (1) (2022) 397-407.

[18] Usman M. H. A., Zaman F. D., Eldin S. M., Symmetry analysis and exact Jacobi elliptic solutions for the nonlinear couple Drinfeld Sokolov Wilson dynamical system arising in shallow water waves, *Results Phys.,* 51 (2023) 106613.

[19] Shahzad M. U., Ur-Rehman H., Awan A. U., Zafar Z., Hassan A. M., Iqbal I., Analysis of the exact solutions of nonlinear coupled Drinfeld-Sokolov-Wilson equation through Φ^6-model expansion method, *Results Phys.,* 52 (2023) 106671.

[20] Iqbal M., Seadawy A. R., Lu D., Zhang Z., Computational approachand dynamical analysis of multiple solitary wave solutions for nonlinear coupled Drinfeld-Sokolov-Wilson equation, *Results Phys.,* 55 (2023) 107099.

[21] Younis I. T., Al-Rawi E. S., Improved finite difference technique via Adominian polynomial to solve the coupled Drinfeld's-Sokolov-Wilson system, *Int. J. Math. Math. Sci.,* 2023 (2023) 6916596.

[22] Aydemir T., New exact solutions of the Drinfeld-Sokolov-Wilson system by the generalized unified method, *J. New Theory*, 44 (2023) 10-19.

[23] Hakkaev S., Spectral stability of periodic waves for the Drinfeld-Sokolov-Wilson equation, *J. Math. Anal. Appl.,* 533 (1) (2024) 128016.

[24] Abassy T. A., El Tawil M. A., El Zoheiry H., Toward a Modified Variational Iteration Method, *J. Comput. Appl. Math.,* 207 (1) (2007) 137-147.

[25] Abassy T. A., El Tawil M. A., El Zoheiry H., Solving Nonlinear Partial Differential Equations Using the Modified Variational Iteration Padé Technique, *J. Comput. Appl. Math.* 207 (1) (2007) 73-91.

[26] Abassy T. A., Modified Variational Iteration Method (Nonlinear Homogeneous Initial Value Problem), *Comput. Math. Appl.,* 59 (2) (2010) 912-918.

[27] Abbasbandy, S., Shivanian, E., Application of the Variational Iteration Method for System of Nonlinear Volterra's Integro-Differential Equations, *Math. Comput. Appl.,* 14 (2) (2009) 147-158.

[28] Aggarwal S., Chaudhary R., A comparative study of Mohand and Laplace transforms, *J. Emerg. Technol. Innov. Res.,* 6 (2) (2019) 230-240.

[29] Aggarwal S., Sharma S.D., Sumudu transform of error function, *J. Appl. Sci. Comput.,* 6 (6) (2019) 1222-1231.

[30] Zhang W. M., Solitary solutions and singular periodic solutions of the Drinfeld-Sokolov-Wilson equation by variational approach, *Appl. Math. Sci.,* 5 (38) (2011) 1887-1894.

Cumhuriyet Science Journal

Some Results on the Oscillation of a Class of Generalized Fractional Integro-Differential Equations

Funda Raziye Mert[1,a] Selami Bayeğ [2,b,*]

[1] Department of Software Engineering, Faculty of Computer and Informatics, Adana Alparslan Türkeş Science and Technology University, 01250, Adana, Türkiye.

[2] Department of Industrial Engineering, Faculty of Engineering, University of Turkish Aeronautical Association, 06790, Ankara, Türkiye.

*Corresponding author

Research Article

ABSTRACT

In this study, we analyze the oscillatory behavior of solutions to a specific class of fractional integro-differential equations. First, we derive sufficient conditions that ensure nonoscillatory solutions exhibit a well-defined asymptotic behavior. Building on this result, we establish a series of oscillation theorems that provide deeper insight into the qualitative nature of solutions. To validate our theoretical findings, we present a concrete example that demonstrates the applicability of our main results. These contributions aim to advance the theoretical framework of fractional equations, offering new perspectives on their dynamic behavior and potential applications in mathematical modeling.

Keywords: Fractional integro-differential equation, Riemann-Liouville Derivative, Riemann-Liouville Integral, Oscillation

[a] rmert@atu.edu.tr   https://orcid.org/0000-0001-6613-2733   [b] sbayeg@thk.edu.tr   https://orcid.org/0000-0001-7014-1739

Introduction

Fractional calculus is an extension of classical differentiation and integration to arbitrary order. Its history is as old as the classical calculus. Fractional derivatives and integrals have been shown to be better than classical tools for describing many real-life phenomena in science and engineering. Hence, many and varied sectors of engineering and science, including fluid mechanics, electromagnetics, electrochemistry, biological population models, viscoelasticity, signals processing, and signals optics use fractional calculus.

Fractional differential equations have recently attracted considerable attention. The study of fractional differential equations is interdisciplinary and is encountered in diverse fields such as plasma physics, biomathematics, fluid dynamics, mathematical biology, control systems, elasticity, biotechnology, quantum mechanics, optics, and complex systems. Since the derivatives there are of fractional order, they can approximate real data more flexibly, see [1].

The variety of fractional operators is what distinguishes fractional calculus from other mathematical disciplines. This allows the scientists working on modeling real life phenomena to choose the best operator for their model. To model real life phenomena more accurately, researchers have needed several other fractional operators in addition to the Riemann-Liouville and Caputo ones. An interested reader can look at [2-7] for some newly introduced fractional operators. These operators are defined as particular cases of fractional operators depending on a kernel function.

Oscillation is a substantial aspect of the qualitative behavior of solutions of differential and difference equations. Its theory is important to study the oscillatory phenomena in technology and natural and social sciences. A major problem in oscillation theory is proving the existence or non-existence of an oscillatory solution to a given equation or system. Additionally, the behavior of other solutions relative to a particular oscillatory (non-oscillatory) solution is also studied. Many articles on theoretical aspects of oscillation theory are published every year. Surprisingly, this significant area of research has substantial applications and is not entirely theoretical. Oscillation theory has important applications in physics, biology, ecology, physiology, etc. Studying oscillations provides a better understanding of the dynamics of solutions of equations that model applied problems encountered in engineering, technology, and science. Despite its importance, when we look at the literature, we see that there are few studies related to the oscillation of fractional differential and difference equations. As far as we know, Grace et al. [8] first studied the oscillation for a fractional differential equation. After that, corresponding results for ordinary differential and difference equations have been extended to fractional differential and difference equations, see [9-19]. There is also very little research on the oscillation theory of fractional integro-differential equations, see [20-23]. This work investigates the oscillatory behavior of solutions to a fractional Volterra integro-differential equation using the method introduced in [24]. We believe that our study will inspire further research on fractional integro-differential equations. We consider the fractional integro-differential equation

$$\begin{cases} D_a^{\mu,\mathfrak{S}}x(t) = \mathfrak{z}(t) - \int_a^t \mathcal{M}(t,v)\mathcal{Y}(v,x(v))\,dv, t \geq a \geq 0, 0 < \mu < 1, \\ \lim_{t \to a^+} I_a^{1-\mu,\mathfrak{S}}x(t) = b_1, \end{cases} \tag{1}$$

where, $\mathfrak{z}$, $\mathcal{M}$, and $\mathcal{Y}$ are continuous, $b_1 \in \mathbb{R}$, and $D_a^{\mu,\mathfrak{S}}$ and $I_a^{1-\mu,\mathfrak{S}}$ are the left fractional general derivative and integral operators in the Riemann-Liouville setting, respectively.

We concentrate only on those solutions of Eq. (1) not identically zero eventually. Henceforth, we mean such solutions. Such solutions are called oscillatory if they are not eventually of one sign and nonoscillatory otherwise. The equation itself is oscillatory in case all its solutions oscillate.

PRELIMINARIES

We now present some basic definitions and important lemmas. Let $\mu \in \mathbb{C}$ with $Re(\mu) > 0$, $I = (a,b)$ be an interval, and $\mathfrak{S} \in C^1(I)$ be an increasing function with $\mathfrak{S}'(t) \neq 0 \; \forall t \in I$. The left fractional integral and derivative in the Riemann-Liouville sense of a function θ with respect to another function $\mathfrak{S}$ are defined in [25, 26] as

$$I_a^{\mu,\mathfrak{S}}\theta(t) = \frac{1}{\Gamma(\mu)} \int_a^t (\mathfrak{S}(t) - \mathfrak{S}(v))^{\mu-1} \mathfrak{S}'(v)\theta(v)dv \tag{2}$$

and

$$\begin{aligned} D_a^{\mu,\mathfrak{S}}\theta(t) &= {}_\mathfrak{S}D_t^n I_a^{n-\mu,\mathfrak{S}}\theta(t) \\ &= \frac{1}{\Gamma(n-\mu)} {}_\mathfrak{S}D_t^n \int_a^t (\mathfrak{S}(t) - \mathfrak{S}(v))^{n-\mu-1} \mathfrak{S}'(v)\theta(v)dv, \end{aligned} \tag{3}$$

respectively, where $n = [\mu]$ and

$${}_\mathfrak{S}D_t^n = \left(\frac{1}{\mathfrak{S}'(t)}\frac{d}{dt}\right)^n.$$

In the special cases $\mathfrak{S}(t) = t$ and $\mathfrak{S}(t) = \ln t$ in Eq. (2) and Eq. (3), we have the Riemann-Liouville and Hadamard fractional operators, respectively.

We assume throughout that $\mathfrak{S}(t) > 0 \; \forall t \in I$.

Lemma 1 [26] Let $\mu \in \mathbb{C}$ with $Re(\mu) > 0$, $n = -[-Re(\mu)]$, $\theta \in L(a,b)$, and $(I_a^{\mu,\mathfrak{S}}\theta)(t) \in AC_\mathfrak{S}^n[a,b]$. Then,

$$I_a^{\mu,\mathfrak{S}}D_a^{\mu,\mathfrak{S}}\theta(t) = \theta(t) - \sum_{j=1}^n \frac{(I_a^{j-\mu,\mathfrak{S}}\theta)(a^+)}{\Gamma(\mu-j+1)}(\mathfrak{S}(t) - \mathfrak{S}(a))^{\mu-j}. \tag{4}$$

Lemma 2 [27] Let $\mu, \nu \in \mathbb{C}$ with $Re(\mu) > 0$ and $Re(\nu) > 0$. Then

$$I_a^{\mu,\mathfrak{S}}(\mathfrak{S}(t) - \mathfrak{S}(a))^{\nu-1} = \frac{\Gamma(\nu)}{\Gamma(\nu+\mu)}(\mathfrak{S}(t) - \mathfrak{S}(a))^{\nu+\mu-1}. \tag{5}$$

Lemma 3 [28] For non-negative real numbers $\mathcal{K}$ and $\mathcal{R}$,

$$\mathcal{K}^\alpha - (1-\alpha)\mathcal{R}^\alpha - \alpha\mathcal{K}\mathcal{R}^{\alpha-1} \leq 0, \; 0 < \alpha < 1. \tag{6}$$

The equality holds if and only if $\mathcal{K} = \mathcal{R}$

Main Results

We assume that the following hypotheses are met:

(H1) $\mathfrak{z}: [a,\infty) \to \mathbb{R}$ is continuous;

(H2) $\mathcal{M}: [a,\infty) \times [a,\infty) \to \mathbb{R}$ is continuous and there exist continuous functions $\zeta_1, \zeta_2: [a,\infty) \to (0,\infty)$ such that

$$0 \leq \mathcal{M}(t,v) \leq \zeta_1(t)\zeta_2(v) \text{ for } t \geq v \geq a;$$

(H3) $\mathcal{Y}: [a,\infty) \times \mathbb{R} \to \mathbb{R}$ is continuous and there exists a continuous function $\eta: [a,\infty) \to (0,\infty)$ and a real number α, $0 < \alpha \leq 1$ such that

$$0 < x\mathcal{Y}(t,x) \leq \eta(t)|x|^{\alpha+1} \text{ for } t \geq a, \; x \neq 0;$$

For a given continuous function $\xi: [a,\infty) \to (0,\infty)$, we define

$$q_\pm(t) := \mathfrak{z}(t) \pm (1-\alpha)\alpha^{\alpha/(1-\alpha)}\zeta_1(t)\int_a^t \xi^{\alpha/(\alpha-1)}(v)\zeta_2^{1/(1-\alpha)}(v)\eta^{1/(1-\alpha)}(v)\,dv, \quad 0 < \alpha < 1.$$

To begin, we provide sufficient conditions for each nonoscillatory solution of Eq. (1) to fulfill

$$x(t) = O(\mathfrak{S}^\mu(t)) \text{ as } t \to \infty.$$

Theorem 1 Let $0 < \alpha < 1$ and the hypotheses (H1)–(H3) hold. Assume that

$$\zeta_1(t) \le M_1 \quad \text{for } t \ge a \tag{7}$$

for some real number $M_1 > 0$ and

$$\int_a^\infty \mathbb{S}^\mu(v)\xi(v)\,dv < \infty. \tag{8}$$

If

$$\limsup_{t\to\infty} \frac{1}{\mathbb{S}^\mu(t)} I_a^{\mu,\mathbb{S}}[q_+(t)] < \infty, \text{ and } \liminf_{t\to\infty} \frac{1}{\mathbb{S}^\mu(t)} I_a^{\mu,\mathbb{S}}[q_-(t)] > -\infty, \tag{9}$$

then every nonoscillatory solution $x(t)$ of Eq. (1) satisfies

$$\limsup_{t\to\infty} \frac{|x(t)|}{\mathbb{S}^\mu(t)} < \infty. \tag{10}$$

Proof 1 Assume that $x(t)$ is a nonoscillatory solution of Eq. (1), say $x(t) > 0$ for $t \ge T_1$, for some $T_1 \ge a$. From Eq. (1), we have

$$\begin{aligned}
D_a^{\mu,\mathbb{S}} x(t) &= \mathfrak{z}(t) - \int_a^t \mathcal{M}(t,v)\mathcal{Y}(v,x(v))\,dv \\
&= \mathfrak{z}(t) - \int_a^{T_1} \mathcal{M}(t,v)\mathcal{Y}(v,x(v))\,dv - \int_{T_1}^t \mathcal{M}(t,v)\mathcal{Y}(v,x(v))\,dv.
\end{aligned}$$

Let $L := \min\{\mathcal{Y}(t,x(t)): t \in [a,T_1]\} \le 0$ and $\kappa := -L\int_a^{T_1} \zeta_2(v)\,dv \ge 0$.
Since $\mathcal{M}(t,v)\mathcal{Y}(v,x(v)) \ge L\mathcal{M}(t,v) \ge L\zeta_1(t)\zeta_2(v), \quad a \le v \le T_1,$

we have

$$\int_a^{T_1} \mathcal{M}(t,v)\mathcal{Y}(v,x(v))\,dv \ge L\zeta_1(t)\int_a^{T_1}\zeta_2(v)\,dv$$

and

$$-\int_a^{T_1} \mathcal{M}(t,v)\mathcal{Y}(v,x(v))\,dv \le -L\zeta_1(t)\int_a^{T_1}\zeta_2(v)\,dv = \kappa\zeta_1(t).$$

In view of $\mathcal{M}(t,v)\mathcal{Y}(v,x(v)) > 0$, we have

$$-\int_{T_1}^t \mathcal{M}(t,v)\mathcal{Y}(v,x(v))\,dv < 0$$

and

$$-\int_{T_1}^t \mathcal{M}(t,v)\mathcal{Y}(v,x(v))\,dv < 0 \le \zeta_1(t)\int_{T_1}^t \zeta_2(v)\eta(v)x^\alpha(v)\,dv.$$

Thus, we get

$$\begin{aligned}
D_a^{\mu,\mathbb{S}} x(t) &\le \mathfrak{z}(t) + \kappa\zeta_1(t) + \zeta_1(t)\int_{T_1}^t \zeta_2(v)\eta(v)x^\alpha(v)\,dv \\
&= \mathfrak{z}(t) + \kappa\zeta_1(t) + \zeta_1(t)\int_{T_1}^t \left(\zeta_2(v)\eta(v)x^\alpha(v) - \xi(v)x(v)\right)dv + \zeta_1(t)\int_{T_1}^t \xi(v)x(v)\,dv.
\end{aligned} \tag{11}$$

In (6), by setting $\mathcal{K} := (\zeta_2\eta)^{1/\alpha}x$ and $\mathcal{R} := \left(\frac{1}{\alpha}\xi(\zeta_2\eta)^{-1/\alpha}\right)^{\frac{1}{\alpha-1}}$, we get

$$\zeta_2(v)\eta(v)x^\alpha(v) - \xi(v)x(v) \le (1-\alpha)\alpha^{\alpha/(1-\alpha)}\xi^{\alpha/(\alpha-1)}(v)\zeta_2^{1/(1-\alpha)}(v)\eta^{1/(1-\alpha)}(v).$$

Hence, inequality (11) gives

$$D_a^{\mu,\mathbb{S}} x(t) \le q_+(t) + \kappa\zeta_1(t) + \zeta_1(t)\int_a^t \xi(v)x(v)\,dv, \quad t \ge a$$

and in view of (7),

$$D_a^{\mu,\mathbb{S}} x(t) \le q_+(t) + \kappa M_1 + M_1 \int_a^t \xi(v)x(v)\,dv, \quad t \ge a. \tag{12}$$

Now, applying $I_a^{\mu,\mathbb{S}}$ to (12) and using (4) and (5) with $\nu = 1$, we get

$$\begin{aligned}
x(t) &\le \frac{b_1}{\Gamma(\mu)}(\mathbb{S}(t) - \mathbb{S}(a))^{\mu-1} + \frac{\kappa M_1}{\Gamma(\mu+1)}(\mathbb{S}(t) - \mathbb{S}(a))^\mu + I_a^{\mu,\mathbb{S}}[q_+(t)] \\
&\quad + M_1 I_a^{\mu,\mathbb{S}}\left[\int_a^t \xi(v)x(v)\,dv\right].
\end{aligned} \tag{13}$$

By interchanging the order of integration, we have

$$I_a^{\mu,\mathfrak{S}}\left[\int_a^t \xi(v)x(v)\,dv\right] = \frac{1}{\Gamma(\mu)}\int_a^t \mathfrak{S}'(v)(\mathfrak{S}(t)-\mathfrak{S}(v))^{\mu-1}\int_a^v \xi(u)x(u)\,dudv$$

$$= \int_a^t \xi(u)x(u)\int_u^t \frac{\mathfrak{S}'(v)(\mathfrak{S}(t)-\mathfrak{S}(v))^{\mu-1}}{\Gamma(\mu)}\,dvdu$$

$$= \int_a^t \xi(u)x(u)I_u^{\mu,\mathfrak{S}}(1)\,du$$

$$= \frac{1}{\Gamma(\mu+1)}\int_a^t (\mathfrak{S}(t)-\mathfrak{S}(u))^\mu \xi(u)x(u)\,du. \tag{14}$$

Using (14) in (13), it follows

$$x(t) \le \frac{b_1}{\Gamma(\mu)}(\mathfrak{S}(t)-\mathfrak{S}(a))^{\mu-1} + \frac{\kappa M_1}{\Gamma(\mu+1)}(\mathfrak{S}(t)-\mathfrak{S}(a))^\mu + I_a^{\mu,\mathfrak{S}}[q_+(t)] + \frac{M_1}{\Gamma(\mu+1)}\mathfrak{S}^\mu(t)\int_a^t \xi(v)x(v)\,dv$$

and hence,

$$\frac{x(t)}{\mathfrak{S}^\mu(t)} \le c_1 + \frac{M_1}{\Gamma(\mu+1)}\int_a^t \mathfrak{S}^\mu(v)\xi(v)\frac{x(v)}{\mathfrak{S}^\mu(v)}\,dv, \quad t \ge t_1 > a,$$

where taking into account (9), $c_1 > 0$ is an upper bound for

$$\frac{b_1}{\Gamma(\mu)}\frac{(\mathfrak{S}(t)-\mathfrak{S}(a))^{\mu-1}}{\mathfrak{S}^\mu(t)} + \frac{\kappa M_1}{\Gamma(\mu+1)}\frac{(\mathfrak{S}(t)-\mathfrak{S}(a))^\mu}{\mathfrak{S}^\mu(t)} + \frac{I_a^{\mu,\mathfrak{S}}[q_+(t)]}{\mathfrak{S}^\mu(t)}.$$

Proceeding as in the proof of the well-known Gronwall's inequality, we obtain

$$\frac{x(t)}{\mathfrak{S}^\mu(t)} \le \left(c_1 + \frac{M_1}{\Gamma(\mu+1)}\int_a^{t_1} \xi(v)x(v)\,dv\right)e^{\frac{M_1}{\Gamma(\mu+1)}\int_{t_1}^t \mathfrak{S}^\mu(v)\xi(v)\,dv}, \quad t \ge t_1,$$

and using (8),

$$\limsup_{t\to\infty}\frac{x(t)}{\mathfrak{S}^\mu(t)} < \infty.$$

If $x(t) < 0$, then we set $y := -x$. It follows that y satisfies Eq. (1) with $\mathfrak{z}(t)$ replaced by $-\mathfrak{z}(t)$ and $\mathcal{Y}(t,x)$ by $-\mathcal{Y}(t,-y)$, respectively. Continuing in the same manner, we obtain

$$\limsup_{t\to\infty}\frac{-x(t)}{\mathfrak{S}^\mu(t)} < \infty.$$

The proof is accomplished.

Now, by using the asymptotic result in Theorem 1, we will construct theorems for the oscillation of Eq. (1) in Theorems 2 and 4. We will provide sufficient conditions in Theorem 3 that, for the case where $\alpha = 1$, nonoscillatory solutions of Eq. (1) fulfill (10).

Theorem 2 Let $0 < \alpha < 1$ and the hypotheses (H1)–(H3) hold. Assume that (7) and (9) are satisfied and that

$$\limsup_{t\to\infty}I_a^{\mu,\mathfrak{S}}[\zeta_1(t)] < \infty \tag{15}$$

and

$$\limsup_{t\to\infty}\mathfrak{S}^\mu(t)\int_a^t \mathfrak{S}^\mu(v)\xi(v)\,dv < \infty. \tag{16}$$

If

$$\liminf_{t\to\infty}I_a^{\mu,\mathfrak{S}}[q_+(t)] = -\infty, \quad \limsup_{t\to\infty}I_a^{\mu,\mathfrak{S}}[q_-(t)] = \infty, \tag{17}$$

then Eq. (1) is oscillatory.

Proof 2 Let $x(t)$ be a nonoscillatory solution of Eq. (1), say $x(t) > 0$ for $t \ge T_1$ for some $T_1 \ge a$. The proof when $x(t) < 0$ is similar.

Continuing as in the proof of Theorem 1, we obtain

$$x(t) \le \frac{b_1}{\Gamma(\mu)}(\mathfrak{S}(t)-\mathfrak{S}(a))^{\mu-1} + I_a^{\mu,\mathfrak{S}}[q_+(t)] + \kappa I_a^{\mu,\mathfrak{S}}[\zeta_1(t)] + \frac{M_1}{\Gamma(\mu+1)}\mathfrak{S}^\mu(t)\int_a^t \mathfrak{S}^\mu(v)\xi(v)\frac{x(v)}{\mathfrak{S}^\mu(v)}\,dv. \tag{18}$$

Moreover, (16) implies (8), and hence the result of Theorem 1 holds. Together with (15), this indicates that the last two integrals of (18) are bounded. Taking limit inferior on both sides and using (17) yields a contradiction with the fact that $x(t)$ is eventually positive. The proof is completed.

Corollary 1 Let $0 < \alpha < 1$ and the hypotheses (H1)–(H3) hold. Assume that (7), (15), and (16) are satisfied and that

$$\limsup_{t\to\infty}\frac{1}{\mathfrak{S}^\mu(t)}I_a^{\mu,\mathfrak{S}}[\mathfrak{z}(t)] < \infty, \quad \liminf_{t\to\infty}\frac{1}{\mathfrak{S}^\mu(t)}I_a^{\mu,\mathfrak{S}}[\mathfrak{z}(t)] > -\infty,$$

$$\limsup_{t\to\infty}\int_a^t \frac{\mathfrak{S}'(v)(\mathfrak{S}(t)-\mathfrak{S}(v))^{\mu-1}}{\Gamma(\mu)}\zeta_1(v)\int_a^v \xi^{\alpha/(\alpha-1)}(u)\zeta_2^{1/(1-\alpha)}(u)\eta^{1/(1-\alpha)}(u)\,du\,dv < \infty.$$

If

$$\liminf_{t\to\infty} I_a^{\mu,\mathfrak{S}}[\mathfrak{z}(t)] = -\infty \quad \text{and} \quad \limsup_{t\to\infty} I_a^{\mu,\mathfrak{S}}[\mathfrak{z}(t)] = \infty, \tag{19}$$

then Eq. (1) is oscillatory.

Analogously, when $\alpha = 1$, we can easily prove the following theorems.

Theorem 3 Let $\alpha = 1$ and the hypotheses (H1)-(H3) hold. Besides (7), assume that
$\int_a^\infty \mathfrak{S}^\mu(v)\eta(v)\zeta_2(v)\, dv < \infty.$
If

$$\limsup_{t\to\infty} \frac{I_a^{\mu,\mathfrak{S}}[\mathfrak{z}(t)]}{\mathfrak{S}^\mu(t)} < \infty \quad \text{and} \quad \liminf_{t\to\infty} \frac{I_a^{\mu,\mathfrak{S}}[\mathfrak{z}(t)]}{\mathfrak{S}^\mu(t)} > -\infty, \tag{20}$$

then, every nonoscillatory solution of Eq. (1) satisfies (10).

Theorem 4 Let $\alpha = 1$ and the hypotheses (H1)-(H3) hold. Assume that (7), (15), (19), and (20) are satisfied. If
$\limsup_{t\to\infty} \mathfrak{S}^\mu(t) \int_a^t \mathfrak{S}^\mu(v)\eta(v)\zeta_2(v)\, dv < \infty,$
then, Eq. (1) is oscillatory.

Example 1 Let $\alpha = 1$. Consider the integro-differential equation

$$\begin{cases} D_1^{1/2,t} x(t) = \frac{1}{t} - \int_1^t \frac{x(v)}{tv^2}\, dv, t \geq 1, \\ \lim_{t\to 1^+} I_1^{1/2,t} x(t) = 1. \end{cases} \tag{21}$$

We have $\mu = 1/2, a = 1, \mathfrak{S}(t) = t, \mathfrak{z}(t) = \frac{1}{t}, \mathcal{M}(t,v) = \frac{1}{t}$, and $\mathcal{Y}(t,x) = \frac{x}{t^2}$. Let's take $\zeta_1(t) = \frac{1}{t}, \zeta_2(v) = 1$, and $\eta(t) = \frac{1}{t^2}$. It is clear that $\zeta_1(t)$ is bounded from above. We have

$$\int_1^\infty \frac{1}{v^{3/2}}\, dv = 2 < \infty$$

and $I_1^{1/2,t}[\frac{1}{t}] = \frac{1}{\Gamma(1/2)} \int_1^t (t-v)^{-1/2} \frac{1}{v}\, dv = \frac{2\ln\left(1+\sqrt{\frac{t-1}{t}}\right) + \ln t}{\sqrt{\pi t}},$

which implies that

$$\limsup_{t\to\infty} \frac{I_1^{1/2,t}[\frac{1}{t}]}{t^{1/2}} = 0 < \infty \quad \text{and} \quad \liminf_{t\to\infty} \frac{I_1^{1/2,t}[\frac{1}{t}]}{t^{1/2}} = 0 > -\infty.$$

Hence, all the conditions of Theorem 3 are satisfied, and every nonoscillatory solution of Eq. (21) has the asymptotic property (10).

Conclusions

In this study, we analyzed the oscillatory behavior of solutions to a class of fractional integro-differential equations. Firstly, in Theorem 1, we gave sufficient conditions under which every nonoscillatory solution of Eq. (1) satisfies the asymptotic property (10). Afterward, by using the asymptotic result obtained in Theorem 1, we established theorems for the oscillation of Eq. (1) in Theorems 2 and 4. In Theorem 3, we presented sufficient conditions under which every nonoscillatory solution of Eq. (1) satisfies (10) for the case $\alpha = 1$. To reinforce the theoretical results, we presented a concrete example that illustrates the applicability and effectiveness of our main findings. These contributions deepen the understanding of fractional integro-differential equations and provide a foundation for further exploration in this area.

Conflict of interests

There are no conflicts of interest in this work.

References

[1] Singh J., Kumar D., Baleanu D., New aspects of fractional Biswas-Milovic model with Mittag-Leffler law, *Math. Model. Nat. Phenom.*, 14(3) (2019).

[2] Kilbas A.A., Hadamard-type fractional calculus, *J. Korean Math. Soc.*, 38(6) (2001) 1191-1204.

[3] Katugampola U.N., New approach to generalized fractional integral, *Appl. Math. Comput.,* 218(3) (2011) 860-865.

[4] Katugampola U.N., A new approach to generalized fractional derivatives, *Bull. Math. Anal. Appl.*, 6(4) (2014) 1-15.

[5] Jarad F., Abdeljawad T., Baleanu D., On the generalized fractional derivatives and their Caputo modification, *J. Nonlinear Sci. Appl.*, 10(5) (2017) 2607-2619.

[6] Jarad F., Abdeljawad T., Baleanu D., Caputo-type modification of the Hadamard fractional derivatives, *Advances in Difference Equations*, 2012 (2012) 1-8.

[7] Jarad F., Uğurlu E., Abdeljawad T., Baleanu D., On a new class of fractional operators, *Adv. Differ. Equ.*, 247 (2017).

[8] Grace S.R., Agarwal R.P., Wong P.J.Y., Zafer A., On the oscillation of fractional differential equations, *Fract. Calc. Appl. Anal.*, 15 (2012) 222-231.

[9] Zhu P., Xiang Q., Oscillation criteria for a class of fractional delay differential equations, *Adv. Differ. Equ.*, 2018:403 (2018).

[10] Bolat Y., On the oscillation of fractional order delay differential equations with constant coefficients, *Commun. Nonlinear Sci. Numer. Simul.*, 19 (2014) 3988-3993.

[11] Chen D.X., Oscillation criteria of fractional differential equations, *Adv. Differ. Equ.*, 2012:33 (2012).

[12] Abdalla B., Abdeljawad T., Oscillation criteria for kernel function dependent fractional dynamic equations, *Discrete & Continuous Dynamical Systems - S*, 14(10) (2021).

[13] Zhou Y., Ahmad B., Chen F., Alsaedi A., Oscillation for fractional partial differential equations, *Bull. Malays. Math. Soc.*, 42 (2019) 449-465.

[14] Aphithana A., Ntouyas S.K., Tariboon J., Forced oscillation of fractional differential equations via conformable derivatives with damping term, *Bound. Value Probl.*, 2019 (2019) 1-16.

[15] Chen D., Qu P., Lan Y., Forced oscillation of certain fractional differential equations, *Adv. Differ. Equ.*, 2013 (2013) 125-134.

[16] Alzabut J., Abdeljawad T., Sufficient conditions for the oscillation of nonlinear fractional difference equations, *J. Fract. Calc. Appl.*, 5(1) (2014) 177-187.

[17] Abdalla B., On the oscillation of q-fractional difference equations, *Adv. Differ. Equ.*, 2017:254 (2017) 1-11.

[18] Abdalla B., Oscillation of differential equations in the frame of nonlocal fractional derivatives generated by conformable derivatives, *Adv. Differ. Equ.*, 2018:107 (2018) 1-15.

[19] Abdalla B., Abdeljawad T., On the oscillation of Hadamard fractional differential equations, *Adv. Differ. Equ.*, 2018:409 (2018).

[20] Aslıyüce S., Güvenilir A.F., Zafer A., Oscillation criteria for a certain class of fractional order integro-differential equations, *Hacet. J. Math. Stat.*, 46(2) (2017) 199-207.

[21] Mert R., Bayeğ S., Abdeljawad T., Abdalla B., On the oscillation of kernel function dependent fractional integro-differential equations, *Rocky Mt. J. Math.*, 52(4) (2022) 1451-1460.

[22] Restrepo J.E., Suragan D., Oscillatory solutions of fractional integro-differential equations, *Math. Methods Appl. Sci.*, 43(15) (2020) 9080-9089.

[23] Restrepo J.E., Suragan D., Oscillatory solutions of fractional integro-differential equations II, *Math. Methods Appl. Sci.*, 44(8) (2021) 7262-7274.

[24] Grace S.R., Zafer A., Oscillatory behavior of integro-dynamic and integral equations on time scales, *Appl. Math. Lett.*, 28 (2014) 47-52.

[25] Kilbas A.A., Srivastava M.H., Trujillo J.J., Theory and Application of Fractional Differential Equations, North Holland Mathematics Studies 204, (2006).

[26] Jarad F., Abdeljawad T., Generalized fractional derivatives and Laplace transform, *Discrete and Continuous Dynamical Systems-S*, 13 (2020) 709-722.

[27] Samko S.G., Kilbas A.A., Marichev O.I., Fractional Integrals and Derivatives: Theory and Applications, Gordon and Breach, Yverdon, (1993).

[28] Hardy G.H., Littlewood J.E., Polya G., Inequalities, Cambridge University Press, (1988).

Cumhuriyet Science Journal

Effect of Quantum Barrier Thickness on the Optical Properties of Triple Triangular GaAs/AlGaAs Quantum Wells

Behçet Özgür Alaydın [1,a,*]

[1] Department of Electronics and Automation, Sivas Cumhuriyet University, 58140, Sivas, Türkiye
*Corresponding author

Research Article

ABSTRACT

This study investigates the electronic and optical properties of a GaAs/Al$_x$Ga$_{1-x}$As triple triangular quantum well (QW) structure, focusing on the $2-4$ and $3-4$ intersubband transitions. By varying the right barrier (R$_B$) thickness from 0 to $6\,nm$, the impact on wave function localization, energy levels, dipole moment matrix elements, absorption coefficients, and refractive index changes was analyzed using a finite element-based Schrödinger solver. Quantitative results indicate that increasing the R$_B$ breaks the symmetry of the potential, enabling the $2-4$ transition and causing variations in absorption coefficients, which peak at $4\,nm$ before declining. The $3-4$ transition exhibits a higher and more stable total absorption coefficient compared to the $2-4$ transition, ranging from 1100 to 1125 cm^{-1}. Additionally, the total refractive index changes for the $3-4$ transition remain constant (±0.006 to ±0.009), while the $2-4$ transition shows more variation (±0.001). Qualitatively, the $3-4$ transition's stability and minimal energy difference from the $2-4$ transition make it a more promising candidate for terahertz device applications, particularly where R$_B$ thickness constraints are present. These findings underscore the importance of barrier engineering in optimizing QW-based devices for advanced semiconductor application.

Keywords: GaAs, AlGaAs, Quantum Well, Absorption Coefficients, Refractive Index Change.

a ✉ balaydin@cumhuriyet.edu.tr 　　 ID https://orcid.org/0000-0003-0935-4836

Introduction

Advances in semiconductor (SC) device technology have increasingly impacted daily life, even though many SC devices have reached a point of efficiency saturation. However, improvements in artificial intelligence (AI) have introduced new perspectives on SC devices due to the microchips used as essential hardware for AI. As a result, research on SC devices has accelerated in recent years.

Researchers are striving to develop more efficient SC devices, with many focusing on fundamental aspects such as nanoscale quantum wells (QWs). State-of-the-art devices and record-breaking performances continue to be achieved with QW-based devices, and enhancing QW efficiency is widely believed to be key to further improvements. For this reason, I have studied the triple triangular QW structure to investigate the electronic and optical properties of the GaAs/Al$_x$Ga$_{1-x}$As QWs structure.

In literature, numerous studies have been published, many of which are still under review. Öztürk et al. [1] examined the dependence of intersubband transitions in QWs on intense laser fields (ILF). Sayrac et al. [2] investigated the modulation of harmonic generation coefficients (HGC) in n-type quadruple δ-doped GaAs QWs under external fields. Restrepo et al. [3] studied mid-infrared linear optical transitions in δ-doped AlGaAs/GaAs triple QWs. Martinez-Orozco et al. [4] focused on nonlinear optical absorption (OA) and refractive index change (RIC) for field-effect transistor under hydrostatic pressure. Ozturk et al. [5] explored the effect of ILFs on

the nonlinear optical properties of triple QWs with parabolic and inverse-parabolic profiles. Alaydin [6] analyzed the optical properties of GaAs/Al$_x$Ga$_{1-x}$As superlattices under an electric field. Dakhlaoui published results on linear and nonlinear OA coefficients and RICs in GaN/Al$_x$Ga$_{1-x}$N double QWs operating at $1.55\,\mu m$ [7]. Durmuslar [8] investigated the nonlinear optical properties of double V-shaped Al$_x$Ga$_{1-x}$As/GaAs QWs, for structural parameters under ILF. Magdaleno et al. [9] examined asymmetric GaAs n-type double δ-doped QWs, focusing on the effects of an applied electric field. Barseghyan et al. [10] studied the donor binding energy and photoionization cross sections in a Pöschl–Teller QW. Karabulut et al. [11] investigated linear and nonlinear intersubband OAs in asymmetric rectangular QWs. Sayrac [12] explored the nonlinear optical properties of semi-exponential QWs. Karimi et al. [13] analyzed linear and nonlinear intersubband OA and RICs in QWs. Niculescu et al. [14] studied the density of impurity states of shallow donors in a QW under ILF. Liu et al. [15] detailed electric field effects on HGC in Al$_x$Ga$_{1-x}$As/GaAs QWs. Altun et al. [16] analyzed the linear and nonlinear optical properties of a superlattice with periodically increased well width under electric and magnetic fields. All these studies have contributed to advancements in QW technology.

In this study, I investigated the absorption coefficients and refractive index changes of the (2-4) and (3-4) transitions of triple triangular QWs. The quantum barrier

(QB) thickness on the right side varies from 0 to $6\,nm$ in $1\,nm$ increments. The paper is organized into three sections: i) Section II provides the theoretical background of the triple triangular QW structure; ii) Section III discusses the computational results; iii) Section IV concludes the paper.

Theory

A time-independent, one-dimensional Schrödinger equation is solved using a custom in-home Matlab code based on the finite element method [16, 17]. During the calculation, all operators are first created, and then the Hamiltonian is constructed. Diagonalization is subsequently performed to compute the eigenfunctions. In the end, the wave functions (WFs) and corresponding energy levels (ELs) are obtained under the effective mass approximation. The Hamiltonian for the triangular GaAs/Al$_x$Ga$_{1-x}$As QWs structure, featuring a periodically increasing right barrier, is provided in Equation (1).

$$H = -\frac{\hbar^2}{2m^*}\frac{d^2}{dz^2} + V(z) \tag{1}$$

where the second-order differential is written as:

$$\frac{d^2}{dz^2} = \left[-2\,\text{diag}\big(\text{ones}(1, N_z)\big) + \text{diag}(\text{ones}(1, N_z - 1), -1) + \text{diag}(\text{ones}(1, N_z - 1), 1)\right]^2 \tag{2}$$

Here, m^* represents the effective mass of the electron, taken as 0.067 m_0 due to the lattice matching between GaAs and Al$_x$Ga$_{1-x}$As (m_0 being the free electron mass). e is the electron charge, N_z defines the matrix length of the total quantum region. The length of N$_z$ determines the size of the diagonalization matrix. A resolution step size of 1 Å is used, which results in a diagonalization matrix size of 600, and $V(z)$ represents the confinement potential. The QW structure consists of three triangular QWs, each with a width of $12\,nm$. The quantum barrier (QB) between the left and middle QWs is 0, while the QB between the middle and right QWs increases from 0 to $6\,nm$ in $1\,nm$ increments. For the GaAs/Al$_x$Ga$_{1-x}$As QW structure, the conduction band offset and potential discontinuity V_0 are set to 0.6 and $228\,meV$ (corresponding to Aluminium concentration of 0.3), respectively [18, 19].

To solve the time-independent Schrödinger equation, diagonalization is performed in one dimension. After obtaining the ELs and their corresponding WFs, the linear absorption coefficients (LACs), third order nonlinear absorption coefficients (NACs), and total absorption coefficients (TACs) for the $(2-4)$ and $(3-4)$ intersubband transitions are calculated for the first four ELs using the density matrix approach [20, 21].

$$\beta_{if}^{(1)}(\omega) = \omega\sqrt{\frac{\mu}{\varepsilon_r}}|M_{if}|^2\,\frac{e^2\,\sigma_v\,\hbar\,\Gamma}{(E_{if}-\hbar\omega)^2+(\hbar\,\Gamma)^2} \tag{3}$$

$$\beta_{if}^{(3)}(\omega, I) = -2\omega\sqrt{\frac{\mu}{\varepsilon_r}}|M_{if}|^4\left(\frac{I}{\varepsilon_0 c\,n_r}\right)\frac{e^4\,\sigma_v\,\hbar\,\Gamma}{\{(E_{if}-\hbar\omega)^2+(\hbar\,\Gamma)^2\}^2} \times \left[1 - \frac{|\delta_{if}|^2}{|2M_{if}|^2}\left(\frac{(E_{if}-\hbar\omega)^2-(\hbar\,\Gamma)^2+2E_{if}(E_{if}-\hbar\omega)}{(E_{if})^2+(\hbar\,\Gamma)^2}\right)\right] \tag{4}$$

$$\beta_{if}(\omega, I) = \beta_{if}^{(1)}(\omega) + \beta_{if}^{(3)}(\omega, I) \tag{5}$$

The linear refractive index change (LRICs), non-linear refractive index change (NRICs), and total refractive index change (TRICs) can be formulated as follows [22, 23]:

$$\frac{\Delta n_{if}^{(1)}(\omega)}{n_r} = \frac{e^2\,\sigma_v}{2\varepsilon_0 n_r^2}|M_{if}|^2\,\frac{(E_{if}-\hbar\omega)}{(E_{if}-\hbar\omega)^2+(\hbar\,\Gamma)^2} \tag{6}$$

$$\frac{\Delta n_{if}^{(3)}(\omega, I)}{n_r} = -\frac{\mu c}{4\,\mathcal{E}_0 n_r^3}|M_{if}|^2\,\frac{e^4\,\sigma_v\,I}{\{(E_{if}-\hbar\omega)^2+(\hbar\,\Gamma)^2\}^2}\times$$
$$\left[4(E_{if}-\hbar\omega)|M_{if}|^2 - \frac{\delta_{if}^2}{(E_{if})^2+(\hbar\,\Gamma)^2}\times\{(E_{if}-\hbar\omega)[E_{if}(E_{if}-\hbar\omega)-(\hbar\,\Gamma)^2]-(\hbar\,\Gamma)^2[2E_{if}-\hbar\omega]\}\right] \tag{7}$$

$$\frac{\Delta n_{if}(\omega, I)}{n_r} = \frac{\Delta n_{if}^{(1)}(\omega)}{n_r} + \frac{\Delta n_{if}^{(3)}(\omega, I)}{n_r} \tag{8}$$

Intersubband dipole moment matrix elements (DMMEs) are obtained by

$$M_{if} = \int \Psi_f^*\,z\,\Psi_i\,dz\,, \qquad (i, f = 1, 2, 3, 4) \tag{9}$$

Here, $\delta_{if} = M_{ff} - M_{ii}$ represents the intra-subband DMMEs, I is the optical light intensity, and ω is the angular frequency of the incident photon. $E_{if} = E_f - E_i = \hbar\,\omega_{if}$, where E_f and E_i represent the quantized ELs of the final and initial states, respectively. $\mathcal{E}_0$ is the vacuum permittivity, $\mathcal{E}_r$ is the real part of the permittivity, μ is the magnetic permeability, n_r is the refractive index, and σ_v is the carrier density.

Result and Discussion

I have theoretically studied the electronic and optical properties for the $(2-4)$ and $(3-4)$ transitions in the triple triangular QW structure. Other transitions, such as $(1-2)$, $(1-3)$, $(1-4)$ and $(2-3)$, were not included in the study due to negligibly small values (the DMME, TAC and RIC values are lower than 10^{-24}). In this study, I have used $\sigma_v = 4\text{x}10^{16}\text{cm}^{-3}$, T $= 1\,/\,\Gamma = 0.14\,\text{ps}$ and an optical intensity $I = 0.5\,\text{MW/cm}^2$ [24, 25].

Figure 1 shows the potential variation of the triple triangular QWs for different right barrier (R$_B$) widths. When the R$_B$ is 0 nm, the ground state EL (blue line) is distributed across the wells, with most localization in the middle QW. A similar behavior is observed for the second excited state (green line). The first excited state (red line), however, localizes in the left and right barriers, while the third excited state (pink line) shows an irregular distribution across the QW region. As the R$_B$ increases from 0 to 2 nm, the symmetry of the potential is broken,

leading to changes in the localization of the states. The ground and second excited states shift to the left and middle QWs, with their probability in the right well dropping to almost zero. In contrast, the first excited state becomes localized in the right QW. The irregular distribution of the third excited state remains but starts to shift toward the left side of the QW region. These changes are attributed to the broken symmetry. With further increases in R_B thickness ($4\ nm$ and $6\ nm$), the localization

of states becomes more defined. The ground and second excited states are primarily confined to the left and middle QWs, with no localization in the right QW. The first excited state is fully localized in the right well, while the third excited state shows significant distribution in the left and middle QWs. It is evident that R_B thickness disrupts the symmetry in the structure, although some coupling between the wells remains.
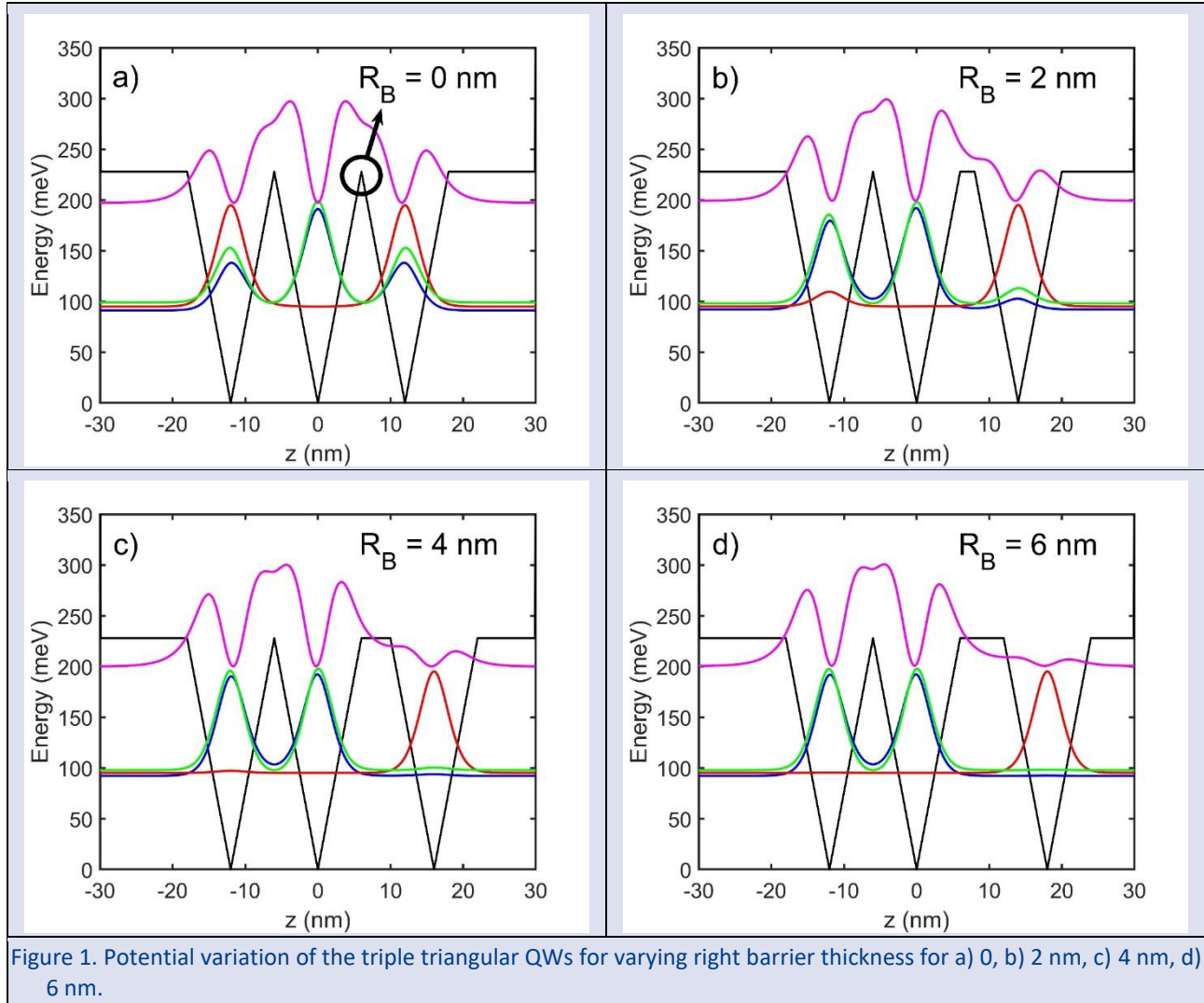
Figure 1. Potential variation of the triple triangular QWs for varying right barrier thickness for a) 0, b) 2 nm, c) 4 nm, d) 6 nm.

Figure 2 illustrates the variation of ELs, energy differences, and DMMEs as a function of the right barrier R_B. As shown in Figure 2a, the ELs are minimally affected by changes in R_B thickness. Consequently, the energy differences for the $2-4$ and $3-4$ transitions vary within a small range, with approximate differences of $3\ meV$ and $5\ meV$, respectively. In Figure 2b, the DMMEs for the $2-4$ and $3-4$ transitions, along with the intersubband transitions for the $2-4$ and $3-4$ levels, are presented. The DMMEs for the $1-2$, $1-3$, $1-4$ and, $2-3$ transitions are zero and are not shown. While it is

understood that the $3-4$ transition is more probable and more than an order of magnitude higher than the $2-4$ transition, both transitions are largely independent of the R_B thickness. The intersubband DMMEs (δ_{34}, δ_{24}) for these transitions are proportional to the R_B thickness, with the rate of increase for the $3-4$ transition consistently higher than that of the $2-4$ transition. This further supports the conclusion that the $3-4$ transition is more probable than the $2-4$ transition.
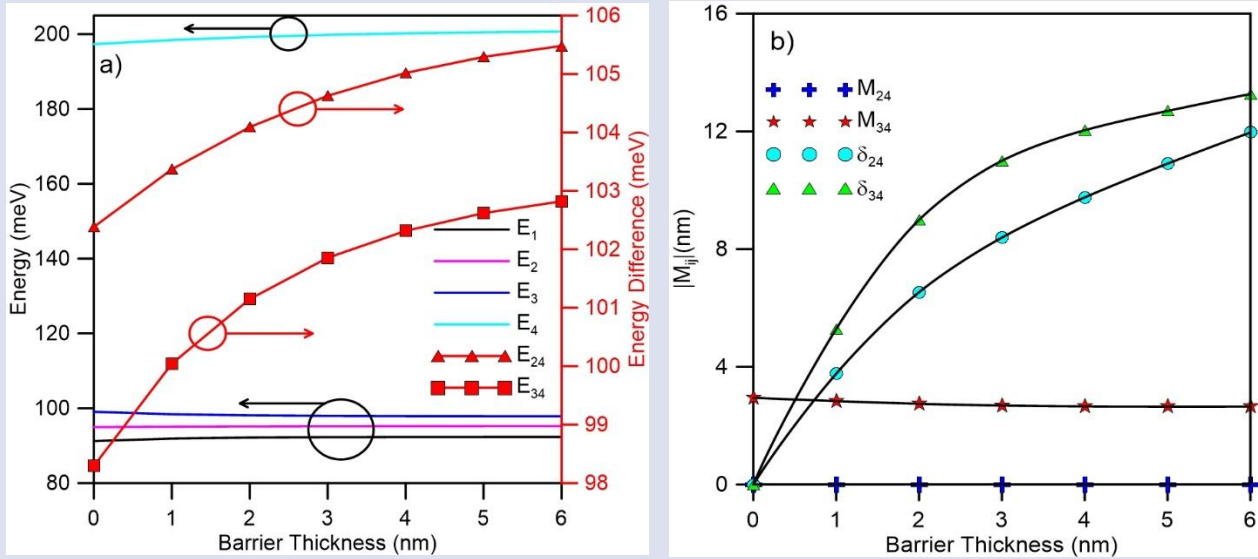
.

Figure 2. a) Variation of the ELs and energy differences, b) variation of the DMMEs.

In Figure 3, LACs, NACs, and TACs of the $2-4$ transition are presented. When the R$_B$ is zero, the absorption coefficients are also zero due to the symmetry of the structure. As the R$_B$ increases, LAC, NAC, and TAC become non-zero due to the broken symmetry and the shift in the WFs, which alters the DMME and enables the $2-4$ transition. With $1\,nm$ increments in R$_B$ thickness, LAC, NAC, and TAC increase up to $4\,nm$, after which further increases in R$_B$ thickness result in a noticeable decrease in the absorption coefficients. The TAC reaches approximately $69\,cm^{-1}$ due to δ_{24} which is increasing. The absorption coefficients for the $2-4$ transition are comparable to values reported in the literature [3, 8, 19]. Additionally, a slight blue shift is observed in the optical

spectrum, resulting from the small increase in energy difference, as mentioned earlier.

In Figure 4, LACs, NACs, and TACs of the $3-4$ transition are plotted. For an R$_B$ of 0 nm, the LAC is approximately $2086\,cm^{-1}$. However, as the R$_B$ increases, the LAC decreases almost linearly, down to around $1760\,cm^{-1}$. This decline is due to the reduction of M_{34}, as shown in Figure 2b. Despite the changes in LAC, the TAC for the $3-4$ transition remains largely unaffected by R$_B$ variation. This is because the NAC decreases in inverse proportion to the linear reduction in LAC, owing to the more significant increase in δ_{34} compared to M_{34}. As a result, the TAC fluctuates between approximately 1100 and $1125\,cm^{-1}$. Similar to the $2-4$ transition, a slight blue shift is also observed in the $3-4$ transition.
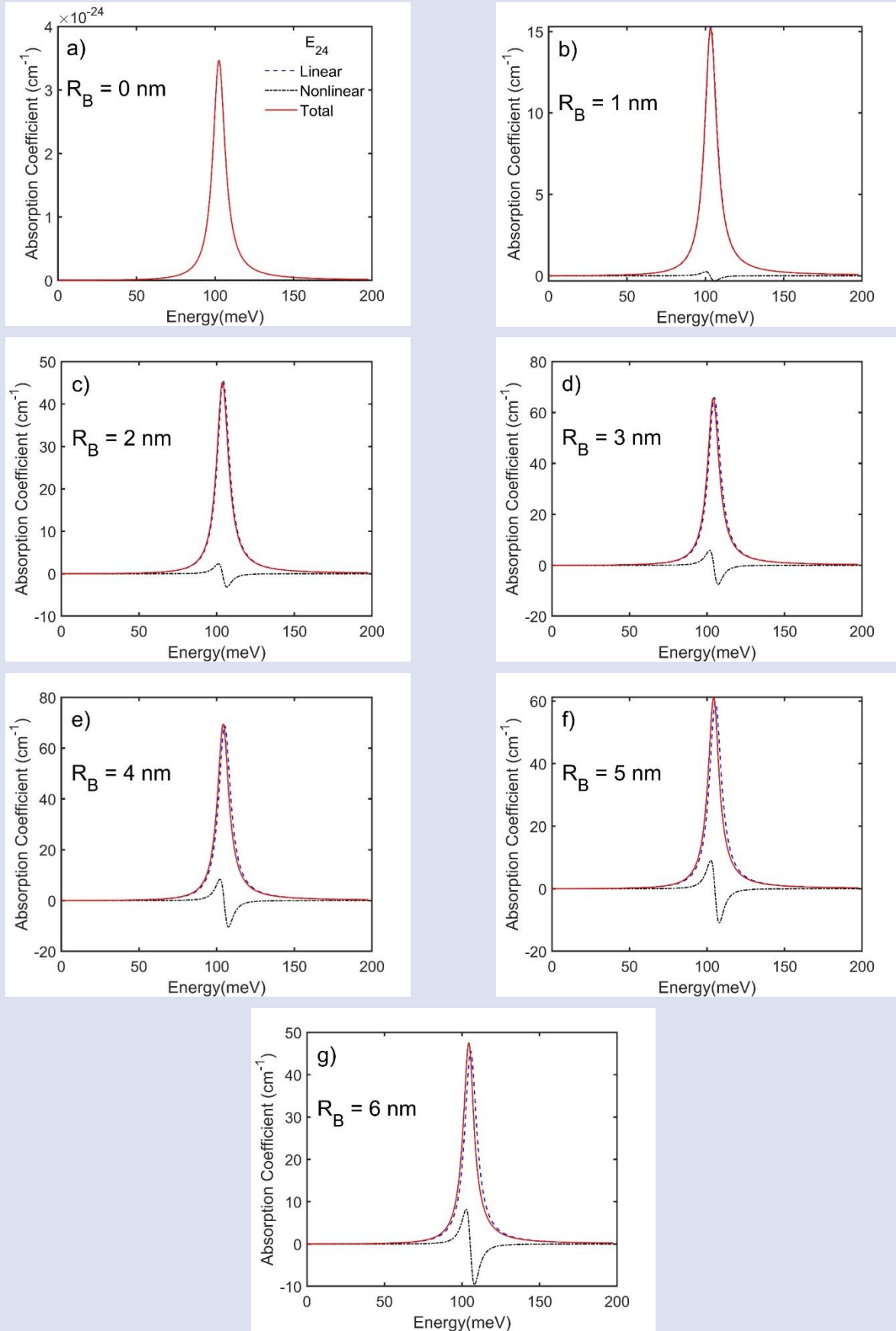
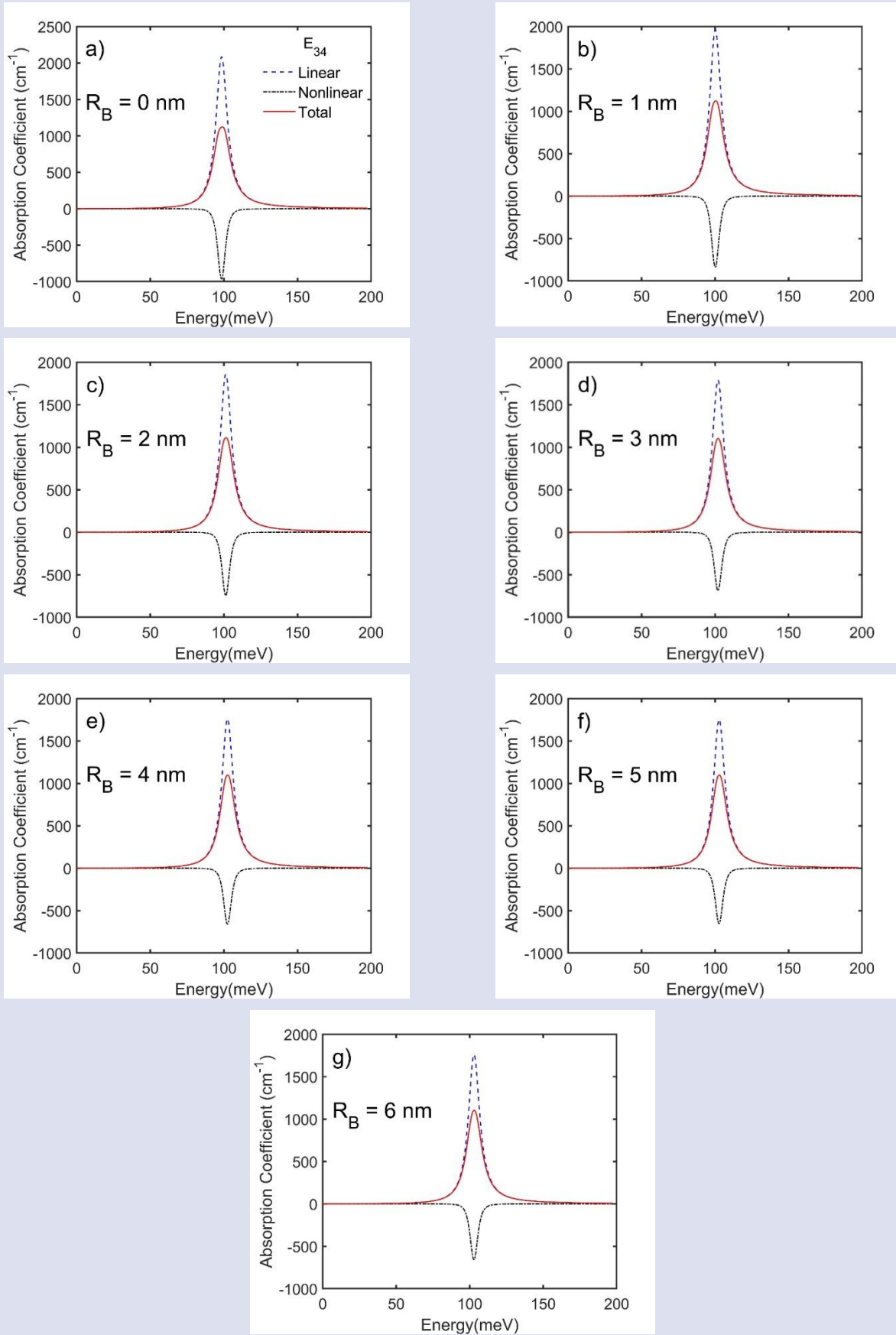Figure 3. LACs, NACs and TACs of the 2 — 4 transition for varying R_B thickness.

Figure 4. LACs, NACs and TACs of the 3 − 4 transition for varying R_B thickness.

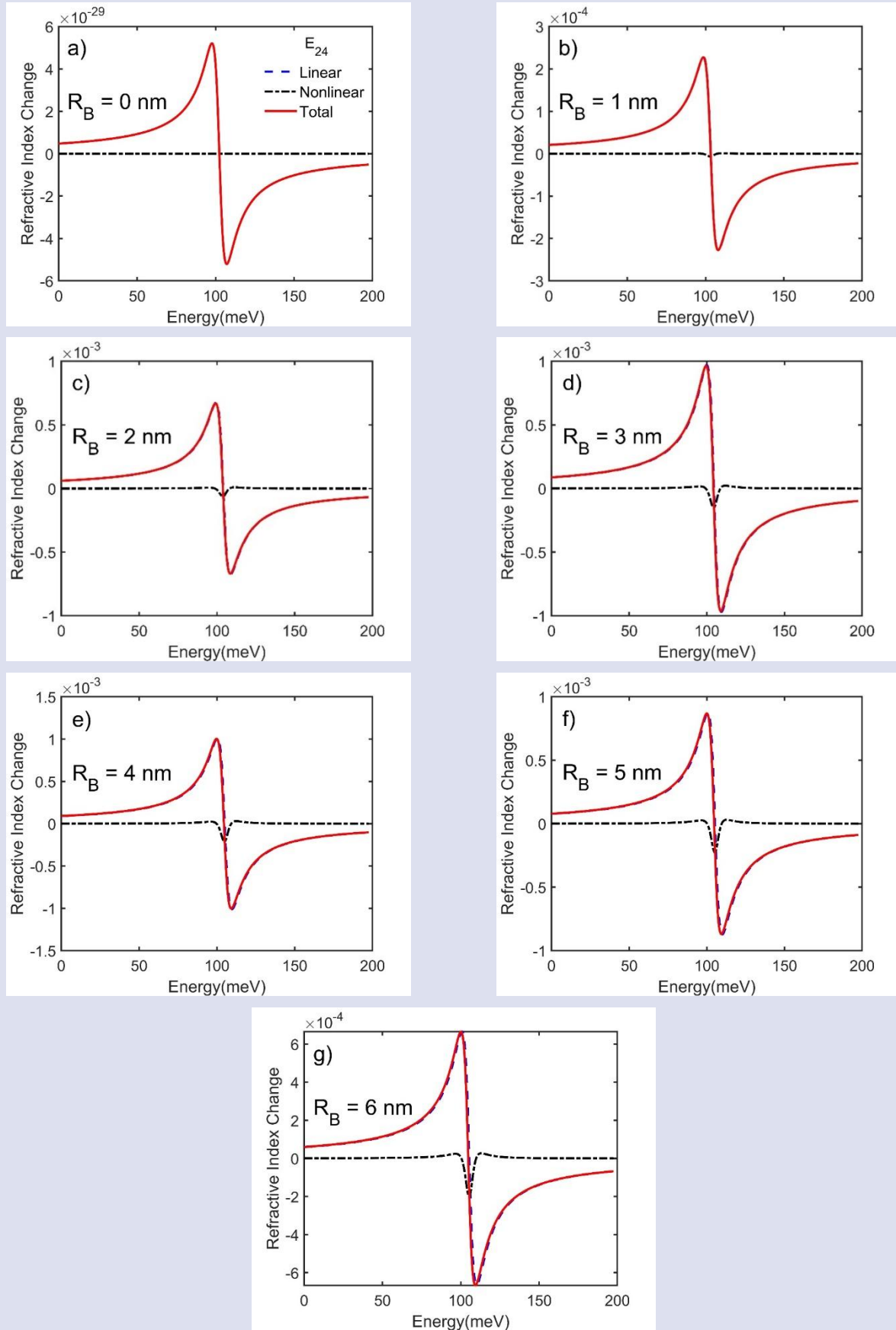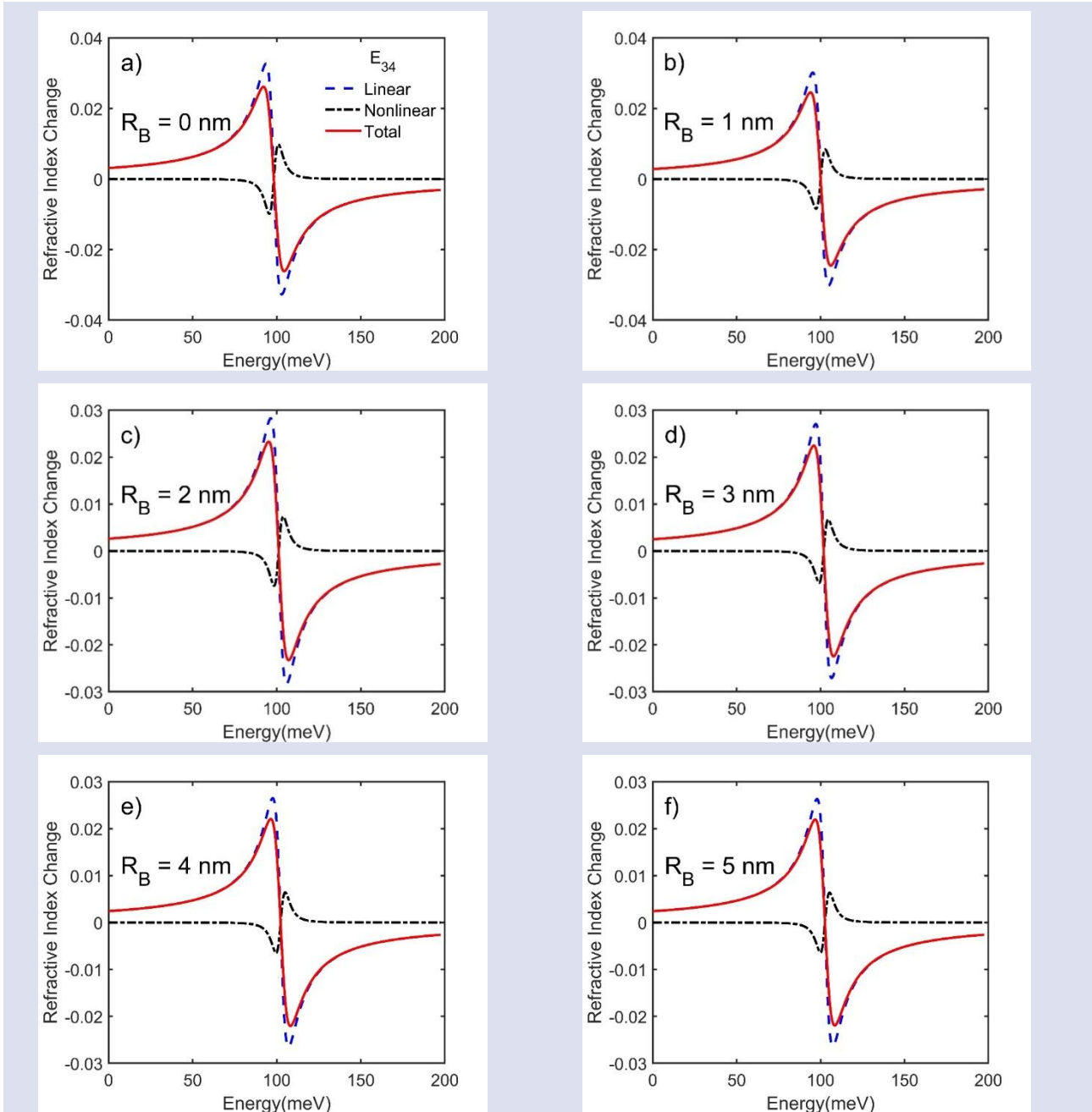Figure 5. LRICs, NRICs and TRICs of the $2-4$ transition for varying R_B thickness.

As shown in Figure 5, the refractive index change for the $2-4$ transition is zero when the R_B is $0\,nm$, as expected. With an increase in R_B to $1\,nm$, very small changes in the LRIC and NRIC are observed. Consequently, a slight variation in the TRIC is noted. Like the TAC, the TRIC reaches its maximum at an R_B thickness of $4\,nm$,

corresponding to the maximum point for M_{ij}. The variation in TRIC is around ±0.001, which is comparable to the values reported in the literature for other transitions [9-11]. While a blue shift is observed in the TRICs, it is negligible due to the steep variation in LRIC and NRIC.

The variation of the R_B affects LRICs and NRICs for the $3-4$ transition in a linear and inverse linear manner, respectively, resulting in an almost constant TRIC, as shown in Figure 6. Consequently, the TRIC varies between

±0.006 and ±0.009 for R_B values ranging from 0 to 6 nm. This indicates that devices based on the $3-4$ transition are only minimally affected by R_B variation, which could be advantageous for semiconductor device applications where thickness limitations are a concern. In addition, the $3-4$ transition can be favored over the $2-4$ transition due to its greater stability. The small energy differences between the $2-4$ and $3-4$ transitions make the $3-4$ transition more suitable for terahertz (THz) device applications.
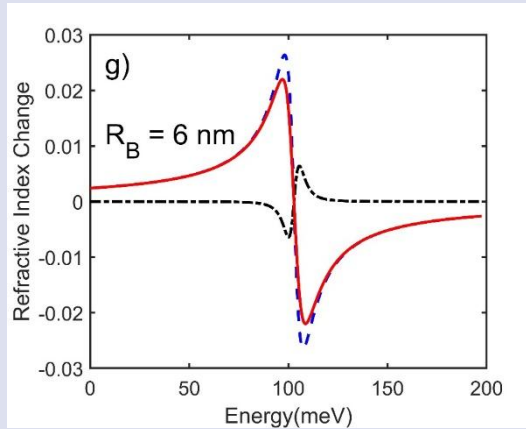
Figure 6. LRICs, NRICs and TRICs of the 3 − 4 transition for varying R$_B$ thickness.

Table 1 presents the maximum values of the total AC and RIC for the 2 − 4 and 3 − 4 transitions. A similar trend is observed for both the AC and RIC coefficients. Breaking the symmetry through variations in the R$_B$ thickness enhances the TAC of the 2 − 4 transitions, reaching its peak for an R$_B$ thickness of 4 nm, while the TAC of the 3 − 4 transitions decreases. This indicates that $4\,nm$ is the critical thickness for maximizing the TAC. Furthermore, the RIC coefficients are only slightly affected by these changes: the RIC of the 2 − 4 transitions increases, whereas the RIC of the 3 − 4 transitions decreases.

Table 1. Maximum values of the total AC and RIC of the 2-4 and 3-4 transitions.

RB (nm)	Total Maximum Values			
	TAC $2 − 4\ (cm − 1)$	TAC $3 − 4\ (cm − 1)$	RIC $(2 − 4)$	RIC $(3 − 4)$
0	0	1124	0	0.026
1	15	1119	0	0.024
2	45	1105	0	0.023
3	65	1101	0.001	0.022
4	69	1098	0.001	0.022
5	61	1090	0.001	0.022
6	48	1104	0.001	0.022

Conclusion

In this study, the electronic and optical properties of a triple triangular QW structure based on GaAs/AlxGa1-xAs were analyzed with a focus on the 2 − 4 and 3 − 4 intersubband transitions. The influence of varying RB thicknesses (from 0 to $6\,nm$) on ELs, DMMEs, absorption coefficients, and refractive index changes were investigated. The results show that the RB thickness has a noticeable impact on the localization of WFs and symmetry of the potential. Specifically, increasing the RB thickness breaks the symmetry, leading to shifts in the energy levels and enabling the otherwise forbidden 2 − 4 transition. In contrast, the 3 − 4 transition remains more probable and consistent throughout the study, being only minimally affected by the RB variation. Quantitative analysis revealed that while both the 2 − 4 and 3 − 4 transitions exhibit slight energy shifts, the absorption coefficients of the 3 − 4 transition are significantly higher, supporting its greater transition probability. Notably, the TACs and TRICs of the 3 − 4 transition are relatively stable with respect to RB variation, unlike the 2 − 4 transition, which shows a peak in absorption at $4\,nm$ RB before declining. This stability suggests that the 3 − 4 transition is more suitable for applications in semiconductor devices, especially where thickness limitations are critical.

Furthermore, the small energy difference between the 2 − 4 and 3 − 4 transitions makes the latter more viable for terahertz (THz) device applications. Overall, the 3 − 4 transition's robustness against structural variations and its high optical response make it a favorable candidate for high-performance THz devices, further supporting the significance of QW-based structures in next-generation semiconductor technologies.

Conflict of Interest

There are no conflicts of interest in this work.

Acknowledge

No acknowledgement

Ethical Approval Statement

No ethical statement required

References

[1] Ozturk E., Sari H., Sokmen I., The dependence of the intersubband transitions in square and graded QWs on intense laser fields, *Solid State Communications*, 132(7) (2004) 497-502.

[2] Sayrac H., Jaouane M., Ed-Dahmouny A., Sali A., Ungan F., Modulation of nonlinear optical rectification, second, and third harmonic generation coefficients in n-type quadruple δ-doped GaAs quantum wells under external fields, *Physica B: Condensed Matter*, 690 (2024) 416252.

[3] Restrepo R.L., Castaño-Vanegas L.F., Martínez-Orozco J.C., Morales A.L., Duque C.A., Mid-Infrared linear optical transitions in delta-doped AlGaAs/GaAs triple-quantum well, *Applied Physics A*, 125(1) (2018) 31.

[4] Martínez-Orozco J.C., Mora-Ramos M.E., Duque C.A., The nonlinear optical absorption and corrections to the refractive index in a GaAs n-type delta-doped field effect transistor under hydrostatic pressure, *Physica Status Solidi B*, 249(1) (2012) 146-152.

[5] Ozturk O., Alaydin B.O., Altun D., Ozturk E., Intense laser field effect on the nonlinear optical properties of triple quantum wells consisting of parabolic and inverse-parabolic quantum wells, *Laser Physics*, 32(3) (2022) 035404.

[6] Alaydin B.Ö., Optical Properties of Gaas/Alxga1-xas Superlattice Under E-Field for Quantum Cascade Laser Application, *Gazi University Journal of Science*, 34(4) (2021) 1179-1191.

[7] Dakhlaoui H., Linear and nonlinear optical absorption coefficients and refractive index changes in GaN/AlxGa(1−x)N double quantum wells operating at 1.55 μm, *Journal of Applied Physics*, 117(13) (2015).

[8] Salman Durmuslar A., Investigation on nonlinear optical properties of symmetric and asymmetric double V-shaped AlxGa1-xAs/GaAs potential wells with structural parameters and external electromagnetic fields, *Philosophical Magazine*, 103(9) (2023) 872-891.

[9] Rodríguez-Magdaleno K.A., Martínez-Orozco J.C., Rodríguez-Vargas I., Mora-Ramos M.E., Duque C.A., Asymmetric GaAs n-type double δ-doped quantum wells as a source of intersubband-related nonlinear optical response: Effects of an applied electric field, *Journal of Luminescence*, 147 (2014) 77-84.

[10] Barseghyan M.G., Hakimyfard A., López S.Y., Duque C.A., Kirakosyan A.A., Simultaneous effects of hydrostatic pressure and temperature on donor binding energy and photoionization cross section in Pöschl–Teller quantum well, *Physica E: Low-dimensional Systems and Nanostructures*, 42(5) (2010) 1618-1622.

[11] Karabulut İ., Atav Ü., Şafak H., Tomak M., Linear and nonlinear intersubband optical absorptions in an asymmetric rectangular quantum well, *The European Physical Journal B*, 55(3) (2007) 283-288.

[12] Sayrac M., Effects of applied external fields on the nonlinear optical rectification, second, and third-harmonic generation in an asymmetrical semi exponential quantum well, *Optical and Quantum Electronics*, 54(1) (2021) 52.

[13] Karimi M.J., Keshavarz A., Poostforush A., Linear and nonlinear intersubband optical absorption and refractive index changes of asymmetric double semi-parabolic quantum wells, *Superlattices and Microstructures*, 49(4) (2011) 441-452.

[14] Niculescu E.C., Burileanu L.M., Radu A., Density of impurity states of shallow donors in a quantum well under intense laser field, *Superlattices and Microstructures*, 44(2) (2008) 173-182.

[15] Liu G., Guo K., Zhang Z., Hassanbadi H., Lu L., Electric field effects on nonlinear optical rectification in symmetric coupled AlxGa1−xAs/GaAs quantum wells, *Thin Solid Films*, 662 (2018) 27-32.

[16] Altun D., Ozturk O., Alaydin B.O., Ozturk E., Linear and nonlinear optical properties of a superlattice with periodically increased well width under electric and magnetic fields, *Micro and Nanostructures*, 166 (2022) 207225.

[17] Nakamura K., Shimizu A., Koshiba M., Hayata K., Finite-element analysis of quantum wells of arbitrary semiconductors with arbitrary potential profiles, *IEEE Journal of Quantum Electronics*, 25(5) (1989) 889-895.

[18] Karimi M.J., Keshavarz A., Second harmonic generation in asymmetric double semi-parabolic quantum wells: Effects of electric and magnetic fields, hydrostatic pressure and temperature, *Physica E: Low-dimensional Systems and Nanostructures*, 44(9) (2012) 1900-1904.

[19] Ozturk E., Nonlinear optical absorption in graded quantum wells modulated by electric field and intense laser field, *The European Physical Journal B*, 75(2) (2010) 197-203.

[20] Alaydin B.O., Altun D., Ozturk E., Linear and nonlinear optical properties of semi-elliptical InAs quantum dots: Effects of wetting layer thickness and electric field, *Thin Solid Films*, 755 (2022) 139322.

[21] Kaynar E., Alaydin B.O., Optical properties of AlxInyGa1−x−yAs/AlzGawIn1−z−wAs quantum wells under electric and magnetic fields for telecommunication applications, *The European Physical Journal Plus*, 138(2) (2023) 121.

[22] Alaydin B.O., Effect of high bandgap AlAs quantum barrier on electronic and optical properties of In0.70Ga0.30As/Al0.60In0.40As superlattice under applied electric field for laser and detector applications, *International Journal of Modern Physics B*, 35(02) (2021) 2150027.

[23] Zhang Z.-H., Yuan J.-H., Guo K.-X., The Combined Influence of Hydrostatic Pressure and Temperature on Nonlinear Optical Properties of GaAs/Ga0.7Al0.3As Morse Quantum Well in the Presence of an Applied Magnetic Field, *Materials*, 11(5) (2018) 668.

[24] Alaydin B.O., Altun D., Ozturk O., Ozturk E., High harmonic generations triggered by the intense laser field in GaAs/AlxGa1-xAs honeycomb quantum well wires, *Materials Today Physics*, 38 (2023) 101232.

[25] Ozturk E., Nonlinear intersubband transitions in different shaped quantum wells under intense laser field, *Superlattices and Microstructures*, 82 (2015) 303-312.

Cumhuriyet Science Journal

The Effect of The Geometry of Side Quantum Wells on The Optical Properties of Triple Quantum Wells Under The Electric Field Influence

Bahadır Bekar [1,a,*]

[1] Keşan Vocational School, Trakya University, Keşan, Edirne, Türkiye.
*Corresponding author

Research Article

ABSTRACT

The electronic and optical properties of the symmetrical $Al_x Ga_{1-x} As/GaAs$ multiple quantum wells were investigated. The system consists of three triangular-shaped quantum wells in which the potentials of left- and right-hand side wells were shallower in comparison with that of the center well. The calculations were carried out for different potential shapes as the triangular shapes of the left- and right-hand side wells varied from triangle to square shape keeping the center well potential constant. The energy levels were calculated using the finite difference method under the effective mass approximation, with and without an electric field. When the geometry of the side wells was changed from shallow triangular side wells to square side wells in the absence of an electric field, the optical transitions were found to shift towards smaller photon energies. When an electric field was applied, the optical absorption and refractive index changes for the (1-2) transition exhibited interesting behavior. It was found that the electronic and optical properties of structures can be controlled by the externally applied electric field by selecting appropriate structural parameters.

Keywords: Quantum well, Optical absorption, Optical refraction.

[a] ✉ bahadirbekar@trakya.edu.tr   🆔 https://orcid.org/0000-0002-7489-2190

Introduction

In the last few decades, the advances in the technology of producing low-dimensional semiconductor structures with different geometries have been extremely significant [1-5], because the devices have come out as new nanostructures. Many electro-optical devices such as LEDs, solar cells, transistors, photodiodes, photodetectors, laser diodes have been designed by combining different semiconductors such as $AlGaAs$ and $InGaN$ [6-25].

Many theoretical studies have been carried out to find out the electronic and optical properties of low-dimensional structures, and to guide experimenters in structure designs [26-47]. The lack of uniform geometric shapes of the structures makes them difficult to solve analytically. Therefore, the numerical solution methods have been developed. G. Bastard et al. used the variation method to calculate the eigenstates of the electron in the quantum well under the electric field [26]. F. K. Boz et al. calculated the binding energy of an impurity atom in double quantum wells with different geometries under magnetic and laser fields using a variational technique [27]. They showed that the potential profile of the structure indicates a strong control mechanism over the binding energy, and the binding energy increases or decreases depending on the position of the impurity atom under the applied laser and magnetic fields. A. Shaer et al. calculated the electronic and optical properties of the double inverse parabolic quantum well in the presence of hydrostatic pressure and magnetic field within the effective mass and parabolic band approximation

depending on temperature. They pointed out that the effects of temperature and hydrostatic pressure are important in practical applications in optoelectronics [28]. D. Altun et al. investigated the linear and nonlinear optical properties of $Al_x Ga_{1-x} As/GaAs$ superlattice with periodically increasing well width under magnetic and electric fields using the finite element method with the effective mass approach. They showed that the refractive index change is affected by the applied electric and magnetic fields [29]. F. Ungan et al. showed the absorption coefficient and refractive index changes for the semi-infinite inverse Gaussian-like $Al_x Ga_{1-x} As$ in the presence of the electric, the laser, and the magnetic fields[30].
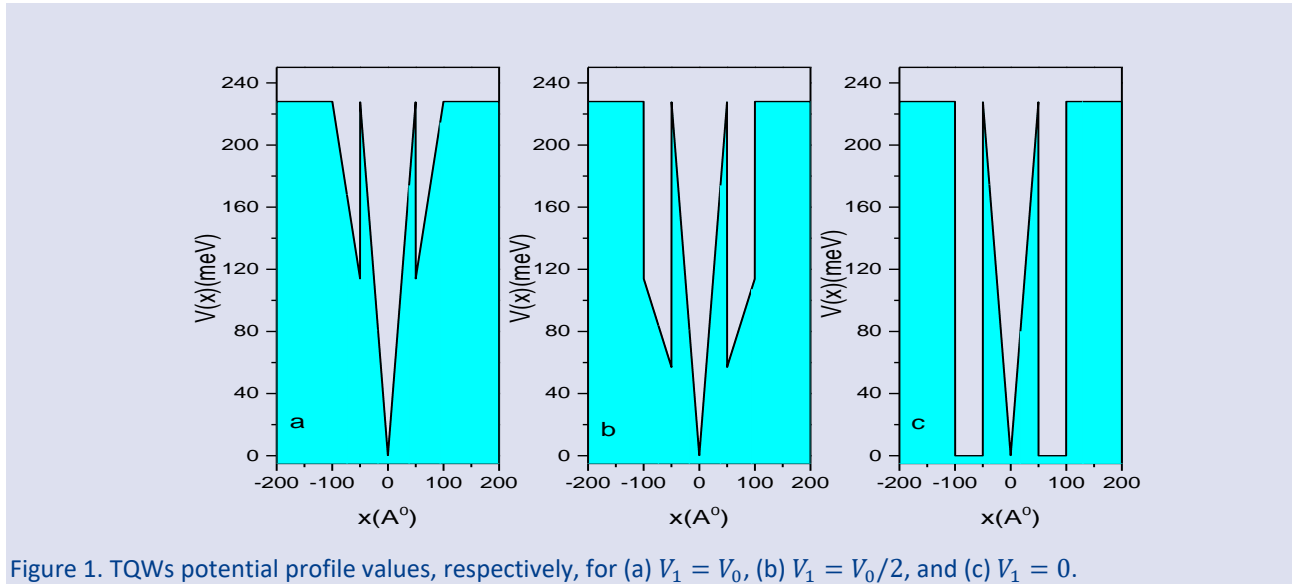
The probability density and the energy states have been seen to be varied by changing the geometries of the structures and re-shaping potential profiles of the structures with externally applied fields. These changes are very effective on the electronic and optical properties of low-dimension structures. For these reasons, a new triple quantum wells structure was considered in this study. The absorption coefficients and the refractive index changes were examined by changing the side well geometries in the triple AlxGa1-xAs/GaAs quantum wells, using the finite difference method, one of the most used methods today [44-47]. The study also shows how choosing appropriate side well geometries affects optical transitions under an electric field.

Theory

Triple quantum wells (TQWs) consist of a triangular well in the center and symmetrical wells of varying shapes on both sides were considered. While the triangular well in the center of the structure remained constant in shape and potential energy, the potential energies of the side wells on either side of the central well were considered with different depths, and also their shapes were converted from triangular into square wells. The confined potential of the TQWs, shown schematically in Fig. 1, along the *x*-axis, is defined as

$$V(x) \begin{cases} V_0, & |x| \geq 100A^0 \\ |x| * \left(\frac{V_1}{T_2}\right), & -100A^0 < x < -50A^0 \\ |x| * \left(2 * \frac{V_0}{T_2}\right) & -50 \leq x \leq 50A^0 \\ |x| * \left(\frac{V_1}{T_2}\right), & 50A^0 < x < 100A^0 \end{cases} \tag{1}$$

where T_2 in the above expression is constant and is taken as $100A^0$. The potential energy profiles of TQWs are plotted by assuming $V_1 = V_0$ in Fig. 1(a), $V_1 = V_0/2$ in Fig. 1(b), and $V_1 = 0$ in Fig. 1(c). V_0 is defined as the barrier height.

Figure 1. TQWs potential profile values, respectively, for (a) $V_1 = V_0$, (b) $V_1 = V_0/2$, and (c) $V_1 = 0$.

The time-independent Schrödinger equation for the TQWs grown along the *x*-axis is as follows

$$H\psi_n(x) = E_n\psi_n(x) \tag{2}$$

Here, H is the Hamiltonian operator and is defined as,

$$H = -\frac{\hbar^2}{2m^*}\nabla^2 + |e|Fx + V(x) \tag{3}$$

In this expression, m^* is the effective mass, e is the electron charge, and F is the electric field strength. The finite difference method is used to obtain the wavefunctions and energy states of the structures by applying the Hamiltonian in Eq.3 to the Schrödinger equation in Eq.2. The details of the method have been given elsewhere [27,47]. Using the wavefunctions and energy values of the first two states, the linear and nonlinear absorption coefficients of the TQWs in the transitions between the two energies were found as follows

$$\beta^{(1)}(\omega) = \frac{\sigma}{c\varepsilon_0 n_s} \frac{\hbar\omega|M_{if}|^2/\tau_{in}}{(E_{if} - \hbar\omega)^2 + (\hbar/\tau_{in})^2} \tag{4}$$

$$\text{and} \beta^{(3)}(\omega, I) = -\frac{2\sigma}{(c\varepsilon_0 n_s)^2} \frac{\hbar\omega I|M_{if}|^4/\tau_{in}}{[(E_{if} - \hbar\omega)^2 + (\hbar/\tau_{in})^2]^2}$$

$$x\left[1 - \left|\frac{M_{ff} - M_{ii}}{2M_{if}}\right|^2 \frac{(E_{if} - \hbar\omega)^2 - (\hbar/\tau_{in})^2 + 2E_{if}(E_{if} - \hbar\omega)}{E_{if}^2 + (\hbar/\tau_{in})^2}\right] \tag{5}$$

The total absorption coefficient $\beta(\omega, I)$ is given as

$$\beta(\omega, I) = \beta^{(1)}(\omega) + \beta^{(3)}(\omega, I) \tag{6}$$

The refractive index changes involving linear and nonlinear terms are calculated from

$$\frac{\Delta n^{(1)}(\omega)}{n_s} = \frac{\sigma}{2\varepsilon_0 n_s^2} \frac{|M_{if}|^2(E_{if} - \hbar\omega)}{(E_{if} - \hbar\omega)^2 + (\hbar/\tau_{in})^2} \tag{7}$$

and

$$\frac{\Delta n^{(3)}(\omega, I)}{n_s} = -\frac{\sigma}{c\varepsilon_0^2 n_s^3} \frac{I|M_{if}|^4(E_{if} - \hbar\omega)}{[(E_{if} - \hbar\omega)^2 + (\hbar/\tau_{in})^2]^2}$$

$$x\left\{1 - \left|\frac{M_{ff} - M_{ii}}{2M_{if}}\right|^2 \frac{E_{if}(E_{if} - \hbar\omega)^2 - \left(\frac{\hbar}{\tau_{in}}\right)^2(3E_{if} - 2\hbar\omega)}{\left[E_{if}^2 + \left(\frac{\hbar}{\tau_{in}}\right)^2\right](E_{if} - \hbar\omega)}\right\} \tag{8}$$

Therefore, the total refractive index change is given by

$$\frac{\Delta n(\omega, I)}{n_s} = \frac{\Delta n^{(1)}(\omega)}{n_s} + \frac{\Delta n^{(3)}(\omega, I)}{n_s} \tag{9}$$

where $\hbar\omega$ is the incident photon energy, ε_0 is the dielectric permittivity of the vacuum, σ is the carrier density in the system, c is the speed of light in a vacuum, τ_{in} is the relaxation time, $n_s = \sqrt{\varepsilon}$ is the refractive index of the system and ε is the dielectric permittivity of the material. I is the optical intensity. E_f and E_i describe the energies of the last and first states respectively, E_{if} is the energy difference between these states which is defined as

$$E_{if} = E_f - E_i \qquad (10)$$

The M_{if} dipole matrix element is calculated from the following equation.

$$M_{if} = |< \psi_i |e.x| \psi_f >| \qquad (11)$$

Here, e is the electron charge. The ψ_i and ψ_f are the wave functions of the first state and the final state, respectively

In the calculations, the effective mass was $m^* = 0.067 m_0$ for the whole structure. The dielectric permeability of the medium was $\varepsilon = 12.58\, \varepsilon_0$. The potential depth of mid-well was taken as $V_0 = 228\, meV$, the electron density in the system $\sigma = 3 \times 10^{22} m^{-3}$, the refractive index for GaAs, $n_s = \sqrt{\varepsilon}$ and the relaxation time between the inner bands $\tau_{in} = 5$ps. The optical density of the external light was $I = 0.06$ MW/cm^2.

Results
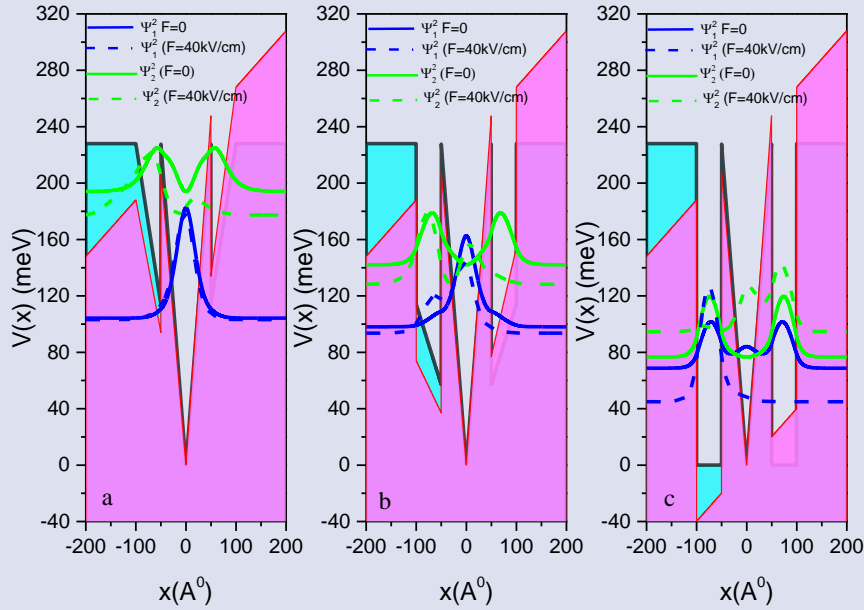
Figure 2. The potential profiles of the TQWs together with the probability densities in the ground and excited states for $F = 0$ and $F = 40\, kV/cm$. (a) $V_1 = V_0$, (b) $V_1 = V_0/2$, and (c) $V_1 = 0$.

The ground and first excited state energies, the probability densities, and the confining potential shapes for different TQWs with and without an electric field are shown in Fig. 2. In Fig. 2(a) where $V_1 = V_0$ case is investigated, it is noteworthy to point out for the ground state that the electron is mostly located in the central well independent from whether the electric field is on or not. The underlying reason is the side wells are so shallow that they cannot hold the electron inside. In the first excited state, it is seen that while the wavefunction is localized in both side wells when the electric field is off, the field application shifts the localization into the left-hand side well. Fig. 2(b) shows the results for $V_1 = V_0/2$ consideration. With no electric field, the probability distribution of the electron in the ground state spreads to the whole structure as the side well depths were increased, and their shapes were changed from right-angled triangles to square-like ones. The electron localization shifts towards the left-hand side when the field is on. The excited state probability distribution entirely leaves the right-hand side well mostly localizing in the left-hand side well. The electron is mostly located in the side wells for its ground state with no electric field as seen in Fig. 2(c) in which the case is $V_1 = 0$ and the side

well shapes were turned into full square shape. Figure 2(c) shows that the ground state wave function is now more localized in the side wells instead of the center well in the absence of the electric field, and is completely localized in the left-hand side well with the electric field. The probability density of finding an electron in its first excited state exhibits a different behavior than previous potential profile choices if the electric field is on. Without an electric field, it is distributed to the side wells leaving the center well completely. With the electric field, however, the shifts of the probability distribution are observed in the center and the right-hand side wells contrary to expectations that it had to have been in the left-hand side well as in previous potential profile considerations. That is because the probability distribution of the ground state occupies the left-hand side well where the first excited level probability distribution is expected to be found if the electric field is on. The above results show that when an electric field is applied to these three different structures, the energy states are reduced for $V_1 = V_0$ and $V_1 = V_0/2$ potential profiles. However, the ground state energy decreased while the first excited state energy increased in the square side wells structure ($V_1 = 0$).

In Fig. 3, the first two energy states concerning the side well potential energies are investigated with and without an electric field. In the absence of an electric field, it was observed that the ground state energy increased up to around $V_1 = 120\ meV$ of the side well potential energy, and after this value, it was seen to be almost constant. In the first excited state, a linear increase was observed. When an electric field is applied, the ground state energies decrease in comparison with that of no-field energies for small values of V_1. When the value of $V_1 = V_0$ is reached, the energies with and without the electric field become equal. The field-on energies of the first excited state are higher than that of the field-off energies for the values $0 \le V_1 \le 50\ meV$. For values greater than $50\ meV$, the field-on energy values of the first excited state become smaller than that of the field-off energies. The changes in all these energy states are in agreement with the energy levels of the quantum wells described in Fig. 2
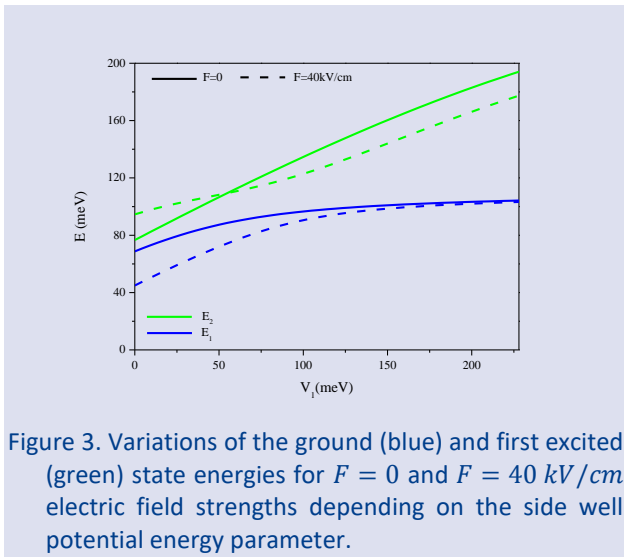

Figure 3. Variations of the ground (blue) and first excited (green) state energies for $F = 0$ and $F = 40\ kV/cm$ electric field strengths depending on the side well potential energy parameter.

In Fig. 4, the effect of electric field strength on the ground and first excited states is shown for three different well structures. For the structure with $V_1 = V_0$, the ground state energy was around $100\ meV$ and is not affected by the electric field. The first excited energy of the same structure decreases if the electric field strength increases. At large strength of the electric field, these energy states are seen to converge with each other. The ground state and the first excited state energies decrease while the electric field increases, and they are almost parallel to each other for $V_1 = V_0/2$. For the structure with a value of $V_1 = 0$, the initial values of the ground and the first excited state energies start from a value close to each other. With the increase of the electric field, the ground state energies decrease against the increase in the first excited state energies. The reason for this behavior is due to the geometry of the structure described in Fig. 2(c). It has been observed that the energy states exhibit different behaviors under the influence of the applied electric field due to the different geometries of the side wells in the TQW structure.
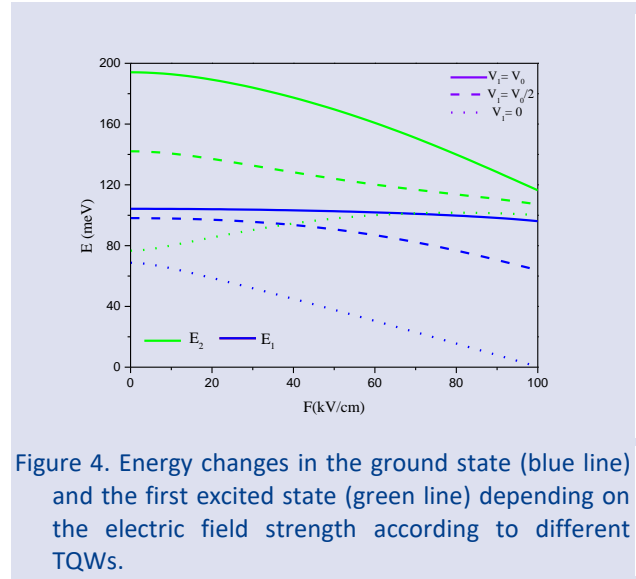

Figure 4. Energy changes in the ground state (blue line) and the first excited state (green line) depending on the electric field strength according to different TQWs.

Fig. 5 shows the photon energy-dependent variation of the linear, nonlinear, and total absorption coefficients for (1-2) optical transitions for all three potential profiles without any electric field application. For the structure with $V_1 = V_0$, the photon energy is approximately $90\ meV$. The required photon energy for $V_1 = V_0/2$ and $V_1 = 0$ values decreased to $45\ meV$ and $10\ meV$, respectively. The required photon energy decreases as the depth of side wells increases. This is because the difference between the E_1 and E_2 energies is small for small values of V_1 as seen in Fig. 3. The nonlinear absorption coefficient is highest for the smallest photon energy obtained for $V_1 = 0$. These two different functions of the linear and nonlinear absorption coefficients are reflected in the total absorption coefficients as seen in Fig. 5.
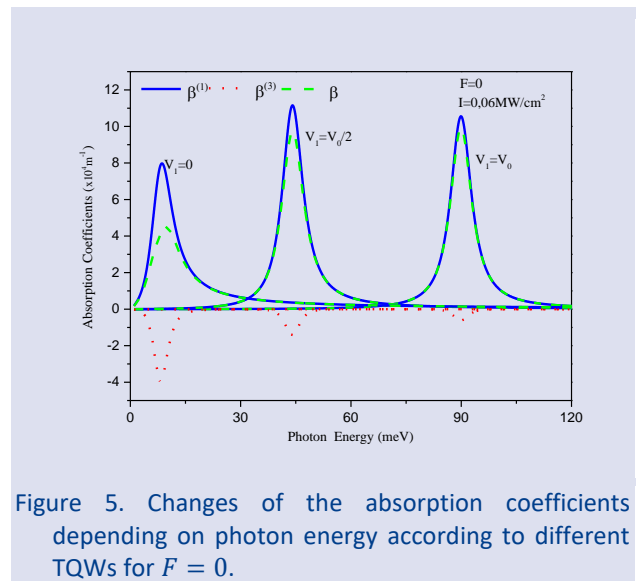

Figure 5. Changes of the absorption coefficients depending on photon energy according to different TQWs for $F = 0$.

The photon energy-dependent change of absorption coefficients for optical transitions (1-2) under the electric field $F = 40\ kV/cm$ strength is shown for all three potential profiles in Fig. 6. When compared with no

electric field case seen in Fig. 5, there is a decrease in the photon energy for the linear absorption coefficient of $V_1 = V_0$ and $V_1 = V_0/2$ TWQs to $75\ meV$ and $35\ meV$, respectively. With a value of $V_1 = 0$, the opposite situation occurred and the photon energy rose to approximately shifted to $50\ meV$. This behavior is sourced from the fact that the E_1 and E_2 energy difference for the $V_1 = V_0$ and $V_1 = V_0/2$ structures are small while it is large for the $V_1 = 0$ TQW when the electric field is applied with $F = 40\ kV/cm$ strength as shown in Fig. 4. For the nonlinear absorption coefficient, the photon energy has its smallest value for $V_1 = V_0/2$ in comparison with the photon energies come across in the other TQWs. The nonlinear absorption coefficient of $V_1 = 0$ and $V_1 = V_0$ TQWs are so low that their total absorption coefficients almost not affected by the nonlinear absorptions as seen in Fig. 6.
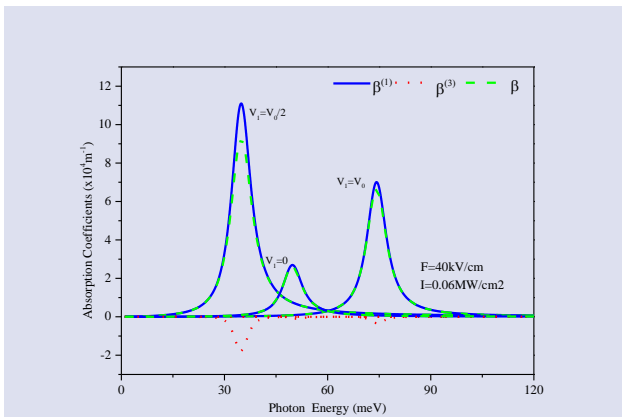

Figure 6. Changes of absorption coefficients depending on photon energy, according to different values of V_1, under $F = 40kV/cm$.
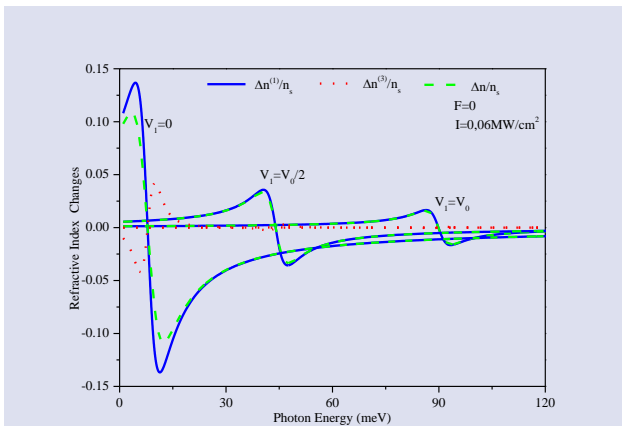

Figure 7. The refractive index changes depending on photon energy for different TQWs for $F = 0$.

The linear, the third-order nonlinear, and the total refractive index changes without any electric field application are depicted according to photon energy for three different values of V_1 in Fig. 7. The refractive index changes are observed in two extrema values. The region between these extrema values gives the region of photon energies where the total absorption coefficients are maximum. The photon energy decreases while the amplitude of the total refractive index changes increases in the order for $V_1 = V_0$, $V_1 = V_0/2$, and $V_1 = 0$ structures, respectively. The $V_1 = 0$ TQWs, where the amplitude of the refractive index changes is greatest, is examined, and the difference between the energies is small, but the squares of electron wave functions without the electric field shown in Fig. 2(c) are maximum in the same regions for both energy states. From these results, it can be said that the forces of the dipole matrix elements are effective in the refractive index changes.
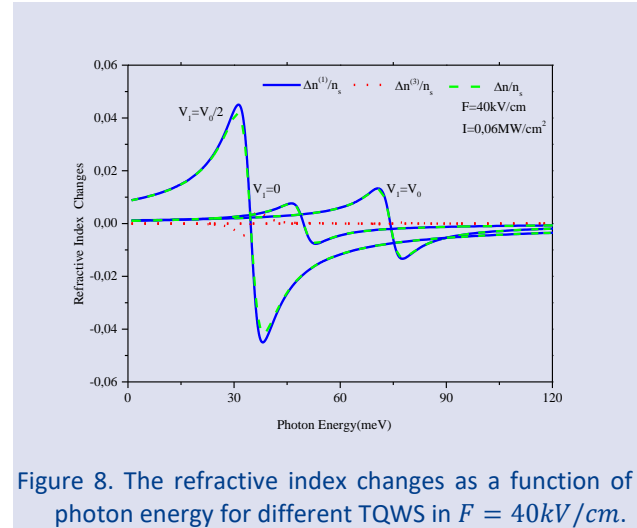

Figure 8. The refractive index changes as a function of photon energy for different TQWS in $F = 40kV/cm$.

In Fig. 8, the linear, nonlinear, and total refractive index changes were presented depending on the photon energy for three different values of V_1 with the electric field strength $F = 40\ kV/cm$. The interesting point in this figure is that the extrema points of the refractive index changes are between -0.05 and 0.05. The refractive index changes depend on both the energy gap and the dipole matrix elements. The largest amplitude change was seen in $V_1 = V_0/2$ TQWs because the dipole matrix element is more effective on the refractive index changes. Another striking point is that for $V_1 = 0$ and $V_1 = V_0$ TQWs, the nonlinear refractive index change is almost not affected by the photon energy.

Conclusion

The study examines how the electronic and optical properties of the triple quantum wells change when the geometry of the side wells changes from a triangular well to a square well, in the absence and presence of an electric field. With the increase in the parameter of V_1, which changes the geometry of the well in the absence of an electric field, it was observed that the ground state energy initially increased but remained constant after a certain value, while the excited state energy showed a linear variation. With the increase of the V1 parameter, it was observed that the photon energy values of the absorption coefficients increased. It has been observed that the side well geometries affect the electronic and optical properties of triple quantum wells. Interesting

changes were observed in the energy states when an external electric field was applied to the structures formed with the values of $V_1 = V_0$, $V_1 = V_0/2$, and $V_1 = 0$ of the side well parameters. These interesting changes in energy values have been found to affect the optical properties of these structures. When a constant electric field strength of $40\ kV/cm$ is applied to the structures, the peak values of the total absorption coefficients are observed for $V_1 = V_0$, $V_1 = V_0/2$ shift to smaller photon energies compared to the case without an electric field. For $V_1 = 0$, it shifts to larger photon energies compared to the case without an electric field. It is thought that these features of triple quantum well structures can be used as switching devices in optoelectronics.

Conflict of interest

There are no conflicts of interest in this work.

Acknowledgment

Ethical Approval Statement

(Statements of ethical approval for studies involving human subjects and/or animals) There is no ethical infringement.

References

[1] Umansky V., Heiblum, M., Levinson Y., Smet, J. Nübler J., Dolev M., MBE growth of ultra-low disorder 2DEG with mobility exceeding 35 X 10(6) cm(2)/V s, *Journal of Crystal Growth.* 311 (7) (2009) 1658-1661.

[2] Fu K., Growth Dynamics of Semiconductor Nanostructures by MOCVD, PD Thesis, School of Biotechnology (BIO), Theoretical Chemistry, (PhD dissertation, KTH), (2009), Retrieved from https://urn.kb.se/resolve?urn=urn:nbn:se:kth:diva-11447 (Retrieved May 2, 2024.)

[3] Hasegawa S., Sato M., Maehashi K., Asahi H., Nakashima, H., Formation of quantum well wire-like structures by MBE growth of AlGaAs/GaAs superlattices on GaAs (110) surfaces, *Journal of crystal growth.* 111 (1-4) (1991) 371-375.

[4] Hara S. Motohisa Ju., Fukui T., Hasegawa H., Quantum Well Wire Fabrication Method Using Self-Organized Multiatomic Steps on Vicinal (001) GaAs Surfaces by Metalorganic Vapor Phase Epitaxy, *Japan Journal Applied Physics.* 34 (1995) 4401-4404.

[5] Sato M., Maehashi K., Asahi H., Hasegawa S, Nakashima H., MBE growth of $AlGaAs/GaAs$ superlattices on GaAs (110) substrates, *Superlattices and Microstructures* 7 (4) (1990) 279-282.

[6] Bozyigit, D., Wood, V., Challenges and solutions for high-efficiency quantum dot-based LEDs, *MRS Bulletin.* 38 (9) (2013) 731–736.

[7] Bozyigit D., Yarema O. Wood V., Origins of Low Quantum Efficiencies in Quantum Dot LEDs. *Advanced Function Materials.* 23 (24) (2013) 3024-3029.

[8] Wood V. , Bulović V., Colloidal quantum dot light-emitting devices, *Nano Reviews*. 1 (2010).

[9] Emin S., Singh S. P., Han L., Satoh N., Islam A., Colloidal quantum dot solar cells, *Solar Energy.* 85 (6) (2011) 1264-1282.

[10] Rühle S., Shalom M., Zaban A., Quantum-Dot-Sensitized Solar Cells, *Chem. Phys. Chem.* 11 (11) (2010): 2290-2304.

[11] Nozik A.J, Quantum dot solar cells, *Physica E: Low-dimensional Systems and Nanostructures.* 14 (1-2) (2002) 115-120.

[12] Gleiter H., Schimmel T., Hahn H., Nanostructured solids – From nano-glasses to quantum transistors. *Nano Today.* 9 (1) (2014) 17–68.

[13] Shi B., Pinna S., Luo W., Zhao H., Zhu S., Brunelli S. T. S., Lau K. M., Klamkin J., Comparison of static and dynamic characteristics of 1550 nm quantum dash and quantum well lasers, *Optics Express.* 28 (18) (2020) 26823-26835.

[14] Li S., Nezami M.S., Rolston D., Liboiron-Ladouceur O., A Compact High-Efficient Equivalent Circuit Model of Multi-Quantum-Well Vertical-Cavity Surface-Emitting Lasers for High-Speed Interconnects, *Applied Sciences.* 10 (11) (2020) 3865.

[15] Hakl M., Lin Q., Lepillet S., Billet M., Lampin J.-F., Pirotta S., Colombelli R., Wan W., Cao J. C., Li H., Peytavit E., Barbieri S., Ultrafast Quantum-Well Photodetectors Operating at 10 μm with a Flat Frequency Response up to 70 GHz at Room Temperature, *ACS Photonics.* 8 (2) (2021) 464-471.

[16] Tokhy M. E. S., Mahmoud I.I., Detectivity analysis of infrared photodetector devices under nonuniform distribution of quantum well and wire, *Optik.* 227 (2021) 166113.

[17] Miyazaki H.T., ManoT., Kasaya T. , Osato H., Watanabe K., Sugimoto Y., Kawazu T., Arai Y., Shigetou A., Ochiai T., Jimba Y. Miyazaki H., Synchronously wired infrared antennas for resonant single-quantum-well photodetection up to room temperature, *Nature Communication.* 11 (1) (2020) 565.

[18] Maximov M.V., Nadtochiy A.M., Mintairov S.A., Kalyuzhnyy, N.A., Kryzhanovskay N.V., Moiseev E.I., Gordeev N.Y., Shernyakov Y.M., Payusov A.S., Zubov F.I., Nevedomskiy V. N., Rouvimov S. S., Rouvimov S S , Zhukov A. E., Light Emitting Devices Based on Quantum Well-Dots, *Applied. Science.* 10 (3) (2020) 1038.

[19] Grenier V., Finot S., Jacopin G., Bougerol C., Robin E., Mollard N., Gayral B., Monroy E., Eymery J., and Durand C., UV Emission from GaN Wires with m-Plane Core–Shell GaN/AlGaN Multiple Quantum Wells, *ACS Applied Materials & Interfaces.* 12 (39) (2020) 44007-44016.

[20] Kochetkov, F.M., Neplokh, V., Mastalieva, V.A., Mukhangali, S., Vorob'ev, A.A., Uvarov, A.V., Komissarenko F.E., Mitin, D.M., Kapoor, A., Eymery, J., Amador-Mendez N., Durand C. , Krasnikov D., , Nasibulin A. G., Tchernycheva M. Mukhin I. S., Stretchable Transparent Light-Emitting Diodes Based on InGaN/GaN Quantum Well Microwires and Carbon Nanotube Films, *Nanomaterials.* 11 (6) (2021) 1503.

[21] Krevchik V. D., Semenov M. B., Shorokhov A. V., Filatov D. O., Baidus N. V., Marychev M. O., Shkurinov A. P., Timoshenko V. Y., Krevchik P. V., Zhurina A. E., Saburova D. A., Antonov I. S., Semenov I. M., Effects of dissipative electron tunneling manifested in the photocurrent of a GaAs p-i-n photodiode with a double InAs quantum dot layer, *Journal of Physics: Conference Series.* 1851 (2021) 012016.

[22] Hsiao F.-C., Hazari A., Chang Y. C., Bhattacharya P., Dallesasse, J. M., Modeling photocurrent spectra of high-indium-content InGaN disk-in-wire photodiode on silicon substrate, *Physica E: Low-dimensional Systems and Nanostructures.* 144 (2022) 115371.

[23] Bayal M., Chandran N., Pilankatta R., Nair S.S., Quantum Wells, Wires and Dotes for Luminescent Device Applications. In: Nanomaterials for Luminescent Devices, Sensors, and Bio-imaging Applications. *Progress in Optical Science and Photonics.* (2021).

[24] Fischer I. A., Wendav T., Augel L., Jitpakdeebodin S., Oliveira F., Benedetti A., Stefanov S., Chiussi S., Capellini G., Busch K., Schulze J., Growth and characterization of SiGeSn quantum well photodiodes, *Optic Expres* . 23 (19) (2015) 25048-25057.

[25] Wegscheider W., Pfeiffer L., Kenneth W., Leibenguth R. E., Current injection GaAs/AlGaAs quantum wire lasers fabricated by cleaved edge overgrowth, *Applied Physics Letters. 65* (20*)* (1994) 2510–2512.

[26] Bastard G., Mendez E. E., Chang L. L., Esaki L. Variational calculations on a quantum well in an electric field, *Physical Review B.* 28 (6) (1983) 3241–3245.

[27] Boz F.K., Aktas S., Bekar B., Okan S.E., Laser filed-driven potential profiles of double quantum wells, *Physics Letters A.* 376 (4) (2012) 590-594.

[28] Shaer A., Yücel M.B., Kasapoglu E., Hydrostatic pressure and temperature dependent optical properties of double inverse parabolic quantum well under the magnetic field, *Physica B: Condensed Matter*. 685 (15) (2024) 416057.

[29] Altun D., Ozturk O., Alaydin B.O., Ozturk E., Linear and nonlinear optical properties of a superlattice with periodically increased well width under electric and magnetic fields, *Micro and Nanostructures*. 166 (2022) 207225.

[30] Ungan F., Bahar M.K., Rodríguez-Magdaleno K.A., Mora-Ramos M.E., Martínez-Orozco J.C., Influence of applied external fields on the nonlinear optical properties of a semi-infinite asymmetric AlxGa1–xAs/GaAs quantum well, *Materials Science in Semiconductor Processing*. 123 (2021) 105509.

[31] H. Sayrac, M. Jaouane, A. Ed-Dahmouny, A. Sali, F. Ungan, Modulation of nonlinear optical rectification, second, and third harmonic generation coefficients in n-type quadruple δ-doped GaAs quantum wells under external fields, *Physica B: Condensed Matter*. 690 (2024) 416252.

[32] Kasapoglu E., Yücel M. B., Duque C. A., Mora-Ramos M. E., Simultaneous effects of the position dependent mass and magnetic field on quantum well with the improved Tietz potential, *Physica B: Condensed Matter*. 679 (2024) 415797.

[33] Vinasco J. A., A. Radu, Niculescu E., Mora-Ramos M. E., Feddi E., Tulupenko V., Restrepo R. L., Kasapoglu E., Morales A. L., Duque C. A., Electronic states in GaAs-(Al,Ga)As eccentric quantum rings under nonresonant intense laser and magnetic fields, *Scientific Reports.* (9) (2019) 1427.

[34] Kes H., A Bilekkaya., Aktas S., Okan S.E., Binding energy of a hydrogenic impurity in a coaxial quantum wire with an insulator layer, *Superlattices and Microstructures*. 111 (2017) 966-975.

[35] Yesilgul U., Al E.B., Martínez-Orozco J.C., Restrepo R.L., Mora-Ramos M.E., Duque C.A., Ungan F., Kasapoglu E., Linear and nonlinear optical properties in an asymmetric double quantum well under intense laser field: Effects of applied electric and magnetic fields, *Optical Materials*. 58 (2016) 107-112.

[36] Al, E.B., Kasapoglu, E., Ungan, F. Dynamics of nonlinear optical rectification, second, and third harmonic generation in asymmetric triangular double quantum wells due to static electric and magnetic fields, *The European Physical Journal Plus.* 137 (2022).

[37] Al, E.B., Peter, A.J., Mora-Ramos, M. E. , Ungan F. Theoretical investigation of nonlinear optical properties of Mathieu quantum well, *The European Physical Journal Plus*. 138 (2023).

[38] Tuzemen, A.T., Dakhlaoui, H., Al, E.B., Ungan F., The nonlinear optical properties of "12-6" tuned GaAs/GaAlAs double quantum well under the external fields, *The European Physical Journal Plus* 138 (2) (2023).

[39] Tuzemen, A.T., Al, E.B., Dakhlaoui, H. , Ungan F., Effects of external electric and magnetic field on the nonlinear optical rectification, second, and third-harmonic generations in GaAs/AlGaAs asymmetric triple quantum well, *The European Physical Journal Plus.* 138 (7) (2023).

[40] Haghighatzadeh, A., Attarzadeh, A., Salman Durmuslar, A. Al E. B., Ungan F., Modeling of electronic spectra and optical responses of a semiconductor AlGaAs/GaAs quantum well with three-step barriers: the role of external perturbations and impurity, *The European Physical Journal Plus* 139 (4) (2024).

[41] Sayrac, M., Belhadj, W., Dakhlaoui, H. Ungan F., Influence of structural variables and external perturbations on the nonlinear optical rectification, second, and third-harmonic generation in the InP/InGaAs triple quantum well structure, *The European Physical Journal Plus.* 138 (2023).

[42] Alaydin B.O., Altun D., Ozturk O., Ozturk E., High harmonic generations triggered by the intense laser field in GaAs/AlxGa1-xAs honeycomb quantum well wires, *Materials Today Physics*. 38 (2023) 101232.

[43] Tirole R., Vezzoli S., Saxena D., Yang, S. Raziman T. V., Galiffi E., Maier S. A., Pendry J. B., Sapienza R., Second harmonic generation at a time-varying interface, *Nature Communications.* 15 (1) (2024).

[44] Cooper J. D., Valavanis A.,Ikonić Z.,Harrison P., Cunningham J. E., Finite difference method for solving the Schrödinger equation with band nonparabolicity in mid-infrared quantum cascade lasers, *J. Appl. Phys.* 108 (11) (2010) 113109.

[45] Yan R.Y., Tang J., Zhang Z.H., Yuan J. H., Optical properties in GaAs/AlGaAs semiparabolic quantum wells by the finite difference method: Combined effects of electric field and magnetic field, *International Journal of Modern Physics B.* 32 (13) (2018) 1850159.

[46] Ma X., Li K., Zhang Z.,; Hu H., Wang Q., Wei X., Song G., Two-band finite difference method for the bandstructure calculation with nonparabolicity effects in quantum cascade lasers, *Journal of Applied Physics.* 114 (6) (2013) 063101.

[47] Bekar B., Boz F.K., Aktas S., Okan S. E., The effect on the optical absorption coefficients due to the positions in the plane of square GaAs/Al(GaAs) quantum well wire under the laser field, *Acta Physica Polonica A.* 136 (6) (2019) 882-888.

Cumhuriyet Science Journal

Thermophysical Properties of Directionally Solidified the Zn-Mg-Al Eutectic Alloy and the Effect of Growth Rates on Electrical Properties

Ümit Bayram [1,2,a,*]

[1] Central Research Facility (AGU-CRF), Abdullah Gül University, Kayseri, Türkiye
[2] Nanotechnology Application and Research Center (ERNAM), Erciyes University, Kayseri, Türkiye
*Corresponding author

Research Article

ABSTRACT

The study aimed to investigate the effect of growth rates (V) on the electrical properties of a Zn–3.0 Mg–2.5 Al (wt.%) eutectic alloy. The alloy was directionally solidified at four different growth rates ranging from 8.28 to 164.12 µm/s. Directional solidification experiments were conducted using a Bridgman-type solidification furnace, which was employed for controlled solidification and minimizing undesirable casting defects, following the alloy's production and casting process. The electrical resistivity (ρ) of the samples, measured using the Four-Point Probe Method (FPPM) available in the laboratory, exhibited an increasing trend ranging from 72.80 to 96.20 (nΩm) with rising growth rates. In other words, the electrical conductivity of the Zn–Mg–Al eutectic alloy varies inversely with the growth rate. Additionally, the thermophysical properties of the eutectic alloy in the casting phase were determined using differential scanning calorimetry (DSC): ΔHf (the fusion enthalpy), ΔCp (the specific heat) and TM (the melting point) (26.69 J/g, 0.043 J/gK, 618.92 K, respectively). The results obtained for the Zn–Mg–Al eutectic alloy reveal that, when compared to Zn-Al-based alloys produced under similar experimental conditions, the elements comprising the alloy and mass proportions lead to microstructural changes, which in turn affect its electrical conductivity.

Keywords: Zn–Mg–Al alloys, Directional solidification, Electrical resistivity, Thermophysical properties.

[a] ✉ umit.bayram@agu.edu.tr   ⓘD https://orcid.org/0000-0001-8760-8024

Introduction

Globally, renewable energy sources are being promoted as a measure to address the global challenges associated with heating and energy consumption. The use of wind and solar energy as primary power sources has seen significant growth in recent years, leading to an increased demand for systems that facilitate the adjustment of electricity generation, particularly from thermal power plants. Thermal energy storage systems are highlighted as a viable solution due to their advantages in energy efficiency and cost [1]. The capacity of energy storage in thermal systems is directly related to the selection of suitable thermal storage materials. Among thermal storage materials, eutectic alloys are preferred due to several superior properties: reduced phase separation compared to non-eutectic alloys, higher energy density due to intermetallic phase formation than pure metals, and superior thermal conductivity compared to inorganic salts [2,3].

Eutectic alloys also play a significant role in sustainable transportation by providing high strength and durability in the automotive industry while increasing fuel efficiency due to their lightweight properties. In other words, reducing vehicle weight is recognized as an effective method for improving fuel consumption in the automotive sector [4,5]. To achieve this, priority is given to materials such as aluminum alloys, which are lighter than steel. However, the primary challenge regarding efficiency and cost arises from applying these materials to

the entire vehicle body. A key solution to this issue involves using multi-material structures incorporating zinc-aluminum (Zn-Al) based eutectic alloys with high strength and rigidity. In addition to their applications in automotive components, these alloys enable significant usage in various important applications, such as radio frequency circuits, disk drives, portable computers, phone antennas, and high-quality filters, due to their superior properties [6-8]. Furthermore, to obtain a coating material with excellent surface corrosion resistance and protective capabilities, zinc-based coatings with varying Al and Mg contents are widely used in the market [9-11].

The solidification microstructure is a critical foundational stage in the material preparation and shaping process, which typically directly determines the final performance and service life of the material. For this reason, eutectic alloys, which are frequently used by researchers and the casting industry, possess not only superior mechanical properties and casting capabilities but also low melting points [12-14]. In eutectic alloys, the solidification process begins when the temperature of the liquid reaches the eutectic temperature. At this stage, the liquid phase starts to transform into two or more solid phases. Directional solidification, on the other hand, is a model of the transition from liquid phase to solid phase and generally encompasses scenarios in which the temperature distribution is arranged in a specific linear manner. This process allows for the investigation of

different growth rates during solidification due to the temperature gradient within the alloy. Furthermore, directional solidification is employed to understand the factors affecting the temperature gradient and growth rates during the solidification process of eutectic alloys. In summary, while eutectic alloys form two or more solid phases during the transition from liquid phase to solid phase at a specific temperature, directional solidification serves as a model to help understand the effects of this solidification process on temperature and time. These two concepts are evaluated together to optimize metallurgical processes and achieve the desired microstructure.

The Bridgman-type controlled solidification technique is one of the fundamental methods used for the controlled directional solidification of metals and alloys. This technique plays a significant role in both fundamental research and industrial applications, particularly in the production of high-quality crystals and alloys. Undesirable casting defects in zinc and aluminum-based alloys can be minimized to the lowest levels using the Bridgman-type controlled solidification technique, as detailed in the literature [15,16].

According to the results obtained from studies on binary and multicomponent eutectic alloys in the literature [17-27], investigations related to directional solidification were predominantly conducted using Bridgman-type controlled solidification equipment within a standard growth rate range of 8-250 µm/s. Following the determination of solidification parameters (V, G, C_o) from the experimental results, the effects of growth rate on the microstructure, mechanical, thermal, and electrical properties were examined. In this context, the primary aim of the study is to experimentally perform directional solidification studies of the Zn–3.0 Mg–2.5 Al (wt.%) eutectic alloy within a fixed temperature gradient (G=4.58 K/mm) and a growth rate range of V=8.28–164.12 µm/s, and to elucidate the relationship between the growth rate values and the changes in electrical resistivity (ρ) using linear regression analysis. Additionally, another significant objective of this study is to determine the thermophysical properties of the eutectic alloy in the casting phase, such as the fusion enthalpy (ΔH_f), the specific heat difference between solid and liquid (ΔC_p), and the melting point (T_M), using a Simultaneous Thermal Analyzer (STA 8000). Finally, the results obtained for the Zn–Mg–Al eutectic alloy will be compared with Zn-Al-based alloys produced under similar experimental conditions, and the effects of changes in the microstructural arrangement on the electrical properties of the alloy will be discussed.

Materials and Methods

Alloy Preparation, Casting, and Solidification Experiments

The most critical part of the experimental procedures followed in this study includes the homogeneous preparation of the alloy, the execution of directional solidification experiments, and the measurement of solidification parameters (G-constant and V) thereafter, as well as the observation and characterization of the microstructure. Initially, high-purity materials were utilized to prevent impurities from accumulating at the interface and to avoid deterioration of the microstructure. These materials consisted of Alfa Aesar - 99.99% pure aluminum and 99.95% pure zinc, and Sigma-Aldrich - ≥99.9% pure magnesium. The appropriate amounts of Zn–3.0 Mg–2.5 Al (wt.%) eutectic alloy were weighed using a precision balance with a sensitivity of ±0.1 mg.

Before the casting of the alloy, a vacuum melting furnace was used to prevent metal oxidation and ensure the formation of a completely molten alloy. This furnace is equipped with a specially designed temperature controller that allows for a temperature accuracy of ±2 °C up to a maximum of 1100 °C, and the melting process is conducted under a pressure of 10^{-3} mbar with the help of a vacuum pump. Due to its superior properties, such as resistance to reaction with metallic materials, ease of processing through engineering applications, and a very high melting temperature (approximately 4000 °C), *Morgan-brand* graphite was preferred for the experimental equipment used before and after casting, including mixing rods, sample molds, and melting pots.

A specially designed casting furnace was utilized for the pouring of the obtained molten alloy and its unidirectional (linear) solidification within the sample molds. The prepared sample molds (Length: 200 mm, ID: 4.0 mm, OD: 6.35 mm) were placed inside the furnace, and the furnace temperature was raised to approximately 100-150 °C above the alloy's melting temperature (~345 °C) before casting. To ensure complete filling of the pots and to prevent one of the undesired casting defects known as shrinkage cavities, solidification was achieved using a graphite rod in 8–10-minute intervals. Simultaneously, while the lower heating zone within the casting furnace was cooled, the upper heating zone was maintained at a high temperature, allowing for unidirectional (linear) solidification within the sample molds. The alloy was allowed to cool for approximately one day, and the sample molds filled with the eutectic alloy were made ready for use in controlled solidification experiments.

At the beginning of the solidification experiments, the cast samples were placed in a Bridgman-type solidification furnace equipped with a protective graphite cylinder at the top. The block diagram of the experimental setup and its visual representation in the laboratory are shown in Figures 1(a) and 1(b). The directional solidification experiments of the samples were conducted using four different synchronous motors with withdrawal rates of 1 (V = 8.28 µm/s), 5 (V = 43.56 µm/s), 10 (V = 87.69 µm/s), and 20 rpm (V = 164.12 µm/s). Many technical details, from the production of alloy samples to the use of equipment shown in the block diagram in Fig. 1 and the calculations performed, as well as information regarding the Bridgman-type solidification furnace, have been provided in detail in previous studies [18, 28, 29].

The controlled solidification furnace was set to the desired temperature (~500 °C) using a temperature

controller, and the attainment of this temperature was monitored with a temperature recorder and thermocouples. A waiting period of approximately 2-3 hours was implemented to stabilize the temperature flow. The driver motor system was then activated to initiate the experiment, after which the solidified sample, approximately 10-12 cm in length, was quickly withdrawn into the cold zone containing the internal water reservoir, where it underwent an abrupt cooling process known as quenching. To ensure the effectiveness of the rapid cooling, the withdrawal process was conducted very quickly, and the temperature of the internal reservoir, designed to create a temperature gradient, was

meticulously controlled. These experimental procedures were conducted at four different growth rates, with two samples for each rate. The reason for performing two samples is to determine the growth rates and the temperature gradient of the material by placing thermocouples inside alumina tubes. Samples containing alumina tubes would not yield reliable results for the electrical properties to be measured. Therefore, two experiments were conducted for each growth rate under the same conditions.
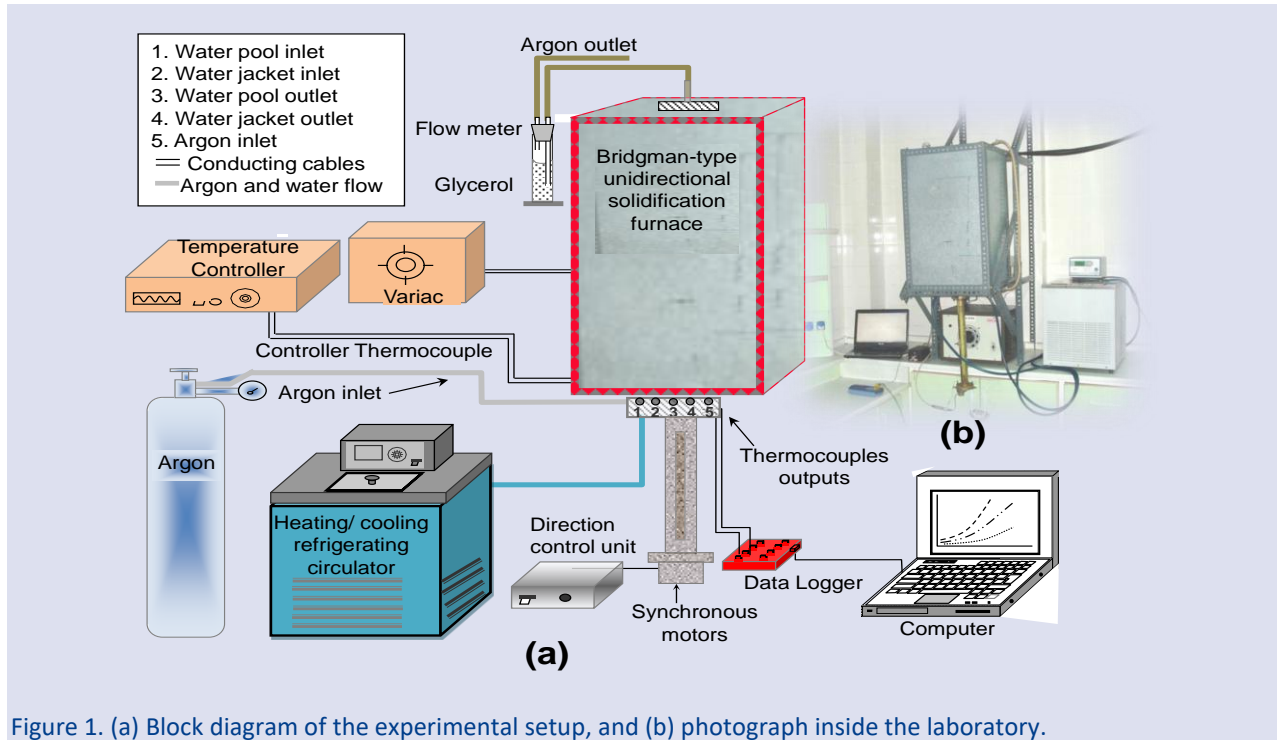

Figure 1. (a) Block diagram of the experimental setup, and (b) photograph inside the laboratory.

The solidified alloys were carefully removed from the graphite crucibles without causing any damage. To identify the microstructure and phases of all samples, the *Struers-Minitom* cutting tool and a *Struers* diamond cutter (127 mm diameter, 0.4 mm thickness) were used to cut the samples to the desired sizes. An important consideration in this process is the necessity of employing a cutting technique that causes minimal structural change and generates the least amount of heat. The samples were polished using sandpapers that gradually changed from coarse to fine, containing silicon carbide (SiC) grains and magnetite powder (320, 500, 1000, 2000 grit). During the polishing process, carried out with an automatic polishing robot (*Struers TegraPol-15*), care was taken to ensure that the surface of each sample remained flat and that deep scratches were removed after each polishing stage. The sections prepared for metallographic procedures were molded using epoxy and hardener chemicals at a 7:1 ratio. Although the surface of the sample appeared smooth, shiny, and mirror-like after polishing, it is not possible to conduct examinations without creating contrast on the sample surface. For microstructure analysis, the samples required etching. Finally, the Zn–3.0 Mg–2.5 Al (wt.%)

eutectic alloy was etched by immersion in a Keller etchant (1.5 ml Hydrochloric acid (HCl), 1 ml Hydrofluoric acid (HF), 2.5 ml Nitric acid (HNO_3), 95 ml water (H_2O)) for 40-45 seconds, preparing it for microstructure analysis.

Microstructure, Phase Analysis, and Solidification Parameters (G and V)

Following metallographic processes such as cutting, polishing, molding, ultrasonic cleaning, and etching of the samples, characterization studies were conducted. To identify the resulting microstructures and phases, images and data obtained from SEM (Scanning Electron Microscope - Zeiss GeminiSEM 300) and SEM-EDX (Energy Dispersive X-ray Spectroscopy) were utilized. Before the microstructure analysis using SEM, the surface of the samples, which were embedded in epoxy, was placed in a Quorum-Q150R Plus coating device and coated with a gold (Au) layer approximately 10-20 nm thick under vacuum to ensure more efficient scattering of the electron beam from the surface, thereby improving image resolution. The gold-coated samples were then positioned on the sample stage within the SEM, and photographs were taken from suitable areas where the phases

exhibited high contrast and could be easily distinguished. EDX-point analysis was performed on the phases to determine the composition of each phase.

To measure the temperature of the alloy, three K-type thermocouples (diameter: 0.25 mm) insulated with capillary ceramic alumina tubes were fixed at intervals of 10 mm. Using the data recorded by a computer-connected data logger for ΔT, ΔX, and Δt, the temperature gradient (G = ΔT/ΔX) and growth rate (V = ΔX/Δt) values were calculated. Here, ΔT (°C) is defined as the difference in temperature values measured by any two thermocouples, ΔX (mm) is the predetermined distance between the thermocouples, and Δt (s) is defined as the transition time of the solid-liquid interface across any two thermocouples. Since the distance between the cold and hot regions of the furnace was kept constant and the experimental parameters were not altered during the solidification process, the temperature gradient value (G) at the solid-liquid interface could be maintained constant. In addition to obtaining the values of Δt, ΔX, and ΔT, detailed information regarding the calculations of V and G has been provided in previous studies [18, 28, 29].

Electrical Resistivity (ρ) Measurement and Details

Electrical resistivity and conductivity are characteristic properties of materials that need to be known. Electrical conductivity can be determined using the relationship between the voltage and current measured across the sample, the calculated resistivity value, and the geometric structure of the sample. Additionally, when determining the electrical resistivity of a homogeneous sample, it is essential to know the geometric properties of the material as well. The expression for electrical resistivity can be given as follows [30]:

$$\rho = \frac{V}{I} G \tag{1}$$

G is defined here as a correction factor dependent on the geometric structure (Resistivity Correction Factor, RCF). This coefficient varies based on factors such as the magnitude of the surface area, the structure of the sample's edge boundaries, the thickness of the sample, its geometric configuration, and the arrangement and position of the contacts on the sample [31]. The electrical resistivity values of each sample (20 mm in length and 4 mm in diameter) were measured using the four-point probe method (FPPM), as shown in the photograph and block diagram of the measurement system presented in Fig. 2, depending on the growth rate of the eutectic alloy.
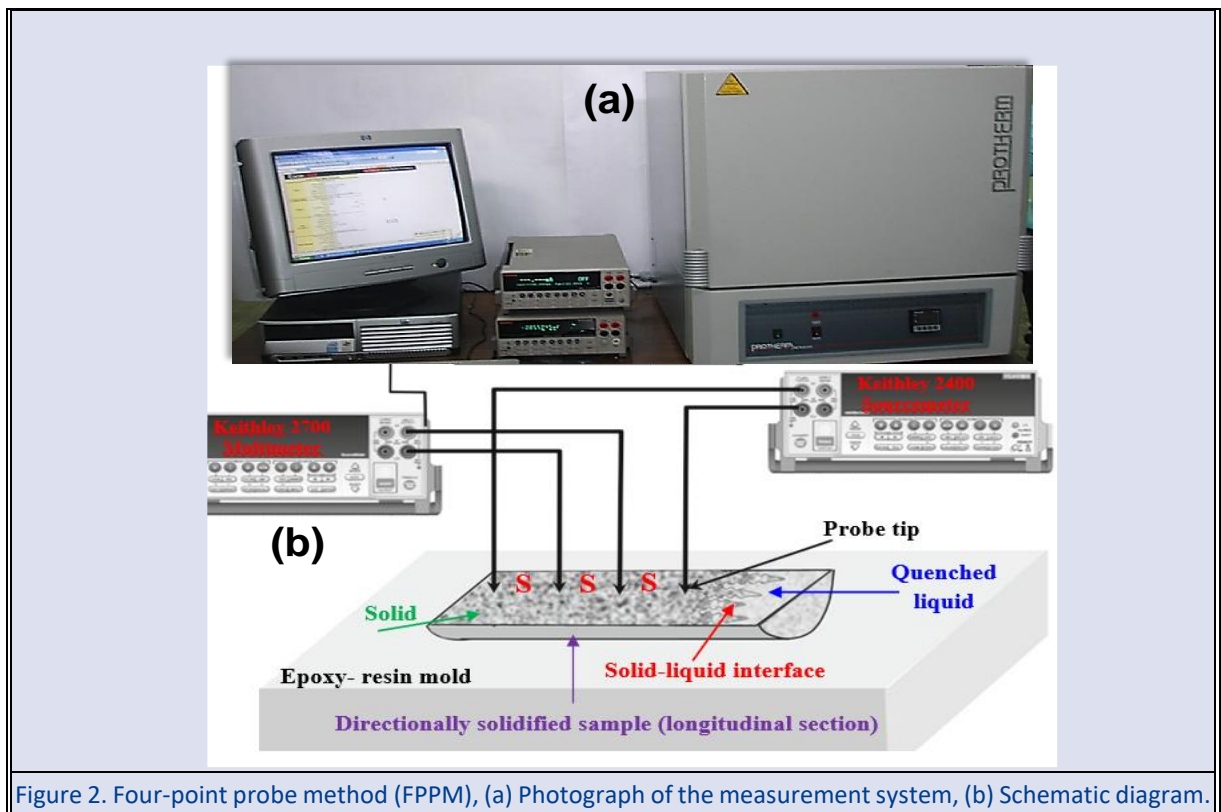

Figure 2. Four-point probe method (FPPM), (a) Photograph of the measurement system, (b) Schematic diagram.

In this study, the four-point probe method (FPPM) was equipped with a Keithley 2700 multimeter and a Keithley 2400 programmable power supply. The method is based on measuring the voltage value against the current applied to the sample through four platinum wires with a diameter of 0.5 mm, positioned within a Protherm-brand ash furnace. The platinum wires were directly in contact

with the surface of the bar-shaped samples at four electrical contact points. Two of the probes were used to measure the potential difference between two points, while the other two were used for sourcing the current. FPPM was preferred in this study due to its superior characteristics, such as eliminating measurement errors arising from the spreading resistance under each probe,

probe resistance, and contact resistance between each platinum probe and the material [32]. In summary, the resistances of the contacts used do not affect the measurement, and the calculated value represents only the resistivity of the sample. To enhance the reliability of the results in determining the electrical resistivity value, a minimum of 40-50 measurements were taken across the same sample to obtain an average value. Details regarding the measurement and use on the sample surface are provided in the work conducted by Smiths [32].

Thermophysical Properties (ΔH_f, ΔC_p and T_M)

The thermophysical properties of the Zn–3.0 Mg–2.5 Al (wt.%) eutectic alloy were determined in the casting phase (before solidification) using a Simultaneous Thermal Analyzer (STA 8000). This method encompasses techniques in which a physical property of the analyzed sample is measured as a function of temperature, or the heat released or absorbed in a chemical reaction is monitored. Specifically, properties such as phase transition, melting, glass transition, and crystallization are measured directly, while ΔC_p (the specific heat difference between solid and liquid, or the specific melting heat—the energy required for the melting of unit mass), ΔH_f (the fusion enthalpy), and T_M (the melting temperature) are calculated from the obtained curves. A suitable amount (8.81 mg) of the Zn–Mg–Al eutectic alloy was placed into the device and heated up to 700 K at a rate of 10 K/min under a nitrogen atmosphere. The ΔH_f value was calculated using the area under the peak derived from the alloy data:

$$\Delta H = \frac{Area}{m} \tag{2}$$

The definition of enthalpy from the equation indicates that it is the energy required for the melting of unit mass (m). The ΔC_p value is calculated using the equation:

$$\Delta C_p = \frac{\Delta H_f}{T_M} \tag{3}$$

Results and Discussion

SEM Analysis and Phase Characterization

In this study, the composition of the Zn–Mg–Al alloy to be investigated at the eutectic point was determined based on the work conducted by Kim *et al.* [33] using CALPHAD analysis. Accordingly, the composition of the alloy was selected as Zn–3.0 Mg–2.5 Al (wt.%), and the phases involved in the eutectic reaction at this point are as follows: E (eutectic reaction): L↔(μ-Zn) + MgZn$_2$ + (α-Al). For the determined eutectic Zn–Mg–Al alloy, microstructure (SEM) images obtained from the cross-sections of directionally solidified samples at four different growth rates are presented in Fig. 3. These images, taken at equal magnification values, demonstrate that the distance between the phases forming the alloy decreases with increasing growth rates, leading to a transition towards a more irregular structure.
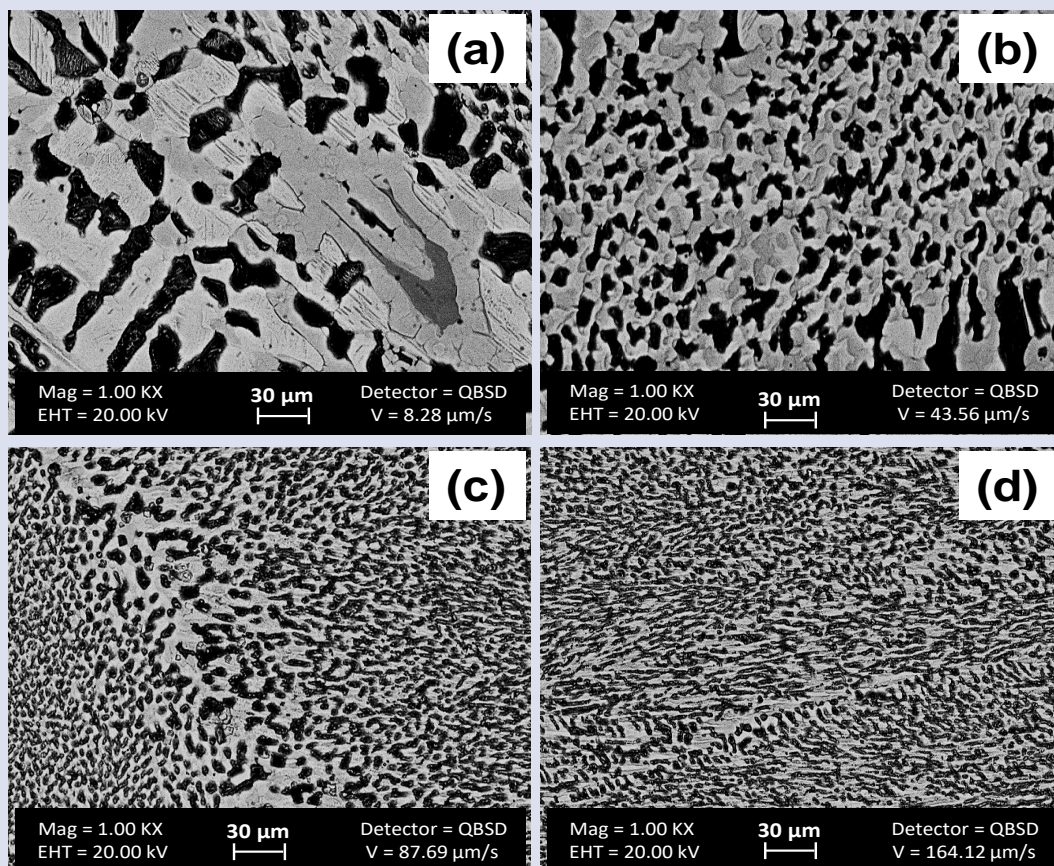

Figure 3. SEM images of cross sections for directionally solidified Zn–3.0 Mg–2.5 Al (wt.%) eutectic alloy. (a) V= 8.28 μm/s, (b) V= 43.56 μm/s, (c) V= 87.69 μm/s, (d) V= 164.12 μm/s.

As a result of solidification experiments, certain phases have separated in the phase diagram [33] as defined and point composition analyses of each distinct phase of the studied eutectic alloy have been conducted. The analyses revealed that three different phases—grey, black, and white—grew eutectically in the Zn–Mg–Al eutectic alloy, as observed from the microstructural photographs presented in Fig. 3. The quantitative chemical composition analyses obtained from SEM-EDX results are shown in Fig. 4.
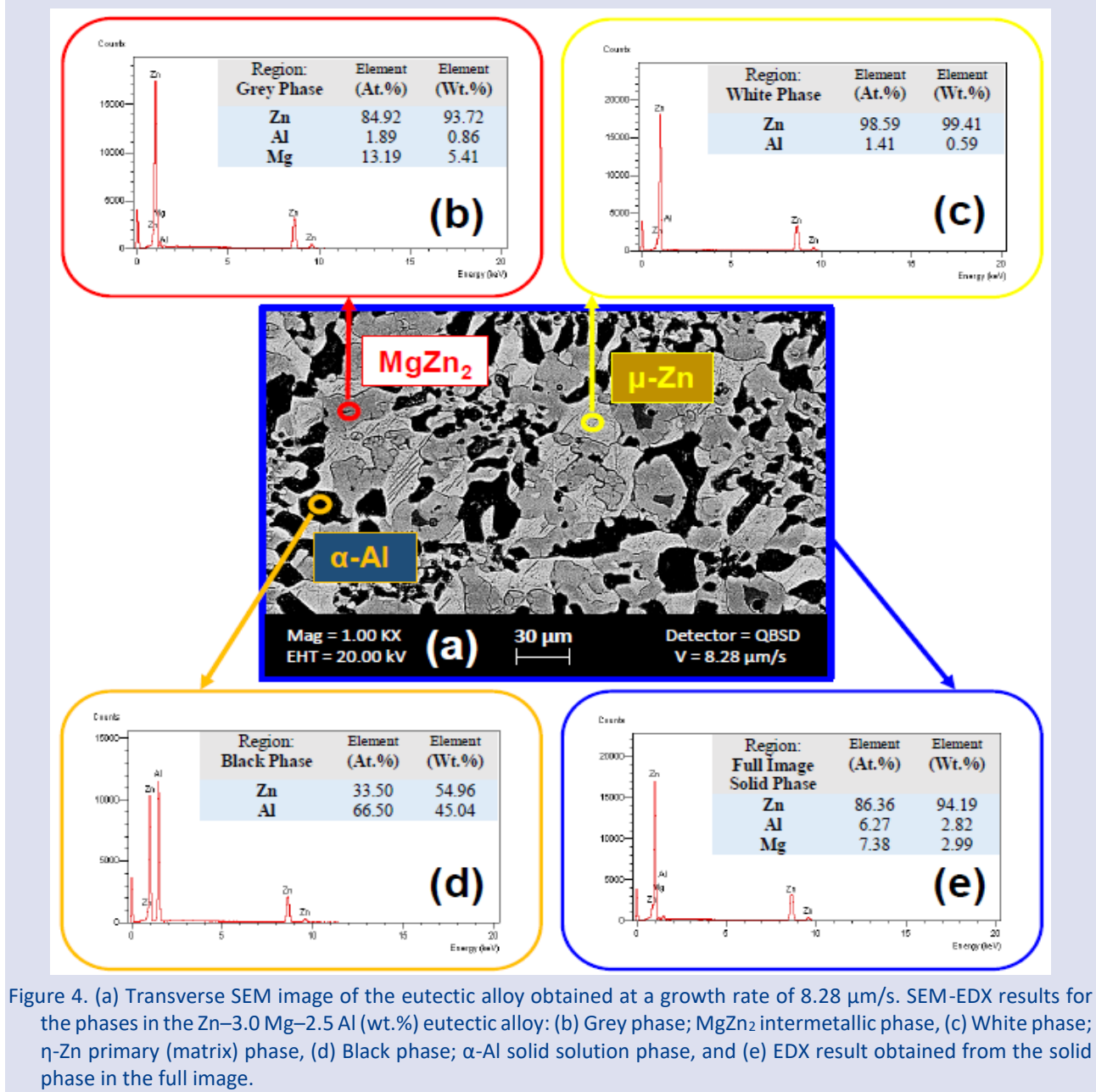

Figure 4. (a) Transverse SEM image of the eutectic alloy obtained at a growth rate of 8.28 µm/s. SEM-EDX results for the phases in the Zn–3.0 Mg–2.5 Al (wt.%) eutectic alloy: (b) Grey phase; $MgZn_2$ intermetallic phase, (c) White phase; η-Zn primary (matrix) phase, (d) Black phase; α-Al solid solution phase, and (e) EDX result obtained from the solid phase in the full image.

Upon examining the results in Fig. 4, it can be observed that the grey phase (Fig. 4b) corresponds to the MgZn2 intermetallic phase (Zn–5.41 Mg–0.86 Al (wt.%)), the white phase (Fig. 4c) corresponds to the η-Zn primary (matrix) phase (Zn–0.59 Al (wt.%)), and the black phase (Fig. 4d) corresponds to the α-Al solid solution phase (Zn–45.04 Al (wt.%)). The EDX result obtained from the solid phase in Fig. 4e is Zn–2.99 Mg–2.82 Al (wt.%), which is found to be quite close and consistent with the eutectic composition prepared in this study (Zn–3.0 Mg–2.5 Al (wt.%)). This consistency suggests that the alloy was produced homogeneously.

The Variation of Electrical Resistivity Values with Growth Rates

The other significant aim of this study is to investigate the electrical properties of the Zn–Mg–Al eutectic alloy, which is frequently used in both industrial and technological applications, and to reveal the effects of growth rates. To this end, each sample was placed in an ash furnace at room temperature, ensuring complete contact of four platinum wires with the sample. The electrical resistivity (ρ) values were then measured in nΩm. To enhance statistical reliability, at least 40-50 measurements were taken for each sample, and the averages were included in the calculations. Subsequently,

the relationship between the measured electrical resistivity values and the varying growth rates was established using linear regression analysis

In this study, the variation of electrical resistivity values with growth rate on a logarithmic scale is linear within the range of growth rates used (V = 8.28–164.12 μm/s), and the proportional equation can be obtained through linear regression analysis as follows:

$$\rho = K_1 . V^{-n} \ (for \ constant \ G) \tag{4}$$

where K_1 is the proportionality constant and n is the exponent of the growth rate. The relationship between the electrical resistivity values obtained from the cross-section and all growth rates (V = 8.28–164.12 μm/s) was determined for the directionally solidified Zn–3.0 Mg–2.5 Al (wt.%) eutectic alloy using the following equation (Fig. 5):

$$\rho = 58.70 \ V^{0.09} (n\Omega m) \tag{5}$$

From the SEM images provided in Fig. 3, it can be observed that increases in the growth rate significantly alter the eutectic microstructure, thereby affecting the other properties of the alloy. In this study, it was concluded that the electrical resistivity values measured using FPPM also increase with the rise in growth rates under a constant temperature gradient (G = 4.58 K/mm). In other words, the electrical conductivity (σ = 1/ρ) of the Zn–3.0 Mg–2.5

Al (wt.%) eutectic alloy varies inversely with the growth rates. The highest electrical resistivity value (96.20 nΩm) was obtained at the highest growth rate (164.12 μm/s), while the lowest electrical resistivity value (72.80 nΩm) was measured at the lowest growth rate (8.28 μm/s).

To compare and discuss the results obtained in this study, the electrical resistivity values and proportional equations of directional solidified Zn–Al-based eutectic alloys under similar experimental conditions are shown in Fig. 5 [21, 23, 25]. The exponent value of 0.09 and the proportionality constant of 58.70 obtained from the electrical resistivity measurements for the growth rates are consistent with the values obtained for the Zn–5.0 Al–0.8 Sb (wt.%) eutectic alloy [23]. However, these values differ significantly from the exponent values of the eutectic alloys containing Bi [21] and Cu [25] (0.11 and 0.06, respectively). The reason for the exponent value being higher for the Zn–5.0 Al–0.5 Cu (wt.%) [25] alloy and lower for the Zn–5.0 Al–0.2 Bi (wt.%) [21] alloy can be attributed to the solubility of the copper and bismuth elements within the zinc matrix rather than the mass proportions of the alloying elements, which prevents the formation of any intermetallic phases. The results of this study and the article conducted for the Zn–5.0 Al–0.8 Sb (wt.%) [23] eutectic alloy, clearly show the formation of $MgZn_2$ and AlSb intermetallic phases in the microstructure images.
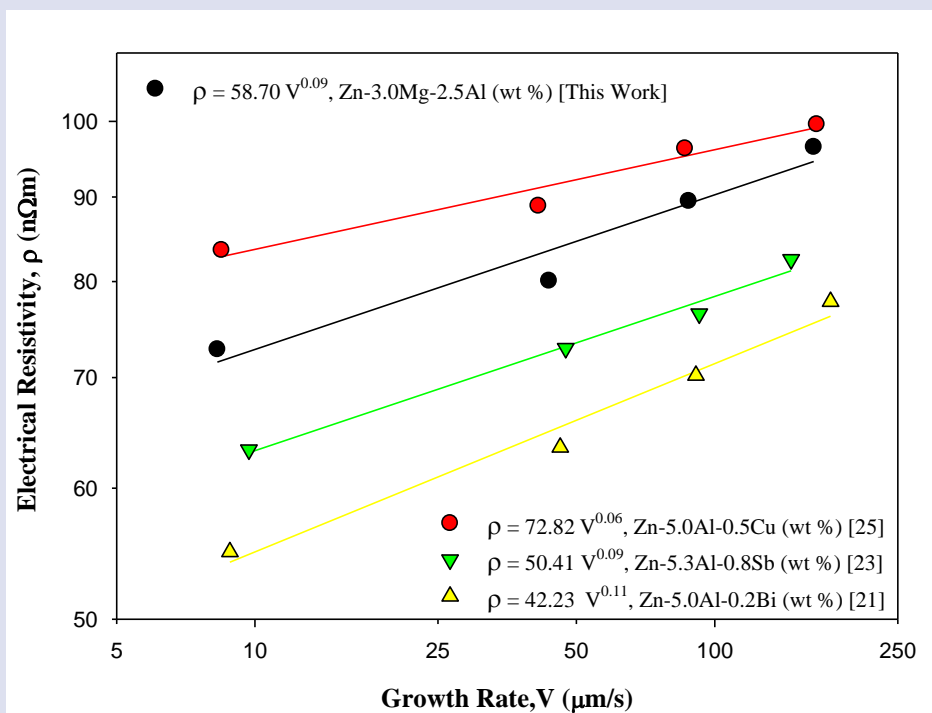

Figure 5. The variation of electrical resistivity values as a function of growth rates for directionally solidified Zn–Mg–Al eutectic alloy under a constant temperature gradient and compared with the experimental results of previous Zn-Al based alloys.

The effect of intermetallic phases on the electrical properties of alloys is influenced by factors such as microstructure, phase distribution, and atomic structure [34,35]. Consequently, the presence and characteristics of
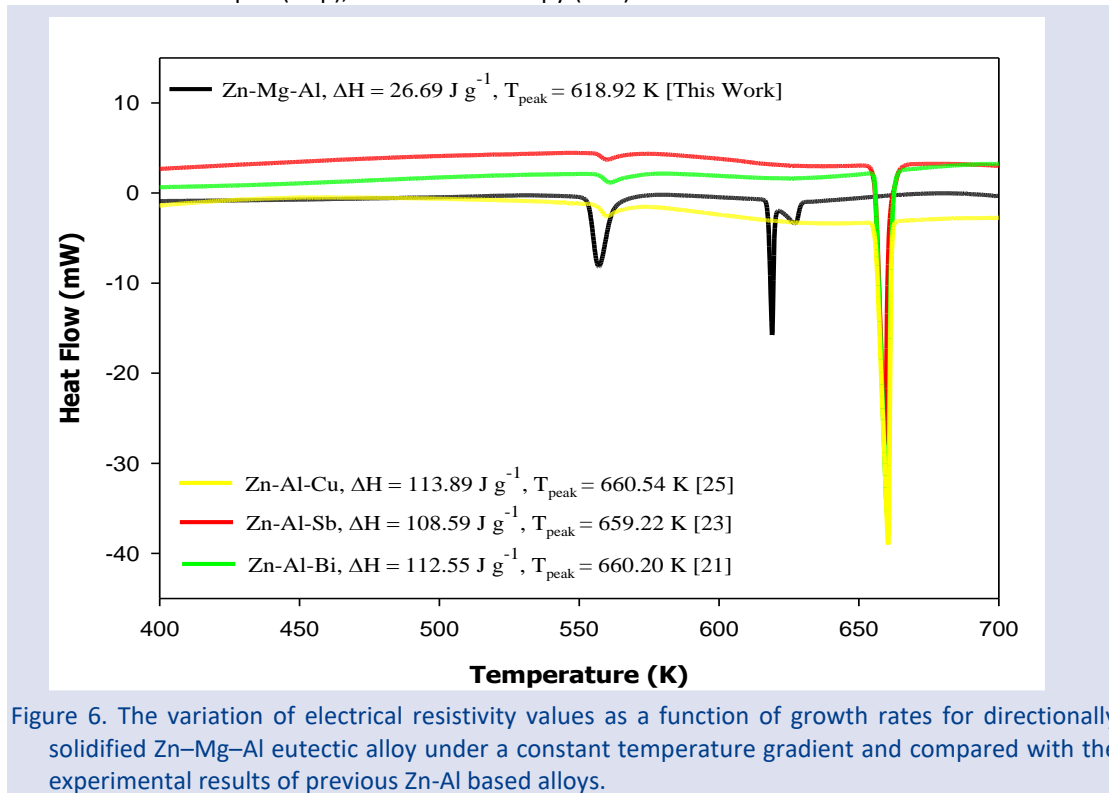
intermetallic phases play a critical role in determining the electrical performance of alloys. Firstly, intermetallic phases generally reduce the electrical conductivity of the alloy. This reduction is due to the distinct atomic

structures and bonding of these phases. The voids and irregularities within these structures lead to a decrease in electron mobility [36]. On the other hand, changes in the alloy's microstructure resulting from intermetallic phases, along with grain boundary and interphase interactions, also impact electrical conductivity. An increase in the grain boundary area can hinder electron flow, thereby reducing conductivity [37]. Both studies referenced, involving these intermetallic phases (MgZn2 [this study] and AlSb [23]), may contribute to the alloys exhibiting similar electrical properties.

The Evaluation of Thermophysical Properties

Understanding the thermal properties of alloys, such as melting point (TM), the specific heat difference between solid and liquid (ΔCp), the fusion enthalpy (ΔHf)

and crystallization temperature, is crucial for determining their suitability for various applications. The DSC (Differential Scanning Calorimetry) graph obtained using the Simultaneous Thermal Analyzer (STA 8000) measures energy changes during the heating processes of the alloy, helping to identify phase transitions (such as melting and crystallization) and related characteristics. For the temperature program of the device, a heating rate of 10 K/min was set, with a starting temperature of 400 K and an ending temperature of 700 K. Thus, within this specified temperature range, the heat flow curve (DSC graph) of the eutectic alloy consisting of 8.18 mg Zn–3.0 Mg–2.5 Al (wt.%) was obtained under a constant nitrogen atmosphere (Fig. 6).

Figure 6. The variation of electrical resistivity values as a function of growth rates for directionally solidified Zn–Mg–Al eutectic alloy under a constant temperature gradient and compared with the experimental results of previous Zn-Al based alloys.

The melting temperature (T_{peak}) of the Zn–3.0 Mg–2.5 Al (wt.%) eutectic alloy was determined to be 618.92 K. The values of ΔH_f and ΔC_P were found to be 26.69 J·g^{-1} and 0.043 J·g^{-1}·K^{-1}, respectively. The calculated value of 26.69 J·g^{-1} is approximately four times lower than the values reported for Zn-Al-Cu [25], Zn-Al-Sb [23], and Zn-Al-Bi [21] alloys, which are 113.89 J·g^{-1}, 108.59 J·g^{-1}, and 112.55 J·g^{-1}, respectively. This difference can be attributed to the presence of magnesium (~8.9 k·J·mol^{-1}) in the Zn–3.0 Mg–2.5 Al (wt.%) eutectic alloy, which has a lower fusion enthalpy compared to copper (~13.1 k·J·mol^{-1}), antimony (~19.7 k·J·mol^{-1}), and bismuth (~10.9 k·J·mol^{-1}). Thus, the inclusion of magnesium in the alloy reduces the overall fusion enthalpy, resulting in a lower melting point and facilitating the melting process [38]. A further difference is observed in the ΔC_P values. Due to its low density, magnesium contributes to a reduction in the overall density of the alloy, which can lead to a decrease in ΔC_P [39, 40].

Conclusion

Due to its superior properties such as high strength, lightweight, and corrosion resistance, the Zn–3.0 Mg–2.5 Al (wt.%) eutectic alloy is used in various industrial applications. Solidification studies were conducted using a Bridgman-type solidification furnace with a constant temperature gradient (G = 4.58 K/mm) and a growth rate range of V = 8.28–164.12 µm/s, at a furnace temperature of approximately 500 °C. Scanning Electron Microscopy (SEM) images were obtained to elucidate the microstructure and characterize the phases constituting the alloy, with quantitative chemical composition analyses (SEM-EDX) presented in graphical form for each phase. The electrical resistivity values of the solidified samples, dependent on each growth rate, were measured using FPPM, and the relationship between the growth rates and electrical resistivity values was established through linear regression analysis. The significant results emerging from this study can be summarized as follows:

1. It has been concluded that as the growth rates increase, the electrical resistivity values also rise proportionally. The highest electrical resistivity value (96.20 nΩm) was measured at the highest growth rate (164.12 μm/s), while the lowest electrical resistivity value (72.80 nΩm) was observed at the lowest growth rate (8.28 μm/s). In other words, the electrical conductivity ($\sigma = 1/\rho$) of the Zn–3.0% Mg–2.5% Al (wt.%) eutectic alloy exhibits an inverse relationship with the growth rates. Furthermore, the equation obtained from linear regression analysis ($\rho = 58.70\ V^{0.09}(n\Omega m)$) indicates that both the exponential value and the proportionality constant may reflect differences observed in some studies in the literature, which could be attributed to the $MgZn_2$ intermetallic phase. The differences arising from the $MgZn_2$ intermetallic phase can be attributed to two characteristics: (1) the distinct atomic structure and bonding of the $MgZn_2$ intermetallic phase, and (2) the emergence of more and tighter phase boundaries due to the increase of grain boundaries, which can hinder the passage of electrons and thus decrease conductivity.

2. The thermophysical properties of the Zn–3.0 Mg–2.5 Al (wt.%) eutectic alloy were determined from the DSC graph obtained using the PerkinElmer-STA8000 model device ($T_M = 618.92$ K, $\Delta H_f = 26.69$ J·g^{-1}, $\Delta C_P = 0.043$ J·g^{-1}·K^{-1}), and the results were compared with Zn-Al based studies in the literature. It was noted that the presence of magnesium in the Zn–3.0 Mg–2.5 Al (wt.%) alloy reduced the overall fusion enthalpy compared to other Zn-Al based alloys, resulting in a lower melting point. Additionally, by making a similar comparison with the ΔC_P value, it was emphasized that magnesium, being a low-density metal, decreases the overall density of the alloy, which could lead to a reduction in ΔC_P.

Conflict of interest

The author declares no conflict of interest in this work.

Acknowledgment

References

[1] Yamamoto K., Domoto K., Tobo M., Kawamizu T., Yamana T., Ota Y., Thermal Storage System to Provide Highly Efficient Electric Power Resilience in The Era of Renewable Energy, *Mitsubishi Heavy Industries Tech. Rev.,* 57 (1) (2020) 1–11.

[2] Nazir H., Batool M., Bolivar Osorio F. J., Isaza-Ruiz M., Xu X., Vignarooban K., Phelan P., Inamuddin, Arunachala I., Kannan A. M., Recent Developments in Phase Change Materials for Energy Storage Applications: A Review, *Int. J. Heat Mass Trans.*, 129 (2019) 491–523.

[3] Zhou, C., Wu S., Medium-and High-Temperature Latent Heat Thermal Energy Storage: Material Database, System Review, and Corrosivity Assessment. *Int. J. Energy Research,* 43 (2019) 621–661.

[4] Hirose A., Trends of Applications and Joining Technologies of Aluminum Alloys in Automobiles, *Journal of JSAE*, 61 (2007) 18-23.

[5] Sasabe S., Dissimilar Metal Joining Technology of Aluminum Alloy to Steel, *Journal of JSAE*, 61 (2007) 24-29.

[6] Porter D.A., Easterlirng K.E., Phase Transformations in Metals and Alloys, 2nd Ed., CRC Press, London, (1992).

[7] Caram R., Milenkovic S., Microstructure of Ni–Ni3Si eutectic alloy produced by directional solidification, *J. Crys. Growth*, 198–199 (1) (1999) 844-849.

[8] Fu H.Z., Liu L., Progress of Directional Solidification in Processing of Advanced Materials, *Mat. Sci. Forum*, 475–479 (2005) Zurich-Uetikon, Switzerland.

[9] Li Z., Li Y., Jiang S., Zhang J., Liu X., Zhang Q., Liu Q., Calculation and Experimental Verification of Zn–Al–Mg Phase Diagram. *Coatings*, 14 (4) (2024) 468.

[10] Delneuville P., Tribological Behaviour of ZnAl Alloys (ZA27) Compared with Bronze When Used as A Bearing Material with High Load and at Very Low Speed, *Wear*, 105 (4) (1985) 283-292.

[11] Auras R., Schvezov C., Wear Behavior, Microstructure, and Dimensional Stability of As-Cast Zinc-Aluminum/SIC (Metal Matrix Composites) Alloys, *Metall. Mat. Trans. A*, 35 (2004) 1579–1590.

[12] Kurz W., Fisher D.J., Fundamentals of Solidification, Chapter 5, 4th revised edition, Trans. Tech. Publications Ltd., Bäch, Switzerland, (1998).

[13] Zhang Y., Song C., Zhu L., Zheng H., Zhong H., Han Q., Zhai Q., Influence of Electric-Current Pulse Treatment on the Formation of Regular Eutectic Morphology in an Al-Si Eutectic Alloy, *Metall. Mat. Trans. B*, 42 (2011) 604–611.

[14] Kakitani R., de Gouveia G.L., Garcia A., Cheung N., Spinelli J.E., Thermal Analysis During Solidification of an Al–Cu Eutectic Alloy: Interrelation of Thermal Parameters, Microstructure and Hardness, *J. Thermal Analy. Cal.,* 137 (2019) 983–996.

[15] Duffar T., Sylla L., Crystal Growth Processes Based on Capillarity. Chapter 6—Vertical Bridgman Technique and Dewetting, Wiley, New York, (2010) 355–411.

[16] Venkataraman R., Handbook of Radioactivity Analysis (4th edition). Chapter 4—Semiconductor detectors, Elsevier Inc., (2020) 458-459.

[17] Rios C.T., Oliveira M.F., Caram R., Botta F.W.J., Bolfarini C., Kiminami C.S., Directional and Rapid Solidification of Al–Nb–Ni Ternary Eutectic Alloy, *Mat. Sci. Eng. A,* 375–377 (2004) 565-570.

[18] Çadırlı E., Kaya H., Gündüz M., Directional Solidification and Characterization of the Cd–Sn Eutectic Alloy, *J. Alloys Comp.*, 431 (1-2) (2007) 171-179.

[19] Li X., Ren Z., Fautrelle Y., Zhang Y., Esling C., Morphological Instabilities and Alignment of Lamellar Eutectics During Directional Solidification Under a Strong Magnetic Field, *Acta Mat.*, 58 (4) (2010) 1403-1417.

[20] Cui C., Zhang J., Xue T., Liu L., Fu H., Effect of Solidification Rate on Microstructure and Solid/Liquid Interface Morphology of Ni–11.5 wt% Si Eutectic Alloy, *J. Mat. Sci. Tech.*, 31 (3) (2015) 280-284.

[21] Karamazı Y., Bayram Ü., Ata P., Aksöz S., Keşlioğlu K., Maraşlı N., Dependence of microstructural, mechanical and electrical properties on growth rates in directional solidified Zn-Al-Bi eutectic alloy, *Trans. Nonfer. Metals Soc. China*, 26 (9) (2016) 2320-2335.

[22] Zuo X., Zhao C., Zhang L., Wang E., Influence of Growth Rate and Magnetic Field on Microstructure and Properties of Directionally Solidified Ag-Cu Eutectic Alloy, *Materials*, 9 (7) (2016) 569.

[23] Bayram Ü., Karamazı Y., Ata P., Aksöz S., Keşlioğlu K., Maraşlı N., Dependence Of Microstructure, Microhardness, Tensile Strength and Electrical Resistivity on Growth Rates for Directionally Solidified Zn-Al-Sb Eutectic Alloy, *Int. J. Mat. Res.*, 107 (11) (2016) 1005-1015.

[24] Hötzer J., Steinmetz P., Dennstedt A., Genau A., Kellner M., Sargin I., Nestler B., Influence of Growth Velocity Variations on the Pattern Formation During the Directional Solidification of Ternary Eutectic Al-Ag-Cu, *Acta Mat.*, 136 (2017) 335-346.

[25] Maraşlı N., Bayram, Ü., Aksöz, S., The variations of electrical resistivity and thermal conductivity with growth rate for the Zn–Al–Cu eutectic alloy. *J. Mater. Sci.: Mater. Electron*, 32 (2021) 18212–18223.

[26] Yan J., Liu T., Wang M., Sun J., Dong S., Zhao L., Wang Q., Constitutional Supercooling and Corresponding Microstructure Transition Triggered by High Magnetic Field Gradient During Directional Solidification of Al-Fe Eutectic Alloy, *Mat. Charact.*, 188 (2022) 111920.

[27] Bayram Ü., Investigation of Changes in Microstructure and Microhardness Properties of Zn-Al Eutectic Alloy as a Result of Directionally Solidification at High Velocities, *Erciyes Uni. J. Ins. Sci. Tech.*, 40 (2) (2024) 408-419.

[28] Çadırlı E., Gündüz M., The Dependence of Lamellar Spacing on Growth Rate and Temperature Gradient in the Lead-Tin Eutectic Alloy, *J. Mat. Proc. Tech.*, 97 (2000) 74–81.

[29] Böyük U., Maraşlı N., Kaya H., Çadırlı E., Keşlioğlu K., Directional solidification of Al–Cu–Ag alloy, *App. Physics A*, 95 (2009) 923–932.

[30] Yamashita M., Resistivity Correction Factor for the Four-Probe Method, *J. Phys. E: Sci. Instrum.*, 20 (1987) 1454-1456.

[31] Caignan A.G., Holt E.M., New 1,4-dihydropyridine Derivates with Hetero, Saturated B Rings, *J. Chem. Cryst.*, 32 (2002) 315-323.

[32] Smits F. M., Measurement of Sheet Resistivities with the Four-Point Probe, *The Bell System Tech. J.*, 37 (1958) 711-718.

[33] Kim J. N., Lee C. S., Jin Y. S., Structure and Stoichiometry of Mg_xZn_y in Hot-Dipped Zn–Mg–Al Coating Layer on Interstitial-Free Steel, *Met. Mater. Int.*, 24 (2018) 1090–1098.

[34] Gancarz T., Pstrus J., Characteristics of Sn–Zn Cast Alloys with the Addition of Ag and Cu, *Arch. Metall. Mater.*, 60 (2015) 1603–1607.

[35] Kamal M., Meikhail M. S., El-Bediwi A. B., Gouda E. S., Study of Structural Changes and Properties for Sn–Zn9 Lead-Free Solder Alloy with Addition of Different Alloying Elements, *Rad. Eff. Defect Solids*, 160 (2005) 45–52.

[36] Lee W. B., Bang K. S., Jung S. B., Effects of Intermetallic Compound on the Electrical and Mechanical Properties of Friction Welded Cu/Al Bimetallic Joints During Annealing, *J. Alloys Comp.*, 390 (1-2) (2005) 212-219.

[37] Zhang L., Luo J., Zhang S., Yan J., Huang X., Wang L., Gao J., Interface Sintering Engineered Superhydrophobic and Durable Nanofiber Composite for High-Performance Electromagnetic Interference Shielding, *J. Mat. Sci. Tech.*, 98 (2022) 62-71.

[38] Abdullaev R. N., Agazhanov A. S., Khairulin A. R., Samoshkin D. A., Stankus S. V., Thermophysical Properties of Magnesium in Solid and Liquid States, *J. Eng. Thermo.*, 31 (2022) 384–401.

[39] Li S., Yang X., Hou J., Du W., A Review on Thermal Conductivity of Magnesium and its Alloys, *J. Magnes. Alloys*, 8 (2020) 78–90.

[40] Song J., She J., Chen D., Pan F., Latest Research Advances on Magnesium and Magnesium Alloys Worldwide, *J. Magnes. Alloys*, 8 (2020) 1–41.

Cumhuriyet Science Journal

Kinetics of the Mixed Spin (1, 3/2) Ising Model in the Presence of an Oscillating Magnetic Field by Using the Path Probability Method

Mustafa Gençaslan [1,a,*], Abdulrahman Mohammed Kaif Awwadee [1,b]

[1] Department of Physics, Erciyes University, Kayseri, Türkiye.
*Corresponding author

Research Article

ABSTRACT

Kinetics of the mixed spin (1, 3/2) Ising ferrimagnetic system on the two interpenetrating square lattices with the bilinear and crystal-field interactions under an oscillating magnetic field were investigated by using the path probability method (PPM). We examined time variations in average dynamic magnetizations and obtained phases and then we investigated the thermal behaviors of dynamic magnetizations to determine the nature of the dynamic phase transitions and find their temperature values. We also constructed the dynamic phase diagrams in (d, T) and (h_0, T) planes. Dynamic phase diagrams display the paramagnetic (p), ferrimagnetic (i), and mixed phases (i+p), and one dynamic tricritical point and dynamic double critical endpoints. We found that the PPM is a more convenient method to investigate the kinetics and dynamics behaviors of ferrimagnetism.

Keywords: Mixed spin-1 and spin- 3/2 Ising system, Path probability method, Dynamic phase transition temperatures, Dynamic magnetic phase diagrams.

a✉ gaslan@erciyes.edu.tr   https://orcid.org/0000-0002-5726-1733   b✉ abd.m.kaif@gmail.com   https://orcid.org/0009-0009-7377-7877

Introduction

The usage areas of molecular-based magnetic materials in today's technology are increasing. Therefore, both theoretical and experimental studies on understanding the magnetic properties of these materials have increased and will continue to increase. Since it is essential to understand the equilibrium and nonequilibrium phase behaviors of these materials, many different theoretical models and methods have been developed in this context, the different Ising spin systems being the origin of most of them, and it has been observed that mixed spin systems give better results than the pure spin system. The mixed spin (1, 3/2) Ising system is one of the most practical prototype system to investigate molecular-based magnetic materials, such as $[NiCr_2(bipy)_2(C_2O_4)_4(H_2O)]H_2O$ [1], Fe_4N [2], and $[Co(hfac)_2]BNO^*$ [3]. Moreover, the system also gives interesting hysteresis loop behavior and rich equilibrium and nonequilibrium critical phenomena. Equilibrium behaviors of the system were studied by using the mean-field theory, the effective-field theory, the renormalization group theory, Green's function technique, Monte Carlo simulations, etc., (see [4-8] and references therein). The system was also used to investigate nanomaterials' thermal and magnetic properties, such as nanowires, nanotubes, and nanoislands [9-12].

On the other hand, less work was performed on the dynamic behaviors of the system. Keskin and co-workers conducted one of the earlier works [13, 14]. They determined the dynamic phase transition [13] and dynamic compensation temperatures using the dynamic mean field approximation (DMFA) and presented the dynamic phase diagrams [14]. The dynamic magnetic properties of the Fe_4N compound structure were investigated by Kantar and Ertaş [2] using the DMFA, and by Shi and Qi [15] using the dynamic effective field theory (DEFT). Also, Ertaş and Keskin [16] investigated the dynamic hysteresis and dynamic compensation temperatures of the system using the DEFT. The dynamic magnetic behavior of double-walled nanotubes was investigated by Benhouria et al., using the dynamic Monte Carlo simulations (DMCs) [18]. The path probability method (PPM) [27] used in the present paper has been very popular in Ising-like systems in recent years. While other methods include only one rate constant, the PPM includes two rate constants, one of which (k_2) corresponds to the wheel speed in the melt spinning technique in the rapid solidification process. (2) Even in the simplest use of the Hamiltonian, the order parameters become coupled. (3) The derivation of the dynamic equations is easier and more systematic than the other methods. Therefore, the application area of this method is quite wide. With the motivation of this information, Gençaslan and co-workers used the PPM to various mixed spin Ising ferrimagnetic systems (IFSs) in the presence of an oscillating magnetic field applied on different crystal fields to investigate the dynamic magnetic properties of molecular-based magnetic materials, namely dynamic hysteresis loops behaviors [19-24] and the dynamic phase diagrams (DPDs) [24-30]. They reported some interesting and rich dynamic phase diagram behaviors and dynamic hysteresis loop behaviors.

In this study, we investigate the dynamic phase transition temperatures (DPTs) and DPDs of the mixed spin (1, 3/2) IFS with the bilinear (*J*) and crystal field interactions (*D*) under a time-varying magnetic field (sinusoidal) by using the PPM. Moreover, we give the time variations of average dynamic magnetizations for different system parameters. After Section 2, where the model and derivations of dynamic equations are presented, the results and discussion are given in Section 3. Finally, concluding remarks are presented in Section 4.

Model and Derivation of Dynamic Equations

As depicted in Fig. 1, the mixed spin-1 and spin-3/2 IFS are defined on two square lattices with interpenetrating sublattices *A* and *B*. Sublattice *A* have spin values $\sigma_i^A = \pm 1, 0$, sublattice *B* have spin values $S_j^B = \pm\frac{3}{2}, \pm\frac{1}{2}$.
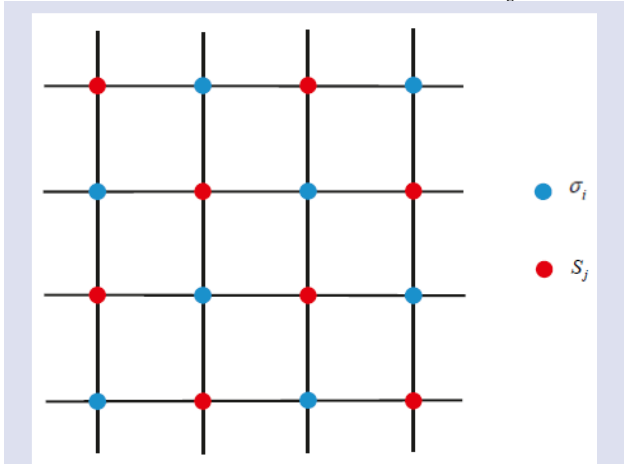

Figure 1. (Color online) The schematic representation of the two interpenetrating square lattices. The lattice is filled by σ_i (solid blue circles) and S_j (solid red circles) spins. *J* is the exchange couplings between the nearest-neighbor pairs of spins $\sigma_i - S_j$.

Hamiltonian of the system with bilinear (*J*) nearest-neighbor pair interaction and a crystal field interaction (*D*), under the presence of a sinusoidal magnetic field is written as

$$\mathcal{H} = -J \sum_{(i,j)} \sigma_i^A S_j^B + D \sum_i [(3\sigma_i^A)^2 - 2] + D \sum_j [(S_j^B)^2 - \frac{5}{4}] - H(\sum_i \sigma_i^A + \sum_j S_j^B) \quad (1)$$

where $< i, j >$ on the sublattices imply a summing of all nearest-neighboring sites. H is a sinusoidal magnetic field with amplitude H_0 and the angular frequency $\omega = 2\pi\nu$, thus $H = H_0 \cos(\omega t)$.

The system has the following five order parameters: (1) The average magnetization or the dipole moment $m^A = < \sigma_i^A >$, (2) the quadrupole moment, $q^A = 3 < (\sigma_i^A)^2 > -2$, for *A* sublattice and (3) The dipole moment or average magnetization $m^B = < S_j^B >$, (4) the quadrupole moment, $q^B = < (S_j^B)^2 > -\frac{5}{4}$, and (5) the octupole moment, $r^B = \frac{5}{3} < (S_j^B)^3 > -\frac{41}{12} < S_j^B >$, for *B* sublattice.

Since the formulation is given and discussed in Refs. [23, 24] in detail, we will briefly summarize it here. At this stage, the set of coupling average dynamic equations for order parameters can be obtained by using Eqs. (2)-(7) in Ref. [23] as

$$\Omega \frac{dm^A}{d\xi} = \{[\frac{1}{2}(sinh(2b) - cosh(2b))k_1 + (sinh(a-b) - cosh(a-b) - sinh(a+b)$$

$$- cosh(a+b))k_2 + \frac{1}{2}(sinh(2b) - cosh(2b))k_3]m^A$$

$$+ \frac{1}{6}[(sinh(2b) - cosh(2b) - 2cosh(a+b) - 2sinh(a+b))k_1 + 2(sinh(a+b)$$

$$+ cosh(a+b) + sinh(a-b) - cosh(a-b))k_2 + (cosh(2b) - sinh(2b) \quad (2)$$

$$+ 2cosh(a-b) - 2sinh(a-b))k_3]q^A$$

$$+ (\frac{1}{3}k_1 + \frac{2}{3}k_2)cosh(a+b) + (\frac{1}{3}k_1 + \frac{2}{3}k_2)sinh(a+b) - (\frac{2}{3}k_2 + \frac{1}{3}k_3)cosh(a-b)$$

$$+ (\frac{2}{3}k_2 + \frac{2}{3}k_3)sinh(a-b) - (\frac{1}{3}k_1 + \frac{1}{3}k_3)cosh(2b) + (\frac{1}{3}k_1 - \frac{1}{3}k_3)sinh(2b)\}/[ke^b(cosh(a) + e^{-3b})],$$

$$\Omega \frac{dq^A}{d\xi} = \{\frac{3}{2}[(sinh(2b) - cosh(2b))k_1 + (cosh(2b) - sinh(2b))k_3]m^A$$

$$+ [\frac{1}{2}(sinh(2b) - cosh(2b) - 2cosh(a+b) - 2sinh(a+b))k_1$$

$$+ (\frac{1}{2}(sinh(2b) - cosh(2b) - 2cosh(a-b) + 2sinh(a-b))k_3]q^A \quad (3)$$

$$+ k_1(cosh(a+b) + cosh(a+b)) + k_3(cosh(a-b) - sinh(a-b)$$

$$+ (k_1 + k_3)sinh(2b) - (k_1 + k_3)cos(2b)\}/[ke^b(cosh(a) + e^{-3b})]$$

and

$$\Omega \frac{dm^B}{d\xi} = \{-\frac{1}{5}[(2\sqrt{k_1k_2} + 9k_2 - k_1)\cosh(a)e^c - (6\sqrt{k_1k_2} + k_2 + 3k_1)\cosh(b)e^{-c}]m^B$$
$$+\frac{1}{2}[(2\sqrt{k_1k_2} - k_2 - k_1)\sinh(b)e^{-c} - (2\sqrt{k_1k_2} - 3k_2 + k_1)\sinh(a)]e^c]q^B \quad (4)$$
$$+\frac{1}{5}[(2\sqrt{k_1k_2} - 3k_2 + k_1)\cosh(b)e^{-c} - 3(2\sqrt{k_1k_2} - k_2 - k_1)\cosh(a)e^c]r^B$$
$$+\frac{1}{2}[(2\sqrt{k_1k_2} + k_2 - k_1)\sinh(b)e^{-c} + (2\sqrt{k_1k_2} + 3k_2 + k_1)\sinh(a)e^c]\}/2k[\cosh(a)e^c + \cosh(b)e^{-c}],$$

$$\Omega \frac{dq^B}{d\xi} = \{\frac{1}{5}(\sqrt{k_1k_2} - k_1)[6\sinh(b)e^{-c} - 2\sinh(a)e^c]m^B$$
$$-(\sqrt{k_1k_2} + k_1)[\cosh(a)e^c + \cosh(b)e^{-c}]q^B \quad (5)$$
$$+\frac{2}{5}(\sqrt{k_1k_2} - k_1)[3\sinh(a)e^c + \sinh(b)e^{-c}]r^B$$
$$+(\sqrt{k_1k_2} + k_1)[\cosh(a)e^c - \cosh(b)e^{-c}]\}/2k[\cosh(a)e^c + \cosh(b)e^{-c}],$$

$$\Omega \frac{dr^B}{d\xi} = \{\frac{1}{5}[(\sqrt{k_1k_2} - 3k_2 + 2k_1)\cosh(a)e^c + 3(\sqrt{k_1k_2} + k_2 - 2k_1)\cosh(b)e^{-c}]m^B$$
$$+\frac{1}{2}[(\sqrt{k_1k_2} + k_2 - 2k_1)\sinh(a)e^c - (\sqrt{k_1k_2} - 3k_2 + 2k_1)\sinh(b)e^{-c}]q^B \quad (6)$$
$$-\frac{1}{5}[(3\sqrt{k_1k_2} + k_2 + 6k_1)\cosh(a)e^c - (\sqrt{k_1k_2} - 9k_2 - 2k_1)\cosh(b)e^{-c}]r^B$$
$$-\frac{1}{2}[(\sqrt{k_1k_2} - k_2 - 2k_1)\sinh(a)e^c + (\sqrt{k_1k_2} + 3k_2 + 2k_1)\sinh(b)e^{-c}]\}/2k[\cosh(a)e^c + \cosh(b)e^{-c}],$$

where $h = \frac{H}{Jz}$, $d = \frac{D}{Jz}$, $T = (\beta Jz)^{-1}$, $k = \frac{k_1}{k_2}$, $k_3 = \sqrt{k_1k_2}$, $\xi = \omega t$, $z = 4$, and $\frac{a=(m^B+h_0\cos\xi)}{T}$, $b = \frac{d}{T}$ in the Eqs. (2, 3), and $a = \frac{3}{2}(m^A + h_0\cos\xi)/T$, $b = \frac{1}{2}(m^A + h_0\cos\xi)/T$ and $c = \frac{d}{T}$ in the Eqs. (4-6). It is worth remembering here that k_1 and k_2 are the rate constants that emerge as an advantage of the PPM. In the PPM, the rate constant k_1 corresponds to spin particle translation, i.e. the insertion or removal of particles across the lattices, and k_2 relates

to spin particle rotation at a given site, and k_3 corresponds to spin translation and rotation at the same time. Using the geometric mean, k_3 can be expressed in terms of k_1 and k_2 as $k_3 = \sqrt{k_1k_2}$. It is expected that two particles cannot be inserted, removed, or rotated at the same time. These constants for sublattices *A* and *B* are given in Table I. In the present paper, we fixed $k_1 = 1.0$ in all numerical calculations.

Table I. The description of rate constants for the *A* and *B* sublattices

		1	0	-1
A sublattice	1		k_1	k_2
	0	k_1		k_1
	-1	k_2	k_1	

		+3/2	+1/2	-1/2	-3/2
B sublattice	+3/2		k_1	k_3	k_2
	+1/2	k_1		k_2	
	-1/2	k_3	k_2		k_1
	-3/2	k_2	k_3	k_1	

We numerically solved these equations by combining the numerical methods of the Romberg integration with the Adams-Moulton predictor-corrector, for a given set of system parameters and initial values. The obtained results and their discussion will be presented in the next section. Since m^A and m^B determine the dynamic magnetic properties of the system, we are only interested in the behaviors of m^A and m^B. Moreover, the total magnetization is defined as $m^T = \frac{(m^A+m^B)}{2}$.

Time Variations in Average Dynamic Magnetizations

To find phases occurring in the system, we examine the stationary solutions of average magnetizations (m^A and m^B), i.e., Eqs. (2) and (4). The stationary solutions of Eqs. (2) and (4) are periodic functions of ξ with period 2π, i.e.,

$$m^{A,B}(\xi + 2\pi) = m^{A,B}(\xi) \quad (7)$$

Furthermore, they can be one of two solutions according to whether they have or do not have the following condition

$$m^{A,B}(\xi + \pi) = -m^{A,B}(\xi) \qquad (8)$$

It is one of the solutions that satisfies Eq. (8), which is called the symmetrical solution and expresses a paramagnetic (p) phase. In this case, m^A and m^B oscillate around zero as seen in Fig. 2(a). The other solution does not satisfy Eq. (8), which is called the nonsymmetric solution, corresponds to a ferrimagnetic (i) phase. For this reason, m^A oscillates around ± 1 and m^B around $\pm 3/2$, as exhibited in Fig. 2(b). The i and p phases are fundamental phases. We found one mixed phase, i.e., p+i where the p and i phases coexist, displayed in Fig. 2(c). We also investigated the effect of rate constants on stationary solutions of m^A and m^B, and we observed the system rapidly relaxes to the p phases while k_2 values increase, as seen in Fig. 3. We should mention that since most systems have a longer relaxation time for a rotation (k_2) than for a translation (k_1), we took $k_2 > k_1$ in numerical calculations. Figs. 2 and 3 exhibit the solutions of m^A and m^B with different initial values, with the same color code. If examined carefully, it is seen that the solutions given as Fig. 2(a) and Fig. 3 are independent of initial values, while the those given as Figs. 2 (b)-(c) are dependent on the initial values. If we look at Fig. 2(a) carefully, we see that m^A and m^B oscillate around zero, which is understood to represent the paramagnetic phase (p). In Fig. 2(b), m^A and m^B oscillate exactly around ± 1 and $\pm \frac{3}{2}$, that is, they show the ferrimagnetic (i) phase. The mixed or hybrid phase (p + i) behavior, that is, m^A and m^B oscillate exactly ± 1, $\pm \frac{3}{2}$ and also around zero, is clearly seen in Fig. 2(c). While the oscillations in the calculations found with the mean field approximation for the same mixed spin system in Refs. [2, 14] occur around approximate values, it is interesting that the oscillations obtained with the PPM in the present study occur exactly around 0, ± 1, $\pm \frac{3}{2}$ as expected. Fig. 3(a)-(d) shows the effect of the changing rate constant on the paramagnetic phase while all system parameters remain the same. It is seen that the system reaches the paramagnetic phase more quickly as the rate constant parameter k_2 increases.
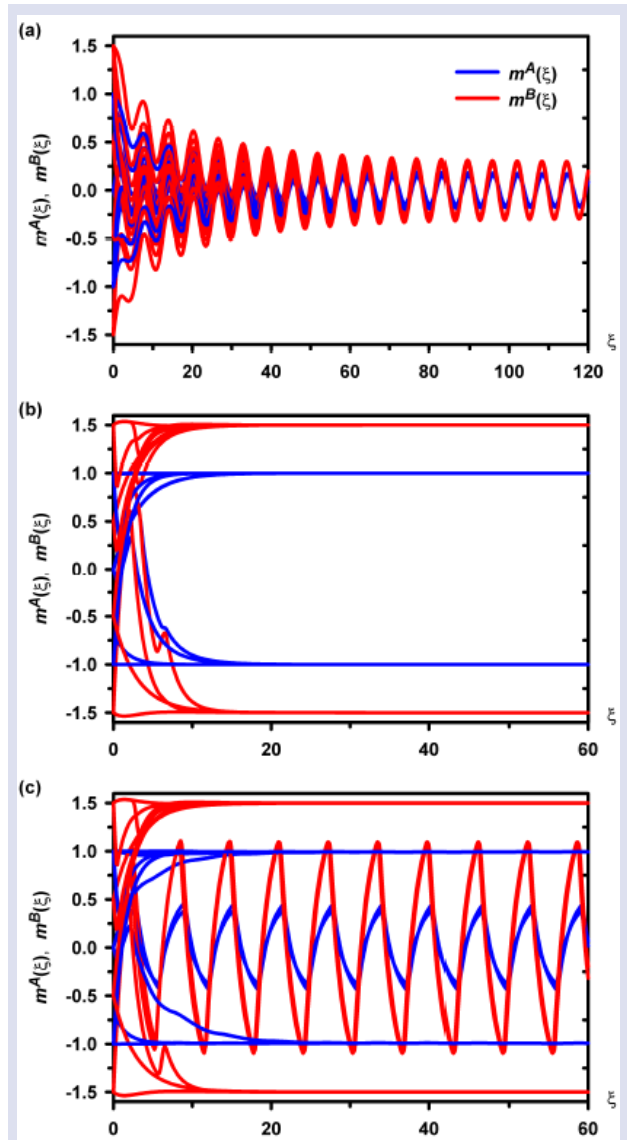

Figure 2. (Color online) Time variations of the magnetizations (m^A and m^B), with $d = 4.0$, $k_1 = 1.0$ and $k_2 = 1.0$. (a) Exhibiting a paramagnetic (p) phase for $T = 1.50$, $h_0 = 0.350$; (b) Illustrating a ferrimagnetic (i) phase for $T = 0.10$, $h_0 = 0.60$; (c) Displaying a mixed or coexistence phase, namely the i+p phase for $T = 0.75$, $h_0 = 0.60$.

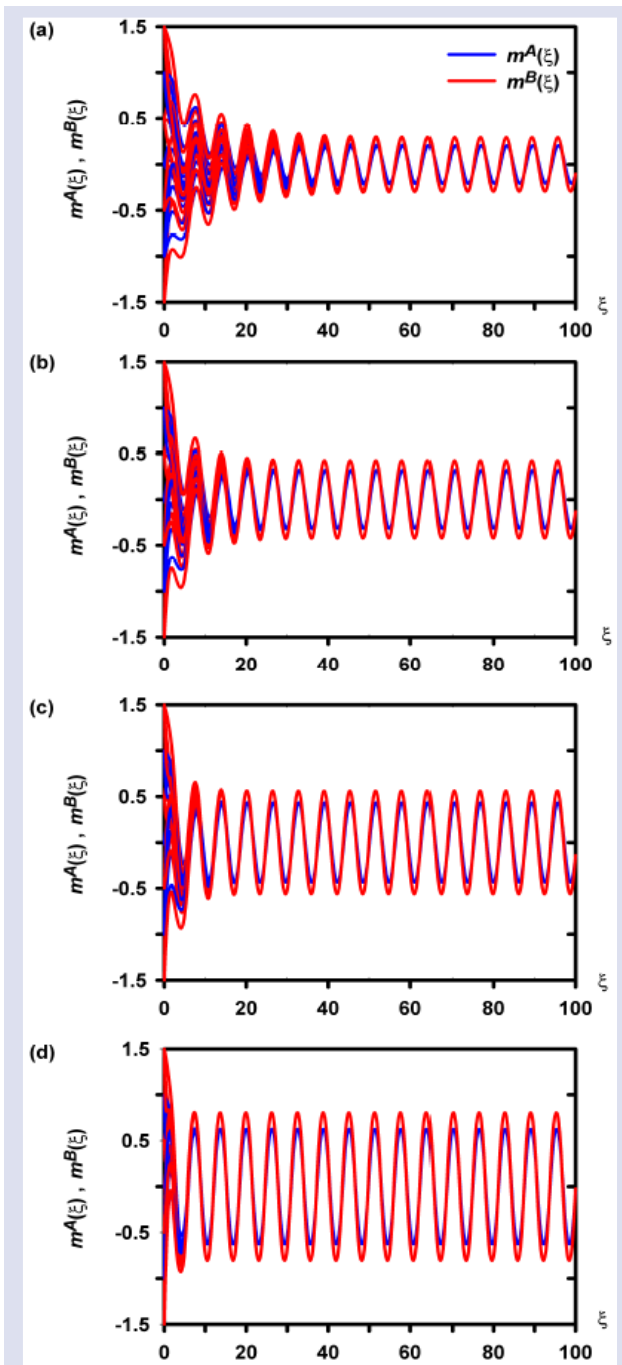Figure 3. (Color online) Time variations of the magnetizations (m^A and m^B) for only paramagnetic (*p*) phase for $T = 1.40$, $d = 0.25$, $h_0 = 0.60$, $k_1 = 1.0$ and four different values of k_2. (a) $k_2 = 2.0$, (b) $k_2 = 2.5$, (c) $k_2 = 3.0$ and (d)

Dynamic Phase Transition Temperatures (DPTs)

Dynamic phase transition temperatures (DPTs) are obtained by investigating the thermal behavior of dynamic magnetizations that are given as [31]

$$M^{A,B} = \frac{1}{2\pi} \int_0^{2\pi} m^{A,B}(\xi)\, d\xi. \tag{9}$$

As we mentioned before, since m^A and m^B determine the dynamic magnetic properties of the system, we only need to examine the behaviors of M^A and M^B. The solutions of Eq. (9) give us to whether a first or second order phase transition occurs and the temperature values of these transitions. Firstly, we numerically solved Eq. (9) for $d = 4.0$, $k_1 = 1.0$, $k_2 = 2.0$, and various values h_0, and obtained the thermal behavior of dynamic magnetizations ($|M^A|$ and $|M^B|$) as seen in Fig. 4. Hence, Fig. 4 (a) is presented for $h_0 = 0.35$. Fig. 4(a) exhibits that $M^{A,B}$ decreases to zero continuously as *T* increases. Therefore, the system undergoes a second-order phase transition at $T_C = 1.40$ and the dynamic transition is from the *i* phase to the *p* phase, for all initial values of $|M^A|$ and $|M^B|$. This fact is very clearly seen in Fig. 6 (c) for $h_0 = 0.35$. Fig. 4(b) is plotted for $h_0 = 0.60$, and it displays that $M^{A,B}$ firstly the *p* phase up to $T_t = 0.075$ for the initial values of $|M^A| = 0.0$, it exhibiting the *i* phase for the $|M^A| = 1.0$; $|M^B| = 0.5, 1.5$ up to $T_C = 1.16$. They are exhibiting two successive phase transitions, namely (b_1) illustrating a first-order phase transition at $T_t = 0.075$, and ($b_2 b_2$) displaying a second-order phase transition at $T_C = 1.16$. Thus, the *i+p* mixed phase takes place between T_t and T_C. Fig. 4(c) is constructed for $h_0 = 0.80$; (c_1)-(c_4) exhibiting four successive phase transitions, namely the first one is (c_1) at $T_{t1} = 0.08$ for initial values $|M^A| = 0.0$; $|M^B| = 0.5$ and $T_{t2} = 0.355$, the second one is (c_2) at $T_{t1} = 0.08$ for initial values $|M^A| = 0.0$; $|M^B| = 1.5$ and $T_{t2} = 0.365$, the third one is (c_3) at $T_{t2} = 0.355$ for initial values $|M^A| = 1.0$; $|M^B| = 0.5$ and finally the fourth one is (c_4) at $T_t = 0.600$ for initial values $|M^A| = 1.0$; $|M^B| = 1.5$. This fact is very clearly seen in Fig. 6 (c) for $h_0 = 0.80$. Thus, the *i+p* mixed phase takes place between $T_t = 0.08$ and $T_t = 0.600$.

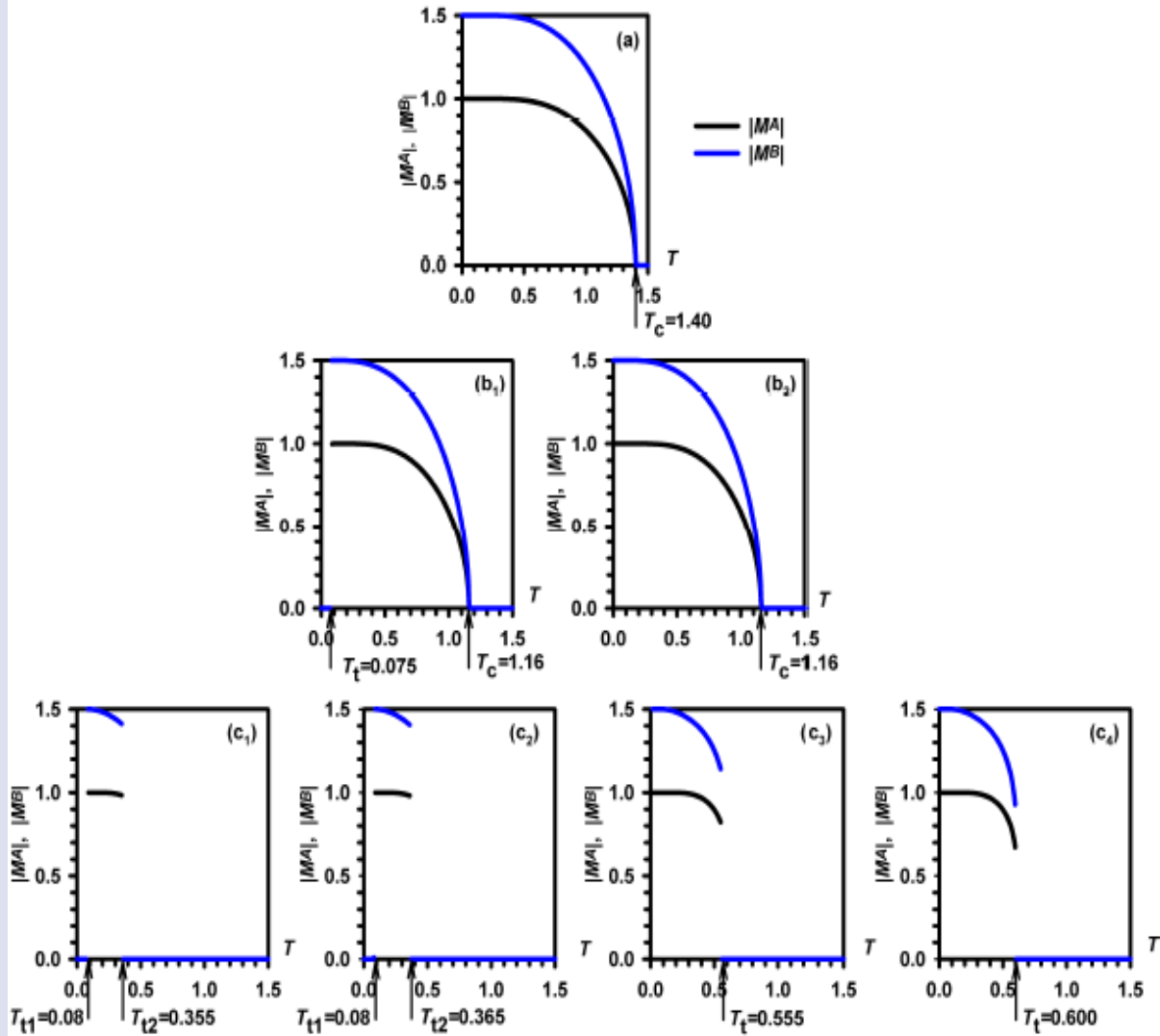Figure 4. (Color online) The thermal behavior of dynamic magnetizations ($|M^A|$) T_c and T_t are the second-order and first-order phase transition temperatures for both $|M^A|$ and $|M^B|$, respectively, with $d = 4.0$, $k_1 = 1.0$, $k_2 = 2.0$. (a) Exhibiting a second-order phase transition from the ferrimagnetic (*i*) phase for $T_C = 1.40$, $h_0 = 0.35$, for all initial values of $|M^A|$ and $|M^B|$; (b_1) and (b_2) were obtained for $h_0 = 0.60$ and two different initial values of $|M^A| = 0.0$; $|M^B| = 0.5, 1.5$ and $|M^A| = 1.0$; $|M^B| = 0.5, 1.5$, respectively, and they are exhibiting two successive phase transitions, namely (b_1) illustrate a first-order phase transition at $T_t = 0.075$, and (b_2) displaying a second-order phase transition at $T_C = 1.16$. For $h_0 = 0.80$, (c_1)-(c_4) exhibiting four successive phase transitions, namely the first one is (c_1) at $T_{t1} = 0.08$ for initial values $|M^A| = 0.0$; $|M^B| = 0.5$ and $T_{t2} = 0.355$, the second one is (c_2) at $T_{t1} = 0.08$ for initial values $|M^A| = 0.0$; $|M^B| = 1.5$ and $T_{t2} = 0.365$, the third one is (c_3) at $T_{t2} = 0.555$ for initial values $|M^A| = 1.0$

To see the nature of the DPT temperatures for the case where h_0 is fixed but for the crystal-field interaction d is varied, we obtained Fig.5 by solving Eq.(9). So that, Fig.5(a) exhibits a second-order phase transition from the ferrimagnetic (*i*) phase for $T_c = 0.765$, $d = 0.10$, for all initial values of $|M^A|$ and $|M^B|$. For $d = 1.0$, Fig.5 (b_1)-(b_3) shows three successive phase transitions, namely the first one is (b_1) at $T_t = 0.365$ for initial values $|M^A| = 0.0$; $|M^B| = 0.5, 1.5$, the second one is (b_2) at $T_t = 0.555$ for initial values $|M^A| = 1.0$; $|M^B| = 0.5$, the third one is (b_3) at $T_t = 0.595$ for initial values $|M^A| = 1.0$; $|M^B| = 1.5$. For $d = 6.0$, very similar results were found as presented

in Fig.4 (c_1)-(c_4) exhibiting four successive phase transitions, namely the first one is (c_1) at $T_{t1} = 0.130$ for initial values $|M^A| = 0.0$; $|M^B| = 0.5$ and $T_{t2} = 0.355$, the second one is (c_2) at $T_{t1} = 0.130$ for initial values $|M^A| = 0.0$; $|M^B| = 1.5$ and $T_{t2} = 0.365$, the third one is (c_3) at $T_t = 0.555$ for initial values $|M^A| = 1.0$; $|M^B| = 0.5$ and finally the fourth one is (c_4) at $T_t = 0.600$ for initial values $|M^A| = 1.0$; $|M^B| = 1.5$. Thus, the *i+p* mixed phase takes place between $T_{t1} = 0.130$ and $T_t = 0.600$.

Dynamic Phase Diagrams (DPDs)

In the previous section, it was explained how to determine the DPTs, and now we can plot the DPDs in the

(h_0, T) and (d, T) planes for various system parameters, as shown in Figures 6 and 7. In the given DPDs, the dashed and solid lines represent the first- and second-order DPT boundaries, respectively, *TCP* and *B* represent the dynamic triple critical point and the dynamic double critical endpoint [32], respectively. All our calculations were made for $k_1 = 1.0$, $k_2 = 2.0$ and various values of h_0 and d.

Figure 6(a) obtained for $d = 0.25$ in which at low temperature (T) and low values of h_0, the DPD exhibits ferrimagnetic (i), while at high T values displays paramagnetic (p) characteristics. The dynamic boundary line separating the i and p phases is the second-order phase line. There is a region at low T and high h_0 values where the i and p phases coexist, named the mixed phase $(i+p)$. The dynamic first-order phase lines separate the $i+p$ phase from the i and the p phases. Moreover, the system

has a dynamic tricritical point (*TCP*) where two first-order phase transition lines merge and transform into a first-order to a second-order phase transition. The DPDs with similar behavior have been reported in various mixed Ising ferrimagnetic systems (see Refs. [27, 33-35] and references therein) and mixed (1, 3/2) IFS [14, 36, 37]. Fig. 6(b) was calculated for $d = 2.50$, which is similar to Fig. 6(a), but the tricritical line becomes shorter and the mixed phase region becomes slightly larger. Additionally, at low temperatures, another mixed phase region appears, terminating in a double critical end point *B*. Fig. 6 (c) and (d) were constructed for $d = 4.0$ and $d = 6.0$, respectively. Figures 6 (c) and (d) are quite similar to Fig. 6(b), except for the broadening of the mixed phase region, terminating in a *B*, that occurs at lower temperatures with increasing d.
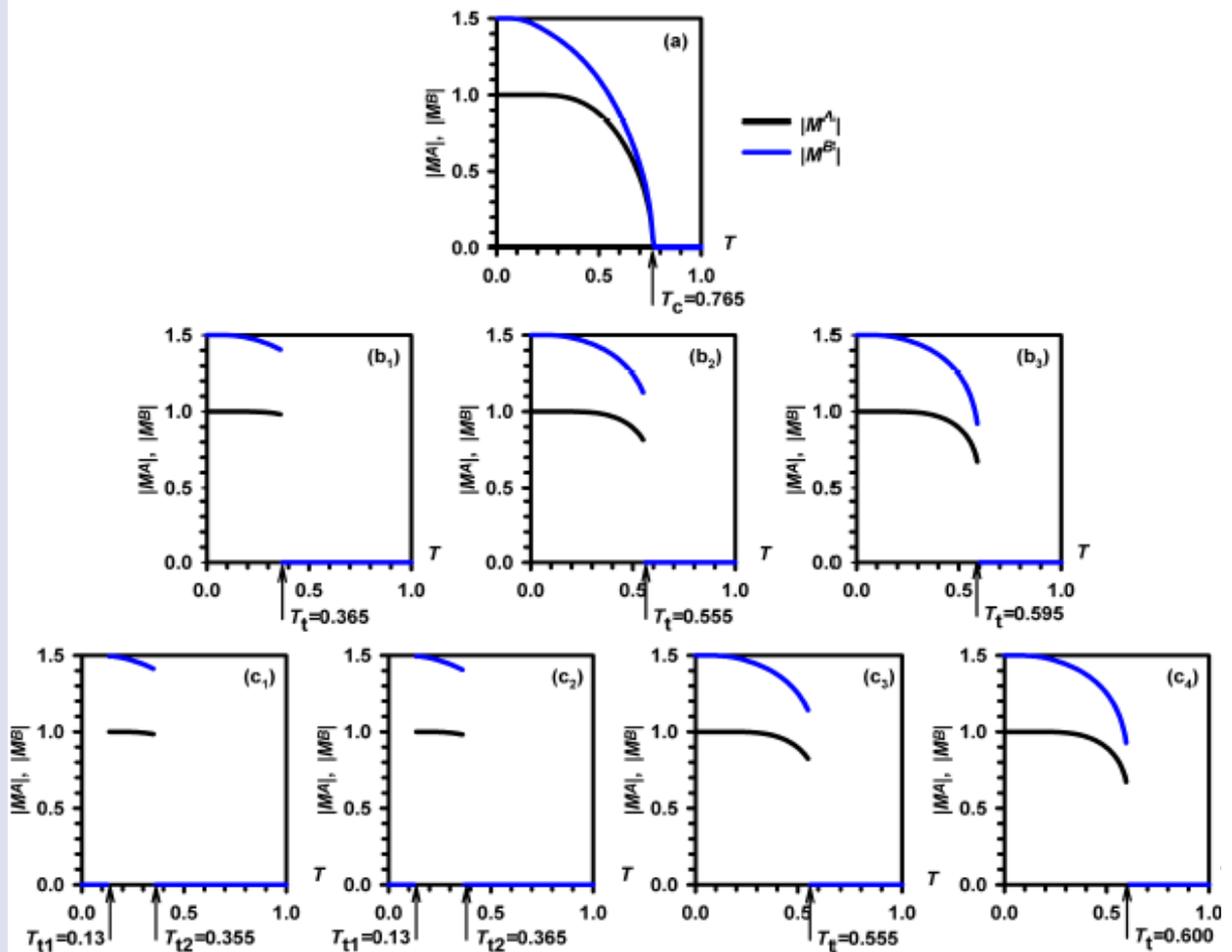

Figure 5. (Color online) The thermal behavior of dynamic magnetizations ($|M^A|$ and $|M^B|$) T_c and T_t are the second-order and first-order phase transition temperatures for both $|M^A|$ and $|M^B|$, respectively, with $d = 4.0$, $k_1 = 1.0, k_2 = 2.0$. (a) Exhibiting a second-order phase transition from the ferrimagnetic (i) phase for $T_c = 0.765$., $d = 0.10$, for all initial values of $|M^A|$ and $|M^B|$. For $d = 1.0$, (b_1)-(b_3) exhibiting three successive phase transitions, namely the first one is (b_1) at $T_t = 0.365$ for initial values $|M^A| = 0.0$; $|M^B| = 0.5, 1.5$, the second one is (b_2) at $T_t = 0.555$ for initial values $|M^A| = 1.0$; $|M^B| = 0.5$, the third one is (b_3) at $T_t = 0.595$ for initial values $|M^A| = 1.0$; $|M^B| = 1.5$. For $d = 6.0$ found the very similar result were found that (c_1)-(c_4) exhibiting four successive phase transitions, namely the first one is (c_1) at $T_{t1} = 0.130$ for initial values $|M^A| = 0.0$; $|M^B| = 0.5$ and $T_{t2} = 0.355$, the second one is (c_2) at $T_{t1} = 0.130$ for initial values $|M^A| = 0.0$; $|M^B| = 1.5$ and $T_{t2} = 0.365$, the third one is (c_3) at $T_t = 0.555$ for initial values $|M^A| = 1.0$; $|M^B| = 0.5$ and finally the fourth one is (c_4) at $T_t = 0.600$ for initial values $|M^A| = 1.0$; $|M^B| = 1.5$.
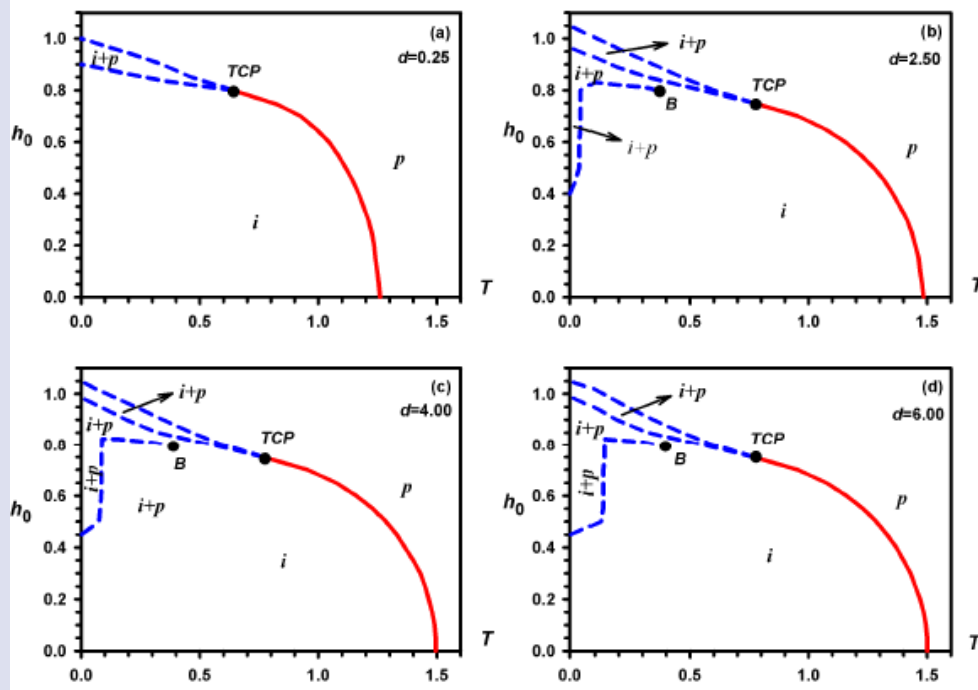
Figure 6. (Color online) The DPDs of the system in the (h_0, T) plane, with $k_1 = 1.0$ and $k_2 = 2.0$. The paramagnetic (p), ferrimagnetic (i), and the $i+p$ mixed phase are observed. Solid and dashed lines are the second-order and first-order phase transitions, respectively. The special dynamic critical points are the dynamic tricritical (TCP) and the dynamic double critical end (B) points. (a) $d = 0.25$, (b) $d = 2.50$, (c) $d = 4.00$, (d) $d = 6.00$.
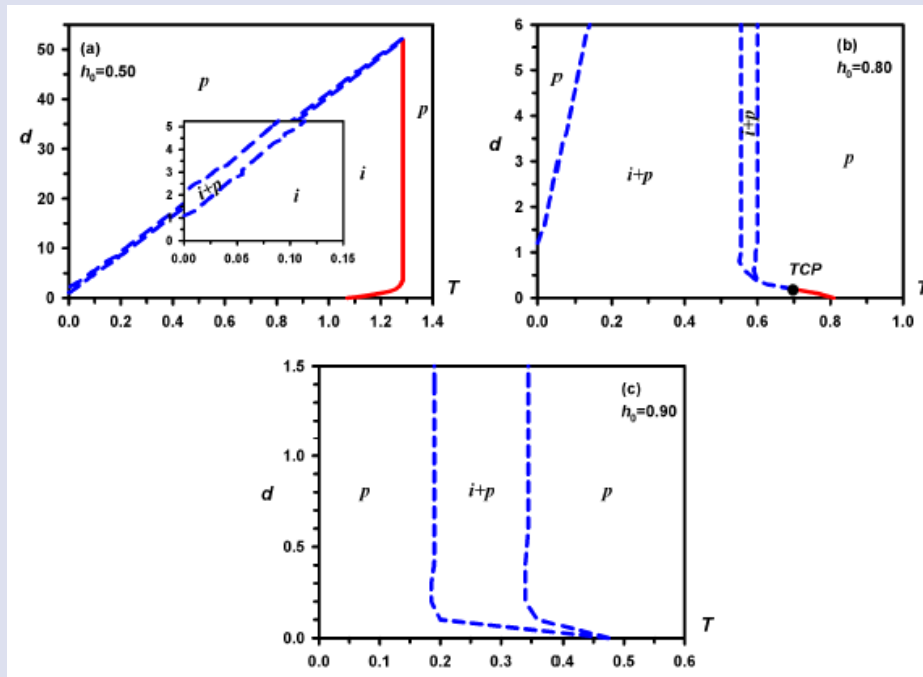

Figure 7. (Color online) The DPDs of the system in the (d, T) plane. It contains TCP but not B. (a) $h_0 = 0.50$, (b) $h_0 = 0.90$

Fig. 7 exhibits the DPDs in the (d, T) plane for three different values of h_0. Fig. 7 (a)-(c) are obtained for $h_0 = 0.50; 0.80$ and 0.90 respectively. If one looks carefully at Fig. 7(a), one sees that it contains a very narrow $i+p$ mixed phase region that starts at low temperatures and small d values, which gradually narrows with increasing d values and merges with the second-order phase transition line at high temperatures and large d values, i.e. they converge at TCP tricritical point. In Figure 7(b),

a third dynamic first-order phase transition line appears starting from low temperature and d values and goes towards asymptotically high temperature and d values. Furthermore, there is also a narrow mixed-phase region, which starts from a TCP point at a low d value. In Figure 7(c) obtained for $h_0 = 0.90$, a third dynamic first-order phase line and TCP point seen in Figure 7(b) disappear, and the $i+p$ mixed phase region widens.

Finally, the DPDs we obtained in both the (h_0, T) and the (d, T) plane have a *TCP* point and a dynamic double critical endpoint, and some similar results have been reported in pure [27, 33-35] and mixed spin Ising ferrimagnetic systems [2, 14, 36, 37].

Concluding Remarks

We studied the dynamic phase transition temperatures and dynamic phase diagrams of the mixed spin (1, 3/2) IFS under a sinusoidal magnetic field by using the PPM, which contains two rate constants. Thus, the dynamic phase behavior of this system was examined for the first time according to these two rate constants. The following important conclusions were obtained. (1) We observed that only the *p*, *i* , and *i+p* phases were present in the system when the PPM was used. (2) We found that as the values of k_2 rate constant increased, the system rapidly relaxed into the *p*, *i* , and *i+p* phases. (3) We obsered that the system contains a special dynamic critical point, such as a dynamic double critical endpoint. (4) When we compared our DPDs with some dynamic theoretical studies of different mixed and pure Ising ferrimagnetic systems, we observed that they were in good agreement. Finally, we hope that our present theoretical work sheds light on theoretical condensed matter physicists or statistical physicists to continue to investigate DPTs and DPDs in different systems within the PPM.

Conflict of interest

The authors report no conflicts of interest in this work.

References

[1] Stanica N., Stager C. V., Cimpoesu M., Andruh M., Synthesis and magnetic properties a of new oxalato-bridged heterotrinuclear complex, [NiCr$_2$ (bipy)$_2$ (μ-C$_2$O$_4$)$_2$(C$_2$O$_4$)$_2$ (H$_2$O)$_2$].H$_2$O. A rare case of antiferromagnetic coupling between Cr(III) and Ni(II) ions, *Polyhedron 17* (1998) 1787-1789.

[2] Kantar E., Ertaş M., Frequency-Dependent Dynamic Phase Diagrams in Ising System with Fe$_4$N Structure, *Journal of Superconductivity and Novel Magnetism 29* (2016) 2319-2326.

[3] Numata Y., Inoue K., Baranov N., Field-induced ferrimagnetic state in a molecule-based magnet consisting of a Co (II) ion and a chiral triplet bis(nitroxide) radical, Kurmoo M., Kikuchi K., *Journal of the AmericanNChemical Society 129* (2007) 9902-9909.

[4] Jiang W., Wei G.-z, Zhang Z.-d,Tricritical behavior and magnetic properties for a mixed spin-1 and spin-3/2 transverse Ising model with a crystal field, *Phys. Rev. B 68* (2003) 134432.

[5] Madani M., Gaye A., El Bouziani M., Migdal–Kadanoff solution of the mixed spin-1 and spin-3/2 Blume–Capel model with different single-ion anisotropies, Alrajhi A., *Physica A 437* (2015) 396-404.

[6] Htoutou K., Oubelkacem A., Benhouria Y., Htoutou K., Oubelkacem A., Benhouria Y., Essaoudi I., Ainane A., Ahuja R., The Magnetic Properties of the Mixed Ferrimagnetic Ising System with Random Crystal Field, *Journal of Superconductivity and Novel Magnetism, 30* (2017) 1247-1256.

[7] Motlagh H. N., Rezaei G., Monte Carlo simulation of magnetic properties of mixed spin (3/2, 1) ferromagnetic and ferrimagnetic disordered binary alloys with amorphous structure, *J. Magn. Magn. Mater., 445* (2018) 26-36.

[8] Lafhal A., El Antari A., Hachem N., Al-Rajhi A., Aharrouch R., Saadi H., Madani M., El Bouziani M., Renormalization Group Study of the Mixed Spin-1 and Spin-3/2 Blume-Emery-Griffiths Model with Attractive Biquadratic Coupling, *International Journal of Theoretical Physics, 59* (2020) 1165-1178.

[9] Zaim A., Kerouad M., Monte Carlo simulation of the compensation and critical behaviors of a ferrimagnetic core/shell nanoparticle Ising model, *Physica A, 389* (2010) 3435-3442.

[10] Feraoun A., Kerouad M., The mixed spin-(1,3/2) Ising nanowire with core/inter-shell/outer-shell morphology, *Applied Physics A-Materials Science & Processing, 124* (2018) 124:735.

[11] Vatansever E., Polat H., Monte Carlo investigation of a spherical ferrimagnetic core–shell nanoparticle under a time dependent magnetic field, *J. Magn. Magn. Mater., 343* (2013) 221-227.

[12] Yang M., Wang W., Li Bo-chen, Wu H. J., Yang Shao-qing, Yang J., Magnetic properties of an Ising ladder-like graphene nanoribbon by using Monte Carlo method, *Physica A, 539* (2020) 122932.

[13] Keskin M., Kantar E., Canko O., Kinetics of a mixed spin-1 and spin-3/2 Ising system under a time-dependent oscillating magnetic field, *Phys. Rev. E, 77* (2008) 051130.

[14] Keskin M., Kantar E., Dynamic compensation temperatures in a mixed spin-1 and spin-3/2 Ising system under a time-dependent oscillating magnetic field, *J. Magn. Magn. Mater., 322* (2010) 2789-2796.

[15] Shi X., Qi Y., Existence of a dynamic compensation temperature of the mixed spin-1 and spin-3/2 Ising model within the effective-field theory, *Physica A, 430* (2015) 93-100.

[16] Ertaş M., Keskin M., Dynamic hysteresis features in a two-dimensional mixed Ising system, *Phys. Letts. A, 379* (2015) 1576-1583.

[17] Benhouria Y., Oubelkacem A., Essaoudi I., Ainane A., Ahuja R.,Dynamic Magnetic Properties of a Mixed Spin Ising Double-Walled Ferromagnetic Nanotubes: A Dynamic Monte Carlo Study, *Journal of Superconductivity and Novel Magnetism, 30* (2017) 839-844.

[18] Kikuchi R., The Path Probability Method, *Progress of Theoretical Physics Supplement,* 3 (1966) 1–64.

[19] Gençaslan M., Keskin M., Dynamic magnetic hysteresis loop features of a mixed spin (1/2, 1) Ising system on a hexagonal lattice using path probability method, *Modern Phys. Letters, B 35* (2021) 2150221.

[20] Gençaslan M., Keskin M., Influences of the interaction parameters on the dynamic hysteresis of a mixed spin (1/2, 3/2) Ising model under the presence of an oscillating magnetic field, *Int. J. Modern Phys., B 35* (2021) 2150217.

[21] Gençaslan M., Keskin M., Dynamic hysteresis features of a mixed spin (1/2,3/2) Ising system within the path probability method, *Phase Transitions, 95* (2022) 372-386.

[22] Gençaslan M., Keskin M., Dynamic magnetic hysteresis features of a mixed spin (2, 5/2) Ising system on a hexagonal lattice under an oscillating magnetic field within the path probability method, *Int. J. Modern Phys. B, 38* (2024) 2450198.

[23] Gençaslan M., AWWADEE A. M. K., Effect of Cooling Rate on Dynamic Magnetic Hysteresis Loop Behaviors of Magnetic Materials by Using as a Model Mixed Spin (1, 3/2) Ising System Under an Oscillating Magnetic Field, *Journal of Superconductivity and Novel Magnetism, 37* (2024) 1105-1117.

[24] AWWADEE A. M. K., Dynamic Magnetic Properties of a Mixed Spin (1, 3/2) Ferrimagnetic Ising System in an Oscilating Magnetic Field Within the Path Probability Method, *M. Sc. Thesis*, Erciyes University (2024), Kayseri, Türkiye.

[25] İnce O., Gençaslan M., Keskin M., Magnetic features and compensation behaviors of a mixed spin (1/2, 1) Ising ferrimagnetic system on a hexagonal lattice, *Physica A, 583* (2021) 126270.

[26] Gençaslan M., Keskin M., Dynamic magnetic properties of the mixed spin (1/2, 3/2) Ising system in the presence of magnetic field within the path probability method, *Physica A, 559* (2020) 125013.

[27] İnce O., Gençaslan M., Keskin M., Dynamic phase of transitions of the mixed spin (1/2, 3/2) Ising model in the presence of a time-varying magnetic field by using the path probability method, *Phys. Letters A, 390* (2021) 127107.

[28] Alhameri M. F. İ., Dynamic phase transitions and compensation behaviors in a mixed spin (1/2,3/2) Ising model on a hexagonal lattice by path probability method, Gençaslan M., Keskin M., *Indian J. Physics, 96* (2022) 3775-3786.

[29] Gençaslan M., Keskin M., Nonequilibrium magnetic features in a mixed spin (2, 5/2) Ising system driven by the external oscillating magnetic field by path probability method, *Physica Scripta, 97* (2022) 085803.

[30] Gençaslan M., Özlü M., Keskin M., Dynamic Magnetic Features of a Mixed-Spin-2 and Spin-5/2 Ising Ferrimagnetic System under a Time-Dependent Oscillating Magnetic Field: Path Probability Method Approach, *Phys. Status Solidi, B 260* (2023) 2200425.

[31] Chakrabarti K., Acharyya M., Dynamic transitions and hysteresis, *Rev. Mod. Phys., 71* (1999) 847-859.

[32] Yunus Ç., Renklioğlu B., Keskin M., Stepwise positional-orientational order and the multicritical-multistructural global phase diagram of the s=3/2 Ising model from renormalization-group theory, Berker A. N., *Phys. Rev. E, 93* (2016) 062113.

[33] Deviren B., Keskin M., Canko O., Kinetics of a mixed spin-1/2 and spin-3/2 Ising ferrimagnetic model, *J. Magn. Magn. Mater., 321* (2009) 458-466.

[34] Ertaş M., Keskin M., Dynamic magnetic behavior of the mixed spin (2, 5/2) Ising system with antiferromagnetic/antiferromagnetic interactions on a bilayer square lattice, *Chin. Phys. B, 22* (2013) 120507.

[35] Ertaş M., Deviren B., Nonequilibrium magnetic properties in a two-dimensional kinetic mixed Ising system within the effective-field theory and Glauber-type stochastic dynamics approach, Keskin M., *Phys. Rev. E, 86* (2012) 051110.

[36] Deviren Ş. A., Deviren B., Dynamic magnetic properties of a mixed-spin (1, 3/2) Ising nanotube: a dynamic mean-field study, *Eur. Phys. J. Plus, 137* (2022) 1067.

[37] Ertaş M., Deviren B., Dynamic magnetic properties of multilayer mixed spin-1 and spin-3/2 Ising model, *Eur. Phys. J. Plus, 137 (2022)* 1031.

Cumhuriyet Science Journal

Electronic, Optical and Mechanical Properties of Ta Doped LiNbO3: Ab Initio Calculation

Furkahan Acar [1,a] Şevket Şimşek [2,b, *]

[1] Department of Material Science and Engineering, Faculty of Engineering, Hakkari University, 30000, Hakkari, Türkiye[3]
*Corresponding author

Research Article

ABSTRACT

In this study, the electronic, optical and mechanical properties of $LiNb_{1-x}Ta_xO_3$ were investigated by ab initio method by adding tantalum (Ta) instead of niobium (Nb) with 0.1 doping step from x=0 to x=1 at different concentrations. The effects of Ta addition on the electronic structure of $LiNbO_3$ were investigated. The results indicate that Ta doping results in an increase in the forbidden band gap of $LiNbO_3$. The real and imaginary parts of the dielectric function of $LiNb_{1-x}Ta_xO_3$ were calculated and the optical transitions between the bands were determined. The second-order elastic constants of Ta doped $LiNbO_3$ were calculated and the mechanical stability of the material was determined. In addition, the calculated elastic constants were used to determine the bulk modulus (B), shear modulus (G), Young's modulus (E), H_{macro} and H_{micro} hardness values. It was determined that the $LiNb_{1-x}Ta_xO_3$ material exhibited a transition from a ductile to a more brittle state with the addition of Ta.

Keywords: $LiNbO_3$, $LiTaO_3$, Electronic properties, Optical properties, Elastic properties.

a acarfurkahan@gmail.com   https://orcid.org/0000-0002-4750-5036   b ssimsek@hakkari.edu.tr   https://orcid.org/0000-0002-7260-6437

Introduction

$LiNbO_3$ (Lithium niobate), a member of the ABO_3-type ferroelectric perovskite family, is one of the most technologically important materials for optoelectronics. Its versatility stems from its considerable piezoelectric coefficient and distinctive electro-optical, acoustic-optical, nonlinear optical, photorefractive and photoconductive characteristics. It is employed in a multitude of applications, including waveguides, solid-state lasers, photorefractive devices and other optoelectronic devices. The LN (Lithium Niobate) crystal has been designated as "Optical Silicon"[1]. The properties of LN crystals can be modified or controlled by the introduction of specific dopants. As an example, the photorefractive (PR) properties of LN crystals can be significantly suppressed when doped with optically damage-resistant (ODR) ions, such as Sc^{3+}, In^{3+}, Zn^{2+}, and Mg^{2+}, at relatively high concentrations. This allows the frequency to double [2]. Furthermore, doping LN with transition metal ions, including Cu, Fe, Mn, and Ce, can result in the formation of crystals with notable photorefractive properties, rendering them as prospective materials for holographic memory applications [3, 4]. It is known that perovskite oxides, characterized by the general formula ABO_3, display a diverse array of physical properties, including superconductivity, substantial magnetoresistance, ferroelectric polarization, and high dielectric constant. As a result, it constitutes one of the most crucial categories of materials for technological applications. LN exhibits a paraelectric phase with a trigonal crystal structure, with the R-3c space group, at high temperatures. When

subjected to low temperatures, the material undergoes a transformation into a ferroelectric phase characterized by R3c symmetry. A slight deformation of the paraelectric phase is observed in what is known as the ferroelectric phase. In the trigonal ferroelectric phase at room temperature, LN is assigned to the 3m point group [5]. It exhibits spontaneous polarization along the [111] crystal direction in the ferroelectric phase, rendering it an appropriate material for use in optoelectronic devices [6, 7].

To the best of our knowledge, there is no study on the effect of Ta doping on the structural, electronic, optical and mechanical properties of $LiNbO_3$ using the virtual crystal approximation (VCA) [8]. The aim of this study is to investigate the effect of Ta doping on the physical properties of LiNbO3 using VCA based on density functional methods (DFT) [9]. For this purpose, the effects of Ta doping on the crystal structure, forbidden band gaps, optical properties such as reflection, refraction, absorption and energy loss function, elastic constants and elastic modulus (such as bulk, shear and Young's modulus) of $LiNbO_3$ with 0.1 doping step from x=0 to x=1 will be investigated.

Materials and Methods

The electronic, optical and elastic properties of Ta-doped $LiNbO_3$ were calculated by means of density functional methods under the generalized gradient approximation (GGA) [9]. The calculations were performed using optimized norm-preserving Vanderbilt

pseudopotentials [10]. The kinetic energy cut-off required for electronic wave functions was determined to be 44 Hartree. In the calculations, the valence electrons of the Li atom were taken to be $1s^2\ 2s^1$, those of the Nb atom $4s^2 4p^6 4d^4 5s^1$, those of the Ta atom $5s^2 5p^6 5d^3 6s^2$, and those of the O atom $2s^2 2p^4$. In order to calculate the electronic and optical properties at specific k points within the Brillouin zone, the 8x8x8 and 16x16x16 Monkhorst-Pack [11] meshes were employed, respectively. In this study, all results were obtained using the VCA. The structural, electronic, optical, and elastic properties of $LiNb_{1-x}Ta_xO_3$ were investigated by ab initio method, wherein Ta was added in place of Nb with a 0.1 doping step from x=0 to x=1 at varying concentrations. All calculations were conducted using the ABINIT software program [12].

Results and Discussion

Structural Properties

LiNbO$_3$ exists in the ferroelectric phase at room temperature, exhibiting a rhombohedral structure (with space group R3c (#161)). Figure 1(a) illustrates the rhombohedral unit cell of the LiNbO$_3$ crystal in its ferroelectric phase. The LiNbO$_3$ unit cell contains two molecules with ten atoms in the rhombohedral structure.

The equilibrium lattice parameter of the LiNbO$_3$ crystal was calculated by minimizing the ratio of the total energy of the crystal to its volume. The resulting lattice parameters are presented in Table 1. The obtained values were compared with the theoretical and experimental lattice parameters that have been previously reported in the literature. As illustrated in Table 1, the lattice constant and the angle between the axes determined in this study using the GGA are slightly bigger than those reported in the literature.

Table 1. The relaxed lattice parameters and angles of LiNbO$_3$ in rhombohedral structure.

Method	$a = b = c$ (Å)	$\alpha = \beta = \gamma$
GGA$^{(Cal.)}$	5.540	58.9
Exp.[13]	5.494	55.8
Exp.[14]	5.496	55.8
GGA[15]	5.509	55.8
GGA[16]	5.495	55.8
LDA[17]	5.488	54.8

Figure 1(b) depicts the variation of lattice parameters for $LiNb_{1-x}Ta_xO_3$ as a function of Ta doping. As illustrated in Figure 1(b), it is clear that the lattice parameters of LiNbO$_3$ exhibit a decrease with Ta doping.

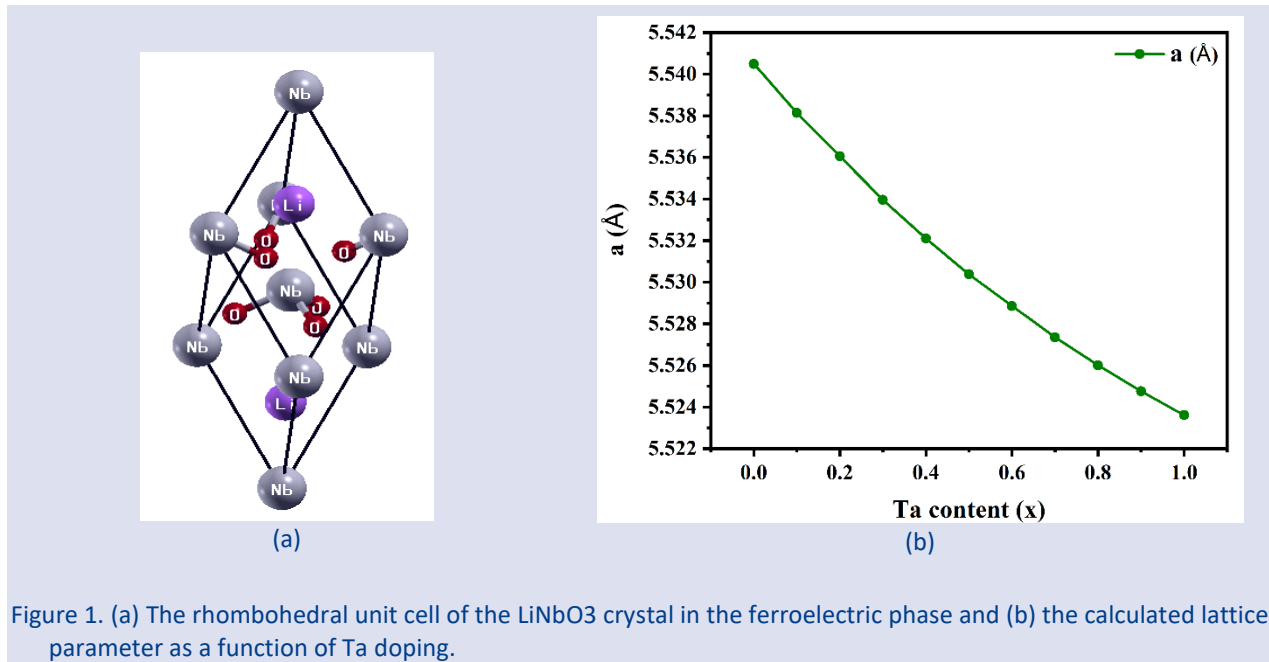(a) (b)

Figure 1. (a) The rhombohedral unit cell of the LiNbO3 crystal in the ferroelectric phase and (b) the calculated lattice parameter as a function of Ta doping.

Electronic Properties

An understanding of the electronic band structure is crucial for the determination of the electrical properties of materials, including their conductive, semiconductive, and insulating characteristics. This knowledge is also essential for technological applications. The electronic band structure and density of state (DOS) plots of $LiNb_{1-x}Ta_xO_3$ for x=0.0 and x=0.5 are presented in Figure 2(a) and (b), respectively. The Fermi energy level is designated as

the zero energy level and is indicated by the red dashed lines. As illustrated in Figure 2(a), the maximum point of the valence band and the minimum point of the conduction band for the LiNbO$_3$ crystal are situated at the Γ point. Consequently, the results of our calculations indicate that the LiNbO$_3$ crystal is a direct bandgap material. In this study, the calculated forbidden energy gap value for LiNbO$_3$ crystal is 3.38 eV. The results obtained in this study and the existing theoretical and

experimental results in the literature are given in Table 2. As illustrated in Table 2, the results obtained are in agreement with the theoretical results available in the literature, but slightly lower than the experimental result obtained by optical measurements. It is known that the forbidden band gaps calculated by DFT are lower than the experimental results obtained by optical measurements because they do not include both quasi-particle effects and excitonic effects [15].
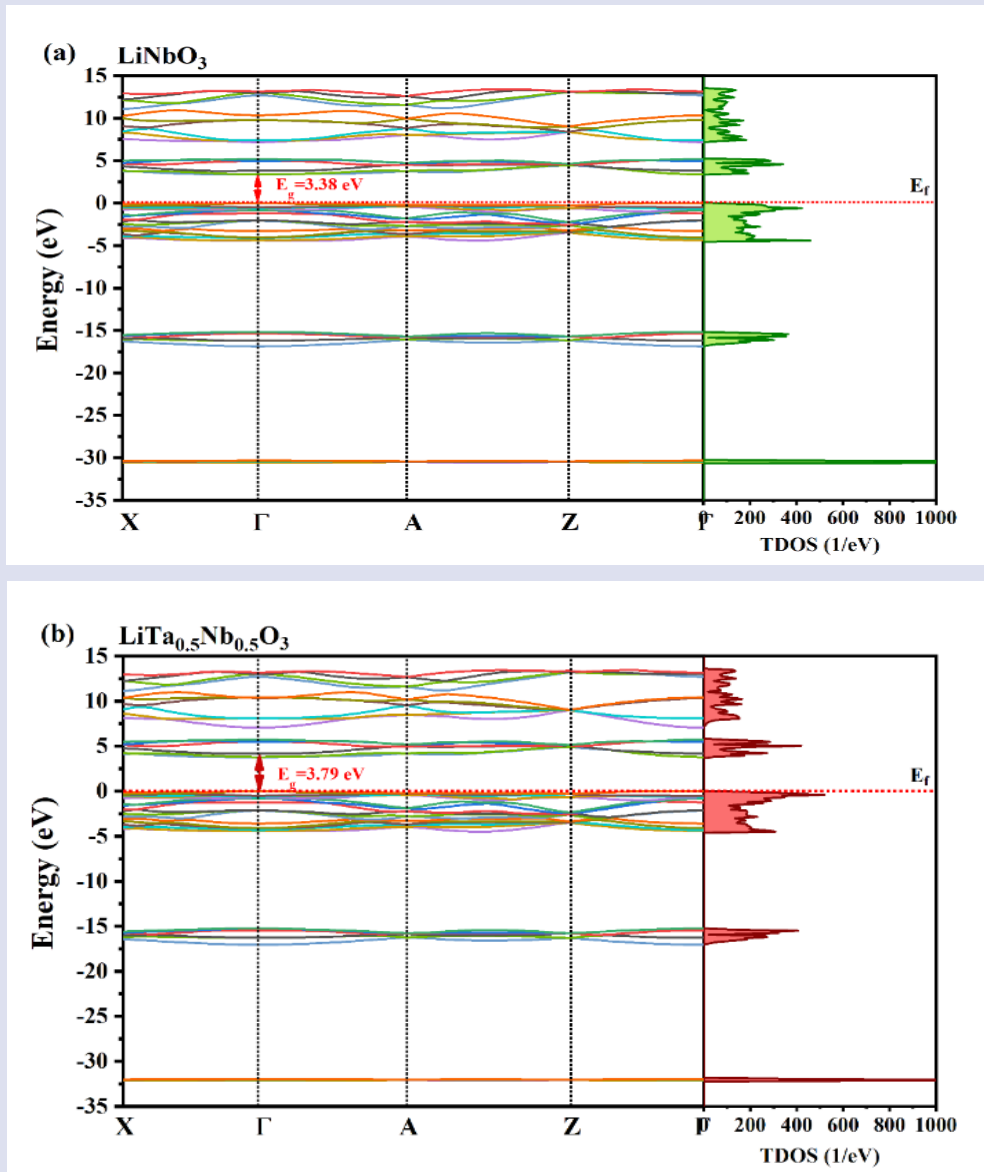

Figure 2. The band structure of LiNb$_{1-x}$Ta$_x$O$_3$ for (a) x= 0.0 and (b) x=0.5.

Table 2. Theoretical and experimental band gaps of LiNbO$_3$ and LiTaO$_3$.

Crystal	E$_{g.}$ LDA (eV)	E$_{g.}$ GGA (eV)	E$_{g.}$ Exp. (eV)
LiNbO$_3$	3.40[5]	3.38[Cal.]	3.78[18]
	2.84[19]	3.48[15]	
	3.59[20]	3.61[21]	
	3.35[22]	3.041[19]	
	3.54[17]	3.32[16]	
LiTaO$_3$		4.15[Cal.]	4.70[23]
		3.93[24]	

In order to better understand the nature of the electronic band structure of the LiNbO$_3$ crystal, the partial (PDOS) and total density of states (TDOS) were calculated. As seen in Figure 3(a), the bands between -30 and -32 eV appear to originate from Nb-4p orbitals. The bands between -15 and -17.5 eV are formed by O-2s orbitals. The bands just below the Fermi energy level (between 0 and -5 eV) are mostly composed of a mixture of O-2p and Nb-4d orbitals. This suggests a partial covalent bond between Nb and O atoms. The conduction bands above the Fermi energy level are mostly composed of Nb-4p orbitals and Li-2s orbitals.
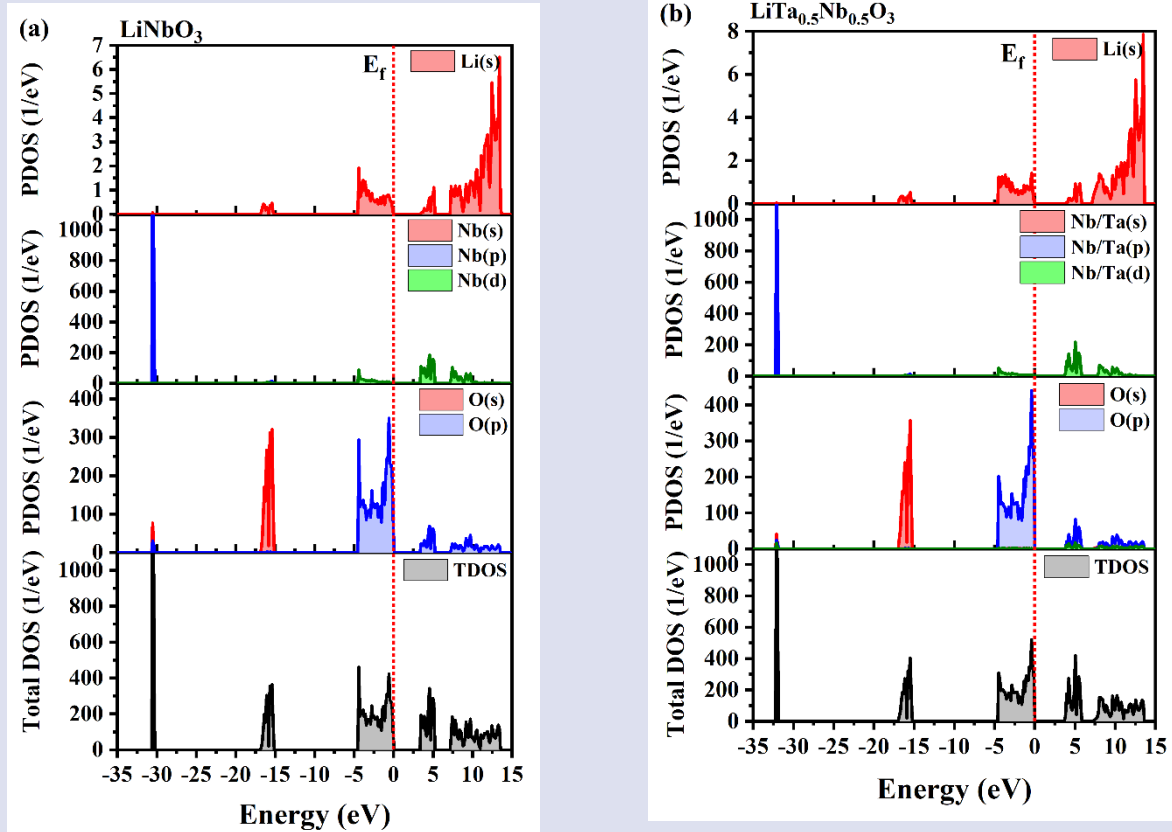
Figure 3. The partial (PDOS) and total density of states (TDOS) of $LiNb_{1-x}Ta_xO_3$ for (a) x= 0.0 and (b) x=0.5.

The electronic band structure and DOS were calculated for $LiNb_{1-x}Ta_xO_3$ by doping Ta at a rate of 0.1 from x=0.0 to x=1.0. However, the electronic band structure plots of $LiNb_{1-x}Ta_xO_3$ calculated for x=0 and x=0.5 are presented in Figure 2(a) and (b). As illustrated in Figure 2(a) and (b), the electronic band structure plots obtained by doping at x=0 and x=0.5 exhibit notable similarities. The band gap of $LiNb_{1-x}Ta_xO_3$ with 50% Ta doping was determined to be 3.79 eV. On the other hand, a closer examination of the DOS plots reveals that the Nb/Ta-4p orbitals exhibit a shift towards lower energies when Ta is introduced in place of Nb. The variation of the forbidden band gap for $LiNb_{1-x}Ta_xO_3$ from x=0.0 to x=1.0 with 0.1 Ta doping is given in Figure 4. As illustrated in Figure 4, the band gap of $LiNb_{1-x}Ta_xO_3$ exhibits an increase with Ta doping.

Optical Properties

Due to the symmetry of the $LiNbO_3$ crystal, the dielectric tensor has components only in the x- and z-directions. The real ($\varepsilon_1(\omega)$) and imaginary parts ($\varepsilon_2(\omega)$) of the calculated frequency-dependent complex dielectric function in the x- and z-axes for $LiNbO_3$ in the rhombohedral structure are given in Figures 5(a) and (b), respectively. The $\varepsilon_1(\omega)$ is related to the electronic polarizations of the materials. The $\varepsilon_2(\omega)$ determines the transition probability of electrons from occupied to unoccupied energy levels and is therefore related to optical absorption. The value of the $\varepsilon_1(\omega)$ in the zero frequency limit ($\varepsilon_1(0)$) is known as the static dielectric

constant. As illustrated in Figure 5 (a) and (b), the values of the static dielectric constant were found to be 5.71 and 5.29 for the x- and z-directions, respectively. Aliabad [16] and et al. found 5.91 and 5.63 for x- and z-directions with GGA, respectively. Mamoun et al. [25] found 5.42 and 5.27 for x- and z-directions with GGA, respectively. It can be observed that the values obtained for the static dielectric constant are aligned with those reported in the existing literature.
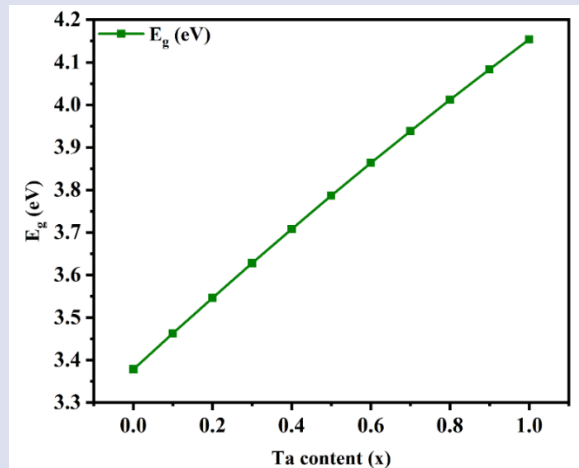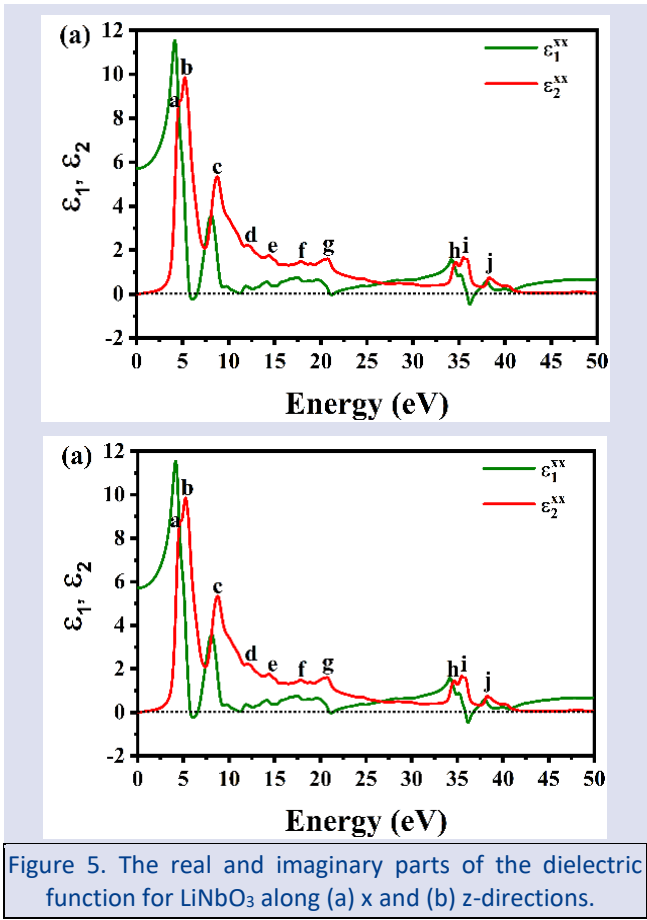

Figure 4. The calculated band gap as a function of Ta doping for $LiNb_{1-x}Ta_xO_3$

Figure 5. The real and imaginary parts of the dielectric function for LiNbO₃ along (a) x and (b) z-directions.

$\varepsilon_1(\omega)$ has negative values in the energy ranges of 5.42-6.09, 20.68-20.91 and 35.48-36.33 eV in the x-direction. The negative ranges of $\varepsilon_1(\omega)$ in the z-direction are in the energy ranges of 9.80-10.30, 20.53-21.62 and 35.41-36.44 eV, respectively. In these energy ranges where $\varepsilon_1(\omega)$ has negative values, the material shows metallic properties. As illustrated in Figure 5 (a) and (b), the first critical points of the $\varepsilon_2(\omega)$ occur around 2.4 eV in both x- and z-direction. These points correspond to the points where the valence band separates from the conduction band and are known as the fundamental absorption edge. After this point, the curves show a rapid increase as the number of points contributing to the $\varepsilon_2(\omega)$ increases abruptly. The $\varepsilon_2(\omega)$ exhibits a pronounced absorption peak at an energy value of 4.6 eV in both the x-direction and z-direction. These energy values correspond to optical transitions from O-2p states to Nb-4d states at Γ. The energy values corresponding to the other maximum peaks of $\varepsilon_2(\omega)$ are given in Table 3 together with the existing theoretical and experimental results. These values correspond to interband transitions at different higher symmetry points. Furthermore, as can be seen from Table 3, the results obtained are consistent with the findings of both theoretical and experimental studies reported in the existing literature.

Table 3. The energy values corresponding to the maximum peaks of $\varepsilon_2(\omega)$ for LiNbO₃ crystal.

ε_2		a	b	c	d	e	f	g	h	i	j
x	GGA(Cal.)	4.6	5.2	8.7	11.9	14.3	17.8	20.8	34.6	35.5	38.3
	GGA[16]	4.2	4.98	8.75							
	GGA[25]	4.39	5.02	8.61							
	LDA[5]	4.97	5.21	8.87							
z	GGA(Cal.)	4.6	5.4	8.6	11.6	14.2	17.1	20.8	34.5	35.4	38.2
	GGA[16]	4.2	5.03	8.75							
	GGA[25]	4.37	5.24	8.67							
	LDA[5]	4.98	5.21	8.84							
	Exp.[26]	4.38	5.07	8.14	12.85	14.6	18.23	20.5			

The plots of the real parts of the dielectric function for LiNb₁₋ₓTaₓO₃ by increasing the Ta doping by 0.1 from x=0 to x=1 are given in Figures 6(a) and (b) for x- and z-directions, respectively. As can be seen from Figures 6(a) and (b), both the energy values corresponding to the maximum peaks of the $\varepsilon_1(\omega)$ and the negative energy values shift to higher energies with Ta doping. In contrast, the variation of the $\varepsilon_2(\omega)$ for LiNb₁₋ₓTaₓO₃ with Ta doping is given in Figures 6(c) and (d). Since Nb and Ta atoms have similar electronic configuration, there is not much difference in the variation of the $\varepsilon_2(\omega)$ for LiNb₁₋ₓTaₓO₃ with Ta doping. Only with Ta doping, the absorption edges and the maximum peaks shift to higher energies. This suggests that the BO₆ octahedron plays a significant role in establishing the upper edge of the valence band and the edge of the conduction band in ABO₃-type perovskite structures. The results obtained are consistent with those presented in Figure 4.
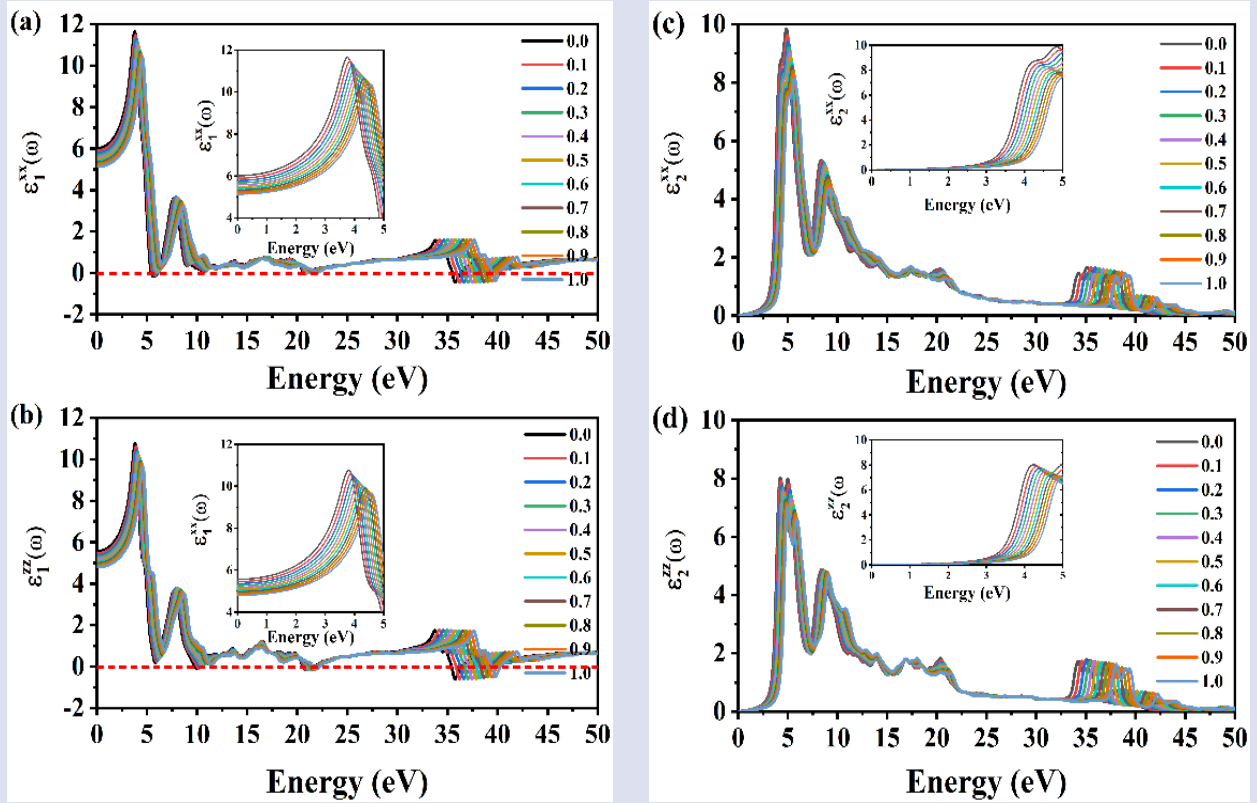
Figure 6. The real and imaginary parts of the dielectric function as a function of Ta doping for LiNb$_{1-x}$Ta$_x$O$_3$.

Mechanical Properties

One of the most essential properties of solids is their elastic constants. An understanding of the elastic constants of solids establishes a connection between the mechanical and dynamic behavior of crystals, and provides valuable insight into the nature of the forces that act within solids. The propagation of an elastic wave in a medium is closely related to the elastic constants of that material. Furthermore, elastic constants are associated with thermodynamic properties, including Debye temperature, coefficient of thermal expansion, melting point, and specific heat. The elastic constants provide insight into the response of a solid material to externally applied forces. The mechanical properties of solids can be ascertained through the utilization of elastic constants. In particular, they provide information regarding the physical properties of materials, including mechanical stability, stiffness, ductility, and brittleness. The elastic moduli, including the bulk modulus (B), shear modulus (G), Young's modulus (E), and Poisson's ratio (v), are derived from single-crystal elastic constants [17]. Due to the symmetry of the LiNbO$_3$ crystal, it has eight components $C_{11}, C_{12}, C_{13}, C_{14}, C_{33}, C_{44}, C_{65}$ and C_{66} in the rhombohedral structure. Since $C_{65} = C_{14}$ and $C_{66} = 1/2 (C_{11} - C_{12})$, the number of independent components is six. For a mechanically stable rhombohedral structure, it is necessary that the elastic constants provide the Born stability criteria, which are as follows [27]:

$$(C_{11} - C_{12}) > 0, \quad (C_{11} + C_{12}) > 0, \quad C_{33} > 0,$$

$$C_{44} > 0 \quad (C_{11} + C_{12})C_{33} - 2C_{13}^2 > 0, \quad (1)$$

$$(C_{11} + C_{12})C_{33} - 2C_{13}^2 > 0, \quad (C_{11} - C_{12})C_{44} - 2C_{14}^2 > 0$$

The calculated elastic constants for the LiNbO$_3$ crystal are presented in Table 4. As shown in Table 4, the calculated elastic constants for the LiNbO$_3$ crystal fulfill the Born stability criteria required for the rhombohedral structure. The elastic constants C_{11} and C_{33} indicate the resistance to linear compression along the x- and z- axes of the crystal, while the elastic constants $C_{12}, C_{13}, C_{14}, C_{44}$ and C_{66} are related to the elasticity in the shape of the crystal. Since $C_{33} > C_{11}$, the z-direction demonstrates more resistance to unidirectional deformation than the x-direction. It is also seen from Table 4 that the calculated results for LiNbO$_3$ crystal are close to the theoretical and experimental results available in the literature.

Table 4. The elastic constants (GPa) of LiNbO3 in the rhombohedral structure.

Ref.	C_{11}	C_{12}	C_{13}	C_{14}	C_{33}	C_{44}	C_{66}
GGA[(Cal.)]	184.5	58.9	60.5	17.5	220.1	39.7	62.7
Exp.[28]	198.39	54.72	65.13	7.88	227.9	59.65	
Exp.[29]	198.86	54.67	67.99	7.83	234.18	59.85	72.09
Exp.[30]	198.86	54.67	67.26	7.83	233.7	59.85	
Exp.[31]	198.9	54.7	67.3	7.8	233.7	70.4	72.1
Exp.[32] (Smp-1)	199.2	54.7	70	7.9	240	59.9	72.2
Exp.[32] (Smp-2)	198.6	54.7	69	7.8	238	59.8	71.9
Exp.[32] (Smp-3)	199.9	55.6	70	7.8	240	60	72.2
GGA[33]	208.77	73.28	75.99	15.68	236.23	49.80	67.74
LDA[17]	205.69	69.28	72.15	12.38	238.34	65.81	70.03

The variation of the second-order elastic constants for LiNb$_{1-x}$Ta$_x$O$_3$ with Ta doping is given in Figure 7(a). As can be seen from Figure 7(a), the elastic constants C_{11} and C_{33} increase linearly with Ta doping. The doping of Ta makes the LiNbO$_3$ compound more resistant to unidirectional compression along the main crystallographic axes. In contrast, as can be seen from Figure 7(a), C_{66} increases slightly with the doping of Ta, but C_{13} does not change very much with the doping of Ta. On the other hand, the C_{12} and C_{14} values of the LiNb$_{1-x}$Ta$_x$O$_3$ decrease with the doping of Ta. This means that LiNb$_{1-x}$Ta$_x$O$_3$ becomes less resistant to lateral deformation. As illustrated in Figure 7(a), the elastic constant C_{44} shows the most different response to Ta doping. The C_{44} shows a rapid increase up to 50% Ta doping and does not change much after 50% Ta doping.
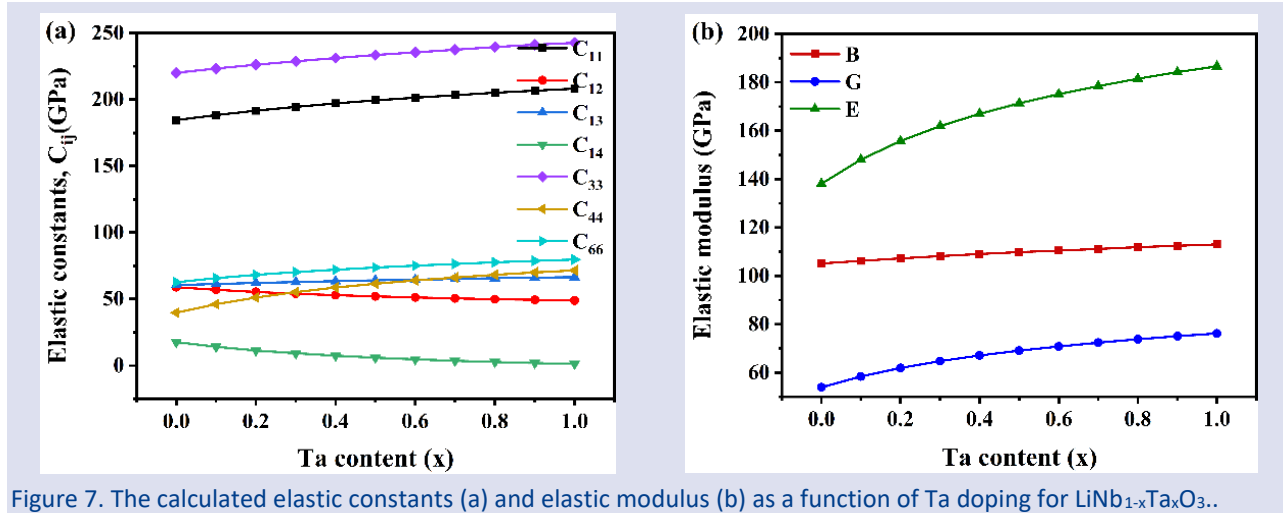
Figure 7. The calculated elastic constants (a) and elastic modulus (b) as a function of Ta doping for LiNb$_{1-x}$Ta$_x$O$_3$.

The mechanical properties of polycrystalline materials can be determined from the single crystal elastic constants using two basic methods, known as the Voigt [34] and Reuss [35] method. In the Voigt method (B$_V$ and G$_V$) and the Reuss method (B$_R$ and G$_R$), the bulk and shear moduli are given by the following equations:

$$B_V = \frac{1}{9}[2(C_{11} + C_{12} + 2C_{13}) + C_{33}] \quad (2)$$

$$G_V = \frac{1}{30}[C_{11} + C_{12} + 2(C_{33} - 2C_{13}) + 12(C_{44} + C_{66})] \quad (3)$$

$$B_R = \frac{(C_{11} + C_{12})C_{33} - 2C_{13}^2}{C_{11} + C_{12} + 2C_{33} - 4C_{13}} \quad (4)$$

$$G_R = \frac{2}{5}\frac{[(C_{11} + C_{12})C_{33} - 2C_{13}^2]C_{44}C_{66}}{3B_V C_{44}C_{66} + [(C_{11} + C_{12})C_{33} - 2C_{13}^2](C_{44} + C_{66})} \quad (5)$$

Using Voigt-Reuss-Hill approximations [36], the bulk and shear moduli are given as follows:

$$B = \frac{1}{2}(B_V + B_R) \quad (6)$$

$$B = \frac{1}{2}(G_V + G_R) \quad (7)$$

E and ν are elastic parameters that are often used to investigate the stiffness of solids, which can be calculated using B and G with the following equations [17].

$$E = \frac{9BG}{3B + G} \quad (8)$$

$$\nu = \frac{3B - 2G}{2(3B + G)} \quad (9)$$

The values of B, G, E and υ of LiNbO₃ calculated in the rhombohedral structure are given in Table 5. As shown in Table 5, the values of B and G found in this study are close to the values found by Tripathy et al. [33]. However, the

values of B and G found by Hossain [17] are larger than our values.

Table 5. The bulk modulus B (GPa), shear modulus G (GPa), Young's modulus E (GPa) and Poisson's ratio (υ) of LiNbO₃ in the rhombohedral structure.

Referans	B_V	B_R	B	G_V	G_R	G	E	B/G	υ
GGA[(Cal.)]	105.4	104.7	105.1	55.7	52.1	53.9	138.1	1.95	0.281
LDA[17]			272.80			138.77	355.95	1.97	0.28
GGA[33]			122.25			62.03			

The variation of B, G and E values calculated for LiNb₁₋ₓTaₓO₃ with Ta doping is given in Figure 7(b). As can be seen from Figure 7(b), B increases linearly with Ta doping. This shows that LiNb₁₋ₓTaₓO₃ is more resistant to compression under hydrostatic pressure with Ta doping. On the other hand, as can be seen from Figure 7(b), the

values of G, which expresses the resistance to plastic deformation, and E, which defines a measure of the hardness of the material, exhibit a more pronounced increase with Ta doping.

Table 6. The bulk modulus (B_V and B_R), shear modulus (G_V and G_R), Poisson's ratio (υ) and B/G ratio as a function of Ta doping for LiNb₁₋ₓTaₓO₃.

Content (x)	B_V	B_R	G_V	G_R	υ	B/G
0.0	105.4	104.7	55.7	52.1	0.281	1.950
0.1	106.5	105.8	59.6	57.2	0.267	1.817
0.2	107.6	106.8	62.8	61.1	0.258	1.731
0.3	108.6	107.6	65.4	64.1	0.250	1.670
0.4	109.5	108.5	67.6	66.6	0.245	1.625
0.5	110.3	109.3	69.5	68.7	0.240	1.589
0.6	111.0	109.9	71.1	70.5	0.236	1.560
0.7	111.7	110.6	72.7	72.1	0.232	1.536
0.8	112.5	111.3	74.0	73.6	0.230	1.516
0.9	113.1	111.9	75.3	74.9	0.227	1.498
1.0	113.7	112.4	76.4	76.0	0.225	1.484

The Poisson's ratio υ provides valuable insight into the nature of interatomic bonds in solids. The value of Poisson's ratio for covalent materials is υ~0.1, for ionic materials υ=0.25 and for metallic materials υ=0.33 [37]. Table 6 shows the value of υ with Ta doping. As shown in Table 6, the ionic contribution is dominant in the interatomic bond for LiNb₁₋ₓTaₓO₃.

As Pugh [38] has previously established, the B/G ratio can be employed to ascertain whether a given material exhibits brittle (B/G < 1.75) or ductile (B/G > 1.75) behavior. As can be seen from Table 6, LiNb₁₋ₓTaₓO₃ exhibits a transition from a ductile to a more brittle state with increasing Ta doping.

The macro (H_{mac}) and micro (H_{mic}) hardness of materials can be determined by a theoretical model, as described in [39],

$$H_{micro} = \frac{(1-2v)Y}{6(1+v)} \qquad (11)$$

The obtained H_{mac} and H_{mic} hardness values of LiNbO₃ are 6.43 GPa and 7.87 GPa, respectively. According to the definition, a material is considered soft if its Vickers hardness is less than 10 GPa [40], while a material is classified as super hard if its Vickers hardness is greater than 40 GPa [37]. According to our calculation, the LiNbO₃ can be classified as a soft material due to its Vickers hardness values lower than 10 GPa. As seen from Figure 8, the H_{mac} and H_{mic} hardness values of LiNb₁₋ₓTaₓO₃ increase with Ta doping, and it can be classified as a medium hard material after approximately 40% Ta doping.
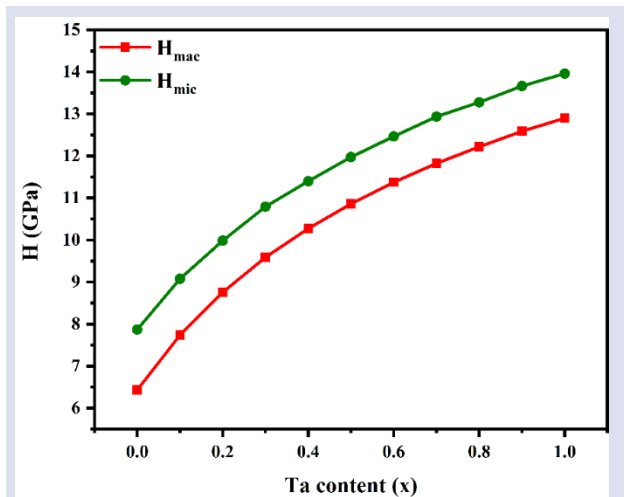
$$H_{macro} = 2\left(\frac{G^3}{B^2}\right)^{0.585} - 3 \qquad (10)$$

Figure 8. The calculated macro (H_{mac}) and micro (H_{mic}) hardnes of LiNb$_{1-x}$Ta$_x$O$_3$ as a function of Ta doping.

Conclusion

In conclusion, the structural, electronic, optical and mechanical properties of pure and Ta doped LiNbO$_3$ in the ferroelectric phase have been obtained by using the DFT with the GGA. It was demonstrated that pure LiNbO$_3$ is a direct bandgap material, exhibiting a forbidden energy gap of 3.38 eV at the Γ point in the Brillouin zone. The calculation results indicated that the lattice parameter of LiNb$_{1-x}$Ta$_x$O$_3$ decreases with Ta doping, but the forbidden energy gap increases. The frequency-dependent complex dielectric functions of pure and Ta doped LiNbO$_3$ are calculated. Both the energy values corresponding to the maximum peaks of the real parts of the dielectric function and the negative energy values shift to higher energies with Ta doping. The results show that the absorption edges of LiNb$_{1-x}$Ta$_x$O$_3$ shift to higher energies with Ta doping. The calculated elastic constants indicated that pure and Ta doped LiNbO$_3$ are mechanically stable. Through the calculated υ and B/G values, it is concluded that the rhombohedral structure of LiNbO$_3$ is ionic and ductile, but with increasing Ta doping, it exhibits a transition from ductile to a more brittle state. Finally, from the calculated H_{mac} and H_{mic} hardness values, it was determined that pure LiNbO$_3$ is a soft material, but after 40% Ta doping, it exhibits a transition to a medium hard material.

Conflict of interest

There are no conflicts of interest in this work.

Acknowledgment

References

[1] Bridges F., Castillo-Torres J., Car B., Medling S., Kozina M., EXAFS evidence for a primary Zn Li dopant in LiNbO$_3$, *Physical Review B—Condensed Matter and Materials Physics*, 85 (2012) 064107-064118.

[2] He Y.L., Xue D.F., Bond-energy study of photorefractive properties of doped lithium niobate crystals, *J Phys Chem C*, 111 (2007) 13238-13243.

[3] Tsuboi T., Grinberg M., Kaczmarek S.M., Site symmetries of Cu^{2+} ions in LiNbO3 crystals, *J Alloy Compd*, 341 (2002) 333-337.

[4] Wang W., Wang R., Zhang W., Xing L.L., Xu Y.L., Wu X.H., A computer study and photoelectric property analysis of potassium-doped lithium niobate single crystals, *Phys Chem Chem Phys*, 15 (2013) 14347-14356.

[5] Cabuk S., First-Principles Study of The Electronic, Linear, and Nonlinear Optical Properties of Li(Nb, Ta)O$_3$, *Int J Mod Phys B*, 24 (2010) 6277-6290.

[6] Ok K.M., Chi E.O., Halasyamani P.S., Bulk characterization methods for non-centrosymmetric materials: second-harmonic generation, piezoelectricity, pyroelectricity, and ferroelectricity, *Chem Soc Rev*, 35 (2006) 710-717.

[7] Xu Y.H., Hao X.F., Franchini C., Gao F.M., Structural, Electronic, and Ferroelectric Properties of Compressed CdPbO$_3$ Polymorphs, *Inorg Chem*, 52 (2013) 1032-1039.

[8] Yu C.J., Emmerich H., An efficient virtual crystal approximation that can be used to treat heterovalent atoms, applied to (1–x)BiScO$_3$–xPbTiO$_3$, *J Phys-Condens Mat*, 19 (2007).

[9] Perdew J.P., Burke K., Ernzerhof M., Generalized gradient approximation made simple, *Phys Rev Lett*, 77 (1996) 3865-3868.

[10] Hamann D.R., Optimized norm-conserving Vanderbilt pseudopotentials, *Phys Rev B*, 88 (2013).

[11] Monkhorst H.J., Pack J.D., Special points for Brillouin-zone integrations, *Phys Rev B*, 13 (1976) 5188.

[12] Gonze X., Amadon B., Antonius G., Arnardi F., Baguet L., Beuken J.M., Bieder J., Bottin F., Bouchet J., Bousquet E., Brouwer N., Bruneval F., Brunin G., Cavignac T., Charraud J.B., Chen W., Côté M., Cottenier S., Denier J., Geneste G., Ghosez P., Giantomassi M., Gillet Y., Gingras O., Hamann D.R., Hautier G., He X., Helbig N., Holzwarth N., Jia Y.C., Jollet F., Lafargue-Dit-Hauret W., Lejaeghere K., Marques M.A.L., Martin A., Martins C., Miranda H.P.C., Naccarato F., Persson K., Petretto G., Planes V., Pouillon Y., Prokhorenko S., Ricci F., Rignanese G.M., Romero A.H., Schmitt M.M., Torrent M., van Setten M.J., Van Troeye B., Verstraete M.J., Zerah G., Zwanziger J.W., The ABINIT project: Impact, environment and recent developments, *Comput Phys Commun*, 248 (2020) 107042.

[13] Megaw H.D., A note on the structure of lithium niobate, LiNbO$_3$, *Acta Crystallographica Section A: Crystal Physics, Diffraction, Theoretical and General Crystallography*, 24 (1968) 583-588.

[14] Bermúdez V., Aragó C., Fernández-Ruiz R., Diéguez E., Evolution of the Structural Properties in Ferroelectric LiNb$_{1−x}$Ta$_x$O$_3$ Compound with Variation in Ta Composition, *Ferroelectrics*, 304 (2004) 989-992.

[15] Schmidt W.G., Albrecht M., Wippermann S., Blankenburg S., Rauls E., Fuchs F., Rödl C., Furthmüller J., Hermann A., LiNbO$_3$ ground- and excited-state properties from first-principles calculations, *Phys Rev B*, 77 (2008).

[16] Aliabad H.A.R., Ahmad I., Optoelectronic properties of Li$_x$A$_x$NbO$_3$ (A: Na, K, Rb, Cs, Fr) crystals, *Physica B*, 407 (2012) 368-377.

[17] Hossain M.M., First principles study on the structural, elastic, electronic and optical properties of LiNbO$_3$, *Heliyon*, 5 (2019).

[18] Dhar A., Mansingh A., Optical properties of reduced lithium niobate single crystals, *J Appl Phys*, 68 (1990) 5804-5809.

[19] Javid M.A., Khan Z.U., Mehmood Z., Nabi A., Hussain F., Imran M., Nadeem M., Anjum N., Structural, electronic and optical properties of LiNbO$_3$ using GGA-PBE and TB-mBJ functionals: A DFT study, *Int J Mod Phys B*, 32 (2018).

[20] Xu Y.-N., Gu Z.-Q., Ching W., Calculation of self-energy corrected band structure of rhombohedral LiNbO$_3$, *Ferroelectrics*, 164 (1995) 225-230.

[21] Thierfelder C., Sanna S., Schindlmayr A., Schmidt W.G., Do we know the band gap of lithium niobate?, *Phys Status Solidi C*, 7 (2010) 362-365.

[22] Nahm H.H., Park C.H., First-principles study of microscopic properties of the Nb antisite in LiNbO$_3$: Comparison to phenomenological polaron theory, *Phys Rev B*, 78 (2008).

[23] Kato H., Kudo A., Water splitting into H$_2$ and O$_2$ on alkali tantalate photocatalysts ATaO$_3$ (A= Li, Na, and K), *The Journal of Physical Chemistry B*, 105 (2001) 4285-4292.

[24] Wang H., Wu F., Jiang H., Electronic band structures of ATaO$_3$ (A= Li, Na, and K) from first-principles many-body perturbation theory, *The Journal of Physical Chemistry C*, 115 (2011) 16180-16186.

[25] Mamoun S., Merad A.E., Guilbert L., Energy band gap and optical properties of lithium niobate from ab initio calculations, *Comp Mater Sci*, 79 (2013) 125-131.

[26] Mamedov A.M., Osman M.A., Hajieva L.C., VUV Reflectivity of LiNbO$_3$ and LiTaO$_3$ Single Crystals, *Appl. Phys. A*, 34 (1984) 189-192.

[27] Wang J.J., Meng F.Y., Ma X.Q., Xu M.X., Chen L.Q., Lattice, elastic, polarization, and electrostrictive properties of BaTiO3 from first-principles, *J Appl Phys*, 108 (2010).

[28] Kovacs G., Anhorn M., Engan H.E., Visintini G., Ruppel C.C.W., Improved Material Constants for LiNbO$_3$ and LiTaO$_3$, *IEEE Ultrasonics Symposium*, 438 (1990) 1-4.

[29] Kushibiki J.I., Takanaga I., Arakawa M., Sannomiya T., Accurate Measurements of the Acoustical Physical Constants of LiNbO$_3$ and LiTaO$_3$ Single Crystals, IEEE Transactions on ultrasonics, ferroelectrics, and frequency control, 1999, 1315-1323

[30] Takanaga I., Kushibiki J.I., A Method of Determining Acoustical Physical Constants for Piezoelectric Materials by Line-Focus-Beam Acoustic Microscopy, IEEE Transactions on ultrasonics, ferroelectrics, and frequency control, 2002, 893-904

[31] Philip T., Menon C.S., Induleka K., Higher Order Elastic Constants, Gruneisen Parameters and Lattice Thermal Expansion of Lithium Niobate, *E-Journal of Chemistry*, 3 (2006) 122-133.

[32] Andrushchak A.S., Mytsyk B.G., Laba H.P., Yurkevych O.V., Solskii I.M., Kityk A.V., Sahraoui B., Complete sets of elastic constants and photoelastic coefficients of pure and MgO-doped lithium niobate crystals at room temperature, *J Appl Phys*, 106 (2009).

[33] Tripathy S.K., Sahu G., Ground state properties of LiNbO$_3$ from first-principles calculations, Advanced Materials and Radiation Physics (AMRP-2015): 4th National Conference on Advanced Materials and Radiation Physics, Longowal, India, 2015, 020005

[34] Voigt W., Lehrbuch der Kristallphysik Teubner Verlag, Leipzig1910.

[35] Reuss A., Berechung der Fliessgrenze von Mischkristallen, *Z. Angew. Math. Mech*, 9 (1929).

[36] Hill R., The elastic behaviour of a crystalline aggregate, *Proceedings of the Physical Society. Section A*, 65 (1952) 349.

[37] Haines J., Léger J.M., Bocquillon G., Synthesis and design of superhard materials, *Ann Rev Mater Res*, 31 (2001) 1-23.

[38] Pugh S., XCII. Relations between the elastic moduli and the plastic properties of polycrystalline pure metals, *The London, Edinburgh, and Dublin Philosophical Magazine and Journal of Science*, 45 (1954) 823-843.

[39] Ali M.A., Hossain M.M., Islam A.K.M.A., Naqib S.H., Ternary boride Hf$_3$PB$_4$: Insights into the physical properties of the hardest possible boride MAX phase, *J Alloy Compd*, 857 (2021) 158264.

[40] Liu W.N., Niu Y.T., Li W.Q., Theoretical prediction of the physical characteristic of Na$_3$MO$_4$ (M = Np and Pu): The first-principles calculations, *Ceram Int*, 46 (2020) 25359-25365.

Cumhuriyet Science Journal

Assessing the Impact of Patient Lung Volume Variations on Absorbed Lung Doses at Y-90 Therapy Using GATE Toolkit

Ayşe Karadeniz Yıldırım [1,a,*]

[1] Opticians Programme, Vocatinal of Health Services, İstanbul Aydın University, İstanbul, Türkiye.
*Corresponding author

Research Article

ABSTRACT

In Y-90 treatment, the dose values received by the target organ and tumour, as well as the dose values received by critical organs, have a significant impact on the treatment planning process and ultimately determine the amount of activity to be used in the treatment. To this end, 10 different phantoms containing lung volumes ranging from small to large for the same activity values in the liver have been designed to evaluate the risk of lung toxicity in Y-90 treatment. Utilizing the GATE toolkit, a 10 mm diameter tumour volume containing 10 mCi activity has been positioned within the liver geometry, and the absorbed dose values have been calculated in lung volumes ranging from 3,103E+06 to 4,727E+06 mm³ in the right lung and from 2,021E+06 to 3,080E+06 mm³ in the left lung. Absorbed dose values have been calculated as maximum 3,046E-07$\pm$1,607E-08 Gy/s, minimum 1,868E-07$\pm$1,177E-08 Gy/s in left lung, maximum 8,772E-08$\pm$6,905E-09 Gy/s, minimum 5,164E-08$\pm$4,963E-09 Gy/s in right lung and maximum 3,923E-07$\pm$1,14852E-08 Gy/s , minimum 2,384E-07$\pm$8,36556E-09 Gy/s in total lung. The results of this study may indicate that the absorbed dose value in the lung increases with an increase in lung volume. A comparison has been made with existing studies in the literature.

Keywords: Lung dose, Lung volume, GATE MC, Dosimetry.

[a] ✉ aysekaradeniz@aydin.edu.tr   https://orcid.org/0000-0001-9301-4775

Introduction

Yttrium-90 (Y-90) radioembolization, also known as selective internal radiation therapy (SIRT), has emerged as a leading treatment modality for liver-dominant cancers, such as hepatocellular carcinoma and metastatic colorectal cancer, particularly for patients who are not eligible for surgery or alternative forms of localized therapy [1-3]. Microspheres carrying the beta-emitting radioisotope Y-90 are inserted into the hepatic artery as part of this treatment (Fig.1). Once inside the tumor vasculature, the microspheres provide the cancer with targeted radiation. This targeted administration reduces the exposure of nearby healthy tissues while simultaneously improving the therapeutic efficacy within the liver. However, the nature of hepatic vasculature and the presence of potential arteriovenous shunts present a risk of microsphere migration to the lungs, resulting in unintended radiation exposure. This migration is quantified by the lung shunt fraction (LSF), which calculates the proportion of microspheres potentially reaching the pulmonary circulation [4,5]. Since too much radiation exposure to lung tissue can cause radiation pneumonitis or even pulmonary fibrosis, both of which have serious morbidities, it is imperative to estimate the absorbed dose to the lungs accurately.

The risk of radiation pneumonitis, a potentially serious side effect of excessive lung exposure, is strongly correlated with the lung dose absorbed, which is typically capped at 30 Gy for single-session exposures and 50 Gy for cumulative exposures in clinical guidelines [7,8] according to dosimetric studies in Y-90 radioembolization. However, individual anatomical variations, especially lung sizes,

which change radiation absorption and dose distribution throughout lung tissues, may not be adequately taken into account by these guidelines.
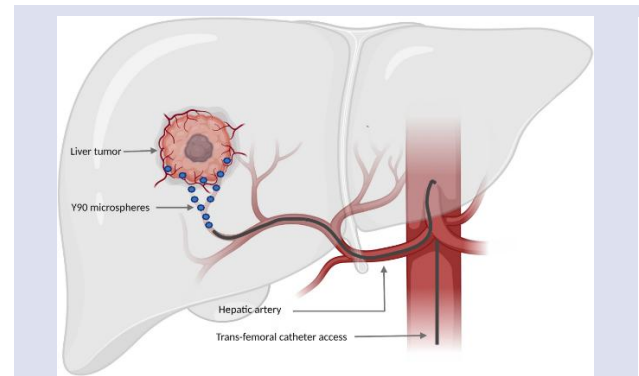
Figure 1. The visualization of Y-90 radioembolization [6].

Lung dosimetry in Y-90 treatment planning is guided by threshold limits that determine safe levels of absorbed dose [9] however, these limits may vary widely among individuals due to patient-specific anatomical differences, particularly lung volume. Variations in lung capacity affect how microspheres are distributed and retained, which changes the overall dose that is absorbed by the lung tissues [10]. For example, the absorbed dose per unit tissue may be lower in patients with higher lung capacities, which could minimize the risk of toxicity. Smaller lung capacities, on the other hand, might lead to a correspondingly higher absorbed dose, raising the risk of radiation-induced harm. However, existing dosimetry

models [11-13], which mainly concentrate on liver dosimetry without adequately accounting for patient-specific features in non-target organs like the lungs, frequently underrepresent these anatomical variances.

This study aims to address this gap by examining the impact of lung volume differences on the absorbed lung doses in patients undergoing Y-90 radioembolization. Our goal is to gain a better knowledge of how lung volumes can alter dose distribution through this study, which will help us improve risk assessment and individualized treatment planning for Y-90 therapy. Our objective is to improve clinical results by reducing the risk of lung toxicity

and guaranteeing safe yet efficient therapeutic radiation delivery to liver cancers by incorporating lung volume as a crucial component in dose modeling.

Material and Method

In this study, Y-90 radioembolization treatment, which is one of the radionuclide treatments applied in nuclear medicine clinics, was selected for internal dosimetry. It is established that the lung dose, liver parenchyma dose and tumour dose are determined by dosimetry [14]. Consequently, the geometry of these three tissues was incorporated into the study.
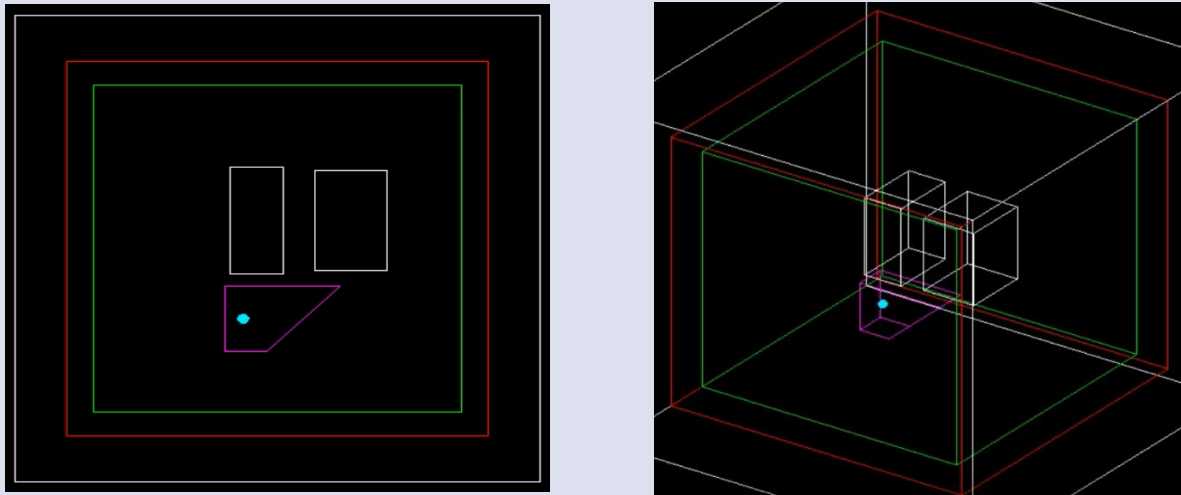

Figure 2. The visualization of virtual phantom geometry. In figures 2-a and 2-b, the lung is represented in white, the liver in magenta, and the tumor tissue in blue.

All Monte Carlo simulations were conducted on a computer with the macOS Monterey Version 12.6.3 operating system, a Core i5 2.7 GHz processor, 8 GB 1867 MHz DDR3 RAM and an Intel Iris 6100 graphics processor. The simulation process commenced with the generation of the phantom geometry in GATE version 8.1. The phantom geometry was designed to include the average volumes of the liver and lungs, and a spherical tumour with a radius of 10 mm was simulated in the liver. The geometry was created in a 700 mm³ cube filled with water. The dimensions of the liver are 220 mm, 140 mm and 80 mm in terms of length (x), height (y) and depth (z), respectively. The shapes of the left and right lungs were represented by rectangles with dimensions of (100 mm x

220 mm x 140 mm) and (137 mm x 230 mm x 150 mm), respectively. A visual representation of the geometry employed is presented in Figure 2.

The effects of lung volume differences on the absorbed lung doses in Y-90 radioembolization were quantitatively analyzed using simulations in the GATE toolkit. Patient-specific models with varying lung volumes were created. The dimensions of the right, left and total lung geometry [15] employed in the simulation are presented in Table 1. These include the width, length and depth in millimeters, as well as the volume in cubic millimeter and mass in kilograms.

Table 1. Size, volume and mass values of different lung volumes for which dose values were calculated in the simulation

	Left Lung				Right Lung				Total Lung	
	X[mm]	Y[mm]	Z[mm]	VL [mm3]	X[mm]	Y[mm]	Z[mm]	VR [mm3]	V [mm3]	m[kg]
1	80	261	135	3,080E+06	137	230	150	4,727E+06	7,807E+06	1,572
2	78	259	133	2,948E+06	135	228	147	4,525E+06	7,473E+06	1,500
3	76	257	131	2,820E+06	133	226	144	4,328E+06	7,148E+06	1,427
4	74	255	128	2,696E+06	131	224	141	4,138E+06	6,833E+06	1,351
5	72	253	126	2,575E+06	129	222	138	3,952E+06	6,527E+06	1,283
6	70	251	124	2,457E+06	127	220	135	3,772E+06	6,229E+06	1,260
7	68	249	122	2,343E+06	125	218	132	3,597E+06	5,940E+06	1,196
8	66	247	120	2,232E+06	123	216	129	3,427E+06	5,659E+06	1,134
9	64	245	118	2,125E+06	121	214	126	3,263E+06	5,388E+06	1,074
10	62	243	116	2,021E+06	119	212	123	3,103E+06	5,124E+06	1,016

The total lung volume used in the simulation was calculated to be between maximum 7,807E+06 m3 and minimum 5,124E+06 m3, between maximum 4,727E+06 m3 and minimum 3,103E+06 m3 for the right lung and between maximum 3,080E+06 m3 and minimum 2,021E+06 m3 for the left lung. Accordingly, lung mass values were calculated as a minimum of 1,016 kg and a maximum of 1,572 kg.

In the context of GATE simulations, the DoseActor is a sensitive detector with the capacity to store the energy present within its added volume and to interact with particle trace information. The DoseActor divides a given volume into three-dimensional voxels, which are then recorded with the associated event information. The volume-weighted algorithm employed by DoseActor entails the calculation of the actor's value by dividing the total energy stored within the defined volume by the total volume and density of the volume material. The dose distributions of all volumes were calculated in 1 mm sections along the y-axis using the C++ analysis code. The simulation was conducted independently for ten distinct lung volumes, as outlined in Table 1.

Finally, electromagnetic interactions (photoelectric event, compton scattering, anhillation etc.) and radioactive decay processes were chosen to create physical processes in simulation. Mersenne Twister algorithm was used as a random number generator. The simulation was executed for a period of one second, utilizing a quantity of 10 mCi of Y-90. All macros were run consecutively for about 1 week to get all the data. The results were obtained as dose, uncertainty in dose, difference (percentage) in TXT file.

Results and Discussion

In the simulation, 10 different phantoms were designed with lung volumes ranging from small to large for an activity value of 10 mCi in the liver to assess the risk of lung toxicity in Y-90 treatment. Dose values and uncertainties in dose values were calculated for right, left and total lung volumes.

Table 2. Absorbed dose values and uncertainties at varying lung volumes and liver as a result of GATE MC simulation

	Lung Left	Lung Right	Total Lung
	Dose Value ± Uncertainty (Gy/s)	Dose Value ± Uncertainty (Gy/s)	Dose Value ± Uncertainty (Gy/s)
1	3,046E-07±1,607E-08	8,772E-08±6,905E-09	3,923E-07±1,14852E-08
2	2,900E-07±1,549E-08	8,238E-08±6,577E-09	3,724E-07±1,10322E-08
3	2,754E-07±1,503E-08	7,773E-08±6,271E-09	3,532E-07±1,06494E-08
4	2,614E-07±1,454E-08	7,299E-08±6,034E-09	3,344E-07±1,02878E-08
5	2,487E-07±1,412E-08	6,983E-08±5,962E-09	3,185E-07±1,00402E-08
6	2,333E-07±1,347E-08	6,617E-08±5,866E-09	2,995E-07±9,66976E-09
7	2,219E-07±1,310E-08	6,223E-08±5,594E-09	2,842E-07±9,34678E-09
8	2,091E-07±1,267E-08	5,840E-08±5,314E-09	2,675E-07±8,99114E-09
9	1,970E-07±1,212E-08	5,473E-08±5,112E-09	2,517E-07±8,61414E-09
10	1,868E-07±1,177E-08	5,164E-08±4,963E-09	2,384E-07±8,36556E-09

The dose values calculated in left, right and total lung volumes are given in Table 2, respectively. Absorbed dose values were calculated as maximum 3,046E-07±1,607E-08 Gy/s, minimum 1,868E-07±1,177E-08 Gy/s in left lung, maximum 8,772E-08±6,905E-09 Gy/s, minimum 5,164E-08±4,963E-09 Gy/s in right lung and maximum 3,923E-07±1,14852E-08 Gy/s, minimum 2,384E-07±8,36556E-09 Gy/s in total lung. The mean liver dose value for all lung volumes presented in Table 1 was determined to be2,963E-03±2,024E-05 Gy/s.

Given the anatomical proximity of the right lung to the liver, the absorbed dose value was measured with greater precision than that of the left lung.

The graph illustrating the relationship between right, left and total lung dose values and volume is presented in Figure 3. It can be observed that the absorbed dose values increase in line with an increase in volume.
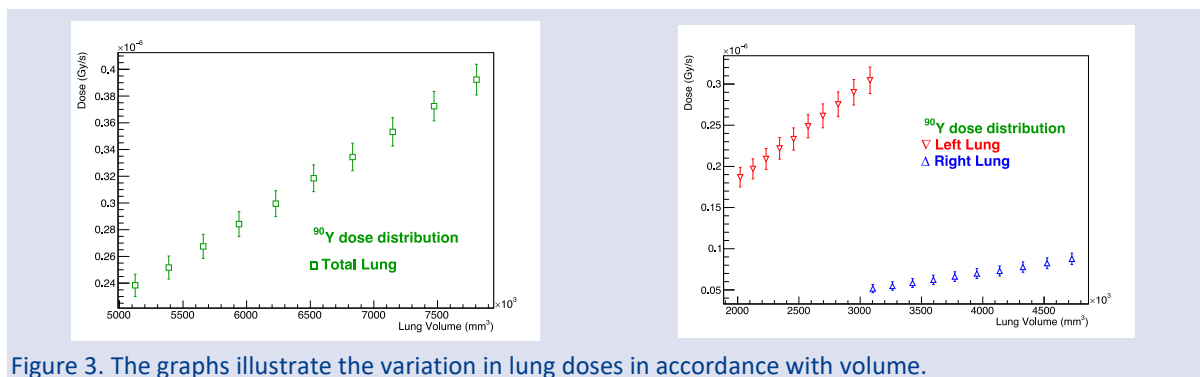

Figure 3. The graphs illustrate the variation in lung doses in accordance with volume.

In the calculation of critical and target organ doses in treatments involving Yttrium-90 radioembolization, the standard approach is to assume a lung mass of 1 kg [16-17]. In the literature, the mass of the lung is known to be 546±207 g and 467±174 g for women, 663±239 g and 583±216 g for men, including the right and left lung [18]. In the treatment of liver cancer, the doses received by organs such as the lung, which are considered critical, directly affect the treatment planning as well as the dose received by the target organ. In literature, it has been demonstrated that different volume values are obtained when various imaging techniques, including planar, SPECT/CT and PET/CT, are used to calculate lung and liver volumes. These differences have been known to have a significant impact on the determination of treatment doses [22, 23]. In this study, the potential risk of lung toxicity was assessed by modelling the impact of changes in lung volume on absorbed dose using Monte Carlo (MC) simulations. It was thus determined that an increase in lung volume resulted in an elevated dose absorption by the lung. In accordance with the findings of [24], when the discrepancies in lung volume were examined under an identical treatment plan, dose variations of up to 65% were observed between the lowest and highest volume values when the volume and dose data in Tables 1 and 2 were compared.

In the simulation, the calculated average absorbed dose value for a total lung volume of 7 litres was 3,726E-07±1,106E-08 Gy/s, while for 5 litres the value was 3,175E-07±9,999E-09 Gy/s and for 3 litres it was 2,604E-07±8,829E-09 Gy/s. This directly proportional relationship between lung volume and absorbed dose per unit volume indicates that larger lung volumes with the same vascularity are exposed to higher doses, which may increase radiation effects. The calculated dose differences for volumes of 3 to 5 litres and 5 to 7 litres were 22% and 17%, respectively. These findings are in agreement with this of previous study in [25], which emphasized a similar dose escalation in patients with larger lung volumes.

The findings of the study reinforce the crucial significance of lung volume in the evaluation of lung toxicity risk during Y-90 radioembolization. The results corroborate the conclusions of [20] that dosimetric models should incorporate anatomical variables such as lung volume to enhance the predictive precision of lung toxicity risk, underscoring that existing dosimetry protocols, which frequently fail to account for individual lung volume variations [10-13], are insufficient.

The results demonstrate the potential of utilizing simulation tools such as GATE to develop more personalized dosimetry models that account for lung volume differences [20, 26-30]. By incorporating patient-specific anatomy into dose calculations, GATE simulations can provide more accurate estimates of absorbed dose and, subsequently, guide safer treatment planning. Personalized models adjusting for lung volume, LSF and applied activity may enable practitioners to more accurately predict the risk of lung toxicity and, therefore, tailor the treatment plan accordingly.

While this study offers valuable insights into the relationship between lung volume and absorbed dose in Y-90 treatments, it is important to acknowledge the limitations of the study. It should be noted that the simulations presented in this study are based on generalized lung volumes, rather than patient-specific anatomical data. This may result in discrepancies when extrapolating the findings to a clinical setting. Furthermore, the shunt was assumed to have standardized vascularity, which inevitably affects the dose calculation. Further studies may benefit from the integration of real patient CT or MRI data, which could be used to refine lung dose estimates and improve the accuracy of dosimetry calculations. Furthermore, the longitudinal evaluation of post-treatment patients could confirm these findings by correlating simulated dose distributions with clinical outcomes of lung toxicity. The expansion of the range of anatomical variation and the investigation of different activity levels may also prove beneficial in optimizing dose thresholds for various patient populations.

Conclusion

This study shows that the amount of lung tissue that is absorbed during Y-90 therapy is significantly influenced by lung volume. The danger of radiation-induced lung damage increases with smaller lung capacities because they receive higher radiation doses per unit volume. Patients with different lung sizes may benefit from customized Y-90 treatments that optimize therapeutic efficacy while lowering toxicity risks by using the GATE toolkit for personalized dosimetry, which could enhance risk assessment.

Conflict of interest

There are no conflicts of interest in this work.

Acknowledgment

Ethical Approval Statement

No animals/humans were used for studies that are the basis of this research.

References

[1] Kouri B.E., Abrams R.A., Al-Refaie W.B., et al., ACR appropriateness criteria radiologic management of hepatic malignancy, *J. Am. Coll. Radiol*., 12(3) (2012) 265–273.

[2] Ahmadzadehfar H., Biersack HJ., Ezziddin S., Radioembolization of liver tumors with yttrium-90 microspheres, *Semin Nucl Med*, 40 (2010) 105-21.

[3] Mulcahy M.F., Lewandowski R.J., Ibrahim S.M., Sato K.T., Ryu R.K., Atassi B., Newman S., Talamonti M., Omary R.A., Benson A., Salem R., Radioembolization of colorectal hepatic metastases using yttrium-90 microspheres, *Cancer*, 115(9) (2009) 1849-58.

[4] Covey A.M., Brody L.A., Maluccio M.A., Getrajdman G.I., Brown K.T., Variant hepatic arterial anatomy revisited: digital subtraction angiography performed in 600 patients, *Radiology*, 224(2) (2002) 542–547.

[5] Lewandowski R.J., Sato K.T., Atassi B., et al., Radioembolization with 90Y microspheres: angiographic and technical considerations, Cardiovasc. *Intervent. Radiol.*, 30(4) (2007) 571–592.

[6] Viñal D., Minaya-Bravo A., Prieto I. et al., Ytrrium-90 transarterial radioembolization in patients with gastrointestinal malignancies, *Clin Transl Oncol* , 24 (2022) 796–808.

[7] Harder E.M., Park H.S., Chen Z.J., Decker R.H., Pulmonary dose-volume predictors of radiation pneumonitis following stereotactic body radiation therapy, *Pract. Radiat. Oncol.*, 6 (2016) 353–359.

[8] Yu N., Srinivas S.M., Difilippo F.P., Shrikanthan S., Levitin A., McLennan G., et al., Lung dose calculation with SPECT/CT for Yittrium-90 radioembolization of liver cancer, *Int J Radiat Oncol Biol Phys*, 85(3) (2013) 834–9.

[9] Salem R., Johnson G.E., Kim E., Riaz A., Bishay V., Boucher E., Fowers K., Lewandowski R., Padia S.A., Yttrium-90 Radioembolization for the Treatment of Solitary, Unresectable HCC: The LEGACY Study, *Hepatology*, 74(5) (2021) 2342-2352.

[10] Yuki B., Josep M., Takeo T., Sara L., Amita K., Pamela A., William S., Lucas F., Rahul S.P., Ganesh G., Edward K., Thomas D.S., Marcelo E. F., A comparative study of portal vein embolization versus radiation lobectomy with Yttrium-90 microspheres in preparation for liver resection for initially unresectable hepatocellular carcinoma, *Surgery,* 169(5) (2021) 1044-1051.

[11] Smits M.L.J., Nijsen J.F.W., van den Bosch M.A.A.J., Lam, M.G.E.H., Vente M.A.D., Huijbregts J.E., van het Schip A.D., Elschot M., Bult W., de Jong H.W.A.M., Meulenhoff P.C.W., Zonnenberg B.A., Holmium-166 radioembolization for the treatment of patients with liver metastases: design of the phase I HEPAR trial, *J. Exp. Clin. Cancer Res.,* 29 (2010) 70.

[12] Bastiaannet, R., Kappadath, S.C., Kunnen, B., Braat A.J.A.T., Lam M.G.E.H., de Jong H.W.A.M., The physics of radioembolization, *EJNMMI Phys.,* 5(1) (2018) 22.

[13] Gulec S.A., Mesoloras G., Stabin M., Dosimetric techniques in 90Y-microsphere therapy of liver cancer: The MIRD equations for dose calculations, *J. Nucl. Med.,* 47(7) (2006) 1209-1211.

[14] Gulec S.A., Mesoloras G., Dezarn W.A., et al., Safety and efficacy of Y-90 microsphere treatment in patients with primary and metastatic liver cancer: the tumor selectivity of the treatment as a function of tumor to liver flow ratio, *J Transl Med*. 14 (2007) 5-15.

[15] D'Angelis C. A., Coalson J. J., Ryan M.R., Pediatric critical care. Chapter 36-Structure of the respiratory system: lower respritory tract, 4nd ed. Mosby, (2011) 490-498.

[16] Margolis L.W., Philips T.L., Whole lung irradiation for metastatic tumour, *Radiology,* 93 (1969) 1173–8.

[17] Stella M., van Rooij R., Lam M.G.E.H., de Jong H.W.A.M., Braat A.J.A.T., Lung Dose Measured on Postradioembolization 90Y PET/CT and Incidence of Radiation Pneumonitis, *J Nucl Med.*, 63(7) (2022) 1075-1080.

[18] Grandmaison G.L., Clairand I., Durigon M., Organ weight in 684 adult autopsies: new tables for a Caucasoid population, *Forensic Science International*, 119(2) (2001) 149-154.

[19] Elsayed M., Cheng B., Xing M., *et al.,* Comparison of Tc-99m MAA Planar Versus SPECT/CT Imaging for Lung Shunt Fraction Evaluation Prior to Y-90 Radioembolization: Are We Overestimating Lung Shunt Fraction?, *Cardiovasc Intervent Radiol,* 44 (2021) 254–260.

[20] Gill H., Hiller J., Systematic review of lung shunt fraction quantification comparing SPECT/CT and planar scintigraphy for yttrium 90 radioembolization planning, *Clin Transl Imaging,* 9 (2021) 181–188.

[21] Mercolli L., Zeimpekis K., Prenosil G.A., Sari H., Rathke H.G., Rominger A., Shi K., Phantom study for ^{90}Y liver radioembolization dosimetry with a long axial field-of-view PET/CT, *Phys Med.*, 118 (2024) 103296.

[22] Allred J.D., Niedbala J., Mikell J.K., *et al.,* The value of ^{99m}Tc-MAA SPECT/CT for lung shunt estimation in ^{90}Y radioembolization: a phantom and patient study, *EJNMMI Res* 8, 50 (2018).

[23] D'Arienzo M., Pimpinella M., Capogni M., *et al.,* Phantom validation of quantitative Y-90 PET/CT-based dosimetry in liver radioembolization, *EJNMMI Res* 7, 94 (2017).

[24] Busse N., Erwin W., Pan T., Evaluation of a semiautomated lung mass calculation technique for internal dosimetry applications, *Med Phys.*, 40(12) (2013) 122503.

[25] Georgiou M.F., Kuker R.A., Studenski M.T., *et al.*, Lung shunt fraction calculation using ^{99m}Tc-MAA SPECT/CT imaging for ^{90}Y microsphere selective internal radiation therapy of liver tumors. *EJNMMI* Res 11**,** 96 (2021).

[26] Karimipourfard M., Sina S., Alavi M.S, Toward three-dimensional patient-specific internal dosimetry using GATE Monte Carlo technique, *Radiation Physics and Chemistry*, 95 (2022) 110046.

[27] Arun G., *et al., Precliinical voxel-based dosimetry through GATE Monte Carlo simulation using PET/CT imaging of mice, Physics in Medicine and Biology,* 64(9) (2019) 095007.

[28] Tanyıldızı- Kokkulunk H., Demir M., Karadeniz-Yildirim A., Ozkorucuklu S., Doğan Y., Akkuş B., Y-90 Dosimetry with Monte Carlo Method: GATE Validation with STL Formatted Phantom, *ACTA PHYSICA POLONICA A* , 138(6) (2020) 801-808.

[29] Karadeniz-Yildirim A., Ozkorucuklu S., Tanyildizi-Kokkulunk H. *et al.*, Monte Carlo Simulation of Liver Dosimetry with Yttrium-90 Radionuclide Using Gate: 3D Phantom, *Bull. Lebedev Phys. Inst,* 51 (2024) 30–37.

[30] Karadeniz-Yildirim A.,Tanyildizi-Kokkulunk H.**,** Comparison of Y-90 and Ho-166 Dosimetry Using Liver Phantom: A Monte Carlo Study, *Anti-Cancer Agents in Medicinal Chemistry (Formerly Current Medicinal Chemistry - Anti-Cancer Agents)*, 22(7) (2022) 1348-1353.

Cumhuriyet Science Journal

Investigation of Step Growth on Nano Surfaces Depending on Temperature and Flux Rates Using the KMC Method

Mehmet Esen [1,a,*]

[1] Adana Vocational School Computer Programming Department, Çukurova University, Adana, Türkiye.
*Corresponding author

Research Article

ABSTRACT

In this study, the growth of nano-sized surface step structures was examined using the Kinetic Monte Carlo (KMC) simulation technique. The step growth and correlation function on the nano surfaces were analyzed at surface energy values of Eb = 100 meV, Ed = 80 meV, Eds = 150 meV, and Ek = 80 meV, where Eb is the bonding enegy, Eds is the step edge diffusion , Ed is the surface diffusion and Ek Schwoebel energy barrier values , with a surface flux of 1 atom every 10 ns directed towards the pre-formed stepped surfaces on the nano surfaces. The simulation temperature was set to T = 250 K. In this case, step growth was limited, but cluster structures played an important role in stepped surface growth. In a different scenario, at T = 300 K, the amplitude increased at a constant rate, and there were no step fluctuations. Surface growth increased, and the surface fluctuation amplitude also grew. At T = 350 K, when the temperature was raised further, step fluctuations has become dominant, the step fluctuation continued to increase at a constant rate, the step amplitude grew, and the number of islands decreased compared to the other two cases. In addition the correlation of steps is investigated for each temperature.

According to these results, the dynamics of step growth can be controlled by selecting an appropriate temperature and balancing the surface energy parameters.

Keywords: KMC method, Nano surfaces, Step growth, Surface diffusion energy, Temperature

a ✉ mehesen@cukurova.edu.tr   https://orcid.org/0009-0000-2057-4536

Introduction

Semiconductor surface production technologies play a crucial role in advancing science and technology. Semiconductor surfaces have an important role in the production of many semiconductor devices. Experimental production of semiconductor surfaces is generally provided by sending atoms or molecules to a sub-surface with different methods. Chemical vapor deposition(CVD), molecular beam epitaxy(MBE) methods are experimental methods that provide experimental surface formation. Before conducting surface formation experiments, the development of the surfaces is guided by predictions from theoretical studies. These theoretical approaches examine factors such as the base material's effect, atom types and their movement to the surface, surface temperature, atomic diffusion properties, temperature variations during the experiment, and the evolution of the formed structures into different configurations. Simulation methods are essential for establishing the theoretical framework. Using these methods, predictions about surfaces and structures can be simulated, guided by the results obtained from the simulations, thereby saving time and resources. In cases where real-world testing is not possible, simulations allow predictions by modeling specific features as parameters. Among surface simulation techniques, Monte Carlo (MC) methods hold significant importance. These include molecular dynamics MC, direct MC, and the Kinetic Monte Carlo (KMC) technique . The KMC method is based on the important studies of Bortz et

al. [1], and Fichthorn and Weinberg [2] and Haneman et al. [3]. There are more recent studies on step simulations using the KMC method [4,5].

Method

In this study, a custom Fortran program utilizing the KMC method was developed, and data were collected using this program. In this method, possible states of the surface sites were analyzed, and their transition probabilities were calculated. The transition probabilities of atoms from one site to another, depend on the energy barriers between them. In the KMC method, atoms moving on the surface, overcome specific energy barriers and settle somewhere on the surface. With a certain probability, these atoms can be displaced by thermal fluctuations (surface diffusion), bond with previously fixed atoms to become part of the structure, or leave the surface and become part of the vapor above the surface. The probability of a particle moving from one site to another on the surface given is as,

$$P \propto e^{-E_b/k_B T} \tag{1}$$

where E_b is the energy barrier the particle must surmount is in going from one site to a neighboring one. If we call this transition probability i events, there can be n total transition events for the particles on the surface. The rate

at which a particle can make transition to state i with a rate r_i is given as,
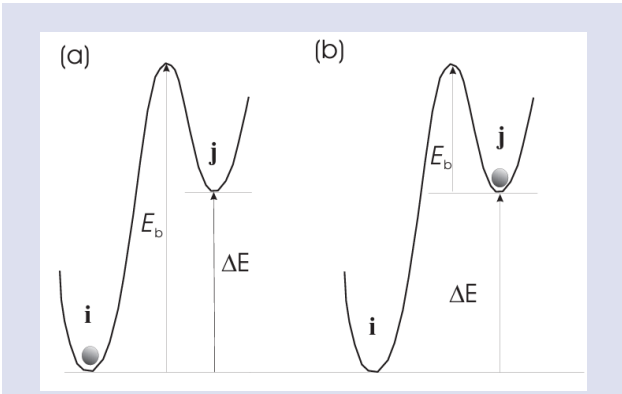
$$r_i = w_i e^{-E_i/k_B T} \tag{2}$$

Figure 1. The barrier energies required to be crossed for states i and j are shown, the probability of transition is low in case (a) but the probability is high compared to the other in case (b). The energy barrier Eb is higher in(a).

In equation(2) w_i represents the number of attempts to pass through the potential well per unit time for the defined event i to occur, and generally $w_i = 10^{12}\,\text{s}^{-1}$. E_i is the size of the energy barrier that the particle tries to cross, k_B is Boltzmann's constant and T is the absolute temperature. As shown in Figure 1, the transition probability from state i to state j is difficult, whereas the transition from j to i is more probable. If the transition probabilities of all particles in all directions are determined by the surface configuration energy, and the probability of one of these events is proportional to the transition probability, then only one particle moves at a time. This is one of the strengths of the KMC method. Another advantage of this method is that a link relation can be established between real time and simulation time [1]. The necessary conditions for establishing this link were outlined by Fichthorn et al. [2]. These criteria are as follows: transitions must be a Poisson event, transition events must be independent of each other, the time between successive events can be calculated in a convenient way, transition probabilities must obey a 'dynamic hierarchy' such that the 'comprehensive equilibrium' condition is satisfied.

The KMC method can be used for systems in equilibrium or far from equilibrium. The current independent Poisson distribution for the transition from state i to state j in the interval from instant t to $t+\tau$ is given by

$$P(n_i) = \frac{(r_i t)^{n_i}}{n_i!} e^{-r_i t} \tag{3}$$

One feature of Poisson events is that a collection of independent events behaves as a single Poisson event. An important property of a Poisson event is that the time elapsed between successive events can be found, and this is the probability of occurring at an instant t can be given as [7],

$$P(t) = R e^{-Rt} \tag{4}$$

Average time between these events

$$\bar{t} = \int_0^\infty t P(t)\,dt = \int_0^\tau t\,R e^{-Rt}\,dt = 1 - e^{R\tau} \tag{5}$$

The right hand side of eqn (5) is between zero and 1, therefore it can be equated to a random number u between 0 and 1, as a result the time elapsed between two consecutive events becomes

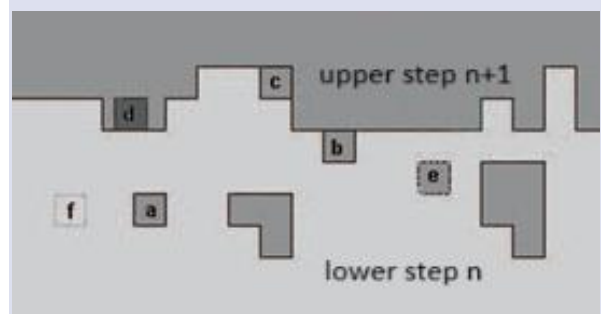$$\tau = -\frac{\ln u}{R} \tag{6}$$

Figure 2. Schematic representation of atoms on a stepped surface, dark regions are one atomic length higher than light colored regions. Only two steps are shown on the surface; a cubic structure located at the step edge, a single atom on the surface, b at the step edge, c attached to the corner, d embedded in the step, e inside the surface, f sample atoms embedded in the crystal depth .

As seen in Figure 2, schematic views of the atoms that can be found on the sample surface are given. The number of nearest (nn), next nearest (nnn) and nex next nearest neigbor (nnnn) atoms for each specific location shown in Figure 2 is given Table 1.

Table 1. Nearest neighboring (nn) atom numbers of crystal atoms [8]

Position	index	nn	nnn	Next nnn
Above the surface	a	1	4	4
Step Edge	b	2	6	4
Around the corner	c	3	6	4
Inside the step	d	4	6	4
Inside the surface	e	5	8	4
Deep in crystal	f	6	12	8

Each bond of the atoms appearing in Table 1 can have different combinations of threshold energies, accordingly the transition barrier energies for several configurations are given in Table 2.

Table 2. Sample transition probabilities of some crystal atoms

Event	Energy Barrier	Probability of occuring
Free diffusion on the surface (a)	E_d	exp(-E_d/$k_B T$)
Step edge detachment (b downward direction)	E_b+ E_d	exp(-(E_b+ E_d)/$k_B T$)
Detaching from the edge of the step to the top (b upward direction)	E_b+ E_k	exp(-(E_b+E_k)/$k_B T$)
Going down from the terrace (d down direction)	E_k	exp(-E_k/$k_B T$)
Movement along the edge of the step (b movement in two directions)	E_{ds}	exp(-E_{ds}/$k_B T$)

When Figure 1 and Table 2 are examined together, it is seen that each atom on the surface has the possibility of moving in 4 different directions, and each atom can make different types of bonds with 4 atoms that may be around it depending on its position on the surface, It should be known that it must break different bond combinations in each direction of movement and the algorithm we developed calculates and groups these probabilities for thousands of different combination cases. In addition, the location of atomic islands and steps were found using specially developed unique difference and fill algorithms [8]. These are necessary for a proper analysis of the resulting surface.

The KMC algorithm used in the present study is given in the following steps:

1. Time is reset *t = 0*
2. All transition rate r_i s for all particles in the system are calculated
3. The cumulative sum of the transition rates are calculated. $R_i = \sum_{j=1}^{i} r_i R = R_N$
4. A random number *u* is chosen between 0 and 1.
5. The i *th* event to occur is chosen to satisfy the equation $R_{i-1} \leq uR < R_i$.
6. The selected *i*.th event is performed (atom location changes)
7. The changed probabilities are recalculated and added to the unchanged ones.
8. A new random number *u* is selected and $\tau = -\frac{\ln u}{R}$ calculated
9. Time is updated $t = t + \tau$
10. Goto step 1.

The step position random walk behavior, related to step movements on the surface, is described by the position correlation function as [9]:

$$G(y) =< ((x(y) - X(y_0))^2 \geq \frac{b^2}{a_\parallel} |y| \qquad (7)$$

In this equation *G(y)*, is a function of distance *y* along the step edge. The term b^2 in the equation is the step

diffusivity term, |y| is the everage position of the step, a|| is the distance between nearest neighbor atoms.

Results And Discussion

The structures formed on the surface were simulated using different surface energy parameters. The growth and fluctuation of the steps were investigated, and it was observed that these properties depend on the particle flux to the surface and the surface energy parameters. In this section, the growth of a single step on a large surface is studied at different temperatures. By choosing a large surface, the effects of periodic boundary conditions and the limited size of the surface are minimized. For all cases considered in this section, the temperature is varied while the other energy parameters are kept constant. These are as follows: the atomic bond energy Eb = 100 meV, free surface diffusion barrier Ed = 80 meV, the step edge diffusion barrier Eds = 150 meV, and the Schwoebel energy barrier Ek = 80 meV. The Schwoebel energy barrier is the the energy a particle must overcome when joining a step edge from an upper step. The atomic flux to the surface is 1 particle per 10 ns. In the first case, T = 250 K was chosen, and the resulting surface morphology is shown in Figure 3. For these parameters, surface diffusion of particles is more difficult, so island formation begins immediately upon particle flux to the surface. Since the binding energy is higher than the diffusion energy, particles bound to steps or islands are more difficult to detach. Furthermore, the particle density near the step edge is low. Because particles in this region are absorbed by the step, sufficient density for island formation near the step cannot be achieved for a long time. However, as the previously formed islands grow and the step edge advances, the islands and the step edge approach each other and eventually merge.
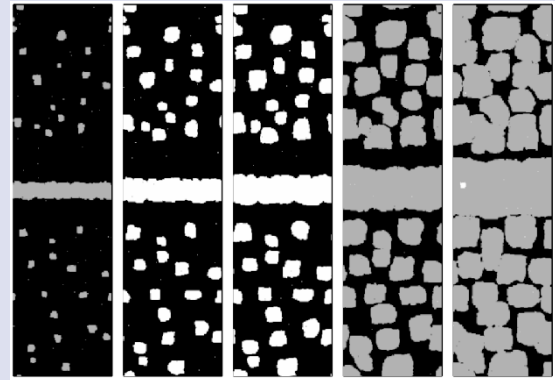

Figure 3. The time evolution of the surface is shown from left to right. The surface size is 160x600, with energy parameters of Eb = 100 meV, Ed = 80 meV, Eds = 150 meV, and Ek = 80 meV at T = 250 K. The flux is 1 atom per 10 ns. As seen in the figure, the growth of islands is more dominant than the growth of steps. A single step is surrounded by two terraces of the same height on each side of the step.

Figure 4 shows the correlation function of the step edge shown in Figure 3. The correlations obtained at later times of the surface are indicated by t₃ in Figure 4. Initially, the step oscillates with small wavelengths. Over time, small wavelength oscillations are eliminated and longer wavelength structures remain on the surface.

When these reach a stable equilibrium, the step grows in this way as expected. The change in correlation varies almost linearly for small step lengths as given in equation(7)[8].
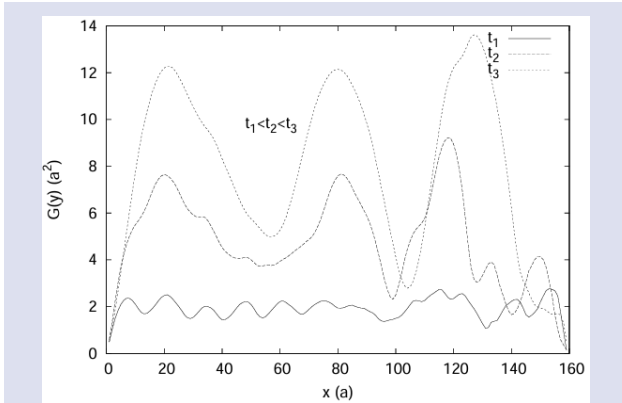

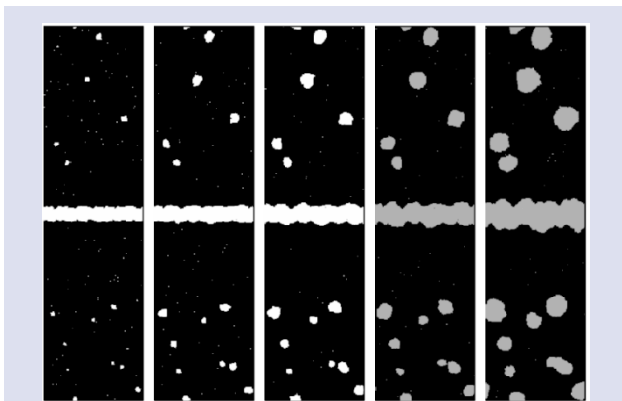Figure 4. Correlation function of a step given in figure 3.

Figure 5. The time evolution of steps and islands on a 160x600 surface at E_b = 100, E_d = 80, E_{ds} = 150 and E_k = 80 meV at T = 300K. The flux is 1 atom at 10 ns. As can be seen in the figure, the growth of the islands is not dominant and the islands grow in small numbers.
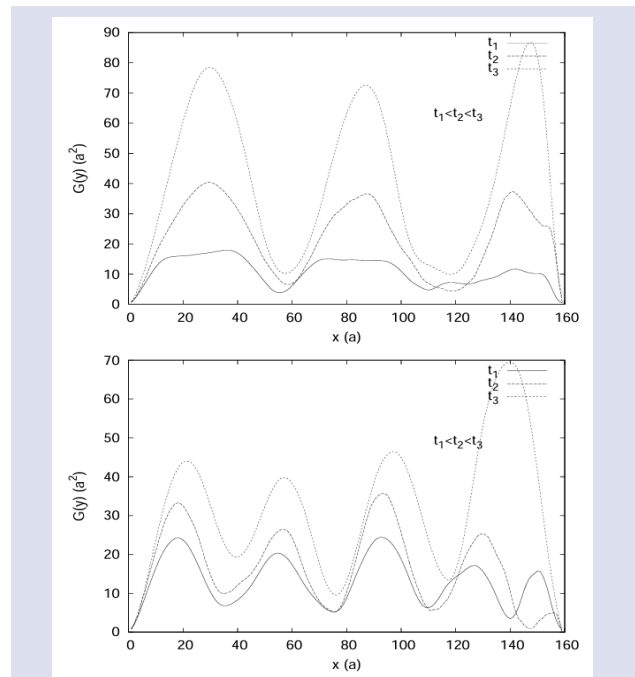

Figure 6. Correlation function for the two sides of the growing step shown in Figure 5. The step fluctuation strength and behavior depends on the cluster distribution near the step edge.

In another case the surface temperature was increased at T=300K. As seen in Figure 5, island formation is low. Since the temperature is higher, the diffusion of particles on the surface is higher. It is easier for atoms to merge and separate at the edges of the step or at the edges of the island. Therefore, island formation is low.
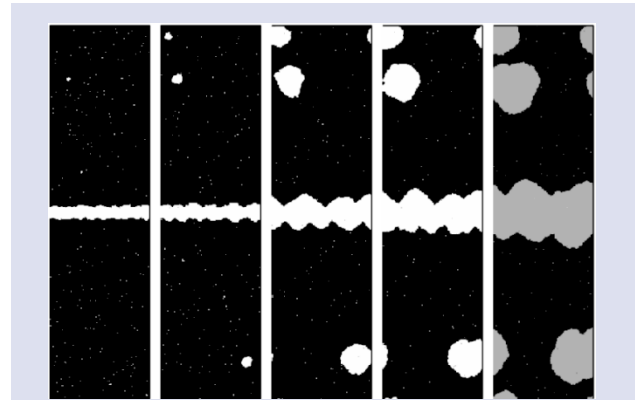

Figure 7. The time evolution of steps and islands on a 160x600 surface at E_b = 100, E_d = 80, E_{ds} = 150 and E_k = 80 meV at T = 350K. The flux is 1 atom at 10 ns. As seen in the figure, the growth of the islands is not dominant and the islands grow in very small numbers.
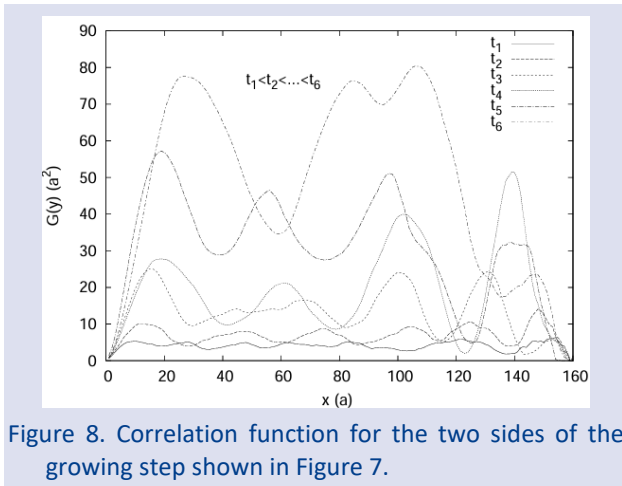
Figure 8. Correlation function for the two sides of the growing step shown in Figure 7.

As in the case of Figures 5 and 6, the step fluctuation behavior depends on the cluster distribution near the step edge. In the present case we have less number of clusters with a considerable size.

In Figure 7, a higher temperature of T = 350 K is simulated. At this temperature, step growth dominates, and no islands form in the terrace region where the step is fed. Instead, a few very large islands form far from the step edges. When the step correlation is analyzed in Figure 8, the amplitude increases significantly and the oscillation mode numbers decrease in the later stages of growth.

Conclusions

Considering all the results, the effect of material parameter selections on step growth processes—a key phenomenon in surface growth—is evident. The selection of growth temperatures suitable for the atomic binding energies of the material plays a crucial role in determining the step growth phases.

Based on these results, if the temperature is increased and the surface flux is maintained at an adequate level, step growth can dominate surface growth. However, if the temperature is increased excessively, step decomposition may become excessive, causing the entire step structure to disappear and the surface to decompose into small clusters of 2 or 3 atoms. This study provides valuable guidance for determining the temperature at which experimental studies should be conducted.

Conflict of interest

The author declare that he has no conflict of interest.

Acknowledgement

References

[1] Bortz A.B., Kalos M.H., Lebowitz J.L.,1975, *J. Comp. Physics*, 17.

[2] Fichthorn K. A., & Weinberg W. H., Theoretical foundations of dynamical Monte Carlo simulations. *The Journal of chemical physics*, 95(2) (1991) 1090-1096.

[3] Haneman D., & Chernov A. A., Thermal conversion of Si (111) 2× 1 cleaved surface structure to Si (111) 7× 7 structure. *Surface science*, 215(1-2) (1989) 135-146.

[4] Nagpal S., Sitapure N., Gagnon Z., & Kwon, J. S. I., Advancing crystal growth prediction: An adaptive kMC model spanning multiple regimes. *Chemical Engineering Science*, 299 (2024) 120472.

[5] Li, Y., Chen, X., & Ai W., Kinetic Monte Carlo simulation study of the early stages of epitaxial SiC (0001) growth. *Journal of Crystal Growth*, 617 (2023) 127291.

[6] Bulmer M. G. *Principles of statistics*. (2012). Courier Corporation.

[7] ÇINLAR E., An Introduction to Stochastic Processes, Prentice-Hall, 1975.

[8] Esen M., Atomik Basamaklı Kristal Yüzeylerinin Kinetik Monte Carlo Yöntemi ile İncelenmesi, Çukurova Üniversitesi, Fen Bilimleri Enstitüsü, Fizik Bölümü Anabilim Dalı, *Doktora Tezi*, tez no: 5907, (2006)

[9] Bartelt N. C. (et al.), Brownian motion of steps on Si(111) *Phys. Rev. B*, 48 (1993) 15453-15456.

Cumhuriyet Science Journal

Design and Fabrication of Single Transverse Mode Passive Large-Pitch Fibers

Bülend Ortaç [1,a,*]

[1] UNAM-National Nanotechnology Research Center and Institute of Materials Science and Nanotechnology, Bilkent University, Ankara 06800, Türkiye
*Corresponding author

Research Article

ABSTRACT

The fabrication processes of single transverse mode passive large-pitch optical fiber (LPF) have been proposed and investigated. The LPF design, combined with the fundamental mode operating principle of delocalizing higher-order modes, has led to impressive performance. In this study, two LPF preform designs were proposed based on the stacking of one type of inner glass tube, two (design of LPF1) or three (design of LPF2) different filler rods, and a core rod placed within an outer tube. The first passive LPF1 is fabricated from a single-step preform drawing process. This fiber exhibits single transverse mode propagation, featuring a core size of 45.5 μm and a normalized hole diameter of 0.454. For the first time, a single transverse mode of light propagation from an LPF with an elliptical-like hole shape was achieved. The second LPF2 design has been proposed and fabricated by using a two-step preform drawing process. Successful production of an LPF with a circular hole shape has been obtained and exhibits single transverse mode propagation, featuring a core size of 42.8 μm and a normalized hole diameter of 0.322. Furthermore, numerical analysis was also performed to study mode propagation for the LPF.

Keywords: Photonic crystal fiber, Large-pitch fiber, Large-mode-area, Single transverse mode

a✉ ortac@unam.bilkent.edu.tr   https://orcid.org/0000-0002-1104-7459

Introduction

Fiber laser oscillator and amplifier systems comprise several critical components, including semiconductor diode lasers, pump combiners, fiber Bragg gratings, saturable absorbers, stretchers, compressors, and active fibers [1-4]. Among these, active fiber is an essential component for generating and amplifying the laser signal. Step-index optical fiber can be effectively utilized for light amplification in fiber laser systems. In such applications, the core of the fiber is doped with rare-earth elements, such as ytterbium or erbium, which serve as the amplifying medium. Power scaling in fiber laser systems initiates non-linear interactions that arise from these effects, including Self-phase modulation (SPM) and Stimulated Raman Scattering (SRS) [1-4]. To control these effects, large-mode-area step-index optical fibers have been proposed [5, 6]. This type of fiber provides a larger core diameter, which helps to reduce nonlinear effects and allows for higher power amplification. The design of large-mode-area step-index fibers enhances the efficiency of the laser system by enabling better control over the beam quality by reducing the core numerical aperture and minimizing signal distortion. However, this approach also creates a platform for the interaction between the fundamental mode and higher-order modes (HOMs) at certain power levels, which can noticeably reduce the quality of the laser beam, called Transverse Mode Instability (TMI) [7]. To increase the power scaling attainable with fiber lasers, one effective strategy is to enlarge the single-transverse mode areas. This approach allows for better handling of higher energy densities, leading to improved performance and efficiency in the

amplification process. By optimizing the new designs of the fiber and its core structures, it becomes possible to achieve higher output powers while maintaining beam quality. Key innovations include chirally-coupled core fibers [8], which improve mode coupling efficiency, and distributed mode filtering rod-type fibers [9] that help suppress unwanted modes. Other notable designs are leakage channel fibers [10], which minimize modal dispersion, and multitrench fibers [11], which maximize mode-field area without compromising single-mode characteristics. Additionally, photonic bandgap fibers [12] and Bragg fibers [13] have been developed to leverage optical bandgap phenomena for better light confinement. Lastly, LPFs offer significant advantages in achieving a large-mode area while ensuring effective single-mode operation [14, 15]. These fibers present transverse mode discrimination through a combination of differential propagation losses on the fundamental mode compared to HOMs and preferential excitation of the fundamental mode, which currently shows records of mode area, power, and energy scaling performances in fiber laser systems [16-19]. In the literature, there is no detailed guidance for single transverse mode LPF fabrication. In this study, the manufacturing processes of single transverse mode passive LPF with different designs are reported. Detailed designs consist of stacking and drawing the LPF preforms from a single- or two-step preform drawing process. LPFs with circular or elliptical-like hole-shaped structures have been produced. Single transverse mode propagations have been confirmed from the LPF featuring a core size of 45.5 μm and a normalized hole

diameter of 0.454 from elliptical-like hole-shaped and the LPF featuring a core size of 42.8 µm and a normalized hole diameter of 0.322 from circular hole-shaped, respectively. In addition, numerical analysis was also investigated to study single-mode propagation for the fiber.

Design of Single Transverse Mode Passive Large-Pitch Fiber

The representative structure of the LPF cross-section is shown in Figure 1. All the LPF designs considered in this paper have hexagonal photonic crystal fiber concepts without an air-cladding ring. The fiber core is formed by one missing hole. The fiber core size can be determined as a region from the corner of holes with a diameter of D. This fiber core is then surrounded by two hexagonal rings of air holes with equidistant air hole distances. In LPF geometry, the pitch Λ is called the hole-to-hole distance, and d is called the diameter of the hole. The normalized hole-diameter d/Λ plays a key role in the fiber guidance properties. The single-mode criteria in the solid-core PCFs can be associated with d/Λ values below 0.4 [20]. To eliminate the index-depressions issue on the light guidance in the core compared to the cladding region, the refractive index of the cladding region ($n_{cladding}$) and core region (n_{core}) are chosen at the same refractive index level shown in Figure 1.
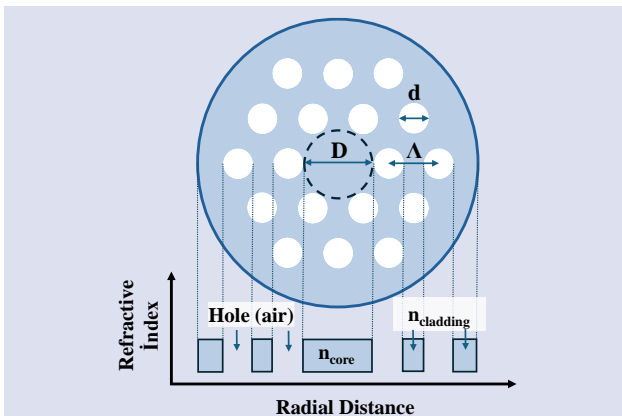

Figure 1. Schematic diagram of an LPF cross-section. The fiber structure consists of a hexagonal two-ring structure with equidistant air holes separated by a pitch Λ and a diameter d with one missing hole as a core (diameter D).

Fabrication of LPF with Single-step Drawing Processing

Figure 2a shows details of the first LPF1 design. It consists of 18 identical (outer diameter and thickness) inner tubes arranged with two hexagonal structures in an outer tube. The inner tube size parameters (inner and outer diameters) determine the LPF fiber pitch Λ and diameter(d) of the hole. The size of the inner tubes has been carefully designed to optimize the d/Λ parameter during the drawing process. A rod with the same diameter as the outer diameter of the inner tube is then placed in the center of the design. To fix this structure into an outer tube, 2 different-sized filler rods (12 pieces each) have been added to this structure, as shown in Figure 2a. An image of this LPF1 preform design without an outer tube has been presented in Figure 2b. The design of the final PCF depends on the preform drawing conditions. The size of the PCF preform is often adjusted to be in a cm scale. The PCF preform can be drawn in one step in which PCFs can be directly obtained upon the fiber drawing. On the other hand, when the PCF is drawn in two step conditions, then a PCF preform with a relatively smaller size called PCF cane is obtained in the order of mm scale. The design of the PCF preform determines what the final PCF structural units are, such as the number of air holes and the size of the PCF core will become. However, the light guiding properties will depend on the drawing conditions and the final fabricated design of the PCFs.
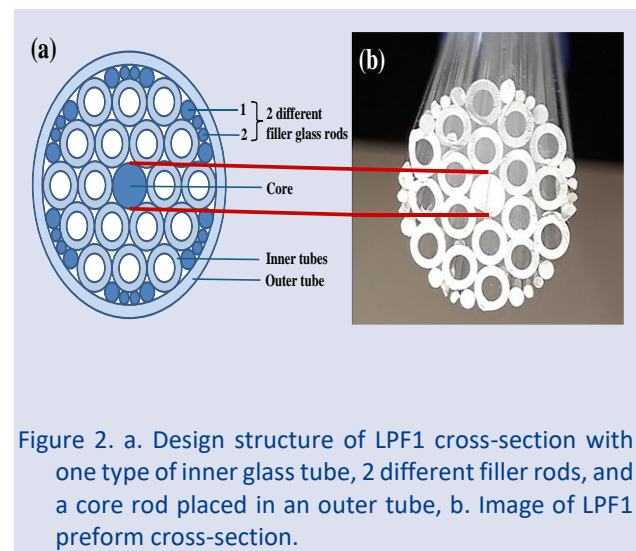

Figure 2. a. Design structure of LPF1 cross-section with one type of inner glass tube, 2 different filler rods, and a core rod placed in an outer tube, b. Image of LPF1 preform cross-section.
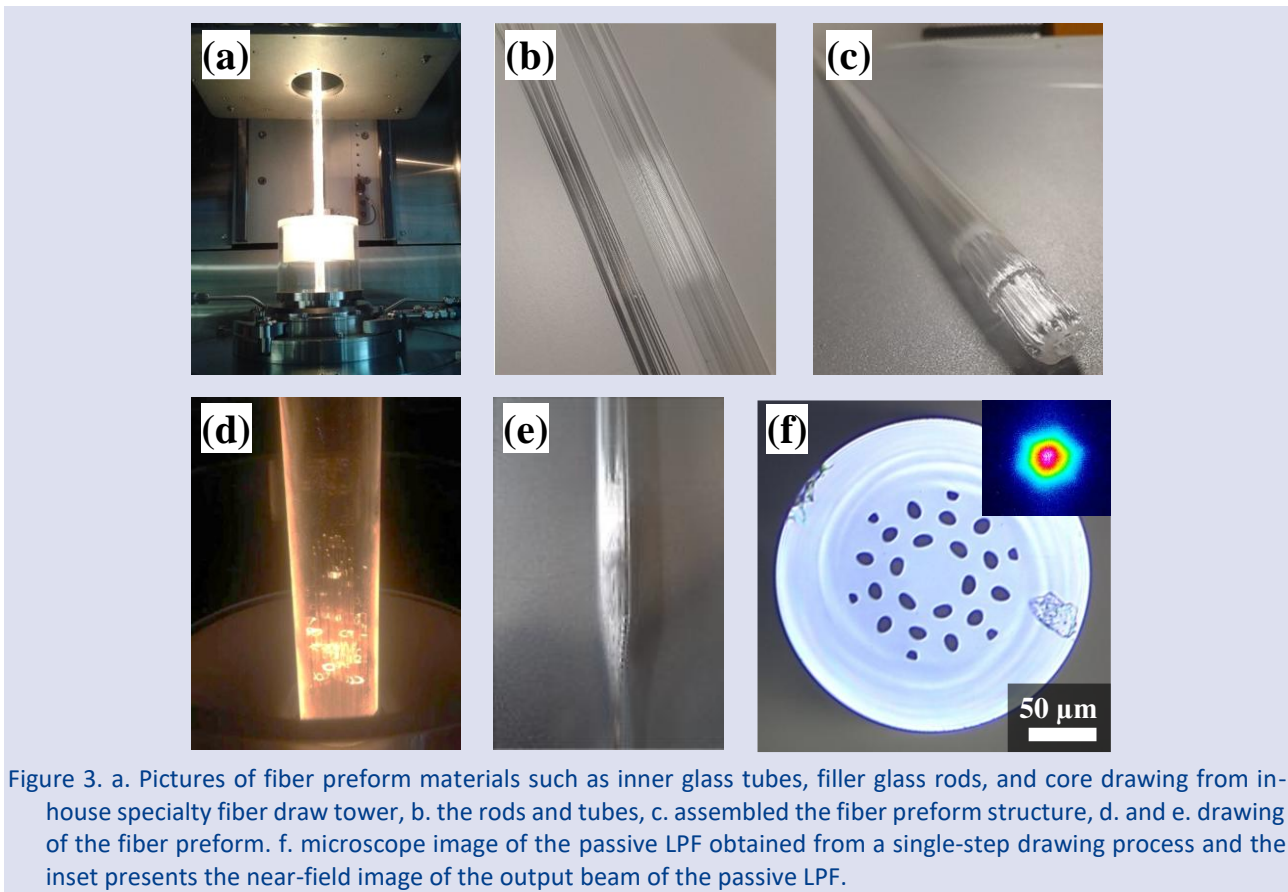
Figure 3. a. Pictures of fiber preform materials such as inner glass tubes, filler glass rods, and core drawing from in-house specialty fiber draw tower, b. the rods and tubes, c. assembled the fiber preform structure, d. and e. drawing of the fiber preform. f. microscope image of the passive LPF obtained from a single-step drawing process and the inset presents the near-field image of the output beam of the passive LPF.

LPF1 preform by using a well-known PCF fiber production method called the "stack-and-draw" procedure was fabricated initially. Figure 3 shows the production steps of an LPF fiber from the fabrication of LPF preform up to fiber. The preform sub-structures targeted in the design (inner tubes, core, and different size rods for fillers) were fabricated first by drawing glass tubes and rods from our high-temperature specialty fiber draw tower (see Figure 3a). In this work, the fused quartz rods and the tubing were purchased by Technical Glass Products, Inc. The index refraction of rquartz for all products is 1.4481 (@ 1200 nm). The quartz rods for the core region and the fillers were produced from the same glass initial rod under different drawing conditions. The inner tube size parameters regarding the inner and outer diameters were optimized by drawing carefully selected initial fused quartz tubing. The glass inner tubes and rods were manually assembled into a preform stack whose structure, as shown in Figure 3b, corresponds to the desired LPF structure. Figure 3c presents the assembled LPF preform structure. The total size of this preform can reach up to 16 mm in diameter.

This LPF preform was drawn to final LPF production using a single-step drawing process. Figure 3d shows an example of the drawn preform down to the final product. During the single-step drawing, the sub-structures (tubes and rods) of the LPF preform are fused to obtain a microstructured preform, which further leads to the final LPF production. The image of the fiber preform drawn is shown in Figure 3e. To optimize fiber structure and parameters such as the pitch, the diameters of the holes,

the hole-diameter ratio, the core, and the outer diameter of the fiber, the effect of drawing process parameters were studied such as furnace temperature directly related to the preform temperature, preform feed speed, and drawing speed on the final product. The drawing speed of the LPF fiber was about 1 m/min. The result of the passive LPF obtained from a single-step drawing process is shown in Figure 3f. The cladding diameter of the produced LPF was measured to be 231 μm. From the fiber structure, the pitch (Λ) of 25.1 μm and the hole diameter of 11.4 μm can be deduced, which corresponds to the normalized hole diameter d/Λ of 0.454. The LPF structure core size could be estimated at 45.5 μm.

The beam localization and propagation into the core region of this LPF were also studied. To optimize the excitation of the fundamental mode (LP01 mode), the modal overlap with the Gaussian-shaped excitation infrared beam within the core area has been carefully performed. To observe the fundamental mode propagation into the fiber, the output beam from the end facet of the fiber onto a CCD camera was also checked. The inset of Figure 3f shows the emitted beam after propagation in a 1 m-long LPF. We didn't observe any leakage of the beam into the cladding region. The propagation loss of the LPF of ~ 1 dB/m was also measured. To prevent the effective single-mode operation of the LPF, the fundamental mode propagation was also disturbed by gently offsetting the coupling condition of the fiber and due to high losses on the HOMs, there is no HOMS propagation observed at the fiber end facet, which proves the evidence of the effective single-

mode operation of the LPF. The divergence and the beam quality of an emitted beam from the LPF are measured by using Thorlabs Complete M² Measurement Systems. The numerical aperture (NA) of the LPF of 0.044 and the M2 value of 1.2 were calculated. With these results, an effective single-mode operation has been performed from our first LPF design. But despite all these results, it has been noticed that the hole shape deformation of LPF has been affected due to the single-step drawing process and mainly missing filler rods between the inner tubes. To better control this issue, it has further developed our second LPF fiber preform design and applied the two-step drawing processing.

Fabrication of LPF with Two-step Drawing Processing

Figure 4a describes the detailed design of the LPF2 preform. In this design, a similar structure template was used shown in Figure 2a, but a thinner diameter of filler glass rods was added (24 pieces in total) to the areas between the inner tubes and the core shown in Figure 4a. To obtain a well-fused glass structure and a microstructured preform called "cane", the drawing of the LPF2 preform has occurred from a 16 mm diameter of LPF2 preform to a 5 mm diameter of the LPF2 cane with a drawing speed of about 1 m/min. The cross-section image of the large-pitch fiber preform of the LPF2 after the first drawing is shown in Figure 4b. As a result of the first drawing on the LPF2 cane, it is seen that the structure of the LPF2 design is preserved without any deformation.
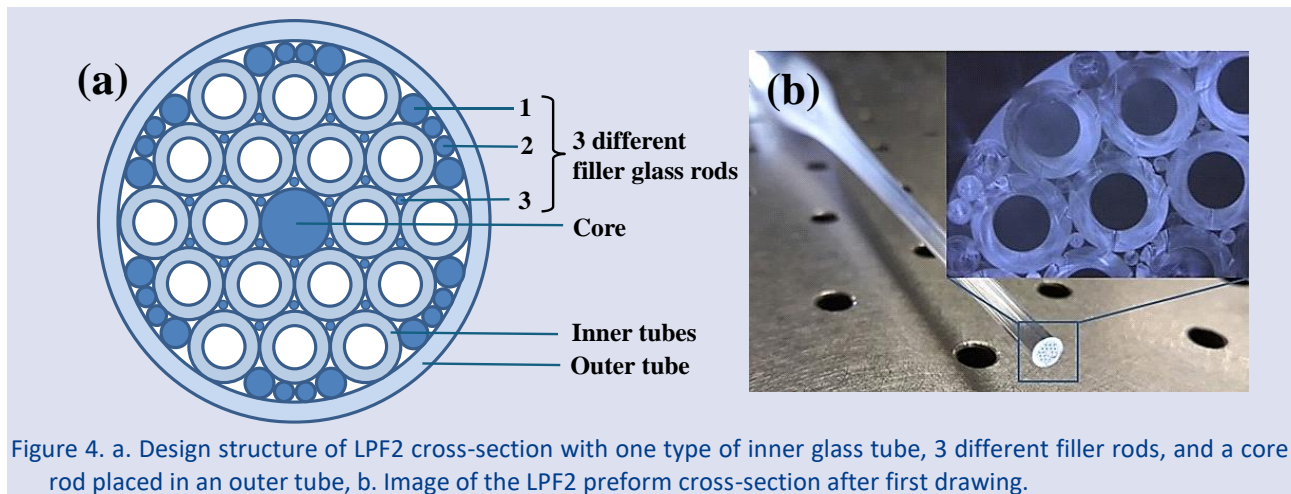

Figure 4. a. Design structure of LPF2 cross-section with one type of inner glass tube, 3 different filler rods, and a core rod placed in an outer tube, b. Image of the LPF2 preform cross-section after first drawing.

The second step in LPF fabrication involves drawing the LPF2 cane into an LPF2 with the desired dimensions and shape, such as pitch size, hole diameter, hole shape, and outer diameter of fiber. To study the effect of the normalized hole-diameter (d/Λ) parameters on the beam propagation behavior into the fiber, the drawing of the LPF2 cane has been performed with and without the air pressure applied inside the LPF2 cane. To eventually reduce the hole diameter value, the drawing of the LPF2 cane is first performed under a vacuum level of 10 mbar. The drawing speed of the LPF2 cane is about 3 m/min. The first fiber from the LPF2 cane is presented in Figure 5a. The pitch (Λ) of the fiber is about 29.2 μm, and the hole diameter is 5.7 μm, which corresponds to the normalized hole diameter d/Λ of 0.195. The LPF core size could be estimated at 55.3 μm. Then, the beam localization and propagation into this core region were studied. Even though it has been tried to excite the fundamental mode by changing the different modal overlaps (beam size, coupling angle, etc.) with the Gaussian-shaped excitation infrared beam within the core area, any fundamental mode propagation into the fiber has been observed at the end facet of the fiber onto a CCD camera. The near-field image of the output beam of the passive LPF with d/Λ ~ 0.195 obtained from a two-step drawing process is shown in Figure 5.

The leakage of the beam into the cladding region and the non-perfectly-localized beam into the core region has been observed.

In the next step, the drawing process of a similar LPF2 cane is then performed under no vacuum conditions with the top of the tube exposed to the ambient atmosphere. The drawing speed of the LPF2 cane is also performed at 3 m/min. The cross-section of fiber produced under these conditions is presented in Figure 5c. The larger hole diameter and smaller pitch size, compared to the fiber presented in Figure 5a, are obtained. From this fiber structure, the pitch (Λ) of 25.4 μm and the hole diameter of 8.2 μm have been deduced, which corresponds to the normalized hole diameter d/Λ of 0.322 with a relatively higher value compared to the fiber obtained in Figure 5a. This LPF core size could be estimated at 42.8 μm, and the cladding diameter of the produced LPF was measured to be 184 μm. Figure 5d presents the near-field image of the output beam of the passive LPF d/Λ ~ 0.322 obtained from a two-step drawing process using Thorlabs' complete M2 measurement system that includes the beam profiler in the near and far fields. The cross-section of beam-shaping 1 m-long LPF fiber at the end facet with a typical hexagonal mode field is obtained without any leakage of the beam into the cladding region. The propagation loss of this LPF of ~ 1 dB/m was also measured. The numerical aperture (NA) of this LPF of

0.044 and the M2 value of 1.2 were also calculated with similar parameters obtained in fiber produced and presented in Figure 3. With these results, an effective single-mode operation has also been performed from our second LPF design with the optimum drawing conditions. In addition, all fibers produced in the LPF2 approach demonstrate a circular hole-shaped structure compared to the approach presented in the LPF1 production.
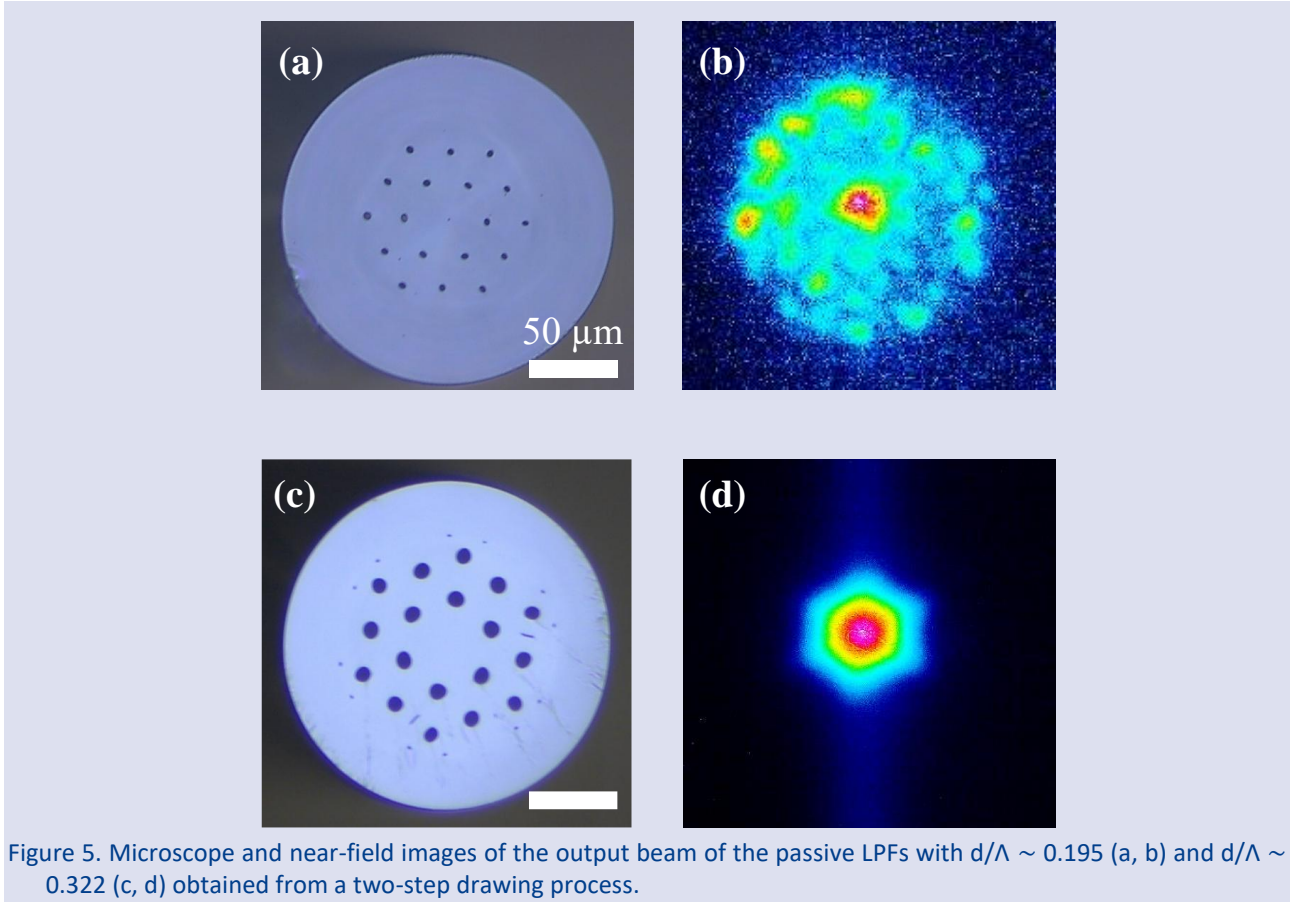

Figure 5. Microscope and near-field images of the output beam of the passive LPFs with d/Λ ~ 0.195 (a, b) and d/Λ ~ 0.322 (c, d) obtained from a two-step drawing process.

Numerical Simulation of LPF

To investigate the guiding properties of our optical fiber, the finite element method based on COMSOL Multiphysics software 5.0 is performed to simulate the proposed LPF2 with d/Λ ~ 0.322. The structural parameters of LPF2 utilized in the simulations are shown in Table 1.

Table 1. The Simulation parameters of the LPF with 2 air rings conducted using the FEM in COMSOL Multiphysics.

Parameters	Value
Air Hole diameter	8.2 µm
Pitch distance	25.4 µm
Normalized hole diameter	0.322
The Refractive index of air	1.0
The refractive index of the cladding	1.4481 (@ 1200 nm)
Number of air rings	2

Modeling the LPF can be more challenging than typical single-mode fibers due to the variation in the estimation of the effective refractive index of the fundamental mode that depends on the LPF parameters and operational wavelength [20]. When the air hole diameter to pitch distance ratio (d/Λ) is around 0.3 and the operational wavelength (λ) is between 0.8 µm and 1.6 µm, the effective refractive index of the fundamental mode must be searched around 1.447 and 1.449. Figure 6 shows the design of the LPF with d/Λ ~ 0.322 and the fundamental mode electric field distribution where the mode field diameter can reach up to 72 µm. On the other hand, the loss due to waveguide geometry in the LPF is calculated using the confinement loss, which is determined using the equation [16, 22]:

$$L_c = -20 \log_{10} \varepsilon^{-kIm[n_{eff}]} = 8.686 k Im[n_{eff}] \qquad (1)$$

Where $\varepsilon^{-kIm[n_{eff}]}$ *the term* suggests an exponential decay, k is the propagation constant in free space that equals to $2\pi/\lambda$ and Im(neff) is the imaginary part of the refractive index
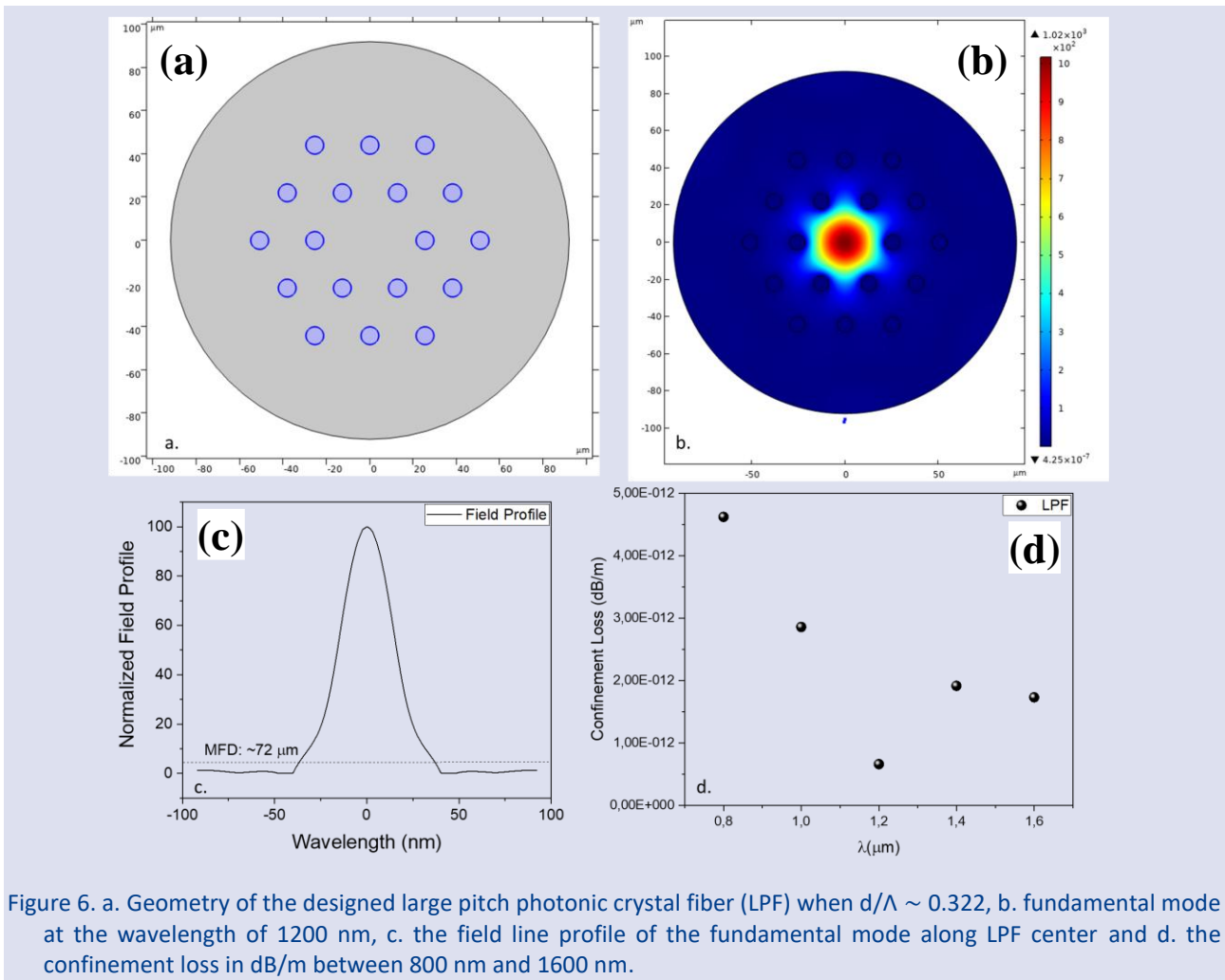
Figure 6. a. Geometry of the designed large pitch photonic crystal fiber (LPF) when d/Λ ~ 0.322, b. fundamental mode at the wavelength of 1200 nm, c. the field line profile of the fundamental mode along LPF center and d. the confinement loss in dB/m between 800 nm and 1600 nm.

The lowest confinement loss of the LPF with d/Λ ~ 0.322 is at the wavelength of 1.2 μm with a loss value of 6.5934×10^{-13} dB/m. This value is consistent with the previous LPF studies where the confinement loss was reported [23]. Such low-loss design of the LPF gives valuable insights, and the numerical simulation demonstrates that the light propagation behaviors of our fiber produced from LPF2 preform agree well with the experiment results.

Conclusions

Two different fabrication processes for the single transverse mode passive LPFs were described. In the first approach, the preform design of LPF with one type of inner glass tube, 2 different filler rods, and a core rod placed in an outer tube was produced by using the draw-and-stack technique. The passive LPF was obtained from a single-step preform drawing process. The single transverse mode propagation from this LPF, which has a core size of 45.5 μm and a normalized hole diameter of 0.454, is observed. The missing filler rods between the inner tubes and direct size reduction from the preform with a mm diameter down to fiber with a diameter of around ~ 200 μm results in the hole shape deformation from the circular hole shape of the initial inner tubes to the elliptical-like hole-shape in the LPF. In the second

approach, the areas between the inner tubes and the core were filled by using the additional filler rods, and a two-step drawing process was performed. This second approach allowed for the control conditions of the fiber structure. The LPF with the circular hole shape was successfully produced. The single transverse mode propagation from this LPF, which has a core size of 42.8 μm and a normalized hole diameter of 0.322, is also demonstrated. In other words, the one-step drawing condition and the two-step conditions do not give the same quality fibers since the latter, where two-step drawing conditions are applied, provides more control in the size and the shape of the air holes. Therefore, the second method yields the PCF satisfying the single-mode criteria. The fundamental mode propagation into the core region was also numerically confirmed for an LPF having a normalized hole-diameter (d/Λ) value around 0.322. These results also reinforced our understanding of how such structural parameters influence mode behavior within the LPF. This development aligns with our findings, as it also resulted in more freedom to control the fiber structure, enhancing the potential applications significantly. Future studies can focus on the fabrication of such fiber structures with double-clad active fiber concepts for further fiber lasers and amplifier systems.

References

[1] Jauregui, C., Limpert, J., Tünnermann, A., High-power fibre lasers, *Nature Photonics.* 7 (2013) 861-867.

[2] Zervas, M., Codemard, C., High Power Fiber Lasers: A Review, *IEEE J. SEL. TOP. QUANT.* 20 (2014) 1-23.

[3] Zuo, J., Lin, X., High-Power Laser Systems, *Laser Photonics Rev.* 16 (5) (2022) 826-831.

[4] Chen, X., Yao, T., Huang, L., An, Y., Hanshuo, W., Pan, Z., Zhou, P., Functional Fibers and Functional Fiber-Based Components for High-Power Lasers, *Advanced Fiber Materials*, 5 (2023) 59-106.

[5] Taverner, D., Richardson, D. J., Dong, L., Caplen, J., 158 μJ pulses from a single-transverse-mode, large-mode-area erbium-doped fiber amplifier, *Optics Letters*, 22 (6) (1997) 378-380.

[6] Broderick, N., Offerhaus, H., Richardson, D. J., Sammut, R. A., Caplen, J., Dong, L., Large Mode Area Fibers for High Power Application, *Optical Fiber Technology*, 5 (1999) 185-196.

[7] Jauregui, C., Stihler, C., Limpert, J., Transverse mode instability, *Advances in Optics and Photonics*, 12 (2020) 429-484.

[8] Xiuquan, M., Cheng Z., I-Ning H., Alex K., Almantas G., Single-mode chirally-coupled-core fibers with larger than 50 μm diameter cores, *Optics Express*, 22 (2014) 9206-9219.

[9] Marko L., Mette M. J., Kristian R. H., Thomas T. A., Jes B., Jesper L., Distributed mode filtering rod fiber amplifier delivering 292W with improved mode stability, *Optics Express*, 20 (2012) 5742-5753.

[10] Liang D., Hugh A. M., Libin F., Michiharu O., Andrius M., Shigeru S., Martin E. F., Ytterbium-doped all glass leakage channel fibers with highly fluorine-doped silica pump cladding, Optics Express, 17 (2009) 8962-8969.

[11] Wang, X., Lou, S., Lu, W., Sheng, X., Zhao, T., Hua, P., Bend resistant large mode area fiber with multi-trench in the core, IEEE J. SEL. TOP. QUANT. 22 (2016).

[12] Gu, G., Kong, F., Hawkins, T. W., Jones, M., Dong, L., Ytterbium-doped all glass leakage channel fibers with highly fluorine-doped silica pump cladding, *Optics Express*, 23 (2015) 9147-9156.

[13] Yehouessi, J. P., Vanvincq, O., Cassez, A., Douay, M., Quiquempois, Y., Bouwmans, G., Bigot, L., Extreme large mode area in single-mode pixelated Bragg fiber, *Optics Express*, 24 (2016) 4761-4770.

[14] Limpert, J., Stutzki, F., Jansen, F., Otto, H.-J. Eidam, T. Jauregui, C., Tünnermann, A., Yb-doped large-pitch fibres: Effective single-mode operation based on higher-order mode delocalisation, *Light: Science & Applications,* 1 (2012) e8.

[15] Stutzki, F., Jansen, F., Otto H.-J., Jauregui, C., Limpert, J., Tünnermann, A., Designing advanced very-large-mode-area fibers for power scaling of fiber-laser systems, *Optica*, 1 (2014) 233-242.

[16] Steinkopff, A., Jauregui, C., Stutzki, F., Nold, J., Hupel, C., Haarlammert, N., Bierlich, J., Tünnermann, A., Limpert, J., Transverse single-mode operation in a passive large pitch fiber with more than 200 μm mode-field diameter, *Optics Letters*, 44 (2019) 650-653.

[17] Stutzki, F., Jansen, F., Eidam, T., Steinmetz, A., Jauregui, C., Limpert, J., Tünnermann, A., High average power large-pitch fiber amplifier with robust single-mode operation, *Optics Letters*, 36 (2011) 689-691.

[18] Martin, B., Florian, J., Fabian S., Cesar J., Ortaç, B., Limpert, J., Tünnermann, A., High average and peak power femtosecond large-pitch photonic-crystal-fiber laser," *Optics Letters*, 36 (2011) 244-246.

[19] Stark, H., Buldt, J., Mueller, M., Klenke, A., Tünnermann, A., Limpert, J., 23 mJ high-power fiber CPA system using electro-optically controlled divided-pulse amplification, *Optics Letters*, 44 (2019) 5529-5532.

[20] Mortensen, N.A., Folkenberg, J.R., Nielsen, M.D., Hansen, K.P., Modal cutoff and the V parameter in photonic crystal fibers, *Optics Letters,* 28 (2003), 1879-1881.

[21] Suslov, D., Komanec, M., Nemecek, T., Bohata, J., Zvanovec, S., Exact modeling of photonic crystal fibers for determination of fundamental properties, *Optical Fiber Technology*, 56. (2020) 102177.

[22] Träger, F., Handbook of Lasers and Optics. Springer, (2012).

[23] Pandey, S., Prajapati, Y., Maurya, J., Design of simple circular photonic crystal fiber having high negative dispersion and ultra-low confinement loss, *Results in Optics*, 1 (2020).

Cumhuriyet Science Journal

Point Estimation for the Inverse Rayleigh Distribution under Type-II Left and Right Censoring

Sümeyra Sert [1,a,*], Coşkun Kuş [1,b]

[1] Department of Statistics, Selcuk University, Konya, Türkiye
*Corresponding author

Research Article

ABSTRACT

The Inverse Rayleigh distribution is frequently utilized in reliability and survival analysis. This study focuses on deriving modified maximum likelihood estimators for the scale parameter of the Inverse Rayleigh distribution under Type-II left and right censoring. The efficacy of the proposed estimators is assessed through comparison with Anderson-Darling, Kolmogorov-Smirnov, and Cramér-von Mises type estimators via Monte Carlo simulations across various censoring schemes and parameter configurations. Additionally, a numerical example is presented to illustrate the proposed methodology. The simulation study demonstrates that the proposed estimators outperform the others. Additionally, given their explicit nature, the proposed estimators can serve as initial values for obtaining the maximum likelihood estimator.

Keywords: Anderson-Darling statistic, Cramér-von mises, Left and right censoring, Kolmogorov-Smirnov statistics, Modified maximum likelihood estimation.

a sumeyra.sert@selcuk.edu.tr   https://orcid.org/0000-0002-4647-1583   b coskun@selcuk.edu.tr   https://orcid.org/0000-0002-7176-0176

Introduction

The Rayleigh distribution has long been a cornerstone in statistical modeling due to its simplicity and broad applicability in diverse fields such as physics, engineering, and environmental studies as a special case of the Weibull distribution. Thanks to its versatility, the Rayleigh distribution has found applications ranging from reliability analysis to quality control. Recent studies, such as [1]-[3], highlight its continued relevance in addressing real-world problems.

The inverse Rayleigh (IR) distribution, derived from the Rayleigh distribution, extends this utility by providing a flexible model for reliability and survival analysis. Specifically, the IR distribution emerges when the reciprocal of a Rayleigh-distributed random variable is considered. If X follows a Rayleigh distribution, then $Y = \frac{1}{X}$ follows an IR distribution. Its probability density function (pdf) and cumulative distribution function (cdf) are given, respectively, by

$$f(x;\theta) = \frac{2\theta^2}{x^3} exp\left\{-\frac{\theta^2}{x^2}\right\}, x > 0, \theta > 0 \qquad (1)$$

$$F(x;\theta) = exp\left\{-\frac{\theta^2}{x^2}\right\}, \qquad (2)$$

where θ is a scale parameter.

The IR distribution has been studied in various contexts. Some recent studies are given as follows: [4] focused on a group acceptance sampling plan for truncated life tests. [5] discussed the estimation problem, both from a Bayesian and non-Bayesian perspective based

on lower record values. [6] studied the characteristics of shrinkage test-estimators considering an asymmetric loss function. [7] explored the Bayesian estimation of parameter and the reliability function of the IR distribution. [8] examined the estimation of parameters for the IR distribution based on Type-I hybrid censored samples. [9] developed a moving average control chart for monitoring failures under a time-truncated test when item lifetimes follow Rayleigh and IR distributions, evaluating its performance using average run lengths (ARL). [10] introduced E-Bayesian and Hierarchical Bayesian estimation methods for estimating the scale parameter and reversed hazard rate of the IR distribution. [11] derived Bayes estimators for the parameter of an IR distribution under symmetric and asymmetric loss functions. Recently, [12] discussed the estimation of process capability index when the underlying distribution follows IR distribution.

Type-II censored samples are frequently encountered in various applications, such as life testing. In this type of censoring, only the smallest or largest observations are not observed. The censoring mechanism involves testing n items until the first non-event or failure time is observed, leading to the termination of the experiment. Statistical inferences based on Type-II censored samples have been addressed in many studies, for example, they can be found in [13-18] and the referenced cited therein. For detailed insights into Type-II censored samples, we refer to the works of [19] and [20].

The motivation for this study arises from the significant gap in the literature regarding the IR distribution under Type II left and right censoring. Existing methods for obtaining maximum likelihood (ML) estimates often rely on search algorithms such as Nelder-Mead or BFGS, which are sensitive to initial values and computationally demanding. To address this issue, we aim to develop a more efficient and robust method that eliminates dependence on initial values, simplifying the estimation process while maintaining accuracy. In this regard, this study discusses point estimation for the IR distribution parameter under Type-II left and right censoring. ML, modified maximum likelihood (MML), least squares (LS), Anderson-Darling type (AD), and Cramér-von Mises type (CvM) estimation methods are proposed in Section 2. The performance of the proposed estimators is compared through a simulation study in Section 3. In Section 4, a numerical example is also proposed for illustrative purposes. Section 5 closes the paper with concluding remarks.

Point Estimation Under Type-II Left and Right Censoring

In this section, we present some explicit estimators by modifing ML estimator under Type-II left and right censoring. We compare the proposed estimators with the ML, AD, CvM, and LS estimation methods based on simulated samples. The AD, CvM, and LS methods are adapted for Type-II censored sample. It is noted that [21-25] used these estimators based on complete sample.

Let $X_{(1)}, X_{(2)}, \ldots, X_{(n)}$ represent the ordered statistics from $IR(\theta)$ distribution. Then, the likelihood function based on Type-II censored data with a censoring of r_1 observations on the left and r_2 observations on the right can be expressed in general form as follows:

$$L(\theta|\mathbf{x}) \propto \left(\prod_{i=r_1+1}^{n-r_2} f\left(x_{(i)};\theta\right) \right) \left(F\left(x_{(a)}\right) \right)^{r_1} \left(1 - F\left(x_{(b)}\right) \right)^{r_2}.$$

Hence, the log-likelihood function is given by

$$\ell(\theta|\mathbf{x}) \propto 2(n - r_1 - r_2) \log(\theta) \\ - \theta^2 \sum_{i=r_1+1}^{n-r_2} \frac{1}{x_{(i)}^2} - \frac{r_1 \theta^2}{x_{(a)}^2} \quad (3) \\ + r_2 \log\left(1 - exp\left\{ -\frac{\theta^2}{x_{(b)}^2} \right\} \right),$$

where $a = r_1 + 1$ and $b = n - r_2$. Then associated gradient found to be

$$\frac{d\ell(\theta|\mathbf{x})}{d\theta} = \frac{2(n - r_1 - r_2)}{\theta} - 2\theta \sum_{i=r_1+1}^{n-r_2} \frac{1}{x_{(i)}^2} \\ - \frac{2r_1 \theta}{x_{(a)}^2} \\ + \frac{2r_2 \theta \, exp\left\{ -\frac{\theta^2}{x_{(b)}^2} \right\}}{x_{(b)}^2 \left(1 - exp\left\{ -\frac{\theta^2}{x_{(b)}^2} \right\} \right)}. \quad (4)$$

The observed information matrix can be obtained by differentiating (4) with respect to the parameter θ and negating the resulting expressions. Hence the observed information matrix is obtained as

$$-\frac{d^2 \ell(\theta|\mathbf{x})}{d\theta^2} = -\frac{2(n - r_1 - r_2)}{\theta^2} - 2\sum_{i=a}^{b} \frac{1}{x_{(i)}^2} - \frac{2r_1}{x_{(a)}^2} \\ - \frac{2r_2 \exp\left\{ -\frac{\theta^2}{x_{(b)}^2} \right\} \left(-x_{(b)}^2 + x_{(b)}^2 \exp\left\{ -\frac{\theta^2}{x_{(b)}^2} \right\} + 2\theta^2 \right)}{x_{(b)}^4 \left(-1 + \exp\left\{ -\frac{\theta^2}{x_{(b)}^2} \right\} \right)^2}.$$

Then, the ML estimator of parameter θ can be defined as

$$\hat{\theta}_1 = \arg\max \ell(\theta|\mathbf{x}).$$

$\hat{\theta}_1$ can be also obtained by the solution of likelihood equation $d\ell(\theta|\mathbf{x})/d\theta = 0$, however it easily be seen that there is no explicit solution for θ. Therefore, numerical methods such as Newton-Raphson or Brent can be used to achieve the solution. Fixed-point iteration, a widely recognized numerical method, can be easily implemented as an alternative. Here, we give a fixed-point iteration for the solution of the likelihood equation. Utilizing the likelihood equation, the fixed-point iterations can be obtained as

$$\theta^{(h+1)} = \frac{G\left(\theta^{(h)}\right) x_{(a)}}{4\left(\sum_{i=a}^{b} \frac{x_{(a)}^2}{x_{(i)}^2} + r_1 \right)} \\ + 4x_{(a)} \left\{ x_{(a)}^2 \left((n - r_2) \sum_{i=a}^{b} \frac{1}{x_{(i)}^2} + \frac{G(\theta^{(h)})}{16} \right) - r_1^2 - \left(\sum_{i=a}^{b} \frac{x_{(a)}^2}{x_{(i)}^2} - n + r_2 \right) r_1 \right\}^{1/2}, \quad (5)$$

where

$$G\left(\theta^{(h)}\right) = \frac{2r_2 \theta^{(h)} \exp\left\{ -\left(\frac{\theta^{(h)}}{x_{(b)}} \right)^2 \right\}}{x_{(b)}^2 \left(1 - \exp\left\{ -\left(\frac{\theta^{(h)}}{x_{(b)}} \right)^2 \right\} \right)}.$$

It is noted that the search methods may suffer from the initial values. It is desired to explicit estimators which do not need an initial value. They can also be used as initial

values for searching algorithms. Let us start to construct the MML estimators. Consider the transformation $Z_{(b)} = X_{(b)}/\theta$. It is clear that $Z_{(b)}$ is the bth order statistic from the IR(1) distribution which is independent of parameter θ. Then, the likelihood equation can be re-written as

$$
\frac{2(n - r_1 - r_2)}{\theta} - 2\theta \sum_{i=r_1+1}^{n-r_2} \frac{1}{x_{(i)}^2} - \frac{2r_1\theta}{x_{(a)}^2} \\
+ \frac{r_2}{\theta} z_b g(z_b) = 0,
\tag{6}
$$

$$
g(z) = \frac{f(z;1)}{1 - F(z;1)} = \frac{2\,exp\left(-\frac{1}{z^2}\right)}{z^3 \left\{1 - exp\left(-\frac{1}{z^2}\right)\right\}}.
\tag{7}
$$

Eq. (6) does not also admit an explicit solution for θ due to the complex nature of $g(z)$. [13] utilized hyperbolic approximation as a method to approach $z_b g(z_b)$, and we intend to employ the same technique initially in addressing our own problem. Hence, we use an equation hyperbola in the first quadrant

$$
zg(z) = K_1,
$$

where the value of K_1 can be obtained by using any two points h_1 and h_2 on the curve that is very close to each other, and denoted by K_1. Then, as $h \to \infty$, h_1 and h_2 tend to a common value of h. Therefore,

$$
-\frac{g(h_2) - g(h_1)}{h_2 - h_1} = \frac{K_1}{h_1 h_2},
\tag{8}
$$

and h is given by

$$
h = \frac{1}{\sqrt{log\left(\frac{n+1}{b}\right)}}
$$

which is solution of the equation $F(h;1) = \frac{n-r_2}{n}$. Then (8) is reduced to

$$
K_1 = -h^2 \left[\frac{d}{dz} g(z)\right]_{z=h} \\
= \frac{2\,exp\left(-\frac{1}{h^2}\right)\left\{3h^2 - 3h^2\,exp\left(-\frac{1}{h^2}\right) + 2\right\}}{h^4 \left\{\left(1 - exp\left(-\frac{1}{h^2}\right)\right)\right\}^2}.
\tag{9}
$$

Substituting (9) into (6), we have the modified likelihood equation

$$
\frac{d\ell(\theta|x)}{d\theta} = \frac{2(n - r_1 - r_2)}{\theta} \\
- 2\theta \sum_{i=r_1+1}^{n-r_2} \frac{1}{x_{(i)}^2} - \frac{2r_1\theta}{x_{(a)}^2} \\
+ \frac{r_2}{\theta} K_1 = 0,
\tag{10}
$$

and the solution to this equation with respect to θ gives the MML, which is given by

$$
\hat{\theta}_2 = x_{(a)} \left(\frac{2(n - r_1 - r_2) + r_2 K_1}{2\left(x_{(a)}^2 \sum_{i=r_1+1}^{n-r_2} \frac{1}{x_{(i)}^2} + r_1\right)}\right)^{\frac{1}{2}}.
\tag{11}
$$

Now, we propose an alternative method for approximate to $z_b g(z_b)$. Traditionally, $E(Z_b)$ can be treated as Z_b, which can be easily approximated by

$$
\hat{z}_b \approx \frac{1}{\sqrt{log\left(\frac{n+1}{b}\right)}},
\tag{12}
$$

where, (12) arises from the facts

$$
Z_b \stackrel{d}{=} F^{-1}(U_{(b)};1)
$$

and

$$
E(Z_b) \approx F^{-1}\left(\frac{b}{n+1};1\right),
$$

where $U_{(b)}$ is the bth order statistic from standard uniform random variable. Then, the second MML is obtained as

$$
\hat{\theta}_3 = x_{(a)} \left(\frac{2(n - r_1 - r_2) + r_2 K_2}{2\left(x_{(a)}^2 \sum_{i=r_1+1}^{n-r_2} \frac{1}{x_{(i)}^2} + r_1\right)}\right)^{\frac{1}{2}},
\tag{13}
$$

where

$$
K_2 = \hat{z}_b g(\hat{z}_b).
$$

The works of [26] and [27] suggest revising the modified Maximum Likelihood Estimation (MMLE). According to the revising methodology, we replace z_b with $z_b = \frac{x_{(b)}}{\theta}$ and calculate the updated estimate $\hat{\theta}$ using Eq.(13). This process is done until $\hat{\theta}$ converges adequately. It is note worthy that more than a few updates (e.g., 3 or 5) may be necessary to stabilize the estimator.

Remark 1. In our simulation study, we observed that the revised MML is almost identical to the ML. From this, it can be concluded that there is no need to employ search methods dependent on the initial values, such as Nelder-Mead or BFGS, to obtain the ML. That is ML estimate can be obtained by updating the MMLE.

Let us define the following modified objective functions to obtain AD, CvM, and LS type estimates for the parameter θ based on Type-II left and right censoring:

$$
Q_{AD}(\theta) = -n + \frac{1}{n} \sum_{j=r^*+1}^{n-r^*} (2j - 1)\left(\frac{\theta^2}{x_{(j)}^2}\right) \\
+ \left[log\left(1 - exp\left\{-\frac{\theta^2}{x_{(n-j+1)}^2}\right\}\right)\right],
$$

$$Q_{CvM}(\theta) = \frac{1}{12n} + \sum_{j=r_1+1}^{n-r_2} \left(exp\left\{-\frac{\theta^2}{x_{(j)}^2}\right\} - \frac{j-0.5}{n} \right)^2,$$

$$Q_{LS}(\theta) = \sum_{j=r_1+1}^{n-r_2} \left(exp\left\{-\frac{\theta^2}{x_{(j)}^2}\right\} - \frac{j}{n+1} \right)^2,$$

where

$$r^* = \begin{cases} r_2 & , \quad r_1 \le r_2 \\ r_1 & , \quad r_1 > r_2. \end{cases}$$

Then, the AD, CvM, and LS type estimates of θ are given, respectively, by

$$\hat{\theta}_4 = \arg\min_{\theta} Q_{AD}(\theta), \tag{14}$$

$$\hat{\theta}_5 = \arg\min_{\theta} Q_{CvM}(\theta), \tag{15}$$

$$\hat{\theta}_6 = \arg\min_{\theta} Q_{LS}(\theta). \tag{16}$$

In this study, all minimization problems are solved via numerical method Nelder-Mead, which is available in the R function optim.

Simulation Study

In this section, we perform Monte Carlo simulation to assess the performance of the estimators given in Section 2. The performances of the proposed estimators are compared in terms of mean squared error (MSE) and bias criteria.

Table 1. MSE and bias (in parantheses) for the estimates of $\theta = 1$

n	r_1	r_2	$\hat{\theta}_1$	$\hat{\theta}_2$	$\hat{\theta}_3$	$\hat{\theta}_4$	$\hat{\theta}_5$	$\hat{\theta}_6$
30	1	1	0.0095	0.0094	0.0095	0.0104	0.0118	0.0117
			(0.0132)	(0.0121)	(0.0132)	(0.0051)	(0.0090)	(0.0062)
	3	3	0.0102	0.0099	0.0102	0.0112	0.0122	0.0121
			(0.0121)	(0.0047)	(0.0122)	(0.0029)	(0.0056)	(0.0034)
	6	6	0.0115	0.0108	0.0116	0.0127	0.0132	0.0131
			(0.0163)	(-0.0145)	(0.0166)	(0.0073)	(0.0086)	(0.0073)
	1	6	0.0093	0.0088	0.0093	0.0124	0.0117	0.0115
			(0.0141)	(-0.0112)	(0.0143)	(0.0083)	(0.0137)	(0.0092)
	6	1	0.0117	0.0117	0.0117	0.0127	0.0132	0.0132
			(0.0155)	(0.0142)	(0.0156)	(0.0067)	(0.0045)	(0.0050)
60	3	3	0.0047	0.0047	0.0047	0.0053	0.0059	0.0059
			(0.0079)	(0.0061)	(0.0079)	(0.0034)	(0.0052)	(0.0039)
	6	6	0.0048	0.0046	0.0048	0.0054	0.0059	0.0058
			(0.0067)	(0.0001)	(0.0067)	(0.0024)	(0.0038)	(0.0027)
	12	12	0.0056	0.0056	0.0056	0.0062	0.0064	0.0064
			(0.0088)	(-0.0201)	(0.0089)	(0.0045)	(0.0050)	(0.0044)
	3	12	0.0047	0.0047	0.0047	0.0063	0.0059	0.0058
			(0.0067)	(-0.0174)	(0.0068)	(0.0035)	(0.0060)	(0.0038)
	12	3	0.0054	0.0054	0.0054	0.0060	0.0063	0.0063
			(0.0073)	(0.0052)	(0.0073)	(0.0024)	(0.0013)	(0.0015)
100	5	5	0.0027	0.0027	0.0027	0.0031	0.0034	0.0034
			(0.0049)	(0.0033)	(0.0049)	(0.0022)	(0.0032)	(0.0024)
	10	10	0.0029	0.0028	0.0029	0.0033	0.0035	0.0035
			(0.0049)	(-0.0013)	(0.0049)	(0.0022)	(0.0030)	(0.00249)
	20	20	0.0033	0.0036	0.0033	0.0037	0.0038	0.0038
			(0.0056)	(-0.0225)	(0.0057)	(0.0026)	(0.0029)	(0.0025)
	5	20	0.0027	0.0030	0.0027	0.0036	0.0033	0.0033
			(0.0038)	(-0.0196)	(0.0039)	(0.0019)	(0.0034)	(0.0021)
	20	5	0.0032	0.0031	0.0032	0.0036	0.0037	0.0037
			(0.0048)	(0.0029)	(0.0048)	(0.0021)	(0.0013)	(0.0014)
200	10	10	0.0013	0.0013	0.0013	0.0016	0.0017	0.0017
			(0.0019)	(0.0004)	(0.0019)	(0.0008)	(0.0014)	(0.0010)
	20	20	0.0014	0.0014	0.0014	0.0016	0.0017	0.0017
			(0.0018)	(-0.0041)	(0.0019)	(0.0005)	(0.0009)	(0.0005)
	40	40	0.0016	0.0022	0.0016	0.0018	0.0019	0.0019
			(0.0020)	(-0.0255)	(0.0021)	(0.0005)	(0.0006)	(0.0004)
	10	40	0.0013	0.0017	0.0013	0.0018	0.0017	0.0017
			(0.0017)	(-0.0213)	(0.0017)	(0.0002)	(0.0011)	(0.0004)
	40	10	0.0015	0.0015	0.0015	0.0018	0.0019	0.0019
			(0.0025)	(0.0008)	(0.0025)	(0.0011)	(0.0008)	(0.0008)
500	25	25	0.0005	0.0005	0.0005	0.0006	0.0007	0.0007
			(0.0007)	(-0.0007)	(0.0007)	(0.0003)	(0.0006)	(0.0004)
	50	50	0.0006	0.0006	0.0006	0.0006	0.0007	0.0007
			(0.0007)	(-0.0051)	(0.0008)	(0.0000)	(0.0002)	(0.0000)
	100	100	0.0006	0.0013	0.0006	0.0007	0.0007	0.0007
			(0.0007)	(-0.0264)	(0.0008)	(0.0003)	(0.0003)	(0.0003)
	25	100	0.0005	0.0010	0.0005	0.0007	0.0007	0.0007
			(0.0009)	(-0.0218)	(0.0009)	(0.0006)	(0.0009)	(0.0006)
	100	25	0.0006	0.0006	0.0006	0.0007	0.0008	0.0008
			(0.0010)	(-0.0006)	(0.0010)	(0.0004)	(0.0002)	(0.0002)

Since the θ is a scale parameter, $\theta = 1$ is considered in the simulations without loss of generality. Various censoring schemes and sample sizes of $n = 30, 60, 100, 200$, and 500 are included in the simulations. Censoring schemes are selected by considering various combinations of right and left censoring, with the number of observations censored from the right and left sides comprising 5%, 10%, and 20% of the dataset. In the case of $n = 30$, r_1 and r_2 are fixed as 1 for a 5% censorship situation. The average of the bias and MSE of the estimators with 10000 replications are given in Table 1.

According to the results from Table 1, the $\hat{\theta}_1$, $\hat{\theta}_2$, and $\hat{\theta}_3$ exhibit similar performance, and they slightly outperform current methods in terms of both MSE and bias considered in this study. When $r_1 = r_2$, an increase in the number of censored observations results in higher MSE values, aligning with expectations. As anticipated, both n and the count of censored observations contribute to an increase in MSE values. Moreover, when $r_1 > r_2$, the MSE tends to be larger. It is possible to reach the ultimate conclusion that censoring should be at right in Type-II scheme. The most significant result extracted from this simulation study is that the proposed estimators perform equally well as the ML estimator and even better than the others. Therefore, there is no objection to using our proposed explicit estimators instead of the ML estimator, which requires numerical methods.

Real Data Analysis

In this section, the strengths of 1.5 cm glass fibres ([28]) dataset is used for illustration purposes. The Table 2 provides the ML estimate of the parameter θ for the complete dataset, along with various goodness of fit values such as the Akaike Information Criterion (AIC), Corrected Akaike's Information Criterion (CAIC), Bayesian Information Criterion (BIC), Anderson-Darling (A), Kolmogorov-Smirnov (KS), and their corresponding p-values (in parentheses). As the p-values for the goodness-of-fit tests shown in Table 2 exceed 0.05, we cannot reject the hypothesis that the data originates from the IR distribution at a significance level of 0.05.

Table 2. Some results fot the glass fibres data for the complete data

$\hat{\theta}$	$\ell(\hat{\theta})$	AIC	CAIC	BIC	A	KS
0.1574	-31.5405	-61.0810	-60.9210	-59.7852	1.4936 (0.1781)	0.1758 (0.3738)

Let us censoring the complete data with scheme $r_1 = 1$ and $r_2 = 2$. Then, the Type-II left and right censored data is produced by: 0.11, 0.12, 0.12, 0.12, 0.12, 0.13, 0.13, 0.14, 0.15, 0.15, 0.15, 0.16, 0.16, 0.16, 0.17, 0.20, 0.20, 0.20, 0.21, 0.23, 0.26, 0.32, 0.33, 0.33. Using this Type-II left and right censored data, point estimates of θ are given in Table 3.

Table 3. Point estimates for the censored glass fibres data

$\hat{\theta}_1$	$\hat{\theta}_2$	$\hat{\theta}_3$	$\hat{\theta}_4$	$\hat{\theta}_5$	$\hat{\theta}_6$
0.1562	0.1558	0.1565	0.1431	0.1435	0.1430

Fixed-point iteration given in (5) is also considered for the censored data. The convergence of the fixed-point iterations to the ML is illustrated in Figure 1, where the dashed line indicates the ML estimate.
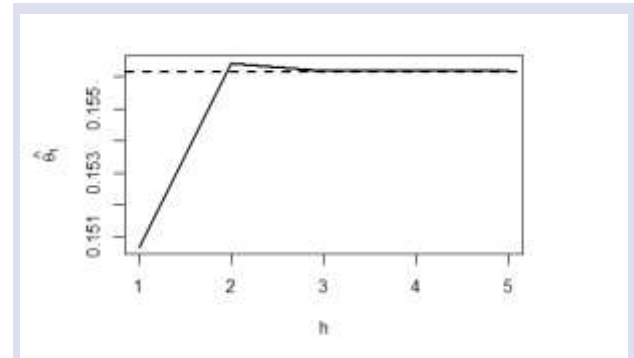

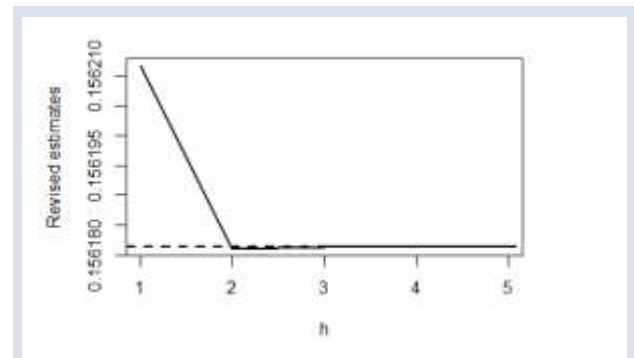Figure 1. The convergence of the fixed-point iterations to the ML

Figure 2. Convergence of the revised estimates of $\hat{\theta}_3$ to the $\hat{\theta}_1$

Figure 2 also demonstrates revising steps for $\hat{\theta}_3$. Based on Figure 2, it can be seen that only a small number of updates are required to reach the ML estimate.

Conclusion

This study is focused on estimating the parameter of the inverse Rayleigh (IR) distribution under Type-II left and right censoring scheme. In this regard, several point estimation methods are introduced, including ML, AD, CvM, and LS. Additionally, two novel MML approaches are proposed, designed to address the challenges of parameter estimation under Type-II left and right censoring. The results of the simulation study demonstrate that the proposed MML estimators consistently outperform the other methods across various scenarios. These estimators are particularly noteworthy for their explicit solutions, which eliminate the need for iterative search methods and simplify the estimation process. This makes the MML estimators promising alternatives for the point estimation of the IR distribution parameter in Type-II left and right censoring contexts. Furthermore, the explicit nature of the proposed MML estimators enhances their computational efficiency and establishes them as excellent initial values for obtaining

the ML estimator. By providing reliable starting points, they help overcome challenges typically associated with iterative methods, such as dependency on initial values and computational complexity. This combination of simplicity and effectiveness underscores the value of the proposed MML estimators as practical tools for parameter estimation in censored data scenarios.

Conflicts of interest

All authors declare that they have no conflict of interest.

References

[1] Adeoti O. A., Rao G. S., Attribute control chart for Rayleigh distribution using repetitive sampling under truncated life test, *Journal of Probability and Statistics*, (1) (2022) 8763091.

[2] Hossain M. P., Omar M. H., Riaz M., Arafat S. Y., On designing a new control chart for Rayleigh distributed processes with an application to monitor glass fiber strength, *Communications in Statistics-Simulation and Computation*, 51(6) (2022) 3168-3184.

[3] Anis M. Z., Okorie I. E., Ahsanullah M., A review of the Rayleigh distribution: properties, estimation & application to COVID-19 data, *Bulletin of the Malaysian Mathematical Sciences Society*, 47(1) (2024) 6.

[4] Aslam M., Jun C. H., A group acceptance sampling plan for truncated life test having Weibull distribution. *Journal of Applied Statistics*, 36(9) (2009) 1021-1027.

[5] Soliman A., Amin E. A., Abd-El Aziz A. A., Estimation and prediction from inverse Rayleigh distribution based on lower record values, *Applied Mathematical Sciences*, 4(62) (2010) 3057-3066.

[6] Prakash G., Shrinkage Estimation in the Inverse Rayleigh Distribution, *Journal of Modern Applied Statistical Methods*, 9 (2010) 209-220.

[7] Dey S., Bayesian estimation of the parameter and reliability function of an inverse Rayleigh distribution, *Malaysian Journal of Mathematical Sciences*, 6(1) (2012) 113-124.

[8] Akdoğan Y., Özkan E., Karakaya K., Tanış C., Estimation Of Parameter For Inverse Rayleigh Distribution Under Type-I Hybrid Censored Samples, *Sigma Journal of Engineering and Natural Sciences*, 38(4) (2020) 1705-1711.

[9] Adeoti O. A., Gadde S. R., Moving average control charts for the Rayleigh and inverse Rayleigh distributions under time truncated life test, *Quality and Reliability Engineering International*, 37(8) (2021) 3552-3567.

[10] Athirakrishnan R. B., Abdul-Sathar E. I., E-Bayesian and hierarchical Bayesian estimation of inverse Rayleigh distribution, *American Journal of Mathematical and Management Sciences*, 41(1) (2022) 70-87.

[11] Kumar R., Gupta R., Bayesian analysis of inverse Rayleigh distribution under non-informative prior for different loss functions, *Thailand Statistician*, 21(1) (2023) 76-92.

[12] Karakaya K., Kınacı İ., Akdoğan Y., Saraçoğlu B., Kuş C., Statistical Inference on Process Capability Index Cpyk for Inverse Rayleigh Distribution under Progressive Censoring, *Pakistan Journal of Statistics and Operation Research*, (2024) 37-47.

[13] Lalitha S., Mishra A., Modified maximum likelihood estimation for Rayleigh distribution, *Communications in Statistics-Theory and Methods*, 25(2) (1996) 389-401.

[14] Wingo D. R., Maximum likelihood estimation of Burr XII distribution parameters under type II censoring, *Microelectronics Reliability*, 33(9) (1993) 1251-1257.

[15] Balakrishnan N., Kundu D., Ng K. T., Kannan N., Point and interval estimation for a simple step-stress model with Type-II censoring, *Journal of Quality Technology*, 39(1) (2007) 35-47.

[16] Jaheen Z. F., Okasha H. M., E-Bayesian estimation for the Burr type XII model based on type-2 censoring, *Applied Mathematical Modelling*, 35(10) (2011) 4730-4737.

[17] Almetwally E. M., Sabry M. A., Alharbi R., Alnagar D., Mubarak S. A., Hafez E. H., Marshall–olkin alpha power Weibull distribution: different methods of estimation based on type-I and type-II censoring, *Complexity*, (2021) 1-18.

[18] Biçer H. D., Öztürker B., Estimation procedures on Type-II censored data from a scaled Muth distribution, *Sigma Journal of Engineering and Natural Sciences*, 39(2) (2021) 148-158.

[19] Schneider H., Weissfeld L. (1986). Inference based on Type II censored samples, *Biometrics*, 531-536.

[20] Balakrishnan N., Aggarwala R., *Progressive censoring: theory, methods, and applications*, Springer Science & Business Media, (2000).

[21] Karakaya K., Tanış C., Different methods of estimation for the one parameter Akash distribution, *Cumhuriyet Science Journal*, 41(4) (2020a) 944-950.

[22] Karakaya K., Tanış C., Estimating the parameters of Xgamma Weibull distribution, *Adıyaman University Journal of Science*, 10(2) (2020b) 557-571.

[23] Tanış C., Karakaya K., On Estimating Parameters of Lindley-Geometric Distribution, *Eskişehir Technical University Journal of Science and Technology A-Applied Sciences and Engineering*, 22(2) (2021) 160-167.

[24] Tanış C., Saraçoğlu B., Kuş C., Pekgör A., Karakaya K., Transmuted lower record type Fréchet distribution with lifetime regression analysis based on type I-censored data, *Journal of Statistical Theory and Applications*, 20(1) (2021) 86-96.

[25] Shen Y., Xu A., On the dependent competing risks using Marshall–Olkin bivariate Weibull model: Parameter estimation with different methods, *Communications in Statistics-Theory and Methods*, 47(22) (2018) 5558-5572.

[26] Lee K. R., Kapadia C. H., Brock D. B., On estimating the scale parameter of the Rayleigh distribution from doubly censored samples, *Statistische Hefte*, 21(1) (1980) 14-29.

[27] Tiku M. L., Akkaya A. D., *Robust estimation and hypothesis testing*, New Age International, (2004).

[28] Elgarhy M., Haq M. A. U., ul Ain Q., Exponentiated generalized Kumaraswamy distribution with applications, *Annals of Data Science*, 5 (2018) 273-292.

AUTHOR GUIDELINES

Thank you for choosing to submit your paper to Cumhuriyet Science Journal. The following instructions will ensure we have everything required so your paper can move through pre-evaluating, peer review, production and publication smoothly. Please take the time to read and follow them as closely as possible, as doing so will ensure your paper matches the journal's requirements.

Submission

Cumhuriyet Science Journal is an international, peer-reviewed, free of charge journal covering the full scope of both natural and engineering sciences. Manuscripts should be submitted by one of the authors of the manuscript as online submission after registration to the Cumhuriyet Sciences Journal. Microsoft Word (.doc, .docx, .rtf), files can be submitted. There is no page limit. If there is a problem while uploading the files of manuscript, please try to reduce their file size, especially manuscripts including embedded figures. Submissions by anyone other than one of the authors will not be accepted. The submitting author takes responsibility for the paper during submission and peer review. If for some technical reason submission through the online submission systme is not possible, the author can contact csj@cumhuriyet.edu.tr for support.

Submission or processing charges

Cumhuriyet Science Journal does not charge any article submission, processing charges, and printing charge from the authors.

Terms of Submission

Papers must be submitted on the understanding that they have not been published elsewhere (except in the form of an abstract or as part of a published lecture, review, or thesis) and are not currently under consideration by another journal. The submitting author is responsible for ensuring that the article's publication has been approved by all the other coauthors. It is also the authors' responsibility to ensure that the articles emanating from a particular institution are submitted with the approval of the necessary institution. Only an acknowledgment from the editorial office officially establishes the date of receipt. Further correspondence and proofs will be sent to the author(s) before publication unless otherwise indicated. It is a condition of submission of a paper that the corresponding author permit editing of the paper for readability. All enquiries concerning the publication of accepted papers should be addressed to csj@cumhuriyet.edu.tr. Please note that Cumhuriyet Science Journal uses iThenticate software to screen papers for unoriginal material. By submitting your paper to Cumhuriyet Science Journal are agreeing to any necessary originality checks your paper may have to undergo during the peer review and production processes. Upon receiving a new manuscript, the Editorial office conducts initial pre-refereeing checks to ensure the article is legible, complete, correctly formatted, original, within the scope of the journal in question, in the style of a scientific article and written in clear English. Any article that has problems with any of the journal criteria may be rejected at this stage.

Peer Review

This journal operates a single blind review process. All contributions will be initially assessed by the editor for suitability for the journal. Papers deemed suitable are then typically sent to a minimum of two independent expert reviewer to assess the scientific quality of the paper. The author is required to upload the revised article to the system within 15 days by making the corrections suggested by the referee. The article will be rejected if there are no fixes in it. The Editor is responsible for the final decision regarding acceptance or rejection of articles. The Editor's decision is final

Title and Authorship Information

The following information should be included

Paper title

Full author names

Full institutional mailing addresses

Corresponding address

Email address

Abstract

The manuscript should contain an abstract. The researchers who are native speakers of Turkish have to add Turkish title and abstract as well. The abstract should be self-contained and citation-free and should be 250-300 words.

Keywords

Keywords of the scientific articles should be selected from the web address of www.bilimadresleri.com

Introduction

This section should be succinct, with no subheadings.

Materials and Methods

This part should contain sufficient detail so that all procedures can be repeated. It can be divided into subsections if required.

Conflicts of interest

Sample sentence if there is no conflict of interest: The authors stated that did not have conflict of interests.

Acknowledgements

Sample sentences for acknowledgements: The work was supported by grants from CUBAP (T-11111). We would like to acknowledge Prof. Mehmet Sözer, MD, for his precious technical and editorial assistance. We would like to thank

References

References to cited literature should be identified by number in the text in square brackets and grouped at the end of the paper in numerical order of appearance. Each reference must be cited in the text. Always give inclusive page numbers for references to journal articles and a page range or chapter number for books. References should be styled and punctuated according to the following examples

[1] Karaca E., Ulusoy S., Morgül Ü., Ulusoy H.I., Development of Analytical Method for Sensitive Determination of Streptozotocin based on Solid Phase Extraction, Cumhuriyet Sci. J., 41 (4) (2020) 826-831. (sample reference for journals)

[2] Keskin B., Ozkan A.S., Inverse Spectral Problems for Dirac Operator with Eigenvalue Dependent Boundary and Jump Conditions, Acta Math. Hungar., 130 (2011) 150-159(sample reference for journals)

[3] Mazur M.T., Kurman R.J., Dysfunctional Uterine Bleeding. In: Mazur M.T., Kurman R.J., (Eds). Diagnosis of endometrial biopsies and curettings, A practical approach. 2nd ed. Berlin: Springer, (2005) 100-120. (sample reference for book chapters)

[4] Mazur M.T., Kurman R.J.,Diagnosis of endometrial biopsies and curettings, A practical approach. 2nd ed. Berlin, (2005) 100-120. (sample reference for book)

[5] National Cancer Institute, Surveillance Epidemiology and End Results. Cancer of the Corpus and Uterus, NOS. Available at: http://seer.cancer.gov/statfacts/html/corp.html?statfacts_page=corp. Retrieved March 2, 2008. (sample reference for websites)

[6] Surname N., Title of thesis, PD or master thesis, Name of university, name of institue, year. (sample reference for thesis)

[7] Surname N., Title of fulltext conference paper, name of conference, city, year, pages. (sample reference for Abstratcs in conferences are not accepted as a valid reference except full text)

Preparation of Figures

Each figure can be integrated in the paper body or separately uploaded and should be cited in a consecutive order. Figure widths can be 4-6 inch as 300 dpi. The labels of the figures should be clear and informative. The name and the subtitles of the figures must be 9-point font.

Preparation of Tables

Tables should be cited consecutively in the text. Every table must have a descriptive title and if numerical measurements are given, the units should be included in the column heading. Tables should be simple with simple borders and text written as left text. The name and the subtitle of the tables must be 9-point font

Proofs

Corrected proofs must be returned to the publisher within 2 weeks of receipt. The publisher will do everything possible to ensure prompt publication. It will therefore be appreciated if the manuscripts and figures conform from the outset to the style of the journal.

Copyright

The use of general descriptive names, trade names, trademarks, and so forth in this publication, even if not specifically identified, does not imply that these names are not protected by the relevant laws and regulations.

While the advice and information in this journal are believed to be true and accurate on the date of its going to press, neither the authors, the editors, nor the publisher can accept any legal responsibility for any errors or omissions that may be made. The publisher makes no warranty, express or implied, with respect to the material contained herein.

Ethical Guidelines

New methods and ethically relevant aspects must be described in detail, bearing in mind the following:

Human Experiments. All work must be conducted in accordance with the Declaration of Helsinki (1964). Papers describing experimental work on human subjects who carry a risk of harm must include:

A statement that the experiment was conducted with the understanding and the consent of the human subject.

A statement that the responsible Ethical Committee has approved the experiments.

Animal Experiments. Papers describing experiments on living animals should provide:

A full description of any anaesthetic and surgical procedure used.

Evidence that all possible steps were taken to avoid animal suffering at each stage of the experiment. Papers describing experiments on isolated tissues must indicate precisely how the donor tissues were obtained.

Submission Preparation Checklist

As part of the submission process, authors are required to check off their submission's compliance with all of the following items, and submissions may be rejected that do not adhere to these guidelines.

The submission has not been previously published, nor is it before another journal for consideration (or an explanation has been provided in Comments to the Editor).

The submission file is in Microsoft Word document file (Times New Roman) format.

Where available, URLs for the references have been provided.

The text is single-spaced; uses a 11-point font; employs italics, rather than underlining (except with URL addresses); and all illustrations, figures, and tables are placed within the text at the appropriate points, rather than at the end.

The text adheres to the stylistic and bibliographic requirements outlined in the Author Guidelines, which is found in About the Journal.

If submitting to a peer-reviewed section of the journal, the instructions in Ensuring a Double-Blind Review have been followed.